Université Paris Cité

Université Paris Cité

École doctorale 561 Hématologie, Oncogenèse, Biothérapies

Laboratoire *Institut de Recherche Saint-Louis (UMR 1342)*

Development of a Microfluidic Tumor-on-Chip Platform for Modeling Host-Tumor Interactions and Predicting Therapeutic Outcomes

Par **Léonard LUGAND**

Thèse de doctorat en Biothérapies et biotechnologies

Dirigée par **Joël LEMAOULT**

Présentée et soutenue publiquement le 10/12/2025

Devant un jury composé de :

Joël LEMAOULT DR-HDR, CEA, Université Paris Cité	Directeur de thèse
Odile FILHOL-COCHET CR-HDR, INSERM, CEA, Université Grenoble Alpes	Rapporteuse
Catherine MONNOT CR-HDR, INSERM, Sorbonne Université	Rapporteuse
Emmanuel DONNADIEU DR-HDR, INSERM, Université Paris Cité	Examinateur
Yves ALLORY PU-PH, Institut Curie, Université de Versailles Saint-Quentin-en-Yvelines (UVSQ)	Examinateur

Titre : Développement d'une tumeur sur puce à des fins de modélisation des interactions hôte-tumeur et de prédiction de réponse aux traitements.

Résumé : Les immunothérapies de nouvelle génération ont profondément transformé la prise en charge oncologique. Les inhibiteurs de points de contrôle immunitaire (ICIs) ciblant l'axe PD-1/PD-L1 et CTLA-4 sont désormais un standard thérapeutique dans la prise en charge de nombreux cancers, y compris le carcinome rénal à cellules claires (ccRCC). Ce cancer présente néanmoins un paradoxe : malgré une infiltration immunitaire dense, seule une fraction des patients présente une réponse durable aux ICI, et aucun biomarqueur prédictif robuste ou cliniquement validé n'est actuellement disponible. Ce paradoxe fait du ccRCC un modèle particulièrement pertinent pour l'étude des mécanismes de résistance à l'immunothérapie. Pour prédire les réponses thérapeutiques, explorer les mécanismes de résistance et évaluer de nouvelles stratégies immunothérapeutiques, des modèles expérimentaux capables de reproduire fidèlement l'écosystème tumoral et immunitaire spécifique à chaque patient sont nécessaires. Or, les modèles précliniques conventionnels ne répondent que partiellement à ce besoin. Les cultures cellulaires classiques, bien que simples et reproductibles, ne tiennent pas compte de la complexité microenvironnementale et de l'hétérogénéité de la niche tumorale. Les modèles animaux, xénogreffes et modèles humanisés compris, permettent d'étudier des dynamiques dans un organisme complet mais sont cependant limités dans leurs applications translationnelles par les questionnements éthiques, leur coût, les différences inter-espèces et l'impossibilité de standardiser les conditions expérimentales dans des délais compatibles avec la pratique clinique. Ainsi, le développement de modèles humains ex vivo alliant pertinence physiologique, reproductibilité et rapidité d'expérimentation demeure nécessaire. Dans ce contexte, cette thèse vise à développer une plateforme ex vivo destinée à modéliser la réponse immunitaire de patients atteints de ccRCC à partir de sphéroïdes tumoraux. Dans un premier temps, des protocoles optimisés ont été mis au point pour générer des sphéroïdes reproductibles issus de lignées cellulaires de ccRCC et d'échantillons tumoraux de patients. Ces sphéroïdes dérivés de tumeurs humaines ont ensuite été réinfiltrés par leurs cellules immunitaires intratumorales. L'analyse transcriptomique a montré que ces sphéroïdes conservaient les principales composantes épithéliales, stromales et immunitaires de la tumeur d'origine. Par ailleurs le modèle montrait, une concordance des signatures géniques associées à la réponse aux ICIs avec la tumeur d'origine. Ce modèle a ensuite été intégré à une plateforme microfluidique conçue sur mesure, assurant la perfusion continue de cellules immunitaires et le contrôle précis de l'écoulement du milieu de culture. Dans ce dispositif, des cellules immunitaires circulantes ont pu infiltrer les sphéroïdes et induire une production mesurable de cytokines, amplifiée en condition de blocage de PD-L1, définissant ainsi un marqueur fonctionnel d'activation immunitaire. A titre de preuve de concept, la même approche a été appliquée à des sphéroïdes dérivés de tumeurs de patients, dans une configuration autologue où des sphéroïdes réinfiltrés ont été exposés à des cellules sanguines du même donneur. La plateforme a été optimisée pour obtenir des lectures fonctionnelles en moins d'une semaine, depuis la préparation de l'échantillon tumoral jusqu'au résultat de l'analyse sur puce, illustrant son potentiel comme base pour le développement de systèmes ex vivo prédictifs de la réponse immunothérapeutique individuelle. Ainsi, ces travaux définissent une démarche translationnelle intégrée, reliant directement l'échantillon tumoral du patient à son évaluation fonctionnelle ex vivo, et ouvrent la voie au développement d'outils prédictifs individualisés en immuno-oncologie, ainsi qu'à l'étude de nouvelles stratégies immunothérapeutiques.

Mots clés : carcinome rénal à cellules claires, immunothérapie, tumeur sur puce, sphéroïdes, organoïdes, microenvironnement tumoral, microfluidique, modèle ex vivo, réponse immunitaire

Title: Development of a Microfluidic Tumor-on-Chip Platform for Modeling Host-Tumor Interactions and Predicting Therapeutic Outcomes.

Abstract: Immunotherapy has profoundly transformed cancer treatment, marking a true paradigm shift in oncology. Immune checkpoint inhibitors (ICIs) targeting the PD-1/PD-L1 axis have become standard-of-care in multiple malignancies, including clear cell renal cell carcinoma (ccRCC). Yet, ccRCC presents a paradox: despite dense immune infiltration, durable clinical responses to ICIs are achieved only in a subset of patients, and no robust or clinically validated biomarkers currently exist. This paradox makes ccRCC a particularly relevant model for investigating mechanisms of resistance to immunotherapy. To predict therapeutic responses, investigate mechanisms of resistance and evaluate novel immunotherapeutic strategies, robust experimental systems that faithfully reproduce the patient-specific tumor-immune ecosystem are required. Conventional preclinical models only partially address this need. Indeed, two-dimensional cell line cultures, while cost-effective and reproducible, fail to integrate the microenvironmental complexity and immune heterogeneity that shape therapeutic response. In vivo animal models, including xenografts and humanized systems, offer a more integrated context but remain limited by ethical constraints, cost, inter-species biological differences, and the inability to achieve standardization or clinically compatible timelines. These limitations underscore the need for ex vivo human models that combine physiological relevance, reproducibility, and rapid experimental turnaround. In this context, this thesis aimed to develop an integrated and standardized ex vivo platform for modeling immune responses in ccRCC using three-dimensional tumor spheroids as a functional core. In a first step, optimized methods were established for generating reproducible spheroids from ccRCC cell lines and from freshly dissociated patient tumors. Building on this method, patient-derived spheroids were next re-infiltrated with autologous tumor-infiltrating immune cells. Transcriptomic profiling confirmed that patient-derived tumor organoids retained the main epithelial, stromal, and immune compartments of their parental tumors and the overall immune composition was preserved. Moreover, predictive gene expression scores associated with response to immune checkpoint inhibitors were comparable between infiltrated spheroids and original tumor tissue fragments. To extend this approach towards dynamic immune interactions, the spheroid model was integrated into a custom microfluidic platform enabling continuous immune perfusion and culture medium flow. Using this setup, circulating immune cells were shown to infiltrate spheroids and induce measurable cytokine release, which further increased upon PD-L1 blockade, establishing a functional readout of immune activation. The workflow was applied to patient-derived spheroids in an autologous proof-of-concept configuration with PD-L1 blockade, in which re-infiltrated spheroids were exposed to peripheral blood mononuclear cells from the same donor. The platform is optimized to deliver functional readouts within a week, from patient sampling to on-chip testing results, illustrating its potential as a promising framework for future patient-specific assessment of immunotherapy efficacy. Together, these results establish a rapid translational workflow, from tumor sampling to on-chip functional testing, providing a physiologically relevant platform to explore immune responsiveness and mechanisms of resistance in ccRCC. Beyond its potential as a personalized medicine approach, this proof-of-concept system may also serve as an experimental basis for the evaluation of emerging immunotherapeutic strategies.

Keywords: clear cell renal cell carcinoma, immunotherapy, tumor-on-chip, spheroids, organoids, tumor microenvironment, microfluidics, ex vivo model, immune response

Acknowledgements / Remerciements

Aux membres du jury

A qui je suis honoré d'avoir confié l'évaluation de cette thèse et qui ont pris de leur temps pour remplir cette tâche. Je remercie le ***Dr Emmanuel Donnadieu*** et le ***Pr Yves Allory*** d'avoir accepté d'être examinateurs de ce travail et d'apporter leurs expertises scientifiques et médicales respectives.

A la Dre Catherine Monnot

Pour son travail de rapporteuse exhaustif et pertinent malgré les contraintes temporelles.

A la Dre Odile Filhol-Cochet

Pour son travail de rapporteuse mais aussi pour le suivi tout au long de ma thèse, pour ses conseils toujours précieux et ses paroles qui m'ont trouvé dans des moments de doute.

A Joël

Pour avoir encadré mes travaux au laboratoire depuis mon premier stage il y a 6 ans. Pour l'accompagnement jamais invasif et toujours arrangeant dont j'ai pu bénéficier en étant ton étudiant. Pour ta disponibilité, ton humanité, les discussions et toute l'aide que tu m'as apportée au cours de mon parcours.

Aux personnes qui ont participé à mes projets et qui ont rendu cette thèse possible

A Joris

Pour avoir rendu la microfluidique accessible en un temps record, pour l'accueil jovial et le travail toujours bien fait.

A Liangwei

Pour son travail acharné et volontaire et ses idées qui ont permis de mener le travail de transcriptomique à bien.

A Christophe

Pour avoir tenu en vie le projet transcriptomique, pour la clarté de sa vision et pour les réunions productives.

Aux membres de la plateforme de l'IRSL

Claire, Christelle et tout particulièrement Niclas qui se sont toujours rendu disponibles pour expliquer, aider, permettre, faciliter ou simplement discuter. Merci d'avoir rendu tous ces readouts possibles et de donne accès à une plateforme de qualité à quasi toute heure.

A Jules et Florent Malloghi

Même si ce projet n'a pas abouti, je garde en tête la volonté du premier meeting et des premiers prototypes.

Au personnel de l'école doctorale

A Maxime DaCunha

Pour l'aide réactive et patiente qu'il témoigne aux étudiants, et pour les tournures de phrase dont lui seul a le secret.

Au Pr Raphaël Itzykson

Pour sa volonté de protéger et accompagner les étudiants à travers l'école doctorale qui transparaît dans son fonctionnement.

Aux membres du SRHI

A Nathalie

Pour ton regard toujours bienveillant et tes paroles encourageantes qui font du SRHI un écosystème sain, exempt de verticalité et de rapports de force.

A Philippe

Pour les rires, les éclats de voix et les moments de vie partagés, à ta retraite.

A Bela

Pour ta présence nocturne toujours rassurante.

Au Pr François Desgrandchamps

Pour sa volonté constante de lier la recherche aux applications, pour son regard bienveillant et enthousiaste ainsi pour son aide plus que précieuse lors de ma passerelle vers la médecine.

A la Pr Alexandra Masson Lecomte

Pour sa volonté d'animer et de motiver la recherche et son engagement pour les étudiants dans la vie universitaire.

A Malika

Tant pour ton travail précieux que pour les matinées passées à parler dans ton bureau en consultant le planning du bloc. Pour les conversations et les rires. Et pour avoir stratégiquement participé à ma rencontre avec Dora.

A la Dre Fatiha Bouhidel

Pour avoir rendu possible l'obtention des échantillons si précieux pour cette thèse. Merci d'avoir toujours ouvert la porte du laboratoire d'anapath même à des horaires improbables, d'avoir toujours été à l'écoute des projets de recherche et d'avoir prêté une oreille attentive à mon évolution, mes moments de surcharge ou plus léger.

Au Dr Clément Dumont

Pour les discussions scientifiques toujours pertinentes que ce soit sur la clinique ou le fondamental, pour tes idées spontanément claires et précises, à la suite de ta carrière universitaire où je te souhaite toute la réussite.

Aux autres cliniciens du laboratoire

Pr Christophe Hennequin, Dr Jérôme Vérine, Pr Stéphane Culine, aux autres membres du service d'Urologie, d'Anatomopathologie et de Cancérologie de l'hôpital Saint-Louis.

Au cœur du laboratoire

Qui a été une famille pour moi depuis mon premier stage lors de ma 2e année d'école d'ingénieur. Aux moments partagés, aux rires, aux coups durs qui sont passés sur chacune de nos routes. Je n'aurais pas imaginé pouvoir être mieux entouré. Nos liens vont bien au-delà du laboratoire et vous avez tous et toutes contribué à transformer ce passage au laboratoire en période de vie, où j'ai appris, grandi et me suis senti à ma place auprès de vous.

A Isabelle

Après maintenant 6 ans à se connaître, je me rappelle encore le premier jour où nos chemins se sont croisés, déjeuner au Street Bangkok, je me souviendrai toujours de ta présence impressionnante mais immédiatement rassurante. Ta manière de tout donner sans compter pour les personnes qui te sont chères. La force avec laquelle tu es capable d'endurer et de soulever des montagnes de problèmes. Merci du fond du cœur pour tous les instants partagés et pour le soutien sans faille que tu m'as apporté.

A Chantal

La charge émotionnelle du laboratoire. Je préfère ne pas imaginer ce qu'auraient été cette thèse et ce laboratoire sans tes réassurances, tes mots de soutien et tes conseils. Pour toi j'ai vu les difficultés et les coups durs s'enchaîner sans jamais que tu ne perdes ton intérêt pour les autres. A ta compréhension naturelle des émotions et ton envie de tout rendre plus léger pour les autres. Pour ta volonté de faire vivre le laboratoire au-delà du travail qui transforme réellement ce lieu en famille.

A Tej

Pour toute l'aide que tu m'as apportée, à ton rire clair lors des repas et des verres et ta gentillesse délicate.

A Jules

Qu'aurait bien pu être cette thèse sans ton arrivée au laboratoire ? Une question à laquelle je n'ai pas vraiment envie d'avoir la réponse. Merci du fond du cœur pour la manière avec laquelle tu as investi ce projet dès ton arrivée, pour l'aide aussi bien technique que scientifique que morale que tu m'as apportée. A nos méthodes de travail complémentaires, ton fonctionnement organisé et toujours tourné vers l'avant. Pour l'amitié et la complicité naturelle rapidement survenue.

Plus que tout à Rebecca

A jamais compagnonne de galère, pour ces quatre années passées en un claquement de doigt. A ton écoute toujours si précieuse, aux cytométries nocturnes, aux goûts musicaux (3.5/10), aux anecdotes sans chutes. Je ne pourrais pas dresser la liste de tout ce que tu m'as apporté, dans la thèse et bien au-delà. A une amitié qui vaut toutes les thèses du monde. Merci d'être toujours présente pour qui a besoin, pour tes vues clairvoyantes, tes conseils et ta manière d'endurer les épreuves avec une force qui m'impressionnera toujours. A ta (très) future thèse qui j'en suis sûr sera mémorable.

A la Dre Joana Gonçalves Araujo

Comment vous séparer même dans mes remerciements tant tout semble une évidence entre vous. Bravo encore pour ta soutenance et pour l'incroyable travail abattu pendant ta thèse malgré les difficultés.

A Louis

Pour ton flegme à toute épreuve, ton engagement sans faille et aux phrases de génie lâchées au détour de la machine à café.

A Noémie

Pour ton investissement, ton humour et ton caractère, je te souhaite toute la réussite dans tes projets futurs.

A Mathieu

A l'année à encadrer ton stage, passée en un instant, à notre amitié, à ton humour naturel à toute épreuve. A la légèreté avec laquelle tu avances sans jamais heurter quiconque, à ton humanité. A la fin de tes études médicales et à ton futur, en médecine comme en dehors.

A Alix

Pour avoir été ma première vision d'une étudiante en thèse, pour m'avoir guidé dans les arcanes du SRHI.

A Guillaume

Pour la douce mais inébranlable volonté de recherche qui t'anime, pour avoir su sublimer les difficultés sur ton parcours et pour l'aide précieuse que tu m'as apportée.

A Amélie

Pour ta sensibilité, pour l'attention que tu portes aux autres, pour tes valeurs et ton énergie

Aux stagiaires de passage au laboratoire

Qui ont tous contribué techniquement ou moralement à cette thèse et qui ont participé à l'ambiance de famille du SRHI. Je vous souhaite le meilleur dans vos carrières scientifiques et médicales et dans vos vies futures. ***A Ronan, Antoine, Pauline, Perla, Anaftali, Riya, Sophie, Séréna, François et les autres.***

A la relève du SRHI

Victor, Jennifer, Astrid, que j'ai moins eu l'occasion de connaitre mais à qui je souhaite le meilleur pour leurs projets au SRHI et pour la suite.

A Marina

Pilier du laboratoire, roc que l'on pensait inébranlable et qui est pourtant partie. Aux souvenirs que tu laisses à toute la famille du SRHI qui était ta maison. A tes enseignements techniques qui ont été mes premiers en biologie cellulaire, à tes farces. Toutes mes pensées à tes proches.

A mes professeur·e·s

Au rendu de ce travail qui pose un jalon particulier de ma vie étudiante, je tenais à remercier tous les membres du corps enseignant qui m'ont permis ou poussé à arriver là où j'en suis, qui m'ont enseigné, souvent avec un intérêt qui dépassait bien au-delà du simple contrat passé avec l'éducation nationale.

Merci aux enseignants et au personnel des écoles, collèges et lycées de Saint-Claude, qui ont pleinement accompagné et conforté mon choix de rester dans ces établissements, et qui m'ont montré combien l'engagement pédagogique et la pluralité sont précieux, même dans un contexte de conditions de travail de plus en plus contraintes.

Je remercie l'ensemble du personnel des classes préparatoires BCPST du lycée du Parc, où j'ai vécu parmi les plus belles années de ma vie, une période ô combien fondatrice au cours de laquelle se sont forgées mes amitiés les plus fortes.

Parmi mes professeurs, je remercie tout particulièrement ***Mme Bronquard***, qui m'a en premier orienté vers ce parcours centré sur la curiosité scientifique, et tout spécialement en biologie. Je remercie également ***Mme Woerhlé, Mme Gardet, Mme Fayemendy, M. Ponton, M. Dutruge, Mme Krajewsky-Bertrand, M. J.-D. Collomb et Mme Couronnes-Geary,*** qui, chacun à leur manière, ont construit et animé l'environnement bienveillant et d'émulation qu'ont été ces deux années de classes préparatoires.

Je remercie également ***Mme Sabine d'Andrea***, qui a su maintenir un parcours de recherche scientifique exigeant au sein d'une école d'ingénieur aussi vaste qu'AgroParisTech.

Plus récemment, et dans mon nouveau cursus, je remercie la ***Dre Elessa-Ngombo***, qui m'a enseigné bien plus que l'examen clinique mais bien l'écoute des patients et la sensibilité médicale. Je remercie également le ***Pr Olivier Lortholary*** pour son accueil et sa volonté d'enseignement et la ***Pr Fanny Lanternier*** pour son attention toute particulière au bien être étudiant, pour son écoute précieuse et son aide pour concilier la fin de cette thèse avec les études médicales.

A ma famille

A mes parents

Qui nous ont toujours placé·e·s mes sœurs et moi au premier plan, privilégié·e·s et plus que tout entouré·e·s.

A ma mère

Pour sa protection, pour tout ce qu'elle m'a transmis, ses enseignements, le goût des études, mais surtout pour ses valeurs. Pour l'empreinte qu'elle a laissée, pour cette volonté de chercher la bonté chez les autres, de comprendre, d'aider sans distinction, avec la gentillesse pour centre, en rejetant l'hypocrisie et les faux-semblants.

A mon père

Qui est, sans doute aucun, à l'origine de ma curiosité scientifique, dont la présence protectrice m'a permis, et me permet encore, d'avancer comme bon me semble. Pour tes valeurs inébranlables et profondément humaines, ta force inépuisable lorsqu'il s'agit d'aider ceux que tu aimes. Je te suis plus que reconnaissant pour les enseignements que tu m'as transmis et pour les clefs que tu m'as données.

A Joséphine

Ma grande sœur, la personne la plus humaine que je connaisse. Pour ton soutien inconditionnel, l'attention constante que tu me témoignes, tes conseils, ton aide et ta compréhension. Je ne te remercierai jamais assez pour tout ce que tu as fait pour moi.

A Bérénice

Ma presque jumelle avec qui je partage tant, pour notre connivence, les années fusionnelles passées ensemble. Merci d'avoir toujours été là pour moi, même dans les moments les plus durs, j'admire toujours la force ardente avec laquelle tu défends tes idéaux et cette idée d'un monde meilleur que jamais tu n'abandonnes.

A Alexis

Une belle personne récemment rencontrée, à ta délicatesse, cette gentillesse évidente et cet idéalisme tranquille qui te rendent si singulier. Merci d'avoir rejoint notre famille et d'aimer Bérénice comme tu le fais.

A Monique

Pour ta sincérité, tes valeurs, ton ouverture d'esprit qui force le respect. Merci pour tous les moments partagés, de mon enfance jusqu'à aujourd'hui.

A la famille Dreyfuss et Tibi

Qui m'a si aisément créé une place à laquelle je me sens bien. Qui sait toujours maintenir un lien malgré mes absences. Merci de m'avoir accompagné pendant une grande partie de ma thèse, merci d'être une fois de plus présents pour ce moment particulier.

A Didier

Pour sa générosité, ses enseignements, sa volonté d'entourer et d'aider les siens et bien sûr, sa cuisine. Merci du fond du cœur pour tous les moments partagés et pour l'accueil si chaleureux qui m'est chaque fois réservé. Votre soutien à beaucoup compté ces dernières années que ce soit pour cette thèse ou pour la médecine.

A Clémentine

Pour sa sollicitude sincère, son oreille attentive, sa gestion des émotions de tout un groupe. Merci de m'avoir accueilli avec simplicité et bienveillance, de m'avoir créé une place dans la famille. Pour les encouragements, précieux à la réussite de cette thèse et de la passerelle vers la médecine.

A Judith

Pour ta manière de toujours avoir su me mettre à l'aise et me faire me sentir à ma place, pour ces attentions si justes que tu sais avoir. Pour ta force combattante, pour ce que tu as su tenir et traverser, et pour cette manière impressionnante de mener de front médecine, maternité et famille, sans laisser personne pour compte.

A Kevin

Pour ton sens profond de la famille, pour ce que tu donnes sans compter. Pour ton ancrage mais aussi pour ton humour.

A Esther et Odaya

Au bonheur de vous voir grandir et aux personnes que vous devenez.

A Aline

Pour son sens aigu de l'autre, pour l'attention vraie qu'elle porte à chacun et qui a marqué chacune de nos rencontres.

A mes ami·e·s

Aux jurassien·nes

A Jules et Jean-Etienne

Amis de lycée avec qui j'ai pu partager le goût pour les sciences mais aussi et surtout aux moments ripisylves et vespéraux.

A Marion B, Léa, Juliette, Vitaline, Corentin, Salwa, Marion G, Aysun, Gwendolyne, Antoine et les autres, pour les moments partagés au lycée et pour rendre les retours dans le Jura chaque fois mémorables et natals.

Au trinôme 7 étendu

La plus précieuse des formations, aux galères, aux rires, aux DM, aux émaux caduques, aux bananes et leur maturation, aux colles, aux pun-intended, à la triple, au cône de déjection, aux éruptions réunionnaises, aux monstres calculateurs, aux paraboles, aux herbiers et aux écrevisses.

A nos amitiés évidentes, depuis 10 ans maintenant, si inébranlables qu'elles ont pavé mon parcours de certitude dans l'adversité. Vous rencontrer au hasard de la prépa a redessiné mon paysage et bâti l'un des socles les plus sûrs de ma vie.

A Nathan

A ta détermination, ton intelligence, tes valeurs et tes principes. Pouvoir partager par proxy ces 4 années de thèses avec un ami si proche a beaucoup compté. J'admirerai toujours ta combativité dans les épreuves, ta manière de tracer ta route qu'importe les embuches. A ta très future thèse qui sera sans nul doute éclatante, tant on t'a donné de la boue et tu en as fait de l'or.

A Lucas

A ta sincérité, ta sensibilité, ta facilité rare à créer du lien, sans jamais le forcer. A ta présence vibrante qui met tout le monde en confiance. A tous les instants d'écoute et de partage, à ton soutien qui jamais ne flanche, merci pour ces dix années d'amitié qui me rendent fier de cheminer aux côtés de personnes comme toi.

A Camille

Pour cette façon si naturelle que tu as eue de trouver ta place parmi nous, pour ta présence évidente dans le groupe, aux instants heureux partagés, à ta force et ta présence radieuse.

A Mehdi

Pour ton intelligence vertigineuse et ta sincérité. A nos sorties lyonnaises aux retours approxi-

matifs, à ton écoute salvatrice quand j'étais au plus mal. A ton humour acerbe et à l'immédiate connivence qui renait à chaque retrouvaille, à ta future thèse qui sera j'en suis sûr d'un tout autre niveau.

A Marine

Pour cette stabilité tranquille que tu donnes à ceux qui t'entourent, pour la droiture de tes principes et la force avec laquelle tu les tiens, pour les rires. A ta manière de veiller sur les liens du groupe, aux vacances et aux week-ends partagés, à ta porte toujours ouverte.

A Alexis

Pour ton hospitalité renouvelée, ton naturel, ton humour et ta douceur.

Au Dr Norman Daurelle

Pour le lien gardé malgré la distance, à la manière dont j'ai toujours pu compter sur toi dans les moments difficiles, à ta sincérité et ton sourire si communicatif.

A Noelle

Pour la finesse de ses analyses, son écoute, sa patience et sa compréhension de l'humain, des épreuves et des relations qui va bien au-delà de son métier.

A tout ceux qui m'ont aidé ou inspiré, de près ou de loin pendant ces 4 dernières années et auparavant, que ce soit en recherche, en médecine ou dans ma vie personnelle.

Et au milieu, Dora,

Qui navigue tous mes mondes, à la fois vent, soleil et vagues. Pour la place que tu m'as laissée prendre auprès de toi, et qui me rend heureux par-dessus tout. Pour l'aide incommensurable que tu m'as apportée dans tous les domaines, pour la finesse avec laquelle tu déchiffres le monde et les gens, pour la joie solaire que tu insuffles partout où tu passes. A ton intelligence ardente, ta résilience, ton engagement total dans le soin comme en dehors. A ta façon de m'aimer et de me comprendre comme jamais je n'aurais cru cela possible. A notre relation que tu fais grandir chaque jour, et qui a été mon refuge ces dernières années, les plus heureuses de ma vie, à tes côtés.

List of Abbreviations

α-KG – Alpha-ketoglutarate

β-2m – Beta-2 microglobulin

AJCC – American Joint Committee on Cancer

ANGPT2 – Angiopoietin-2

ATP – Adenosine Triphosphate

BALB/c – Bagg Albino strain c (inbred laboratory mouse strain)

BAP1 – BRCA1 Associated Protein-1

BRB-seq – Bulk RNA Barcoding and sequencing

CA – Cryoablation

CAFs – Cancer-Associated Fibroblasts

CAR – Chimeric Antigen Receptor

CAR-T – Chimeric Antigen Receptor T cells

CD – Cluster of Differentiation

CDX – Cell line-derived xenograft

CFSE – Carboxyfluorescein succinimidyl ester

CXCL / CXCR – Chemokine (C-X-C motif) ligand / receptor

ccRCC – Clear Cell Renal Cell Carcinoma

chRCC – Chromophobe Renal Cell Carcinoma

CT26 – Murine colorectal carcinoma cell line (BALB/c origin)

CTLA-4 – Cytotoxic T-Lymphocyte Antigen 4

DCs – Dendritic Cells

DFS – Disease-Free Survival

ECM – Extracellular matrix

EGLN – Egl-9 family hypoxia-inducible factor (prolyl hydroxylases)

EMT – Epithelial-to-Mesenchymal Transition

EpCAM – Epithelial Cell Adhesion Molecule

ESMO – European Society for Medical Oncology

EV – Extracellular Vesicles

FH – Fumarate Hydratase

GEMM – Genetically Engineered Mouse Model

H&E – Hematoxylin and Eosin

HIF – Hypoxia-Inducible Factor

HLA – Human Leukocyte Antigen

HLRCC – Hereditary Leiomyomatosis and Renal Cell Carcinoma

HNF – Hepatocyte Nuclear Factor

HUVECs – human umbilical vein endothelial cell

ICIs – Immune Checkpoint Inhibitors

IDO1 – Indoleamine 2,3-Dioxygenase 1

IFN-α – Interferon-alpha

IFN-γ – Interferon-gamma

IL-2 – Interleukin-2

IL-10 – Interleukin-10

ILT2 / ILT4 – Immunoglobulin-like Transcript 2 / 4

IMDC – International Metastatic RCC Database Consortium

IO – Immuno-Oncology

ISUP – International Society of Urological Pathology

KPS – Karnofsky Performance Status

LAG-3 – Lymphocyte Activation Gene 3

MC38 – Murine colon adenocarcinoma cell line (C57BL/6 origin)

MCBS – ESMO Magnitude of Clinical Benefit Scale

MDSCs – Myeloid-Derived Suppressor Cells

MHC – Major Histocompatibility Complex

mRCC – Metastatic Renal Cell Carcinoma

MSKCC – Memorial Sloan Kettering Cancer Center

mTOR – Mechanistic Target of Rapamycin

NKG2A – Natural Killer Group 2 member A

NK – Natural Killer cells

NKp80 – Natural Killer Protein 80

NOD – Non-Obese Diabetic (mouse strain)

OS – Overall Survival

PBRM1 – Polybromo 1

qPCR – Quantitative Polymerase Chain Reaction

PD-1 – Programmed Cell Death Protein 1

PDGF – Platelet-Derived Growth Factor

PD-L1 – Programmed Death-Ligand 1

PDOTS – Patient-Derived Organotypic Tumor Spheroids

PDO – Patient-Derived Organoids

PDTO – Patient-Derived Tumor Organoids

PDX – Patient-Derived Xenograft

PFS – Progression-Free Survival

PN – Partial Nephrectomy

pRCC – Papillary Renal Cell Carcinoma

RCC – Renal Cell Carcinoma

REMCA – Renal Murine Clear Cell Adenocarcinoma model

RFA – Radiofrequency Ablation

RN – Radical Nephrectomy

RNAseq – RNA sequencing

SABR / SBRT – Stereotactic Ablative Body Radiotherapy / Stereotactic Body Radiotherapy

SASP – Senescence-Associated Secretory Phenotype

SCID – Severe Combined Immunodeficiency (mouse strain)

SDH – Succinate Dehydrogenase

SETD2 – SET domain containing 2

SIRPα – Signal Regulatory Protein Alpha

TAMs – Tumor-Associated Macrophages

TAMR / TAMR polarization (M1/M2) – Tumor-Associated Macrophage Reprogramming

TCGA – The Cancer Genome Atlas

TIGIT – T cell Immunoreceptor with Ig and ITIM domains

TILs – Tumor-Infiltrating Lymphocytes

TIM-3 – T cell Immunoglobulin and Mucin-domain containing-3

TLS – Tertiary Lymphoid Structures

TMB – Tumor Mutational Burden

TME – Tumor Microenvironment

TKI – Tyrosine Kinase Inhibitor

Tregs – Regulatory T cells

TNM – Tumor, Node, Metastasis classification

TSC – Tuberous Sclerosis Complex

UICC – Union for International Cancer Control

VEGF – Vascular Endothelial Growth Factor

VEGFR – Vascular Endothelial Growth Factor Receptor

VHL – von Hippel–Lindau

VISTA – V-domain Ig Suppressor of T cell Activation

WES – Whole-Exome Sequencing

WHO – World Health Organization

Table of Contents

ACKNOWLEDGEMENTS / REMERCIEMENTS V

LIST OF ABBREVIATIONS XVII

INTRODUCTION 1

Chapter 1: Cancer Immunology 1

I. Cancer as a Genetic and Evolving Disease 1
II. The Hallmarks of Cancer 3
III. Cancer Immunology: Elimination, Equilibrium, and Escape 7
IV. Cancer Immunotherapy 25

Chapter 2: Renal Cell Carcinoma 31

I. Epidemiology, Risk Factors, and Hereditary Syndromes 31
II. Diagnosis and Prognosis 32
III. Molecular and Biological Characteristics of Clear Cell RCC 43
IV. Immune Landscape and Tumor Microenvironment of Clear Cell RCC 46
V. Current Management of RCC 48
VI. Place of immunotherapy in RCC 52

Chapter 3: Preclinical Models for Immuno-Oncology 60

I. Classical 2D Culture Cell Line Model 60
II. In Vivo Models 66
III. Complex in Vitro Models for Immuno-Oncology 80

RESULTS 111

Chapter 1: Methods for Establishing a Renal Cell Carcinoma Tumor Spheroid Model with Immune Infiltration for Immunotherapeutic Studies 112
Summary and perspectives 127

Chapter 2: Transcriptomic evaluation of immune-infiltrated patient-derived tumor spheroids as preclinical models in renal cell carcinoma 128
Summary and perspective 149

Chapter 3: A Tumor-on-Chip Platform for Modeling Immunotherapy Response in Clear Cell Renal Cell Carcinoma 151
Summary and perspectives 218

GENERAL DISCUSSION 221

I. Current state and limitations 221
II. Positioning of the model 224
III. Perspectives 225

APPENDIX 230

BIBLIOGRAPHY 233

RÉSUMÉ SUBSTANTIEL EN FRANÇAIS 260

Introduction

This general introduction is organized into three chapters. The first outlines the basic principles of cancer immunology. The second focuses on renal cell carcinoma (RCC), highlighting its biological and immunological specificities. The third reviews experimental models used in oncology, with particular emphasis on immunocompetent systems, and synthesizes findings derived from preclinical models of RCC in the context of immunotherapy, thereby setting the stage for the work presented in this thesis.

Chapter 1: Cancer Immunology

Cancer is one of the leading causes of morbidity and mortality worldwide. In 2022, an estimated 20.0 million new cases and 9.7 million deaths were reported globally (1), making cancer the second leading cause of death after cardiovascular disease, and representing a major global health burden. The number of cases is expected to rise to 29.9 million by 2040, mainly due to population growth and aging, but also to increased exposure to environmental factors (2). Given its incidence, mortality, and complexity, cancer remains one of the foremost priorities of biomedical research.

In this chapter, we will first introduce the biological basis of cancer as a genetic and evolving disease, before presenting the conceptual framework of the Hallmarks of Cancer. We will then describe how the immune system interacts with tumors through the processes of immunosurveillance, equilibrium, and escape, and how these interactions shape tumor development. Finally, we will review the principles of modern immunotherapies and the challenges that remain in integrating them into cancer care.

This section aims to provide the conceptual framework of cancer immunology, highlighting the major mechanisms of immune recognition, evasion, and therapeutic targeting. These principles serve as essential keys to understanding the particularities of RCC immunobiology and the rationale for developing advanced preclinical models, which will be addressed in the subsequent sections.

I. Cancer as a Genetic and Evolving Disease

Cancer is a group of diseases characterized by the uncontrolled growth and survival of abnormal cells that acquire the capacity to invade surrounding tissues and, in many cases, to metastasize to distant organs. The recognition of cancer as a distinct pathological entity dates back to

antiquity. Hippocrates used the term karkinos (crab) to describe the invasive nature of tumors, while Galen later distinguished between benign and malignant growths. For centuries, theories on the origins of cancer remained speculative, ranging from humoral imbalance to chronic irritation or infections. A major conceptual breakthrough occurred in the 19th century with Rudolf Virchow, who established the cellular theory of disease and emphasized that cancers arise from the uncontrolled proliferation of cells. In 1914, Theodor Boveri further hypothesized that chromosomal abnormalities could drive tumor development, foreshadowing the genetic paradigm that dominates modern oncology (3).

By the late 20th century, the discovery of oncogenes and tumor suppressor genes, together with the identification of DNA repair pathways, cemented the view of cancer as a disease of the genome. This genomic paradigm was further reinforced by the launch of large-scale molecular characterization initiatives in the early 2000s. The Cancer Genome Atlas (TCGA) and the International Cancer Genome Consortium (ICGC) initially employed array-based platforms to systematically profile gene expression, copy number alterations, and DNA methylation across multiple tumor types. These efforts soon evolved to incorporate next-generation sequencing, including whole-exome sequencing (WES) and RNA sequencing (RNA-seq), enabling a more detailed cataloging of somatic mutations and transcriptomic landscapes. Building on this foundation, the Pan-Cancer Analysis of Whole Genomes (PCAWG) project analyzed over 2,600 whole-genome sequences from 38 tumor types, uncovering non-coding driver mutations, complex structural variations, and signatures of genome evolution (4). Remarkably, these studies also identified cancer-associated mutations in histologically normal tissues, suggesting that oncogenic processes may be initiated well before overt morphological changes are detectable. Despite these advances, genomic data alone has proven insufficient to fully explain tumor behavior or therapeutic response. More recent pan-cancer projects have expanded to include additional layers of molecular regulation, such as epigenetic modifications, chromatin organization, proteogenomics, and post-translational modifications, offering a more integrated and dynamic understanding of tumor biology.

Figure 1 provides a chronological overview of key conceptual and technological milestones that have shaped our current understanding of cancer as a genetic and evolving disease.

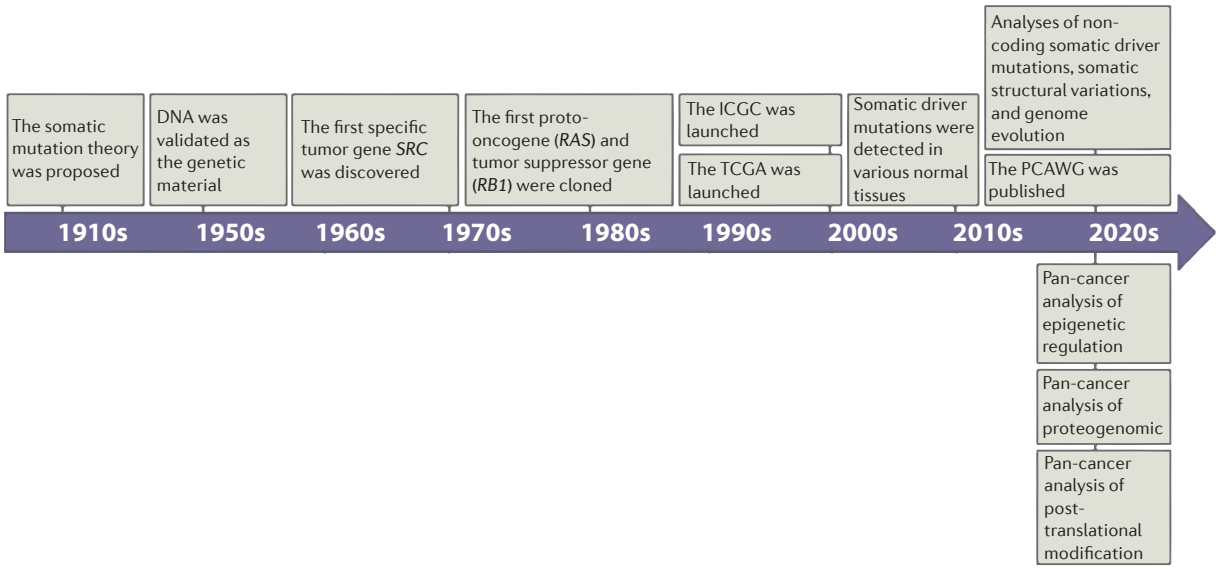

Figure 1. Historical milestones in the development of the somatic mutation theory of cancer.
From the early 20th century conceptualization of cancer as a disease of accumulated somatic mutations, to the discovery of oncogenes and tumor suppressor genes, and the emergence of large-scale genome sequencing programs, our understanding of cancer as a genetic and evolving disease has been progressively refined. Recent pan-cancer studies now integrate epigenetic, proteogenomic, and post-translational data.

Source: adapted from (5), under CC BY 4.0

At its core, cancer arises from the progressive accumulation of genetic and epigenetic alterations in somatic cells. These changes affect genes involved in the regulation of cell proliferation, apoptosis, DNA repair, and cellular differentiation, ultimately disrupting the homeostatic mechanisms that maintain tissue integrity.

Oncogenesis typically involves the activation of proto-oncogenes into oncogenes, which promote proliferation, and the inactivation of tumor suppressor genes, which normally restrain growth or promote cell death in the presence of genomic damage. The instability of the genome, either through defective DNA repair mechanisms or mitotic errors, further accelerates the accumulation of mutations, allowing cancer cells to adapt to selective pressures from their environment, including therapy (6).

The result is a clonal expansion of cells that progressively acquire traits favoring survival, growth, and dissemination. However, despite this underlying clonal origin, most tumors are highly heterogeneous due to genetic diversification, epigenetic remodeling, and interactions with their surrounding environment. This heterogeneity represents a major challenge to effective treatment and is a driving force behind therapeutic resistance.

II. The Hallmarks of Cancer

The accumulation of genetic and epigenetic alterations in somatic cells occurs in a largely stochastic manner. However, during tumor evolution, selective pressures within the host environment favor alterations that provide survival and growth advantages. As a result, malignant cells,

despite their diverse origins, tend to converge toward a limited set of functional capabilities that collectively define the cancer phenotype. This conceptual framework was elegantly formalized by Hanahan and Weinberg in 2000 and subsequently refined in 2011 and 2022, under the term *Hallmarks of Cancer* (7–9). We will use this framework as a simple base to describe tumor biology.

The original framework described six core hallmarks that capture the fundamental deregulations of cell-autonomous processes driving malignant transformation:

- Sustaining proliferative signaling: Unlike normal cells, which require external growth factors to divide, tumor cells become self-sufficient by producing their own mitogenic signals or by constitutively activating downstream pathways, through mechanisms such as autocrine signaling or activating mutations in receptors like epidermal growth factor receptor (EGFR).
- Evading growth suppressors: cancer cells acquire the ability to bypass signals that normally restrict proliferation, such as those mediated by tumor suppressors like retinoblastoma protein (pRb) or p53.
- Resisting cell death: programmed cell death, or apoptosis, is a fundamental safeguard against damaged or abnormal cells; tumor cells often harbor alterations that disrupt apoptotic pathways, resulting in enhanced survival under stress or genomic instability.
- Enabling replicative immortality: while most normal somatic cells undergo senescence after a finite number of divisions, cancer cells frequently present activated telomerase or alternative lengthening mechanisms that maintain telomere integrity and support unlimited replication.
- Inducing angiogenesis: Beyond a critical size, tumors require a dedicated vasculature to meet their metabolic demands. This is facilitated by the expression of pro-angiogenic factors, such as vascular endothelial growth factor (*VEGF*).
- Activating invasion and metastasis: malignant cells acquire properties that enable degradation of the extracellular matrix, remodeling of surrounding tissues, and dissemination to distant sites, where they may establish secondary tumors.

In 2011, this model was expanded to include two additional hallmarks. The first: reprogramming of cellular energy metabolism, refers to the altered metabolic states observed in cancer cells, enabling them to meet increased bioenergetic and biosynthetic demands under variable oxygen and nutrient conditions. This often involves a preference for aerobic glycolysis (the "Warburg effect") even in the presence of sufficient oxygen. The second: evasion of immune destruction, describes the capacity of tumor cells to suppress or escape immune recognition and elimination by the host immune system, a phenomenon we will discuss in more detail later in this chapter.

In addition, two enabling characteristics were emphasized. Genomic instability provides the mutational diversity that fuels the acquisition of other hallmarks, while tumor-promoting inflammation supplies growth factors, cytokines, and matrix remodeling enzymes that not only sustain proliferation but also alter the local tissue environment, bolstering tumor progression (9).

Most recently, in 2022, the framework was further enriched by incorporating additional hallmarks that reflect the expanding understanding of tumor biology (7):

- Phenotypic plasticity refers to the ability of cancer cells to transition between different cellular states, such as epithelial-to-mesenchymal transition (EMT), a process associated with increased adaptability and metastatic potential.
- Epigenetic reprogramming involves modifications in chromatin organization and DNA methylation patterns that regulate gene expression without altering the DNA sequence, contributing to the maintenance of malignant phenotypes.
- Cellular senescence, historically viewed as a tumor-suppressive mechanism, has emerged as a dual-faceted process: while it halts proliferation, senescent cells can also acquire a pro-inflammatory secretory phenotype (SASP) that influences the tumor milieu and may support progression.
- The tumor microenvironment (TME), composed of non-malignant stromal, vascular, and immune elements, has been recognized as a major determinant of tumor behavior. Interactions within this heterogeneous cellular network shape the dynamics of tumor progression and underscore the notion that cancer is not solely a cell-autonomous disease, but also a pathology driven by tissue-level dysregulation.

A graphical overview of all established and emerging hallmarks, including those not explicitly discussed in the text, is provided in **Figure 2**.

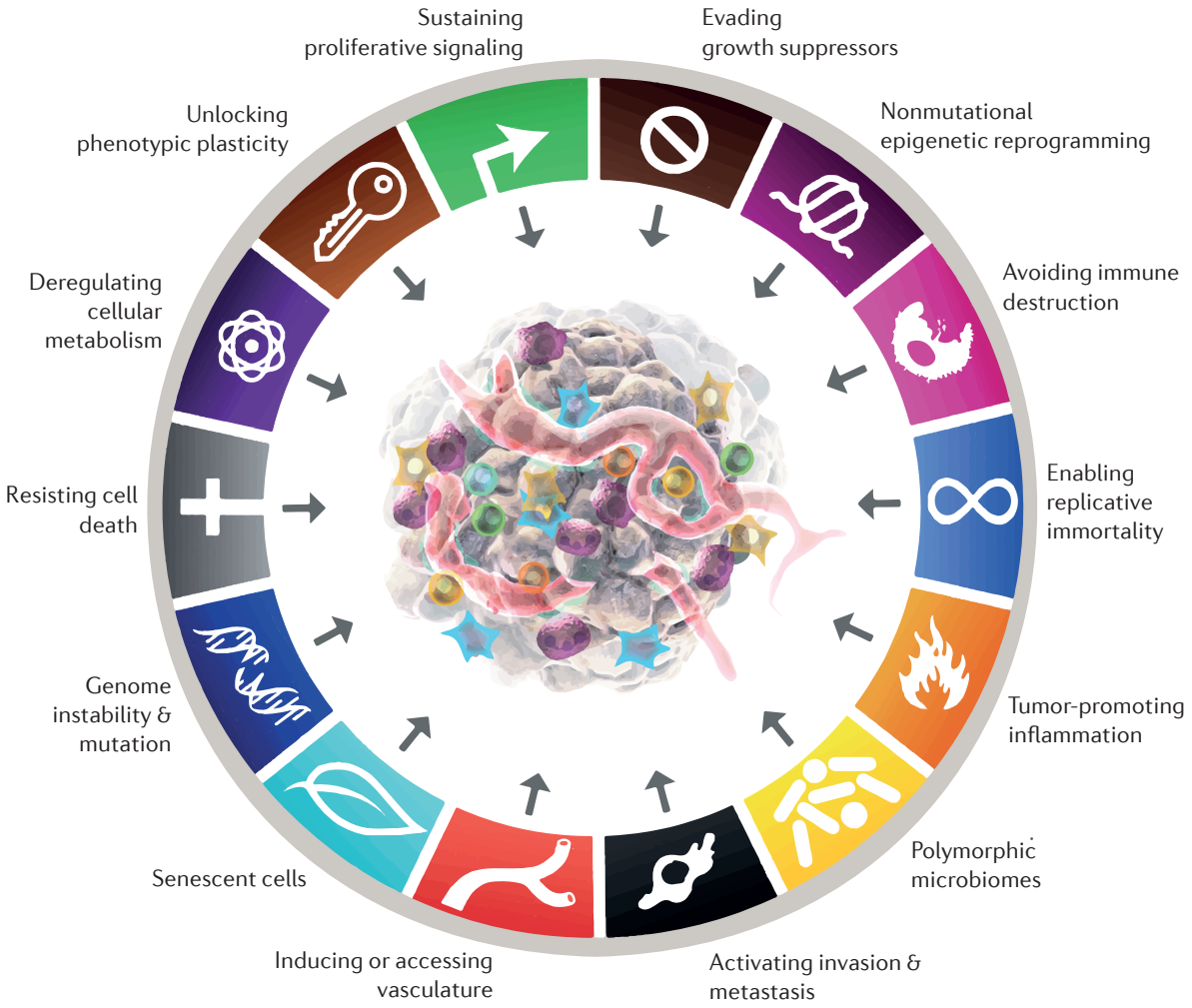

Figure 2. Updated framework of the hallmarks of cancer as proposed by Hanahan (2022).
The model encompasses established hallmarks (e.g., sustaining proliferative signaling, resisting cell death), enabling characteristics (e.g., genome instability, tumor-promoting inflammation), and newly recognized dimensions such as polymorphic microbiomes, nonmutational epigenetic reprogramming, and cellular senescence. These features collectively reflect the evolving understanding of tumor biology and the multifactorial nature of cancer progression.

Source: (7) reproduced with permission from Springer Nature, license number 6140750281084

By providing a unifying lens through which the immense complexity of cancer biology can be interpreted, the hallmarks framework highlights both the diversity and the convergence of tumorigenic processes. Ultimately, cancer emerges as the consequence of an evolutionary process in which genetic and epigenetic alterations, shaped by selective pressures, give rise to cells that progressively acquire survival and growth advantages. The resulting disease is therefore not a single molecular defect, but rather the integration of multiple functional capabilities that collectively sustain malignancy.

III. Cancer Immunology: Elimination, Equilibrium, and Escape

The idea that the immune system might play a role in controlling cancer dates back to Paul Ehrlich, who speculated in the early 20th century that immune mechanisms could eliminate nascent tumor cells before they became clinically apparent (10). This notion was later revisited and formalized in the 1950s by Macfarlane Burnet and Lewis Thomas, who articulated the concept of cancer immunosurveillance (11,12). Drawing on evidence that mice could be immunized against tumor antigens, they proposed that immune cells act as sentinels, recognizing and eliminating emerging neoplastic cells through the detection of tumor-associated structures at the cell surface (13,14).

Over time, it became clear that the relationship between tumors and the immune system was more complex than simple elimination. Tumors were found to persist in a state of dynamic balance with immune defenses, where immune pressure could restrain growth without achieving complete eradication. To capture this dual role of the immune system in both suppressing and shaping tumor development, Dunn, Old, and Schreiber introduced in the early 2000s the concept of cancer immunoediting. This framework describes three sequential phases: elimination, equilibrium and escape. In the elimination phase, immune effector cells recognize and destroy tumor cells. During equilibrium, residual tumor cells survive under continuous immune pressure, undergoing selection for variants with reduced immunogenicity. In the escape phase, tumor cells acquire the ability to circumvent or suppress immune attack, leading to uncontrolled expansion and clinically detectable disease (15).

In the following sections, we will use this evolutionary sequence as a guide to describe how the immune system interacts with tumors, first through mechanisms of immunosurveillance and elimination, and later through processes of escape and tolerance that ultimately allow tumor progression. A graphical illustration of the three phases is provided in **Figure 3**.

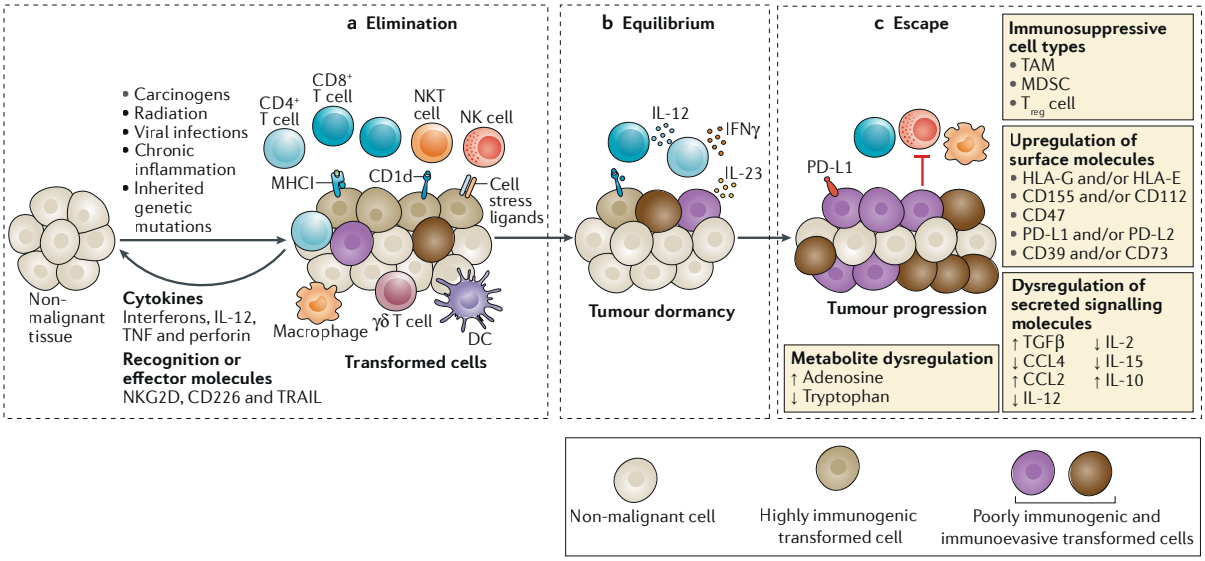

Figure 3. Cancer immunoediting.

The interactions between transformed cells and the immune system proceed through three phases: (a) Elimination, during which innate and adaptive immune cells cooperate to recognize and destroy highly immunogenic tumor cells; (b) Equilibrium, in which surviving variants are maintained in a dormant state under continuous immune pressure; and (c) Escape, where tumor cells acquire immunoevasive and immunosuppressive traits that allow unrestrained growth and clinical progression. Key cellular players, cytokines, immune checkpoints, and immunosuppressive mechanisms are indicated.

Source: (16), reproduced with permission from Springer Nature, license number 6140750666905

A. Elimination

1. Neoantigens and tumor immunogenicity

The first step in this sequence relies on the ability of the immune system to recognize transformed cells as abnormal. This recognition is mediated by tumor antigens, which can arise from several sources. Somatic mutations generate neoantigens, peptides with novel amino acid sequences absent from the normal proteome. In addition, tumor-associated antigens can result from aberrant expression patterns, such as the re-expression of normally silenced germline genes (for example, cancer–testis antigens), the ectopic expression of tissue-restricted proteins (such as melanocyte differentiation antigens in melanoma), or the overexpression of normal proteins beyond physiological thresholds **Figure 4**. Once produced, these proteins are degraded into peptides by the proteasome, transported into the endoplasmic reticulum via the transporter associated with antigen (TAP), and loaded onto major histocompatibility complex class I (MHC-I) molecules together with β2-microglobulin (β2m). The resulting peptide–MHC complexes are then displayed at the cell surface, where they become accessible to surveillance by cytotoxic $CD8^+$ T lymphocytes **Figure 4**.

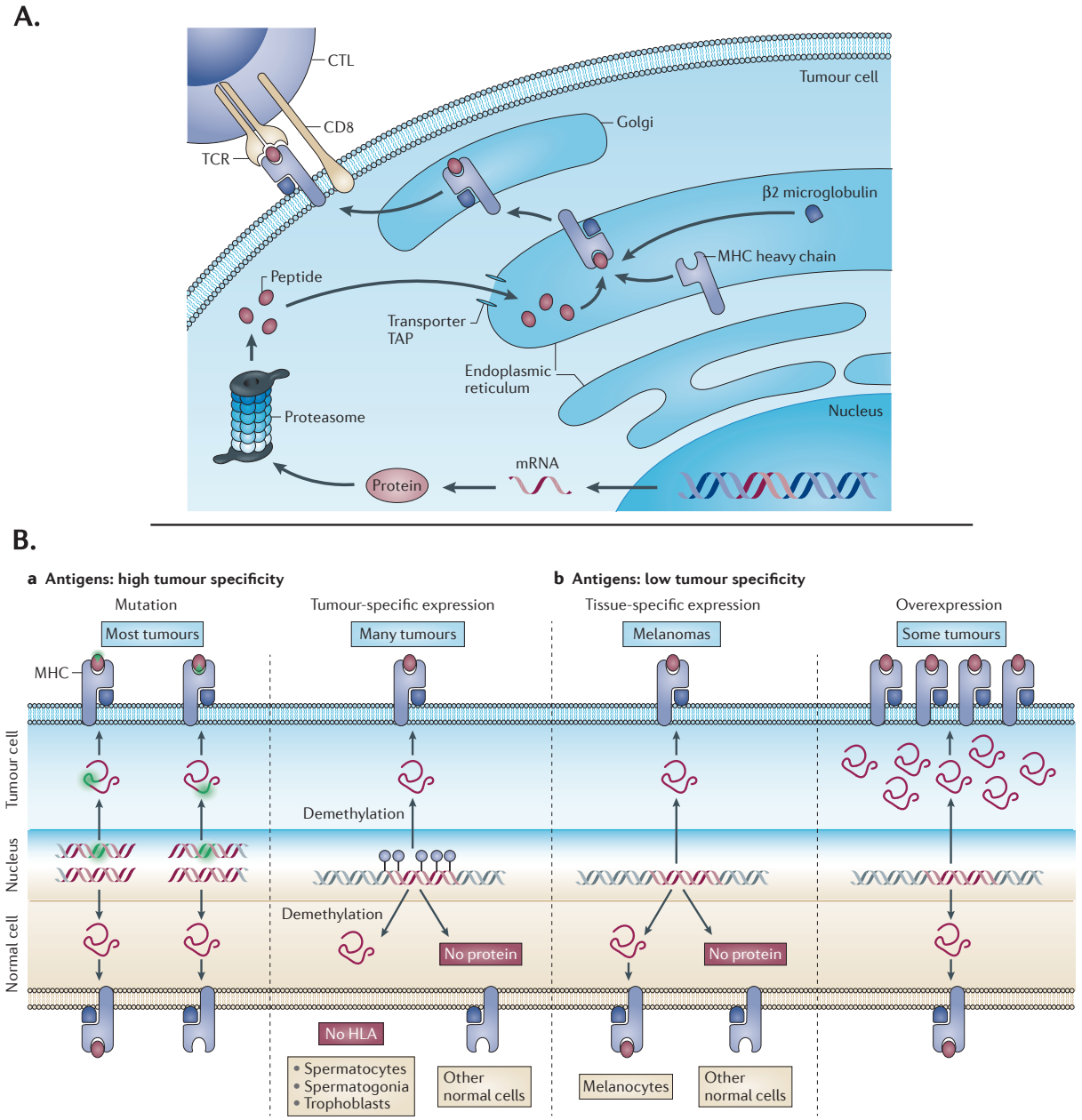

Figure 4. Processing and sources of tumor antigens.

A. Antigen processing. Intracellular proteins are degraded by the proteasome into peptides, which are transported into the endoplasmic reticulum by the transporter associated with antigen processing (TAP). There, they bind to major histocompatibility complex class I (MHC-I) molecules together with β2-microglobulin before being exported to the cell surface for recognition by $CD8^+$ cytotoxic T lymphocytes (CTLs). B. Classes of tumor antigens. Tumor antigens may arise from different mechanisms: (a) mutations generating neoantigens with high tumor specificity; (b) aberrant re-expression of normally silenced germline or tissue-specific genes or (c) overexpression of normal proteins beyond physiological thresholds.

Source: (17), reproduced with permission from Springer Nature, license number 6153531282917

The extent to which a tumor can be recognized by the immune system, often referred to as tumor immunogenicity, is influenced by the tumor mutational burden (TMB). Tumors with a high number of mutations, such as melanoma, smoking-associated lung cancers, or tumors with microsatellite instability tend to generate more immunogenic neoantigens, whereas tumors with

a low TMB often fail to elicit robust immune recognition unless other mechanisms contribute to antigenicity. Importantly, in addition to antigen presentation, transformed cells can emit danger-associated molecular patterns danger-associated molecular patterns (DAMPs), such as high mobility group box 1 (HMGB1), adenosine triphosphate ATP, or calreticulin. These molecules serve as endogenous alarm signals, providing the inflammatory context necessary for antigen-specific T cell priming and linking cellular stress responses to adaptive immune activation.

Once tumor antigens are generated and presented in an immunogenic context, they can be detected and acted upon by both the innate and adaptive arms of the immune system, initiating the process of tumor immunoediting.

2. Effectors of immunosurveillance

Cells of the innate immune system provide the first line of defense against emerging tumors. Natural killer (NK) cells play a central role by recognizing and killing cells that have downregulated MHC class I molecules, a common feature of tumor cells selected to evade T cell recognition. Macrophages can also participate in antitumor immunity, particularly when polarized toward a pro-inflammatory M1 phenotype, where they secrete cytotoxic mediators such as reactive oxygen species (ROS), nitric oxide (NO), and tumor necrosis factor-α (TNFα). In addition to their effector functions, macrophages contribute to antigen presentation and the amplification of adaptive responses, although dendritic cells (DCs) remain the primary professional antigen-presenting cells. DCs capture tumor antigens and initiate adaptive immune responses through cross-presentation to $CD8^+$ T cells (18).

The adaptive immune system provides specificity and memory. $CD8^+$ cytotoxic T lymphocytes (CTLs) recognize tumor antigens presented on MHC class I and are capable of directly killing malignant cells through perforin–granzyme release and death receptor signaling. $CD4^+$ T helper 1 (Th1) cells support this response by secreting cytokines such as interleukin-2 (IL-2) and interferon-γ (IFNγ), which activate CTLs and macrophages (19).

Within tumors, B cells often organize into tertiary lymphoid structures (TLS), ectopic lymphoid aggregates that recapitulate features of secondary lymphoid organs. In TLS, dendritic cells prime $CD4^+$ and $CD8^+$ T cells, while naive and memory B cells undergo affinity maturation and class switching in the presence of follicular helper T cells (Tfh) and follicular dendritic cells. The resulting plasma cells migrate along CXCL12-expressing fibroblastic tracks into the tumor bed, where they secrete high-affinity IgG antibodies. These antibodies mediate tumor cell destruction via Antibody-Dependent Cellular Cytotoxicity (ADCC) by NK cells, phagocytosis by macrophages, or complement-dependent cytotoxicity. In addition, IgG-tumor antigen immune complexes formed in situ further stimulate local immune responses by activating myeloid cells and enhancing antigen presentation. These integrated responses enable TLS to act as intratumoral immune niches that both initiate and amplify anti-tumor immunity (20).

Cytokines serve as crucial mediators of this antitumor immunity. IFNγ enhances antigen presentation and promotes CTL activity, while TNFα can induce apoptosis in tumor cells and contribute to inflammatory activation.

Together, these innate and adaptive effectors form the backbone of immunosurveillance, enabling the elimination of transformed cells during the earliest stages of tumorigenesis. This dynamic process of immune activation, recruitment, tumor infiltration, and cancer cell killing is often conceptualized as a cyclic sequence: the cancer-immunity cycle as proposed by Chen and Mellman (21). It represents the stepwise development of effective anti-tumor immune responses, as illustrated in Figure 4.

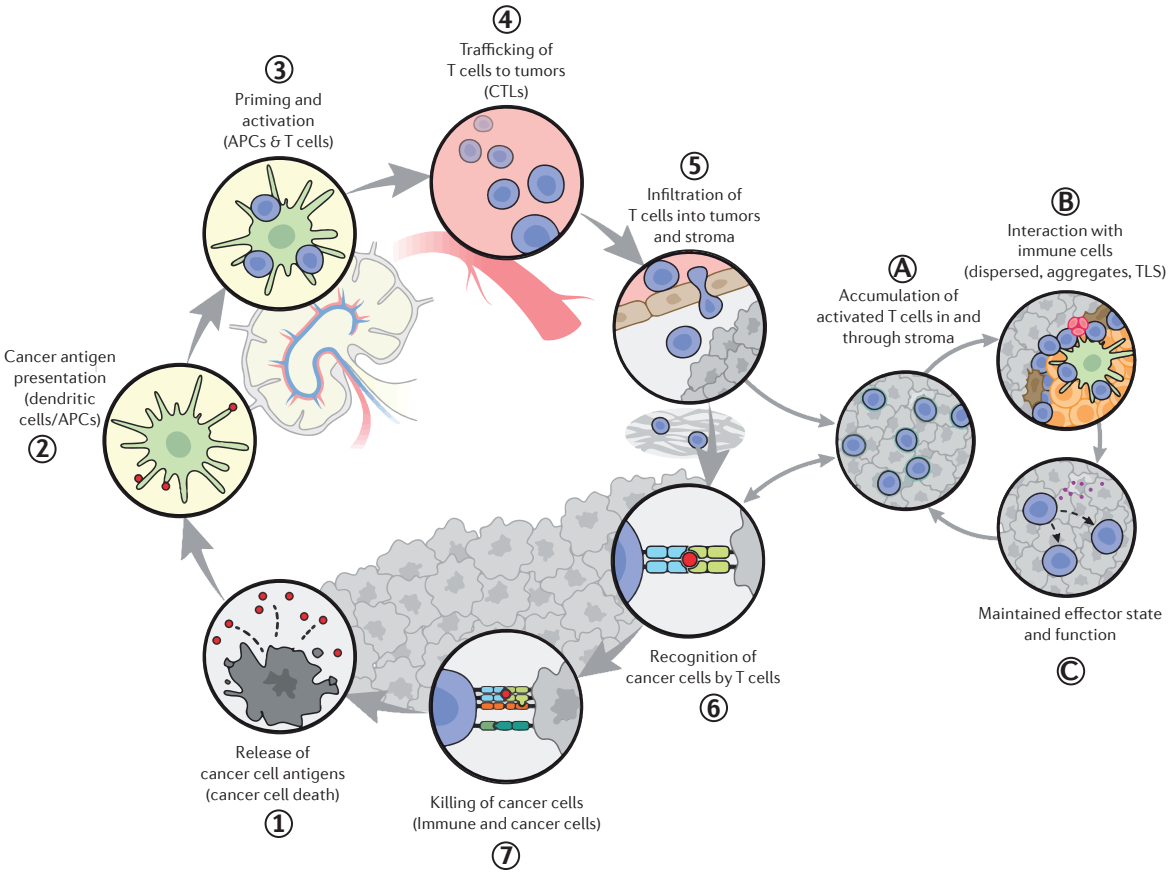

Figure 5. The cancer-immunity cycle and its intratumoral subcycle.

The cancer-immunity cycle describes the stepwise process through which the immune system identifies and eliminates malignant cells. Following the release of tumor antigens (1), antigen-presenting cells (APCs) such as dendritic cells capture and process these antigens (2), then migrate to draining lymph nodes where they prime $CD4^+$ and $CD8^+$ T cells (3). Activated cytotoxic T lymphocytes (CTLs) then traffic to the tumor via the bloodstream (4), infiltrate the TME (5), recognize tumor cells via peptide–MHC complexes (6), and induce cell death through cytotoxic mechanisms (7). Within the tumor, a localized "immunologic subcycle" can occur, reflecting the same sequence of activation, expansion, and effector activity but restricted to the TME. This includes accumulation of activated T cells in the stroma (A), interaction with intratumoral immune cells, including within dispersed aggregates or tertiary lymphoid structures (TLS) (B), and concludes with maintenance of effector function (C). While this cycle enables effective immune surveillance and tumor cell killing, it can be disrupted by immunosuppressive cells, stromal barriers, metabolic constraints, or T cell exhaustion, thereby impeding tumor eradication.

Source: (22), under CC-BY-NC-ND 4.0

B. Equilibrium: selection and coevolution

When immune elimination is incomplete, residual tumor cells can survive under the continuous selective pressure of the immune system. This stage, termed equilibrium, represents a dynamic balance in which immune effector mechanisms prevent tumor outgrowth but fail to fully eradicate malignant cells. During this phase, tumor cells may remain clinically undetectable for extended periods, existing in a subclinical or dormant state.

Importantly, equilibrium is not a static condition but an evolutionary process. Immune pressure acts as a selective force, favoring the survival and expansion of tumor cell variants with reduced immunogenicity. This phenomenon, known as immunoediting, progressively sculpts the antigenic landscape of the tumor. Cells that downregulate antigen expression, lose major histocompatibility complex (MHC) molecules, or develop resistance to immune-mediated killing gain a growth advantage, while highly immunogenic clones are eliminated.

The outcome of this coevolution is a heterogenous tumor cell population with varying levels of susceptibility to immune attack. From a clinical perspective, this process underlies the distinction often made between “hot” tumors, characterized by abundant immune infiltration and pro-inflammatory activity, and “cold” tumors, which are poorly infiltrated and largely immunologically silent. The equilibrium phase thus represents a critical turning point in tumor–immune interactions: it restrains tumor expansion but simultaneously drives the selection of variants that are more likely to escape immune control (16).

C. Escape: tolerance and progression

The final stage of cancer immunoediting is immune escape, in which tumor cells acquire the ability to withstand or suppress immune attack, allowing progressive expansion and clinically detectable disease. Multiple, often overlapping mechanisms contribute to this process, involving both tumor-intrinsic changes and the establishment of an immunosuppressive microenvironment (**Figure 3**).

1. Loss of antigenicity

One major mechanism of escape is the reduction of tumor immunogenicity. Tumor cells may downregulate, lose the expression of tumor antigens, or acquire mutations that render these antigens less recognizable. In parallel, defects in antigen processing and presentation pathways, such as loss of β2-microglobulin or downregulation of MHC class I molecules, impair the ability of cytotoxic T cells to detect malignant cells.

2. Immune checkpoints

A central mechanism contributing to the suppression of antitumor immunity in cancer is the upregulation and engagement of immune checkpoints. Immune checkpoints are regulatory pathways formed by receptor–ligand pairs that modulate the intensity and duration of immune responses. Under physiological conditions, these interactions maintain tolerance and prevent excessive immune activation. In tumors, both malignant and non-malignant cells may express checkpoint receptors or their ligands, generating inhibitory signals that affect multiple immune populations. These include reduced proliferation, cytokine secretion, and cytotoxicity of effector T and NK cells, as well as modulation of B cell responses and myeloid cell activity. Over time, the persistence of such inhibitory interactions favors immune dysfunction and tolerance within the tumor microenvironment.

a. Canonical checkpoints

Two checkpoint pathways have been most extensively characterized and clinically targeted. CTLA-4 (cytotoxic T lymphocyte–associated antigen 4) is expressed on activated T cells and competes with the costimulatory receptor CD28 for binding to CD80/CD86 on antigen-presenting cells. By outcompeting CD28, CTLA-4 dampens T cell priming in lymph nodes, limiting the initiation of immune responses. In contrast, the PD-1/PD-L1 axis primarily regulates T cell activity in peripheral tissues. Programmed cell death protein 1 (PD-1) is expressed on chronically stimulated T cells, while its ligands Programmed cell death ligand 1 (PD-L1) and PD-L2 can be upregulated on tumor cells and immune cells in the tumor microenvironment. Engagement of PD-1 by its ligands inhibits TCR signaling, leading to reduced proliferation, impaired cytokine secretion, and diminished cytotoxic function.

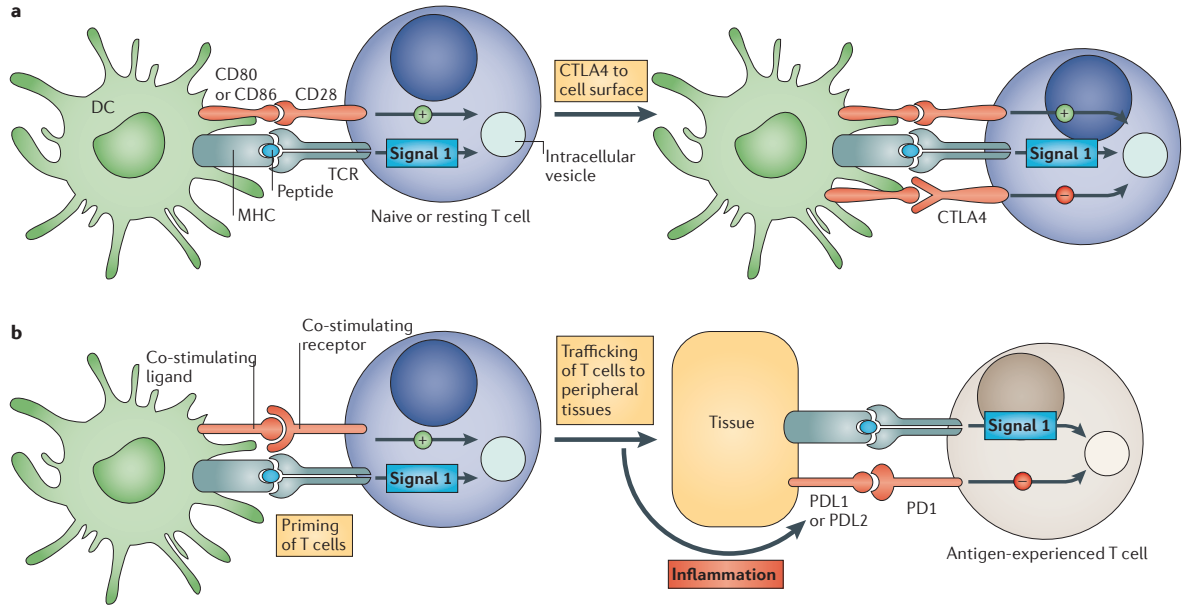

Figure 6. Distinct roles of CTLA-4 and PD-1 in regulating T cell responses.

(a) During priming in lymph nodes, naïve T cells require two signals for activation: antigen recognition (signal 1, via TCR–MHC–peptide complexes) and co-stimulation (signal 2, e.g., CD28 binding to CD80/CD86 on dendritic cells). CTLA-4, upregulated upon T cell activation, competes with CD28 for CD80/CD86 binding and attenuates T cell priming. (b) In peripheral tissues, antigen-experienced T cells are further regulated by co-stimulatory and inhibitory interactions. Engagement of PD-1 on T cells by its ligands PD-L1 or PD-L2, which can be induced by inflammation and are frequently expressed on tumor or stromal cells, inhibits TCR signaling and effector functions. Thus, CTLA-4 predominantly limits the initiation of immune responses, whereas PD-1/PD-L1 primarily regulates T cell activity in peripheral tissues, including the tumor microenvironment.

Source: (23), Reproduced with permission from Springer Nature, license number 6153540567645

b. Additional inhibitory checkpoints

Beyond CTLA-4 and PD-1, numerous other inhibitory receptors and ligand–receptor pairs contribute to immune evasion, often acting redundantly or synergistically. TIM-3 (T cell immunoglobulin and mucin-domain containing-3) marks dysfunctional or exhausted T cells and suppresses Th1 and CTL responses upon binding to ligands such as Galectin-9. LAG-3 (lymphocyte activation gene-3) is upregulated on exhausted T cells and binds MHC class II, delivering inhibitory signals that limit T cell expansion. TIGIT (T cell immunoreceptor with Ig and ITIM domains) interacts with CD155 and CD112 on antigen-presenting cells, counterbalancing stimulatory signals from CD226 (24). In fact, numerous co-stimulatory and inhibitory signals regulate T cell response as can be seen in **Figure 7**.

In addition, non-classical HLA molecules play a major role. HLA-G, normally restricted to placental tissues to maintain maternal–fetal tolerance, can be aberrantly expressed by tumor or stromal cells and exert broad immunosuppressive effects. By engaging inhibitory receptors such as ILT2 and ILT4, HLA-G impairs cytotoxicity of T and NK cells, promotes Treg differentiation, skews macrophage polarization toward a tolerogenic phenotype, and supports the expansion of tolerogenic myeloid cells (25). HLA-E interacts with the inhibitory receptor NKG2A on NK and $CD8^+$ T cells, dampening cytotoxic activity and promoting immune escape

(26).

Other ligand–receptor pairs also contribute. CD70, which is usually expressed transiently on activated lymphocytes, can be aberrantly upregulated on tumor cells. Its persistent expression chronically stimulates CD27 on T cells, driving their functional exhaustion rather than effective activation. The SIRPα–CD47 axis is another well-recognized pathway: CD47, widely overexpressed on tumor cells, delivers a "don't eat me" signal by engaging SIRPα on macrophages and dendritic cells, thereby inhibiting phagocytosis and reducing innate clearance of malignant cells. Finally, other inhibitory pathways, such as VISTA (V-domain Ig suppressor of T cell activation), further contribute to the suppression of immune activity (27).

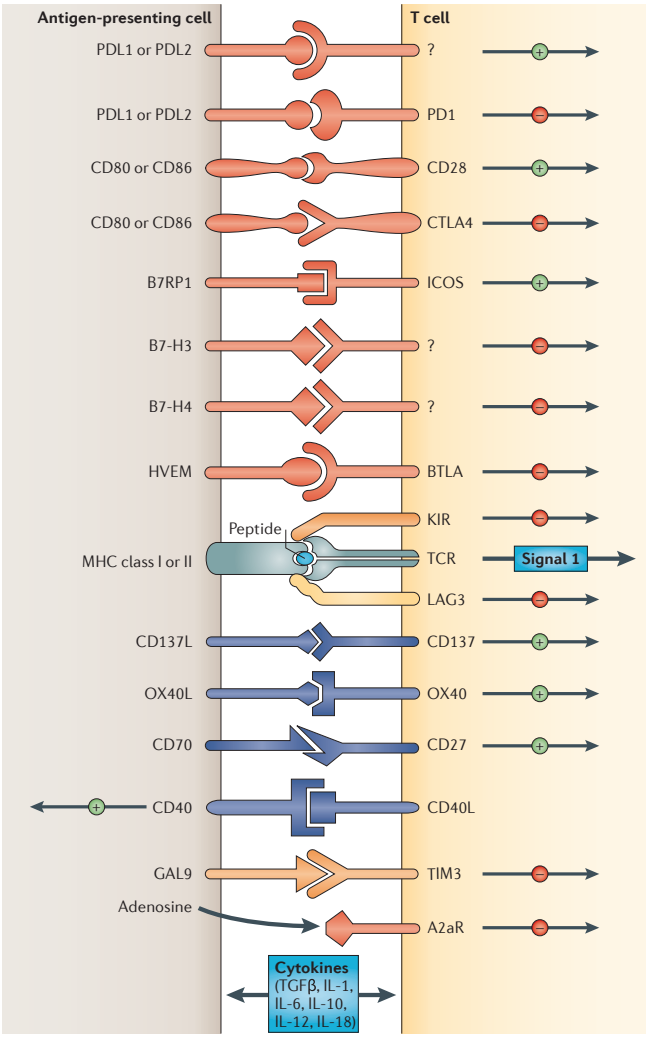

Figure 7. Co-stimulatory and inhibitory interactions regulating T cell responses.

T cell activation is controlled by antigen recognition (signal 1, mediated by peptide–MHC binding to the T cell receptor, TCR) and by co-regulatory signals delivered through ligand–receptor interactions with antigen-presenting cells (APCs). Co-stimulatory pathways (e.g., CD28–CD80/86, ICOS–B7RP1, OX40–OX40L, CD137–CD137L, CD27–CD70, CD40–CD40L) promote proliferation, cytokine secretion, and effector differentiation, while inhibitory checkpoints (e.g., CTLA-4–CD80/86, PD-1–PD-L1/2, TIM-3–Galectin-9, LAG-3–MHC-II, BTLA–HVEM, A2aR–adenosine) attenuate activation and foster T cell dysfunction. These interactions occur both during priming in lymph nodes and in peripheral tissues, including tumors, where they critically shape antitumor immune responses. The balance between stimulatory and inhibitory pathways ultimately determines whether T cells mediate effective tumor rejection or become functionally exhausted.

Source: (23), reproduced with permission from Springer Nature, license number 6153540567645

Collectively, these checkpoints constitute a complex and redundant network that dampens both innate and adaptive immunity, reinforcing tolerance. By co-opting these inhibitory mechanisms, tumors exploit regulatory pathways originally evolved to maintain immune homeostasis and prevent autoimmunity, thereby turning them into barriers to immune elimination. This insight into the biology of immune escape underpins the rationale for targeting immune checkpoints in cancer immunotherapy.

3. The immunosuppressive tumor microenvironment

Beyond tumor-cells-intrinsic mechanisms, the tumor surroundings undergo profound remodeling, giving rise to a microenvironment that suppresses immunity. This tolerogenic TME, composed of immune, stromal, and vascular elements, is now recognized as a distinct hallmark of cancer. Far from being a passive bystander, the TME displays active immunoregulatory properties that lead to immune tolerance and support tumor progression.

Within the TME, immunosuppressive cell populations accumulate, including regulatory T cells (Tregs), myeloid-derived suppressor cells (MDSCs), and alternatively activated M2 macrophages: Tumor Associated Macrophages (TAMs). These cells inhibit effector lymphocyte function through direct contact, secretion of suppressive cytokines, and metabolic regulation. The release of IL-10 and TGF-β further dampens immune activation, while pro-angiogenic factors such as VEGF contribute to immune exclusion by altering the tumor vasculature. In parallel, metabolic constraints, including hypoxia, acidosis, nutrient depletion, and accumulation of adenosine or lactate, create a hostile environment for effector lymphocytes, limiting their survival and activity (28).

a. Regulatory T cells (Tregs)

Tregs are key mediators of tolerance within the TME. They suppress immune responses by consuming IL-2, thereby depriving effector T cells of this essential growth factor, and by secreting immunosuppressive cytokines such as IL-10 and TGF-β. In addition, they express CTLA-4, which reduces the availability of costimulatory ligands (CD80/CD86) on antigen-presenting cells. These mechanisms collectively blunt cytotoxic T cell and NK cell activity and help sustain an immunosuppressive milieu (29), illustrated on **Figure 8**.

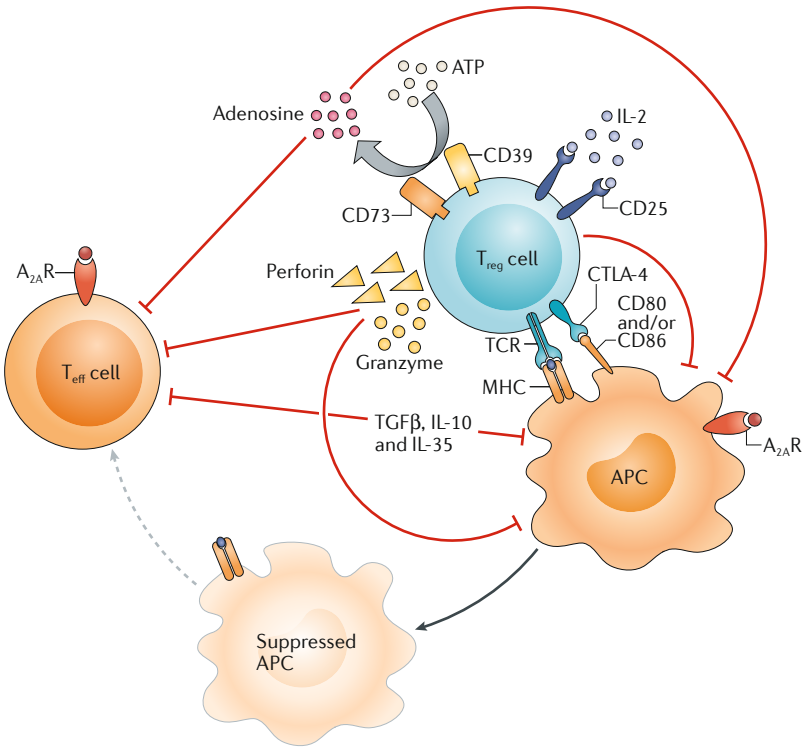

Figure 8. Mechanisms of immune suppression mediated by regulatory T cells (Tregs).

Tregs suppress antitumor immune responses through multiple mechanisms. They express high-affinity IL-2 receptor (CD25), limiting IL-2 availability for effector T cells, and secrete immunosuppressive cytokines such as TGF-β, IL-10, and IL-35. Tregs also inhibit antigen-presenting cells (APCs) via CTLA-4 binding to CD80/CD86 and by inducing an immunoregulatory phenotype. In addition, Tregs generate extracellular adenosine by sequential expression of CD39 and CD73, further dampening Teff responses through adenosine receptor (A2AR) signaling. Cytolytic mechanisms including perforin and granzyme secretion can directly eliminate effector T cells or APCs. Collectively, these pathways converge to restrain antitumor immunity and sustain immune tolerance within the tumor microenvironment.

Source: (29), reproduced with permission from Springer Nature, license number 6153540866810

b. Myeloid-derived suppressor cells (MDSCs)

MDSCs are immature myeloid cells that expand during tumor development. They inhibit immunity through both metabolic and signaling pathways. By expressing arginase-1, they deplete arginine and other amino acids required for T cell proliferation. In parallel, they express inducible nitric oxide synthase (iNOS), which generates high levels of NO. NO can combine with reactive oxygen species to form reactive nitrogen species (RNS) such as peroxynitrite, which disrupt T cell receptor signaling and induce oxidative stress in lymphocytes. Beyond these metabolic effects, MDSCs secrete IL-10 and TGF-β and promote the expansion of Tregs, amplifying the immunosuppressive circuitry (30). The main distinguishing features of MDSCs compared with classical neutrophils and monocytes, as well as their suppressive mechanisms, are summarized in **Figure 9**.

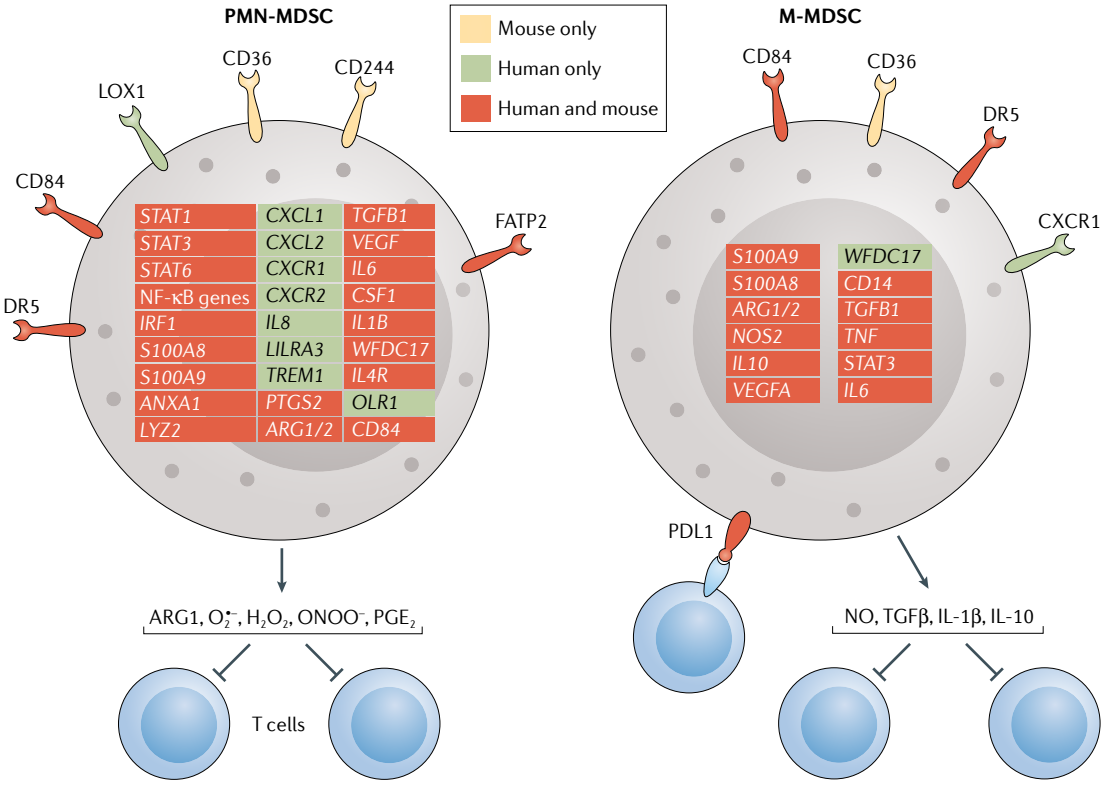

Figure 9. Distinguishing MDSCs from classical neutrophils and monocytes.

The figure shows genes (inside the cells) and surface molecules that distinguish polymorphonuclear myeloid-derived suppressor cells (PMN-MDSCs, left) and monocytic MDSCs (M-MDSCs, right) from neutrophils and monocytes. Color coding indicates whether factors are reported in mouse only (yellow), human only (green), or both mouse and human (red). Arrows indicate major immunosuppressive mechanisms used by MDSCs, including production of reactive oxygen species, nitric oxide, prostaglandin E_2, and immunosuppressive cytokines. CXCR1, CXC-chemokine receptor 1; FATP2, fatty acid transport protein 2; LOX1, lectin-type oxidized LDL receptor 1; NO, nitric oxide; PGE_2, prostaglandin E_2.

Source : (30), Reproduced with permission from Springer Nature, license number 6140730747035

c. Tumor-associated macrophages (TAMs)

TAMs often acquire an immunoregulatory “M2-like” phenotype, characterized by the secretion of IL-10, TGF-β, and pro-angiogenic factors such as VEGFA. Beyond promoting tissue remodeling, angiogenesis, and stromal expansion, TAMs directly suppress cytotoxic lymphocytes through the expression of inhibitory ligands such as PD-L1 and B7-H4, as well as through metabolic mechanisms, including arginase-1–mediated arginine depletion and the generation of reactive oxygen species. TAMs also secrete chemokines such as CCL22 and CCL17 that recruit regulatory T cells, and their release of IL-10 contributes to dendritic cell dysfunction, thereby amplifying immunosuppressive networks. At the structural level, TAMs interact with cancer-associated fibroblasts to promote extracellular matrix remodeling and immune exclusion, while their secretion of VEGFA, PIGF, ANG2, and WNT7B contributes to abnormal angiogenesis and altered vascular integrity. Notably, in several tumor types, TAMs accumulate at the invasive front to form a macrophage mantle, a dense cellular layer that restricts T cell infiltration into the tumor core, exemplifying how the spatial organization of the TME enforces

immune exclusion (31), These direct and indirect mechanisms of immune suppression are summarized in **Figure 10**.

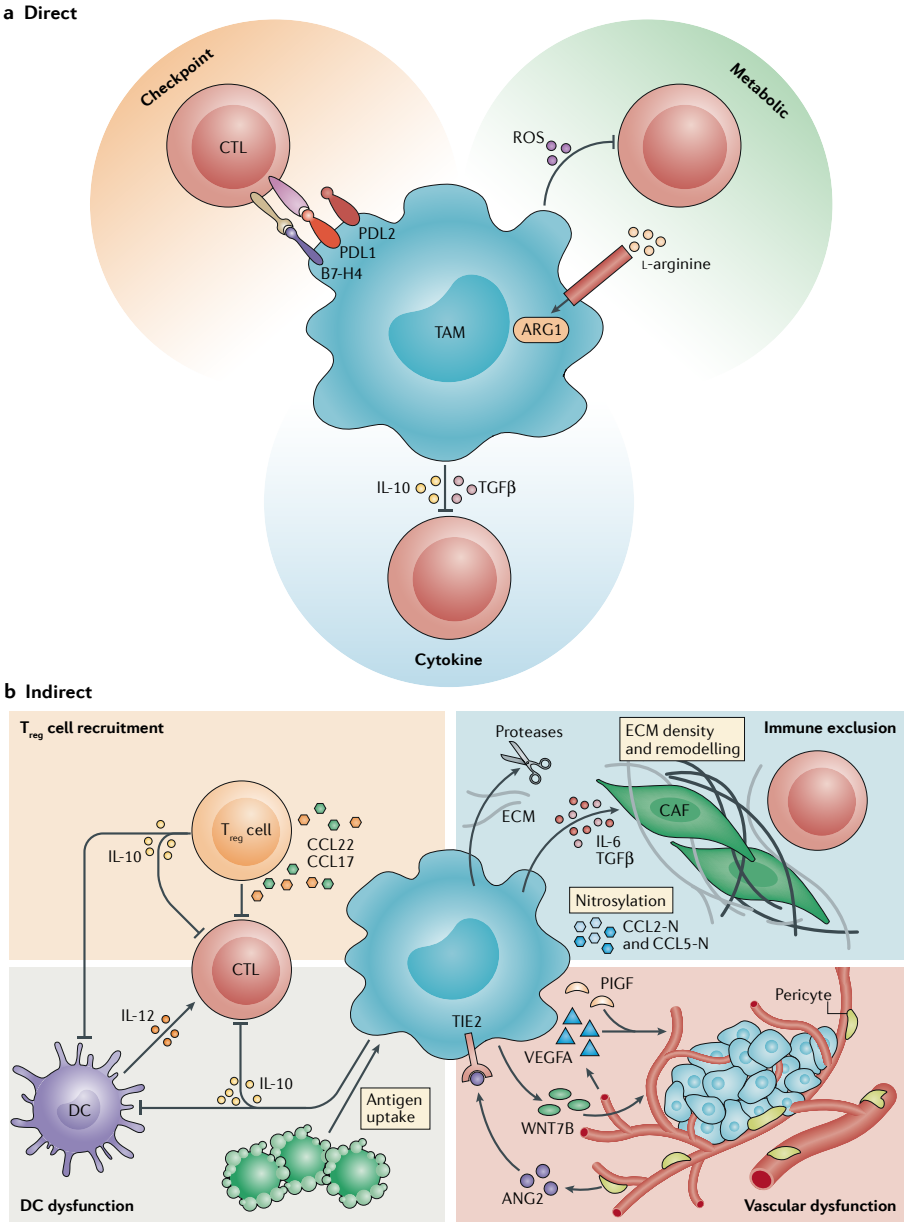

Figure 10. Direct and indirect mechanisms of immunosuppression mediated by TAMs.

(a) Direct mechanisms include the expression of immune checkpoint ligands (PD-L1, PD-L2, B7-H4) inhibiting cytotoxic T lymphocytes (CTLs), metabolic suppression through arginase-1 (ARG1)-mediated arginine depletion and generation of reactive oxygen species (ROS), and secretion of immunosuppressive cytokines such as IL-10 and TGF-β. (b) Indirect mechanisms comprise the recruitment of regulatory T cells (Tregs) via chemokines (CCL22, CCL17), induction of dendritic cell (DC) dysfunction with impaired antigen presentation, and remodeling of the extracellular matrix (ECM) by cancer-associated fibroblasts (CAFs), leading to immune exclusion. TAMs also contribute to vascular dysfunction through secretion of VEGFA, PlGF, WNT7B, and ANG2, which alter vessel stability and promote tumor angiogenesis.

Source: (31), reproduced with permission from Springer Nature, license number 6140730747035

d. Cancer-associated fibroblasts (CAFs) and the extracellular matrix

Cancer-associated fibroblasts (CAFs) are abundant stromal components that reinforce immune tolerance through both biochemical and structural mechanisms. They secrete immunoregulatory mediators such as TGF-β, IL-6, and CXCL12, which recruit suppressive immune populations and inhibit cytotoxic T cells. In addition, CAFs release pro-angiogenic and tumor-promoting factors, thereby supporting tumor growth and neovascularization. CAFs also shape the metabolic microenvironment by exporting lactate, which fuels oxidative metabolism in cancer cells but acidifies the TME and suppresses T and NK cell activity. They release alanine and aspartate, which serve as biosynthetic substrates for proliferating tumor cells. In parallel, CAFs contribute to amino acid depletion, depriving effector lymphocytes of key nutrients such as arginine and tryptophan, thereby limiting their proliferation and cytotoxic capacity. Structurally, they produce large amounts of extracellular matrix (ECM) proteins, generating a dense stromal barrier that restricts T cell infiltration and limits the penetration of antibodies and therapeutic agents. ECM stiffening and altered architecture further impair immune cell migration and function, thereby reinforcing immune exclusion (32). The main mechanisms by which CAFs shape the immunosuppressive tumor microenvironment are summarized in **Figure 11**.

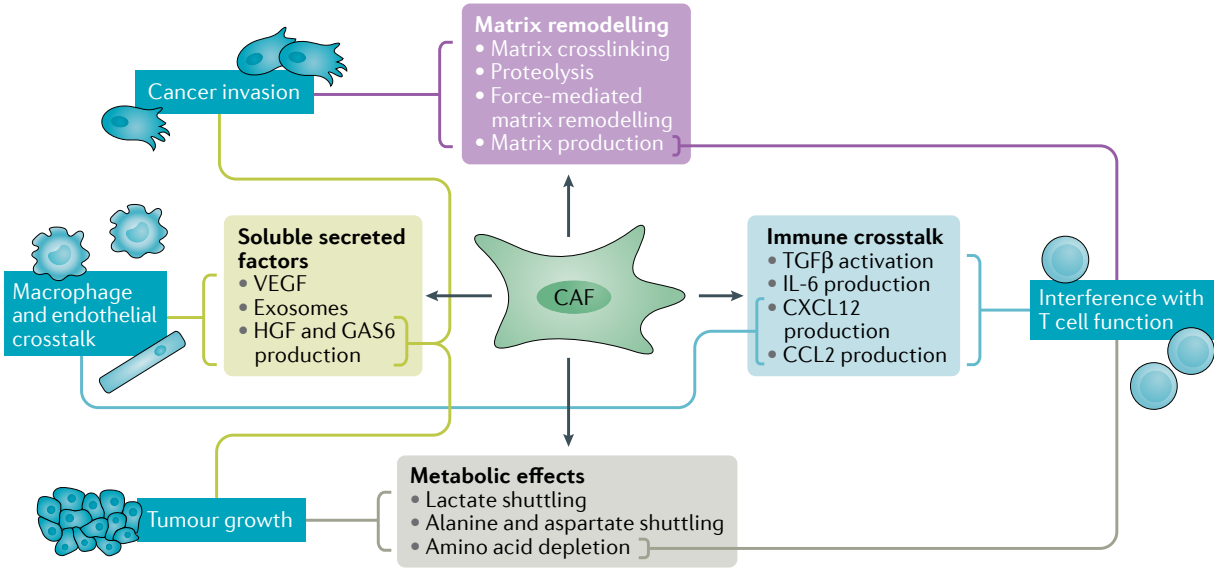

Figure 11. Summary of cancer-associated fibroblast functions and the mechanisms by which they are achieved.

CAFs influence tumor progression through multiple mechanisms. They remodel the extracellular matrix (ECM) by matrix crosslinking, proteolysis, force-mediated remodeling, and matrix production. CAFs secrete soluble mediators including VEGF, hepatocyte growth factor (HGF), growth arrest-specific 6 (GAS6), and exosomes, supporting angiogenesis and tumor growth. Metabolic activities include lactate and amino acid shuttling as well as nutrient depletion, thereby fueling cancer cells while restraining immune responses. Crosstalk with immune cells involves the production of TGF-β, IL-6, CXCL12, and CCL2, which interfere with T cell function and promote immunosuppression. CAFs also interact with macrophages and endothelial cells to facilitate tumor growth and invasion.

Source: (33), under CC BY 4.0

e. Endothelium and angiogenesis

Tumor vasculature, largely driven by VEGF, is aberrant in both structure and function. Irregu-

lar vessels and altered expression of adhesion molecules limit lymphocyte trafficking into the tumor parenchyma, a phenomenon often described as immune exclusion. Angiogenesis thus simultaneously sustains tumor nutrition and imposes a barrier to effective immunity. These vascular abnormalities develop together with stromal elements, especially CAFs and TAMs, which reinforce immune evasion through extracellular matrix remodeling and cytokine secretion (34). However, this phenotype is not uniform across cancers: desmoplastic tumors such as pancreatic ductal adenocarcinoma show strong stromal barriers and immune exclusion, whereas other malignancies, including RCC, are highly vascularized and can remain permissive to immune infiltration.

f. Metabolic constraints

In addition to cellular interactions, physical and metabolic constraints within tumors act as primary drivers of the transition toward a tolerogenic microenvironment. Hypoxia, acidosis, and nutrient depletion not only impair effector T and NK cell function but also promote the emergence of immunosuppressive populations. For example, as seen above, hypoxia skews macrophages toward an M2-like TAM phenotype, lactate accumulation fosters Treg differentiation, and extracellular acidification favors MDSC expansion. Thus, the metabolic landscape of the tumor not only suppresses existing immune responses but actively shapes the recruitment and polarization of CAFs, Tregs, and other stromal components that sustain immune evasion.

g. Conclusion

Together, these cellular, metabolic, and structural mechanisms create a highly immunosuppressive tumor microenvironment. Its recognition as a hallmark of cancer highlights that immune escape results not only from tumor-intrinsic alterations but also from the broader ecosystem that emerges through interactions between malignant cells and their surrounding stroma. Over the past decade, accumulating evidence has firmly established the tumor microenvironment as a key determinant of therapeutic response, particularly to immunotherapies. This underscores that preclinical models cannot rely solely on tumor cell–intrinsic properties, but must incorporate the complexity of the microenvironment, including stromal, vascular, and immune compartments, as well as their fine-grained interactions. Recapitulating these dimensions is crucial for experimental systems to accurately predict treatment outcomes and guide the development of strategies designed to overcome the barriers imposed by the TME.

4. T cell exhaustion

CTLs are universally recognized as the main effectors of antitumoral immunity. They contribute both to the early elimination of transformed cells and to the establishment of long-term protective memory against cancer. However, in the setting of chronic tumor exposure, persistent antigen stimulation combined with sustained inhibitory signaling progressively reprograms

CTLs into dysfunctional states collectively termed “exhaustion”. Exhausted T cells are characterized by impaired proliferation, reduced cytokine secretion, and diminished cytotoxic activity, ultimately compromising immune control of tumor growth. First described in chronic viral infections such as lymphocytic choriomeningitis virus (LCMV) in mice, exhaustion is now recognized as the predominant functional state of T cells within tumors and a central feature of antitumor immune evasion. Compared with effector T cells, exhausted lymphocytes remain antigen-specific and persist in the tumor microenvironment but progressively lose function while acquiring sustained expression of inhibitory receptors including PD-1, TIM-3, LAG-3, and TIGIT. They also undergo profound transcriptional and metabolic reprogramming, exemplified by the induction of the transcription factor TOX and mitochondrial dysfunction (**Figure 12**). Importantly, because tumor-infiltrating T cells are largely exhausted, the current generation of immunotherapies fundamentally relies on reversing or alleviating this dysfunctional state (35).

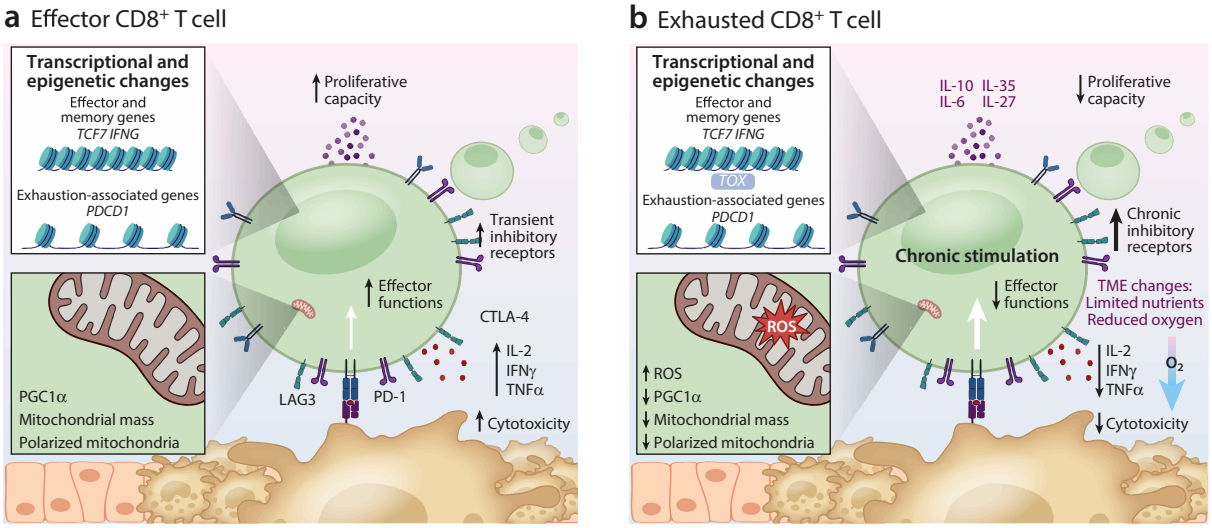

Figure 12. Functional and molecular differences between effector and exhausted CD8⁺ T cells.

(a) Effector CD8⁺ T cells display high proliferative capacity, robust cytokine secretion (IL-2, IFN-γ, TNF-α), and cytotoxic activity. They express effector and memory-associated genes (e.g., *TCF7*, *IFNG*), maintain polarized mitochondria with preserved metabolic fitness, and only transiently express inhibitory receptors. (b) Exhausted CD8⁺ T cells arise under chronic antigen stimulation and tumor microenvironmental stress. They progressively lose proliferative potential, cytokine secretion, and cytotoxicity, while upregulating inhibitory receptors (e.g., PD-1, LAG-3, CTLA-4). This phenotype is transcriptionally enforced by *TOX*, a master regulator that drives and stabilizes the expression of exhaustion-associated genes, including checkpoint molecules such as *PDCD1*. Exhausted T cells also show mitochondrial dysfunction and increased ROS production, further reinforced by hypoxia, nutrient depletion, and immunosuppressive cytokines (IL-10, IL-6, IL-35, IL-27).

Source: (36), under CC BY 4.0

Importantly, T cell exhaustion is not defined by a single, fixed phenotype, but rather represents a dynamic continuum of states shaped by chronic antigen exposure, as observed in chronic infections and cancer. Along this trajectory, exhausted CD8⁺ T cells can be subdivided into distinct subpopulations (**Figure 13**).

Stem-like progenitor exhausted cells, maintained by the transcription factor TCF1 (T cell factor 1), are characterized by high proliferative potential, self-renewal capacity, and responsiveness

to cytokines such as IL-21.

Intermediate or transitory exhausted cells, partly regulated by T-bet (TBX21), begin to lose proliferative potential and show limited cytotoxicity, despite retaining partial effector function. They express multiple inhibitory receptors such as PD-1 and TIM-3, indicating an early commitment toward dysfunction.

At the end of the spectrum, terminally exhausted cells, driven by TOX and EOMES, display high expression of inhibitory molecules (e.g., PD-1, LAG3, TIGIT, CD39), profound epigenetic imprinting, and minimal capacity for proliferation, migration, or cytolysis. These cells accumulate within the tumor core and show poor responsiveness to current immunotherapies. Overall, the severity of functional impairment increases along this differentiation axis, while the potential for reinvigoration by therapeutic agents, such as anti-PD-1 or anti-CTLA-4 antibodies, is largely restricted to the TCF1$^+$ stem-like pool. Understanding and targeting these subsets is therefore critical for improving the efficacy of cancer immunotherapies (35,37).

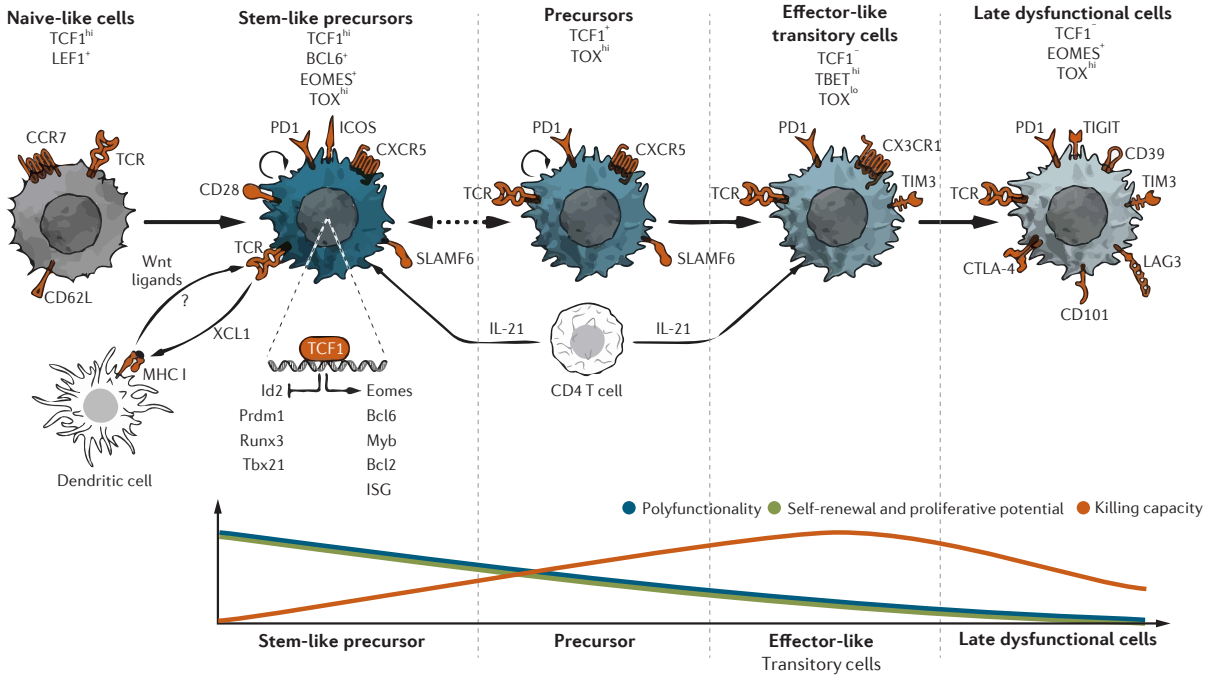

Figure 13. Differentiation trajectory of exhausted CD8$^+$ T cells during chronic antigen exposure.
In settings of persistent antigen stimulation, such as chronic infection or cancer, CD8$^+$ T cells undergo progressive differentiation from naive-like cells (characterized by TCF1^{hi} and LEF1$^+$ expression) toward terminally dysfunctional populations. This continuum includes intermediate subsets such as stem-like precursors, transitory precursors, and effector-like cells, each defined by distinct transcriptional regulators (e.g., *TCF1*, *TOX*, *EOMES*) and surface markers (e.g., PD1, SLAMF6, TIM3, LAG3). Functional properties evolve along this trajectory: cytotoxic capacity transiently increases before declining, while polyfunctionality and proliferative potential progressively diminish. Maintenance of stem-like subsets is supported by extrinsic signals such as IL-21 from CD4$^+$ T cells, and Wnt or XCL1-dependent cues from dendritic cells.

Source: (37), reprinted with permission from AAAS

Thus, T cell exhaustion exemplifies the paradox of tumor immunity: an antigen-specific response is maintained but rendered ineffective through functional reshaping. By locking T cells into dysfunctional states, exhaustion constitutes a major barrier to tumor control and provides a key rationale for immunotherapies designed to restore or bypass exhausted lymphocyte func-

tion.

Taken together, these mechanisms illustrate that immune escape is not solely the result of tumor-intrinsic changes, but rather emerges from the interplay between malignant cells, the immunosuppressive tumor microenvironment, and the progressive dysfunction of effector lymphocytes. A comprehensive overview of these immune evasion mechanisms is provided in **Figure 14**, which schematically summarizes the major strategies by which tumors suppress or avoid immune responses. This includes impaired antigen presentation, immunosuppressive cytokines and regulatory cells, stromal and metabolic modulation of the tumor microenvironment, and the upregulation of inhibitory immune checkpoints.

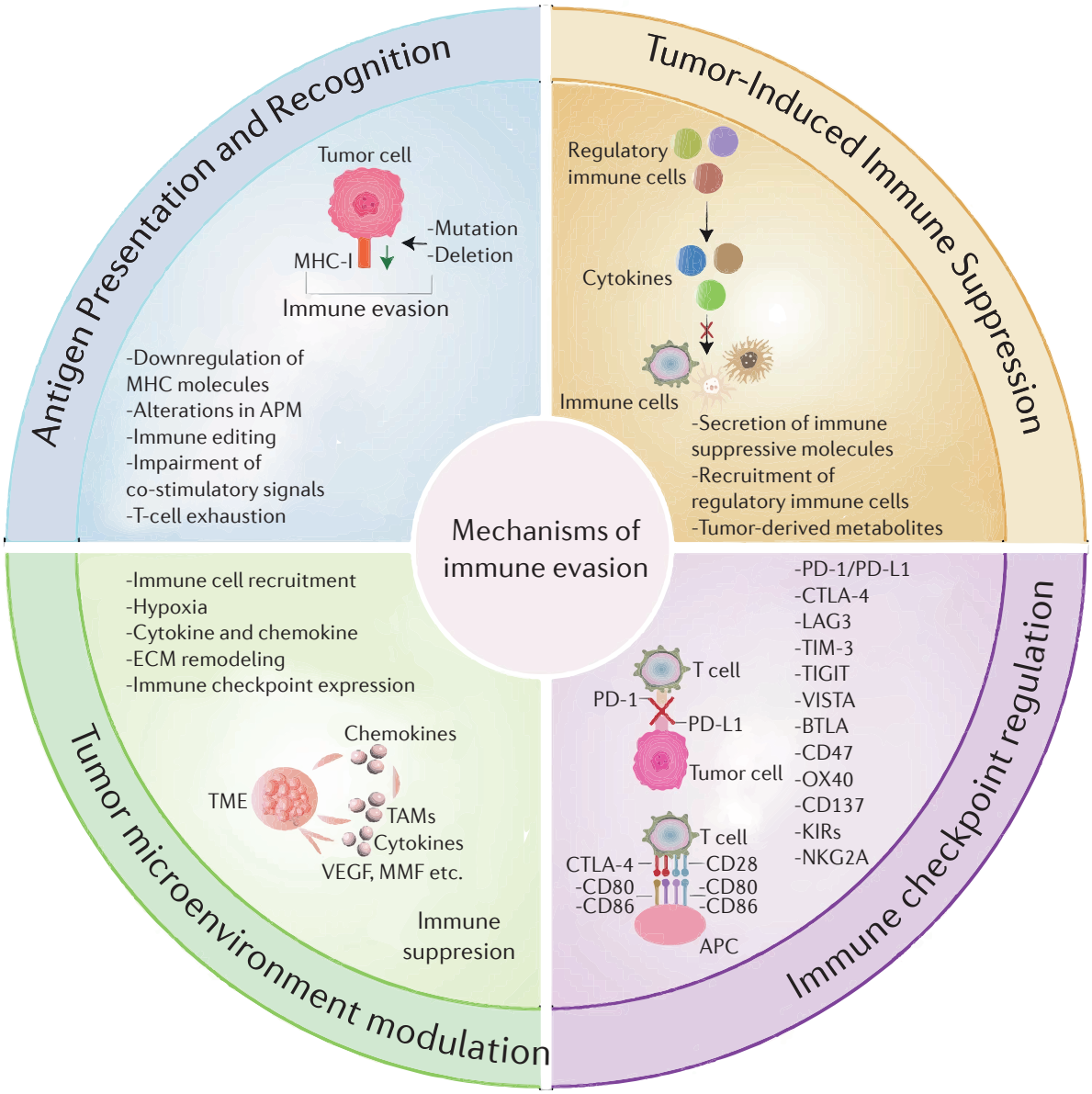

Figure 14. Mechanisms of immune evasion in cancer.

The major strategies employed by tumors to escape immune recognition and elimination are summarized. The central concept of "immune evasion" is organized into four main, interconnected mechanisms: 1- Tumor-induced immune suppression: Cancer cells actively shape an immunosuppressive environment through the secretion of inhibitory cytokines (e.g., TGF-β, IL-10), recruitment of regulatory immune cell populations such as regulatory T cells (Tregs) and myeloid-derived suppressor cells (MDSCs), and the production of tumor-derived metabolites. 2- Immune checkpoint regulation: Tumors exploit co-inhibitory pathways, including PD-1/PD-L1, CTLA-4, LAG-

3, TIM-3, TIGIT, and others, to inactivate cytotoxic T lymphocytes and suppress antitumor immunity. These checkpoints are expressed not only on tumor cells, but also on stromal and immune components within the TME. 3- Tumor microenvironment modulation: Hypoxia, metabolic reprogramming, extracellular matrix (ECM) remodeling, stromal cell interactions, dysregulated chemokine and cytokine networks collectively generate physical and biochemical barriers that impair immune cell infiltration, function, and survival. 4- Impairment of antigen presentation and recognition: Tumor cells reduce their immunogenicity through the downregulation or loss of MHC class I molecules, mutations or deletions in components of the antigen processing machinery (APM), immune editing, and suppression of co-stimulatory signals. This limits effective T cell priming and antigen-specific cytotoxic responses.

Source: (38), under CC BY 4.0

Because these processes critically shape the outcome of antitumor immunity, experimental models designed to study or test immunotherapies must take them into account. Models that incorporate key features of the TME and capture the diversity of T cell subsets, including exhausted populations, are essential to accurately evaluate therapeutic strategies and to predict their clinical relevance.

The recognition of these barriers has directly inspired the development of cancer immunotherapies. By targeting the molecular and cellular pathways that underlie immune tolerance, modern treatments seek not only to restore effective antitumor responses but also to harness the unique potential of the immune system for durable tumor control.

IV. Cancer Immunotherapy

A. General principles

For decades, cancer therapy relied primarily on surgery, radiotherapy, and cytotoxic chemotherapy. These approaches, although effective in certain settings, are limited by a lack of specificity, considerable toxicity, and frequent resistance. The advent of targeted therapies, such as kinase inhibitors, brought important advances by interfering with oncogenic signaling pathways, but durable responses remained uncommon outside of a few tumor types (39).

A major conceptual shift occurred with the emergence of immunotherapies, which aim not to attack tumor cells directly but to stimulate or restore the patient's own immune responses against cancer. By mobilizing immune mechanisms, most prominently the adaptive T cell response, these treatments have the potential to provide specificity, adaptability, and long-term memory, features that set them apart from other therapeutic modalities.

The idea of mobilizing the immune system to treat cancer is not new. As early as the late 19th century, William Coley attempted to stimulate anticancer immunity by injecting bacterial toxins, an approach that, despite inconsistent results, laid the groundwork for the concept of immunotherapy (40). However, throughout much of the 20th century, the field remained largely theoretical, with sporadic clinical applications such as interferon or interleukin-2 therapies. It was not until the turn of the 21st century that immunotherapy achieved transformative clinical

success, ushered in by the development of immune checkpoint inhibitors (ICIs). While current breakthroughs largely rely on T cell–mediated immunity, other immune compartments, including innate and humoral responses, are increasingly being explored as complementary therapeutic targets.

In the following sections, we will review the main classes of immunotherapies, their mechanisms of action, and the challenges that remain in achieving sustained benefit across different cancer types.

1. Immune Checkpoint Inhibitors (ICIs): Canonical Targets

Two checkpoint pathways, CTLA-4 and PD-1/PD-L1, have been most extensively targeted in cancer therapy. While their inhibitory biology has been described above, their blockade with monoclonal antibodies provided the first clinical proof that suppressive pathways of the immune system could be therapeutically reversed. CTLA-4 inhibition with ipilimumab, approved in 2011 for metastatic melanoma (41,42), established the feasibility of checkpoint blockade. In parallel, Tasuku Honjo's discovery of PD-1 (43) paved the way for the development of antibodies targeting PD-1 (nivolumab, pembrolizumab) and PD-L1 (atezolizumab, durvalumab, avelumab), which have since shown efficacy across multiple malignancies, including melanoma, lung cancer, RCC, and Hodgkin lymphoma (44).

The seminal contributions of James Allison on CTLA-4 and Tasuku Honjo on PD-1 were jointly recognized with the 2018 Nobel Prize in Physiology or Medicine, underlining the paradigm-shifting impact of checkpoint inhibition on cancer therapy. Mechanistically, CTLA-4 blockade acts during T cell priming in lymph nodes, enhancing the generation of new effector clones and diversifying the antitumor response (42). In contrast, PD-1/PD-L1 blockade primarily restores the function of exhausted T cells already present within tumors, enabling them to proliferate, secrete cytokines such as IFNγ, and recover cytotoxic activity. This reinvigoration is typically partial rather than complete, but sufficient to shift the balance toward effective tumor control. The complementary mechanisms of these pathways explain why their combination can yield synergistic clinical benefit.

The main therapeutic goal of current ICI strategies is to reverse or prevent T cell exhaustion. As shown in **Figure 15**, anti-PD-1 blockade is thought to act at different stages of $CD8^+$ T cell dysfunction, restoring effector function, promoting clonal replacement, and potentially fostering the emergence of new states that sustain antitumor responses.

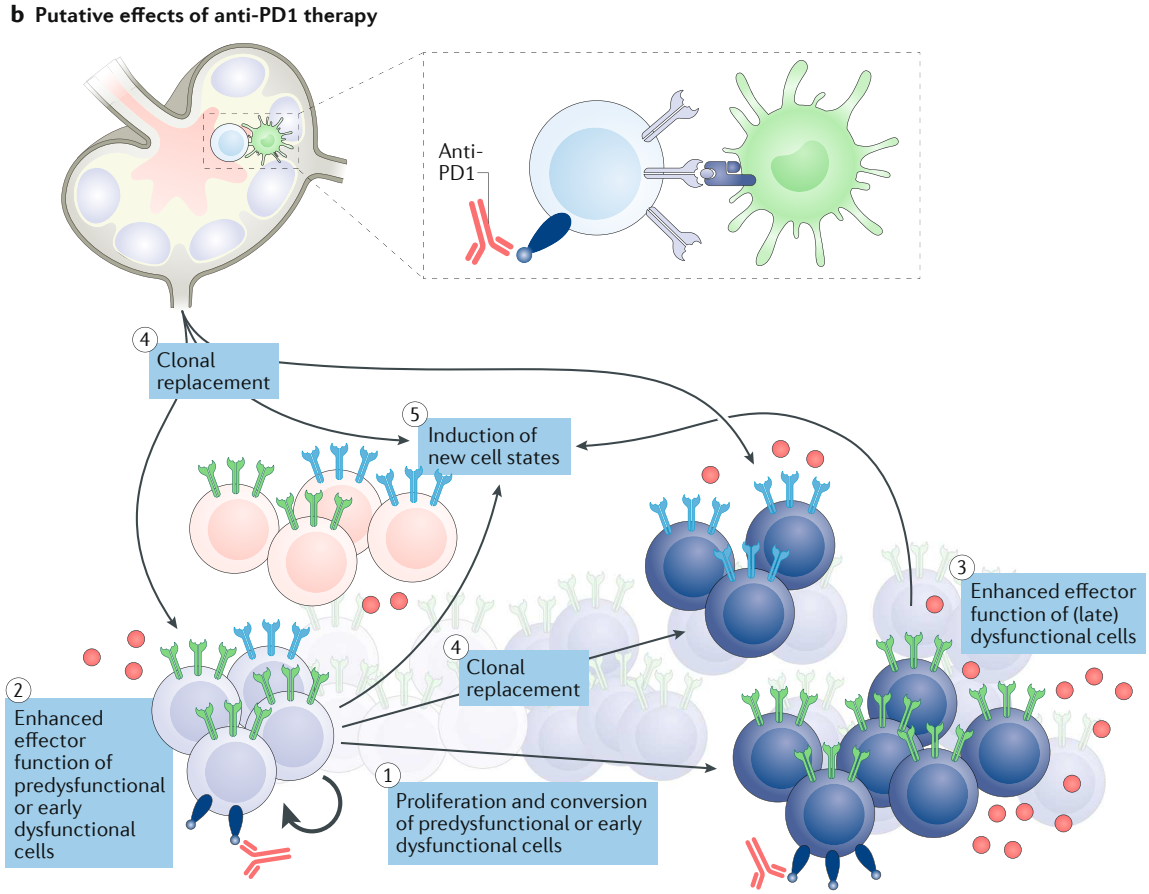

Figure 15. Proposed effects of anti-PD-1 therapy on CD8⁺ T cell states.

Anti-PD-1 blockade is hypothesized to act on different stages of dysfunctional T cells within and outside the tumor microenvironment. Mechanisms include proliferation and conversion of pre- or early dysfunctional T cells (TCF1⁺), partial restoration of effector function in early and late dysfunctional populations, potential replacement of the TCR repertoire through influx or expansion of clones, and the emergence of novel T cell states. Together, these processes may contribute to durable antitumoral responses.

Source: (35), reproduced with permission from Springer Nature, license number 6154811399242

On the other hand, the mechanism of action of anti-CTLA-4 therapy remains under investigation. Initially, these antibodies were thought to act primarily by blocking the CTLA-4/B7 interaction, thereby restoring the priming phase of T cell activation. However, more recent findings indicate that their therapeutic efficacy largely depends on the depletion of regulatory Tregs. Antibodies such as ipilimumab can mediate Fc receptor–dependent cytotoxicity against intratumoral Tregs, reducing their suppressive influence and thereby enhancing effector T cell activity (45).

Together, CTLA-4 and PD-1 blockade have laid the foundations of modern immuno-oncology, demonstrating that therapeutic targeting of immune regulatory pathways can elicit durable tumor regressions, sometimes lasting years after treatment cessation. Their clinical success has not only revolutionized the management of several malignancies but has also established immunotherapy as the fourth pillar of cancer treatment, alongside surgery, radiotherapy, and targeted therapies.

2. Immune checkpoint blockade: non canonical

In addition to CTLA-4 and PD-1, multiple other immune checkpoints have been identified, many of which are co-expressed with PD-1 on exhausted T cells. Several of these have been pursued as therapeutic targets. LAG-3 was the first to achieve clinical validation: the anti–LAG-3 antibody relatlimab, combined with nivolumab, improved progression-free survival in advanced melanoma and obtained FDA approval in 2022. TIM-3 is being investigated with agents such as sabatolimab, mainly in hematologic cancers but also in early-phase studies in solid tumors. TIGIT blockade has generated considerable interest, with antibodies including tiragolumab and ociperlimab under clinical evaluation, though recent results have been mixed. Other checkpoints, such as VISTA, remain at earlier stages of development.

Although these approaches extend the reach of checkpoint inhibition, they largely converge on exhausted T cell populations already modulated by PD-1/PD-L1, raising concerns about redundancy and limiting incremental benefit. This has prompted growing interest in checkpoints that regulate other immune compartments, such as NK cells, macrophages, and myeloid populations, where novel therapeutic strategies may provide non-overlapping mechanisms of action.

Examples include the NKG2A–HLA-E axis, which suppresses both NK and $CD8^+$ T cell activity and is targeted by monalizumab, and the CD47–SIRPα pathway, a macrophage "don't eat me" signal currently being blocked by agents such as magrolimab. HLA-G represents another promising axis: this non-classical MHC class I molecule suppresses T cells, NK cells, and myeloid populations via ILT2 and ILT4. The anti–HLA-G antibody TTX-080 (Tizona Therapeutics) exemplifies ongoing efforts to broaden checkpoint inhibition beyond the adaptive T cell axis.

By diversifying beyond T cell–centric pathways, these strategies aim to overcome resistance to PD-1 blockade and extend the benefits of immunotherapy to a broader patient population.

3. Combination strategies

Despite their success, immune checkpoint inhibitors benefit only a fraction of patients, and resistance remains a major limitation. This has motivated extensive efforts to combine checkpoint blockade with other treatments. Broadly, three strategies have been pursued:

- Dual checkpoint inhibition, exemplified by CTLA-4 plus PD-1 blockade, enhances both T cell priming and effector reinvigoration.
- Checkpoint plus anti-angiogenic therapy, which counters the immunosuppressive effects of VEGF and improves lymphocyte infiltration.
- Checkpoint plus conventional modalities such as chemotherapy, radiotherapy, or targeted therapies, which can increase tumor immunogenicity and synergize with immune activation.

These approaches share a common rationale: to overcome resistance by reshaping the tumor–immune interface and converting poorly infiltrated “cold” tumors into inflamed “hot” tumors more susceptible to immune attack. The clinical development of such combinations has been particularly impactful in RCC, which will be discussed in detail in the following chapter.

4. Other classes of cancer immunotherapy

While immune checkpoint inhibitors have been the most transformative immunotherapies to date, they represent only one facet of a much broader field. Several other strategies are being developed to stimulate or redirect antitumoral immunity.

a. Cytokine therapies

Cytokines were among the earliest immunotherapies tested in cancer. High-dose IL-2 and interferon-α (IFNα) demonstrated that systemic activation of immunity could induce durable remissions in selected patients, particularly in melanoma and RCC, albeit at the cost of significant toxicity. Both agents reached regulatory approval in the 1990s and remain in limited use today. Building on these pioneers, next-generation cytokine therapies are being engineered to enhance activity while reducing systemic side effects. Agents based on IL-15, which supports NK and memory T cell survival, or IL-12 and IL-7, which promote T cell expansion and function, are under active investigation. Modified IL-2 variants such as aldesleukin or pegylated IL-2 derivatives aim to selectively expand effector over regulatory T cells.

b. Adoptive cell therapies (ACT)

ACT consists in the infusion of autologous or engineered immune cells with enhanced antitumoral activity. The first approach to show efficacy was tumor-infiltrating lymphocyte (TIL) therapy, where lymphocytes expanded ex vivo are reinfused into patients. More recently, chimeric antigen receptor (CAR) T cells, genetically engineered to recognize tumor antigens independently of MHC, have revolutionized the treatment of hematologic malignancies and are now approved for multiple B cell leukemias, lymphomas, and multiple myeloma. Efforts are ongoing to adapt CAR-T and TCR-engineered T cells for solid tumors, and NK-based cellular therapies are in early clinical testing.

c. Cancer vaccines

Therapeutic cancer vaccines aim to prime or boost adaptive immunity by presenting tumor antigens in an immunogenic context. While no therapeutic vaccine has yet achieved broad approval in solid tumors, the dendritic cell–based vaccine sipuleucel-T is approved for prostate cancer, and mRNA- or neoantigen-based strategies are currently being evaluated in clinical trials, particularly in melanoma.

d. Oncolytic viruses

Oncolytic virotherapy exploits viruses engineered to selectively infect and lyse tumor cells while stimulating local immune responses. The first FDA-approved agent, talimogene laherparepvec (T-VEC), a modified herpes simplex virus expressing GM-CSF, has demonstrated efficacy in advanced melanoma. Several other viral platforms, including adenoviruses, vaccinia, and reoviruses, are under clinical investigation both as direct cytotoxic agents and as immune adjuvants that enhance responses to checkpoint blockade.

Together, these approaches highlight the diversity of strategies in cancer immunotherapy. Among them, only a few: high-dose IL-2 and IFNα, CAR-T cells in hematologic malignancies, sipuleucel-T, and T-VEC, have achieved regulatory approval. The vast majority remain under active clinical development. By harnessing cytokines, adoptive cells, vaccines, or oncolytic viruses, these strategies complement checkpoint blockade and underscore the central role of the immune system as a therapeutic partner in oncology.

5. Conclusion on immunotherapy

Over the past two decades, immunotherapy in the form of ICIs has profoundly transformed the therapeutic landscape of oncology. For the first time, patients with cancers of historically dismal prognosis, such as metastatic melanoma, non-small cell lung cancer (NSCLC), and RCC, can experience durable responses and long-term survival. This paradigm shift has redefined expectations in advanced disease and firmly established immunotherapy as a cornerstone of modern cancer care.

Yet, these advances remain incomplete. A substantial proportion of patients fail to respond from the outset, while others relapse after an initial response due to the emergence of adaptive resistance. The mechanisms underlying these limitations are diverse, encompassing tumor-intrinsic loss of antigenicity, exclusionary or suppressive tumor microenvironments, and progressive dysfunction of effector lymphocytes. Overcoming these barriers requires not only novel therapeutic strategies but also robust experimental models capable of faithfully reproducing tumor–immune interactions, capturing cellular heterogeneity, and providing functional readouts of immune activity to predict patient response, study mechanisms of resistance, and test innovative immunotherapies.

Among solid tumors, RCC represents a unique paradigm: despite being one of the most immune-infiltrated cancers, antitumor responses are often limited, reflecting profound immunosuppressive mechanisms within its microenvironment. This paradox, together with the central role of ICIs in its management, makes RCC an ideal setting to investigate both the achievements and the limitations of immunotherapy, and underscores the need for experimental models capable of elucidating and predicting mechanisms of resistance. The following chapter will therefore focus on RCC, with an emphasis on its biological and immunological specificities.

Chapter 2: Renal Cell Carcinoma

This chapter provides an overview of current knowledge on renal cell carcinoma, with a particular emphasis on clear cell renal cell carcinoma (ccRCC). It highlights the biological and immunological hallmarks of this malignancy and outlines the need for preclinical models able to recapitulate these features in order to support the development of innovative immunotherapeutic strategies.

I. Epidemiology, Risk Factors, and Hereditary Syndromes

Kidney cancer accounts for approximately 2–3% of adult malignancies. According to GLOBOCAN 2022, around 435,000 new cases and 156,000 deaths were reported globally in 2022, with Europe contributing nearly one third of the burden, i.e. ~146,000 new diagnoses and 52,000 deaths. In France, kidney cancer represents a significant health issue, with approximately 14,500 new cases and 5,000 deaths annually (metropolitan France). Incidence increases with age, peaking in the sixth to seventh decades, and RCC is nearly twice as frequent in men as in women (male-to-female ratio ~2:1) (46) . RCC constitutes the vast majority of kidney cancers, accounting for approximately 90% of kidney cancers.

Several modifiable risk factors have been consistently associated with RCC development. Cigarette smoking remains one of the strongest, increasing RCC risk by approximately 1.5- to 2-fold, with risk declining progressively after cessation. Obesity and metabolic syndrome are also contributors. Hypertension and long-term antihypertensive therapy further increase RCC risk, while chronic kidney disease and prolonged dialysis predispose to acquired cystic disease–associated RCC. Occupational exposures, particularly to trichloroethylene, have also been implicated.

In addition, diabetes, family history of kidney cancer, and certain lifestyle factors such as dietary habits, alcohol consumption, and physical activity have been suggested to influence RCC risk, although the strength and consistency of supporting evidence remain lower compared to the major established factors (47).

Although most RCC cases are sporadic, 3–5% arise in the context of hereditary cancer syndromes. The most prominent is von Hippel–Lindau (VHL) disease, caused by germline mutations in VHL, and characterized by bilateral, multifocal clear cell RCC (ccRCC), retinal angiomas, and hemangioblastomas (48). The study of these syndromes has been instrumental in elucidating oncogenic drivers of RCC. Most notably, the VHL/HIF axis first identified in hereditary VHL disease is now recognized as the central oncogenic pathway in sporadic ccRCC,

shaping its biology and therapeutic vulnerabilities.

II. Diagnosis and Prognosis

RCC (RCC) is most often diagnosed incidentally, as the widespread use of cross-sectional imaging has led to the detection of small renal masses during investigations performed for unrelated conditions. The classic clinical triad of hematuria, flank pain, and palpable mass is now rarely observed, as most tumors are asymptomatic at presentation. Nevertheless, approximately 15–20% of patients present with metastatic disease at diagnosis (47).

Imaging is the cornerstone of RCC diagnosis and staging. Contrast-enhanced computed tomography (CT) and magnetic resonance imaging (MRI) allow precise characterization of the renal mass, evaluation of local extension, venous involvement, lymph node status, and distant metastases. Percutaneous renal mass biopsy is now considered a standard component of the diagnostic work-up in non-surgical management of localized RCC and in advanced disease. It should be systematically performed in patients with small renal masses of uncertain nature, prior to any focal or ablative treatment, or in the context of metastatic disease to confirm histology and guide systemic therapy selection (49).

A. Histological subtypes of RCC

Renal cell carcinoma comprises a heterogeneous group of malignancies with distinct histological, molecular, and clinical features. The 2022 World Health Organization (WHO) classification recognizes several major subtypes, each associated with specific prognostic and therapeutic implications (50).

Clear cell RCC (ccRCC) is the most prevalent subtype, representing approximately 70–75 % of cases. It arises from the proximal tubule epithelium and is histologically characterized by cells with optically clear cytoplasm and a dense capillary network. Genetically, ccRCC is defined by chromosome 3p loss and recurrent mutations in VHL, PBRM1, SETD2, and BAP1, which collectively shape angiogenesis, chromatin remodeling, and tumor aggressiveness. Clinically, ccRCC is the most aggressive and heterogeneous subtype, accounting for the majority of advanced and metastatic presentations. Importantly, ccRCC is also considered the most immunogenic form of RCC, explaining why immune checkpoint inhibitors have become a cornerstone of its treatment (**Figure 16**).

Papillary RCC (pRCC) accounts for approximately 10–15 % of cases and arises from the proximal tubule. In earlier classifications, pRCC was subdivided into type 1 and type 2, but this distinction has been abandoned in WHO 2022. Tumors formerly categorized as “type 2” have

proven to be a heterogeneous group and have now been partly reclassified into molecularly defined RCC entities, including FH-deficient RCC (often associated with hereditary leiomyomatosis and RCC, HLRCC), SDH-deficient RCC, ALK-rearranged RCC, ELOC-mutated RCC, and eosinophilic solid and cystic RCC. The remaining cases are grouped as pRCC, a heterogeneous entity characterized by variable histological appearances, frequent chromosome 7 and 17 gains, MET alterations, and mutations in chromatin modifiers. Overall, papillary RCC is associated with an intermediate prognosis and variable therapeutic sensitivity (**Figure 16**).

Chromophobe RCC (chRCC) represents about 5 % of cases and is thought to arise from the distal nephron. It is characterized histologically by pale cytoplasm with perinuclear halos and by frequent chromosomal losses. chRCC is typically associated with a favorable prognosis compared to ccRCC and pRCC, as it has a lower metastatic potential. A related but distinct entity is the renal oncocytoma, a benign tumor also derived from distal nephron cells. Oncocytomas share imaging and morphological similarities with chRCC but lack metastatic capacity, making their distinction crucial, particularly in small biopsy samples (**Figure 16**).

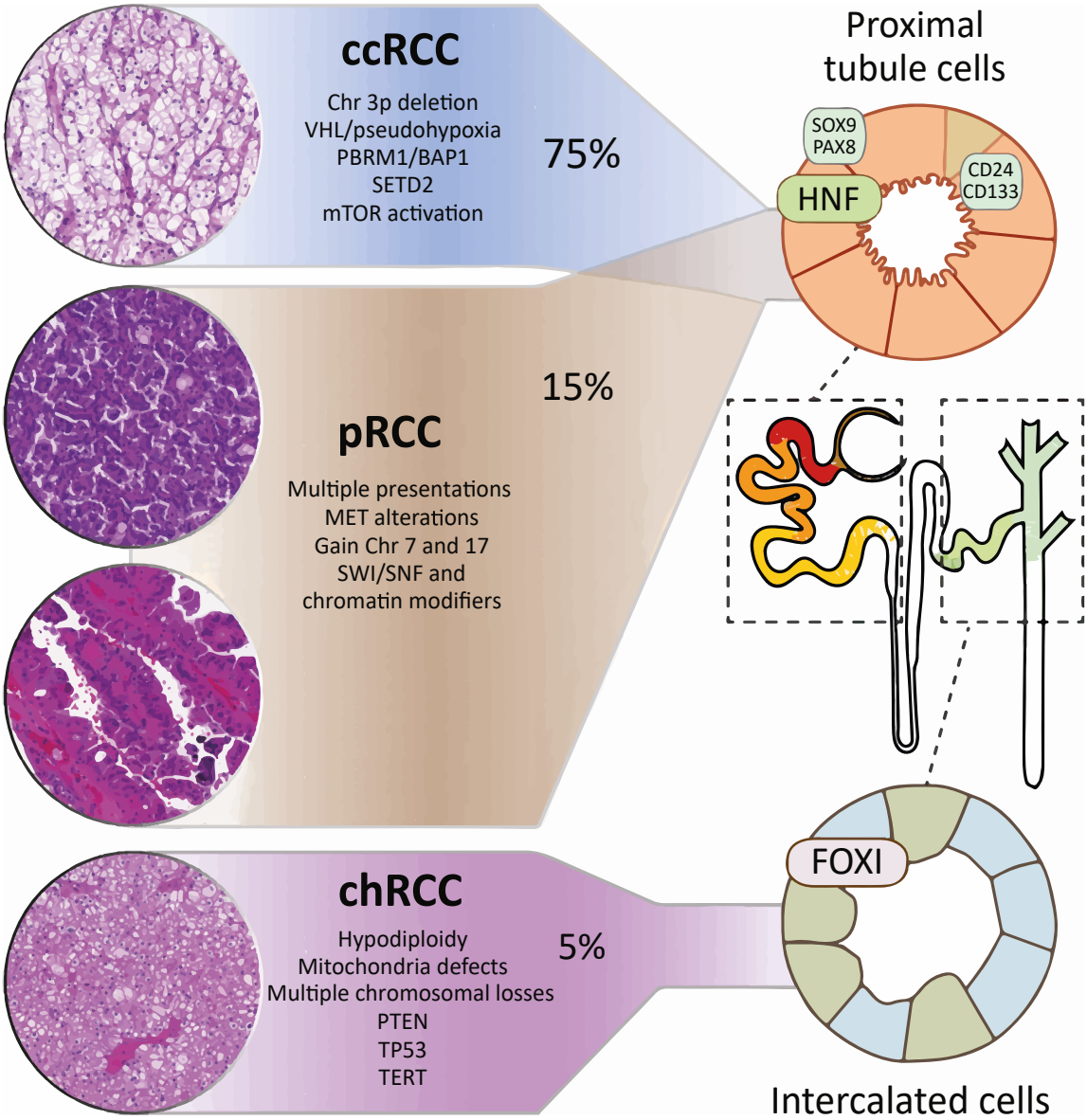

Figure 16. Major RCC subtypes and their cellular origins.

Clear cell RCC (ccRCC) and papillary RCC (pRCC) originate from proximal tubule or parietal epithelial cells (top right), whereas chromophobe RCC (chRCC) arises from intercalated cells of the distal nephron and collecting ducts (bottom right). These epithelial lineages are governed by transcriptional networks regulated by HNF and FOXI transcription factors, respectively, and transcriptional imprints of these programs can be identified in RCC subtypes. Representative hematoxylin–eosin (H&E) staining of each RCC subtype (left) and prototypical genomic/molecular alterations (center) are shown. ccRCCs almost invariably display loss of chromosome arm 3p encompassing VHL and chromatin modifiers such as PBRM1, BAP1, and SETD2. pRCCs, now considered a single heterogeneous entity in WHO 2022, show variable histological appearances and recurrent MET alterations, chromosome 7 and 17 gains, and mutations in chromatin modifiers. Hallmarks of chRCC include hypodiploidy, mitochondrial defects, multiple chromosomal losses, and TP53, PTEN, or TERT mutations. Collectively, RCCs frequently harbor alterations in metabolic and epigenetic pathways.

Source: adapted from (51), reproduced with minimal modification with permission from Elsevier, license number 6154820458036

Rare and aggressive subtypes include the collecting duct carcinoma (also known as Bellini duct carcinoma) and renal medullary carcinoma. Collecting duct carcinoma arises from the renal medullary collecting ducts and is associated with highly aggressive clinical behavior and poor outcomes. Renal medullary carcinoma, strongly associated with sickle cell trait, is one of the

most lethal renal malignancies, with rapid progression and resistance to conventional therapy. Unclassified RCCs represent a small residual category of tumors that do not fit established histological patterns.

In summary, although RCC comprises several histological subtypes with variable prognoses, ccRCC dominates both in frequency and in clinical impact. Its high prevalence, molecular complexity, and particular immunogenicity explain why it has become the primary focus of biological research and therapeutic innovation, and consequently the central focus of the present thesis.

B. Macroscopic pathology, staging, and grading

Grossly, most renal cell carcinomas are well-circumscribed masses separated from the renal parenchyma by a pseudocapsule. Clear cell RCC typically appears golden-yellow due to lipid and glycogen content, with frequent areas of hemorrhage and necrosis and occasional cystic change. Larger tumors may distort the collecting system and can extend into the renal vein and inferior vena cava as a tumor thrombus (**Figure 17**).

protected element - unauthorized distribution

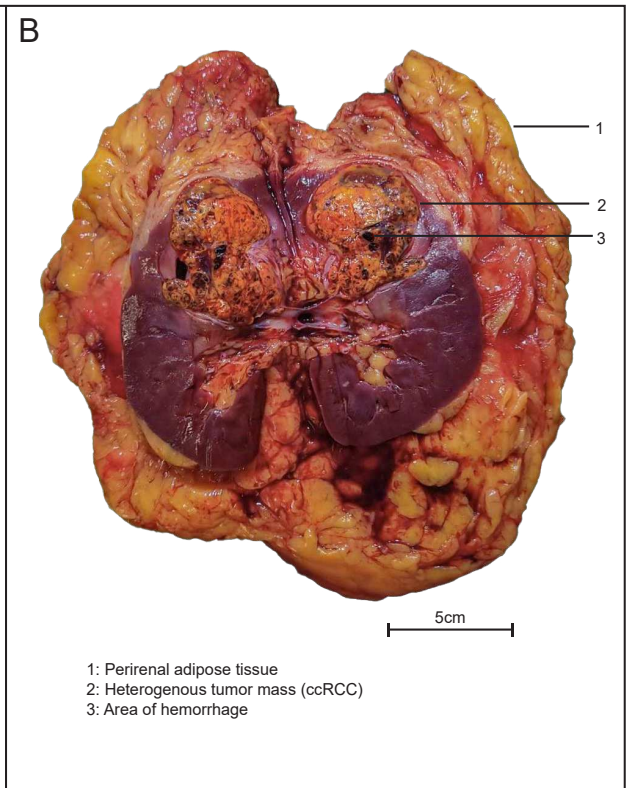

Figure 17. Macroscopic features of clear cell renal cell carcinoma (RCC).

A. Schematic illustration of gross pathologic findings in RCC, highlighting pseudocapsule, necrosis, hemorrhage, cystic changes, and venous extension. B. Gross specimen of nephrectomy: bisection showing a tumor mass in the upper pole with (1) perirenal adipose tissue, (2) a clear cell RCC mass with heterogenous surface, and (3) hemorrhagic areas.

Source: A. Adapted from (52); B. Personal photograph (Department of Pathology, Saint-Louis Hospital)

While macroscopic examination provides important insights into tumor morphology and patterns of local extension, a standardized and reproducible assessment of disease extent requires formal staging and grading systems.

In oncology, staging refers to the assessment of the anatomical extent of a tumor, i.e. its size, local invasion, lymph node involvement, and presence of distant metastases. By contrast, grading evaluates the histological aggressiveness of the tumor, based on microscopic features such as nuclear atypia and cellular morphology. Both parameters are complementary and essential for prognosis and therapeutic decision-making.

For RCC, the TNM classification (Tumor, Node, Metastasis), established by the UICC/AJCC (8th edition), is the international standard for clinical and pathological staging (53). This system codes three dimensions of tumor spread:

- T (Tumor): describes the size and local extent of the primary renal tumor.
- N (Node): indicates whether regional lymph nodes are involved.
- M (Metastasis): specifies the presence or absence of distant metastases.

The combination of T, N, and M categories defines the overall stage (I to IV), which strongly correlates with prognosis.

- T1 tumors are confined to the kidney and measure ≤ 7 cm.
- T2 tumors are also limited to the kidney but are > 7 cm.
- T3 tumors extend into the renal vein, vena cava, or perinephric fat but remain within Gerota's fascia fascia (the fibrous capsule surrounding the kidney and the perirenal fat, serving as an anatomical barrier to local tumor spread).
- T4 tumors invade beyond Gerota's fascia or into the ipsilateral adrenal gland.

Regional lymph node involvement (N1) and distant metastases (M1) are associated with a significant worsening of prognosis.

Based on the combination of T, N, and M categories, RCCs are grouped into four stages:

- **Stage I**: T1, N0, M0
- **Stage II**: T2, N0, M0
- **Stage III**: T3 or N1 disease without distant metastasis
- **Stage IV**: T4 or M1 disease

A more detailed version of the TNM classification can be found in **Table 1** and a graphical illustration is provided as **Figure 18**.

Table 1. TNM classification of renal cell carcinoma (AJCC 8th edition)

T – Primary tumor			
TX	Primary tumor cannot be assessed		
T0	No evidence of primary tumor		
T1	Tumor ≤ 7 cm or less in greatest dimension, limited to the kidney		
	T1a Tumor ≤ 4 cm or less		
	T1b Tumor > 4 cm but ≤ 7 cm		
T2	Tumor > 7 cm in greatest dimension, limited to the kidney		
	T2a Tumor > 7 cm but ≤ 10 cm		
T2b	T2b Tumors > 10 cm, limited to the kidney		
T3	Tumor extends into major veins or perinephric tissues but not into the ipsilateral adrenal gland and not beyond Gerota fascia		
	T3a Tumor extends into the renal vein or its segmental branches, or invades the pelvicalyceal system or invades perirenal and/or renal sinus fat, but not beyond Gerota fascia		
	T3b Tumor grossly extends into the vena cava below diaphragm		
T3c	T3c Tumor grossly extends into vena cava above the diaphragm or invades the wall of the vena cava		
T4	Tumor invades beyond Gerota fascia (including contiguous extension into the ipsilateral adrenal gland)		
N – Regional Lymph Nodes			
NX	Regional lymph nodes cannot be assessed		
N0	No regional lymph node metastasis		
N1	Metastasis in regional lymph node(s)		
M – Distant metastasis			
M0	No distant metastasis		
M1	Distant metastasis		
pTNM stage grouping			
Stage I	T1	N0	M0
Stage II	T2	N0	M0
Stage III	T3	N0	M0
	T1, T2, T3	N1	M0
Stage IV	T4	Any N	M0
	Any T	Any N	M1

source: adapted from (53)

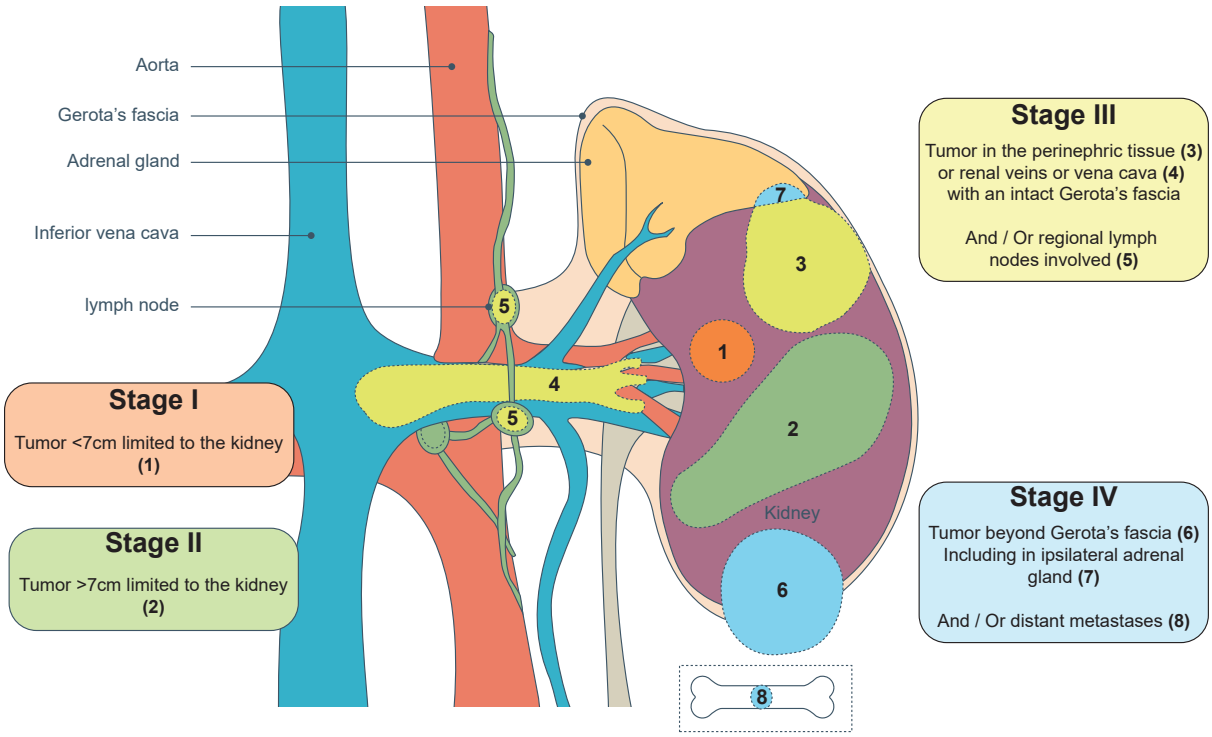

Figure 18. Schematic representation of renal cell carcinoma staging according to the TNM classification (UICC/AJCC, 8th edition).

Stage I corresponds to tumors ≤7 cm confined to the kidney (1). Stage II includes tumors >7 cm but still limited to the kidney (2). Stage III refers to invasion of perinephric fat (3), renal veins or vena cava (4), or the involvement of regional lymph nodes (5). Stage IV is defined by tumor extension beyond Gerota's fascia, including invasion of the ipsilateral adrenal gland (7), or by the presence of distant metastases, such as bone metastasis (8).

Source: adapted from (54), with permission from Springer Nature, license number 6154830539440

These stages are clinically relevant because they provide a standardized framework to estimate prognosis, guide treatment decisions, and allow comparison of outcomes across studies.

Stages I–II generally correspond to localized disease, often managed with surgical resection (partial or radical nephrectomy).

Stage III reflects locally advanced tumors or regional lymph node involvement, requiring surgery with curative intent but carrying a higher risk of recurrence.

Stage IV denotes advanced or metastatic disease, for which systemic therapies (immune checkpoint inhibitors, targeted therapies) are the mainstay of treatment.

Thus, staging not only stratifies patients by outcome but also serves as a cornerstone for therapeutic algorithms and clinical trial design.

This TNM system remains the international standard for RCC staging; however, it has changed little over the past decades, whereas clinical management of RCC has evolved substantially. Its limitations are most apparent for small renal masses, nodal disease, and metastatic burden,

where current categories may not accurately capture prognosis or guide treatment. Moreover, AJCC stage groupings do not always correlate with survival: for example, patients with T1–3N1M0 (stage III) show similar outcomes to T4N0M0 (stage IV), and worse than T3N0M0 (stage III) in some studies (55). Beyond this inconsistency, further criticisms have been raised: current size thresholds for small renal masses may not optimally guide active surveillance and focal therapy, the binary N0/N1 classification does not account for the heterogeneity of nodal disease, and the M0/M1 distinction fails to capture the prognostic differences between oligometastatic and polymetastatic disease. These discrepancies highlight the need for refined staging models, and several modifications have been proposed to better align prognostic classification with contemporary therapeutic strategies (56).

Histological grading provides complementary prognostic information by assessing tumor aggressiveness under the microscope. The WHO/ISUP grading system, now the international standard, has replaced the older Fuhrman system. Fuhrman grading was based on three nuclear parameters (size, shape/irregularity, and nucleolar prominence), which often evolved independently and could yield contradictory results. It also suffered from poor interobserver reproducibility and limited prognostic discrimination, with no consistent progression free survival between grade 2 and grade 3. By contrast, the WHO/ISUP system relies primarily on nuclear features: nucleolar prominence defines grades 1–3, while pleomorphic, sarcomatoid, or rhabdoid morphology defines grade 4. This simplified four-tiered scale has demonstrated greater reproducibility and stronger prognostic accuracy, particularly in ccRCC, where high grade is associated with aggressive behavior and poor survival. (57,58) both these systems are described in **Table 2**. Representative immunohistochemical images illustrating the different ccRCC grades are presented in **Figure 19**.

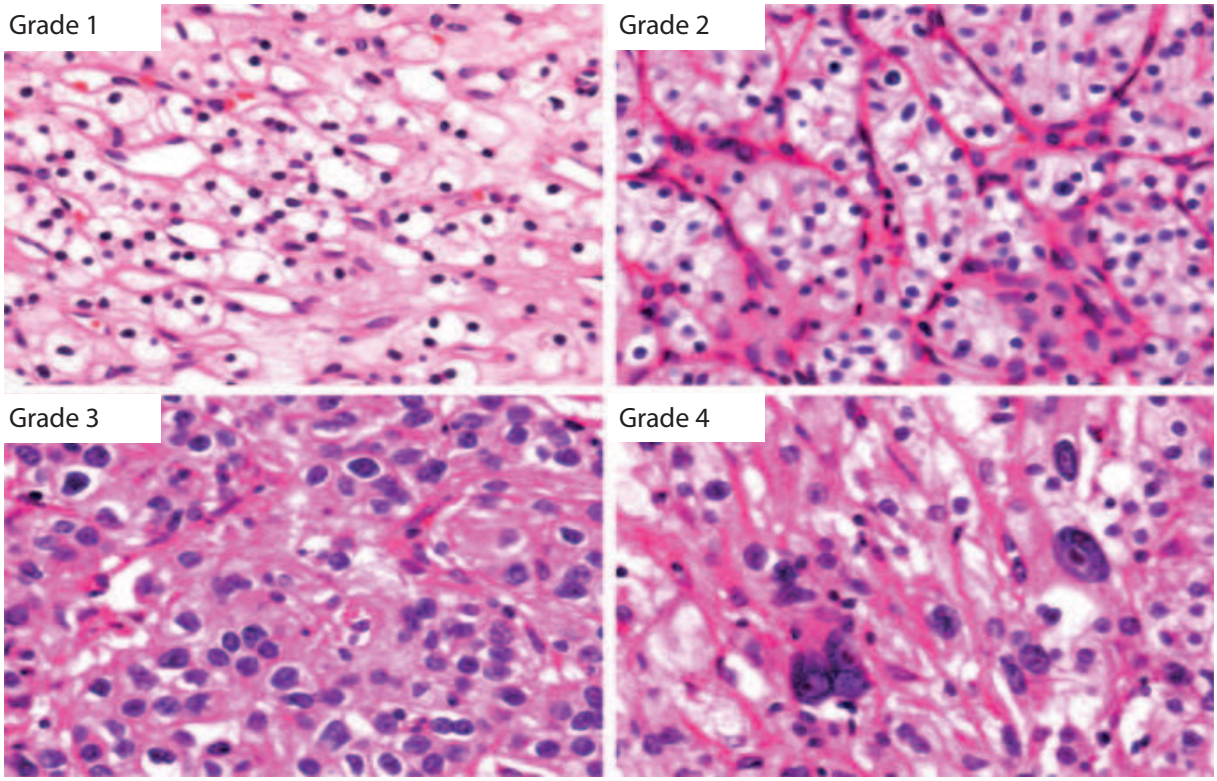

Figure 19. WHO/ISUP grade of ccRCC.

Grade 1 cells have small hyperchromatic nuclei resembling mature lymphocytes, and grade 2 cells have finely granular chromatin. Nucleoli can be easily recognized in grade 3 cells, and nuclear pleomorphism, hyperchromasia, and macronucleoli are observed in grade 4 cells.

Source: (59), reproduced with permission from Springer Nature, license number 6154830793150

Table 2. World Health Organization (WHO)/International Society of Urological Pathology (ISUP) and Fuhrman grading systems.

WHO/ISUP grading system	
Grade 1	Nucleoli absent or inconspicuous and basophilic at ×400 magnification
Grade 2	Nucleoli conspicuous and eosinophilic at ×400 magnification, and visible but not prominent at ×100 magnification
Grade 3	Nucleoli conspicuous and eosinophilic at ×100 magnification
Grade 4	Extreme nuclear pleomorphism and/or sarcomatoid and/or rhabdoid differentiation and/or tumor giant cells

Furhman grade	Nucleoli	Nuclear shape	Nuclear size (μm)
Grade 1	Inconspicuous or absent	Small, round, uniform, irregular	~10
Grade 2	Visible at ×400 magnification	Irregular in outline at ×400 magnification, variable in size	~15
Grade 3	Prominent/large even at ×100 magnification	Obvious irregular outline, large, hyperchromasia, marked variability in size and shape	~20
Grade 4	Cells large, pleomorphic with bizarre multilobed giant cells and heavy chromatic clumps, extreme irregular outlines		

Source: (57)

C. Prognosis

Survival outcomes in RCC depend largely on stage and histological subtype. Overall, the 5-year survival rate for RCC in developed countries is around 80 %. Patients with localized disease (T1–T2) have favorable outcomes, with 5-year survival exceeding 90 %, whereas those with locally advanced tumors (T3–T4) have intermediate prognoses, with survival rates of around 80 %. In contrast, metastatic RCC remains associated with poor outcomes, with 5-year survival of less than 20 % despite recent therapeutic advances, highlighting the need for better therapies for these patients (**Figure 20**A). When compared to other common solid tumors, the prognosis of RCC is less favorable than that of prostate or breast cancer, where 5-year survival rates approach 90–95 %, but generally better than for lung (~30 %) or pancreatic cancer (~13.5 %) **Figure 20**B. This intermediate position underscores the substantial clinical burden of RCC and the critical importance of therapeutic innovation, particularly in advanced disease.

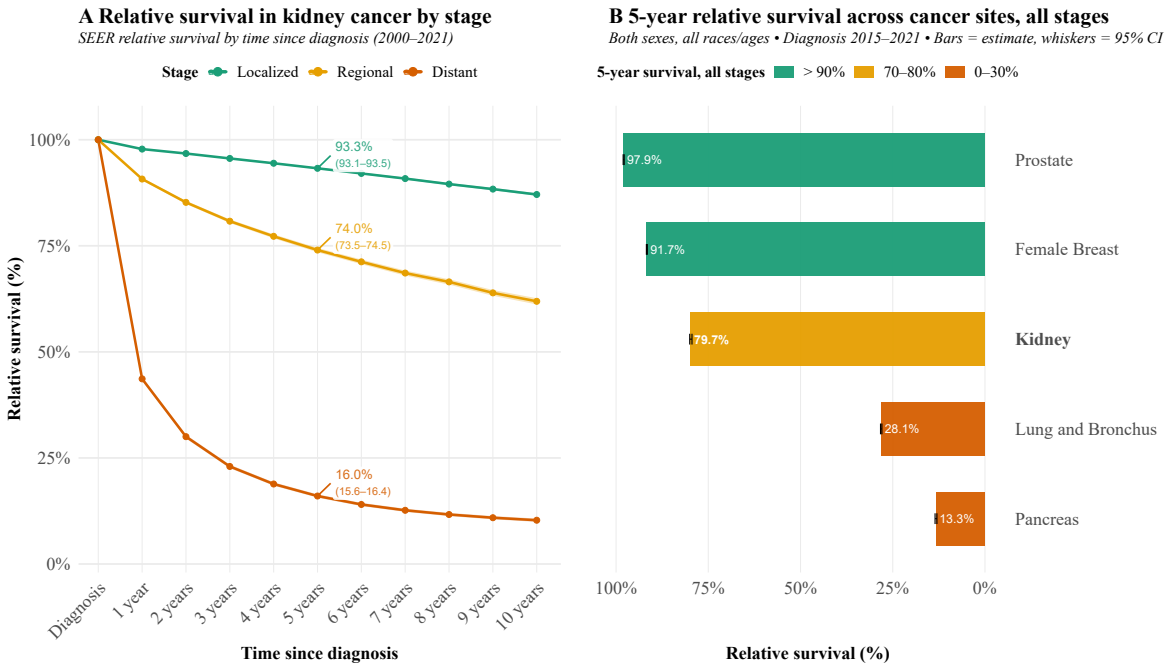

Figure 20. Relative survival in kidney cancer by stage and comparison with other major cancer sites.

A. Ten-year relative survival in patients with kidney cancer according to stage at diagnosis (SEER data, 2000–2021). Relative survival (%) is plotted over time since diagnosis for localized, regional, and distant stages. Shaded areas represent 95% confidence intervals. Labels highlight 5-year survival, with corresponding point estimates and confidence intervals indicated. B. Five-year relative survival across selected cancer sites (prostate, female breast, kidney, lung, pancreas) based on SEER data (2015–2021, both sexes, all ages, all races/ethnicities). Bars indicate survival estimates with 95% confidence intervals. Colors classify cancer sites by survival range: >90% (green), 70–80% (orange), and 0–30% (red).

Plotted from data source: (60).

Prognostic models have been developed to refine outcome prediction and guide therapeutic decision-making. In metastatic RCC, historically, the MSKCC score was used in the cytokine era. Currently, the International Metastatic RCC Database Consortium (IMDC) score is the standard in clinical practice and clinical trials. It incorporates six clinical and laboratory variables: performance status, hemoglobin, corrected calcium, platelet count, neutrophil count, and interval from diagnosis to treatment (**Figure 21**). The IMDC model stratifies patients into favorable, intermediate, or poor risk groups, with significant implications for expected survival and for the selection of first-line systemic therapies.

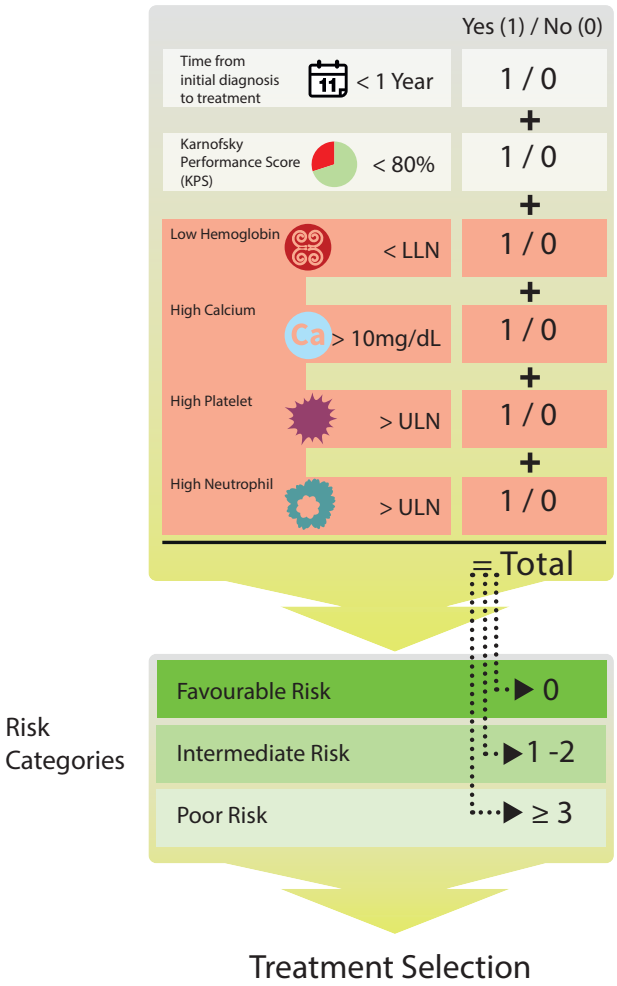

Figure 21. International Metastatic RCC Database Consortium (IMDC) risk stratification model for metastatic renal cell carcinoma.

The IMDC model, also known as the Heng criteria, integrates six adverse prognostic factors: time from diagnosis to systemic therapy < 1 year, Karnofsky performance score (KPS) < 80 %, low hemoglobin, high corrected calcium (> 10 mg/dL), elevated platelet count, and elevated neutrophil count. Patients are stratified into favorable (0 factors), intermediate (1–2 factors), or poor risk (≥ 3 factors) groups. This classification provides prognostic information and is routinely used to guide first-line treatment selection in metastatic RCC.

Source: IKCC.org, used with permission

III. Molecular and Biological Characteristics of Clear Cell RCC

Clear cell RCC (ccRCC) has a distinctive molecular landscape that has been elucidated by large-scale sequencing efforts, most notably The Cancer Genome Atlas (TCGA) and subsequent studies. Its defining alteration is the loss of chromosome 3p, which harbors several critical tumor suppressor genes as seen in **Figure 22**. Among them, VHL (von Hippel–Lindau) is the most frequently inactivated gene, affected in ~70–80 % of cases by mutation, deletion, or epigenetic silencing. Loss of VHL function leads to constitutive stabilization of hypoxia-inducible factors (HIF-1α and HIF-2α). These transcription factors drive angiogenesis (e.g., VEGF,

PDGF), metabolic adaptation, and tumor progression. This aberrant activation of the HIF pathway explains the highly vascular phenotype of ccRCC and its historical sensitivity to anti-angiogenic therapies (61).

Beyond VHL, recurrent mutations in chromatin remodeling genes define biologically and clinically distinct subsets. PBRM1, altered in ~40 % of cases, encodes a subunit of the SWI/SNF complex and exerts tumor-suppressive functions. SETD2, mutated in ~15–20 %, regulates histone H3K36 trimethylation, with roles in transcriptional fidelity, RNA splicing, and DNA repair. BAP1, altered in ~10–15 %, encodes a deubiquitinase that controls chromatin structure and cell cycle progression; its loss is strongly associated with high-grade tumors, aggressive clinical behavior, and poor outcomes. These mutations are largely mutually exclusive and define divergent biological phenotypes. For instance, PBRM1-mutant tumors often display an inflamed microenvironment, whereas BAP1-mutant tumors are more aggressive and resistant to therapy. Such distinctions may influence sensitivity to immunotherapies (62).

In addition to genomic alterations, ccRCC exhibits profound metabolic reprogramming. HIF stabilization promotes aerobic glycolysis (Warburg effect), glutamine dependence, and lipid accumulation. This metabolic rewiring underlies the characteristic clear cytoplasm of ccRCC cells, filled with glycogen and lipids. Mitochondrial dysfunction disrupted redox homeostasis, and accumulation of oncometabolites further contribute to tumor aggressiveness. Importantly, these metabolic changes also modulate the immune microenvironment, fostering immune suppression and therapeutic resistance, for example through lactate accumulation, which impairs T cell function (63).

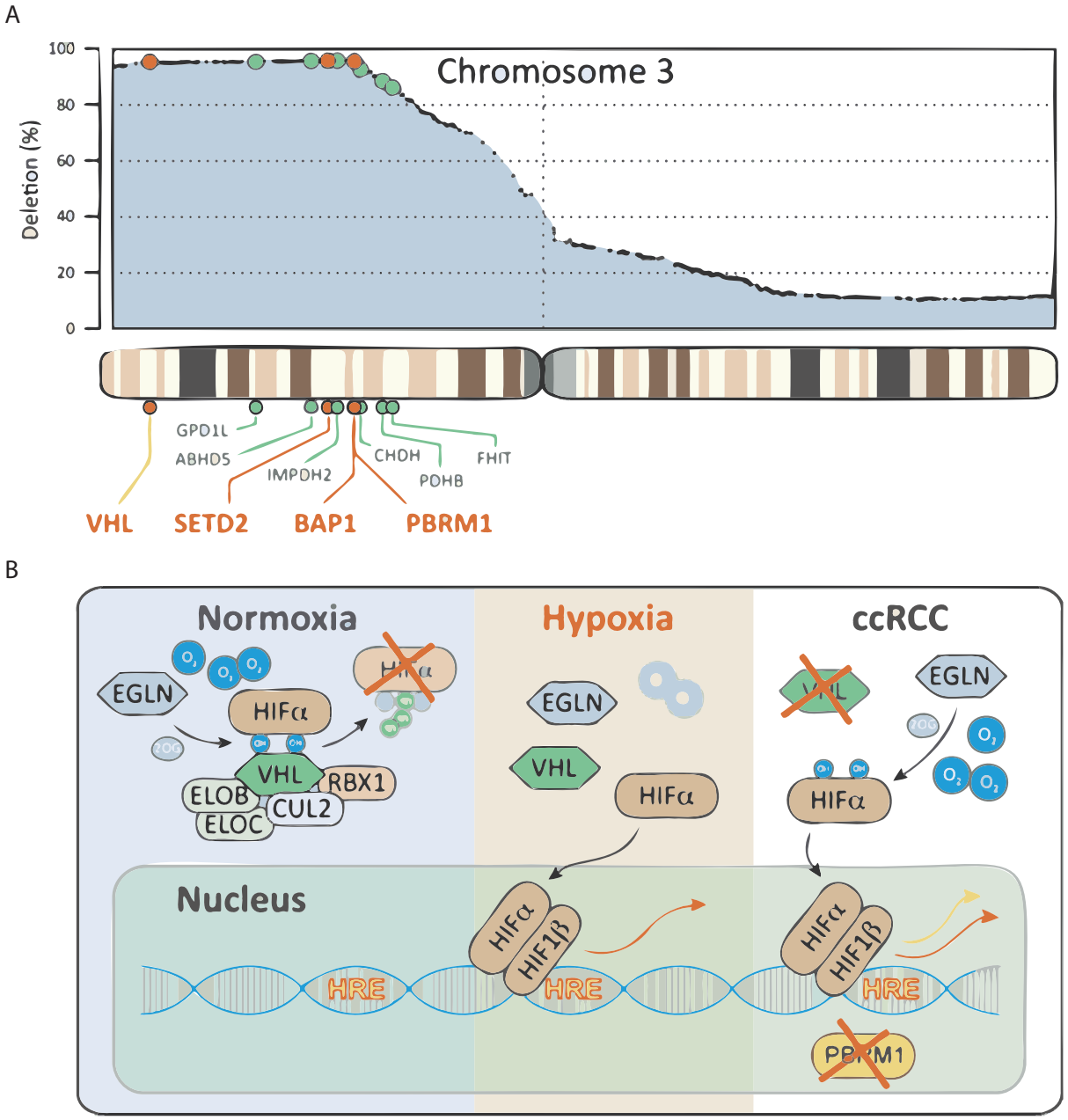

Figure 22. Chromosome 3 Deletions in CcRCC and the VHL/HIF Signaling Cascade.

A. frequency of chromosome 3p deletions in ccRCC. This region contains several tumor suppressor genes frequently mutated in ccRCC, including VHL, PBRM1, BAP1, and SETD2 (highlighted in orange), as well as metabolic regulators implicated in tumorigenesis (green). B. The VHL/HIF signaling pathway under normoxia, hypoxia, and in ccRCC. Under normoxia, prolyl hydroxylases (EGLN family) hydroxylate HIFα, targeting it for ubiquitination by the VHL E3 ligase complex and subsequent proteasomal degradation. Under hypoxia, HIFα escapes degradation, accumulates, and activates transcription of hypoxia-response genes after nuclear translocation. In ccRCC, VHL inactivation results in constitutive HIFα stabilization and pseudohypoxia, leading to sustained expression of HIF target genes. Inactivation of PBRM1 further enhances the hypoxic transcriptional response.

Source: (51), reproduced with permission from Elsevier, license number 6154820458036

Altogether, ccRCC biology is characterized by angiogenic dependency, defects in chromatin remodeling, and remarkable metabolic plasticity. These hallmarks interact dynamically with the tumor microenvironment, shaping tumor progression, therapeutic response, and mechanisms of resistance. A thorough understanding of these features is essential for the development of novel therapeutic approaches and for the design of preclinical models that faithfully recapitulate

ccRCC biology in an immuno-oncological context. In addition, the pronounced genetic heterogeneity across patients, and its consequences on both tumor biology and immune interactions, highlights the need for personalized modeling strategies.

IV. Immune Landscape and Tumor Microenvironment of Clear Cell RCC

Clear cell RCC (ccRCC) harbors one of the most immune-infiltrated yet immunosuppressive tumor microenvironments (TME) among solid cancers. This paradoxical coexistence underlies both its sensitivity to ICIs and the frequent emergence of resistance (64).

A. Immune infiltration and immunogenicity

ccRCC is characterized by abundant infiltration of tumor-infiltrating lymphocytes (TILs), particularly $CD8^+$ T cells, consistent with its intrinsic immunogenicity. Although ccRCC exhibits only a moderate tumor mutational burden, recurrent driver mutations generate immunogenic neoantigens. Antigen presentation, however, is frequently impaired through heterogeneous or reduced HLA class I expression (65), contributing to immune escape. Functionally, infiltrating T cells often display an exhausted phenotype with reduced cytotoxicity, highlighting the paradox of an "inflamed but ineffective" immune microenvironment. In addition to T cells, NK cells and B cells are frequently detected, and the presence of tertiary lymphoid structures (TLS) has been associated with improved response to ICIs (66). Historically, this immunogenic profile explains why ccRCC was among the first solid tumors responsive to cytokine-based therapies (IL-2, IFN-α) and why ICIs have since become central in its management.

B. Canonical immune checkpoints

The PD-1/PD-L1 axis is the best-characterized immune escape pathway in ccRCC. PD-1 is expressed on exhausted T cells, while PD-L1 is found on both tumor cells and tumor-associated myeloid cells. Although PD-L1 expression is heterogeneous and does not consistently predict response to ICIs, blockade of the PD-1/PD-L1 pathway remains the backbone of immunotherapy in ccRCC. Clinical benefit has been demonstrated with PD-1 inhibitors (nivolumab, pembrolizumab) and PD-L1 inhibitors (avelumab, atezolizumab), particularly in combination with VEGF-targeted therapies or CTLA-4 blockade. The CTLA-4 axis, though less dominant, also contributes to immunosuppression by dampening early T cell priming, and dual PD-1/CTLA-4 blockade has shown efficacy in advanced ccRCC (67).

C. Non-classical and emerging checkpoints

Beyond PD-1/PD-L1, several additional inhibitory pathways drive immune escape in ccRCC. HLA-G (described in the previous chapter) is frequently and heterogeneously expressed and suppresses cytotoxic T and NK cell activity through ILT2 and ILT4 (68,69). HLA-E is also expressed fostering exhaustion (70); co-blockade of PD-1 and NKG2A has shown synergistic activity ex vivo (71). Other checkpoints from the B7 family, including VISTA, B7-H3 (CD276), and B7-H4 (VTCN1), are frequently overexpressed in ccRCC and associated with poor prognosis (72–75). Finally, exhaustion markers such as LAG-3, TIGIT, and TIM-3 are commonly co-expressed by TILs (76), and the CD47–SIRPα axis protects tumor cells from macrophage phagocytosis (77,78). Together, these pathways highlight the multiplicity of immune escape mechanisms and support the rationale for combination immunotherapies beyond PD-1 blockade.

D. Regulatory populations and myeloid suppression

The ccRCC TME is enriched in regulatory T cells (Tregs), many of which express high levels of PD-1. PD-1$^+$ Tregs have been associated with lack of benefit from PD-1 blockade, raising the concern that checkpoint inhibition may enhance suppressive functions in certain contexts (79). In parallel, myeloid-derived suppressor cells (MDSCs) accumulate and suppress T and NK cell activity via arginase, nitric oxide, and reactive oxygen species (80). TAMs, particularly CD163$^+$ M2-like subsets, correlate with poor prognosis and tumor progression (81). Reprogramming TAMs or targeting CD47–SIRPα interactions represent promising approaches to counteract myeloid-driven immunosuppression (78).

E. Angiogenesis and hypoxia

The angiogenic signature of ccRCC is a direct consequence of VHL loss and constitutive HIF stabilization, which upregulates VEGFA, PDGFB, and angiopoietin, particularly ANGPT2. This promotes abnormal, poorly pericyte-covered vasculature and deep intratumoral hypoxia (63). Hypoxia not only sustains angiogenesis but also impairs dendritic cell priming, favors recruitment of MDSCs and M2-like TAMs, and promotes Treg expansion. Anti-VEGF therapies can induce a transient vascular-normalization window that alleviates hypoxia and facilitates T cell infiltration, thereby synergizing with PD-1/PD-L1 blockade (82). This mechanistic rationale underpins the clinical success of VEGF-TKI plus ICI combinations, now standard of care in metastatic ccRCC, while direct HIF-2α inhibition further underscores the centrality of this pathway.

F. Transcriptomic TME subtypes

Comprehensive transcriptomic studies in ccRCC, notably the phase II IMmotion150 trial, have identified three TME-associated molecular subtypes: (1) an angiogenic subtype enriched for VEGF-driven signatures and sensitive to VEGF-TKIs; (2) a T-effector/immune-inflamed subtype characterized by $CD8^+$ infiltration, IFN-γ signaling, and heightened sensitivity to ICIs; and (3) a myeloid-inflamed/immunosuppressive subtype dominated by TAMs, MDSCs, and cytokines (e.g., IL-10, TGF-β), often resistant to ICIs alone. These subtypes correlate with treatment outcomes and serve as a foundation for stratifying patients in clinical trials, though they remain exploratory and are not yet implemented in routine practice (83,84).

G. Summary

The ccRCC microenvironment is shaped by a convergence of immune infiltration, checkpoint heterogeneity, regulatory and myeloid suppression, and angiogenic signaling. This complexity might explain the variable responses to immunotherapy and emphasizes the need for preclinical models that faithfully reproduce the cellular diversity, checkpoint mosaicism, and spatial heterogeneity of the ccRCC TME. Such models are critical to explore novel checkpoint targets, test rational therapeutic combinations, and advance personalized immunotherapy strategies, The key requirements for such preclinical models are summarized in **Box 1** (end of the chapter).

Furthermore, with its paradoxical coexistence of abundant immune infiltration and profound immunosuppression, ccRCC constitutes a natural laboratory to study mechanisms of immune resistance and to evaluate novel immunotherapeutic strategies.

V. Current Management of RCC

A. Localized disease

According to the 2025 European Association of Urology (EAU) Guidelines, partial nephrectomy (PN) remains the standard of care for most patients with localized RCC, including those with T1 tumors, whenever technically feasible. This nephron-sparing approach is preferred over radical nephrectomy (RN) in order to preserve renal function (47).

When histological confirmation has been obtained by prior biopsy, focal therapies such as cryoablation or radiofrequency ablation (RFA) may also be considered. More recently, stereotactic ablative radiotherapy (SABR) has emerged as a promising non-invasive alternative for patients with localized RCC who are not candidates for surgery (49). Current recommendations are summarized in **Figure 23**.

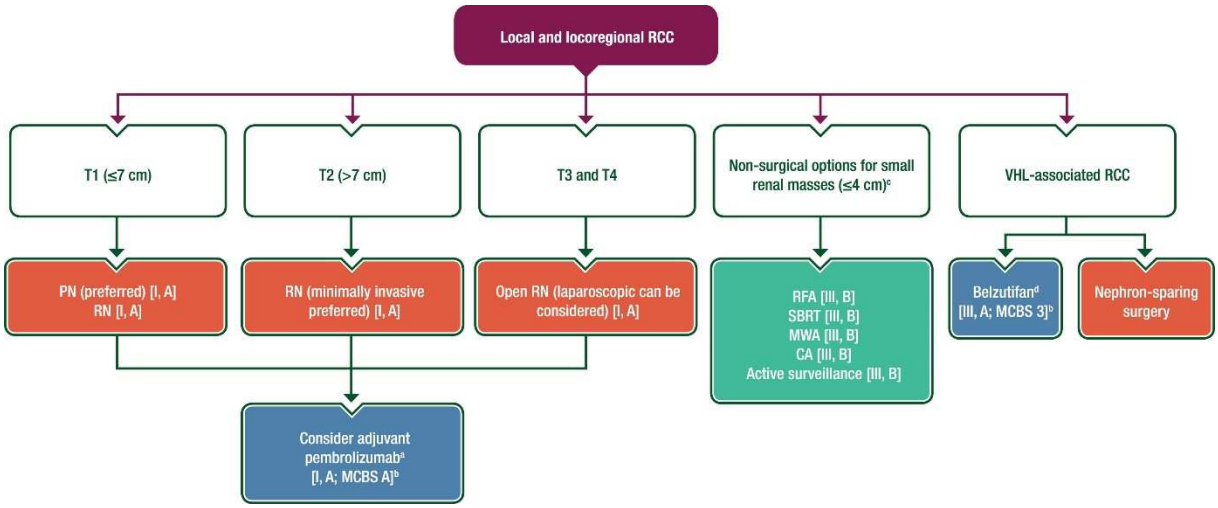

Figure 23. Current ESMO-recommended treatment algorithm for localized and locoregional RCC.
Partial nephrectomy (PN) is the preferred approach for T1 tumors (≤7 cm), while radical nephrectomy (RN) is considered for larger (T2) or more advanced tumors (T3–T4). Minimally invasive RN is preferred when PN is not feasible. Non-surgical options, including radiofrequency ablation (RFA), cryoablation (CA), microwave ablation (MWA), and stereotactic body radiotherapy (SBRT), are reserved for selected patients with small renal masses (≤4 cm) and are supported by level III evidence. Active surveillance is an acceptable strategy in patients with limited life expectancy or significant comorbidities. Adjuvant pembrolizumab is considered in patients with intermediate-high or high-risk disease following nephrectomy. In VHL-associated RCC, nephron-sparing surgery remains the standard, while belzutifan is a systemic alternative for patients not requiring immediate surgical intervention. Levels of evidence and recommendation strength are shown in brackets: [I, A] indicates evidence from high-quality randomized trials with strong recommendation; [III, B] denotes lower-level evidence with moderate recommendation. MCBS refers to the ESMO Magnitude of Clinical Benefit Scale, which evaluates the expected benefit of an oncologic intervention, ranging from A (highest) to C in the adjuvant/curative setting, and 1 (lowest) to 5 (highest) in the palliative/metastatic setting.

Source: (49)

B. Metastatic disease — first-line systemic therapies

In metastatic clear-cell renal cell carcinoma (mccRCC), initial therapeutic decisions are guided by the International Metastatic RCC Database Consortium (IMDC) risk classification as seen above. According to ESMO recommendations, for patients with intermediate or poor risk, the combination of nivolumab and ipilimumab (anti PD-1 and anti CTLA-4) is a recommended first-line regimen. Across all IMDC risk groups, VEGFR tyrosine kinase inhibitors (TKIs) combined with PD-1 blockade, such as pembrolizumab plus axitinib, lenvatinib plus pembrolizumab, or cabozantinib plus nivolumab, are also approved as standard first-line options. No combination has shown superiority in head-to-head comparisons (49).

In patients who are ineligible for immunotherapy, VEGFR-targeted monotherapies including sunitinib, pazopanib, or tivozanib may be used.

C. Metastatic Disease — Subsequent-Line Treatments

Following progression after first-line systemic therapy for metastatic clear-cell renal cell carcinoma (ccRCC), treatment selection is primarily guided by the nature of prior exposure. In

patients previously treated with PD-1-based combinations, further ICI therapy is not recommended. Cabozantinib monotherapy, is therefore the preferred second-line option if not already used upfront.

Alternative VEGFR-targeted agents such as axitinib, lenvatinib–everolimus, pazopanib, sunitinib, and tivozanib may also be used, with modest efficacy reported in retrospective or exploratory studies. Although the quality of evidence is limited, these agents continue to be considered valid options in the sequencing of therapy.

Belzutifan, a HIF-2α inhibitor, has emerged as a promising therapy beyond the first line. While its benefit in the second-line setting appears modest and less compelling than cabozantinib, belzutifan remains an alternative option in this context. In the third-line setting, belzutifan showed a significantly higher response rate and improved tolerability compared with everolimus and is therefore preferred in heavily pretreated patients.

Overall, sequencing VEGFR-targeted therapies remains the mainstay beyond progression, while further ICI use should be avoided outside of clinical trials or highly selected contexts (49).

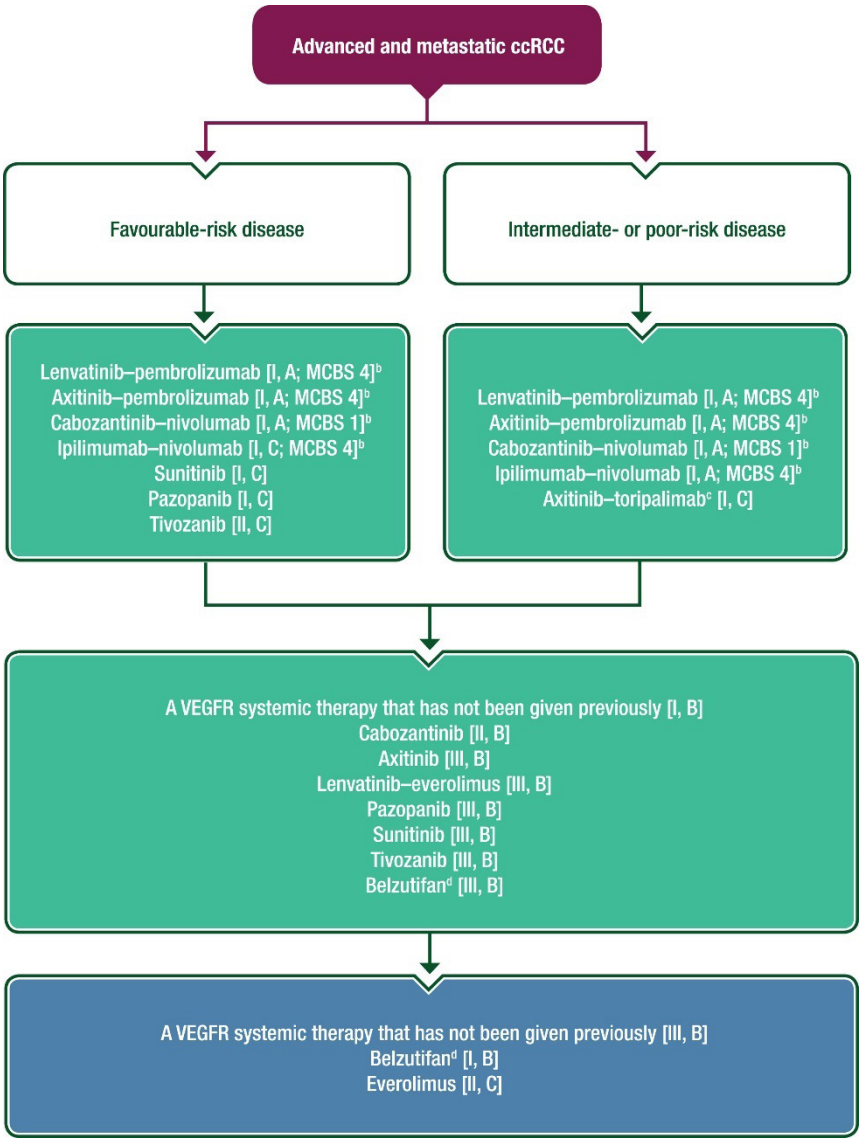

Figure 24. Current ESMO-recommended treatment algorithm for advanced and metastatic clear-cell renal cell carcinoma (ccRCC), stratified by IMDC risk group.

For both favorable and intermediate/poor-risk disease, recommended first-line regimens include combinations of PD-1 inhibitors with VEGFR tyrosine kinase inhibitors (TKIs) such as pembrolizumab plus axitinib or lenvatinib, or with CTLA-4 inhibition (ipilimumab). These regimens are supported by phase III clinical trials and assigned high levels of evidence (e.g., [I, A]) and a meaningful clinical benefit as per the ESMO-Magnitude of Clinical Benefit Scale (MCBS 4). In later lines, sequential VEGFR-targeted therapies not previously administered are recommended, including cabozantinib, axitinib, lenvatinib–everolimus, and belzutifan. Belzutifan and everolimus are also proposed as options beyond second-line therapy. Level of evidence and recommendation grade are based on the ESMO grading system, where [I, A] corresponds to evidence from phase III randomized trials and a strong recommendation. The MCBS (Magnitude of Clinical Benefit Scale) ranges from 1 to 5, with 4–5 indicating high clinical benefit.

Source: (49)

VI. Place of immunotherapy in RCC

A. Historical background

RCC is historically recognized as an immunogenic malignancy, a notion supported by early systemic treatments based on cytokines such as IL-2 and IFN-α (85). Although high-dose IL-2 induced durable complete responses in a small proportion of patients, its use was limited by severe toxicity and applicability only to highly selected individuals. IFN-α, though more broadly accessible, provided only modest benefits and was rapidly replaced by VEGF-targeted therapies (86). Nonetheless, these early immunotherapeutic strategies were foundational, providing proof-of-concept that durable control, and potentially cure, of RCC through immune modulation was achievable.

B. The immune checkpoint inhibitor revolution

The treatment landscape of RCC was transformed by the advent of ICIs. In the landmark CheckMate-025 trial, nivolumab significantly extended median overall survival compared with everolimus, while also achieving a better objective response rate and inducing fewer severe adverse events. For the first time, an immunotherapy proved both more effective and better tolerated than standard targeted therapy, establishing PD-1 blockade as the reference in the second-line setting (87).

In the frontline setting, the CheckMate-214 study demonstrated that dual ICI therapy with nivolumab (anti PD-1) plus ipilimumab (anti CTLA-4) produced durable benefits in intermediate- and poor-risk patients, with overall survival significantly improved and complete responses occurring in 12% of cases compared with 3–4% with sunitinib. Importantly, these responses proved exceptionally long-lasting, with a median duration exceeding 6 years at long-term follow-up (88,89).

Building on these results, combinations of PD-1 blockade with VEGF tyrosine kinase inhibitors (TKIs) have become standard first-line options for metastatic clear-cell RCC across IMDC risk groups. The KEYNOTE-426 (pembrolizumab + axitinib), CheckMate-9ER (nivolumab + cabozantinib), and CLEAR (lenvatinib + pembrolizumab) trials each demonstrated significant improvements in progression-free and overall survival compared with sunitinib. These regimens consistently yielded objective response rates above 55–70%, with complete responses reported in up to 16% of patients. This supports their capacity to achieve higher efficacy and a greater likelihood of durable disease control compared to VEGF-TKI monotherapy (90–95).

Equally important, quality of life outcomes have consistently favored ICI-based regimens. CheckMate-214 showed better global health-related quality of life (HRQoL), as measured by patient-reported outcomes, and delayed symptom deterioration with nivolumab + ipilimumab

compared with sunitinib. Similar improvements were seen with nivolumab + cabozantinib and lenvatinib + pembrolizumab (96–98). This reflects not only more durable disease control but also a different treatment experience: whereas VEGF-TKIs are administered continuously and often lead to chronic toxicities (fatigue, diarrhea, hypertension), ICI-based regimens may allow treatment discontinuation after a fixed duration (e.g. 2 years of PD-1 therapy in most trials), with some patients maintaining long-term disease control off treatment. This strategy reduces cumulative exposure to therapy, although ICIs can also cause distinct immune-related toxicities, sometimes permanent.

At the population level, the arrival of ICIs has translated into real-world gains: registry data show that median survival for patients presenting with de novo metastatic RCC improved from around 8 months in the pre-ICI era (2011–2015) to 11 months after their introduction (2016–2020). While still modest at the population scale, this represents a meaningful improvement in outcomes and underscores the paradigm shift brought by immunotherapy (99).

As a summary of therapeutic advances in metastatic clear-cell RCC, **Figure 25** illustrates the successive treatment eras, from cytokine therapy to targeted agents and immunotherapy-based combinations. **Figure 26** complements this overview by detailing the timeline of pivotal clinical trials specifically involving immune checkpoint inhibitors and immunotherapy-based regimens.

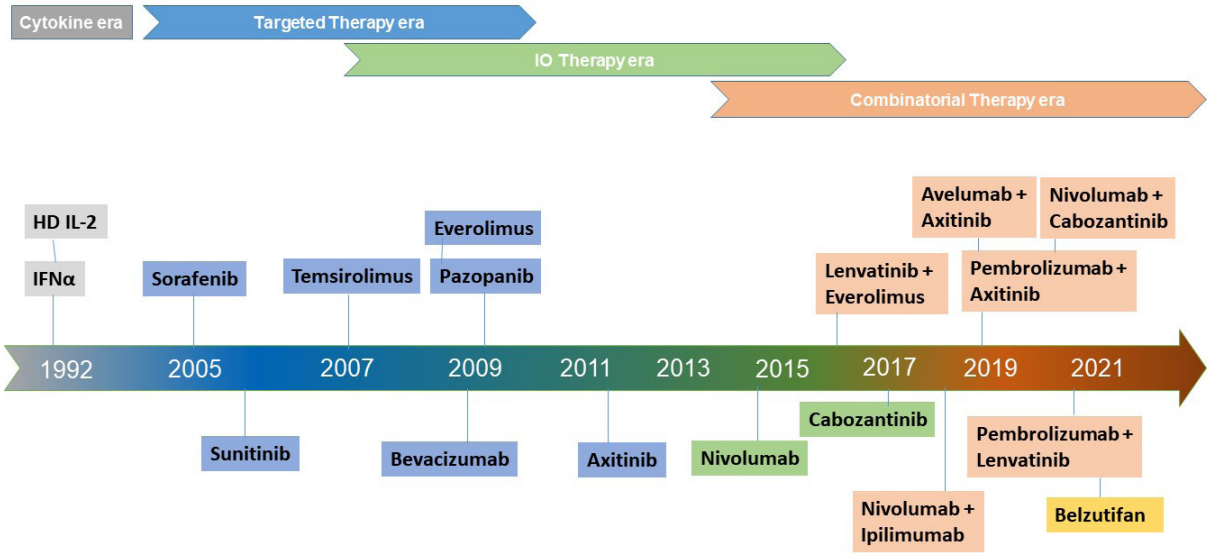

Figure 25. Evolution of systemic therapies for metastatic renal cell carcinoma (mRCC).
Treatment development can be divided into successive therapeutic eras: the cytokine era (interleukin-2 [IL-2], interferon-α [IFNα]); the targeted therapy era with VEGF and mTOR inhibitors (sorafenib, sunitinib, temsirolimus, everolimus, pazopanib, bevacizumab, axitinib, cabozantinib); the immune-oncology (IO) era with the introduction of immune checkpoint inhibitors (nivolumab, ipilimumab); and the combinatorial era with dual ICI regimens (nivolumab + ipilimumab) or ICI–TKI combinations (avelumab + axitinib, pembrolizumab + axitinib, nivolumab + cabozantinib, lenvatinib + everolimus, pembrolizumab + lenvatinib). More recently, HIF-2α inhibition with belzutifan has been incorporated as a novel option in later-line treatment.

Source: (100), under CC-BY-NC-ND

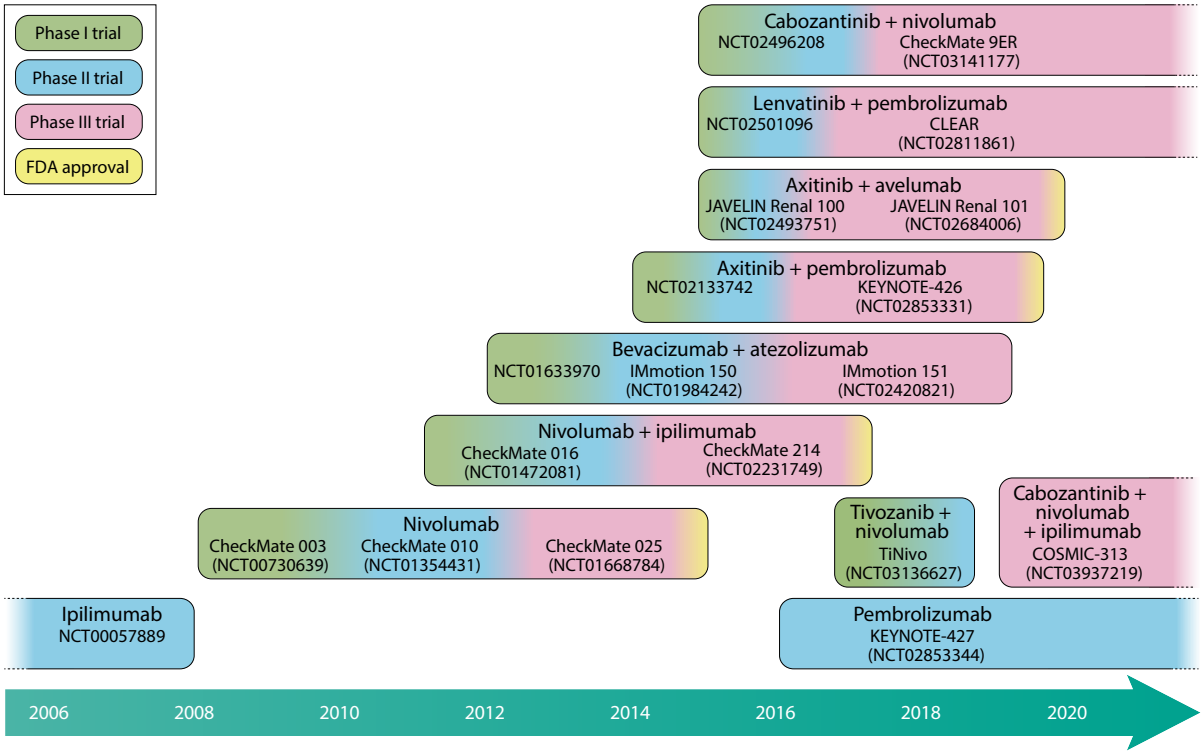

Figure 26. Timeline of pivotal clinical trials of ICIs in metastatic renal cell carcinoma (mRCC).

The figure highlights phase I–III studies that established the role of ICIs, alone or in combination with VEGFR tyrosine kinase inhibitors (TKIs) or other ICIs, leading to subsequent regulatory approvals. Landmark trials include CheckMate 025 (nivolumab vs everolimus), CheckMate 214 (nivolumab + ipilimumab vs sunitinib), KEYNOTE-426 (pembrolizumab + axitinib vs sunitinib), CheckMate-9ER (nivolumab + cabozantinib vs sunitinib), and CLEAR (lenvatinib + pembrolizumab vs sunitinib), among others.

Source : (101), reproduced with permission from Springer Nature, license number 6154850135248

C. Immunotherapy in the adjuvant and neoadjuvant setting

While metastatic RCC has been the main setting where immunotherapy has revolutionized management, its benefits are not confined to advanced disease. In more localized forms, adjuvant immunotherapy administered after complete surgical resection aims to eradicate minimal residual disease and reduce the risk of recurrence. This strategy is particularly relevant in patients with a high risk of relapse, such as those with locally advanced tumors, nodal involvement, or resected oligometastatic disease.

The phase III KEYNOTE-564 trial established pembrolizumab (anti PD-1) as the first effective adjuvant ICI in RCC. Initially demonstrating a significant improvement in disease-free survival (102), its benefit has now been reinforced by the recently reported 5-year update (ASCO 2025), which confirmed a significant overall survival (OS) and five-year disease-free survival (DFS) (103). These results firmly establish pembrolizumab as the standard of care in the adjuvant setting for high-risk ccRCC.

By contrast, other phase III adjuvant trials have been negative. IMmotion010 (atezolizumab:

anti-PD-L1) and CheckMate-914 (nivolumab plus ipilimumab) failed to show disease-free survival benefit over placebo (104,105). These discrepancies suggest that the efficacy of adjuvant immunotherapy in RCC depends on the specific agent, treatment schedule, and patient selection, and they raise ongoing questions regarding the optimal design of perioperative strategies.

Neoadjuvant immunotherapy is administered prior to surgery with the dual intent of tumor downstaging and systemic priming while the full tumor antigen repertoire is present. The phase III PROSPER RCC trial tested perioperative nivolumab (a single preoperative dose followed by postoperative therapy) but was terminated early for futility, as it failed to demonstrate an improvement in recurrence-free survival over surgery alone (106). Although PROSPER RCC failed to demonstrate a recurrence-free survival advantage, it incorporated extensive translational studies, including on pre- and post-treatment tumor tissues, to assess immunologic changes induced by neoadjuvant nivolumab, peer-reviewed results are awaited to determine whether such changes can be translated into optimized perioperative immunotherapeutic strategies.

In summary, immunotherapy has now expanded beyond metastatic disease into the perioperative space. Adjuvant pembrolizumab has become a standard of care following nephrectomy for high-risk ccRCC, supported by both DFS and OS benefit, while neoadjuvant immunotherapy remains experimental. These developments underscore the clinical progress achieved but also highlight persistent uncertainties in patient selection and strategy optimization, reinforcing the need for functional preclinical models capable of predicting response and guiding individualized use of immunotherapy in RCC.

D. Future directions in RCC immunotherapy

Combination strategies beyond standard doublets have also been explored. The phase III COSMIC-313 trial evaluated the triplet of nivolumab, ipilimumab, and cabozantinib. Results, presented at ASCO 2025, demonstrated a significant improvement in progression-free survival compared with nivolumab–ipilimumab, but no overall survival benefit and a higher incidence of toxicity, thereby limiting its clinical use to very select patients (107).

Similarly, the phase III CONTACT-03 trial tested immunotherapy rechallenge with atezolizumab (anti PD-L1) plus cabozantinib after prior ICI exposure. Data presented at ASCO 2025 demonstrated no additional survival benefit compared with cabozantinib monotherapy and higher toxicity, reinforcing cabozantinib alone as the preferred second-line approach (108). These findings suggest that acquired resistance to immunotherapy in RCC is largely irreversible under current immunotherapeutic strategies. This underscores the need not only for rational sequencing strategies in the clinic, but also for robust preclinical models capable of dissecting mechanisms of resistance and guiding the design of novel therapeutic combinations and sequential treatments.

Cell-based immunotherapies are emerging as innovative strategies in RCC. The phase I TRAVERSE trial evaluated ALLO-316, an allogeneic CAR-T product directed against CD70, in heavily pretreated ccRCC. CD70 is highly expressed in most clear-cell RCCs while largely absent from normal tissues, making it an attractive target for adoptive approaches. Results presented at ASCO 2025 showed manageable safety and early antitumor activity, particularly in CD70-high tumors (109). These findings provide proof-of-concept for adoptive cellular approaches, including CAR-T cells, TILs, and NK-based therapies, in the future management of RCC.

In parallel, novel checkpoints such as LAG-3, TIGIT, HLA-G, CD47, and VISTA are being investigated in early-phase trials.

Beyond currently approved immune checkpoint inhibitors and early experiences with cellular therapies, multiple novel immunotherapeutic strategies are being investigated in RCC. These include cytokine-based approaches, adoptive T cell therapies, therapeutic vaccines, and novel checkpoint or metabolic modulators. **Table 3** provides selected examples and highlights how each of these strategies targets distinct steps of the cancer–immunity cycle.

In summary, the therapeutic landscape of RCC continues to expand rapidly. Trials such as COSMIC-313, CONTACT-03, and TRAVERSE, illustrate both the opportunities and limitations of emerging strategies. The heterogeneity of responses underscores the critical need for preclinical models that faithfully recapitulate the tumor–immune microenvironment. Such models are essential not only to investigate mechanisms of resistance but also to guide patient stratification and accelerate the development of next-generation immunotherapies.

Table 3. Selected emerging immunotherapies for RCC.

Examples of novel immunotherapeutic strategies under clinical investigation in RCC, categorized by mechanism of action and their respective targets within the cancer–immunity cycle. Agents include cytokine-based therapies, cell-based approaches (e.g. CAR-T, TILs), therapeutic vaccines, novel checkpoint inhibitors, and pathway modulators.

Compound	Mechanism of action	Combination	ClinicalTrials.gov identifier	Modified step of the cancer–immunity cycle
Proinflammatory cytokines				
High-dose IL-2	T cell growth factor	Nivolumab	NCT02989714	T cell priming and activation
		Radiation therapy	NCT02306954	Recognition of cancer cells by T cells
Bempegaldesleukin	T cell growth factor	Nivolumab ± ipilimumab	NCT02983045	Killing of cancer cells
Inhibitors of anti-inflammatory cytokines, cytokine receptors or growth factors				
Mavorixafor	CXCR4 inhibitor	Axitinib	NCT02667886	Trafficking of immune cells into tumours Infiltration of immune cells into tumours
Cell therapies				
Anti-hCD70 CAR T cells	Recognition and killing of CD70-expressing cells	High-dose IL-2	NCT02830724	Recognition of cancer cells by T cells
Adoptive T cell therapy with TILs	Recognition of HLA-restricted tumour antigens	IL-2	NCT02926053	Killing of cancer cells
HERV-E TCR transduced autologous T cells	Recognition of HLA-A11:01-restricted HERVE-E-derived peptide	None	NCT03354390	
Therapeutic vaccines				
NEOVAX	Neoantigen peptides plus an adjuvant leading to an antigen-specific T cell response	Ipilimumab (local administration)	NCT02950766	Cancer antigen presentation T cell priming and activation
RO7198457	Neoantigen RNA leading to an antigen-specific T cell response	Atezolizumab	NCT03289962	
Immune-checkpoint inhibitors				
MK-7684	Anti-TIGIT antibody	Pembrolizumab	NCT02964013	T cell priming and activation Killing of cancer cells
Co-stimulatory immune receptor agonists				
Utomilumab	Agonistic anti-4-1BB antibody	Pembrolizumab	NCT02179918	Killing of cancer cells
Tryptophan metabolism pathway inhibitors				
Linrodostat	IDO1 inhibitor	Nivolumab	NCT03192943	Killing of cancer cells (alters immunosuppressive microenvironment)
Adenosine signalling pathway inhibitors				
Ciforadenant	A2AR inhibitor	None, or atezolizumab	NCT02655822	Killing of cancer cells (alters TAM, DC, NK cell function and ameliorates immunosuppressive microenvironments)
BMS-986179	CD73 inhibitor	Nivolumab	NCT02754141	Killing of cancer cells (alters TAM, DC, NK cell function and ameliorates immunosupressive microenvironments)

A2AR, adenosine A_{2A} receptor; DC, dendritic cell; HERV-E, human endogenous retrovirus envelope; IDO1, indoleamine 2,3-dioxygenase 1; NK, natural killer; TAM, tumour-associated macrophage; TCR, T cell receptor; TIGIT, T cell immunoreceptor with immunoglobulin and ITIM domains; TILs, tumour-infiltrating T lymphocytes.

Source: (110), reproduced with permission from Springer Nature, license number 6154850357520

E. Current positioning and unmet needs

Immunotherapy now occupies a central role in the management of RCC: it is the backbone of systemic therapy in the metastatic setting, has become a standard option in the adjuvant setting, and is under active investigation in the perioperative context. Nevertheless, important limitations persist. Even with optimal combinations, 30–45% of patients fail to respond, and complete responses remain limited to ~10–16%. Resistance, both primary and acquired, continues

to restrict durable benefit (88).

Crucially, no clinically validated biomarkers currently exist to predict response. PD-L1 expression has consistently failed to provide reliable predictive value, and although exploratory candidates such as RNA-based gene expression signatures (angiogenic, T-effector, myeloid inflammatory), tumor mutational or neoantigen burden, PBRM1 mutations, $CD8^+$ T cell density, and IFNγ-related profiles have been proposed, their utility remains inconsistent and confined to research settings (101). These limitations translate into persistent uncertainty in clinical decision-making, both in the metastatic and perioperative settings.

This creates a critical unmet need for treatment testing approaches capable of rapidly anticipating treatment sensitivity and guiding personalized therapy. At the same time, the development of emerging checkpoint targets (e.g., LAG-3, TIGIT, HLA-G, CD47) and novel immunotherapeutic strategies requires robust preclinical models that reproduce tumor–immune interactions, preserve heterogeneity, and enable functional readouts (cytotoxicity, cytokine release, immune profiling).

Such systems could serve three complementary purposes: (i) as functional tools to predict individual patient response in the absence of validated biomarkers; (ii) as platforms to evaluate novel immunotherapies and rational combinations prior to clinical translation; and (iii) as research instruments to dissect mechanisms of resistance and identify new therapeutic targets. Together, these objectives highlight the dual clinical and scientific value of advanced models and define the translational rationale underlying the present thesis the requirements of such models are summarized in **Box 1**.

In summary, ccRCC stands out by its frequency, molecular complexity, and paradoxical immune microenvironment, characterized by dense infiltration yet impaired antitumor activity. Despite major therapeutic advances with immune checkpoint inhibitors, both primary and acquired resistance remain key clinical challenges. The absence of reliable biomarkers and the heterogeneity of responses further underscore the necessity of developing relevant experimental models. Such models must capture tumor heterogeneity, the multiplicity of immune escape mechanisms, and the metabolic constraints specific to ccRCC. These requirements define the scientific and methodological framework that will be addressed in the following chapter, dedicated to preclinical models.

Box 1. Requirements for a Relevant Preclinical Model of ccRCC

Requirements for a relevant preclinical model of ccRCC

- Preservation of tumor heterogeneity and key immune components (TILs, Tregs, TAMs, MDSCs).
- Maintenance of extracellular matrix and stromal compartments.
- Representation of multiple immune checkpoints involved in immune escape (PD-L1, HLA-G/E–NKG2A, B7-H3, B7-H4, LAG-3, TIGIT, TIM-3, CD47…).
- Faithful reproduction of tumor–host interactions.
- Incorporation of oxygen gradients and metabolic rewiring (glycolysis, lactate accumulation), mimicking hypoxia and aberrant angiogenesis.
- Compatibility with functional readouts (cytotoxicity assays, cytokine secretion, immunophenotyping, transcriptomic, flow cytometry).
- Rapid implementation to support personalized immunotherapy testing.
- Autologous context

Chapter 3: Preclinical Models for Immuno-Oncology

Thus, despite major breakthroughs, substantial progress is still required to fully understand and optimize the outcomes of immunotherapy. In this context, the choice of appropriate preclinical models becomes critical. Broadly defined, a preclinical model is an experimental system designed to reproduce specific aspects of human tumors, thereby enabling the study of their biology and the evaluation of therapeutic strategies. In immuno-oncology, such models can serve multiple purposes: elucidating mechanisms of tumor–immune interactions, screening candidate therapies, and identifying determinants of response and resistance. Ultimately, they hold the potential to predict patient responses to immunotherapy and support the development of personalized treatment approaches.

Historically, preclinical cancer research has relied heavily on two-dimensional monocultures of clonal cell lines (111). These systems have been invaluable for understanding basic tumor biology and testing cytotoxic drugs, but their lack of three-dimensional architecture, stromal components, and immune context makes them poorly suited for immuno-oncology studies. Immunotherapy efficacy depends on dynamic, spatially complex interactions between tumor and immune cells, which require models that better recapitulate the tumor microenvironment. To address this challenge, a variety of preclinical systems have been developed, ranging from traditional cell lines to in vivo models and advanced 3D platforms. Their respective advantages and limitations in the context of immuno-oncology will be reviewed in the following sections.

I. Classical 2D Culture Cell Line Model

A. Cancer cell lines in oncology and in RCC research

Since their establishment in the 1950s, immortalized cancer cell lines have represented a cornerstone of experimental oncology. The introduction of the HeLa line, derived from cervical carcinoma, demonstrated for the first time the possibility of propagating human tumor cells indefinitely under laboratory conditions (112). This breakthrough provided researchers with an unprecedented renewable source of homogeneous tumor material, enabling systematic studies of cancer biology outside the patient.

By the mid-1980s, cancer cell lines had become central not only for mechanistic research but also for therapeutic discovery. Until 1985, the U.S. National Cancer Institute (NCI) drug screening program had relied primarily on murine leukemias (L1210, P388) and a handful of transplantable tumor models to evaluate compound activity. This approach, although effective

in identifying cytotoxic agents, was poorly representative of the diversity of human cancers. In 1990, the NCI therefore launched a landmark initiative based on a panel of 60 human cancer cell lines (NCI-60) encompassing major tumor types (113,114). This shift enabled systematic in vitro drug screening across multiple histologies, allowed rapid elimination of inactive compounds before animal testing, and generated a reference framework still widely used today.

As comprehensively reviewed by Brodaczewska et al., the same trajectory has occurred RCC research. RCC cell lines have been generated from both primary tumors and metastatic sites, reflecting different aspects of the disease. For example, the 786-O and Caki-2 lines were derived from primary renal tumors, while Caki-1 originated from a skin metastasis and ACHN from a pleural effusion. Together, these models have provided the backbone of RCC research for decades, forming the entry point for both basic biological discoveries and translational investigations (115). Representative examples of RCC histology and the corresponding cell line morphology are shown in **Figure 27**.

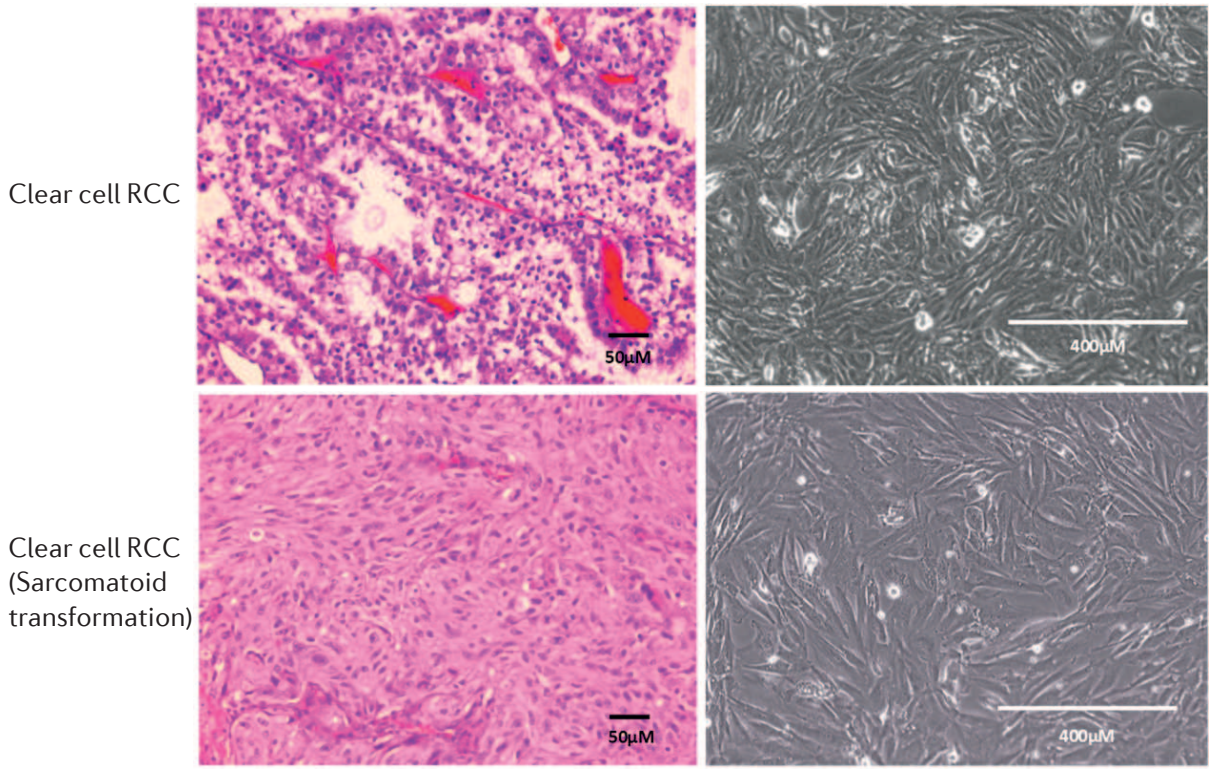

Figure 27. Histological sections of clear cell RCC (top) and sarcomatoid-transformed ccRCC (bottom) compared with the corresponding cell line cultures.

While tissue architecture is highly complex in vivo, cultured cells adopt a more uniform morphology typical of established RCC cell lines.

Source: adapted from (116), reproduced with permission from John Wiley and Sons, license number 6154850536924

B. Molecular and phenotypic characterization of RCC cell lines

1. RCC subtypes

As explained earlier, RCC represents a heterogeneous group of tumors comprising several histological subtypes: clear-cell RCC (ccRCC, ~75%), papillary RCC (~15%), chromophobe RCC (~5%), and a collection of rarer entities defined in the recent WHO/ISUP classifications (50). Despite this diversity, ccRCC, is by far the most represented subtype in established cell line collections, while papillary and chromophobe models are underrepresented and rare subtypes are essentially absent.

A long-standing difficulty in RCC cell line research is the misclassification of histological subtypes. While many lines are broadly considered "clear-cell," careful genomic and phenotypic analyses have revealed that some may in fact derive from papillary RCC or present hybrid features. For example, Caki-2, historically described as a ccRCC line, forms papillary-like tumors in xenografts and exhibits elevated MET expression and chromosome 8 aberrations characteristic of papillary histology (117,118). Similarly, the ACHN line, derived from a pleural effusion, harbors a c-MET polymorphism and chromosomal patterns consistent with papillary RCC, despite sharing certain ccRCC-like transcriptional programs. Even the "classical" A-498 line, part of the NCI-60 panel, has been questioned, with some studies suggesting papillary origin (115). These examples illustrate the pitfalls of relying solely on historical annotation without molecular validation, a factor that continues to complicate data interpretation in RCC research.

2. Genetic alterations captured in RCC lines

As detailed in the previous chapter, the genetic landscape of ccRCC is dominated by mutations in genes located on chromosome 3p. Inactivating alterations of VHL, leading to stabilization of HIF-1α and HIF-2α, are observed in up to 90% of sporadic ccRCC tumors and are mirrored in many RCC cell lines such as 786-O, 769-P, RCC4, and A-498. Additional recurrent alterations in PBRM1 (~50%), BAP1 (~15%), and SETD2 (~15%) are also represented across different lines, though often with inconsistencies compared to clinical frequencies. For example, 786-O carries a VHL mutation and expresses wild-type PBRM1, while Caki-2 and A-704 display PBRM1 loss-of-function alterations. Mutations in BAP1 have been reported in UM-RC-6 and SN12C, whereas SETD2 defects occur in A-498, Caki-1, and A-704 (115,119).

At the chromosomal level, recurrent features of ccRCC such as loss of 3p, loss of 14q (HIF1A), and gain of 5q are variably preserved. For instance, 769-P, 786-O, A-704, and Caki-1 display concomitant 3p and 14q losses (120). However, comprehensive karyotypic information remains incomplete for many RCC lines, limiting direct comparisons with patient tumors. A complete table of the culture medium, histological type and mutated genes in the main RCC cell lines can

be found in Appendix 1.

3. Phenotypic features and tumorigenic potential

Beyond genetics, RCC cell lines differ in their functional behavior. Caki-1, derived from a metastatic lesion, exhibits high tumorigenicity and metastatic potential in xenograft models, making it a preferred system to study invasion and dissemination. 786-O, is often used to model bone metastasis, and 769-P often fails to form robust tumors in vivo (115). Some lines, such as Caki-1, also display epithelial polarity and kidney-like features in vitro, providing opportunities to explore RCC differentiation biology (121).

C. RCC cell lines in immuno-oncology: applications, strengths and limitations

1. Applications in immuno-oncology

With the advent of immune checkpoint inhibitors and adoptive cell therapies, immuno-oncology has become central to RCC research. As reviewed by Wang et al., classical RCC cell lines have been extensively used as first-line tools to model immune–tumor interactions, supporting applications ranging from PBMC co-cultures to checkpoint studies and antibody-mediated cytotoxicity assays (111). Tumor–peripheral blood mononuclear cell (PBMC) co-cultures represent the most common setting, enabling rapid assessment of T cell or NK cell activation and tumor lysis. NK cell cytotoxicity against RCC lines has been extensively characterized, particularly in models such as Caki-1 and 786-O. More advanced settings include the use of TILs expanded from patient tumors or engineered lymphocytes, such as CAR-T cells targeting RCC antigens (e.g., carbonic anhydrase IX, CAIX) (122). Moreover, RCC cell lines are suitable for functional assays modeling antibody-mediated effects, such as antibody-dependent cellular cytotoxicity (ADCC), complement-dependent cytotoxicity (CDC), or macrophage-mediated phagocytosis (123). These readouts have been particularly used to validate antibody-based therapies and Fc-engineered constructs in vitro before testing in in vivo models.

Another application lies in the characterization of immune checkpoint expression on RCC cells. Several lines, including 786-O, Caki-1, and ACHN, express PD-L1 at variable levels, which can be modulated by cytokine exposure, especially interferon-γ (124). This provides a controlled system to study checkpoint dynamics and resistance mechanisms.

Collectively, these applications position RCC cell lines as a first-line tool for IO research, bridging basic immunobiology and translational immunotherapy development.

2. Strengths of RCC cell lines in immuno-oncology research

The major advantages of RCC cell lines mirror their general utility in oncology. They are inexpensive, scalable, and easy to manipulate, offering a virtually unlimited supply of material. Their experimental reproducibility across laboratories has enabled benchmarking of immune assays and facilitated comparison between studies. Moreover, RCC lines are genetically tractable: CRISPR-mediated editing, overexpression, or knockdown strategies can be readily implemented to dissect immune-related pathways (125,126). Finally, they remain the standardized entry point for immuno-oncology drug development, enabling rapid elimination of ineffective agents before costly preclinical or clinical testing.

3. Limitations and partial alternatives

Despite their utility, RCC cell lines suffer from profound limitations when applied to immuno-oncology. They lack stromal, vascular, and immune compartments, thereby omitting the cellular diversity of the tumor microenvironment. Cultivation in 2D monolayers further imposes artificial conditions, with supraphysiological oxygen tension and nutrient composition that poorly replicate the metabolic landscape of RCC.

Furthermore, with time, lines undergo genetic drift and clonal selection, deviating from the original patient tumor (127).

A central point is that cancer is pluriclonal: tumors are mosaics of subclones with distinct mutational and epigenetic profiles, shaped by evolutionary pressures and selective bottlenecks. Established cell lines, in contrast, typically originate from a single dominant clone and are further homogenized by long-term in vitro propagation. Consequently, while they preserve certain driver events of the parental tumor, they fail to recapitulate the full clonal diversity and microenvironmental complexity of RCC.

As a partial solution, primary low-passage RCC cultures can be employed. These retain a broader clonal spectrum and sometimes residual stromal or immune interactions. However, they require constant donor supply, their success rate remains modest, their lifespan limited, and they inevitably converge toward monoclonality with serial passaging.

4. Positioning and conclusion

In summary, RCC cell lines provide an indispensable model for immuno-oncology research. Their accessibility and reproducibility across laboratories have facilitated the comparison of experimental results worldwide. At the same time, it is acknowledged that cell lines represent a profound simplification of cancer, as they are deprived of microenvironmental interactions, stromal support, and host immune responses.

They nonetheless remain a foundation of cancer biology, having enabled the discovery of oncogenes, tumor suppressors, and signaling pathways, and serving as a first-pass screening platform for countless therapeutic agents.

However, these limitations necessitate cautious interpretation. Findings derived from cell lines must be contextualized within the broader tumor ecosystem and complemented by more physiologically relevant models, both in vitro and in vivo.

In particular, in vivo models remain indispensable to capture the full dynamics of tumor–immune interplay, as discussed in the next section.

II. In Vivo Models

The second major category of classical oncology models comprises in vivo systems, which leverage the biological complexity of living organisms to recapitulate both tumor biology and immune responses. In this section, we focus on murine models, which remain the most widely used in preclinical immunotherapy research due to their genetic tractability, cost-effectiveness, and extensive reagent availability. Other animal species are occasionally employed in specific contexts, including rats for imaging or pharmacology studies, and in rare cases, non-human primates for evaluating highly species-specific immunotherapeutic strategies (128). Emerging animal models are also under investigation, including zebrafish (*Danio renio*), which offers unique advantages such as optical transparency for real-time imaging and relatively low maintenance costs (129). In-vivo models can take many forms each with distinct strengths and purpose **Figure 28**, (130).

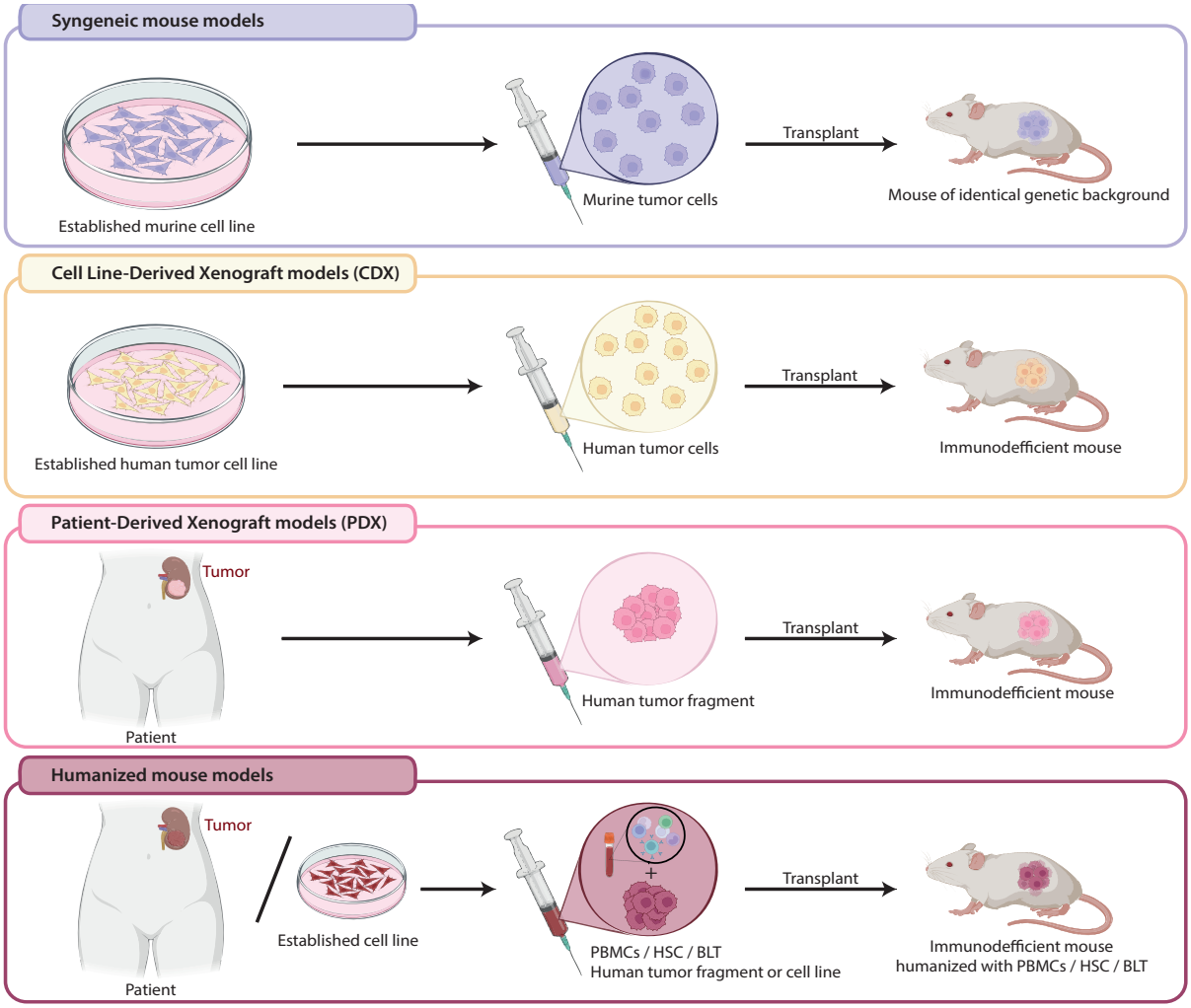

Figure 28. Summary of mouse models.

Syngeneic models are established by transplanting murine tumor cells into immunocompetent mice of identical genetic background, thereby preserving intact immune–tumor interactions. Cell line-derived xenograft (CDX) models involve implantation of established human tumor cell lines into immunodeficient mice, providing a reproducible system but lacking immune components. Patient-derived xenograft (PDX) models use fresh human tumor fragments transplanted into immunodeficient mice. Humanized mouse models combine patient-derived tumor cells or fragments with human immune components such as peripheral blood mononuclear cells (PBMCs), hematopoietic stem cells (HSCs), or BLT (bone marrow–liver–thymus) tissues. BLT humanized mice are generated by engrafting immunodeficient hosts with human fetal liver and thymus tissue together with autologous hematopoietic stem cells, allowing robust reconstitution of a human immune system.

Adapted from: (130), under CC BY-NC-ND 4.0

A. Syngeneic murine models

First established more than 50 years ago, syngeneic animal models represent some of the earliest experimental platforms used to study tumor development in animals. They are made by implanting murine tumor cell lines into immunocompetent mice of the same genetic background. Because the host immune system is intact, these models enable evaluation of antitumor immunity, pharmacodynamics of immunotherapies, and mechanisms of sensitivity and resistance in a living organism with full immune, hematopoietic and stromal compartments rendering different response to immunotherapy according to the model (131). In renal cancer research specifically, RENCA (Renal Adenocarcinoma) in BALB/c (Bagg Albino, substrain c) has been widely used (132–134) even more recently for immune checkpoint inhibition (135). Once the model chosen, several approaches are available: subcutaneous implantation offers speed and accessibility, while orthotopic implantation beneath the renal capsule better captures organ-specific vasculature, and immune trafficking. Other routes (intraperitoneal, intravenous, intrasplenic) can model experimental metastatic RCC.

Syngeneic models allow for a wide range of potential readouts, both clinical and mechanistic. They include tumor growth inhibition, objective response rate, and survival, with bioluminescent imaging available when tumor cell lines are engineered with reporter constructs. Mechanistic analyses can interrogate the tumor microenvironment through flow or mass cytometry of tumor-infiltrating lymphocytes and myeloid populations, multiplex immunohistochemistry or imaging cytometry to capture spatial organization, cytokine and chemokine quantification in plasma or interstitial fluid, TCR and BCR repertoire profiling, and transcriptomic or single-cell analyses to identify pathway modulation. Furthermore, a unique feature of vivo models is the possibility to perform rechallenge experiments to assess immunological memory following complete tumor regression. However, the validity of such experiments remains debated, as studies have highlighted that tumor rejection upon rechallenge after immunotherapy in animal models may not necessarily be attributable to the immunotherapeutic intervention itself (136).

Syngeneic tumor models are straightforward to establish and have proven effective in demonstrating the antitumor activity of several clinically approved immune checkpoint inhibitors, including CTLA-4, PD-1, and PD-L1 blockade (137,138), However, with the rise of targeted therapies, research priorities shifted toward interventions directed at human-specific tumor antigens, sometimes absent from simple syngeneic models. This led to a need for other models, a gradual replacement of purely murine systems by human xenografts and genetically engineered mouse models (GEMMs).

Beyond the absence of human targets, syngeneic systems face additional limitations. The typically rapid progression of murine tumors in these settings does not allow sufficient time for

establishing chronic inflammatory conditions that are characteristic of human cancer. Furthermore, murine tumors generally fail to capture the full genetic complexity of their human counterparts, as they tend to harbor a comparatively lower mutational burden (139).

B. Genetically Engineered Mouse Models (GEMMs)

Advances in our understanding of tumorigenesis, combined with the development of genetic engineering technologies, have enabled the generation of mouse models in which tumors arise spontaneously. These systems offer a tumor microenvironment that is closer to physiological conditions, restricting tumor initiation to the relevant organ site, thereby preserving the native tissue context (140).

The resulting systems are referred to as Genetically Engineered Mouse Models (GEMMs). They thus capture elements of tumor initiation and progression absent from simple transplantation models. For example, in ccRCC, while syngeneic RENCA tumors are widely used in renal cancer research, they fail to reproduce key features of human clear-cell renal cell carcinoma such as *VHL* inactivation and downstream HIF-2α–dependent pathways, which can be modeled in tailored GEMMs (141). However, a major limitation of GEMMs is their typically low tumor mutational burden (TMB), which contrasts with the high neoantigen load observed in many human tumors. This low TMB may result in reduced antigenicity and impaired modeling of immune responses, particularly for studies on immunotherapy. By contrast, carcinogen-induced tumors, though less genetically defined, often present a higher mutational burden and enhanced immunogenicity, making them valuable for studying immune responses despite limited modeling of specific oncogenic drivers. Several GEMMs model exist for ccRCC, covering a variety of driver mutations (134). Notably, recent GEMMs provide more physiologically relevant platforms for modeling early ccRCC. Recent GEMMs employ kidney-targeted CRISPR/Cas9 to inactivate VHL and inducible systems combining 3p tumor suppressor loss (e.g., BAP1, PBRM1) with stabilized HIF, thereby reproducing the sequential genetic events of ccRCC initiation (142,143).

However, despite their utility, syngeneic, whether classical or GEMMs models use murine tumors in murine microenvironments and show limitations in recapitulating human tumors in human hosts. Indeed, human-specific targets may lack cross-reactivity (144), Fc receptor biology differs (145,146), and checkpoint pathways are not fully conserved (147). The immunogenicity of such models can be artificially high or low depending on the line, triggering responses that may not mirror human tumors. Tumor heterogeneity and key biological dynamics lack resemblance to human tumors and the nonclassical checkpoint repertoire; myeloid composition and MHC architecture also diverge from human RCC, which can shift immunotherapy response patterns (134).

Thus, while syngeneic models offer a rapid, immunocompetent, and reproducible in vivo plat-

form, interspecies differences necessitate the incorporation of human tumor antigens and microenvironmental components. In animal-based systems, this can be achieved through a range of xenograft approaches, each offering distinct advantages and limitations.

C. Cell line-Derived Xenografts

To prevent rejection of implanted human material, all xenograft models rely on immunodeficient hosts. Cell line-derived xenografts (CDX) are among the earliest and most established of these systems. Developed in the 1960s with athymic “nude” mice (148) and later refined through strains with deeper immune deficits such as NOD/SCID (149) and NSG allowing for better tumor take rate, CDX involve the implantation of well-characterized human cancer cell lines into such hosts, in subcutaneous or orthotopic sites. These models provide reproducible tumor take rates, predictable growth kinetics, and technical simplicity.

However, just like with traditional 2D cell culture models described earlier, the extensive in vitro passaging of these lines often leads to genetic and phenotypic drift away from the clinical disease (150), diminishing their relevance for modeling tumor heterogeneity and adaptive resistance , they also lack the TME and spatial organization of human tumors (151).

D. Patient-Derived Xenografts (PDX)

These limitations have driven the development of patient-derived xenografts (PDX), in which tumor fragments from individual patients are implanted directly into immunodeficient mice without prior in vitro culture. This approach helps to preserve genetic, phenotypic, and histopathological complexity of the original tumor (152), including clonal heterogeneity and other key components of the tumor microenvironment, notably in ccRCC (153,154). Furthermore it has been shown that PDX model preserve the molecular subtype of the original ccRCC tumors (155).

By better mirroring the architecture and biology of human cancers, PDX models offer enhanced predictive value for drug response compared to CDX, particularly in studies aiming to capture mechanisms of resistance and disease progression (152). In ccRCC, they also represent a privileged platform to study tumor vasculature: for up to 35 days post-implantation, the neovasculature within ccRCC PDX remains predominantly composed of human endothelial cells, unlike in colorectal cancer PDX, where murine endothelial cells rapidly replace the human component (156). This unique feature has been exploited to investigate anti-angiogenic strategies, including the activity of VEGF-targeted therapies (157). ccRCC PDX models have been successfully used to reproduce therapeutic responses and resistance patterns to targeted agents such as sunitinib and mTOR inhibitors (158,159).

While these attributes make PDX a valuable translational tool, they share with CDX major limitations. They typically have a long engraftment time of several months and high rate of failure (160), even though it has been improved with more deeply immunocompromised mouse strains (134). This engraftment time renders this technique almost completely useless for clinical decision support where time to biological answer must match the fast-paced requirement of medical decisions.

Of course, both these models do not come with any functional immune system due to the profound immunodeficiency of their host strains. Thus, their use for evaluating immune checkpoint inhibitors, adoptive cell therapies, or other immune-based therapies is done only using more advanced models, constituted of CDX or PDX engrafted in humanized models.

E. Humanized PDX models

1. Principles

Humanized animal models are based on the engraftment of functional human immune components into severely immunodeficient mice, enabling the study of human-specific immune–tumor interactions in vivo (161). The concept emerged in the late 1980s and early 1990s with the development of SCID mice (Bosma et al., 1983). This was followed by the development of NOD/SCID (149), and later Il2rg-null strains such as NOG, NRG and NSG (163) which eliminated residual NK cell activity and significantly improved engraftment of human hematopoietic cells (Figure 29). These models can then be engrafted with CDX or PDX.

Three principal strategies are currently employed to humanize immunodeficient mice for preclinical studies in immuno-oncology:

- Peripheral blood mononuclear cell (PBMC) engraftment involves the intravenous injection of mature human immune cells, primarily T cells, into highly immunodeficient mice such as NSG or NOG strains. This approach enables the rapid reconstitution of a functional human T cell compartment within 2 to 4 weeks. However, this rapidity comes at a cost as PBMC-engrafted mice typically develop xenogeneic graft-versus-host disease (xeno-GVHD), limiting the experimental window and restricting longitudinal applications (164,165).
- $CD34^+$ hematopoietic stem cell (HSC) engraftment relies on transplantation of human hematopoietic progenitors, usually derived from cord blood, mobilized peripheral blood, or fetal liver, into preconditioned neonatal or adult hosts. Over 10 to 16 weeks, this strategy supports multilineage immune reconstitution, including T cells, B cells, NK cells, and myeloid compartments (166,167). Nonetheless, they often suffer from incomplete maturation of immune subsets, low myeloid and NK cell levels, and donor-to-donor variability that can impact experimental reproducibility.

- BLT (bone marrow–liver–thymus) humanization represents an advanced configuration in which human fetal liver and thymus tissues are implanted under the kidney capsule of immunodeficient mice, alongside intravenous injection of matched $CD34^+$ HSCs $CD34^+$ HSCs. The presence of a human thymic microenvironment allows proper thymic selection and maturation of T cells, generating a more diverse and physiologically educated TCR repertoire (168,169).

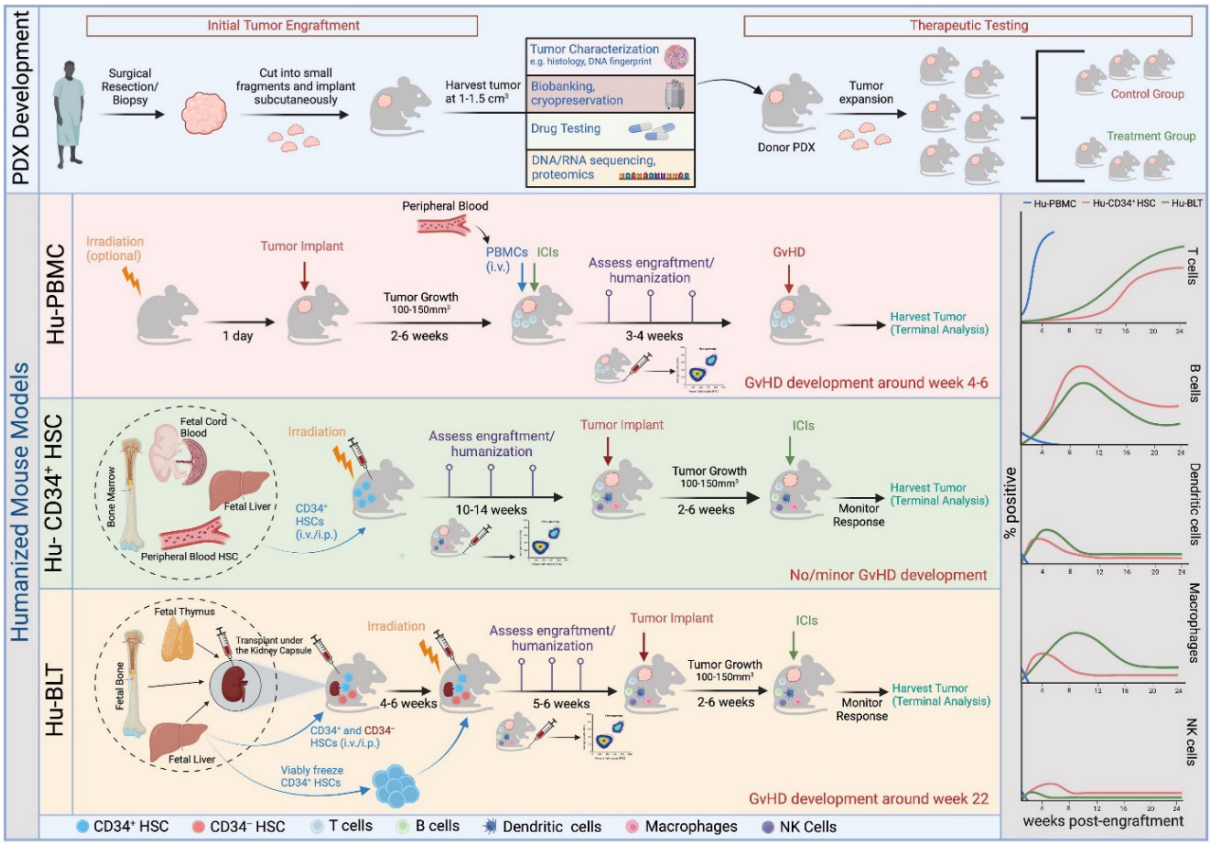

Figure 29. Methods of immune engraftment for humanized mouse models.

PDX models are established from patient tumors resected or biopsied, fragmented, and implanted into immunodeficient mice. Expanded PDX tumors can be biobanked and used for molecular characterization or drug testing. To evaluate tumor–immune interactions, PDXs can be combined with different strategies of immune humanization. In the Hu-PBMC model, peripheral blood mononuclear cells (PBMCs) are injected intravenously, leading to rapid T cell engraftment but frequent graft-versus-host disease (GvHD) within 4–6 weeks. The Hu-CD34+ HSC model relies on transplantation of hematopoietic stem cells from cord blood, fetal liver, or peripheral blood after irradiation, with multilineage human immune reconstitution achieved after 10–14 weeks and minimal GvHD. The Hu-BLT model provides the most robust and functional multilineage reconstitution, including T cells, B cells, dendritic cells, macrophages, and NK cells, with GvHD onset typically delayed until around week 22. The extent and kinetics of human immune reconstitution therefore differ between models (right panel): Hu-PBMC mice display rapid but skewed T cell–dominant engraftment; Hu-CD34+ HSC mice show slower but balanced immune reconstitution; and Hu-BLT mice achieve the most complete and stable reconstitution, allowing extended therapeutic testing.

Source: (170), under CC BY-NC-ND 4.0

2. Applications in immuno-oncology

PBMC-engrafted mice are suited for short-term, T cell–focused investigations thanks to their rapid T cell reconstitution. Traditionally constrained by a narrow experimental window, their utility has been extended in more recent double MHC class I/II–deficient strains (171–173), which delay the onset of xeno-GVHD and enable longer-term monitoring. Being the only hu-

manized model allowing to co-engraft PBMCs and tumor tissue from the same patient, they remain widely used for preclinical immuno-oncology studies. These include immune checkpoint inhibition (174–177), adoptive cell transfer (178), bispecific T cell engagers (BiTES) (179–182), and even demonstrated enhanced adoptive cell transfer efficacy in combination with BiTES (183). They have also yielded valuable mechanistic insights into the role of Tregs (184,185), cytokine-driven modulation of tumor control (186), and optimization of Fc-engineered antibodies for superior ADCC (187). In the context of ccRCC, applications are scarcer, yet notable examples include PBMC-humanized xenografts being used as a proof of efficacy for anti-CAIX antibodies via NK cell-mediated ADCC, CDC, and macrophage-mediated Antibody-Dependent Cellular Phagocytosis (ADCP) as well as T cell activation (123), a proof of concept using PD-L1-secreting CAR-T cells against a ccRCC cell line in immunodeficient hosts (188), and the validation of CAIX-targeted multifunctional immunotherapy nanoparticles (MINPs) co-delivering anti-CAIX, anti-4-1BB, and anti-CD27 antibodies, which effectively inhibited the growth of human ccRCC in PBMC-humanized mouse models (189).

However, as PBMC-engrafted models primarily reconstitute the human T cell compartment, with minimal recovery of B cells, NK cells, and myeloid subsets, they cannot fully recapitulate the complex immunosuppressive tumor microenvironment of cancer, particularly its myeloid component, which should be considered when interpreting preclinical findings (170).

Due to their capacity to reconstitute multiple human immune lineages as described earlier, $CD34^+$ HSC–humanized mice are particularly valuable for long-term immuno-oncology studies that require sustained immune activity. Compared to PBMC-engrafted models, they offer an extended experimental window and reduced, though not completely eliminated, risk of xeno-GVHD (190). Their partial reconstitution of myeloid and NK cell compartments also makes them suitable for evaluating therapies targeting these lineages, although functional deficits remain in conventional strains due to species-specific cytokine incompatibility, giving rise to other models of humanized HSC mice (191,192). HSC-humanized models generally do not allow for the co-engraftment of tumor and immune cells from the same donor, thereby limiting the direct translational relevance of immunotherapeutic studies. Nonetheless, pseudo-matching approaches, in which partially HLA-compatible tumors and immune cells are combined, have been explored to improve model fidelity and predictive value (193).

HSC-humanized Models have been developed and validated for the study of CTLA-4 and PD-1/PD-L1 immune checkpoint inhibitors (194–197), NK cells (198), myeloid cells (199,200), combinatory therapy between TKI and PD-1 blockade (201), and antitumor vaccination using DC-cells (192). While applications of $CD34^+$ HSC–humanized mouse models in ccRCC remain limited compared to PBMC-based systems, a few studies have nevertheless been reported. Notably, Wang et al. achieved tumor regression in a partially HLA-matched humanized orthotopic ccRCC CDX model using the same CAIX-directed CAR-T cells engineered to secrete anti–PD-L1 as described in PBMC-humanized systems, demonstrating profound reshaping of TME

(202). In addition, a proof of concept was provided by Kang et al., who developed an autologous HSC-humanized PDX model from a patient with metastatic ccRCC by reconstituting the immune system with $CD34^+$ progenitors from the patient's bone marrow aspirate reproducing the patient's response to immunotherapy (203).

Despite their capacity for multilineage immune reconstitution, HSC-humanized models display several important limitations that need to be considered when interpreting preclinical findings. The variability in engraftment efficiency remains a major challenge, strongly influenced by the source of $CD34^+$ cells (cord blood, mobilized peripheral blood, or fetal liver), with cord blood generally yielding higher lymphoid reconstitution (191). Furthermore, donor age exerts a critical influence: neonatal HSCs typically support more robust lymphoid engraftment, whereas adult- or elderly-derived HSCs show features of immunosenescence, including reduced T cell function, myeloid skewing, and increased tolerance to tumor growth (204,205). Given the logistical challenges of obtaining autologous bone marrow or mobilized peripheral blood samples from patients with cancer, most Hu-SRC models are allografts with few notable exceptions (206), and pseudo-matching strategies only partially address this limitation. Together, these factors underline the need for careful donor selection, standardized protocols, and complementary approaches when applying HSC-humanized systems to immuno-oncology research.

As previously described, BLT mice combine the implantation of human liver and thymus tissues with $CD34^+$ HSC engraftment, providing a functional human thymic environment. This allows for the development of a diverse and HLA-restricted T cell repertoire. In the context of immuno-oncology, this feature could translate into superior modeling of T cell–driven mechanisms, including priming, exhaustion, and checkpoint regulation (207). Despite these advantages, applications of BLT mice in the study of solid tumors remain rare. Nonetheless, they have been used to reproduce the effect of anti-PD-1 and investigate the effect of other checkpoints blockade (208,209), to generate antigen-specific $CD8^+$ T cells capable of mediating tumor control in melanoma (210), in studies on adoptive T cell or NK cell therapies (211–213), on lymphoid-myeloid crosstalk unveiling resistance to PD-1 (209), and to explore the feasibility of interleukin-1β blockade (208). To date, however, no applications have been reported in ccRCC specifically.

Despite their robust human T cell reconstitution, BLT mice still display incomplete immune engraftment. B cells often remain immature, NK cell frequencies are low, and myeloid lineage reconstitution is limited, with most monocytes and macrophages confined to secondary lymphoid organs (214). Moreover xeno-GVHD still occurs in long-term experiments (215). In addition to these immunological shortcomings, the reliance on human fetal tissue raises logistical concerns due to its restricted availability, and immune reconstitution remains variable across individuals. To address these issues, alternative approaches have been developed. Notably, the NeoThy model replaces fetal tissue with neonatal thymic tissue, often obtained as surgical discards from pediatric cardiac procedures, in combination with cord blood–derived $CD34^+$ cells.

This strategy provides a scalable source of thymic tissue, as up to 1,000 humanized mice can be generated from a single surgical specimen, while preserving functional T cell development comparable to that achieved in conventional BLT models and alleviating concerns regarding the potential immaturity of T cells generated in classical BLT systems (216).

Altogether, BLT mice represent one of the most physiologically relevant systems for modeling human T and non-T cell–mediated immunity in vivo. However, their complexity and limited accessibility confine their use to specialized laboratories and proof-of-concept studies rather than routine preclinical screening and deep mechanistic studies.

F. Conclusion on animal models

The diversity of available animal models in immuno-oncology, from syngeneic murine systems to increasingly sophisticated humanized xenografts, offers a wide array of experimental tools, each with distinct advantages and imitations as described earlier and summarized in **Table 4**. Syngeneic models provide rapid, immunocompetent, and genetically stable platforms ideal for in vivo evaluation of immune responses in fully functional murine hosts. Genetically engineered mouse models (GEMMs) enable tumor initiation and progression within native tissue architecture, thereby preserving key features of tumor evolution. Xenograft systems, including cell line-derived xenografts (CDX) and patient-derived xenografts (PDX), improve translational relevance by introducing human tumor material, while humanized models incorporating peripheral blood mononuclear cells (PBMCs) or $CD34^+$ hematopoietic stem cells permit the partial reconstruction of a human immune context within the murine host and allows homologous human tumor-immune interactions.

However, no single model fully recapitulates the complexity of human tumor–immune interactions. Consequently, the choice of model must be carefully aligned with the specific biological questions and therapeutic strategies under investigation. In ccRCC, recent reviews have proposed guidelines on which models may be best suited to different experimental purposes (Sobczuk et al., 2020), as illustrated on **Figure 30**.

Table 4. Comparative advantages and limits of animal models for ccRCC immunotherapeutic studies.

Model type	Advantages	Limitations
Syngeneic models	✓ Functional murine immune system ✓ Enables immunotherapeutic testing ✓ Low cost, easy to establish	- Limited relevance to human biology - Absence of patient-specific tumor heterogeneity - Non-human tumor genetic background - Non-human tumor microenvironment
Genetically engineered mouse models (GEMMs)	✓ Functional murine immune system ✓ Targeted oncogenic mutations (VHL, HIF) ✓ Allow preclinical testing and mechanistic studies of immunotherapies ✓ Partial genetic overlap with human tumors	- Off-target induction of lesions in other organs - Findings relevant only to tumors harboring specific engineered mutations - Low metastatic frequency - Expensive and technically demanding to establish
Cell-derived xenografts (CDX)	✓ Use of human cancer cell lines ✓ High reproducibility ✓ Can generate metastases ✓ Low cost and straightforward	- No intratumoral heterogeneity - Lack of human stromal and immune components - Requirement for immunodeficient hosts - Long engraftment time
Patient-derived xenografts (PDX)	✓ Direct use of patient tumor samples ✓ Retention of native human tumor architecture and microenvironment ✓ Translational value for the donor patient ✓ Potential tool for therapy personalization	- Limited tissue availability from donor tumors - Often reduced heterogeneity over serial passages - Requirement for immunodeficient hosts - Long engraftment time
Humanized mouse models	✓ Functional human immune system within a murine host ✓ Compatible with human tumor samples or cell lines ✓ Enable investigation of tumor–immune microenvironment interactions ✓ Suitable for immunotherapy evaluation	- Expensive and resource-intensive - Technically complex to establish and maintain - Long engraftment time

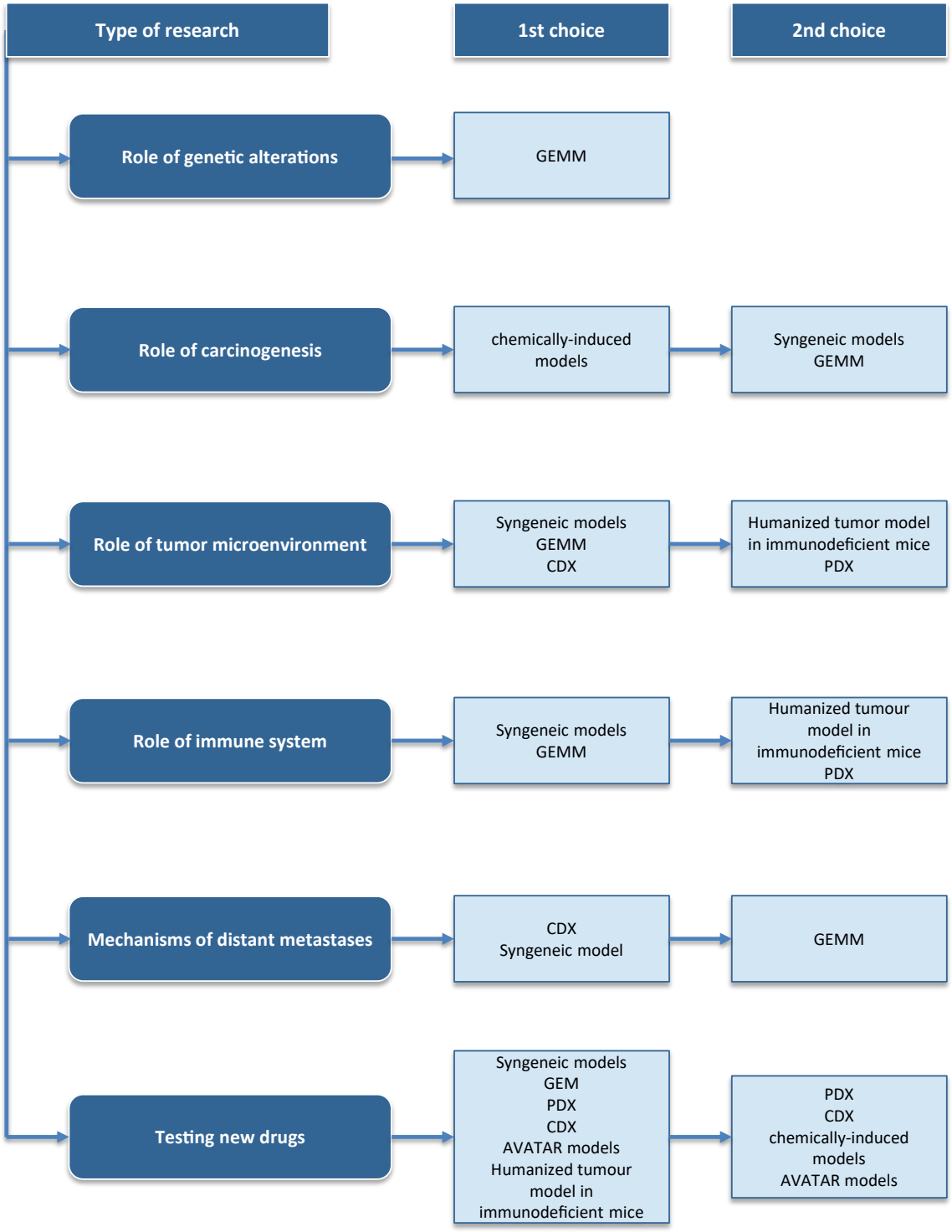

Figure 30. Proposed animal model selection for ccRCC biological research.

Source: Adapted from (134), under CC BY-NC-ND 4.0

While animal models remain essential for investigating whole-organism dynamics, they present several limitations that restrict their translatability, particularly in the field of immuno-oncology where the interplay between tumor cells, non-immune, and immune components is central to therapeutic efficacy.

First, animal models come with significant operational complexity. They require mandatory daily monitoring, specialized housing facilities, and trained personnel, which collectively result in high maintenance costs. In addition, large cohorts occupy substantial laboratory space, further limiting scalability and accessibility for translational studies.

As developed in the paragraphs covering each model, interspecies differences have long been recognized in immuno-oncology (217). Human cytokines are often poorly cross-reactive with murine receptors, while divergences in MHC expression, TCR repertoire, and Fcγ receptor polymorphisms limit the accurate modeling of adaptive and antibody-mediated responses giving rise to complex humanized and genetically engineered models expressing human MHC and cytokines (218). An extensive list of the models available for immune-oncology for all solid tumors is available in the supplementary materials of (170) and a list with a focus on ccRCC is available in (134).

Similarly, standard laboratory mice or hHSC donors for humanized mice are generally young, and free of comorbidities such as obesity, hypertension, or chronic kidney disease, in contrast with the typical RCC patient population adding another bias in immune-oncology studies (205).

On the biological side, a major concern lies in the reconstruction of the TME. Indeed, even in models where a human tumor microenvironment is present (PDX and PDX in humanized models), the human stromal compartment is progressively replaced by murine fibroblasts and endothelial cells, resulting in a hybrid TME of limited fidelity (219). In ccRCC, a notable exception is the transient persistence of human endothelial cells, typically for around 35 days post-engraftment, which can be exploited for angiogenesis studies (156).

Furthermore, the accelerated tumor growth observed in murine hosts contrasts with the slower progression of human cancers, preventing the modeling of chronic inflammation, progressive immune evasion, and clonal evolution, three hallmarks that are particularly relevant in immunotherapy-resistant diseases (9). In line with proliferation-related biases, engraftment in PDX models represents a low-efficiency step, with reported success rates not exceeding ~36% in ccRCC. Tumor grade (Furhman score) has been shown to directly influence engraftment rates, thereby restricting PDX applicability predominantly to high-grade ccRCC tumors (220).

Engraftment time is a major factor that hinders the application of animal models in precision medicine for immuno-oncology. Indeed, this concept relies on autologous patient-derived models to evaluate drug efficacy and tolerance in each individual. However, with engraftment times extending over several months, humanized PDX models are not compatible with the fast-paced timeline required for clinical decision-making. Importantly, any delay between patient tumor

sampling and the establishment of a usable patient-derived model is time during which the tumor, now removed from its native context, begins to diverge. Adaptation to artificial culture conditions or murine hosts alters its cellular composition, gene expression, and microenvironmental interactions, so that the resulting model may no longer faithfully reflect the biology of the original tumor.

Moreover, autologous humanized systems required for precision medicine, clinical decision support or faithful recapitulation of tumor-host interactions, can in principle be generated using patient-derived PBMCs, although this rapidly induces GVHD, or with patient-derived HSCs, which would require engraftment of bone marrow or mobilized blood progenitors from the same individual, adding considerable complexity. Nevertheless, so-called "Avatar models" of this type have been reported (221), including in ccRCC (203).

Another major challenge is reproducibility. Inter-laboratory variability, including differences in microbiota composition, animal housing conditions, and procedural techniques can markedly influence immune response phenotypes and treatment outcomes. Such variability undermines the robustness and generalizability of findings, especially in immuno-oncology where immune contexture is a critical determinant of therapeutic response. To address these issues authors have worked on guidelines for humanized mouse models (222).

Beyond technical and biological issues, animal experimentation raises specific ethical challenges. Mice, like other vertebrates used in research, are sentient beings (223), capable of experiencing pain and stress. This recognition has led to the establishment of the 3Rs principle (Replacement, Reduction, Refinement) (224), now implemented as a cornerstone of animal research ethics. The European regulatory framework has since incorporated these principles, imposing strict requirements on project authorization, daily animal welfare monitoring, and justification of animal use, all of which complicate and slow down research involving animal models (225).

According to the latest data published by the European Commission, a total of 4,108,635 animals were used in Europe in 2022 for human-centered research, of which 82.1% were mice. Oncology alone accounted for 887,742 new animal uses (21.6% of all human-centered research), while research on the immune system represented 505,346 uses (12.3%).

Trends over recent years show a slight overall decrease in animal use for human-centered research (−5.4% in 2021 vs. 2018 and +1.4% in 2022 vs. 2021). However, oncology research stands out as an exception, with a clear increase in animal use (+14.6% in 2021 vs. 2018 and +11.8% in 2022 vs. 2021), underlining the growing reliance on animal models in cancer research despite guidelines aimed at reducing animal use (226).

Moreover, public perception of animal experimentation remains highly heterogeneous and often contentious. Surveys on public acceptance of animal research vary widely across countries and methodologies. Among these, a detailed Danish study is particularly informative. It identified three reproducible stances: ~30% consistently support animal research (*Approvers*), ~15–20%

consistently reject it (*Disapprovers*), and ~50% remain ambivalent (*Reserved*), evaluating case by case. When asked specifically about cancer research on pigs with moderate pain (taken as a "medium" level), acceptance reached 96% among Approvers, 69% among Reserved, and 23% among Disapprovers, highlighting the fact that oncology is considered as a legitimate rationale for animal studies, yet remains the subject of ethical controversy.

Humans tend to express greater empathy and compassion for animals that are phylogenetically closer to them (227). This creates a paradox: the closer an animal is to humans evolutionarily, the more relevant it may be as a model, but the stronger the ethical unease it provokes. Miralles et al. demonstrated that rodents elicit some of the highest empathy and compassion scores among non-primate species (227). This highlights the tension inherent in the use of mice, which are central to biomedical research yet belong to a clade that triggers strong empathic responses. Psychological studies suggest that such unease may be alleviated through cognitive dissonance, as individuals informed that an animal is used in laboratory testing tend to downgrade its perceived cognitive capacities (228).

Altogether, while animal models have played and continue to play a pivotal role in immuno-oncology, their cumulative limitations, from interspecies immunological gaps and distorted tumor–immune interactions to operational constraints and increasing ethical scrutiny, converge toward a central conclusion: they cannot, on their own, provide the comprehensive and clinically faithful insights required for modern immunotherapy development. This is particularly critical in clear-cell renal cell carcinoma (ccRCC), where immune resistance, tumor heterogeneity, and patient-specific variability demand experimental systems capable of capturing human biology with greater fidelity.

Consequently, there has been a progressive paradigm shift toward human-relevant preclinical models. These encompass complex in vitro platforms such as organoids, tumor slices, and spheroids, as well as advanced microphysiological systems that integrate human immune and stromal components within controlled environments. Beyond their translational promise, such models also respond to the ethical and societal call for reduction of animal use, aligning with the "Replacement" principle of the 3Rs.

In the following section, we will examine these emerging alternatives, which aim to overcome the translational barriers inherent to animal models and provide more faithful human-based platforms for immuno-oncology.

III. Complex in Vitro Models for Immuno-Oncology

A. Introduction and comparative framework

Complex in vitro models have historically emerged as a pragmatic compromise between oversimplified monolayer cultures and complex in vivo systems. Over the past decades, this intermediate space has diversified considerably, giving rise to a continuum of approaches that vary in complexity, scalability, and fidelity to the TME. A central premise underlying all these systems is that each represents a specific balance between experimental throughput and biological fidelity. At one end of the spectrum, simplified, rapidly assembled models provide high reproducibility and compatibility with semi–high-throughput assays, but lack the architectural realism and microenvironmental cues of tumors in situ. At the other end, models that conserve native tissue structure and immune context more faithfully recapitulate the patient's tumor ecosystem yet are technically demanding and less scalable. Choosing the appropriate platform for a given experimental question therefore requires a deliberate evaluation of these trade-offs.

In immuno-oncology, the requirements of such models diverge substantially from those of classical cytotoxic drug screening (**Box 1**). Beyond measuring direct tumor-cell killing, they must be able to capture the dynamics of tumor–immune interactions, including immune cell recruitment and trafficking, the interplay between tissue-resident and circulating effectors, antigen presentation and TCR engagement, and the regulation of immune checkpoints, all in the absence of the systemic physiological support provided by animal models. This constraint shapes the suitability of complex in vitro models for immuno-oncology studies, depending on the specific question being addressed. Readouts must also extend beyond viability to encompass infiltration metrics, activation and exhaustion phenotypes, checkpoint activity, cytokine profiling, and, where feasible, spatially resolved analyses.

Given the vast diversity of available platforms, a structured comparative framework is essential to facilitate both comprehension and positioning. 6 axes appear to be particularly interesting to study when comparing 3D models:

1. **Origin**: from established cell lines to patient-derived samples.
2. **Structural support**: scaffold-free systems relying on spontaneous aggregation vs. scaffold-based formats relying on exogeneous extracellular matrix (ECM) components or engineered devices.
3. **Spatial organization**: ranging from systems with lost native architecture to formats preserving intact tissue organization.
4. **Cellular complexity**: from monocellular tumor-only systems to heterotypic structures including stromal, endothelial, or immune populations.

5. **Immune content**: considering the inclusion, diversity, and autologous versus allogeneic nature of immune components.
6. **Time to result and possible duration for experimenting**: from models that can be established within hours or days to those requiring weeks or months before readouts, and from short-term systems maintained only a few days to long-term systems stable for weeks or months.

These parameters jointly determine not only the biological fidelity of a given model but also its throughput, scalability, and suitability for specific immuno-oncology readouts. A summary matrix is provided as an orientation tool for the reader in **Table 5**. These axes are therefore of uttermost importance in the search for a model meeting the requirements summarized in **Box 1**.

Building on this framework, the following subsections will introduce the main categories of complex in vitro tumor models. For each, we provide a concise overview of its defining principles, typical formats, and positioning within the broader landscape.

Table 5. Axes of classification for ex vivo models.

Model type	Origin	Support	Spatial organization	Cellular complexity	Immunity	Formation Time / Experimental Window after formation
Cell line–derived spheroids	Established cell lines	Scaffold-free	Reconstituted aggregates	Tumor cells only	Immune cells can be added (PBMCs, T cells, macrophages)	48-72h, / 2-3 weeks
PDT-spheroids (patient-derived tumor spheroids)	Freshly dissociated tumor cells	Scaffold-free	Reconstituted aggregates	Tumor cells ± residual stroma (+ endothelial)	Re-infiltration with autologous TILs or activated PBMCs	48-72h, weeks according to techniques / several weeks
PDOs (epithelial organoids)	Patient-derived tumor epithelium	ECM (e.g. Matrigel)	Reconstituted epithelial structures	Tumor epithelium only; stroma/immune lost (except ALI-PDOs)	Requires immune co-culture; ALI-PDOs preserve native TILs	Weeks to months / several weeks, cryopreservation available
PDOTs (organotypic spheroids)	Partially dissociated tumor fragments	ECM-embedded	Preserved partial native architecture	Tumor + stromal + endothelial + immune (autologous)	Native immune context partially preserved	24h / 3 days to 1 week
PDEs (explants)	Mechanically cut tumor fragments	depends	Preserved partial native architecture	Tumor + stromal + endothelial + immune (autologous)	Native immune context partially preserved	24h / 3 days to 1 week
Tissue slices	Fresh tumor explants	depends	Fully preserved architecture	Complete multicellular TME	Full autologous immune context	24h / 3 days to 1 week

B. Complex in vitro model types

1. Spheroids

Spheroids are three-dimensional aggregates of tumor cells forming compact spherical structures. Among 3D tumor models, they are by far the most widely used, owing to their simplicity, robustness, and ease of implementation. Their earliest applications date back to the 1970s, when they were developed as a first attempt to move beyond oversimplified two-dimensional monolayers (229).

The most classic format is the multicellular tumor spheroid (MCTS), which arises from the spontaneous aggregation of tumor cells cultured under non-adherent conditions. Aggregation may occur naturally or be facilitated by centrifugation or viscous agents such as methylcellulose. Alternatively, spheroids can be generated from a single cell or a small cluster of cells that proliferate and progressively self-organize into a spherical mass. This process typically requires support from extracellular matrix components (e.g., Matrigel, collagen, alginate) or dynamic culture systems (spinner flasks, magnetic levitation, bioreactors). While slower to establish, such formats allow the study of clonal growth and tumor cell organization in a three-dimensional context. Spheroids can be established by multiple, partly overlapping strategies, the main ones are illustrated in **Figure 31**.

Depending on their cellular origin and culture strategy, spheroids can be broadly classified into three categories: homotypic spheroids, composed of a single tumor cell type; heterotypic spheroids, which combine tumor cells with one or several additional cell types such as fibroblasts, immune cells or endothelial cells; and organotypic spheroids, which aim to integrate a broader spectrum of TME components, including stromal and immune compartments, thereby approaching the complexity of native tumor tissue. Each of these categories presents distinct characteristics and technical considerations, illustrated below.

Cell-line spheroids (classically multicellular tumor spheroids, MCTS) are generated from established tumor cell lines such as 786-O, Caki-1, or RCC7 in the case of ccRCC. They are typically produced by seeding defined numbers of cells in non-adherent culture plates, refered to as liquid overlay technique, hanging drops, or ultra-low-attachment wells. These systems yield relatively homogeneous spheroids ranging from ~100 to 800 µm in diameter, with size being primarily determined by the initial seeding density. Their robustness, reproducibility, and scalability have made them a staple model in cancer biology and preclinical drug screening. Additional advantages include their low cost and the possibility of genetic engineering, which broadens experimental flexibility. However, reliance on immortalized tumor cell lines inherently eliminates inter- and intra-tumoral heterogeneity. In the context of immuno-oncology, such spheroids can be co-cultured with immune cells to serve as standardized targets, enabling the modeling of allogeneic cytotoxic responses and the testing of immunotherapeutic interventions

such as immune checkpoint inhibitors (ICI) (229).

Primary spheroids are derived directly from patient tumors. They can be generated either from dissociated tumor cells briefly expanded in two-dimensional culture, or directly from freshly dissociated cells without prior amplification. Although conceptually similar to cell-line spheroids, their generation is technically more challenging, particularly in the absence of an intermediate flask-expansion step and is associated with lower and more variable success rates of aggregation. When successful, however, primary spheroids retain elements of patient-specific variability and thus provide a more clinically relevant platform (230). Aggregation efficiency can be improved by centrifugation, or the addition of extracellular matrix (ECM) components, but overall reproducibility remains limited (231). Notably, primary spheroids may also incorporate stromal and immune subsets originally present in the tumor, thereby partially preserving the complexity of the native microenvironment and providing opportunities to study autologous interactions (cf infra).

Heterotypic and organotypic spheroids can be generated using cell line spheroids or primary spheroids, they extend the principle of homotypic spheroids containing only tumor cells by deliberately incorporating multiple cell populations. Heterotypic spheroids are assembled by combining tumor cells with other cell types at the time of seeding, or by co-culture after spheroid formation (232). This enables the study of tumor–stroma interactions, angiogenesis, or immune cell infiltration within a three-dimensional structure. Organotypic spheroids aim to recapitulate a more comprehensive tumor ecosystem by simultaneously incorporating multiple stromal and immune compartments, ideally, preserving all major cell types present in the original tumor (**Figure 31**). Although these models offer enhanced biological relevance, their standardization remains challenging. Variability in aggregation efficiency and survival across cell populations often leads to structural heterogeneity and limited reproducibility between experiments (231).

However, the terminology surrounding these patient-derived 3D models remains somewhat ambiguous. In some contexts, the term tumoroid is employed to highlight the substantial differences between a patient-derived organotypic spheroid and a conventional cell-line spheroid. Similarly, the term organoid is sometimes used to refer to patient-derived spheroids, although the precise definition of organoids will be addressed in the following chapter.

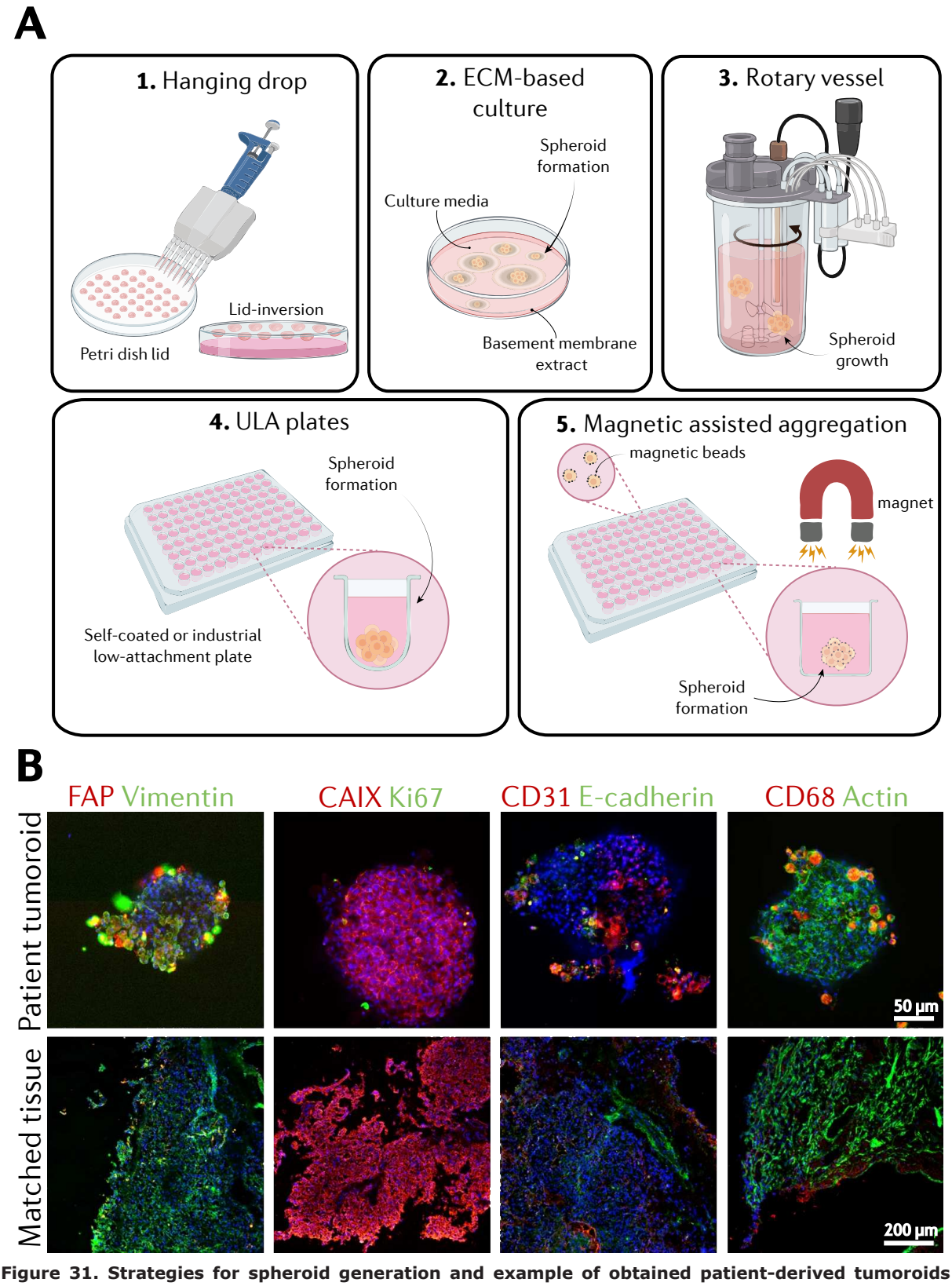

Figure 31. Strategies for spheroid generation and example of obtained patient-derived tumoroids (spheroids equivalent).

(A) Schematic overview of the main approaches used for spheroid generation. (1) Hanging drop: cell suspensions are seeded as droplets on the inverted lid of a Petri dish, where gravity promotes cell aggregation at the drop apex. (2) ECM-based culture: tumor cells are embedded in basement membrane extracts or other extracellular matrix components, providing structural support for spheroid growth. (3) Rotary vessel bioreactors: continuous agitation prevents sedimentation and promotes aggregation into compact spheroids. (4) Ultra-low attachment (ULA) plates: culture surfaces are coated to prevent adhesion, thereby forcing spontaneous cell aggregation. (5) Magnetic bead–assisted aggregation: cells are labeled with magnetic nanoparticles that associate with the cell

surface, and an external magnet drives rapid spheroid compaction. (B) Immunofluorescent images of whole-mounted patient-derived tumoroids compared with matched tumor tissue sections. Each column illustrates a distinct co-labeling: (1) fibroblast activation protein (FAP, red) and vimentin (green), (2) carbonic anhydrase IX (CAIX, red) and Ki67 (green), (3) CD31 (red) and E-cadherin (green), and (4) CD68 (red) and actin (green). Tissue sections are 8 µm thick. Images were acquired using a CellInsight CX7 high-content imaging system (ThermoFisher) with a 20× objective (NA 0.45) for tumoroids and a 10× objective (NA 0.4) for tissue sections. Scale bars: 50 µm (tumoroids) and 200 µm (tissue).

Source: panel A: adapted from (233), under CC BY 4.0, panel B: adapted from (230), under CC BY 4.0

Collectively, spheroids represent the most accessible and versatile entry point into 3D tumor modeling. Their adaptability, ranging from simple monocultures to complex organotypic assemblies, has made them a key platform for exploring immune infiltration, effector functions, and responses to immunotherapies in a controlled three-dimensional context.

In the context of precision medicine and prediction of immunotherapy response, these models offer a relatively scalable and reproducible platform, with the potential to deliver results within two weeks of tumor sampling. This rapid turnaround could allow their integration into clinical decision-making and help prevent therapeutic divergence. Nevertheless, their use inevitably entails a complete loss of the native tumor architecture.

2. Patient-derived organotypic tumor spheroids (PDOTs)

A particular subtype of 3D “spheroid” models is the patient-derived organotypic tumor spheroid (PDOT) approach, first described by Jenkins and colleagues (234). Unlike conventional spheroids generated from fully dissociated single-cell suspensions or scaffold-based cultures, PDOTs are formed directly from partially dissociated tumor fragments. This method enables the retention of native tissue architecture, stromal elements, and resident immune infiltrates, thereby placing PDOTs at the interface between primary spheroids and tissue slice models (**Figure 32**). Notably, each PDOT represents only the specific tumor region from which it was derived, thus potentially lacking original tumor heterogeneity if used in an insufficient number. Furthermore, their use is restricted to short-term applications (~72 h), as both structural integrity and cell viability decline beyond this timeframe. Nevertheless, their hybrid nature provides improved biological fidelity while retaining a level of scalability and manipulability, making them an attractive platform for immuno-oncology applications.

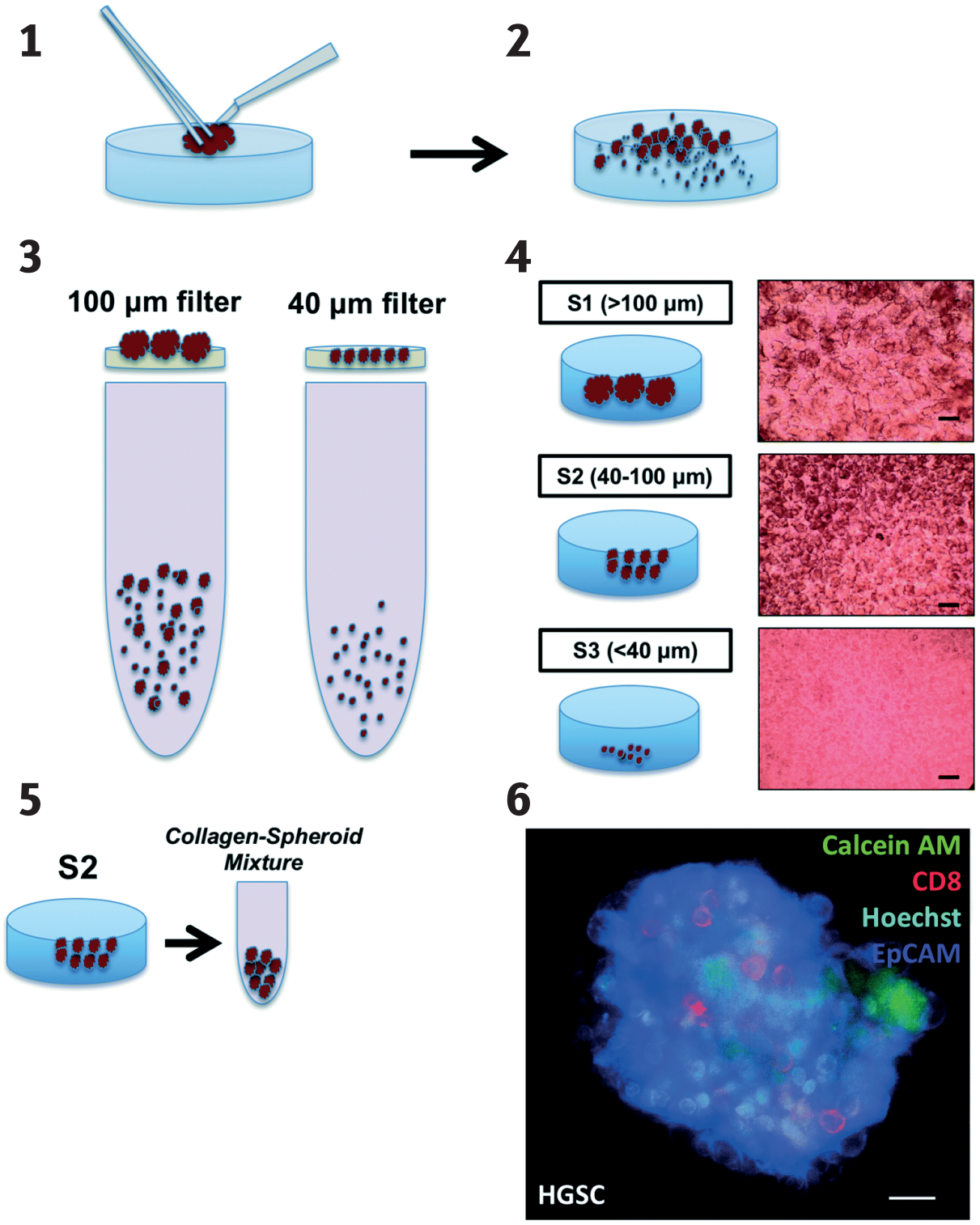

Figure 32. Generation and immunofluorescence characterization of patient-derived organotypic tumor spheroids (PDOTS).

(1) Tumor tissue is manually minced and enzymatically dissociated to release multicellular structures. (2) The resulting suspension contains a mixture of single cells, small fragments, and intact spheroids. (3) Sequential filtration through 100 µm and 40 µm filters allows separation into three size-based fractions. (4) Three populations are isolated: S1 (>100 µm), S2 (40–100 µm), and S3 (<40 µm). Brightfield images illustrate the composition of each fraction. Scale bars: 100 µm. (5) The S2 fraction, enriched in compact spheroids, is embedded in collagen for downstream analysis. (6) Representative baseline immunofluorescence image of a PDOT derived from high-grade serous carcinoma (HGSC), showing viable cells (Calcein AM, green), $CD8^+$ T cells (red), $EpCAM^+$ tumor cells (blue), and all nucleated cells (Hoechst, cyan). Scale bar: 20 µm.

Source: adapted from (235), under CC BY 3.0

While time efficient and relatively simple, spheroids are generally restricted to short-term cultures and lack stem cell–driven self-organization, these limitations inherently confine their use to applications requiring rapid readouts rather than long-term modeling of tumor evolution. In contrast, organoids constitute a distinct class of 3D models, based on developmental biology principles, that enable extended growth and structural fidelity, making them more suitable for studies of self-renewal, differentiation, and long-term treatment dynamics.

3. Organoids

Organoids are three-dimensional cellular structures that arise from stem or progenitor cells cultured under conditions that support self-organization, proliferation, and differentiation (236). Typically embedded in extracellular matrix (ECM) hydrogels such as Matrigel or collagen, these structures recapitulate key aspects of the architecture, polarity, and functionality of their tissue of origin (237). Originally developed in the field of developmental and regenerative biology, organoids gained prominence with the establishment of intestinal organoids from $Lgr5^+$ stem cells (238) and have since been generated from a wide array of epithelial tissues.

Tumor organoids apply this principle to malignant tissues. Derived from dissociated patient tumor samples, they rely on ECM scaffolds and defined growth factor cocktails to support the expansion of tumor epithelial cells. While highly faithful in recapitulating tumor epithelial architecture and conserving patient-specific genetic and phenotypic traits, they often lack stromal and immune components unless these are deliberately incorporated (237).

An important terminological caveat, as previously noted, is that in oncology the term organoid is sometimes applied to patient-derived spheroids generated directly after tumor dissociation and short-term aggregation of tumor cells. Although these structures do constitute three-dimensional tumor-derived aggregates, they conceptually differ from canonical organoids, which are defined by stem cell–driven self-organization within an extracellular matrix scaffold. In parallel, the term tumoroid is inconsistently employed in the literature, at times referring to organoids, and in other cases to patient-derived spheroids themselves, further contributing to semantic ambiguity in the field.

Patient-derived organoids (PDOs) represent one of the most widely adopted tumor organoid formats. They are established by embedding dissociated tumor epithelial cells into ECM hydrogels such as Matrigel, supplemented with growth factors, Wnt agonists, and inhibitors of lineage-restricting pathways (236). Under these conditions, epithelial cells undergo clonal expansion and self-organization into polarized, gland-like structures that preserve many histological and molecular features of the original tumor (239).

PDOs offer several key advantages. They can be propagated over extended periods, providing renewable experimental material from a single patient sample. They maintain intra-patient genetic and phenotypic heterogeneity, and are amenable to biobanking, high-throughput drug

screening, and molecular profiling.

However, PDOs also present important practical limitations. Their establishment and expansion require several weeks before stable cultures can be obtained, in stark contrast with spheroid systems that can be generated within a few days. This slow kinetics restricts their suitability for rapid clinical applications. Instead, PDOs are particularly well suited for studying tumor initiation, clonal evolution, and progression, where long-term stability and preservation of intra-patient heterogeneity are essential. Moreover, by design, PDO cultures are almost exclusively epithelial: stromal fibroblasts, endothelial cells, and most immune populations are lost during enzymatic dissociation and selective culture, meaning that PDOs do not intrinsically recapitulate the TME. In immuno-oncology, they must therefore be combined with exogenous immune cells, such as PBMCs, T cells, or macrophages, to assess infiltration, cytotoxicity, and responses to immune checkpoint inhibitors (ICI) (240).

Innovations have sought to address these limitations. Air–liquid interface (ALI) cultures preserve not only epithelial cells but also tumor-resident immune infiltrates, thereby capturing elements of the autologous immune context (239). A summary of these two methods is provided in **Figure 33**. Other strategies use engineered ECM scaffolds to introduce stromal and vascular compartments alongside PDOs.

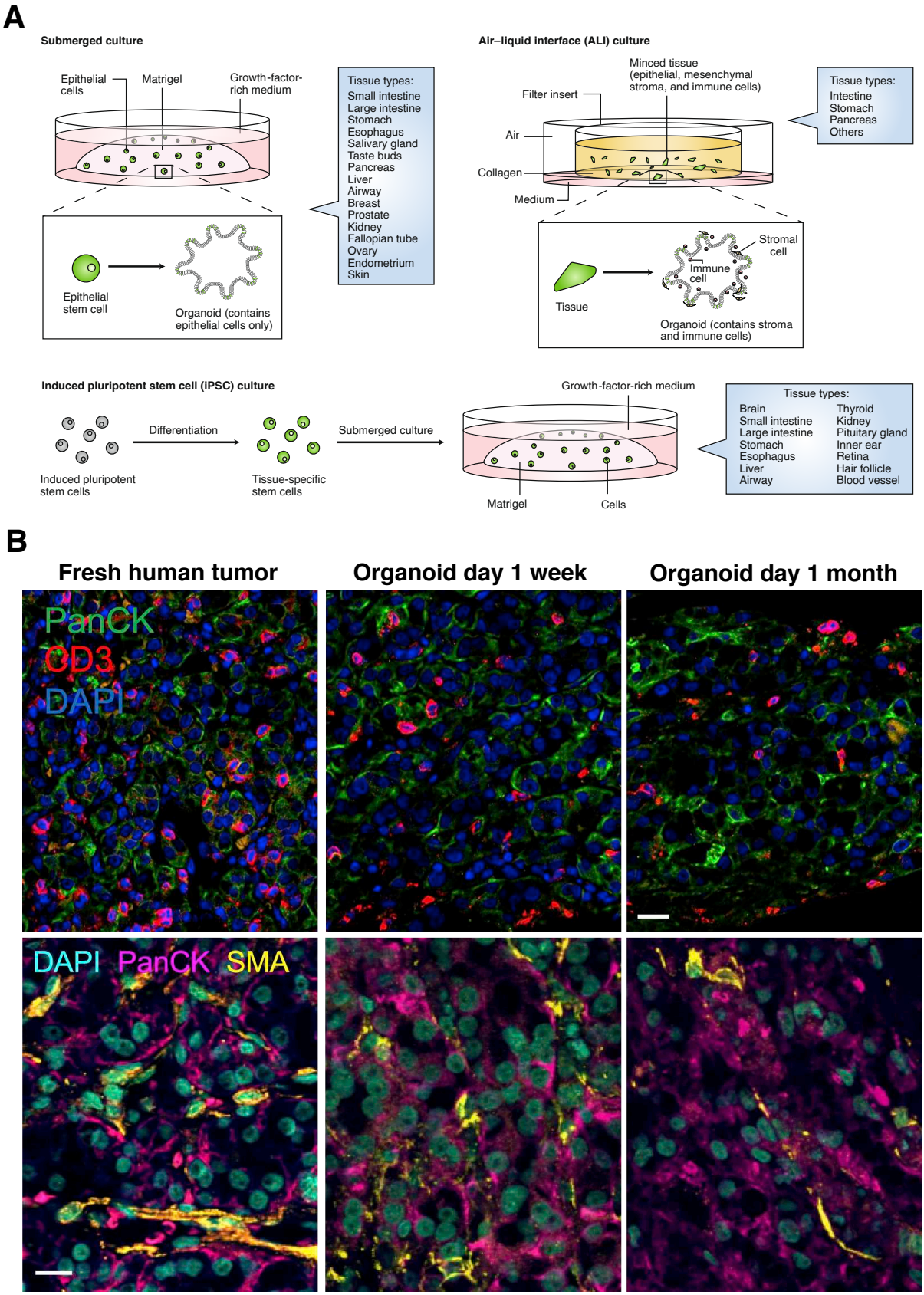

Figure 33. Organoid methodologies and preservation of tumor microenvironment components in ccRCC patient-derived organoids cultured under air–liquid interface conditions.

(A) Overview of organoid methodologies. Submerged culture systems typically generate epithelial-only organoids from adult tissue. Air–liquid interface (ALI) culture maintains epithelial cells together with stromal and immune components, thereby providing a more organotypic context. Organoids can also be derived from induced plu-

ripotent stem cells (iPSCs) after differentiation into tissue-specific progenitors. (B) Representative ccRCC PDOs established using ALI culture, compared with the matched fresh tumor (day 0) and organoids at days 7 and 30. Top: immunofluorescence (IF) staining for epithelial tumor cells (PanCK, green), tumor-infiltrating lymphocytes (CD3, red), and nuclei (DAPI, blue). Bottom: time course of cancer-associated fibroblast (CAF) preservation, with IF staining for PanCK (magenta), SMA (yellow), and DAPI (cyan). Scale bars: 20 μm.

Sources: panel A adapted from (241), reproduced with permission from Elsevier, license number 6154860183522 ; panel B adapted from (239), reproduced with permission from Elsevier, license number 6154860424057

Altogether, PDOs represent a powerful 3D model that recreates key aspects of tumor epithelial organization while supporting long-term expansion. Their scalability, biobanking potential, and ability to preserve patient-specific heterogeneity make them an invaluable tool for molecular profiling, functional studies, and longitudinal drug testing. However, the very features that underpin these strengths, namely prolonged culture times and dependence on defined growth factor cocktails, also constrain their applicability for rapid clinical purposes. The extended time required to establish PDOs is incompatible with clinically relevant decision-making windows, and prolonged expansion may introduce selection biases, particularly under growth factor–driven conditions.

4. Tumor slices

Tissue slices, also referred to as organotypic tumor slices culture (TSCs), represent an alternative to reconstructed three-dimensional models by preserving intact fragments of native tumor tissue. They are typically generated by cutting freshly resected tumor material into thin sections (100–400 μm) using a vibratome and maintaining them on porous membranes at an air–liquid interface. This approach allows preservation of the full cellular diversity and spatial organization of the tumor, including epithelial, stromal, vascular, and immune compartments (**Figure 34**).

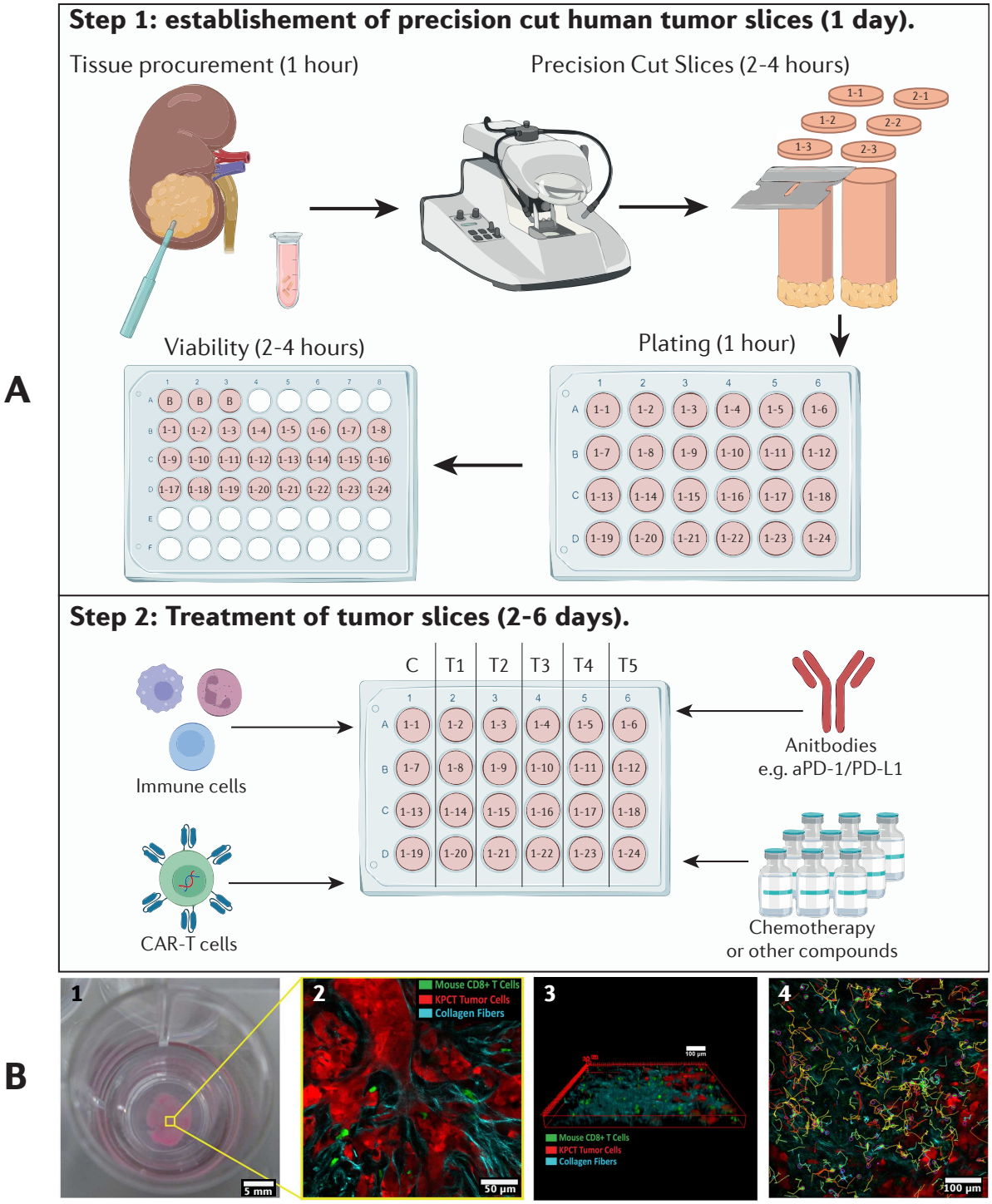

Figure 34. Workflow and example of application of tumor slice model.

(A) Overview of the preparation and treatment of tumor slices. Tumor tissue is collected, sectioned using a vibratome to obtain standardized slices, plated in 24-well plates, and assessed for viability before treatment. Immune cells (e.g., PBMCs, CAR-T cells), immune checkpoint inhibitors (e.g., anti-PD-1/PD-L1), or chemotherapeutic agents can be added to evaluate therapeutic response. (B) Representative imaging of tumor slices (pancreatic cancer). (1) Macroscopic view of a tumor slice in an organotypic culture insert (24-well plate). Scale bar: 5 mm. (2) Two-photon microscopy image showing KPCT tumor cells (red), murine $CD8^+$ T cells labeled with CellTracker Green (green), and second harmonic generation signal from collagen fibers (cyan). Scale bar: 50 µm. (3) 3D reconstruction of a 75 µm z-stack showing T cell infiltration through tumor tissue and surrounding matrix. Scale bar: 100 µm. (4) Migration tracks of $CD8^+$ T cells within the slice, extracted from the z-stack shown in (3). Scale bar: 100 µm.

Source: panel A adapted from (242), under CC BY 4.0 using Biorender.com ; panel B adapted from (243), under CC BY-NC-ND 4.0

The major advantage of tissue slices lies in their ability to conserve the autologous TME in situ, thereby providing an exceptionally faithful ex vivo platform. They enable direct interrogation of immune–tumor interactions, drug penetration, and therapeutic responses under conditions that closely reflect the patient's tumor. Several studies have exploited this format to evaluate ICIs or adoptive immune cell therapies in the context of the preserved autologous immune infiltrate, offering unique insights into mechanisms of response and resistance (244–246).

However, TSCs are constrained by important limitations. Their viability is short-lived, usually restricted to 48–72 hours, although optimized protocols may extend this to about one week. Scalability is inherently limited, as each slice requires fresh surgical tissue and only a finite number of sections can be obtained per specimen. Reproducibility is further hampered by the pronounced "zone effect": slices originating from different regions of the same tumor (necrotic core, invasive front, vascularized zones) may yield divergent results. These constraints limit the use of TSCs for large-scale or long-term studies, in contrast to more manipulable systems such as spheroids or organoids.

A variant of this model is represented by patients derived explant (PDEs) which use mechanically cut fragments of tumors instead of precision cut slices (247).

Conceptually, tissue slices and patient derived explants share similarities with patient-derived organotypic spheroids (PDOTs) discussed above, in that both formats preserve native architecture and multiple cellular compartments. However, while PDOTs derive from partially dissociated fragments, tissue slices conserve an even more intact snapshot of the tumor ecosystem with minimal manipulation. In contrast to reconstructed models that trade fidelity for scalability, tissue slices maximize fidelity at the expense of throughput and duration. This complementary positioning not only links them to PDOTs but also makes them an important reference model for validating reconstructed systems and for providing high-resolution insights into the genuine patient tumor microenvironment.

C. Key features and advantages of 3D tumor models

Unlike 2D cultures, which fail to reproduce spatial organization and microenvironmental constraints, 3D models capture key features of solid tumors. Indeed, solid tumors in vivo are inherently three-dimensional structures, shaped not only by the intrinsic properties of malignant cells but also by their spatial organization, stromal context, and interaction with vascular and immune compartments. This three-dimensionality imposes unique biophysical and biological constraints, such as gradients of oxygen, nutrients, and metabolites; zones of proliferation versus quiescence or necrosis; and complex cell–cell and cell–matrix interactions, that are absent in flat monolayer cultures. Conventional two-dimensional systems therefore fail to capture many of the hallmarks of tumor growth and therapy response. In contrast, 3D models recreate at least part of these features, thereby providing a closer approximation of the in vivo tumor

ecosystem and offering distinct advantages for both mechanistic studies and translational applications **Figure 35**.

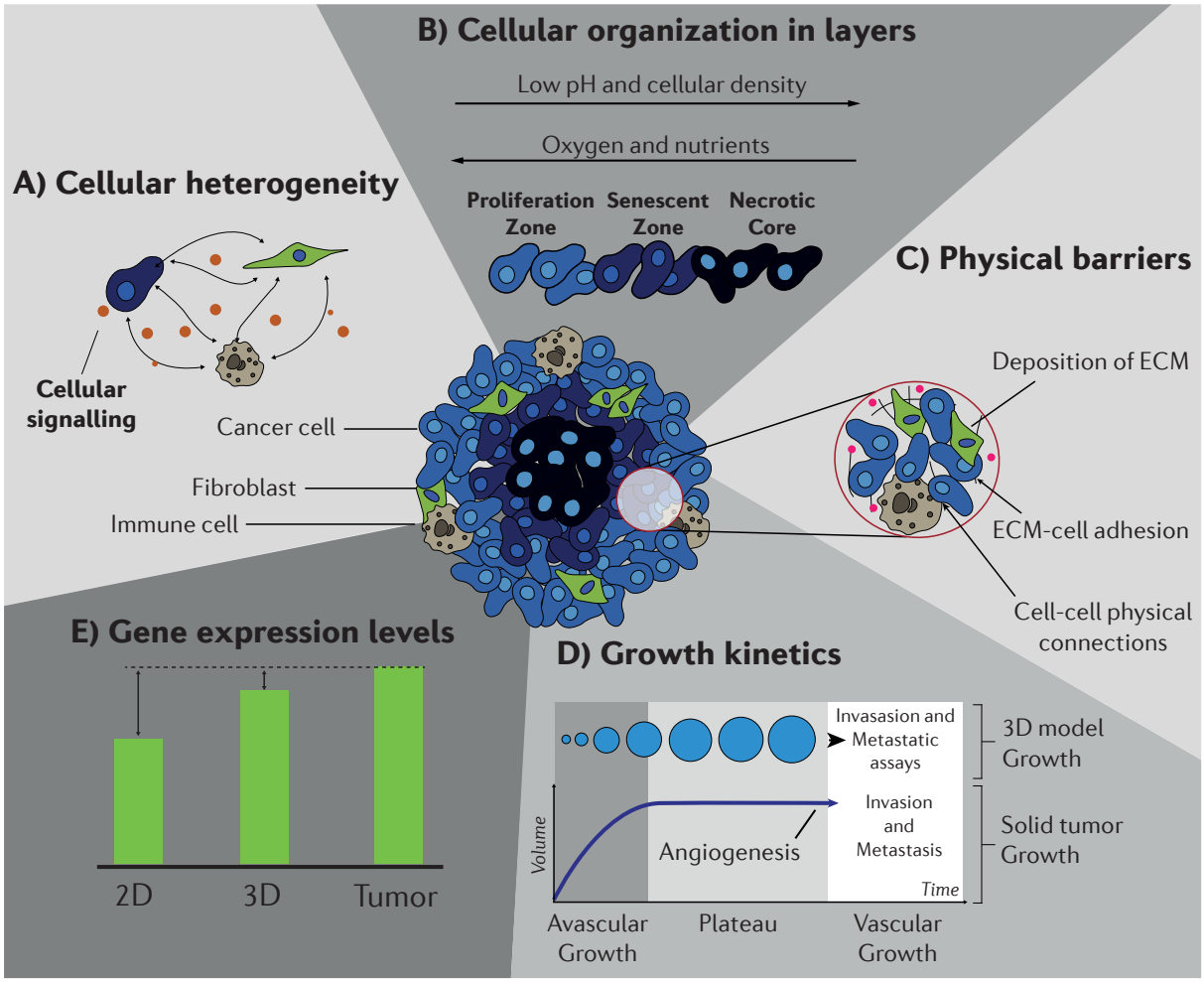

Figure 35. Main features of 3D tumor models compared with 2D cultures.

(A) Representation of cellular heterogeneity through the inclusion of cancer, stromal, and immune cells. (B) Layered cellular organization generates gradients of nutrients, oxygen, and pH, leading to distinct proliferative, senescent, and necrotic zones. (C) Extracellular matrix generates physical barriers and interactions. (D) Growth kinetics shows phases of avascular expansion, plateau, and need for angiogenesis, with the possibility to assess invasion and metastasis. (E) Comparison of gene expression profiles between 2D, 3D, and tumor samples, illustrating the closer resemblance of 3D models to tumor tissues.

Source: (248), reproduced with permission from Elsevier, license number 6154860738961

1. Gradients

A defining feature of solid tumors is the presence of steep gradients in oxygen, nutrients, metabolites, and drugs. Cells near blood vessels remain proliferative, whereas those deeper within the mass face hypoxia, acidosis, and nutrient deprivation, leading to metabolic shifts, quiescence, or necrosis. Such gradients critically shape tumor biology and therapy response, with hypoxia being particularly linked to immune escape and resistance to immunotherapy as seen in the previous chapter.

Unlike two-dimensional cultures, which expose all cells to uniform conditions, 3D tumor models such as spheroids and organoids recreate diffusion-limited microenvironments with pro-

liferative rims, quiescent layers, and necrotic cores, resembling avascular tumor regions. This enhances biological relevance and allows investigation of drug penetration, hypoxia signaling, and the heterogeneous sensitivity of tumor subpopulations (248).

2. Enhanced cell–cell and cell–matrix interactions

Another defining feature of three-dimensional tumor models is the restoration of dense and multidirectional cellular contacts, as well as interactions with extracellular matrix (ECM) components. In two-dimensional monolayers, each cell is restricted to lateral contacts on a rigid plastic surface, which profoundly distorts adhesion, polarity, and signaling. In contrast, cells within 3D structures engage with multiple neighbors simultaneously and establish integrin-mediated contacts with ECM, thereby reproducing the biomechanical and biochemical cues encountered in vivo (249).

3. Immune–tumor interactions

Three-dimensional tumor models also provide a more faithful framework to study immune–tumor interactions. Unlike 2D cultures, their compact and stratified organization reproduces the physical barrier encountered by lymphocytes in solid tumors. In addition, the metabolic and hypoxic gradients established within 3D structures shape the functional state of infiltrating immune cells, often promoting exhaustion and reduced cytotoxic activity (cf. previous chapter). Together, these features make 3D models uniquely suited for probing mechanisms of immune exclusion and resistance.

4. Heterogeneity and translational relevance

In addition to these features, three-dimensional tumor models spontaneously generate cellular heterogeneity, with proliferative, quiescent, and therapy-resistant subpopulations coexisting within the same structure. This mirrors the functional diversity observed in clinical tumors and provides a natural setting for studying mechanisms of drug resistance and clonal evolution.

Based on the requirements outlined in **Box 1**, several models appear particularly promising. Although PDOs provide long-term expansion and biobanking potential, their lengthy initiation time makes them unsuitable for clinical decision purpose in most situations and raises concerns about progressive divergence from the native tumor. By contrast, patient-derived spheroids and PDOTs fulfill many of the outlined criteria. Spheroids offer a simple and versatile platform where multiple parameters can be experimentally controlled, yet they do not preserve the original spatial organization of the tumor. PDOTs, on the other hand, maintain native architecture and immune infiltrates from the outset, but because they are established from small tumor fragments, one must ensure that sufficient material is available to adequately capture patient

heterogeneity.

D. Microfluidic systems

Despite these advantages, static 3D cultures remain limited in their ability to reproduce the dynamic nature of the TME. Solid tumors are constantly subjected to interstitial flow, variable perfusion, mechanical stress, and sequential recruitment of stromal and immune populations, all of which profoundly affect tumor biology and therapeutic response. To address these shortcomings, microfluidic systems, often referred to as “organ-on-a-chip” or “tumor-on-a-chip” platforms, have emerged as a powerful complement to spheroids, organoids, and tissue slices. These devices use miniaturized channels, chambers, and porous membranes to control the spatial organization of cells and the flow of fluids with micrometer precision. By integrating flow, perfusion, and controlled cell–cell interactions, microfluidics provides a bridge between simplified 3D constructs and the complex, perfused environment of living tissues.

In some cases, microfluidic platforms may be used to directly form organoids or spheroids (250,251).

1. Microfluidic systems advantages for immuno-oncology

One of the major reasons for the adoption of microfluidic systems in tumor modeling lies in their ability to reproduce biophysical cues that are inherently absent in static cultures. Among these, shear stress, the tangential force exerted by fluid flow on cells, plays a central role in shaping both vascular and tumor biology. In tumors, capillary flow generates shear stresses in the range of 0.1–1 dyn/cm² (252). Indeed, the vasculature is structurally abnormal: vessels are tortuous, leaky, and poorly organized, leading to highly heterogeneous shear profiles, ranging from near-stagnant zones to transient bursts of elevated flow.

This variability has profound biological consequences. Endothelial cells exposed to low or irregular shear stress adopt a dysfunctional phenotype, characterized by increased permeability, aberrant polarity, and enhanced pro-angiogenic signaling (253). Tumor cells, when subjected to interstitial flow or direct shear, show altered adhesion dynamics, cytoskeletal remodeling, and in some cases, increased invasive potential (252), and shear stress resistance is considered a conserved biophysical property in malignant cells (254). From an immuno-oncology perspective, immune cells such as T lymphocytes and NK cells rely on shear-dependent mechanisms for vascular adhesion, rolling, and extravasation (255); in microfluidic tumor models, applying physiological levels of shear has been shown to critically influence the recruitment and infiltration efficiency of these cells, including CAR-T cells . Thus, incorporating controlled flow into 3D tumor models not only enhances their physiological relevance but also enables interrogation

of dynamic processes, vascular crosstalk, immune trafficking, and drug delivery, that are otherwise inaccessible in static spheroid or organoid cultures.

Beyond shear stress, microfluidic systems also recapitulate other tumor-specific physical constraints. Continuous perfusion maintains nutrient and oxygen gradients closer to in vivo conditions. Microfluidic systems enable dynamic and sequential treatments, which is crucial in modern oncology. In vivo, therapies are rarely delivered as single bolus exposures; instead, tumors experience fluctuating concentrations and ordered sequences of drugs, targeted agents, and immunotherapies. Microfluidic perfusion reproduces these dynamics, allowing the modeling of treatment schedules, washout effects, and synergistic or antagonistic interactions between therapeutic modalities.

Beyond these advantages, microfluidics can be regarded primarily as a technological layer to be integrated with 3D tumor models. Beyond recreating dynamic biophysical cues, microfluidic designs can be equipped with sensors and analytical modules and offer opportunities for standardization and automation of assays. The scale of microfluidics is well adapted to clinical samples. Devices operate with very small fluid volumes and cell numbers, which means that a single biopsy can be sufficient to establish multiple parallel assays. This makes tumor-on-chip systems particularly attractive in the context of personalized medicine, where patient material is often scarce and must be maximized for experimental use.

2. Types of microfluidic devices

Microfluidic systems designed for tumor modeling encompass a wide variety of architectures, ranging from standardized commercial platforms to highly customized research devices. Several commercial solutions are now available, providing user-friendly chips with predefined channel geometries and perfusion setups, which lower the technical barrier for laboratories without microfabrication expertise. In parallel, academic and industrial groups continue to design bespoke platforms optimized for specific biological questions. Explanations on the techniques used to fabricate microfluidic chips are included in **Box 2.**

The simplest category consists of single or parallel perfusion channels, which enable controlled exposure of tumor spheroids or organoids to defined flow conditions. Building on this, barrier- or membrane-based systems introduce a porous interface that separates two compartments, for instance, an endothelial monolayer and a tumor chamber, thereby allowing the study of extravasation, immune transmigration, or drug diffusion across a vascular barrier. More advanced compartmentalized chips feature multiple interconnected chambers, supporting the co-culture of tumor cells with stromal, vascular, and immune populations in spatially defined niches. At the other end of the spectrum, droplet-based systems rely on microfluidic emulsions to encapsulate defined cell numbers or spheroids into nanoliter-scale droplets, offering high-throughput and

highly standardized conditions for screening. Moreover, dedicated “metastasis-on-chip” designs allow the modeling of tumor cell dissemination, intravasation, and colonization of distant niches, thereby extending the scope of microfluidic platforms to the study of metastatic processes. Finally, vascularized-on-chip systems incorporate engineered endothelial networks, either self-assembled in hydrogels or lithographically patterned, to generate perfusable microvessels. These platforms are particularly powerful for modeling tumor angiogenesis, intravasation, and immune cell trafficking under physiologically relevant flow.

Collectively, these diverse device designs provide a continuum of complexity, ranging from accessible commercial chips to highly integrated tumor-on-chip platforms that closely mimic in vivo dynamics.

3. Flow control in microfluidic culture

A defining strength of microfluidic systems lies in their ability to impose controlled and reproducible flow conditions. Several strategies exist, each with distinct advantages and limitations. The simplest relies on gravity-driven flow, in which reservoirs of different heights generate a hydrostatic pressure gradient. This approach is inexpensive and requires minimal equipment, but flow rates are relatively unstable and difficult to precisely control.

More precise regulation is achieved using external pumping systems. Syringe pumps deliver highly stable, continuous flows with defined shear profiles, making them well suited for long-term culture under constant conditions. Peristaltic pumps, by contrast, allow recirculation of medium and can maintain multiple chips in parallel, though they introduce pulsatile flow patterns that may themselves influence cellular behavior.

An increasingly popular alternative is the use of pressure controllers, in which compressed air or nitrogen applies pressure directly to medium reservoirs connected to the chip. This setup allows for rapid and precise adjustments of flow rates, smooth transitions between flow conditions, and parallel operation of multiple channels. While requiring more specialized equipment, pressure-driven systems offer excellent stability and fine control, making them particularly well suited for sensitive applications such as immune cell trafficking assays.

Finally, a newer generation of integrated micropumps and capillary-driven systems has enabled “self-contained” chips, where flow is maintained through on-chip microvalves, pneumatic actuation, or passive capillary forces. These designs minimize the need for bulky external equipment and improve reproducibility across laboratories, while also facilitating high-throughput setups (256).

Box 2. How are microfluidic chips made?

Microfluidic devices can be manufactured using several fabrication principles, each with specific strengths and trade-offs:

- **Soft lithography (PDMS prototyping):** This is the most common approach in academic labs. First, a master mold is created on a silicon wafer using a photosensitive resin patterned by UV photolithography. The mold contains the positive relief of the future channels. Liquid PDMS is then poured onto the mold, cured by heat, and peeled off, yielding an elastomeric replica with the microchannels as negative impressions. The PDMS slab is finally bonded (e.g., to glass or another PDMS layer) to enclose the channels. This method is inexpensive and flexible but requires access to cleanroom facilities for mold fabrication.
- **Injection molding / hot embossing:** Using thermoplastics such as COC, PMMA, or PC, a mold is either pressed against heated sheets (embossing) or filled under pressure (molding). This is close to industrial plastic production and enables high-volume manufacturing with excellent reproducibility, though less accessible in academic settings.
- **Laser micromachining:** A focused laser beam directly ablates material from a solid plate (glass or polymer) to carve channels. This approach avoids mold fabrication and allows rapid prototyping with fine resolution, but throughput is limited and equipment is expensive.
- **Precision milling:** Computer-controlled micromilling machines (CNC) can directly cut microchannels into plastic blocks. While resolution is typically lower than photolithography or laser methods (tens of microns), it is inexpensive and does not necessarily require cleanrooms.
- **3D printing:** Additive manufacturing builds channels layer by layer from photosensitive resins. Stereolithography achieves tens of microns of resolution, whereas two-photon polymerization can reach sub-micron precision, enabling very complex vascular-like geometries. Current limitations include material biocompatibility, optical clarity, and cost.

Once the channel structures are formed, they are sealed by bonding to a flat plate (e.g., PDMS–glass, polymer–polymer), producing enclosed channels that can be perfused with fluids. Depending on the material and sealing method, chips may be intended for single use (simplifying sterility and contamination control) or multiple uses with more robust bonding and sterilization protocols.

4. Possible readouts

One of the strengths of microfluidic tumor models is their compatibility with a wide spectrum of analytical readouts, ranging from real-time monitoring to high-content molecular profiling. The choice of readout strongly depends on the biological question and the device architecture, but several approaches have become standard.

a. Live imaging

Most microfluidic devices are fabricated from optically transparent materials such as PDMS or COC, which makes them highly compatible with advanced microscopy. Confocal and multiphoton imaging allow dynamic visualization of tumor–immune interactions, including lymphocyte migration, infiltration depth, and cytotoxic activity. Lightsheet microscopy can provide volumetric imaging of large spheroids or organoids embedded in chips, while high-content automated microscopy facilitates screening applications.

b. Effluent analysis

Because microfluidic systems operate with perfused channels, secreted factors and metabolites can be collected continuously in the outlet effluent. This enables longitudinal quantification of cytokines, chemokines, growth factors, and metabolites using ELISA, mass spectrometry, or multiplex bead-based assays. In addition, cells flushed out of the chip can be recovered for single-cell RNA sequencing or functional assays, providing snapshots of evolving cellular states under defined microenvironmental conditions.

c. End-point assays

At the conclusion of experiments, chips can be fixed, stained, and processed for immunofluorescence or histology. This permits spatial analysis of proliferation, apoptosis, or immune infiltration, complementing live-cell readouts. Increasingly, protocols are also adapted for on-chip clearing and 3D reconstruction, allowing high-resolution mapping of cellular interactions across the entire device.

d. Integration with omics and high-throughput platforms

Recent advances couple microfluidics to transcriptomic and proteomic profiling, either by directly barcoding effluent samples or by isolating defined regions of chips for bulk or spatial omics. Parallelization of chip arrays further enables medium-throughput testing of drug combinations or immune interventions, bridging mechanistic studies with translational screening.

Altogether, the versatility of readouts, ranging from real-time imaging to molecular profiling, positions microfluidic tumor models as highly integrative tools, while requiring considerably less effort and complexity than animal models. They capture not only the dynamic interplay

between tumor, stromal, and immune components but also the molecular signatures underlying these interactions, thereby expanding their utility for both basic research and applied clinical applications.

Collectively, complex in vitro tumor models, ranging from simple cell line–derived spheroids to highly sophisticated microfluidic systems, provide a continuum of experimental platforms that balance fidelity and manipulability. Their increasing relevance for immuno-oncology stems from their ability to recapitulate not only the cellular and structural components of the tumor microenvironment, but also its functional interactions with the immune system. In the following sections, we explore how these models have been applied to elucidate key immune mechanisms and therapeutic responses.

E. In vitro complex models applications in immuno-oncology

3D tumor models have become essential tools to investigate tumor–immune interactions, offering higher physiological relevance than conventional 2D cultures as detailed earlier. They reproduce key features of the TME, such as cell–cell contacts, extracellular matrix organization, and spatial constraints, thereby enabling functional studies of effector lymphocytes, stromal elements, and therapeutic responses. Such platforms range from simple tumor cell line spheroids to more complex patient-derived organoids PDOs, tumor explants, and microfluidic systems. Increasingly, they are positioned not only as research tools but also as translational platforms with potential applications in personalized immuno-oncology.

Although significant progress has been made in several cancer types, including colorectal, lung, ovarian, pancreatic cancer and melanoma, the situation in ccRCC remains different. Indeed even if 3D models of ccRCC exist, only a limited number of studies have applied complex 3D systems to immunotherapeutic studies, and existing work is often fragmented, focusing separately on aspects such as immune infiltration, checkpoint blockade, or vascularization. This underlines the need for integrated approaches capable of capturing the immune and vascular hallmarks that are central to ccRCC biology.

1. T cell cytotoxicity and canonical checkpoint blockade

T cell cytotoxicity has been widely investigated in 3D tumor models, particularly in the context of ICIs such as PD-1/PD-L1 blockade (257). These systems illustrate how 3D approaches can reproduce patient responses, identify predictive biomarkers, and uncover mechanisms of resistance. While most studies have been performed in cancers such as colorectal, lung, and melanoma, they provide important proof-of-concept examples that can inform applications to ccRCC.

For example, patient-derived spheroids have been used to detect cytokines associated with ICI response and to evaluate combination strategies, such as PARP inhibition with PD-1 blockade in ovarian cancer (258).

Similarly, PDOs co-cultured with autologous TILs or peripheral blood mononuclear cells (PBMCs) supported the selective expansion of tumor-reactive $CD8^+$ T cells in mismatch repair-deficient colorectal cancer and NSCLC (259). In a landmark study, Neal et al. demonstrated that ALI PDOs derived from melanoma, non-small cell lung cancer, and ccRCC could preserve the endogenous T cell repertoire and recapitulate differential responses to ICI observed in vivo (239). More recently, lung cancer PDOs enabled the derivation of transcriptional signatures distinguishing tumor-reactive T cells (260).

Models preserving native architecture have also provided key insights. PDOTs provided a platform to evaluate PD-1 and CTLA-4 blockade (234) and to show that CDK4/6 inhibition enhanced T cell infiltration, thereby augmenting PD-1 blockade efficacy (261). Conversely, patient-derived tumor fragments captured mechanisms of resistance, as Voabil et al. showed that tumors with immune exclusion phenotypes remained refractory to PD-1 blockade (262).

These models have also shed light on the dynamics of T cell migration and exclusion within the tumor microenvironment. In PDOTs, Jenkins et al. reported that increased CCL19 and CXCL13 expression under PD-1 blockade correlated with improved responses (234). Patient-derived explants retaining tissue architecture linked clinical benefit from PD-1 therapy in melanoma to increased spatial separation between cytotoxic T cells and regulatory T cells (247). Tumor slice cultures demonstrated that the orientation and density of the extracellular matrix restrict T cell entry into tumor islets in NSCLC (263), and were further used to show that CXCR4 inhibition in combination with PD-1 blockade enhanced T cell expansion and antitumor efficacy (264).

Together, these studies demonstrate the versatility of 3D systems for modeling T cell responses to ICIs, but also highlight that applications to ccRCC remain limited, with only a handful of studies to date. This underscores the need to develop kidney cancer–specific patient-derived platforms to explore mechanisms of sensitivity and resistance to checkpoint blockade.

2. NK cell activity in 3D tumor models

NK cell activity has also been investigated in 3D systems, where these models offer the possibility to study NK infiltration, recognition, and killing within more physiological tumor contexts. Studies in non-renal cancers have illustrated this potential across diverse approaches. In colorectal cancer spheroids derived from cell lines and patients, NKG2D–MICA/B interactions promoted NK entry, an effect enhanced by NKG2A blockade (265).

Using cell line–derived spheroids in micropillar–microwell assays that mimic hypoxic conditions, NK92-CD16 cells exhibited enhanced killing of pancreatic and breast cancer spheroids when combined with therapeutic antibodies such as trastuzumab or atezolizumab, thereby mod-

eling antibody-dependent cell-mediated cytotoxicity (ADCC) (266). Similarly, microfluidic "tumor-on-chip" systems integrating cancer, immune, endothelial, and fibroblast cells enabled visualization of NK–tumor interactions in $HER2^+$ breast cancer, where trastuzumab promoted prolonged NK–tumor contacts and recapitulated effective ADCC responses (267).

By contrast, studies in renal cancer remain scarce. A recent work using ccRCC spheroids demonstrated that restoring VHL function or inhibiting hypoxia-inducible factors (HIFs) enhanced NK infiltration and sensitized tumors to immune checkpoint blockade, thereby revealing kidney cancer–specific barriers to NK activity (268). Altogether, these findings highlight the need to establish dedicated patient-derived 3D systems in ccRCC to better capture NK–tumor dynamics and evaluate strategies aimed at overcoming tumor-specific resistance mechanisms.

3. CAR-engineered immune cells in 3D systems

Beyond studies of endogenous lymphocytes, 3D models have also been exploited to evaluate the efficacy and behavior of CAR-engineered immune cells, which represent a major axis of next-generation immunotherapy.

Most proof-of-concept studies have been performed in non-renal cancers. In hepatocellular carcinoma PDOs, CAR-T cells engineered with simultaneous checkpoint silencing (PD-1, Tim-3, Lag-3) showed improved infiltration and persistence, underscoring the ability of organoid models to reveal mechanisms of resistance and evaluate potential strategies to overcome them (269). At a more advanced technological scale, the BEHAV3D platform, a high-throughput single-cell imaging and analysis pipeline, was applied to live-track more than 150,000 engineered T cells co-cultured with patient-derived solid tumor organoids. This approach enabled the combined phenotypic and behavioral profiling of CAR-T cells, leading to the identification of a distinct "super engager" cluster with potent serial killing capacity (270).

Similarly, CAR-NK strategies have been explored: CAR-NK92 cells targeting EPCAM or EGFRvIII selectively killed tumor spheroids (271), while ROR1-specific CAR-T cells demonstrated enhanced activity in triple-negative breast cancer spheroids when combined with TGF-β inhibition (272)

The scope of CAR engineering has also been expanded beyond lymphocytes. Greiner et al. developed CAR-macrophages (CAR-Ms) targeting CSPG4, a melanoma antigen, and demonstrated that these cells specifically infiltrated melanoma spheroids and performed antigen-dependent phagocytosis (273).

Importantly, applications to renal cancer are beginning to emerge. In a study involving 33 patients, RCC-derived PDOs were validated as translational platforms for CAR-T efficacy testing, directly confirming the feasibility of applying patient-derived organoid systems to ccRCC (274). Building on this, Wang et al. recently generated patient-derived organotypic tumor spheroid (PDOTS) cultures from ccRCC and demonstrated that G9 CAR-T cells exhibited superior

efficacy, migration, and cytokine release in these ex vivo models (275). Together, these studies mark a critical step forward in adapting CAR-T strategies to kidney cancer, which remains underexplored compared with other solid tumors.

4. Myeloid cells in 3D tumor models for immuno-oncology

Myeloid cells represent a central component of the TME, where they contribute to angiogenesis, immunosuppression, and tumor progression. Among them, TAMs are the most extensively studied population in 3D models. These systems have been used to reproduce macrophage polarization and functional interactions with tumor, stromal, and immune cells, thereby providing mechanistic insights into their role in shaping tumor–immune dynamics and responses to immunotherapy.

Early studies highlighted the pro-invasive functions of macrophages. In breast carcinoma spheroids, tumor cells grown as aggregates failed to invade surrounding Matrigel, but invasive behavior was restored in the presence of macrophages, underscoring their pro-tumoral activity (276).

Beyond invasion, heterotypic and multicellular models have shown that macrophages can be polarized toward immunosuppressive phenotypes within the tumor context. For example, in NSCLC tri-cultures with fibroblasts and monocytes (THP1 cell line or PBMC-derived) encapsulated in alginate microcapsules, monocytes acquired features of so-called “M2-like” TAMs, a phenotype reversed by CSF1R inhibition, a therapeutic strategy aimed at blocking macrophage survival and differentiation (277). Similarly, in pancreatic spheroids, fibroblasts and monocytes promoted macrophage polarization into suppressive M2-like states that inhibited $CD4^+$ and $CD8^+$ T cell activation; this effect was partially rescued by arginase-I blockade, which targets a metabolic enzyme involved in depriving T cells of essential nutrients (278). In ovarian hetero-spheroids, cancer stem cells drove macrophages toward a $CD206^+$ phenotype, further illustrating how tumor cell subsets can shape the immunosuppressive myeloid compartment (279).

Importantly, Li et al. developed a PDO-based TME-mimicry culture integrating tumor cells, TAMs, and antigen-specific T cells, which reproduced macrophage-mediated suppression of $CD8^+$ cytotoxicity and showed that this inhibition could be reversed by immune checkpoint blockade (anti–PD-1/PD-L1) or by metabolic inhibition (280).

Additional mechanisms of TAM-driven suppression have been captured in tissue-based 3D models. Ex vivo slices from lung squamous carcinoma showed that macrophages formed long-lasting contacts with $CD8^+$ T cells, physically excluding them from tumor islets, a mechanism associated with poor clinical outcome (281).

By contrast, studies addressing myeloid biology in renal cancer remain limited. Rausch et al.

generated heterotypic spheroids incorporating THP-1 myeloid cells (232), while Séraudie et al. recently reported a patient-derived tumoroid model that retained $CD68^+$ cells, likely macrophages, thus preserving part of the myeloid compartment in renal cancer organoids (230). These studies suggest that macrophages can be integrated into renal cancer organotypic systems, but comprehensive patient-derived models specifically dedicated to interrogating myeloid biology in ccRCC are still lacking.

5. Fibroblasts and stromal immunoregulation in 3D models

Cancer-associated fibroblasts (CAFs) are key stromal components of the TME, where they regulate extracellular matrix (ECM) deposition, tumor cell motility, and immune exclusion. Some studies used 3D models to reproduce and decipher their dual role as architects of stromal barriers and as modulators of immune responses.

The ability of CAFs to promote immunosuppressive myeloid differentiation has been reproduced in 3D settings. In pancreatic spheroids combining tumor cells, fibroblasts, and monocytes, CAFs drove polarization into M2-like TAMs and myeloid-derived suppressor cells (MDSCs), thereby suppressing T cell activity (278). In parallel, chip-based 3D systems have captured the capacity of CAFs to establish stromal barriers that limit immune cell access. In a tumor-on-chip model incorporating CAFs, fibroblasts increased cancer cell motility and provided protective niches even under trastuzumab treatment, consistent with mechanisms involving ECM remodeling and paracrine signaling rather than direct contact (267). More recently, the MIRO platform, an open fluidic device allowing the self-organization of cancer cell line spheroids, CAFs, and ECM, demonstrated that such stromal barriers can block immune infiltration and protect tumor cells from antibody-dependent cellular cytotoxicity. Importantly, IL-2 stimulation enhanced immune cell dynamics and spreading, thereby overcoming CAF-driven suppression and restoring antitumor activity (282).

In ccRCC, desmoplasia and fibroblast-rich tumors correlate with poor prognosis, and CAF-driven exclusion likely contributes to resistance to immune checkpoint blockade (283,284). Fibroblasts have been incorporated into ccRCC 3D models (230,232) providing a first basis for exploring stromal immunoregulation in patient-derived settings.

6. Next-generation immunotherapies in 3D models

Beyond canonical checkpoint blockade, 3D systems have also been exploited to evaluate next-generation immunotherapies. These models allow not only the study of endogenous tumor–immune interactions but also the preclinical testing of novel therapeutic modalities in physiologically relevant contexts.

In pancreatic ductal adenocarcinoma PDOs that incorporated stromal and immune elements,

the combination of epigenetic inhibitors with PD-1 blockade was shown to remodel the tumor microenvironment. By interfering with chromatin regulators, these drugs enhanced the expression of antigen-presentation machinery and turned an immunosuppressive context into an immunoactive one, thereby facilitating T cell infiltration and cytotoxicity (285)

T cell–engaging bispecific antibodies (TCEs), which redirect T cells toward tumor cells by simultaneously binding a tumor antigen and the CD3 receptor, have also been tested in 3D systems. In cell line–derived heterotypic spheroids combining tumor, fibroblasts, and immune cells, the combination of IL-2 variants with TCEs enhanced immune infiltration, activation, and tumor clearance compared with single agents (286). Building on this, patient-derived colorectal and intestinal organoids supplemented with immune cells showed that TCE efficacy depends on antigen density and stromal context, and that co-stimulatory bispecifics can further amplify T cell activity (287).

Other modalities have also been explored using organoid platforms. Oncolytic viruses, engineered to selectively replicate in and lyse tumor cells while stimulating immunity, were shown to enhance $CD8^+$ T cell cytotoxicity in patient-derived ascites organoids (288). Similarly, nanoparticles designed to stimulate innate immunity promoted infiltration and activation of endogenous T cells across organoids from multiple tumor types (289).

Notably, in clear cell renal cell carcinoma, chemokine-armed oncolytic adenoviruses encoding immune attractants such as CXCL9, CXCL10, or IL-15 promoted $CD8^+$ migration via CXCR3 signaling, induced cytokine secretion, and enhanced NK cell infiltration, providing direct proof-of-concept for viral immunotherapy in kidney cancer (290).

These studies show that 3D models are emerging as versatile translational tools to evaluate innovative immunotherapies. While most advances have been achieved in other cancers, early data in ccRCC highlight both the feasibility and the need to develop dedicated patient-derived systems to explore novel therapeutic strategies in this context.

7. 3D personalized platforms for immunotherapy response prediction

A major challenge in immuno-oncology is the lack of reliable assays to predict whether a patient will benefit from a given treatment. While biomarkers such as PD-L1 expression, tumor mutational burden, or gene signatures are being explored, they remain imperfect and do not capture the functional complexity of tumor–immune interactions. In this context, 3D patient-derived models have emerged as promising complementary tools, as they can incorporate both stromal and immune compartments while enabling functional testing of immunotherapies within clinically relevant timelines.

Several groups have therefore developed 3D systems explicitly designed as predictive assays

for immunotherapy, aiming to deliver readouts that could ultimately guide therapeutic decision-making.

Micro-organospheres (MOS) (a form of tumoroid or PDOs), generated by droplet microfluidics from small patient samples, represent one of the most advanced examples. These miniaturized tumoroids retain stromal and immune cells and can be produced in large numbers within days, making them suitable for rapid functional testing. In metastatic colorectal cancer and NSCLC, MOS were used to evaluate PD-1 blockade, bispecific antibodies, and T cell therapies, reliably reproducing immune responses within a two-week window compatible with clinical decision-making. Notably, MOS derived from kidney cancer patients demonstrated that nivolumab alone was insufficient to induce tumor killing, whereas its combination with T cell activation enhanced cytotoxicity, illustrating both the feasibility and the specificity of this approach (291). Other groups have used organoid-based systems to preserve immune interactions. Immune-enhanced patient tumor organoids (iPTOs), established from melanoma biopsies while retaining stroma and lymphocytes, enabled parallel testing of immune checkpoint inhibitors and targeted therapies, with organoid responses matching clinical outcomes in the majority of patients. These models could even activate autologous T cells to kill naïve organoids, suggesting a role in modeling adaptive immunity (292). Similarly, lung tumor-on-chip systems combining autologous tumor cells, T cells, and FAP^+ fibroblasts captured stroma-dependent resistance to PD-1 blockade and allowed patient-specific assessment of treatment response ex vivo (293). Humanized microfluidic chips incorporating tumor cells, serum, and immune cells from head-and-neck cancer patients further demonstrated that checkpoint inhibitors or metabolic modulators such as IDO1 blockade can elicit highly patient-dependent responses (294).

Crucially, such concepts are beginning to extend to renal cancer. Xue et al. established air–liquid interface PDOs from ccRCC surgical specimens, preserving tumor cells, fibroblasts, endothelial cells, and infiltrating T lymphocytes. Drug testing showed that toripalimab, a PD-1 antibody, could restore $CD8^+$ T cell activity and overcome exhaustion, correlating with tumor cell apoptosis. This proof-of-concept validates PDOs as preclinical models for predicting immunotherapy response in ccRCC patients (295)

Altogether, these studies highlight that 3D systems can be engineered as clinically relevant predictive tools for immunotherapy, with turnaround times compatible with treatment planning. While most work has been performed in melanoma, lung, and colorectal cancers, the first applications in ccRCC underscore both the feasibility and the urgency of developing robust, immune-competent personalized platforms in kidney cancer.

This body of work highlights the range of immuno-oncology applications enabled by 3D tumor models, from canonical checkpoint blockade to NK and CAR-based therapies, myeloid and stromal regulation, and innovative modalities such as bispecific antibodies, viral immunotherapies, or predictive personalized assays. While most of these advances have been made in cancers such as colorectal, lung, or melanoma, they collectively establish a proof-of-concept

framework that can directly inform applications to ccRCC. However, despite these advances, important limitations inherent to in vitro models remain to be addressed, most notably their lack of vascularization.

F. General conclusion on preclinical models in immuno-oncology

The study of tumor–immune interactions has historically relied on a wide spectrum of preclinical models, each offering unique advantages but also facing intrinsic limitations. Two-dimensional (2D) cultures, while simple and standardized, fail to capture the three-dimensional architecture and cellular diversity of the tumor microenvironment. Conversely, animal models provide a systemic context, but their translational value is constrained by interspecies differences, their inability to fully recapitulate human immunobiology, and ethical considerations.

In this landscape, complex in vitro systems, referred to as 3D models, have progressively emerged as intermediate and highly versatile platforms. These models encompass a wide range of formats and can preserve inter- and intra-patient heterogeneity, cell–cell contacts, extracellular matrix organization, and spatial constraints, key features that support their potential to recapitulate patient-specific therapeutic responses. They provide a more physiologically relevant context to study immune infiltration, stromal regulation, and treatment efficacy than conventional 2D cultures, while remaining simpler and faster to implement than animal models (**Figure 36**).

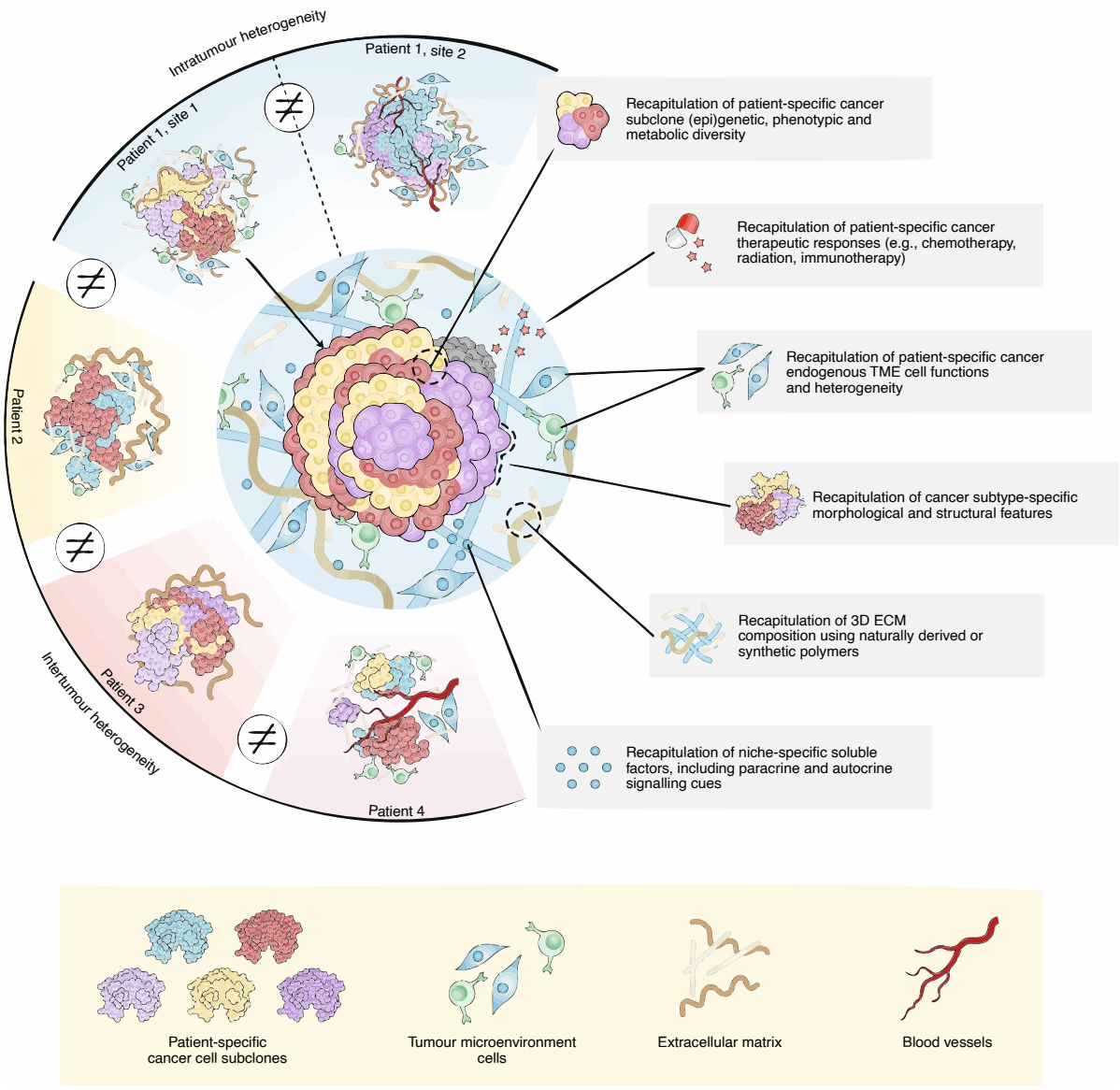

Figure 36. Biological complexity that 3D cancer models can potentially recapitulate.

Patient-derived 3D cancer models have the potential to reproduce key aspects of both intra- and intertumoral heterogeneity. These include: (epi)genetic, phenotypic, and metabolic diversity of patient-specific cancer cell subclones, tumor-specific morphological and structural features, the presence and functions of non-malignant TME cells, the composition of the extracellular matrix (ECM), whether naturally derived or synthetic, and the activity of niche-specific soluble signals, including paracrine and autocrine factors. Some models may also allow for the evaluation of patient-specific therapeutic responses to chemotherapy, radiotherapy, or immunotherapy.

Source: (296), reproduced withe permission from Springer Nature, license number 6154860986875

These models have enabled mechanistic insights into T- and NK cell cytotoxicity, the suppressive functions of myeloid and stromal cells, as well as the evaluation of next-generation immunotherapies, from checkpoint inhibitors, bispecific antibodies, and oncolytic viruses, to CAR-based approaches. More recently, personalized organoid-based platforms have demonstrated predictive value for immunotherapy response, thereby paving the way for precision immuno-oncology.

Yet, these advances also underscore a fundamental principle: no model is universal. Highly complex systems integrating vascularization, automation, or bioprinting represent powerful

proofs of concept, but they remain technically demanding and limited in scalability. At the same time, simpler models such as multicellular tumor spheroids retain strong value for their reproducibility and rapid implementation. Ultimately, the relevance of any given model depends less on its intrinsic sophistication than on its suitability for the biological or therapeutic question at hand.

This perspective is reinforced by the FDA Modernization Act 2.0 (2022), which removed the long-standing requirement for animal testing prior to human clinical trials (297). This landmark regulatory shift recognizes the potential of advanced in vitro systems as credible alternatives, and further legitimizes their development as translational tools in oncology.

It is within this evolving scientific and regulatory context that the present thesis is situated. By building on insights derived from diverse 3D models, the work seeks to adapt these approaches to ccRCC, establishing models tailored to the study of immunotherapies in this context. The overarching aim is to develop platforms that are pragmatic yet biologically relevant, capable of dissecting the unique immunobiology of ccRCC while supporting the exploration of both established and emerging immunotherapeutic strategies.

G. Project Rationale and Methodological Framework

This thesis project was initiated with the goal of establishing a patient-derived 3D model that would be both rapidly implementable and technically accessible, in order to preserve tumor representativity and support timely investigation of immunotherapeutic responses. While the long-term vision was to build a functional tumor-on-chip platform for patient-specific testing, the starting point required the development of core technical capabilities within the team.

At the time, 3D culture systems, microfluidics, and associated analytical techniques were not yet established within the laboratory. The project therefore focused on progressively building a robust experimental pipeline, starting from fundamental steps such as tumor dissociation and primary cell culture, and advancing toward reproducible spheroid formation, immune cell reinfiltration, and functional assessment.

Based on the comparative framework established in **Table 5** and the criteria outlined in **Box 1,** patient-derived tumor spheroids were selected as the most appropriate starting point for model development. This approach combined essential features of representativity and feasibility: it preserved part of the tumor heterogeneity and stromal components while allowing rapid formation and manipulation within experimentally compatible timelines. Unlike tissue slices or ECM-embedded organoids, spheroids offered a standardized, scalable, and modifiable system, aligning with the requirements defined for a relevant preclinical ccRCC model.

Results

The experimental results of this thesis are presented in the form of three articles. The first, already published in 2022, lays the methodological foundation for the development of a three-dimensional spheroid model derived from ccRCC tissues and cell lines. The two subsequent articles, currently under preparation, follow a logical progression toward the implementation of an autologous ex vivo platform for modeling immune-tumor interactions. The second article describes the development and transcriptomic characterization of a patient-derived tumor spheroid model generated from freshly dissociated tumor tissue and re-infiltrated with autologous TILs. Finally, the third article describes the integration of this model into a custom-designed microfluidic chip and explores its potential for modeling dynamic immune-tumor interactions under immunotherapeutic conditions, laying the groundwork for a functional tumor-on-chip platform in both basic and translational immuno-oncology.

Chapter 1: Methods for Establishing a Renal Cell Carcinoma Tumor Spheroid Model with Immune Infiltration for Immunotherapeutic Studies

Leonard Lugand, Guillaume Mestrallet, Rebecca Laboureur, Clement Dumont, Fatiha Bouhidel, Malika Djouadou, Alexandra Masson-Lecomte, Francois Desgrandchamps, Stephane Culine, Edgardo D. Carosella, Nathalie Rouas-Freiss and Joel LeMaoult

Published in Frontiers in Oncology on July, 28 2022

In this first study, we established an initial experimental pipeline spanning from tumor dissociation to spheroid formation and preliminary functional assays. The work focused on optimizing key technical parameters required to develop a reproducible 3D model of ccRCC. We first refined tumor dissociation protocols and optimized culture media to improve the viability and growth of primary tumor cells. Several methods for spheroid formation were compared to identify conditions yielding consistent and homogeneous structures.

We then implemented co-culture systems with immune cells to determine the conditions under which immune infiltration could occur. In parallel, preliminary strategies were outlined to address variability among spheroids and improve reproducibility across experiments. Together, these advances provided the methodological foundation for subsequent studies aiming to model patient-specific tumor–immune interactions in ccRCC.

frontiers | Frontiers in Oncology

ORIGINAL RESEARCH
published: 28 July 2022
doi: 10.3389/fonc.2022.898732

Check for updates

Methods for Establishing a Renal Cell Carcinoma Tumor Spheroid Model With Immune Infiltration for Immunotherapeutic Studies

Leonard Lugand[1†], Guillaume Mestrallet[1†], Rebecca Laboureur[1], Clement Dumont[1,2], Fatiha Bouhidel[3], Malika Djouadou[4], Alexandra Masson-Lecomte[4], Francois Desgrandchamps[4], Stephane Culine[2], Edgardo D. Carosella[1], Nathalie Rouas-Freiss[1‡] and Joel LeMaoult[1‡]*

[1] Hemato-Immunology Research Department, CEA, DRF-Francois Jacob Institute, Saint-Louis Hospital, Paris, France - U976 HIPI Unit, IRSL, Paris University, Paris, France, [2] Department of Medical Oncology, Saint-Louis Hospital, AP-HP.Nord - Université de Paris, Paris, France, [3] Service d'Anatomopathologie Saint-Louis Hospital, AP-HP.Nord - Université de Paris, Laboratory of Pathology, UMR-S728, Paris, France, [4] Department of Urology, Saint-Louis Hospital, AP-HP.Nord - Université de Paris, Paris, France

Tumor spheroids play an increasingly important role in cancer research. Their ability to recapitulate crucial features of tumor biology that are lost in the classically used 2D models along with their relative simplicity and handiness have made them the most studied 3D tumor model. Their application as a theranostic tool or as a means to study tumor-host interaction is now well-established in various cancers. However, their use in the field of Renal Cell Carcinoma (RCC) remains very limited. The aim of this work is to present methods to implement a basic RCC spheroid model. These methods cover the steps from RCC tumor dissociation to spheroid infiltration by immune cells. We present a protocol for RCC dissociation using Liberase TM and introduce a culture medium containing Epithelial Growth Factor and Hydrocortisone allowing for faster growth of RCC primary cells. We show that the liquid overlay technique allows for the formation of spheroids from cell lines and from primary cultures. We present a method using morphological criteria to select a homogeneous spheroid population based on a Fiji macro. We then show that spheroids can be infiltrated by PBMCs after activation with OKT3 or IL-15. Finally, we provide an example of application by implementing an immune spheroid killing assay allowing observing increased spheroid destruction after treatment with PD-1 inhibitors. Thus the straightforward methods presented here allow for efficient spheroid formation for a simple RCC 3D model that can be standardized and infused with immune cells to study immunotherapies.

Keywords: spheroid, renal cell carcinoma, immune checkpoint inhibitors, standardization, PD-1, heterogeneity, personalized medicine

OPEN ACCESS

Edited by:
Thierry Massfelder, Institut National de la Santé et de la Recherche Médicale (INSERM), France

Reviewed by:
Wanhe Wang, Northwestern Polytechnical University, China
Daxiang Cui, Shanghai Jiao Tong University, China
Elvis Pandzic, University of New South Wales, Australia

****Correspondence:***
Joel LeMaoult
joel.lemaoult@cea.fr

[†]These authors have contributed equally to this work and share first authorship

[‡]These authors have contributed equally to this work and share last authorship

Specialty section:
This article was submitted to Genitourinary Oncology, a section of the journal Frontiers in Oncology

Received: *17 March 2022*
Accepted: *01 June 2022*
Published: *28 July 2022*

Citation:
Lugand L, Mestrallet G, Laboureur R, Dumont C, Bouhidel F, Djouadou M, Masson-Lecomte A, Desgrandchamps F, Culine S, Carosella ED, Rouas-Freiss N and LeMaoult J (2022) Methods for Establishing a Renal Cell Carcinoma Tumor Spheroid Model With Immune Infiltration for Immunotherapeutic Studies. Front. Oncol. 12:898732. doi: 10.3389/fonc.2022.898732

INTRODUCTION

Advanced clear cell renal cell carcinoma (ccRCC) is primarily treated with systemic treatments targeting the tumor microenvironment (TME) These treatments include immune checkpoint inhibitors (mainly PD-1 inhibitors) or VEGFR tyrosine kinase inhibitors (TKIs), as single agents or as part of combination treatments depending mostly on patient's prognosis. To this day, apart from the clinical IMDC prognostic criteria, which are associated with decreased sensitivity to VEGFR-TKIs, no reliable biomarkers are available in the clinic to select the best therapeutic options for each patient. The use of standardized patient-derived individual predictive models may help solve this unmet clinical need, as well as serve in the translational research setting.

Current ccRCC models regroup *in vivo* and *in vitro* models, each with advantages and disadvantages. While *in vivo* models provide the possibility to study tumor biology in a dynamic and more complete TME, they come with cost, poor handiness, and ethical limitations. Furthermore, their application as a theranostic tool, mostly in the form of patient-derived xenografts (PDXs) remains far remote from clinical routine. Thus, relevant *in vitro* ccRCC models are essential both as research tools and as theranostic tools. As a research tool, while established cell lines grown in monolayers are cost-effective, easy to maintain and allow high replicability and standardization, they include neither the clonal heterogeneity nor the rich TME that are characteristic of ccRCC (1). Conversely, primary cultures of tumor cells directly isolated from patient samples may retain some heterogeneity (including the conservation of several tumor clones as well as TME components) and allow patient-level applications. Two-dimensional culture of either cell lines or primary cultures were successfully used for decades to select, grow and study tumor cells. However, 2D models find their limit when tumor heterogeneity and structural characteristics are key parameters, because those are completely lost (2). These characteristics include tumor physical structure, the impact of hypoxia or the contribution of stromal cells and immune infiltrate to tumor biology. Furthermore, by using 2D models, even for primary culture, a selection still occurs. It is not based on the capability to escape immune destruction or survive and grow in a chemically inadequate environment, but on the cell's capability to grow attached to plastic in an artificial medium. This has important consequences, among which (i) loss of cell diversity, to the point to which a primary culture becomes a « cell line », and (ii) alteration of the tumor cell characteristics due to culture conditions. In particular, it should be expected that tumor cell characteristics dependent on parameters of the TME may be impacted. For instance, neo-expression of the immune checkpoint HLA-G, which is common in ccRCC cells and is an immune escape mechanism, is usually lost in culture within a few passages (3).

To best preserve tumor structural components, it is possible to work with tissue slices (4–9). However, this model is not suited for studies focusing on individual tumor elements that are heterogeneously distributed within the tumor. In particular, it was shown that immune checkpoints ligands and receptors are heterogeneously expressed in RCC tumors (10). Thus, if focusing on such heterogeneously distributed parameters, tissue slices might not be a good model, being only representative of themselves.

Multicellular tumor spheroids are an intermediate model between 2D cultures and tissue slices, in which tumor components are dissociated and then reassembled in a spheroid of defined parameters. In such spheroids, tumor structure is lost, but they may include tumor cells from different tumor areas along with stromal cells, be of various sizes, possess a necrotic core or not (11, 12) and be infused with immune cells, including autologous Peripheral Blood Mononuclear Cells (PBMCs) and Tumor-Infiltrating Lymphocytes (TILs) (13). Thus, tumor spheroids have the advantages of flexibility, standardization, and parallelization while preserving some tumor heterogeneity. As such, this model seems well adapted to test the effects of immune therapies, as it was shown for colorectal cancer (14–16), breast cancer (17), non-small cell lung cancer (18–20), or liver cancer (21) for instance.

It is clear that such models would be very useful in the context of ccRCC as well, but methodological information on how to generate a basic spheroid model infiltrated with immune cells starting from ccRCC tissue is scarce. Providing such information was our goal here: we present our approach for establishing an immune-infiltrated ccRCC spheroid model. It includes tumor dissociation, primary cell culture, and generation of multicellular tumor spheroids from cell lines or primary cells, and infiltration by immune cells. We also provide a method to select a homogeneous population of spheroids based on morphologic criteria to increase the relevance of the data obtained in the spheroid model. Lastly, we present one application of our model by analyzing the effect of blocking PD-1 with therapeutic antibodies on tumor cell survival in a live-imaging spheroid-killing assay.

MATERIALS AND METHODS

All specific materials used are summarized in **Supplementary Table 1** with references. A complete protocol can be found in **Supplementary Data Sheet 1**.

Human Tissue and Cells

RCC Cell Line

The RCC7 cell line originated from ccRCC was kindly provided by Dr. Anne Caignard, St Louis Hospital, Paris (22).

Tumor Samples

Human ccRCC tissues were collected as surgical waste from adult patients undergoing nephrectomy at our center (Urology Department, Saint-Louis Hospital, Paris, France), after informed consent. Tumor samples were selected on nephrectomy specimens by a pathologist, rinsed with phosphate-buffered saline (PBS), and placed in Roswell Parks Memorial Institute (RPMI) 1640 medium (Sigma-Aldrich) at 4°C prior to dissociation.

Cell Culture

In this study, we describe a custom culture medium suitable for ccRCC cell culture, referred to as RCCM. It is composed of Dulbecco's Modified Eagle Medium (DMEM, Gibco) and Ham's F12 media (Gibco) (v/v, 3/1 mixture) supplemented with 10% fetal calf serum (FCS, Sigma-Aldrich), 2 mM L-glutamine (Gibco), 100 U/ml penicillin/streptomycin (Gibco), 10 ng/ml epidermal growth factor (EGF) (Sigma-Aldrich) and 0.4 µg/ml hydrocortisone (Sigma-Aldrich)

Cultures were kept in a humidified atmosphere with 5% (v/v) CO2 at 37°C. Cell transfer and preparation of single-cell suspensions from monolayers were performed by mild enzymatic dissociation using a 0.05% (w/v) trypsin and 0.02% (w/v) EDTA solution in PBS (Gibco).

PBMC Preparation

Blood samples were collected from healthy donors from Etablissement Français du Sang (Paris). Peripheral blood mononuclear cells (PBMCs) were isolated using gradient Ficoll (Histopaque, Sigma-Aldrich) according to the manufacturer's recommendations and stored at −150°C.

ccRCC Dissociation

Within 30 minutes after nephrectomy, ccRCC samples were rinsed in RPMI 1640 medium at 4°C. Fibrous parts were discarded and the remaining was finely minced until reduced to approximately $1mm^3$ pieces.

We chose to avoid further mechanical dissociation as it leads to poor final viability.

For enzyme comparison, the minced samples were incubated in 15mL conical tubes containing 6mL of dissociating solution composed of Hank's Balanced Salt Solution and 20µL recombinant DNase I (Sigma-Aldrich) with either Liberase TM (Sigma-Aldrich) at concentrations ranging from 0.07 to 0.28 WU/mL or collagenase IV (Worthington) at concentrations ranging from 0.25 to 1 mg.mL-1 at 37°C, in a hot-water bath, for 10 to 60 minutes. Every 10 minutes, the tubes were hand-shaken to help dissociation. No vortexing or repeated up-and-down-pipetting was involved to avoid damaging ccRCC cells. Once the dissociation complete, the solution was filtered through a 100µm nylon cell-strainer and collected in a 50mL conical tube. To rinse the filter and stop the dissociation, 35mL of RPMI 1640 at 4°C supplemented with 10% FCS (Sigma-Aldrich), L-glutamine (300 µg/mL), gentamicin (50 µg/mL) and amphotericin B (2.5 µg/mL, Gibco), referred to as complete RPMI, were poured on top of the strainer and collected in the same tube. Cells were then washed and red blood cells were lysed using red blood cell lysis solution (Miltenyi Biotec) according to the manufacturer's instructions. After another washing step, cells were resuspended in DMEM and counted. Viability was assessed by trypan blue exclusion. CD45+ immune infiltrating cells and non-immune cells were then separated using CD45 magnetic beads on a QuadroMACS Separator (Miltenyi Biotec) according to the manufacturer's instructions. Both fractions were collected, washed, and counted. ccRCC patient-derived primary cell cultures were initiated by seeding 10^6 cells of the CD45-negative fraction in $75cm^2$ flasks. The remaining part of the primary cells was frozen.

After optimization, 0.28 $WU.mL^{-1}$ Liberase TM during 30 to 40 minutes were chosen for dissociation. A complete protocol is provided in **Supplementary Data Sheet 1**.

Optimization of Culture Medium

ccRCC tumor cells were cultured in a medium constituted of DMEM and Ham's F12 media (Gibco) (v/v, 3/1 mixture), 10% fetal calf serum (Sigma), 2 mM L-glutamine (Gibco), and 100 U/ml penicillin/streptomycin (Gibco). When indicated, 10 ng/ml epidermal growth factor (EGF) (Sigma-Aldrich), 5 µg/ml insulin (Sigma-Aldrich), 0.4 µg/ml hydrocortisone (Sigma-Aldrich) or 180 µM adenine (Sigma-Aldrich) were added in the medium. Medium was renewed thrice a week.

For growth data collection, tumor cells were seeded at 1,000 cells/cm^2 and sub-cultured every week. All cultures were performed in flasks. Upon each passage, once per week, numbers of population doublings (PD) achieved by cultures were calculated as follows: PDs = log(N/N0)/log(2), where N0 represents the number of seeded cells and N represents the number of cells obtained after 7 days of growth.

For cell confluence data, confluence was calculated with the Incucyte S2 system (Sartorius) using the dedicated function. ccRCC cells from 3 patients were seeded at 500 cells per well in a 96-well plate and placed in the Incucyte for brightfield imaging every 4 hours for 7 days. Cell confluence was calculated automatically.

Spheroid Formation

When primary ccRCC cultures or established cell lines reached 80 percent cell-confluence, they were processed for spheroid formation, using the following methods.

Liquid Overlay Technique

Cells were detached with trypsin, washed, and counted. They were then diluted with RCCM to reach 50,000 cells/mL. 200µL of this suspension were distributed in each well of a cell-repellent 96-well round bottom plate (Greiner Bio-one). The plate was centrifuged at 500g for 1 minute to initiate contact between cells. Spheroid formation was monitored each day on an inverted microscope.

Hanging-Drop Technique:

After detachment, 25µL of a 40,000 cells/mL unicellular suspension of the chosen cells in RCCM were seeded in droplets in the lid of a petri dish. The bottom of the dish was covered in PBS to prevent evaporation and the lid was placed on the dish resulting in hanging drops. Spheroid formation was monitored each day on an upright microscope.

Spheroid Morphological Parameters Calculation

70 RCC7 spheroids were formed with the hanging-drop technique and imaged every day for five days using brightfield imaging. Obtained images were analyzed using Fiji software (23) for Area, Circularity = $(4\pi \times Area)/(Perimeter)^2$, Roundness = 4×Area/

($\pi \times$major axis^2) and Solidity = Area/(convex hull) measurements using a recorded macro (**Supplementary Data Sheet 2**). This macro was used through the plugin>macro>run option on Fiji, it requires the "shape-smoothing" package. The macro improves contrast, uses a threshold to select the spheroid, operates a smoothing of the selection's border, saves the selection mask in the output folder and measures circularity, roundness, area and solidity along with other shape descriptors. The results are saved in a table at the end of macro execution.

Spheroid Infiltration

PBMC Preparation

To avoid too many washing steps causing cell loss and optimize flow-cytometry results from spheroids, PBMCs were stained for 20 minutes at room temperature with a CD45 APC antibody (eBioscience). PBMCs were then washed and counted. For activation, 30,000 healthy donors PBMCs were seeded in the wells of a 96-well round-bottom plate in 200µL complete RPMI 1640 medium containing 40 ng/mL IL-15 (Miltenyi Biotec) or 100 ng/mL OKT3 (Biolegend) and cultured for 2 days.

Monocyte-Derived Cell Preparation

To isolate and differentiate macrophages from human PBMCs, 20 millions healthy donor PBMCs were plated on a standard 100 mm petri dish in RPMI medium. Cells were left 2 hours for adherence and the petri dish was then thoroughly rinsed 4 times using PBS to remove non-adherent cells. The remaining cells were cultured for 3 days in RPMI medium completed with human AB serum (Corning).

Spheroid Infiltration With PBMCs

Two days prior to coculture, PBMCs were prepared as described above and 10,000-cell RCC7 spheroids were formed with the liquid overlay technique in RCCM. After these 48 hours, the medium surrounding the spheroids was carefully removed with a 200µL micropipette. CD45-labeled activated or non-activated PBMCs were then added to the spheroids and cocultured for 24 hours. At the end of coculture, the wells were carefully mixed by up and down pipetting without aspirating the spheroid. The supernatants of the resuspended wells were removed, leaving the spheroid in the bottom. Spheroids were then washed twice in PBS following the same process so as to remove all non-infiltrated PBMCs. They were then transferred to 1,5mL Eppendorf tubes, pooling 3 spheroids per tube, and washed once more. PBS was then replaced with 50µL Accutase (Stemcell Technologies) to dissociate the spheroids. Every 10 minutes each well underwent 10 up and down pipetting to combine mechanical and enzymatic dissociation as described by Grässer et al. (24). After 30 minutes of dissociation at room temperature, 450µL of complete RPMI at 4°C were added and the dissociated spheroids + infiltrating PBMCs were analyzed on an Attune NxT flow cytometer (ThermoFisher).

Spheroid Infiltration With Monocyte-Derived Cells

10,000-cell RCC7 spheroids were formed with the liquid overlay technique in RCCM were prepared 2 days prior to coculture. 3 days prior to coculture, macrophages were prepared as described above. After these 72 hours, the medium surrounding the spheroids was carefully removed with a 200µL micropipette. Macrophages were detached from the petri dish using trypsin and 30,000 macrophages were added to the spheroids-containing wells. After 24 hours of coculture, the spheroids were processed as described before for washing and dissociation. The obtained single cells suspension was then stained usingCD14-APC (Miltenyi) and anti HLA-DR-PE (Miltenyi) mouse anti human antibodies. Results were analyzed on an Attune NxT flow cytometer (ThermoFisher)

Spheroid Killing Assay

As described above, 48h before the experiment, 10,000-cell RCC7 spheroids were formed using the liquid overlay technique in RCCM and 100,000 PBMCs were seeded in the wells of a 96-well round-bottom tissue culture plate and activated with IL-15 for 48h. Then, 10 µg/mL nivolumab (Bristol Myers Squibb), 10 µg/mL pembrolizumab (Merck) or no treatment were added to the wells containing PBMCs and incubated for 20 minutes. Cocultures were then initiated: the medium surrounding spheroids was removed and activated PBMCs, non-activated PBMCs or no PBMCs were added to the wells at a 10:1 effector:target ratio. 5 µg/mL of Propidium Iodide (PI) were added to monitor cell death by red fluorescence.

Spheroids were monitored using the Incucyte S2 system (Sartorius), taking 4× images (0.2 NA) with red (585/635 nm excitation/filter) and green (460/524 nm) fluorescence every 2 hours for 5 days. Background red fluorescence was corrected by setting the Green into Red setting at 60 percent so that the control spheroids cultured without PBMCs showed no signs of red fluorescence. Incucyte analysis settings were set with the "spheroid" mode, with the Background to Cell option set to 100 towards background and a minimum object size limit set at "10,000", allowing selecting only the spheroids. Red fluorescence was analyzed with the option "Largest brightfield object red mean intensity".

Statistical Analysis

For ccRCC growth data, analyses were performed with GraphPad Prism 7 (GraphPad Software), statistical significance was tested using paired t-tests.

Other analyses were performed with R (version 4.0.5). Comparisons between categorical and numerical variables for infiltration data were performed using t-tests. For morphological criteria, comparisons between timepoints were performed using paired Wilcoxon-test comparing each group against all (base mean), a global Kruskal-Wallis test was performed, denoting if at least one group is different from the others.

p-values were adjusted for multiple when appropriate using Bonferroni correction, a p-value threshold of 0.05 was chosen for significance. Values are written as mean ± SEM.

RESULTS

ccRCC Dissociation

In order to obtain patient-derived RCC cells, dissociation of fresh tumor samples is necessary. Reliable dissociation protocols based

on collagenase IV or collagenase cocktails such as Liberase are published, even for ccRCC tumors (25), and even compared (26–28). We will not present data for the optimization of this part, but since the dissociation step is an integral part of the process we present, we felt necessary to individualize this step in a paragraph. Thus, in this study, we used Liberase TM at 0.28 WU/mL for 30 to 40 minutes (**Supplementary Table 1**), which routinely yielded up to 80% viable cancer cells (data not shown).

Optimization of Culture Medium for Survival, Short-Term and Long-Term Growth of ccRCC Primary Cells

It is common knowledge that ccRCC primary cells do not survive well in basic culture media such as RPMI and DMEM, and even if obtaining tumor lines by using just those is possible, it is highly inefficient, yielding to death of the entire primary culture in most cases, to weak growth in some, and very rarely in long term growth. Out of commercially available and published primary line culture media we tested, a keratinocyte primary line culture medium proved most reliable. This culture medium is published elsewhere (29) and is composed of base medium (DMEM/F12), i.e. DMEM and Ham's F12 media (Gibco) (*v*/*v*, 3/1 mixture), 10% fetal calf serum (Hyclone), supplemented with the following components: 10ng/mL epidermal growth factor (EGF) (Sigma-Aldrich), 5 µg/mL transferrin (Sigma-Aldrich), 5 µg/mL insulin (INS) (Sigma-Aldrich), 0.4µg/mL hydrocortisone (HC) (Sigma-Aldrich), 180µM adenine (AH) (Sigma-Aldrich), 2mM tri-iodothyronine (TIT) (Sigma-Aldrich), 2mM L-glutamine (Gibco), and 100U/mL penicillin/streptomycin (Gibco). From this base, we sought to establish a simplified medium suitable for primary culture of ccRCC cells. Tumors from 3 patients were used for this. First, we compared primary ccRCC cell growth when cultured in complete keratinocyte culture medium or in medium with one component removed (**Supplementary Figure 1**). As shown the removal of only 4 of the medium's components had a negative effect on cell growth: EGF, HC, INS, and AH. Next, we compared the growth of 3 primary ccRCC lines in DMEM/F12 medium alone, supplemented individually with each component, or with the 4 components together (**Figure 1**). As shown in **Figure 1A**, after 7 days of culture, only EGF and HC permitted a significant increase in cell growth compared to DMEM/F12 alone, whereas no effect was observed for INS or AH.

To determine the kinetics of cell growth, we measured cell confluence every 4 hours with the IncuCyte S2 system for one week. We observed that cells showed accelerated growth in DMEM/F12 medium supplemented with EGF and HC compared with DMEM/F12 (**Figure 1B**), yielding to 100% confluence in 5 days, while only 40% confluence was obtained after 7 days in unsupplemented DMEM/F12 medium. This medium will be referred to as RCCM (Renal Cell Carcinoma Medium).

We then determined if EGF and HC could sustain long-term proliferation of primary ccRCC cells. Cells from three patients were amplified in DMEM/F12 or in DMEM/F12 supplemented with EGF and Hydrocortisone (RCCM). Obtaining sufficient amplification in unsupplemented DMEM/F12 became difficult starting from week 4 whereas cells could be amplified for more than 8 weeks in RCCM. Cells amplified in RCCM also showed growth rates twice as high as in unsupplemented DMEM/F12 after 4 weeks (17 population doublings (PDs) vs 9 PDs, respectively), and 30 PDs were obtained after 8 weeks (**Figure 1C**).

RCCM (DMEM/F12+EGF+HC) is therefore a simple medium that reliably sustains survival and growth of tumor cells obtained from dissociated ccRCC samples.

Taken together, our selected methods for ccRCC tumor dissociation followed by culture in RCCM routinely allow us to successfully obtain primary ccRCC cell cultures from 9 out of 10 tumor samples.

Spheroid Formation Methods From Both ccRCC Cell Lines And ccRCC Primary Cell Cultures

Depending on the research topic, spheroids may be required either from cell lines or from primary lines, or even directly from dissociated ccRCC cells. Because the successful generation of spheroids directly with ccRCC cells is extremely patient-dependent, we will only present data obtained with established cell lines and primary lines (1 to 2 *in vitro* passages). For the reassembly of spheroids starting from heterogeneous dissociated ccRCC tumor cells, two main methods are described: the hanging drop technique and the liquid overlay technique. In the hanging drop technique, spheroids are formed within droplets of culture medium hanging from the lid of a petri dish, and no specific material is required. In the liquid overlay technique, cells are seeded in wells of commercially available non-stick plates, specially coated to prevent cell adhesion. In both these methods, spheroids form because cells have only each other to adhere to. We compared the formation of spheroids by these two methods by seeding 10,000 cells in droplets or in 96 well cell-repellent plates and by imaging the spheroids in formation every day for 3 days. **Figure 2** shows the results obtained for an established cell line, RCC7 (**Figure 2A**), and for two primary ccRCC cell cultures dissociated from ccRCC tumors and cultured for 1 passage following the procedures presented above (**Figure 2B**).

For the RCC7 cell line (**Figure 2A**), we found that spheroids could easily be formed using both techniques, but that spheroids formed faster (within 24 hours) with the liquid overlay method than with the hanging drop technique (72 hours).

Whereas both techniques seemed suitable for the formation of cell line spheroids of comparable quality, this was not the case with primary ccRCC cultures. We compared spheroid formation by both methods using primary ccRCC cell cultures from 7 patients. Cells from one patient did not form spheroids by either method. Of the remaining 6 patients, results were either similar by both methods (3 out of 6 patients), or better with the liquid overlay method (3 out of 6 patients). **Figure 2B** shows representative results obtained with 1 patient of each category. As can be seen, primary cells from Patient#83 formed spheroids in 72 hours by either method, with no obvious difference observed in spheroids. On the contrary, primary cells from

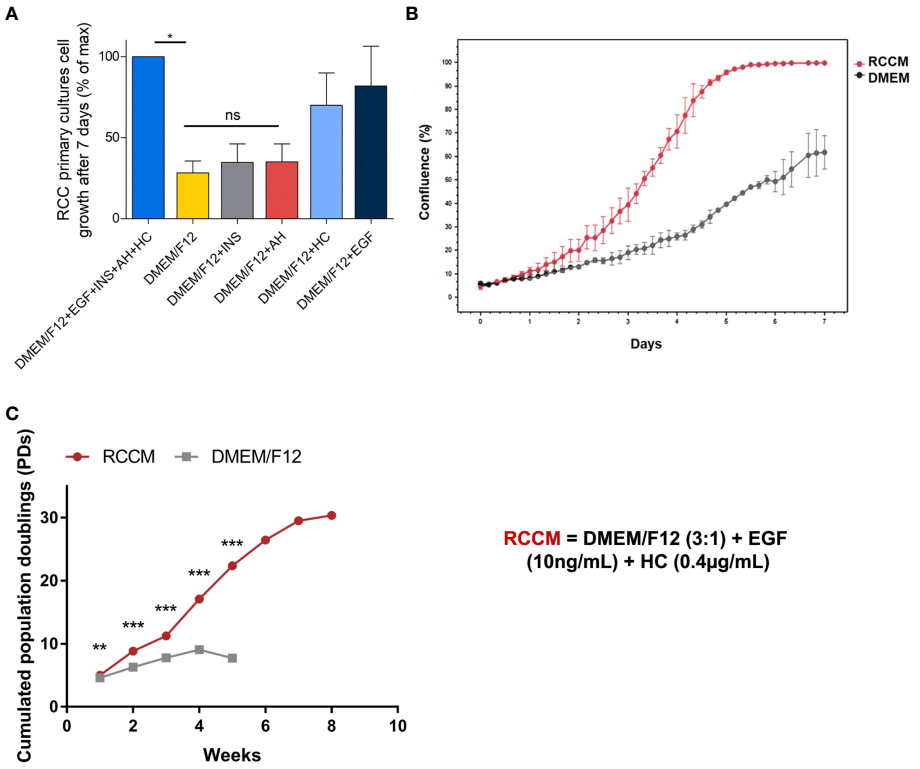

FIGURE 1 | Optimization of RCC cell growth with cytokines. Dissociated cells from ccRCC tumors from 3 patients were amplified in culture media containing the indicated cytokines. EGF: Epithelial Growth Factor, INS: insulin, AH: adenin, HC: hydrocortisone. RCCM: medium supplemented with EGF and HC. **(A)** 7-day proliferation index of ccRCC cells from 3 patients in media supplemented with the indicated cytokines. Maximum proliferation was obtained with the 4 cytokines added to the medium and constituted the 100% mark. All other proliferation results were indexed on this mark. **(B)** RCCM permits faster growth. Confluence % obtained with of primary ccRCC cells over 7 days in RCCM, compared with DMEM/F12 medium alone for one representative patient Confluence % was measured every 4 hours with the Incucyte S2 system and raw values are plotted. **(C)** RCCM permits long-term growth. Long-term FDTR ccRCC cell growth from one selected patient in RCCM or in DMEM/F12 medium alone were compared over an 8-week period. The numbers of population doublings (PDs) attained by cultures were calculated and are plotted. *p < 0.05; **p < 0.01; ***p < 0.001; ns, non-significant.

patient#97 formed more spherical and compact spheroids in 72 hours by the liquid overlay than by the hanging drop method.

Thus, in our hands, when working with freshly dissociated cells and primary lines, the liquid overlay method was more reliable and more user-friendly. The spheroids formed by this technique also seemed more regular in shape as described before (30).

Selection of a Homogeneous Spheroid Population, Based on Automatic Analysis of Morphological Criteria

As a simple 3D model, spheroids are expected to provide an intermediate level between *in vivo* models and cells grown in monolayers. Thus, many authors see them as a "semi high-throughput model" enabling the collection of biologically relevant results with substantial statistical force and relative ease of use. As such, there is a need to optimize the production and analysis of spheroids to reach even higher-throughput and more relevant results. Morphological variation among the tested population of spheroids is known to be a source of inconstancy in the obtained results. This is particularly important in patient-derived spheroids, often subjected to more variability in shape and size than spheroids from established cell lines. Two solutions are possible to mitigate the variations due to spheroid heterogeneity: conducting experiments on a population large enough to reach significant statistical power, or limiting the population heterogeneity itself. For the latter, our approach consists in selecting a homogeneous population, based on morphological criteria. It has been designed to be simple and fast and requires no specific material or software.

To monitor spheroid heterogeneity, 10,000 cell RCC7 spheroids (N=70) were formed with the hanging drop technique, and imaged by simple brightfield every day for 4 days starting on day 4 after cell seeding. The obtained images were automatically analyzed with a recorded Fiji macro (see **Supplementary Data Sheet 2**) calculating the Area of the spheroid along with three shape descriptors: Circularity, Roundness and Solidity. Circularity indicates the degree of similarity to a perfect circle, a value of 1 indicating a perfect circle. Solidity describes the extent to which a shape is convex or concave, a value of 1 indicating a completely convex shape. Roundness is somewhat similar to Circularity but less sensitive to

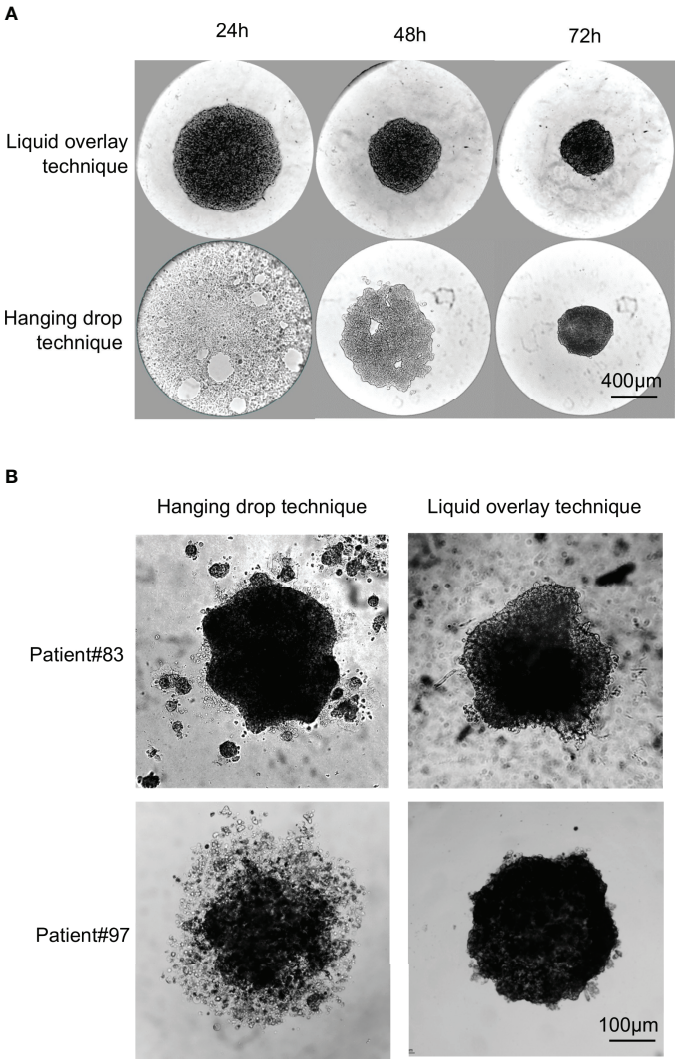

FIGURE 2 | Comparison of spheroid formation from established long-term cell lines and primary lines using the hanging drop or liquid overlay techniques. 10,000 cells from RCC7 cell line or from primary cultures were seeded in droplets and left hanging from the lid of a petri dish (Hanging drop technique) or in the wells of a 96-wells cell-repellent plate (Liquid overlay technique). **(A)** Representative brightfield images of RCC7 spheroid formation using the hanging drop technique or the liquid overlay technique taken every 24h for 72h post-seeding. **(B)** Representative brightfield images of spheroid formation from primary cultures after 72h of culture using the hanging drop technique or the liquid overlay technique.

irregularities along the perimeter and more sensitive to elongated shapes (31).

Figure 3A shows that the Area of the spheroids formed in this experiment decreased gradually from day 4 to day 8, indicating compaction. Several studies have used area as an indicator of the size of spheroids in terms of growth but we show here that in a model such as ours with short culture times, growth is negligible compared to compaction. Therefore, in short term experiments with little cell growth, area is to be used as an indicator of compactness and not of growth. We observed no significant variation in circularity, roundness and solidity from day 4 to day 8, (**Figures 3B–D**) indicating that these shape descriptors do not correlate with compactness. Consequently, when selecting spheroids for subsequent experiments, both area as an indicator of size/compactness and shape descriptors have to be taken into account.

To better explain the usefulness of each shape descriptors, a set of particular spheroids is shown in **Figure 3E**. First, it is worth noting that abnormal spheroids such as spheroid number 1 present poor scores in each shape descriptor and would therefore not be included in a subsequent experiment. As shown with spheroid 1 and 5, poor roundness is characteristic of elongated spheroids. Spheroids 2 and 7 show that poor solidity is linked to empty spaces or protuberances on the spheroid's side. Spheroids 2 and 3 link poor circularity to irregularities on the perimeter. In regard to spheroid selection before an experiment, eliminating spheroids 1, 2, 3, and 5 would be preferable. Indeed, spheroid number 1 is unlikely to produce reproducible results,

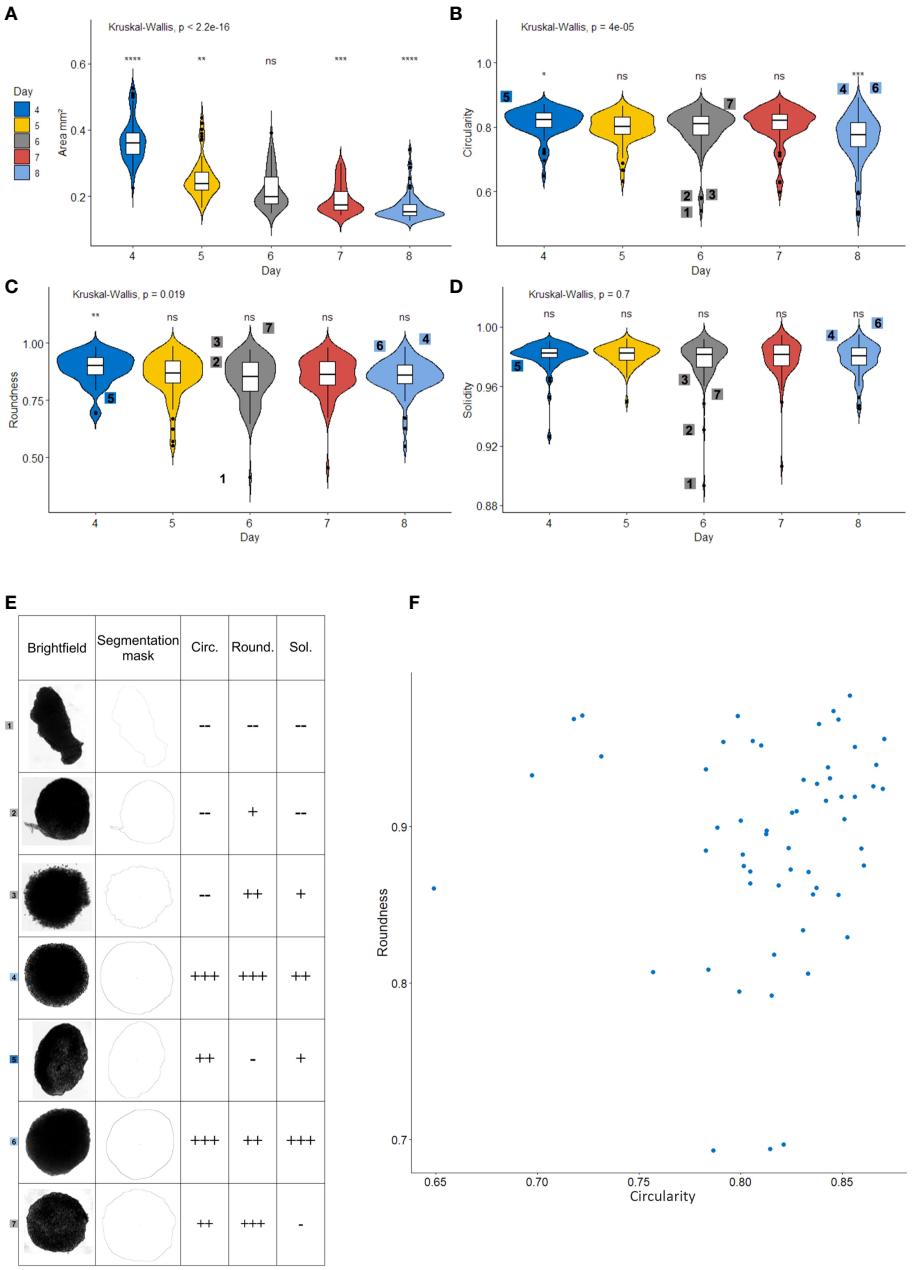

FIGURE 3 | Area, Circularity and Roundness are relevant morphological parameters for selecting a homogeneous spheroid population. Measurement of area **(A)**, circularity **(B)**, roundness **(C)** and solidity **(D)** of Renal Cell Carcinoma cell line Spheroids (N=70) with a recorded Fiji macro. Violin-plots show box-and-whisker plots (white) representing the 1st and 4th quartiles, the line in the middle denotes the median. Whiskers notify the min and max values. The violin part represents the density plot for each group. Digits on the plot relate to the spheroids shown in **(E)**, global Kruskal-Wallis test is given above the chart and pairwise Wilcoxon-Mann-Whitney tests represented above each group, comparing the group to every other (base). **(E)** Illustrative spheroids for roundness, solidity and circularity. Brightfield images, ImageJ masks and levels of measured parameters (–, -, +, ++, and +++). Each of these spheroids is identified with a digit on other graphs. **(F)** Roundness and circularity scatter-plot of the entire spheroid population. all parameters calculated with Fiji software. *p < 0.05; **p < 0.01; ***p < 0.001; ****p < 0.0001; ns, non-significant.

spheroid number 2 presents an abnormal protuberance, spheroid 3 seems to be disintegrating and the elongation on spheroid 5 would lead to an increased surface exposed to the medium during the experiment. On the other hand, it appears that solidity correlates with circularity except for spheroid number 7, which presents a poor solidity due to slightly concave parts along the perimeter. However, this spheroid does not present any particularities that would justify its elimination from the selection. Therefore, we chose not to use solidity in our selection process.

This experiment shows that even when formed from an established cell line, the population of spheroids presents a substantial level of heterogeneity in shape. The scatter plot on **Figure 3F** illustrates this heterogeneity in circularity and roundness on day 4. For subsequent experiments, spheroids should be selected from the population with higher scores for both circularity and roundness.

Altogether, these results suggest that area, circularity, and roundness are relevant quality criteria to select homogeneous spheroids for functional experiments. Priority should be given to Area, as it is an indicator of size and compactness that dictates the surface exposed to the medium as well as the ease of penetration for treatments or immune cells, and then to circularity and roundness. These criteria are of interest mostly when when the number of spheroids for each condition of an experiment is limited by technical issues. Otherwise, increasing the number of spheroids included in the analysis may also be an option.

Immune Infiltration of RCC Spheroids

The obtained tumor spheroids offer a simple 3D model suitable for many cancer studies. When formed from established cell lines, they contain only cancer cells, making them suitable for studies on cancer cells themselves, such as response to chemical treatments. Heterotypic tumor spheroids such as those obtained from primary cultures or directly after tumor dissociation contain not only a more heterogeneous population of cancer cells, but may also include other cells, such as stromal cells. This makes them suitable for studies involving interactions between cancer cells and other elements of the tumor mass. However, for studies involving interactions between cancer cells and an immune component, immune cells must be introduced and infiltrate the spheroids. These cells can be allogeneic or autologous Peripheral Blood Mononuclear Cells (PBMCs) or even the very Tumor Infiltrating Lymphocytes (TILs) that were extracted from the tumor that formed the spheroid. Thus, we will describe one method to infiltrate spheroids with allogeneic PBMCs and we will illustrate the use of such infiltrated spheroids in the context of checkpoint blockade with therapeutic anti-PD-1 antibodies.

In order for PBMCs lymphocytes to significantly infiltrate spheroids, activation is necessary. This activation can be T-Cell Receptor (TCR)-dependent, using anti-CD3 (OKT3) for instance, or TCR-independent, with IL-15 for example. TCR-dependent activation can be used when TCR function is not required in downstream experiments, and to ensure activation of T cells only. Alternatively, for downstream experiments in which blocking the TCR might be an issue, cytokine activation is preferable, even though cells other than T cells might also be activated by this method, such as Natural Killer (NK) cells. In the experiments presented here, PBMCs were activated for 48 hours prior to the experiment, with either 30 U/mL IL-15 or 100 ng/mL OKT3. Non-activated PBMCs and spheroids cultured alone were used as controls. At the start of the experiment, 30,000 PBMC, activated or not were added to individual spheroids formed with the RCC7 cell line by the liquid overlay method as described above. After 24 hours of coculture, spheroids were thoroughly washed to remove non-infiltrated PBMCs remaining in the supernatant and the spheroids were dissociated using Accutase (see *Materials and Methods*). Infiltration was then measured by flow cytometry, using CD45 positivity as a marker of infiltrating leukocytes. The results were analyzed to show the percentage of CD45+ cells within the total cells obtained from the dissociation.

Figure 4A shows representative examples of the results obtained when non-activated and IL-15-activated PBMCs were used to infiltrate spheroids. As can be seen, even though some non-activated PBMCs could infiltrate the spheroids, activation yielded a much more significant infiltration.

Figure 4B shows the extent of the infiltration obtained from one representative experiment out of five performed for this report, with all conditions done in quadruplicate. In non-activated conditions, infiltrated PBMCs represented only 5.52% ± 1.33 of the overall population of cells obtained after spheroid dissociation. By contrast, OKT3-activated and IL-15-activated PBMCs represented respectively 22.8% ± 4.84 and 26.2% ± 5.2 of cells obtained after spheroid dissociation

Both OKT3 and IL-15 can be used to activate PBMCs and induce spheroid activation. The choice between the two methods depends on the downstream experiment: if TCR implication is not an issue, either can be used, whereas if TCR interaction is required, IL-15 would be preferable. In the next set of experiments, since TCR interaction with tumor HLA is required, IL-15 activation was used.

Monocytes can also infiltrate spheroids:after isolation from donor's PBMCs, 30,000 monocyte derived cells were cocultured with 10,000-cell RCC7 formed spheroids. After 24 hours, the spheroids were washed and dissociated as described above. The obtained cells were characterized by flow cytometry, looking for CD14 expressing cells and HLA-DR expressing cells to assess myeloid monocyte derived antigen presenting cells infiltration.

Figure 5 shows the proportion of CD14+/HLA-DR+, CD14-/HLA-DR+, CD14-/HLA-DR- in controls (monocyte-derived cells alone or dissociated non-infiltrated spheroids alone) and in dissociated infiltrated spheroids.

As shown in **Figure 5**, spheroids cultured alone contained no CD14 or HLA-DR expressing cells while monocyte-derived cells contained 96% of HLA-DR positive cells. By contrast, dissociated spheroids that had been cocultured with monocyte-derived cells contained 41% HLA-DR+ cells. Interestingly, while the original HLA-DR positive monocyte-derived cells contained roughly equal amounts of CD14- and CD14+ cells, spheroid-infiltrating monocyte derived cells contained 2/3 CD14+ cells and 1/3 CD14- cells.

Thus spheroid can be infiltrated by several cell types according to the specific needs of a subject of study and can therefore constitute an immunocompetent *in-vitro* model for studies in immuno-oncology.

Live Imaging Spheroid Killing Assay for the Assessment of Immune Checkpoint Blockade Efficacy

One of the possible and most explored applications of spheroids is to serve as a preclinical model for drug efficacy assessment. Thus, as an example of an application for an infiltrated spheroid

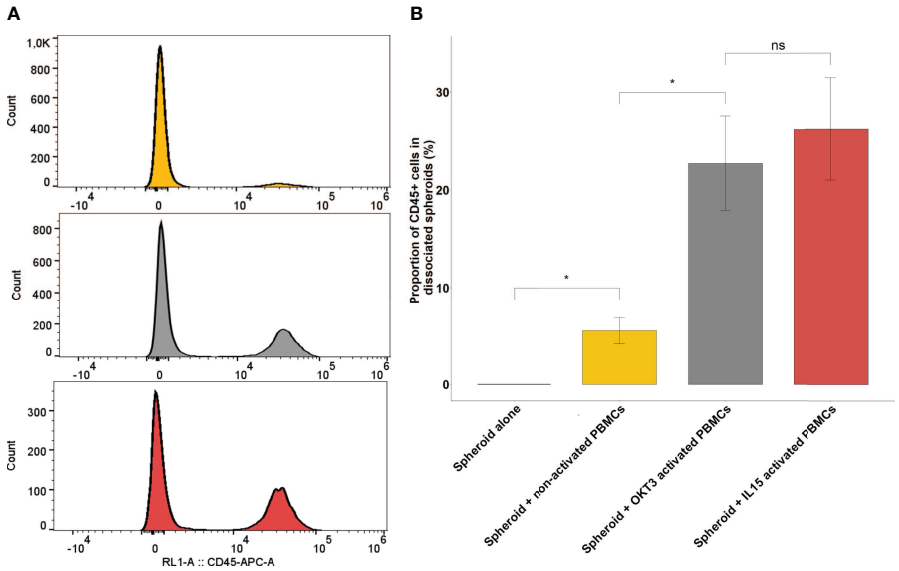

FIGURE 4 | Immune infiltration following co-culture between RCC spheroids and activated or non-activated PBMCs. **(A)** Representative CD45 flow cytometry histograms of 3 pooled, washed and dissociated spheroids after 24h of culture, alone, in co-culture with non-activated PBMCs or with PBMCs activated with IL-15. **(B)** Barplots representing the percentage of CD45 positive cells found by flow cytometry in the dissociated spheroid after co-culture in the indicated conditions of activation. Results for a representative experiment out of 3, performed in quadruplicates. Error bars represent standard error, statistical significance ($p<0.05$) of the Student test is notified by a star. *$p < 0.05$; ns, non-significant.

model, we chose to implement a live spheroid immune killing assay. In this type of assay, immune cells are expected to cause spheroid destruction by exerting cytotoxicity. In the experiments presented here, spheroids are generated with PD-L1-positive RCC7 cells, effector cells are IL-15-activated allogeneic PBMCs, and treatments are 2 therapeutic anti-PD-1 antibodies: nivolumab and pembrolizumab. Both these checkpoint inhibitors are currently used as a treatment for metastatic ccRCC. In this experiment, it is expected that PD-L1 expressed by spheroid cells will interact with PD-1 expressed by activated cytotoxic cells, reducing their killing capabilities, and that nivolumab and pembrolizumab anti-PD-1 antibodies will block PD-1-PD-L1 interaction and increase tumor cell destruction.

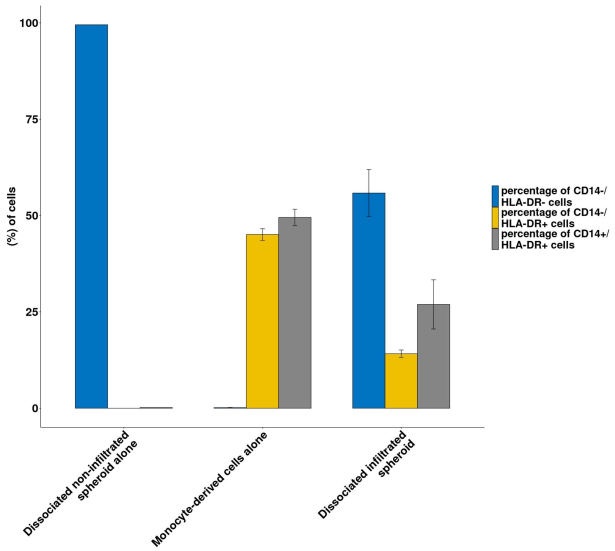

FIGURE 5 | Immune infiltration following co-culture between RCC spheroids and monocyte-derived cells. Histograms representing the proportion of CD14-/HLA-DR- cells (spheroid cells) or CD14+/HLA-DR$^+$ and CD14$^-$/HLA-DR$^+$ from the monocyte-derived population in the dissociated spheroid cultured alone or monocyte derived cells cultured alone or dissociated infiltrated spheroids are shown Results from a representative experiment; N=3; all conditions done in triplicate. Means ± SE are represented.

All procedures for the experiment are detailed in the Materials and Methods section. Briefly, after 48 hours of IL-15 activation, treatments (10 µg/mL of either nivolumab or pembrolizumab) were added to the wells containing the PBMCs, leaving non-treated wells as control. In order to ensure spheroid killing, we used 100,000 PBMCs per well (10:1 effector:target ratio). They were then added to the wells of a 96-well cell-repellent plate containing 2-day old spheroids composed of 10,000 RCC7 cells. Wells with either no PBMCs, or non-activated PBMCs served as control for each condition. Finally, 5 µg/mL of Propidium Iodide were added to track cell death. Using the Incucyte S2 system, each well was imaged for brightfield and red fluorescence every 2 hours for five days.

Brightfield + red fluorescence live images presented in **Figure 6A** show two key parameters: spheroid disruption and tumor cell death, on non-treated spheroids. Spheroids cocultured with IL-15-activated PBMCs started disaggregating after 24h compared to control spheroids cultured alone.

For immune-cell induced tumor cell death measurement using PI fluorescence, red-fluorescence was adjusted so that background from control spheroids was null. After fluorescence background removal, increasing levels of PI red fluorescence were observed in cocultured spheroids, indicating cell death throughout the experiment (**Figure 6A**), implying that activated PBMCs lead to spheroid disruption and killing.

Figure 6B presents the mean Propidium Iodide red-fluorescence of the spheroids calculated by the Incucyte system during the five-day experiment. An increase in red fluorescence means an increase in cell death. As shown, coculturing spheroids with allogeneic PBMCs, activated or not, lead to increased levels of red fluorescence indicating increased spheroid cell death. However, regardless of treatment, this effect remained limited with non-activated PBMCs: fluorescence started increasing after 50 hours and reached 2-6 Red Calibrated Unit (RCU) at day 5, whereas with IL-15-activated PBMCs, fluorescence increased sharply to plateau in 16-20 hours. Significantly higher levels of cell death were reached when treating PBMCs with nivolumab or pembrolizumab. The largest difference was measured after 36 hours when red fluorescence reached 23 RCU in presence of nivolumab or pembrolizumab, representing a 40% increase compared to non-treated controls (16 RCU). No differences between the effects of nivolumab or pembrolizumab were observed.

In this type of experiment, the most favorable timeframe for observing the effect of the immunotherapeutic compounds was therefore between 16 and 84 hours. Videos for each condition can be found in **Supplementary Data**.

DISCUSSION

It is now well-established that the spheroid model can provide relevant insight on cancer biology while remaining relatively simple and straightforward. Its ability to recapitulate key tumor characteristics has been extensively studied in several cancers. A

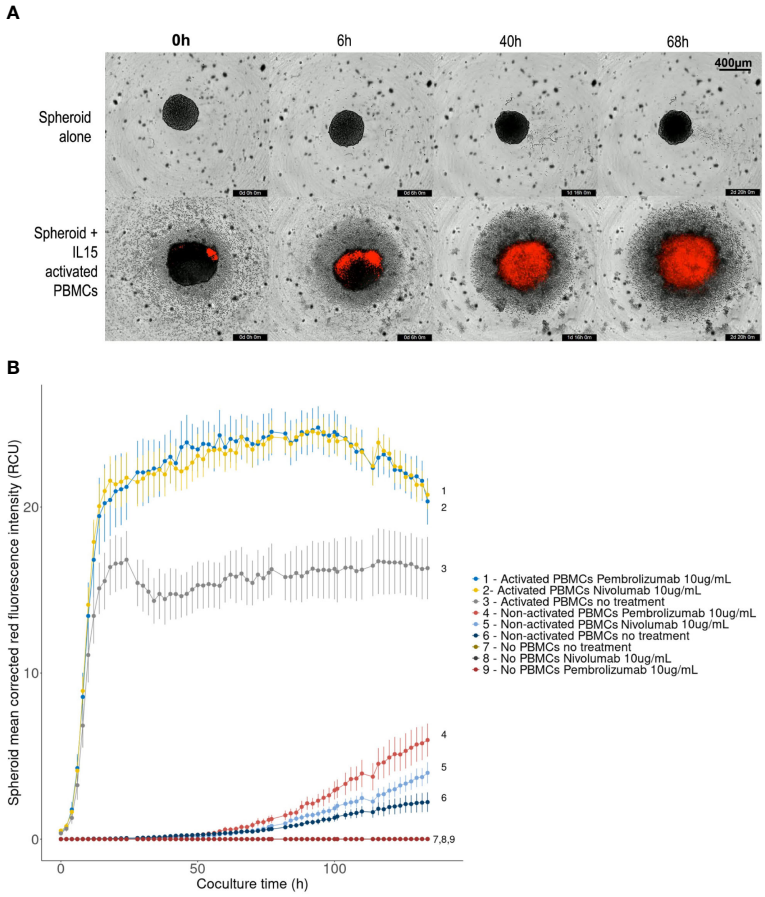

FIGURE 6 | Effect of PD-1 blockade on spheroid destruction by IL-15 activated allogeneic PBMCs. 10,000-cell RCC7 spheroids were cultured alone or co-cultured with activated or non-activated PBMCs for 5 days, in the presence or absence of nivolumab or pembrolizumab. The wells were imaged every 2 hours with the Incucyte S2 system. Propidium Iodide staining was used to track cell death. **(A)** Representative 4× brightfield images with superimposed red fluorescence (Propidium Iodide), background level was set by fixing control spheroid red fluorescence to zero. **(B)** Linechart of spheroid red fluorescence measurement (Red Calibrated Unit) over time as calculated by the Incucyte S2 system in the given conditions. Means of 10-plicates, representative results out of 3 experiments. Error bars represent the Standard Error of the means, digits correspond to conditions.

particularly relevant feature is its ability to conserve a certain amount of complexity from the original tumor. ccRCC has long been known as a cancer of high heterogeneity, both in terms of tumor cell clonality and TME characteristics and there is increasing evidence of the role of tumor heterogeneity in treatment resistance and disease progression (32–34). ccRCC could therefore benefit from the use of the spheroid model. In particular, patient-derived spheroids as described in this work retain a fraction of the original tumor complexity, and allow culturing these heterogeneous cells in close contact, offering possibilities for enhanced cell-to-cell interaction as compared to 2D models.

While the spheroid model appears to take an increasingly important place in cancer research, there are very few occurrences of its application to ccRCC. Remarkably, Rausch et al. described a model of infiltrated ccRCC spheroid composed of controlled proportions of cancer cells, fibroblasts, endothelial cells and immune cells subsets, all from established cell lines (13). In light of this work, we were able to confirm the infiltration of different subsets of immune cells in ccRCC spheroids and to complete the methods used for the formation of spheroids with patient-derived spheroids.

The aim of this study was to present standardized methods to constitute a simple and adaptable toolbox to establish ccRCC spheroid models. It is addressed to researchers wishing to initiate studies relying on the spheroid model. We introduced methods and a new medium for cultivating primary ccRCC cells and forming spheroids, from both established cell lines and primary ccRCC cell cultures. We proposed a method to improve the reliability of the data obtained in this model by selecting the spheroids for subsequent experiments based on morphological criteria. We showed that the spheroids can be infiltrated by activated immune cells, resulting in a 3D model suitable for cancer immunology studies. As an example, we implemented a live-imaging spheroid killing assay showing the effect of PD-1 blockade on spheroid destruction by activated allogeneic immune cells.

This method is highly adaptable and changes can be made if necessary: the size of the spheroids can easily be adapted by changing the number of cells used to form the spheroid and other elements can be mixed in the cell suspension before the formation of the spheroid as it has been done before with stromal or endothelial element (30).

Because they are harder to handle than 2D models, spheroids can only be used in small numbers during studies. Thus, reproducibility and representativity and therefore parallelization can be an issue (12, 35). As shown, morphological criteria measured on routinely taken images can help limit this heterogeneity by selecting a homogeneous population of spheroids before subsequent experiments and thus enhance the relevance of the data obtained. Here, a Fiji macro permitted fast and semi-automatized spheroid quality analysis.

The methods presented here allow for the formation of heterotypic spheroids. However, it remains to be seen if the spheroids generated following these methods are representative of the original tumor complexity. Indeed, there are several key steps that could lead to a loss in representativity. First, complete tumor dissociation leads to the loss of original structure. A different approach to forming spheroids that partially retain this structural information has been carried out before by Jenkins et al. on different cancer types (36). These "Patient-Derived Organotypic Tumor Spheroids" were formed by partial tumor digestion until the desired size is reached. While this approach retains a form of the original tumor structure, it raises reproducibility issues as each formed spheroid contains specific elements not shared among all other spheroids, therefore hindering parallelization. Secondly, to reach maximum representativity, it would be preferable to avoid any 2D culture step and form spheroids directly after tumor dissociation to retain a maximum of tumor elements. Indeed, it is very likely that the amplification step carried out in plastic flasks leads to the selection of certain tumor elements, based on their capacity to adhere to plastic. Complementary studies on the representativity of patient-derived ccRCC spheroids such as transcriptomic studies would provide precious data on the level of complexity recapitulated by this model, along with their resemblance with the original tumor. This is critically important if the final aim is to test therapeutic molecules in the context of personalized medicine, particularly in the case of checkpoint inhibitors as checkpoint molecule expression may vary during cultures. To conclude, forming patient-derived ccRCC spheroids can be done using simple techniques. Further studies to assess the preservation of tumor complexity and improve the assessment of cell interactions within this model are ongoing to validate its relevance, both as a translational research tool but also as a candidate theranostics assay.

DATA AVAILABILITY STATEMENT

The raw data supporting the conclusions of this article will be made available by the authors, without undue reservation.

AUTHOR CONTRIBUTIONS

LL conceived and designed the analysis, collected the data, performed the analysis and wrote the manuscript. GM conceived, designed the analysis, collected the data, performed the analysis and wrote the manuscript. RL collected the data and performed the analysis. CD wrote the manuscript. FB provided tumor samples. MD provided tumor samples, AM-L provided tumor samples. FD provided tumor samples. EC conceived and designed the analysis and acknowledged the final version. NR-F conceived and designed the analysis, revised and acknowledged the final version. JL conceived and designed the analysis, wrote the manuscript, revised and acknowledged the final version. All authors contributed to the article and approved the submitted version.

FUNDING

This study was funded by CEA. LL is recipient of a PhD grant through the CEA-focus program "organoids-on-a-chip". GM was a recipient of a CEA PhD grant.

ACKNOWLEDGMENTS

We would like to thank the Saint-Louis Research Institute Core Facility and particularly Niclas Setterblad for his precious advice and kind help regarding imaging experiments.

SUPPLEMENTARY MATERIAL

The Supplementary Material for this article can be found online at: https://www.frontiersin.org/articles/10.3389/fonc.2022.898732/full#supplementary-material

REFERENCES

1. Brodaczewska KK, Szczylik C, Fiedorowicz M, Porta C, Czarnecka AM. Choosing the Right Cell Line for Renal Cell Cancer Research. *Mol Cancer.* (2016) 15(1):83. doi: 10.1186/s12943-016-0565-8
2. Jensen C, Teng Y. Is It Time to Start Transitioning From 2D to 3D Cell Culture? *Front Mol Biosci* (2020) 7:33. doi: 10.3389/fmolb.2020.00033
3. Rouas-Freiss N, Bruel S, Menier C, Marcou C, Moreau P, Carosella ED. Switch of HLA-G Alternative Splicing in a Melanoma Cell Line Causes Loss of HLA-G1 Expression and Sensitivity to NK Lysis. *Int J Cancer* (2005) 117 (1):114–22. doi: 10.1002/ijc.21151
4. Bougherara H, Mansuet-Lupo A, Alifano M, Ngô C, Damotte D, Le Frère-Belda MA, et al. Real-Time Imaging of Resident T Cells in Human Lung and Ovarian Carcinomas Reveals How Different Tumor Microenvironments Control T Lymphocyte Migration. *Front Immunol* (2015) 6:500. doi: 10.3389/fimmu.2015.00500
5. Roelants C, Pillet C, Franquet Q, Sarrazin C, Peilleron N, Giacosa S, et al. *Ex-Vivo* Treatment of Tumor Tissue Slices as a Predictive Preclinical Method to Evaluate Targeted Therapies for Patients With Renal Carcinoma. *Cancers. janv* (2020) 12(1):232. doi: 10.3390/cancers12010232
6. de Hoogt R, Estrada MF, Vidic S, Davies EJ, Osswald A, Barbier M, et al. Protocols and Characterization Data for 2D, 3D, and Slice-Based Tumor Models From the PREDECT Project. *Sci Data.* (2017) 4(1):170170. doi: 10.1038/sdata.2017.170
7. Koerfer J, Kallendrusch S, Merz F, Wittekind C, Kubick C, Kassahun WT, et al. Organotypic Slice Cultures of Human Gastric and Esophagogastric Junction Cancer. *Cancer Med* (2016) 5(7):1444–53. doi: 10.1002/cam4.720
8. Misra S, Moro CF, Del Chiaro M, Pouso S, Sebestyén A, Löhr M, et al. *Ex Vivo* Organotypic Culture System of Precision-Cut Slices of Human Pancreatic Ductal Adenocarcinoma. *Sci Rep* (2019) 9(1):2133. doi: 10.1038/s41598-019-38603-w
9. Donnadieu E, Michel Y, Hansmann ML. Live Imaging of Resident T-Cell Migration in Human Lymphoid Tissue Slices Using Confocal Microscopy. In: NK Verma, editor. *T-Cell Motility: Methods and Protocols*. New York, NY: Springer (2019). p. 75–82. doi: 10.1007/978-1-4939-9036-8_10
10. Rouas-Freiss N, LeMaoult J, Verine J, Tronik-Le Roux D, Culine S, Hennequin C, et al. Intratumor Heterogeneity of Immune Checkpoints in Primary Renal Cell Cancer: Focus on HLA-G/Ilt2/Ilt4. *Oncoimmunology* (2017) 6(9):e1342023. doi: 10.1080/2162402X.2017.1342023
11. Costa EC, Moreira AF, de Melo-Diogo D, Gaspar VM, Carvalho MP, Correia IJ. 3D Tumor Spheroids: An Overview on the Tools and Techniques Used for Their Analysis. *Biotechnol Adv* (2016) 34(8):1427–41. doi: 10.1016/j.biotechadv.2016.11.002
12. Vinci M, Gowan S, Boxall F, Patterson L, Zimmermann M, Court W, et al. Advances in Establishment and Analysis of Three-Dimensional Tumor Spheroid-Based Functional Assays for Target Validation and Drug Evaluation. *BMC Biol* (2012) 10(1):29. doi: 10.1186/1741-7007-10-29
13. Rausch M, Blanc L, De Souza Silva O, Dormond O, Griffioen AW, Nowak-Sliwinska P. Characterization of Renal Cell Carcinoma Heterotypic 3d Co-Cultures With Immune Cell Subsets. *Cancers* (2021) 13(11):2551. doi: 10.3390/cancers13112551
14. Zboralski D, Hoehlig K, Eulberg D, Frömming A, Vater A. Increasing Tumor-Infiltrating T Cells Through Inhibition of CXCL12 With NOX-A12 Synergizes With PD-1 Blockade. *Cancer Immunol Res* (2017) 5(11):950–6. doi: 10.1158/2326-6066.CIR-16-0303
15. Courau T, Bonnereau J, Chicoteau J, Bottois H, Remark R, Assante Miranda L, et al. Cocultures of Human Colorectal Tumor Spheroids With Immune Cells Reveal the Therapeutic Potential of MICA/B and NKG2A Targeting for Cancer Treatment. *J Immunother Cancer* (2019) 7:74. doi: 10.1186/s40425-019-0553-9
16. Herter S, Morra L, Schlenker R, Sulcova J, Fahrni L, Waldhauer I, et al. A Novel Three-Dimensional Heterotypic Spheroid Model for the Assessment of the Activity of Cancer Immunotherapy Agents. *Cancer Immunol Immunother.* (2017) 66(1):129–40. doi: 10.1007/s00262-016-1927-1
17. Aung A, Kumar V, Theprungsirikul J, Davey SK, Varghese S. An Engineered Tumor-On-a-Chip Device With Breast Cancer–Immune Cell Interactions for Assessing T-Cell Recruitment. *Cancer Res* (2020) 80(2):263–75. doi: 10.1158/0008-5472.CAN-19-0342
18. Fortunato O, Belisario DC, Compagno M, Giovinazzo F, Bracci C, Pastorino U, et al. CXCR4 Inhibition Counteracts Immunosuppressive Properties of Metastatic NSCLC Stem Cells. *Front Immunol* (2020) 11:2168/full. doi: 10.3389/fimmu.2020.02168/full
19. Evans L, Milward K, Attanoos R, Clayton A, Errington R, Tabi Z. Macrophage Plasticity and Function in the Lung Tumour Microenvironment Revealed in 3D Heterotypic Spheroid and Explant Models. *Biomedicines* (2021) 9(3):302. doi: 10.3390/biomedicines9030302
20. Liello RD, Ciaramella V, Barra G, Venditti M, Corte CMD, Papaccio F, et al. Ex Vivo Lung Cancer Spheroids Resemble Treatment Response of a Patient With NSCLC to Chemotherapy and Immunotherapy: Case Report and Translational Study. *ESMO Open* (2019) 4(4):e000536. doi: 10.1136/esmoopen-2019-000536
21. Cherradi S, Almeida N, Saviano A, Durand S, Felli E, Pessaux P, et al. A Robust and Simple Patient-Derived Multicellular Spheroid Model Enables Liver Cancer Precision Drug Screening. (2021). doi: 10.21203/rs.3.rs-183605/v1
22. Wittnebel S, Jalil A, Thiery J, DaRocha S, Viey E, Escudier B, et al. The Sensitivity of Renal Cell Carcinoma Cells to Interferon Alpha Correlates With P53-Induction and Involves Bax. *Eur Cytokine Netw* (2005) 16(2):123–7.
23. Schindelin J, Arganda-Carreras I, Frise E, Kaynig V, Longair M, Pietzsch T, et al. Fiji: An Open-Source Platform for Biological-Image Analysis. *Nat Methods* (2012) 9(7):676–82. doi: 10.1038/nmeth.2019
24. Grässer U, Bubel M, Sossong D, Oberringer M, Pohlemann T, Metzger W. Dissociation of Mono- and Co-Culture Spheroids Into Single Cells for Subsequent Flow Cytometric Analysis. *Ann Anat - Anat Anz* (2018) 216:1–8. doi: 10.1016/j.aanat.2017.10.002
25. Loudon K. Human Kidney / Tumour Tissue Disaggregation for Single Cell RNA Sequencing (10x Genomics Platform). (2018). doi: 10.17504/protocols.io.mjyc4pw
26. Dolmans MM, Michaux N, Camboni A, Martinez-Madrid B, Van Langendonckt A, Annarita Nottola S, et al. Evaluation of Liberase, a Purified Enzyme Blend, for the Isolation of Human Primordial and Primary Ovarian Follicles. *Hum Reprod* (2006) 21(2):413–20. doi: 10.1093/humrep/dei320
27. Linetsky E, Bottino R, Lehmann R, Alejandro R, Inverardi L, Ricordi C. Improved Human Islet Isolation Using a New Enzyme Blend, Liberase. *Diabetes* (1997) 46(7):1120–3. doi: 10.2337/diabetes.46.7.1120
28. Olack BJ, Swanson CJ, Howard TK, Mohanakumar T. Improved Method for the Isolation and Purification of Human Islets of Langerhans Using Liberase^{TM} Enzyme Blend. *Hum Immunol* (1999) 60(12):1303–9. doi: 10.1016/S0198-8859(99)00118-4
29. Mestrallet G, Auvré F, Schenowitz C, Carosella ED, LeMaoult J, Martin MT, et al. Human Keratinocytes Inhibit CD4+ T-Cell Proliferation Through TGFB1 Secretion and Surface Expression of HLA-G1 and PD-L1 Immune Checkpoints. *Cells* (2021) 10:1438. doi: 10.3390/cells10061438
30. Metzger W, Sossong D, Bächle A, Pütz N, Wennemuth G, Pohlemann T, et al. The Liquid Overlay Technique Is the Key to Formation of Co-Culture Spheroids Consisting of Primary Osteoblasts, Fibroblasts and Endothelial Cells. *Cytotherapy* (2011) 13(8):1000–12. doi: 10.3109/14653249.2011.583233
31. Zdilla MJ, Hatfield SA, McLean KA, Cyrus LM, Laslo JM, Lambert HW. Circularity, Solidity, Axes of a Best Fit Ellipse, Aspect Ratio, and Roundness of the Foramen Ovale: A Morphometric Analysis With Neurosurgical

Considerations. *J Craniofac Surg* (2016) 27(1):222–8. doi: 10.1097/SCS.0000000000002285
32. Mier JW. The Tumor Microenvironment in Renal Cell Cancer. *Curr Opin Oncol* (2019) 31(3):194–9. doi: 10.1097/CCO.0000000000000512
33. Berlato C, Khan MN, Schioppa T, Thompson R, Maniati E, Montfort A, et al. A CCR4 Antagonist Reverses the Tumor-Promoting Microenvironment of Renal Cancer. *J Clin Invest.* (2017) 127(3):801–13. doi: 10.1172/JCI82976
34. Hajiran A, Chakiryan N, Aydin AM, Zemp L, Nguyen J, Laborde JM, et al. Reconnaissance of Tumor Immune Microenvironment Spatial Heterogeneity in Metastatic Renal Cell Carcinoma and Correlation With Immunotherapy Response. *Clin Exp Immunol* (2021) 204(1):96–106. doi: 10.1111/cei.13567
35. Zanoni M, Piccinini F, Arienti C, Zamagni A, Santi S, Polico R, et al. 3D Tumor Spheroid Models for *In Vitro* Therapeutic Screening: A Systematic Approach to Enhance the Biological Relevance of Data Obtained. *Sci Rep* (2016) 6(1):19103. doi: 10.1038/srep19103
36. Jenkins RW, Aref AR, Lizotte PH, Ivanova E, Stinson S, Zhou CW, et al. *Ex Vivo* Profiling of PD-1 Blockade Using Organotypic Tumor Spheroids. *Cancer Discov* (2018) 8(2):196–215.

Conflict of Interest: The authors declare that the research was conducted in the absence of any commercial or financial relationships that could be construed as a potential conflict of interest.

Publisher's Note: All claims expressed in this article are solely those of the authors and do not necessarily represent those of their affiliated organizations, or those of the publisher, the editors and the reviewers. Any product that may be evaluated in this article, or claim that may be made by its manufacturer, is not guaranteed or endorsed by the publisher.

Copyright © 2022 Lugand, Mestrallet, Laboureur, Dumont, Bouhidel, Djouadou, Masson-Lecomte, Desgrandchamps, Culine, Carosella, Rouas-Freiss and LeMaoult. This is an open-access article distributed under the terms of the Creative Commons Attribution License (CC BY). The use, distribution or reproduction in other forums is permitted, provided the original author(s) and the copyright owner(s) are credited and that the original publication in this journal is cited, in accordance with accepted academic practice. No use, distribution or reproduction is permitted which does not comply with these terms.

Summary and perspectives

This first article confirmed the feasibility of generating spheroids from patient-derived ccRCC samples and demonstrated that co-culture assays could be used to monitor immune–tumor interactions in a simplified, rapid format using cell line–based systems. Two distinct co-culture configurations were explored: one optimized for the reinfiltration of TILs into pre-formed spheroids, and another designed to evaluate immune-mediated spheroid destruction.

However, generating patient-derived spheroids remained labor-intensive and required an intermediate expansion step in flasks. The subsequent objective was therefore to establish an autologous model that could be generated directly from dissociated tumor material, without prior culture. Through incremental optimization and improved workflow efficiency, we increased the spheroid formation success rate to approximately 70%. To further secure this process, we now routinely include a parallel condition using growth factor–depleted Matrigel, which significantly enhances spheroid aggregation in less favorable samples.

Under our experimental conditions, we initially aimed to maintain the entire tumor cell suspension intact, preserving both tumor and immune components, in the hope that this "complete mixture" would spontaneously aggregate into spheroids. However, this approach consistently failed to produce compact and reproducible structures. Aggregation was incomplete, heterogeneous, or excessively slow, with only partial adhesion of tumor cells and widespread variability between wells. As a result, we found it necessary to separate immune cells from tumor cells prior to spheroid formation.

This separation step, while enabling robust and uniform spheroid generation, created a new challenge: maintaining TIL viability and promoting their reinfiltration into spheroids at a later stage. To preserve TIL viability and function, we introduced an activation step using IL-15, which supports T cell survival and proliferation without direct TCR engagement. While this approach inevitably introduces some degree of activation bias, it provided a practical compromise at this stage of model development. Future refinements will aim to reduce or eliminate this requirement, particularly in autologous configurations.

Building on these methodological advances, the next study aimed to validate the Patient-Derived Spheroid formed directly after dissociation and reinfiltrated with its own TILs by assessing its cellular composition and transcriptional fidelity relative to the original tumor. This work, conducted in collaboration with Liangwei Lin and Christophe Battail from the Biosciences and Bioengineering for Health laboratory (BGE), employed BRB-seq, a cost-effective transcriptomic method enabling the use of identical RNA extraction protocols for both tumor tissue and spheroids. This standardized workflow facilitated direct comparisons and was successfully applied to samples from three patients.

Chapter 2: Transcriptomic evaluation of immune-infiltrated patient-derived tumor spheroids as preclinical models in renal cell carcinoma

Liangwei Yin, Leonard Lugand, Jules Russick, Joel Lemaoult, Christophe Battail

Article draft to be submitted in November 2025

In this work, RNA samples were collected at each key step of model generation, enabling the characterization of how cellular composition and transcriptional features changed during tumor dissociation, spheroid formation, and immune reinfiltration. We specifically examined the potential biases introduced by tumor dissociation, the impact of spheroid assembly on tumor and microenvironmental components and the nature and phenotype of immune populations that successfully reintegrated the model.

The initial objective of this study was to accurately deconvolute the cellular composition of patient-derived tumor spheroids and to evaluate how it evolved throughout model establishment. However, it quickly became apparent that existing reference datasets commonly used for transcriptomic deconvolution were not suitable for our spheroid samples. Their composition and gene expression profiles differed substantially from conventional bulk tumor or single-cell references, particularly at intermediate stages such as post-dissociation and pre-reinfiltration. We therefore turned to more robust and conventional analytical strategies to assess cellular dynamics across the different experimental stages.

Finally, the resulting spheroids were compared to their matched parental tumors. Particular attention was given to the expression of key renal cancer markers, immune checkpoint molecules, and transcriptional signatures associated with immune responsiveness, in order to evaluate the representativity and functional relevance of the final model.

Transcriptomic evaluation of immune-infiltrated patient-derived tumor spheroids as preclinical models in renal cell carcinoma

Liangwei Yin[1], Léonard Lugand[2], Jules Russick[2], Joel Lemaoult[2*], Christophe Battail[1*]

[1]Université Grenoble Alpes, CEA, INSERM, UA13 BGE, CEA, Grenoble, France.
[2]Hemato-Immunology Research Department, CEA, DRF-Francois Jacob Institute, Saint-Louis Hospital, Paris, France – INSERM UMR1342, IRSL, Paris University, Paris, France.
*co-senior authors

Main contact: Christophe.BATTAIL@cea.fr

Abstract

Patient-derived tumor spheroids (PDTS) have emerged as valuable preclinical models for studying tumor biology and therapeutic responses. However, despite the development of protocols for tumor dissociation and immune cell infiltration, their fidelity in representing clear cell renal cell carcinoma (ccRCC) tumors remains poorly characterized. To address this, we established matched samples, including tumor tissue, enzymatically dissociated tumor, formed PDTS, and immune-infiltrated PDTS from three ccRCC patients, and performed bulk RNA sequencing to capture dynamic molecular changes across the experimental workflow. Our analyses revealed that tumor dissociation triggered stress-related transcriptional changes, marked by the upregulation of heat shock genes (e.g., *HSPA1A*) and the downregulation of the hypoxia pathway, while PDTS recapitulated hypoxic signaling. Immune-infiltrated PDTS retained critical immune signatures including T-effector, and exhibited an enhanced pro-inflammatory phenotype (*CXCL10*, JAK-STAT). Furthermore, predictive gene signatures and immunotherapy response scores further underscored the clinical relevance of immune-infiltrated PDTS consistent with the original tumor tissue. Collectively, these findings validate immune-infiltrated PDTS as robust, patient-specific models for personalized therapeutic exploration, offering a platform to optimize immunotherapy strategies in ccRCC.

Key words: clear cell renal cell carcinoma, patient-derived tumor spheroids, tumor infiltrating lymphocytes, transcriptomics, immunotherapy response

Introduction

Clear cell renal cell carcinoma (ccRCC) is the most common subtype of renal cancer, characterized by a highly heterogeneous tumor microenvironment that drives tumor progression and confers resistance to therapies[1,2]. While surgical treatment remains the standard for localized ccRCC, metastatic ccRCC relies on systemic therapies, including combinations of tyrosine kinase inhibitors (TKIs) and immune checkpoint blockade (ICB) or dual ICBs, as strongly recommended by the EAU guidelines[3]. Despite the advancements in immunotherapy, treatment outcomes remain suboptimal in terms of variable patient response rates between 7-59%[4–6]. This variability underscores therapeutic challenges posed by tumor heterogeneity and complex resistance mechanisms, which have hindered the identification of reliable molecular biomarkers for predicting therapeutic efficacy[7]. To address these limitations, patient derived tumor spheroids (PDTS) have emerged as promising clinical tools for precision oncology, in drug screening, treatment optimization, and outcome predictions[8–10].

Conventional preclinical models, such as two-dimensional culture of cell lines or tumor cells, inadequately replicate the physical structure and tumor microenvironment (TME)[11]. These systems often fail to preserve hypoxia gradients, immune cell activity, and tumor-immune cells interactions, which are essential for modeling immunotherapy responses. Recently, a standardized protocol of patient derived tumor spheroids (PDTS) with infiltrated lymphocytes has been established to retain the original tumor complexity, in terms of tumor cell heterogeneity and TME characteristics[12]. These immune-infiltrated PDTS (infiltrated-PDTS) offer a transformative platform to study immunotherapy mechanisms and resistance in a clinically relevant setting.

However, it remains to be further characterized for the artifacts of experimental steps in the formation of spheroids, and the representativeness of formed spheroids in the original tumor. For examples, tumor dissociation disrupted the physical structure of the original tumor[13], which may impact the composition of formed spheroids. The re-infiltration of immune cells, also raised of the question on how the spheroids mimicked TME and modeled immune evasion of the original tumor. Critically, transcriptomics profiles of experimental samples may indicate the extent of the resemblance between the original tumor and matched spheroids, and immune checkpoint genes could exhibit the fidelity of spheroids in preclinical trials of immunotherapy.

Therefore, we evaluate the fidelity and translational potential of infiltrated-PDTS as preclinical models for immunotherapy in ccRCC. Using a standardized protocol, we generated matched patient samples including primary tumor tissue, dissociated tumor cells, PDTS, and infiltrated-PDTS from three ccRCC patients. Through transcriptomic profiling, we characterized molecular and cellular changes during tumor dissociation and spheroids formation, identifying differentially expressed genes, transcription factors, and pathways. We further validated infiltrated-PDTS using tumor- and immune-specific signatures, and assessed their suitability as preclinical models by correlating organoid responses with clinical predictive biomarkers. By bridging the gap between in vitro models and clinical complexity, this work establishes infiltrated-PDTS as a robust platform for advancing personalized immunotherapy in ccRCC.

Materials and Methods

Tumor collection

Fresh tumor specimens were obtained from patients undergoing nephrectomy for localized clear cell renal cell carcinoma (ccRCC) (Saint-Louis Hospital, Paris, France) (Table 1). These specimens, classified as surgical waste, were collected with the patients' written informed consent prior to inclusion in the study. Tumors were collected by a pathologist under sterile conditions, and immediately transferred to Roswell Parks Memorial Institute (RPMI, Gibco) medium, supplemented with antibiotics on ice for transport to the laboratory within 30 min of excision.

FDTR number	ISUP grade	PD-L1 CPS	Date of birth	Sex	Tumor long axis cm	TNM	Anatomopthology commentary	Anatomopathlgy diagnosis
FDTR114	4	Positive	18276	F	5.5	pT3aNxR0	rhabdoid component	ccRCC
FDTR115	2	Positive	20760	F	5.5	pT3aNxR0	N/A	ccRCC
FDTR127	2	Positive	21592	M	4	PT1aNxR0	N/A	ccRCC

Table 1. Clinical information of patients with kidney cancer.

Tumor digestion

Tumor samples were finely minced into ~1 mm fragments and suspended in 2 mL Roswell Park Memorial Institute (RPMI) medium (Gibco, Thermo Fisher Scientific) at the bottom of a Petri dish. Three replicates of 100 ul each were aliquoted into a U-bottom 96-well plate (labeled "tumor tissue") and stored on ice until RNA extraction.

The remaining minced tumor material was digested in 6 mL Hank's Balanced Salt Solution with calcium and magnesium (HBSS; Gibco, Thermo Fisher Scientific), containing 0.125 WU/mL LiberaseTM (Sigma-Aldrich) and 100 U/mL DNase I (Sigma-Aldrich), for 35 min at 37 °C in a water bath. The digested suspension passed through a 100 µm cell strainer to remove undigested debris, and the reaction was stopped by adding 40mL cold RPMI, supplement with 10% fetal bovine serum (FBS; Sigma-Aldrich). Cells were pelleted by centrifugation at 400 ×g for 5 min. The red blood cells were lysed using RBC Lysis Buffer (BioLegend) according to the manufacturer's instructions.

Three 100 µL aliquots of the dissociated tumor cell suspension were transferred into the same 96-well plate (labeled "dissociated tumor"). For separation of tumor and immune cells, magnetic-activated cell sorting (MACS) was performed using CD45 MicroBeads (Miltenyi Biotec) according to the manufacturer's instructions.

RNA extraction for Bulk RNA Barcoding and sequencing (BRB-seq)

RNA extraction from both "tumor tissue" and "dissociated tumor" samples was performed using the Organoid DRUG-seq Kit (Alithea Genomics) according to the manufacturer's instructions. Extracted RNA was stored in the provided 96-well plate at −80 °C until shipment.

Patient-Derived Tumor Organoid (PDTS) formation

Non-immune ($CD45^-$) and immune ($CD45^+$) fractions were collected after MACS separation. $CD45^-$ cells were rinsed and resuspended in Renal Cell Carcinoma Medium (RCCM), consisting of Dulbecco's Modified Eagle Medium (DMEM; Gibco) and Ham's F-12 medium (Gibco) mixed at a 3:1 ratio (v/v), supplemented with 10% FBS, 2 mM L-glutamine (Gibco), 100 U/mL penicillin–streptomycin (Gibco), 10 ng/mL

epidermal growth factor (EGF; Sigma-Aldrich) and 0.4 µg/mL hydrocortisone (Sigma-Aldrich).

For organoid formation, 10 000 $CD45^-$ cells were seeded in 100 µL RCCM into a 96-well cell-repellent plate (Greiner Bio-One) and centrifuged at 500 ×g for 1 min to promote aggregation. In parallel, $CD45^+$ cells were activated in a 96-well U-bottom plate (30 000 cells/well) with 40 ng/mL IL-15 (PeproTech).

After 48 h, activated $CD45^+$ cells from 10 wells were transferred to 10 wells containing formed PDTS, achieving a 3:1 ratio (30 000 immune cells per 10 000 $CD45^-$ cells initially seeded). Another 10 PDTS wells were left untreated.

After 24 h, all PDTS (labeled "PDTS") and co-cultured PDTS with immune cells (labeled "infiltrated PDTS") were washed three times in PBS to remove non-infiltrated immune cells. RNA extraction was then performed in each well using the Organoid DRUG-seq Kit (Alithea Genomics) as described above. Extracted RNA was added to the Alithea sample plate and stored at −80 °C until shipment.

Library construction and sequencing

Extracted RNA from samples described above was sent to Alithea Genomics SA (Lausanne, Switzerland) for library preparation and sequencing using extraction-free, highly multiplexed, 3′-end bulk RNA barcoding and sequencing (MERCURIUSTM Organoid DRUG-seq service). Bulk RNA Barcoding and sequencing (BRB-seq) libraries were prepared using the MERCURIUSTM Organoid DRUG-seq library preparation kit for Illumina, according to the manufacturer's manual (Alithea Genomics, #10861). The constructed libraries were sequenced on an Illumina NovaSeq 6000 platform.

RNA-seq reads generated from BRB-seq were then aligned and quantified using STAR (version 2.7.9) against the GRCh38 HUMAN reference genome and quality control was performed using FastQC (version 0.11.9) and RSeQC (version 4.0.0)[14–16]. Unique molecular identifiers (UMIs) count per gene were used for downstream analyses. For sample with biological duplicates, duplicates were excluded if they had a lower number of detected genes (CPM: counts per million > 0) or a Pearson correlation coefficient below 0.4 compared to other duplicates.

Transcriptional analysis

Differential gene expression (DGE) analysis, Transcription factors (TF) analysis, and pathway activity (PA) analysis were performed and visualized using decoupleR (python version 1.8.0)[17]. Briefly, raw reads count of samples were used as the input and genes were excluded if number of their reads was less than 10. Differential expressed genes (DEGs) were inferred with the embedded Deseq2, analyzing the statistics of genes between two conditions[18]. DEGs were taken as significant genes, if fold changes of DEGs were greater than 2 with an adjusted p-value less than 0.05. TF activity inference was conducted using the univariate linear model, with the statistics results of DEGs and a CollecTRI network database (The regulations between TF and genes were included)[19]. Pathway activity was inferred using multivariate linear model on the statistics results of DEGs and a PROGENy resource (14 curated pathways, containing weights for the interaction between genes and pathways)[20].

In addition, over representation analysis (ORA) and gene set enrichment analysis (GSEA) were also performed using gene ontology (GO) terms and curated KEGG (Kyoto Encyclopedia of Genes and Genomes) pathways from Molecular Signature Database (MsigDB)[21].

Transcriptional signature estimation

For signature analysis, raw read counts were normalized to transcripts per million (TPM) and $\log_2$-transformed ($log_2\ (TPM + 1)$). Molecular signature analysis was conducted using ccRCC-specific subset signatures collected from the paper of Motzer et al (Signatures: T effector, angiogenesis, myeloid Inflammation signatures, cell cycle, stroma, the complement cascade, small nucleolar RNAs (snoRNAs), and metabolism-related pathways, including fatty acid oxidation (FAO)/AMP-activated protein kinase (AMPK) signaling, fatty acid synthesis (FAS)/ pentose phosphate, and biological oxidation pathways)[22].

Tumor signatures were also assessed by the ESTIMATE R package (Estimate of Stromal and Immune Cells in Malignant Tumor Tissues from Expression Data), including stromal, immune, tumor purity and ESTIMATE scores[23].

Tumor immune infiltration analysis

Tumor immune infiltration levels were evaluated by single sample gene set enrichment analysis (ssGSEA), with immune-related gene sets derived from a pan-cancer study[24]. Calculations were performed with GSVA using the ssGSEA algorithm[25].

Immunotherapy response prediction

To predict patients' response to immunotherapy, TIDE (Tumor Immune Dysfunction and Exclusion) scores were computed based on the gene expression profiles of our samples using the website online: http://tide.dfci.harvard.edu/[26]. Based on TIDE output, samples were classified as predicted responders or non-responders. In parallel, expression levels of canonical immune checkpoint genes were directly compared across samples.

Results

Generation of infiltrated-PDTS from ccRCC patients

To derive patient-derived tumor spheroids (PDTS), a tumor spheroids model has been established and evaluated in the context of immunotherapies[12]. We obtained tumor samples from three patients (patient ID-114, patient ID-115, and patient ID-127) (Table 1), and generated spheroids following the established protocol[12], including tumor dissociation, selection of non-immune fraction and immune fraction, PDTS formation, and PDTS with infiltrating lymphocytes (infiltrated-PDTS) (Figure 1).

Tumor tissue was firstly dissociated into fragments, homogenized, and enzymatically digested (dissociated tumor). Then, single-cell suspensions were separated into $CD45^-$ (tumor-enriched) and $CD45^+$ (immune cells) fractions using magnetic-activated cell sorting (MACS) with anti-CD45 microbeads. For PDTS generation, $CD45^-$ cells (10,000/well) were seeded in cell-repellent 96-well plates with Renal Cell Carcinoma Medium (RCCM), centrifuged (500 ×g, 1 min), and cultured for 48 hours to form spheroids Concurrently, $CD45^+$ cells were activated with 30 ng/mL IL-15 in complete RPMI for 48 hours. Activated tumor-infiltrating lymphocytes (TILs, 30, 000 cells) were co-cultured with spheroids (a ratio of tumor to immune cells: 1:3) for 24 hours, while control spheroids remained untreated. Post-co-culture, spheroids were washed, lysed, and processed for RNA extraction to profile infiltrated and non-infiltrated models.

Based on sequencing data, most of samples were kept for transcriptional analysis, except 1 PDTS in patient 114, 1 PDTS and 1 infiltrated-PDTS in patient 115 (Table S1). The filtration was based on the Pearson correlation between samples inside their category, the number of expressed genes, and principal component analysis (Figure S1-2). Using the transcriptional profile, we then evaluated the fidelity of infiltrated-PDTS as preclinical models in ccRCC for treatment response.

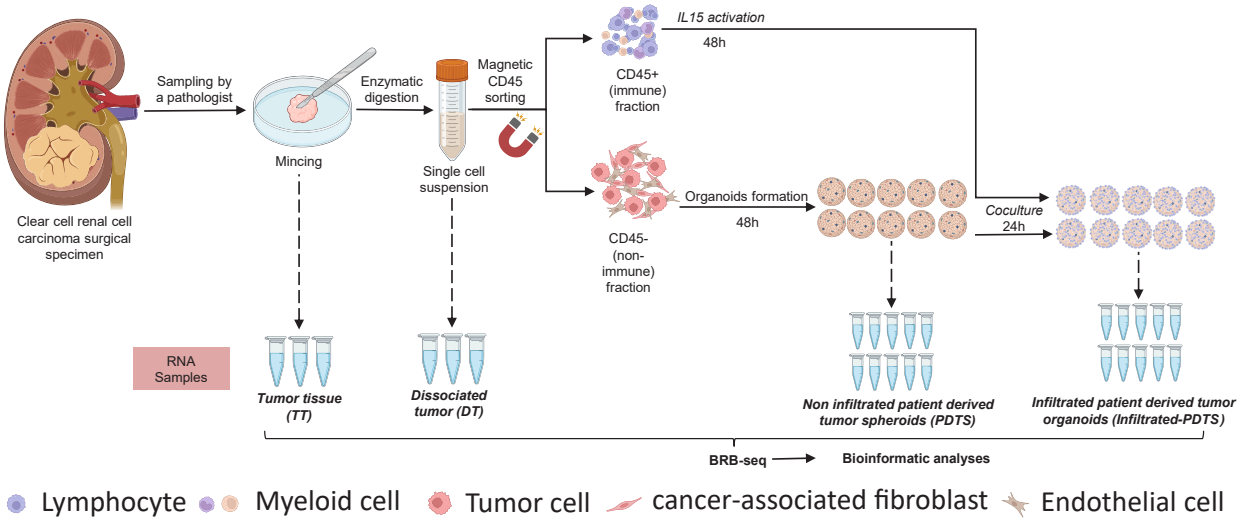

Figure1. Experimental design for the establishment of patient-derived tumor spheroids (PDTS), and patient-derived tumor spheroids with infiltrating lymphocytes (infiltrated-PDTS).

Molecular characterization of tumor dissociation and PDTS formation

To explore how tumor dissociation and cell culture influence PDTS formation, we set out to investigate differences in gene expression, transcription factors (TFs), and cancer pathways. Differential gene expression (DGE) analyses were performed for two

comparisons: tumor tissue versus dissociated tumor (effect of enzymatic dissociation), and dissociated tumor versus PDTS (effect of PDTS formation). In our representative case (patient 115), 18,131 genes were kept based on their total reads count across all samples. During tumor dissociation, 1,980 genes were significantly up-regulated and 1,482 genes were down-regulated in dissociated tumor relative to tumor tissue (fold change > 2; adjusted p-value < 0.05; Figure 2A; Table S2). Out of top differentially expressed genes (DEGs), *RGS2, HSPA8, HSPA6*, and *ATF3* were canonical stress-responsive genes, triggered by dissociation stress[27,28]. Consistently, inference of TFs activity revealed activated TFs such as HSF1 (Heat shock transcription factor 1), RELA, NFKB1, and JUN in the dissociated tumor (Figure 2A), mediating cellular responses to enzymatic dissociation. Moreover, analysis of canonical cancer pathways indicated an active EGFR pathway alongside an inactive hypoxia pathway, indicating cell proliferation and reverse low oxygen of dissociated tumors (Figure 2A). No significant pathway was found using gene set enrichment analysis (GSEA) (Table S3).

In the progression from dissociated tumor to PDTS, 1,086 up-regulated and 1,920 down-regulated DEGs were identified in PDTS (fold change > 2; p-value < 0.005; Figure 2B). The p-value was stricter due to imbalance of samples (Figure S3). Top DEGs such as *HLA-DRB1*, and *HLA-DPA1* encode components of the MHC class II complex, likely expressed by immune cells, highlighting the depletion of immune cells in PDTS. Inactive TFs such as RFXAP, RFXANK, and RFX5 were inferred (Figure 2B), which were essential for activating MHC class II genes. Relative to dissociated tumor, hypoxia was restored, and activation of the PI3K and MAPK pathway indicated the proliferation of tumor cells in PDTS (Figure 2B). The suppression of the JAK-STAT pathway further highlights the depletion of immune components in PDTS, which was also validated by the down-regulation of KEGG pathways such as T cell receptor signaling pathway and chemokine signaling pathway (Table S3).

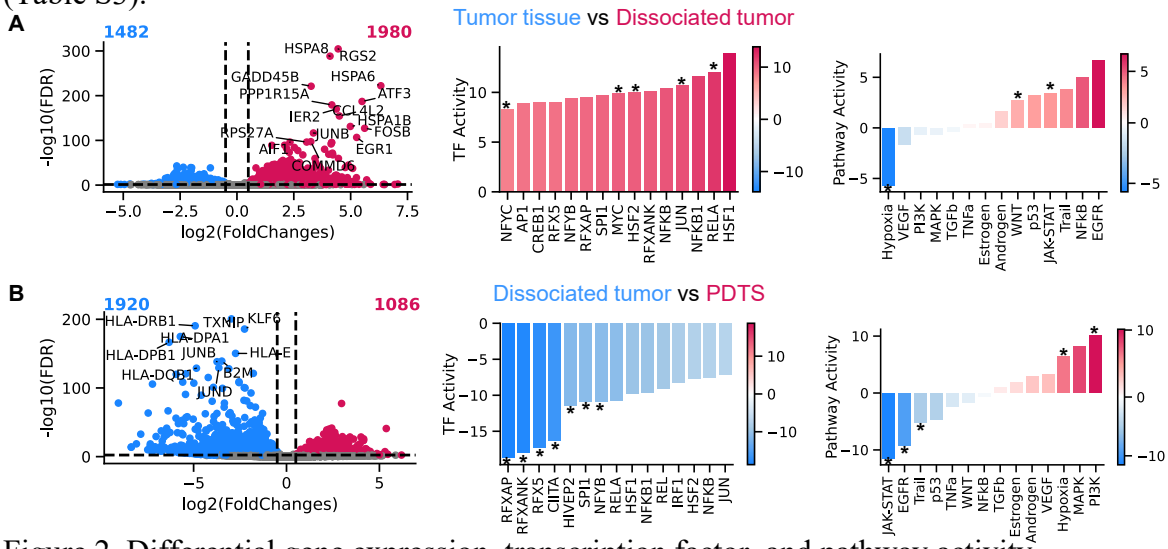

Figure 2. Differential gene expression, transcription factor, and pathway activity analysis in tumor dissociation, and the formation of PDTS for patient 115.
A. Comparisons between tumor tissues to dissociated tumor. B. Comparisons between dissociated tumors and PDTS. Red color indicated the upregulation, and blue color indicated the downregulation. Left plots were volcano plots of differential expressed genes (DEGs), middle plots were of TF activity inferred from DEGs, and right plots were of pathway activity inferred from DEGs. Note that "*" refers to shared TFs and pathways across three patients.

In patient 114 and patient 127, fewer DEGs were detected in tumor dissociation and PDTS formation, relatively compared to patient 115 (Figure S4-5; Table S4-5). In tumor dissociation, the upregulation of ribosome related genes and heat shock genes (*RPL37A*, *HSPA8*) was highlighted for both patients. Consistent with stress response and cell proliferation genes, patient 114 exhibited inactive TFs (SP53, ARNT) and activation of the JAK-STAT pathway, and patient 127 was characterized with an active PI3K pathway (Figure S4A-5A). The downregulation of hypoxia pathway was present in all patients, introducing a bias of the hypoxic microenvironment for dissociated tumor[29]. In PDTS formation, despite different DEGs, inactive TFs (RFXAP, RFXANK), active PI3K, inactive JAK-STAT pathway, and down-regulation of immune related KEGG pathways were observed in PDTS from all three patients (Figure S4B-5B; Table S6-7). Notably, the hypoxic microenvironment was restored in the formation PDTS from tumor dissociation (Figure 2B, Figure S4B-5B).

To investigate the technical effects of experimental procedures, we identified common DEGs across three patients for these two comparisons, thereby minimizing patient-specific tumor heterogeneity. In tumor dissociation, we identified 90 upregulated and 165 downregulated DEGs common to all patients (Figure S6A; Table S2,4-5). Gene ontology (GO) analysis reported that up-regulated genes were enriched in processes such as protein refolding, cytosolic ribosome, and C3HC4 type ring finger domain binding (Figure S6A), suggesting stress response activation. Down-regulated genes were associated with the ERBB3 signaling pathway, and xenobiotic transmembrane transporter (Figure S6A), suggesting the loss of tumor 3D structure. In PDTS formation, 58 up-regulated DEGs were enriched in GO terms such as negative regulation of granulocyte chemotaxis and cyclooxygenase pathway, and 233 down-regulated DEGs were mainly associated with the MHC protein related process, emphasizing the depletion of immune cells in PDTS (Figure S6B).

Collectively, our analysis highlights the heterogeneity and commonality at transcriptional level during tumor dissociation, and PTDS formation for patient derived tumor. While individual patients exhibited varying number of DEGs and dysregulated TFs and pathways, several pathways as hypoxia, PI3K and JAK-STAT emerged, underscoring oxidative stress and cell proliferation in tumor culture and PDTS development.

Molecular differences between tumor tissue, PDTS, and infiltrated-PDTS

In order to investigate the molecular distinction of infiltrated-PDTS, we next performed DGE analysis directly between tumor tissue and PDTS or infiltrated-PDTS. In patient 115, PDTS exhibited 1,799 up-regulated and 2,204 down-regulated DEGs compared to tumor tissue, while infiltrated-PDTS showed 2,579 up-regulated and 2,844 down-regulated genes relative to tumor tissue (fold change > 2, p-value < 0.005; Table S2). Integrated with DEGs between dissociated tumor and tumor tissue, a heatmap of 7747 DEGs illustrates these differences (Figure 3A).

Compared to tumor tissue, several TFs (ELF4, JUNE, etc.) were consistently dysregulated in dissociated tumor, PDTS, and infiltrated-PDTS (Figure 3B). While PDTS demonstrated inactive TFs such as ZFX, RFXANK, RFX5, CIITA, and RFXAP, likely due to the absence of immune cells, infiltrated-PDTS showed activation of E2F3, ELF4, TFDP1, and E2F1 (cell cycle TFs), suggesting tumor cells remained proliferative after the re-infiltration of immune cells. Furthermore, pathway analysis indicated the expected absence of immune cells with the inactive JAT-STAT and TNFa pathways in PDTS. In contrast, infiltrated-PDTS exhibited activation of JAK-STAT, PI3K, VEGF pathway, with an inactive p53 pathway,

indicating cytokine signaling and interactions between tumor cells and immune cells. GSEA also revealed the enrichment of downregulation of immune cells related KEGG pathway in PDTS, and downregulation of metabolism related pathways in infiltrated-PDTS (Table S3)

For patient 114 and patient 127, PDTS had 1,529 up-regulated, and 3,357 down-regulated DEGs, and 340 up-regulated, 1,269 down-regulated DEGs, respectively (Figure S7-8A; Table S4-5). Infiltrated-PDTS showed 1,357 up-regulated, and 3,068 down-regulated genes, and 274 up-regulated, 1,716 down-regulated genes, respectively (Figure S7-8A). All DEGs were illustrated in the heatmap (Figure S7-8B). Both patients displayed inactive MHC class II related TFs and inactive JAK-STAT pathway in PDTS, and a highly active JAK-STAT pathway in infiltrated-PDTS (Figure S7-8CD).

Common DEGs across all patients included 190 up-regulated and 937 down-regulated genes in PDTS, and 138 up-regulated genes and 726 down-regulated genes in infiltrated-PDTS (Figure S9). GO analysis highlighted enrichment of MHC-related and immune cell-related terms among down-regulated genes in PDTS, and enrichment of small nuclear ribonucleoproteins (snRNPs) among up-regulated genes in infiltrated-PDTS. Upregulation of snRNPs were associated with immune evasion[30]. This was complemented by down-regulated KEGG pathways such as hematopoietic cell lineage and T cell receptor signaling pathway in PDTS and down-regulation of metabolism and signaling pathways (e.g., Alanine aspartate and glutamate metabolism, MAPK signaling pathway) in infiltrated-PDTS.

The modest number of DEGs (90 upregulated and 165 downregulated) between tumor tissue and dissociated tumor suggests minimal transcriptomic alterations due to dissociation. In contrast, PDTS exhibited a substantial number of DEGs (190 upregulated and 937 downregulated), while infiltrated-PDTS had fewer DEGs (138 upregulated and 726 downregulated) compared to tumor tissue. This pattern indicates that the presence of infiltrating immune cells enhances the transcriptomic resemblance of PDTS to the original tumor tissue.

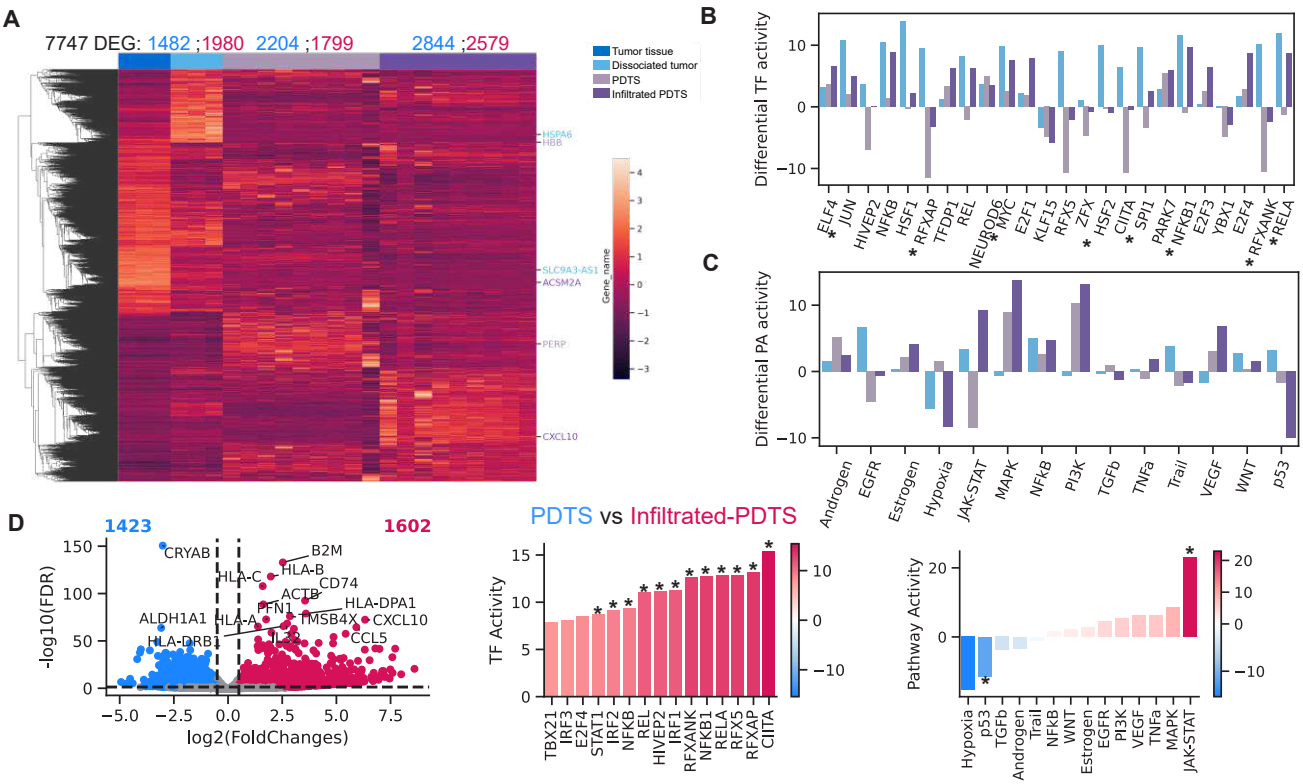

Figure 3. Differential gene expression, transcription factor, and pathway activity analysis in the formation of PDTS for patient 115.

A. A heatmap for all DEGs from the comparison between tumor tissue and dissociated tumor or PDTS or infiltrated-PDTS. B. TF analysis for the comparison between tumor tissue and dissociated tumor or PDTS or infiltrated-PDTS. Top 10 significant TFs were selected for three comparisons, and 24 TFs were obtained. C. PA analysis for the comparison between tumor tissue and dissociated tumor or PDTS or infiltrated-PDTS. D. Comparisons between PDTS vs infiltrated-PDTS.

Noted that "" refers to shared TFs and pathways across three patients.*

Comparisons between PDTS **and infiltrated-**PDTS

To further investigate the impact of immune fraction on PDTS, we conducted a comparative transcriptomic analysis between PDTS and infiltrated-PDTS. In patient 115, we identified 1,602 up-regulated and 1,423 down-regulated genes in infiltrated-PDTS relative to PDTS (Figure 3D, left panel; p value < 0.05, fold change > 2; Table S3). TFs and pathway analyses revealed highly active TFs such as CIITA, RFXAP, etc. and activation of the JAK-STAT pathway (Figure 3D, right panel), suggesting tumor-immune interaction in infiltrated-PDTS.

Although patients 114 and 127 exhibited different numbers of DEGs (396 up-regulated and 148 down-regulated for patient 114; 337 up-regulated and 337 down-regulated for patient 127; Figure S10; Table S4-5), notably, there was increased activity of CIITA, IRF1, and RELA, along with heightened activity of the JAK-STAT pathway (Figure S10). Based common genes and pathways across patients, GO analysis reported the enrichment of MHC related biological function (Figure S11), and GSEA indicated the up-regulation of cytokine-cytokine receptor interaction, antigen processing and presentation, and natural killer cell mediated cytotoxicity.

While only a small subset of DEGs was common across all three patients (155 up-regulated and 36 down-regulated), the consistent enrichment of immune-related

pathways underscores the specificity of immune cell infiltration effects in infiltrated-PDTS compared to PDTS.

Tumor and immune signatures of infiltrated-PDTS

The re-infiltration of immune fraction into PDTS plays an important role in recapitulating tumor immune microenvironment of the original tumor. Hence, we analyzed specific tumor and immune signatures across our categories of samples. Building upon previously established pathway signatures of molecular subsets in ccRCC (T effector, Cell Cycle, FAS (fatty acid synthesis)/pentose phosphate, Complement Cascade, Omega Oxidation, Myeloid Inflammation, Angiogenesis, FAO/AMPK (fatty acid oxidation/ AMP-activated protein kinase), Stroma, snoRNA)[22], we characterized our samples from tumor tissue to infiltrated-PDTS (Figure 4A). In patient 115, tumor tissue was characterized with high levels of angiogenesis and complement cascade. Dissociated tumor exhibited elevated T effector and myeloid inflammation, with a decrease in other signatures. PDTS showed a significant decline in T effector, while other signatures remained similar to dissociated tumor. Notably, infiltrated-PDTS exhibited increased levels of T effector, cell cycle, and myeloid inflammation, and reduced levels of angiogenesis and FAO/AMPK, relative to tumor tissue.

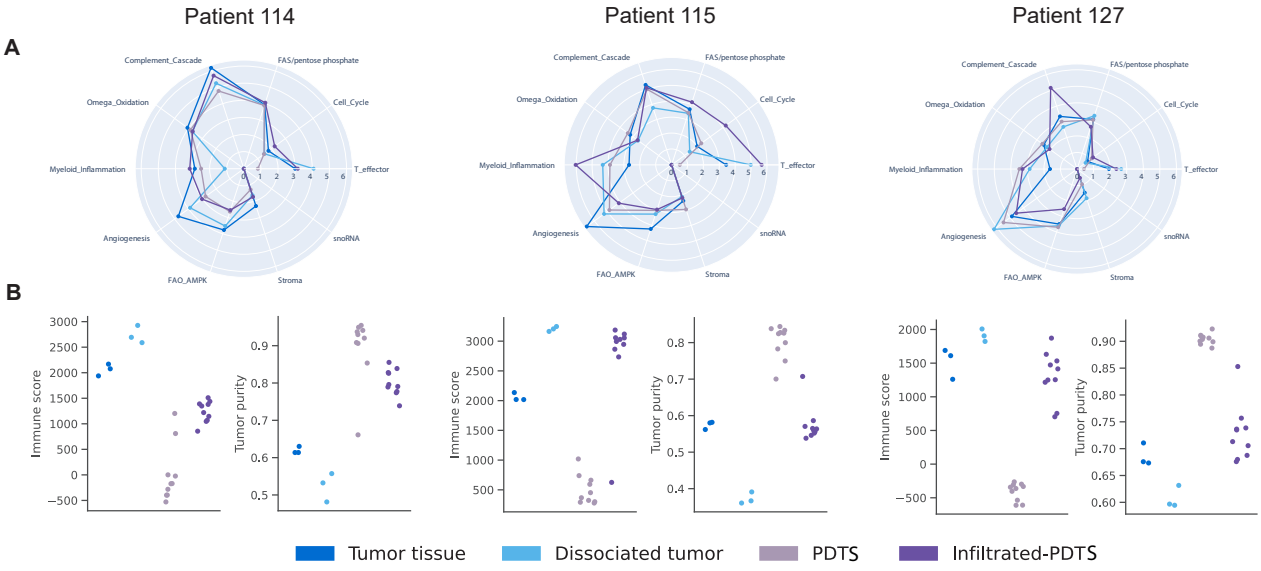

Figure 4. The signatures of cccRCC subtypes and EstimateScore of tumor tissue, dissociated tumor, PDTS, and infiltrated-PDTS from three patients. A. Ten simplified signatures of ccRCC subtypes. B. Immune score and tumor purity.

In patients 114 and 127, tumor tissues were characterized by high level of complement cascade and angiogenesis, respectively. Consistently, dissociated tumor presented higher T effector than tumor tissue. While other signatures remain lower in dissociated tumor of patient 114, myeloid inflammation, angiogenesis, and stromal cell signatures were higher in dissociated tumor of patient 127. As the control, PDTS also showed the lowest level of T effector in both patients. Infiltrated-PDTS maintained T effector signature levels comparable to tumor tissue and exhibited lower levels of angiogenesis and FAO/AMPK, despite differing subtypes. These may suggest the similar characteristic of TME and a restored metabolic reprogramming in infiltrated-PDTS to tumor tissue.

To assess tumor and immune cell composition, we employed the ESTIMATE algorithm to infer immune infiltration level and tumor purity[23]. Consistently, dissociated tumor had higher immune infiltration level (immune score) and lower proportion of tumor cells (tumor purity) than tumor tissue across three patients (Figure 4B; Table S8). While PDTS exhibited the lowest levels of immune cells due to the depletion of immune cells, infiltrated-PDTS displayed comparable levels of immune infiltration, and tumor percentage, compared to tumor tissue.

To accurately investigate which type of immune cells compose the immune microenvironment of infiltrated-PDTS, we performed single sample gene set enrichment analysis (ssGSEA) of 20 immune cell populations to quantify their infiltrating level in our samples (Figure 5; Table S9). Since PDTS were depleted of immune cells, their inferred infiltration levels of PDTS were taken as a control to adjust the immune infiltration level of other samples. In patient 115, tumor tissue, dissociated tumor, and infiltrated-PDTS had similar infiltration levels of activated CD8 T cell, effector memory CD8 T cell, regulatory T cell, natural killer T cell, natural killer cell, myeloid-derived suppressor cell (MDSC), and eosinophil. Infiltrated-PDTS exhibited a decrease in activated B cell, activated dendritic cell, central memory CD8 T cell, and a total loss of effector memory CD4 T cell, gamma delta T cell, macrophage, mast cell, monocyte, neutrophil, immature dendritic cell (Figure 5). These suggest infiltrated-PDTS retained similar infiltration levels of key T cells, with a strong diminution of myeloid cells subtypes.

In patient 114 and 127, infiltrated-PDTS also exhibited comparable infiltration levels of activated CD8 T cell as tumor tissue showed (Figure S12). This was corroborated by similar immune scores between tumor tissue and infiltrated-PDTS (Figure 4B). It was noted that infiltrated-PDTS samples from patient 127 exhibited significant variability in immune infiltration levels.

These findings underscore the critical role of immune cell re-infiltration in PDTS, to accurately replicate the immune microenvironment of the original tumor. The observed variability of ccRCC subset signatures, tumor purity, and immune cell populations suggests these factors can influence the fidelity of infiltrated-PDTS, in modeling the original tumor's characteristics. Therefore, meticulous control over tumor composition during spheroid formation is essential to ensure that infiltrated-PDTS serve as reliable models for studying tumor biology.

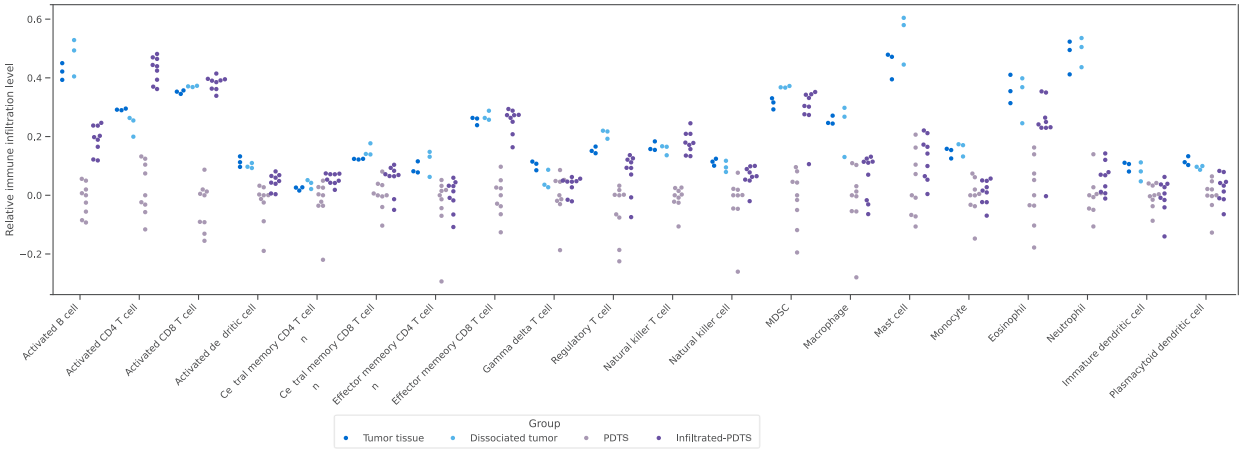

Figure 5. Immune infiltration level analysis of 20 immune cell types using single sample gene set enrichment analysis (ssGSEA). GSEApy was employed to compute immune cell infiltration scores based on the transcriptomics of each sample. Since PDTS were depleted of immune cells, the median of immune infiltration levels of

PDTS were taken as the control to adjust the estimated levels of immune cells in tumor tissue, dissociated tumor, and infiltrated-PDTS.

Prediction of immunotherapy response (Figure 6)

To evaluate the potential of infiltrated-PDTS can be used as reliable models the therapeutic studies, we analyzed Tumor Immune Dysfunction and Exclusion (TIDE) scores, and expression of predictive genes across various samples. A lower TIDE score suggests a higher likelihood of positive response to immunotherapy, and samples with TIDE score below 0 were classified as responders. In patient 115, both tumor tissue and infiltrated-PDTS samples exhibited comparable TIDE scores, with all samples (3/3 tumor tissue and 9/9 infiltrated-PDTS) classified as responders to immunotherapy (Figure 6; Table 14). In contrast, PDTS samples, which lack immune components, showed elevated TIDE scores and were uniformly labeled as non-responders. In patient 114 and patient 127, TIDE scores varied, resulting in 5 out of 10 (50%) and 2 out of 10 (20%) infiltrated-PDTS samples being classified as responders, respectively, compared to 1 out 3 (33.34%) in tumor tissue (Figure 6). These findings reveal that PDTS might have the capacity to be clinical non responders even though they are artificially re-infiltrated with immune cells and that their computed response is close to that of the original tumor, advocating, for their relevance in immunooncology

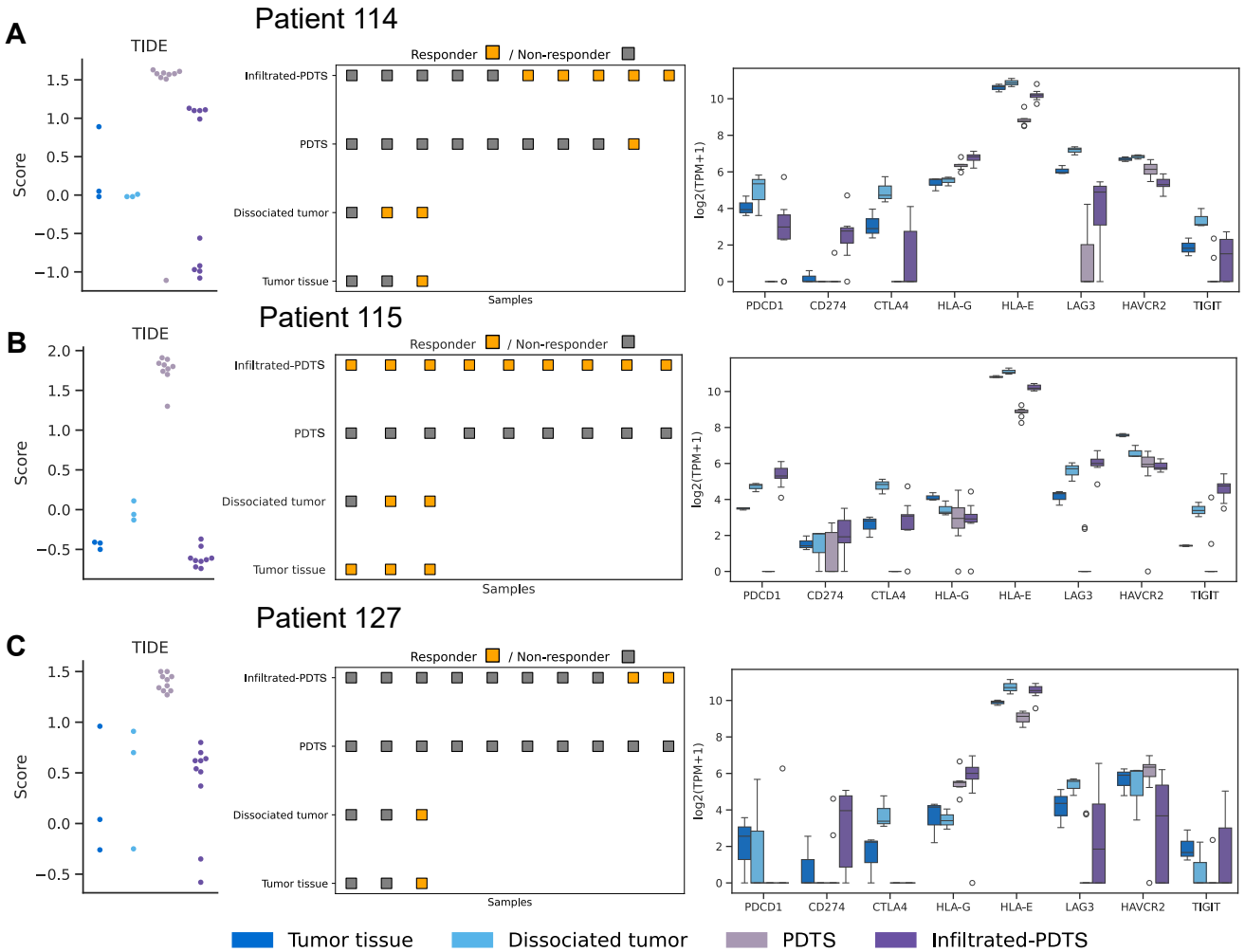

Figure 6. The TIDE scores, responder classification, and immune checkpoint genes expression for samples of tumor tissue, dissociated tumor, PDTS, and infiltrated-PDTS from three patients.

TIDE scores were calculated through the web tool: http://tide.dfci.harvard.edu/. Sample were classified as responders if their TIDE score was below zero.

We further examined the expression of specific genes, including immune checkpoints (*PDCD1*: encoding PD-1, *CD274*: encoding PD-L1, *CTLA-4*, *HLA-G*, *LAG3*, *HAVACR2*: encoding Tim3, *TIGIT*), tumor-intrinsic mutators (*VHL, PBRM1, BAP1, SETD2, KDM5C*), and inflammatory genes (e.g., CXCL9, CXCL10) (Figure 6; Figure S13). In patient 115, *PDCD1*, *CD274*, *CTLA4*, and *HLA-G* were expressed in tumor tissue, indicating tumor immune evasion, and potential resistance to immunotherapy. Infiltrated-PDTS demonstrated even higher expression levels of these genes, suggesting a restoration of immune suppression within the spheroid model. *HLA-G* expression was slightly reduced, potentially reflecting differences in cell composition. *LAG3* and *TIGIT* expressed higher but *HAVCR2* expressed lower in infiltrated-PDTS compared to tumor tissue, possibly reflecting the early or intermediate exhaustion status of T cells in infiltrated-PDTS, as opposed to the terminal exhaustion status of T cells in tumor tissue. While tumor-intrinsic gene expression remained similar, suggesting retained mutation profile of infiltrated-PDTS, inflammatory genes expressed higher in infiltrated-PDTS, indicating the potential effect of IL-15 (Figure S13).

Compared with patient 115, gene of PD-L1 was barely expressed in tumor tissue of patient 114 and 127 (Figure 6), indicating less immune suppressive environment and poor response to immunotherapy. Infiltrated-PDTS displayed lower expressions of *PDCD1* and *CTLA4*, but higher *CD274* expression. This effect could also be related to the IL-15 activation step necessary for PDTS infiltration by immune cells. The cytokine,when activating immune cells could induce the expression of PD-L1 in infiltrated-PDTS in an indirect manner via IFNg pathway. For infiltrated-PDTS, the lower expression of *HAVCR2* in patient 114, and the slightly higher expression of *LAG3* and *TIGIT* in patient 127, indicated the early or intermediate exhaustion status of T cells. Consistent with patient 115, tumor-intrinsic genes remained unchanged between infiltrated-PDTS and tumor tissue, and inflammatory genes expressed higher in infiltrated-PDTS.

In summary, TIDE scores and immunotherapy markers suggested that infiltrated-PDTS can serve as predictive models for immunotherapy response. While tumor-intrinsic gene expression remained stable, variations in immune checkpoint in infiltrated-PDTS may influence their predictive accuracy for treatment response.

Discussion & Conclusion:

Patient derived spheroids have become widely used as preclinical models in cancer research due to their ability to preserve tumor-specific characteristics. However, their representativeness is challenging to estimate, given experimental artifacts and the absence or alteration of the native tumor micro-immune environment. In this study, transcriptomic profiling across various stages of spheroid formation was employed to dissect technical biases and patient-specific variability, offering critical guidance for the application of matched spheroids in immunotherapeutic applications.

Tumor dissociation, in the for of enzymatic digestion in our protocol, is an essential step to initiate spheroids culture. Although it facilitates the isolation and manipulation of specific cell populations, it also disrupts essential features such as the extracellular matrix, spatial architecture, and native cellular interactions within the tumor[13]. Previous studies have demonstrated that dissociation process may trigger immediate early genes (IEGs), heat shock proteins, and stress response pathways[28]. Our findings align with this, revealing the up-regulation of ATP related genes (eg. *ATP5F1A*), ribosomal related genes (eg, *RPL10A*), heat shock related genes (eg. *HSPA1A*), and IEGs (eg. *JUNB*). Moreover, we observed the down-regulation of solute carrier family genes (eg. *SLC12A7*), ERBB3 signaling pathway, and hypoxia pathway, likely triggered by the loss of tumor structure. Notably, *SLC12A7* and *ERBB3* have been reported to be prognostic markers in ccRCC[31,32], suggesting a disrupted role of dissociated tumor samples as potential models. Additionally, tumor dissociation may lead to an increase in the activity of immune cells, a bias that could overestimate treatment response of tumors. These findings highlight biased transcriptomics following tumor dissociation representing the starting material of number of experimental models.

Post-dissociation, the generation, and analysis of both standard PDTS and immune-infiltrated PDTS revealed further insights into tumor reconstitution. In the absence of immune components (used as a control), PDTS restored hypoxia pathway and displayed down-regulation of immune cell markers, immune signatures, and inflammatory pathways In contrast, immune-infiltrated PDTS displayed upregulation of proinflammatory genes such as *CXCL10* and *STAT1*, along with activation of the type II interferon signaling pathway[33] Simultaneously, there was downregulation of IEGS, and stress response genes in infiltrated-PDTS relative to the dissociated tumor. Importantly, robust activation of the JAK-STAT pathway was consistently observed in infiltrated-PDTS across all three patients, supporting the successful recruitment of immune cells into the spheroid structure, and a partial restoration of tumor-immune crosstalk[34].

The primary objective of this study was to evaluate the extent to which infiltrated-spheroids can mimic the original tumor, and their potential for studying immunotherapy resistance. Our results indicate infiltrated-PDTS preserved several key immune signatures, including the T effector signature, immuneScore, and activated $CD8^+$ T cell signatures, as well as comparable proportions of predicted responders inferred by TIDE score. These findings collectively suggest infiltrated-PDTS are representative of the original tumor in the context of immunotherapeutic profiling. This representativeness may be attributed to the preservation of native immune components, reconstitution of the tumor microenvironment (TME), and structural resemblance to the parent tumor similarity[35,36].

Nevertheless, several limitations must be acknowledged. First, the efficiency and fidelity of infiltrated spheroids are influenced by inter-patient tumor heterogeneity.

The number of DEGs varied largely across three patients, resulting in distinct TFs and pathway signature. For instance, PDTS from patient 115 displayed heightened myeloid inflammation, whereas those from patient 127 showed enrichment in complement cascade pathways. T cell exhaustion markers also varied between patients, highlighting the intrinsic heterogeneity of ccRCC. Second, while IL-15 was employed to activate $CD8^+$ T cells, promoting their proliferation, survival, and distribution[37], its use carries limitations. The observed strong activation of the JAK-STAT pathway in infiltrated-PDTS is consistent with IL-15 engagement. However, high concentrations of IL-15 may introduce cytokine-driven toxicity, checkpoint upregulation, and potentially distort the immune landscape compared to the native tumor environment, a fine balance has to be found between sufficient activation to allow immune-tumor crosstalk and strong immune activation that could lead to misleading results. Third, critical components of the TME, particularly myeloids, were diminished in infiltrated-PDTS. These cell populations are key regulators of immune cell behavior and T cell responsiveness, with a particular place for macrophages. Their absence may limit the model's accuracy in fully representing tumor-immune interactions. Future efforts to incorporate these missing cell types will be essential for enhancing the fidelity and translational relevance of infiltrated-PDTS as immunotherapy testing platforms.

In conclusion, this study demonstrates that immune-infiltrated PDTS can effectively preserve tumor-specific immune signatures and structural features, making them a promising model for investigating immune responses and therapy resistance in ccRCC. By systematically evaluating the effects of tumor dissociation, spheroid formation, and immune cell reconstitution, we provide a framework to improve the biological fidelity of these models. Further refinement of this infiltrated-PDTS platform will advance personalized immunotherapy and translational cancer research.

DATA AVAILABILITY

The data and codes were deposited in the GitHub repository (https://github.com/liangwei01/Patient-derived-tumor-organoids).

AUTHOR CONTRIBUTION

LY, LL, JR, JL, and CB conceived the study. LL performed the experiments. LY developed and performed the analysis. LY, LL, JR, JL, and CB wrote the manuscript. LY, LL, JR, JL, and CB contributed to the revision of the manuscript.

FUNDING

This study was supported by EDISCE grant from University of Grenoble Alpes. This work was supported by the KATY project, which has received funding from the European Union's Horizon 2020 research and innovation program under grant agreement no. 101017453, by the CANVAS project, which has received funding from the Horizon Europe twinning program under grant agreement no. 101079510, and by the DIGPHAT project (Multi-scale and longitudinal data modeling in pharmacology: toward digital pharmacological twins), which has received funding from the French research initiative ''France 2030'' through the program PEPR Digital Health under ANR grant agreement no. 22-PESN-0017.

ACKNOWLEDGMENTS

Part of the computations were carried out using the GRICAD infrastructure (https://gricad.univ-grenoble-alpes.fr), which is supported by Grenoble research communities.

SUPPLEMENTARY MATERIAL

Supplementary tables and figures are available online: https://github.com/liangwei01/Patient-derived-tumor-organoids.

Reference

1. Zhang, Y. et al. Single-cell analyses of renal cell cancers reveal insights into tumor microenvironment, cell of origin, and therapy response. Proceedings of the National Academy of Sciences 118, e2103240118 (2021).
2. Zvirblyte, J. et al. Single-cell transcriptional profiling of clear cell renal cell carcinoma reveals a tumor-associated endothelial tip cell phenotype. Commun Biol 7, 1–15 (2024).
3. Bex, A. et al. European Association of Urology Guidelines on Renal Cell Carcinoma: The 2025 Update. European Urology (2025) doi:10.1016/j.eururo.2025.02.020.
4. Tabbara, M. M., González, J., Martucci, M. & Ciancio, G. Current Approaches in Surgical and Immunotherapy-Based Management of Renal Cell Carcinoma with Tumor Thrombus. Biomedicines 11, 204 (2023).
5. Stewart, G. D. et al. A Phase II study of neoadjuvant axitinib for reducing the extent of venous tumour thrombus in clear cell renal cell cancer with venous invasion (NAXIVA). Br J Cancer 127, 1051–1060 (2022).
6. Bex, A. et al. Efficacy, safety, and biomarker analysis of neoadjuvant avelumab/axitinib in patients (pts) with localized renal cell carcinoma (RCC) who are at high risk of relapse after nephrectomy (NeoAvAx). JCO 40, 289–289 (2022).
7. Raimondi, A. et al. Predictive Biomarkers of Response to Immunotherapy in Metastatic Renal Cell Cancer. Front Oncol 10, 1644 (2020).
8. Tong, L. et al. Patient-derived organoids in precision cancer medicine. Med 5, 1351–1377 (2024).
9. Grassi, L. et al. Organoids as a new model for improving regenerative medicine and cancer personalized therapy in renal diseases. Cell Death Dis 10, 1–15 (2019).
10. Calandrini, C. et al. An organoid biobank for childhood kidney cancers that captures disease and tissue heterogeneity. Nat Commun 11, 1310 (2020).
11. Esposito, A. et al. Three-Dimensional In Vitro Cell Cultures as a Feasible and Promising Alternative to Two-Dimensional and Animal Models in Cancer Research. International Journal of Biological Sciences 20, 5293–5311 (2024).
12. Lugand, L. et al. Methods for Establishing a Renal Cell Carcinoma Tumor Spheroid Model With Immune Infiltration for Immunotherapeutic Studies. Front Oncol 12, 898732 (2022).
13. Ren, J. et al. The pros and cons of mechanical dissociation and enzymatic digestion in patient-derived organoid cultures for solid tumor. Cell Organoid (2024) doi:10.26599/CO.2024.9410009.

14. Dobin, A. et al. STAR: ultrafast universal RNA-seq aligner. Bioinformatics 29, 15–21 (2013).
15. Dyer, S. C. et al. Ensembl 2025. Nucleic Acids Research 53, D948–D957 (2025).
16. Wang, L., Wang, S. & Li, W. RSeQC: quality control of RNA-seq experiments. Bioinformatics 28, 2184–2185 (2012).
17. Badia-i-Mompel, P. et al. decoupleR: ensemble of computational methods to infer biological activities from omics data. Bioinformatics Advances 2, vbac016 (2022).
18. Love, M. I., Huber, W. & Anders, S. Moderated estimation of fold change and dispersion for RNA-seq data with DESeq2. Genome Biology 15, 550 (2014).
19. Müller-Dott, S. et al. Expanding the coverage of regulons from high-confidence prior knowledge for accurate estimation of transcription factor activities. Nucleic Acids Research 51, 10934–10949 (2023).
20. Schubert, M. et al. Perturbation-response genes reveal signaling footprints in cancer gene expression. Nat Commun 9, 20 (2018).
21. Subramanian, A. et al. Gene set enrichment analysis: a knowledge-based approach for interpreting genome-wide expression profiles. Proc Natl Acad Sci U S A 102, 15545–15550 (2005).
22. Motzer, R. J. et al. Molecular Subsets in Renal Cancer Determine Outcome to Checkpoint and Angiogenesis Blockade. Cancer Cell 38, 803-817.e4 (2020).
23. Yoshihara, K. et al. Inferring tumour purity and stromal and immune cell admixture from expression data. Nat Commun 4, 2612 (2013).
24. Charoentong, P. et al. Pan-cancer Immunogenomic Analyses Reveal Genotype-Immunophenotype Relationships and Predictors of Response to Checkpoint Blockade. Cell Rep 18, 248–262 (2017).
25. Hänzelmann, S., Castelo, R. & Guinney, J. GSVA: gene set variation analysis for microarray and RNA-seq data. BMC Bioinformatics 14, 7 (2013).
26. Prosz, A. et al. Nucleotide excision repair deficiency is a targetable therapeutic vulnerability in clear cell renal cell carcinoma. Sci Rep 13, 20567 (2023).
27. O'Flanagan, C. H. et al. Dissociation of solid tumor tissues with cold active protease for single-cell RNA-seq minimizes conserved collagenase-associated stress responses. Genome Biol 20, 210 (2019).
28. van den Brink, S. C. et al. Single-cell sequencing reveals dissociation-induced gene expression in tissue subpopulations. Nat Methods 14, 935–936 (2017).

29. Kumano, K. et al. Hypoxia at 3D organoid establishment selects essential subclones within heterogenous pancreatic cancer. Front. Cell Dev. Biol. 12, (2024).
30. Wang, H. et al. The diagnostic and prognostic significance of small nuclear ribonucleoprotein Sm D1 aberrantly high expression in hepatocellular carcinoma. Journal of Cancer 13, 184–201 (2022).
31. Fangning, W. et al. Identification and validation of soluble carrier family expression signature for predicting poor outcome of renal cell carcinoma. Journal of Cancer 8, 2010–2017 (2017).
32. Wang, Z. et al. The Role of ERBB Signaling Pathway-Related Genes in Kidney Renal Clear Cell Carcinoma and Establishing a Prognostic Risk Assessment Model for Patients. Front Genet 13, 862210 (2022).
33. Borcherding, N. et al. Mapping the immune environment in clear cell renal carcinoma by single-cell genomics. Commun Biol 4, 1–11 (2021).
34. Parveen, S., Fatma, M., Mir, S. S., Dermime, S. & Uddin, S. JAK-STAT Signaling in Autoimmunity and Cancer. Immunotargets Ther 14, 523–554 (2025).
35. Magré, L. et al. Emerging organoid-immune co-culture models for cancer research: from oncoimmunology to personalized immunotherapies. J Immunother Cancer 11, e006290 (2023).
36. Yang, G. et al. Metabolic heterogeneity in clear cell renal cell carcinoma revealed by single-cell RNA sequencing and spatial transcriptomics. Journal of Translational Medicine 22, 210 (2024).
37. Alpdogan, Ö. & Brink, M. R. M. van den. IL-7 and IL-15: therapeutic cytokines for immunodeficiency. Trends in Immunology 26, 56–64 (2005).

Useful supplementary figures for Chapter 2 that were not yet included in the article:

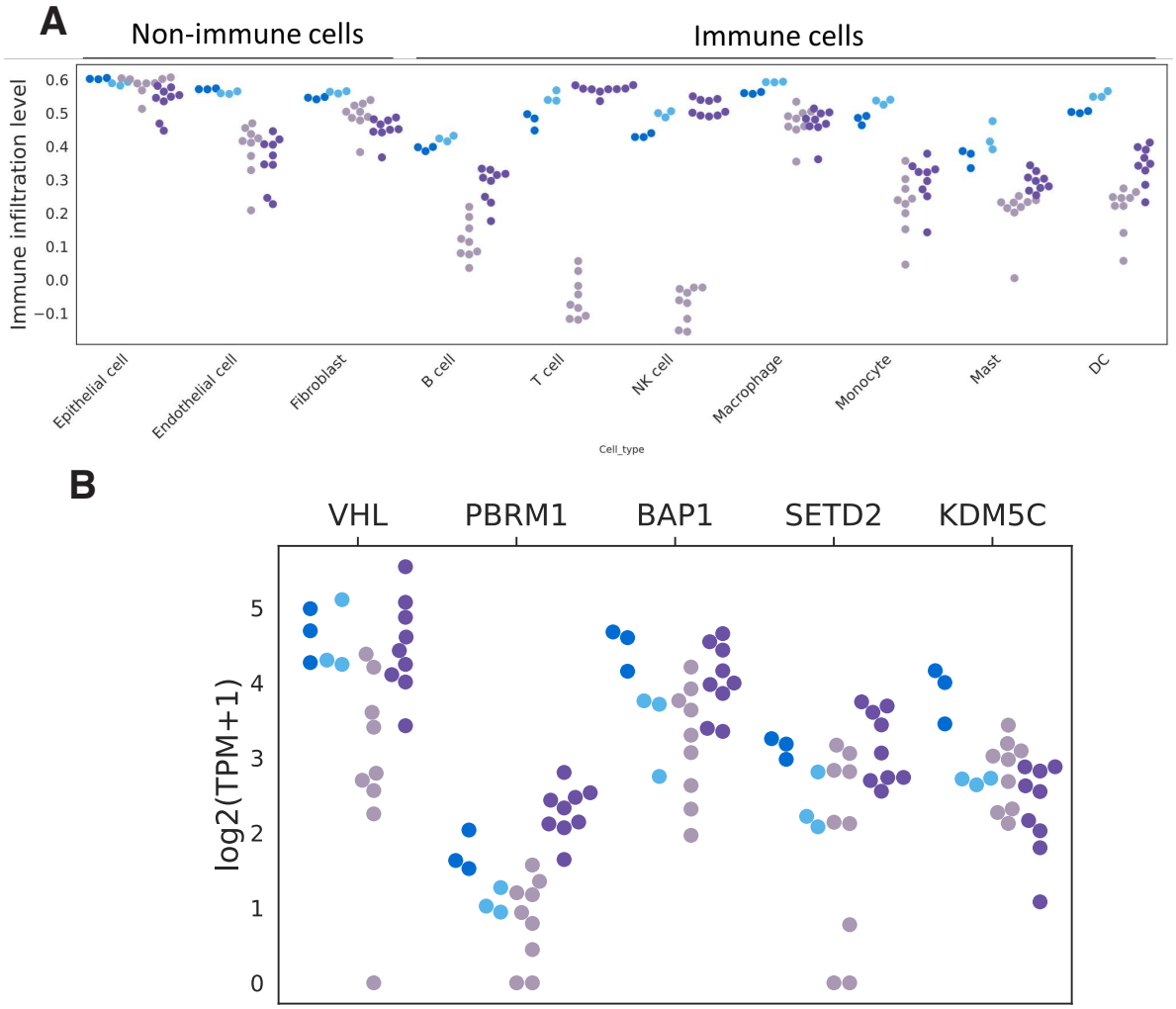

Figure 37: Estimation of non-immune cells and immune cells signatures in tumor tissues, dissociated tumors, PDTOs, and infiltrated-PDTOs.

A. Diverse cell types signatures analyses, including non-immune cells (epithelial cells, and stromal cells), and immune cells. B. Signatures of tumor mutated genes. Data for patient 115.

Summary and perspective

This second study provided valuable insights into the cellular composition and transcriptional dynamics of our patient-derived tumor spheroid model. By comparing samples across successive step, tumor dissociation, spheroid formation, and immune reinfiltration, we were able to identify both methodological biases and encouraging signals of biological relevance. Despite the use of IL-15 activation, not all spheroids displayed uniformly high immune response scores, suggesting that the model retains a degree of heterogeneity reflective of interpatient variability. Major cellular subsets, including epithelial, fibroblastic, endothelial, and immune populations, were consistently detected with relevant gene signatures (also seen in **Figure 37**). Upon reinfiltration, immune cells reappeared in proportions compatible with those observed in the original

tumors, with the possible exception of myeloid populations, whose recovery was likely affected by the 48h culture period in conditions optimized for lymphocytes, including plastic adherence and IL-15 supplementation. As indicated in the first study, dedicated reinfiltration protocols may be needed to better preserve or reintroduce these cells.

However, proteic validation at the tissue level is still required to confirm the bioinformatic observations. To this end, two complementary approaches have been initiated. First, a workflow for comparative slide preparation has been established, enabling direct histological comparison between native tumor tissue and corresponding spheroids. Paraffin-embedded spheroids have been sectioned, and staining protocols are currently being optimized to assess the presence of key cellular subsets, including epithelial cells, lymphocytes, macrophages, endothelial cells, and fibroblasts. Notably, slides have been prepared for Patient 127, included in the transcriptomic study. Immunohistochemistry and immunofluorescence protocols are still being developed and will be applied to matched samples to support and validate transcriptomic findings. Additionally, the bioinformatics team is analyzing flow cytometry data routinely collected from TILs after tumor dissociation, with the aim of evaluating whether ssGSEA-based immune deconvolution recapitulates trends observed in cytometric analyses.

At the transcriptomic level, spheroid profiles showed a strong overall resemblance to their matched tumors but remained distinct in several aspects. They appeared more inflamed and did not fully recapitulate the molecular subtypes of renal cancer described in the introduction. Despite these differences, this study successfully established a reproducible autologous model integrating tumor and immune components, a key milestone toward functional ex vivo immunotherapy testing.

With this autologous platform in place, the next objective was to move beyond static culture conditions and introduce a dynamic dimension to the system. In the tumor microenvironment, immune–tumor interactions are modulated by biophysical and metabolic factors such as interstitial flow, nutrient gradients, and spatial constraints. These parameters play a key role in shaping immune cell migration, activation, and effector functions, aspects that static culture systems fail to recapitulate. Moreover, in static systems, cytokines and metabolites accumulate, generating uniform and artificial inflammatory conditions.

To overcome these limitations, we designed a custom microfluidic chip allowing controlled perfusion of immune cells, nutrients, and treatments. This system was conceived with the goal in mind to enable sequential drug exposure, mimic physiological flow, and provide a more realistic framework to study immune infiltration and tumor destruction under dynamic conditions.

Chapter 3: A Tumor-on-Chip Platform for Modeling Immunotherapy Response in Clear Cell Renal Cell Carcinoma

Leonard Lugand, Jules Russick, Joris Kaal Liangwei Yin, Rebecca Laboureur, Isabelle Poras, Fatiha Bouhidel, Malika Djouadou, Clément Dumont, François Desgrandchamps, Christophe Battail, Fabrice Navarro, Nathalie Rouas-Freiss, Joel Lemaoult

Article Draft to be submitted in 2026

In this final study, we implemented our autologous immune infiltrated spheroid model in a custom microfluidic chip. This study also served as an opportunity to establish and consolidate a series of functional readouts applicable to both the current project and future developments. A significant part of the work was dedicated to benchmarking these assays using a calibrated ccRCC cell line model expressing PD-L1 at controlled levels. This approach enabled us to assess both the performance and reproducibility of the spheroid model in studying immune responses to PD-L1 blockade, and to establish a reliable panel of readouts that can serve for the evaluation of additional immunotherapeutic strategies and targets in the future.

To design the microfluidic chip, we first revisited the BRB-seq data generated in the previous work to further evaluate the representativity of the model and determine the minimal number of spheroids required to capture the main transcriptional features of the tumor. This analysis aimed to assess whether pooling ten spheroids per condition was sufficient to reach a plateau in transcriptomic similarity with the parental tumor.

Building on this foundation, we designed and optimized a microfluidic chip derived from a prototype developed at CEA–LETI, and established the entire experimental workflow required for its operation. The system was then used to validate the ability of circulating immune cells to infiltrate tumor spheroids within this dynamic environment.

Finally, a proof of concept was conducted using the autologous patient-derived model, combining cytokine quantification in the circulating medium with spectral flow cytometry analysis. A 37-color panel was developed to enable detailed immune profiling in future applications of this autologous tumor-on-chip platform.

To accommodate the format of this thesis and provide a methodological resource for future users, the Materials and Methods section of this draft article is presented in greater detail than in a standard journal manuscript.

An Autologous Tumor-on-Chip Platform for Modeling Immunotherapy Response in Clear Cell Renal Cell Carcinoma

Léonard Lugand[1], Jules Russick[1], Joris Kaal[2], Liangwei Yin[3], Rébecca Laboureur[1], Isabelle Poras[1], Fatiha Bouhidel[4], Malika Djouadou[5], Clément Dumont[6], François Desgrandchamps[5], Christophe Battail[3], Fabrice Navarro[2], Nathalie Rouas-Freiss[1], Joël Lemaoult[1].

[1] CEA/DRF/François Jacob Institute/Hemato-Immunology Research Department, Saint-Louis Research Institute (IRSL) – INSERM U1342, Paris Cité University, Saint-Louis Hospital, Paris, France

[2]Univ. Grenoble Alpes, CEA, LETI, DTBS, 38000, Grenoble, France

[3] Université Grenoble Alpes, IRIG, Laboratoire Biosciences et Bioingénierie pour la Santé, UA 13 INSERM-CEA-UGA, 38000 Grenoble, France

[4] Department of Pathology, Saint-Louis Hospital (Assistance Publique-Hôpitaux de Paris), Paris, France

[5] Department of Urology, Saint-Louis Hospital (Assistance Publique-Hôpitaux de Paris), Paris, France

[6] Department of Medical Oncology, Saint-Louis Hospital (Assistance Publique-Hôpitaux de Paris), Paris, France

Background:

The 21st century has witnessed the rise of immunotherapy as a cornerstone of cancer treatment, profoundly reshaping the management of many solid tumors. Among them, clear cell renal cell carcinoma (ccRCC) has emerged as one of the first malignancies to benefit from immune checkpoint inhibitors (ICIs) targeting PD-1/PD-L1 and CTLA-4 pathways. Yet, despite its exceptionally high level of immune infiltration, ccRCC remains paradoxically resistant to immunotherapy: only a subset of patients achieves durable responses, and no reliable biomarker currently predicts therapeutic outcome. This clinical paradox highlights the critical influence of the tumor microenvironment (TME), in modulating immune activation, exclusion, and exhaustion.

To better understand these interactions and improve response prediction, preclinical models that faithfully recapitulate both the structural and immune complexity of ccRCC are needed. Conventional two-dimensional (2D) cultures lack spatial and immune context, whereas animal models cannot reproduce autologous human immunity within clinically relevant timeframes. Three-dimensional (3D) tumor models have addressed part of

this gap by preserving epithelial and microenvironmental diversity, yet their static nature precludes modeling of dynamic immune trafficking and cytokine signaling.

Microfluidic "tumor-on-chip" technologies now offer a promising next step by enabling continuous perfusion, immune cell circulation, and therapeutic delivery under physiologically relevant flow. Such systems provide an opportunity to functionally model immunotherapy response in an autologous, patient-specific context, bridging the gap between static organoid cultures and in vivo complexity.

Methods:

Building upon a previously validated patient-derived, immune-reinfiltrated ccRCC spheroid model, we developed an autologous microfluidic platform combining tumor spheroids, reinfiltrated tumor-infiltrating lymphocytes (TILs), and circulating peripheral blood mononuclear cells (PBMCs). Transcriptomic modeling of BRB-seq datasets guided the inclusion of ten spheroids per condition to ensure representative tumor heterogeneity. The system was first calibrated using RCC cell lines to validate PD-L1–dependent responses and to confirm immune infiltration under flow. The autologous on-chip configuration was then implemented for two patients using their matched tumor and immune cells.

Results:

We successfully established an immune-competent, autologous ccRCC-on-chip model providing functional readouts within six days from surgery. Multiple analytical endpoints were developed, including confocal imaging of retrievable spheroids, cytokine quantification in the circulating medium, and 37-color spectral flow cytometry of immune cells after 72 hours of perfusion. Under these dynamic conditions, activated autologous PBMCs trafficked and infiltrated immune-reconstituted spheroids, both in control and anti–PD-L1 (avelumab)–treated settings. Cytokine concentrations were within detection ranges and showed treatment-dependent variations. Post-culture recovery enabled deep immune phenotyping, confirming the feasibility of high-dimensional single-cell analysis.

Conclusions:

This work establishes a rapid, fully autologous, and immunotherapy-compatible ccRCC-on-chip model that enables dynamic assessment of immune–tumor interactions under checkpoint blockade. The workflow, achievable within three days from tumor sampling, integrates microfluidic perfusion with patient-derived material, offering a practical and physiologically relevant tool for functional precision immuno-oncology, individualized prediction of immunotherapy response, or novel immunotherapy testing.

BACKGROUND

Renal cell carcinoma (RCC) represents 2–3% of adult cancers, accounting for over 430,000 new cases and 156,000 deaths worldwide in 2022 (1). Clear cell RCC (ccRCC) is the predominant subtype, comprising 70–75% of cases, and displays aggressive behavior with frequent metastatic presentation (2) (3). Surgical resection remains the standard treatment for localized disease, while systemic therapy is required in the metastatic setting. Over the past two decades, therapeutic advances have successively transitioned from cytokine-based regimens to VEGF/mTOR-targeted agents and, more recently, immune checkpoint inhibitors (ICIs) administered alone or in combination with tyrosine kinase inhibitors (TKIs) or CTLA-4 blockade (e.g. CheckMate 025, 214; KEYNOTE-426; CheckMate-9ER and CLEAR trials) (4–12). These strategies have significantly improved patient outcomes, and immunotherapy is now gaining ground beyond the metastatic setting, with adjuvant ICI approved following nephrectomy in high-risk patients (13,14).

Although ICIs have markedly improved survival, up to 40% of patients derive no benefit, and durable complete responses remain uncommon (~10–15%) (15). Both primary and acquired resistance constrain efficacy, driven by multiple mechanisms including insufficient T-cell infiltration, the emergence of alternative inhibitory checkpoints, and immunosuppressive stromal or myeloid components (16). Predictive biomarkers such as PD-L1 expression, tumor mutational burden, or gene expression signatures have shown inconsistent performance, leaving clinicians without reliable tools to stratify responders.

Paradoxically, ccRCC ranks among the most immune-infiltrated solid tumors yet exhibits only partial sensitivity to ICIs (17). This “immune-infiltrated but refractory” phenotype makes ccRCC a particularly valuable model for studying resistance to immunotherapy. Dissecting these mechanisms and developing translational tools to predict therapeutic response requires preclinical systems that faithfully reproduce native tumor–immune interactions.

Conventional two-dimensional cultures are easy to manipulate but lack the structural and cellular complexity of human tumors. Animal models, including patient-derived xenografts, provide an in vivo context but lose the human immune component unless humanized, which is costly and time-consuming (18). Organoid and patient-derived tumor models preserve tumor heterogeneity and allow the recapitulation of key tumor features (19). However, they remain static and poorly suited for dynamic immune co-culture. Microfluidic “tumor-on-chip” technologies address these limitations by allowing perfused 3D architectures that support immune-cell circulation, cytokine gradients, and real-time imaging of immune infiltration, features absent from conventional static systems (20).

Building upon our previously described patient-derived, immune-reconstituted ccRCC spheroid model that preserves the tumor’s epithelial, stromal, and immune compartments

(Liangwei Yin, 2025), the present study sought to expand its functional and translational potential through microfluidic integration. We first validated the model's sensitivity to PD-L1 blockade using fluorescently labeled RCC spheroids derived from engineered cell lines, enabling real-time monitoring of spheroid integrity under allogeneic co-culture and quantification of PD-L1–mediated protection. A spatially heterogeneous version of the model was then established to assess intra-spheroid variability in PD-L1 expression and its impact on immune–tumor interactions.

We next reused transcriptomic data from the autologous ccRCC spheroid model to estimate the minimal number of spheroids required to achieve representative sampling of the parental tumor. Guided by these insights, we designed a robust and reusable microfluidic chip optimized for the integration of patient-derived spheroids with autologous tumor-infiltrating lymphocytes (TILs), allowing continuous perfusion of medium, immune cells, and therapeutic antibodies.

Finally, we demonstrated that circulating immune cells can infiltrate trapped spheroids under flow, that cytokine release can be directly quantified in chip effluents with or without PD-L1 blockade, and that a complete autologous workflow, from fresh tumor dissociation to chip-based co-culture combining spheroids, TILs, and PBMCs, can be successfully implemented. Using this setup, spectral cytometry and multiplex cytokine assays were performed on two patients, establishing a proof of feasibility for fully autologous, immune-competent tumor-on-chip assays.

RESULTS

FUNCTIONAL CALIBRATION AND SENSITIVITY ASSESSMENT OF PD-L1–DEPENDENT IMMUNE RESPONSES IN RCC SPHEROIDS

1. *FUNCTIONAL CALIBRATION USING ISOGENIC PD-L1 WT AND KO RCC7 SPHEROIDS*

To functionally validate immune checkpoint interactions, we focused on the PD-1/PD-L1 axis, a key reference in immuno-oncology. Among renal carcinoma cell lines, RCC7 was selected for its strong basal PD-L1 expression, providing a suitable basis for isogenic manipulation. A PD-L1 knockout (KO) line was generated using CRISPR/Cas9, and both parental (WT) and KO lines were stably labeled with fluorescent reporters (mCherry and/or GFP) for real-time tracking and future dual-color assays. Single-cell cloning ensured homogeneity, and PD-L1 loss was confirmed by flow cytometry and Western blotting.

This isogenic pair provided a reproducible framework to quantify PD-L1–dependent protection from immune killing before extending the approach to patient-derived spheroids. PD-L1 WT and KO RCC7 spheroids expressing mCherry were co-cultured with allogeneic IL-15–activated PBMCs (E:T = 10:1) in the presence or absence of the anti-PD-L1 antibody

avelumab (10 µg/mL). Live imaging with the IncuCyte system enabled kinetic tracking of red fluorescence over 96 h as a quantitative readout of cytotoxicity.

Representative images (Fig. 1C) show progressive fluorescence loss during co-culture, consistent with immune-mediated tumor destruction. Despite identical seeding, PD-L1 KO spheroids appeared smaller and lost fluorescence within 48 h, whereas WT spheroids retained strong signal up to 72 h, indicating PD-L1–mediated protection. Avelumab accelerated fluorescence decline in WT spheroids, consistent with restored immune killing.

Normalized red-fluorescence intensity over time (Fig. 1A) provided a dynamic measure of spheroid integrity (t/t_0), reflecting the fraction of viable tumor cells.

In the absence of PBMCs (dotted lines), both PD-L1 WT (dark blue) and KO (light blue) spheroids showed a modest fluorescence increase over 96 h, consistent with baseline growth. Co-culture with IL-15–activated PBMCs (solid lines) instead caused fluorescence loss, reflecting immune-mediated killing, most pronounced in PD-L1 KO spheroids, which lost signal within 48–72 h. PD-L1 WT spheroids displayed delayed, partial decline, indicating checkpoint-mediated protection. Avelumab (dark yellow) markedly enhanced killing of PD-L1 WT spheroids, reducing persistence toward KO levels, whereas it had minimal effect in PD-L1 KO spheroids (light yellow), consistent with the absence of target PD-L1.

The overall pattern was conserved across donors, although kinetics varied, with donor 3 showing slower cytotoxicity and a weaker Avelumab response.

PBMC-mediated tumor killing was quantified by the fluorescence decay area under the curve ($AUC_{0–96}$ h): high AUC = limited killing; low = efficient cytotoxicity (Fig. 1B). A mixed-effects model confirmed a significant Treatment × PD-L1 interaction ($p < 0.001$). Avelumab reduced AUC only in PD-L1 WT spheroids ($97.5 \pm 2.4 \rightarrow 63.8 \pm 11.1$, $p < 0.001$), a 34 % fluorescence loss, whereas PD-L1 KO spheroids were unaffected ($32.6 \pm 8.6 \rightarrow 39.1 \pm 9.6$, n.s.). Baseline comparison showed PD-L1 expression conferred clear protection ($\Delta = +64.9 \pm 2.4$, $p < 0.0001$). After Avelumab, WT spheroids approached but did not reach KO/no-treatment levels ($\Delta = +32.2 \pm 2.5$, $p < 0.0001$); the TOST test (±3.26 AUC; 90 % CI [28.1, 36.4]) confirmed only partial reversal of PD-L1–mediated resistance.

Thus, PD-L1 expression protects RCC7 spheroids from PBMC killing, and Avelumab restores roughly half of this sensitivity in 3D co-culture.

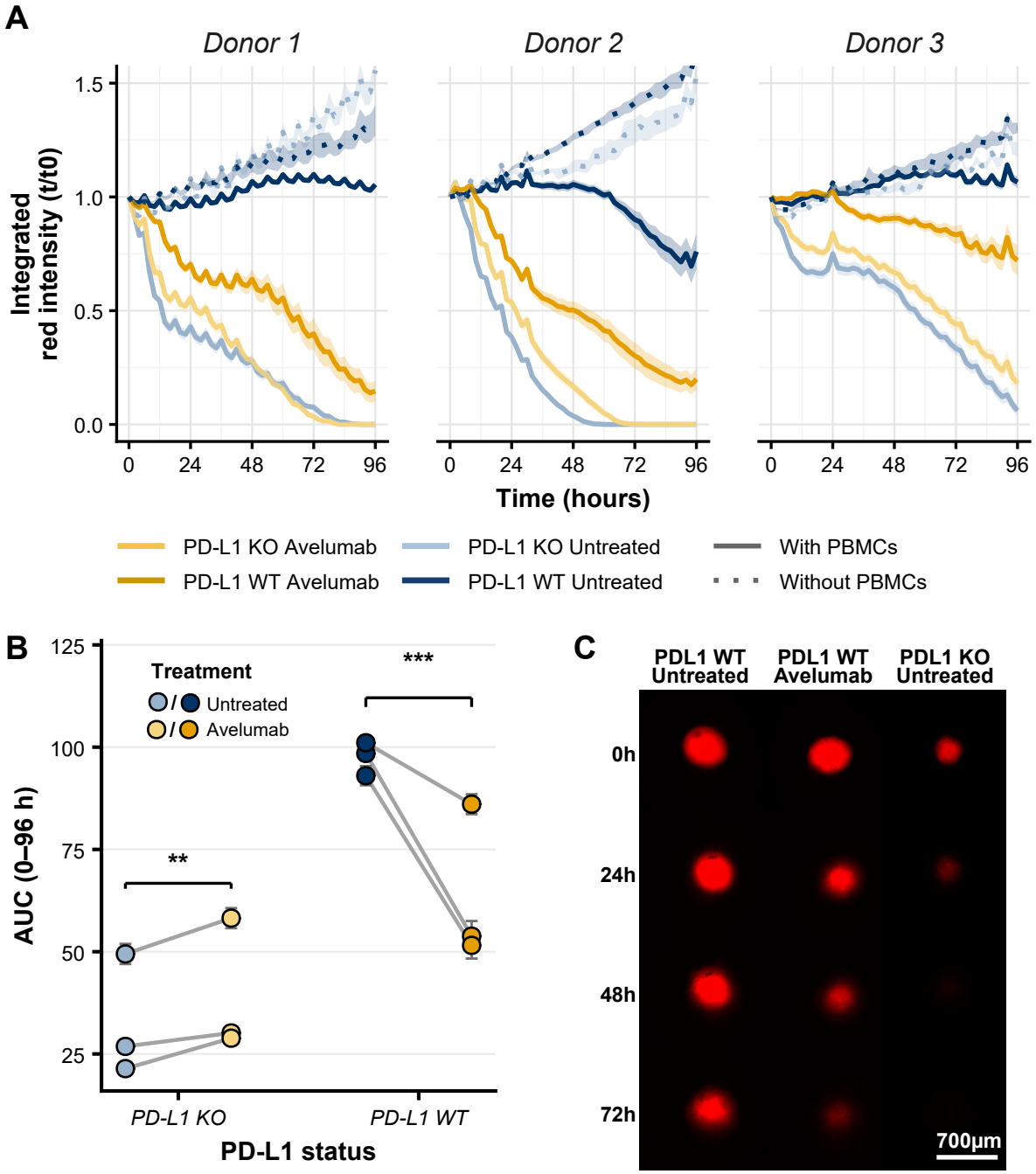

Figure 1: *PD-L1 expression protects RCC spheroids from PBMC-mediated killing, reversed by Avelumab.*
(A) Time-lapse kinetics of PD-L1 WT and KO RCC7 spheroids expressing mCherry, co-cultured with allogeneic IL-15–activated PBMCs (E:T = 10:1) ± Avelumab (10 µg/mL). Curves show mean red-fluorescence ratio to baseline (t/t_0 ± SEM; n = 3 donors). Loss of fluorescence indicates immune-mediated cytotoxicity. (B) Area under the curve ($AUC_{0–96}$ h) quantifies cumulative spheroid persistence. Each dot = donor mean ± technical SEM; lines connect paired donors. Linear mixed-effects model with donor as random intercept (Kenward–Roger correction). (C) Representative mCherry fluorescence images of PD-L1 WT and KO spheroids after co-culture with PBMCs (Donor 2).

2. *SENSITIVITY OF THE SPHEROID CO-CULTURE ASSAY TO GRADED PD-L1 EXPRESSION*

Having established that PD-L1 expression confers a quantifiable advantage against immune cytotoxicity, we next tested how this protection scales with the fraction of PD-L1$^+$ tumor cells within a spheroid. Mixed RCC7 spheroids containing defined ratios of PD-L1 WT and KO cells were co-cultured with IL-15–activated allogeneic PBMCs (E:T = 10:1) ± Avelumab (10 µg/mL). Red fluorescence (mCherry) was monitored over time as a proxy for tumor persistence (Fig. 2A).

In untreated conditions, higher PD-L1$^+$ fractions produced slower fluorescence loss, indicating resistance to PBMC-mediated killing. Avelumab progressively restored cytotoxicity with increasing PD-L1$^+$ content, becoming evident from 50 % PD-L1$^+$ onward. At 25 %, recovery was inconsistent across donors; donor 2 displayed accelerated killing that likely masked PD-L1-dependent differences. Representative images (Fig. 2C) illustrate fluorescence persistence with increasing PD-L1 proportion and its loss upon Avelumab treatment.

Quantification of normalized fluorescence (t/t_0) by area under the curve (AUC; Fig. 2B) confirmed a strong main effect of PD-L1 proportion ($F_{1,84} = 80.7$, $p < 10^{-13}$, Fisher's exact test) and a significant Treatment × PD-L1 interaction ($F_{1,84} = 22.5$, $p < 10^{-5}$). Avelumab had no impact at 0–25 % PD-L1$^+$ (n.s.) but significantly reduced AUC at ≥ 50 % PD-L1$^+$ ($\Delta \approx 20$–26 AUC units; $p \leq 0.05$). The absence of effect at 25 % aligns with donor 2's high cytotoxic baseline.

Thus, PD-L1 expression provides graded protection from immune killing, efficiently counteracted by Avelumab only when PD-L1$^+$ cells represent at least half of the spheroid. Although these PD-L1 levels exceed those typical of ccRCC (<10%), they define the threshold required to detect functional modulation under allogeneic conditions.

Spheroids containing ≤10% PD-L1$^+$ cells (1, 2,5, 5 and 10 were tested) showed no measurable modulation of fluorescence kinetics (data not shown). These observations likely reflect the assay's detection limits and donor-specific effector potency under these conditions. Importantly, these results do not necessarily predict PD-L1 behavior in autologous contexts, where tumor and immune compartments have co-evolved and checkpoint interactions may operate at lower expression thresholds.

Overall, this experiment demonstrates the assay's capacity to resolve graded checkpoint interactions and establishes a methodological basis for subsequent analyses in autologous patient-derived models.

Next, to enable spatially resolved analysis of immune–tumor interactions under identical environmental conditions, we engineered composite spheroids containing juxtaposed

PD-L1^{+} and PD-L1^{-} regions within a single 3D structure.

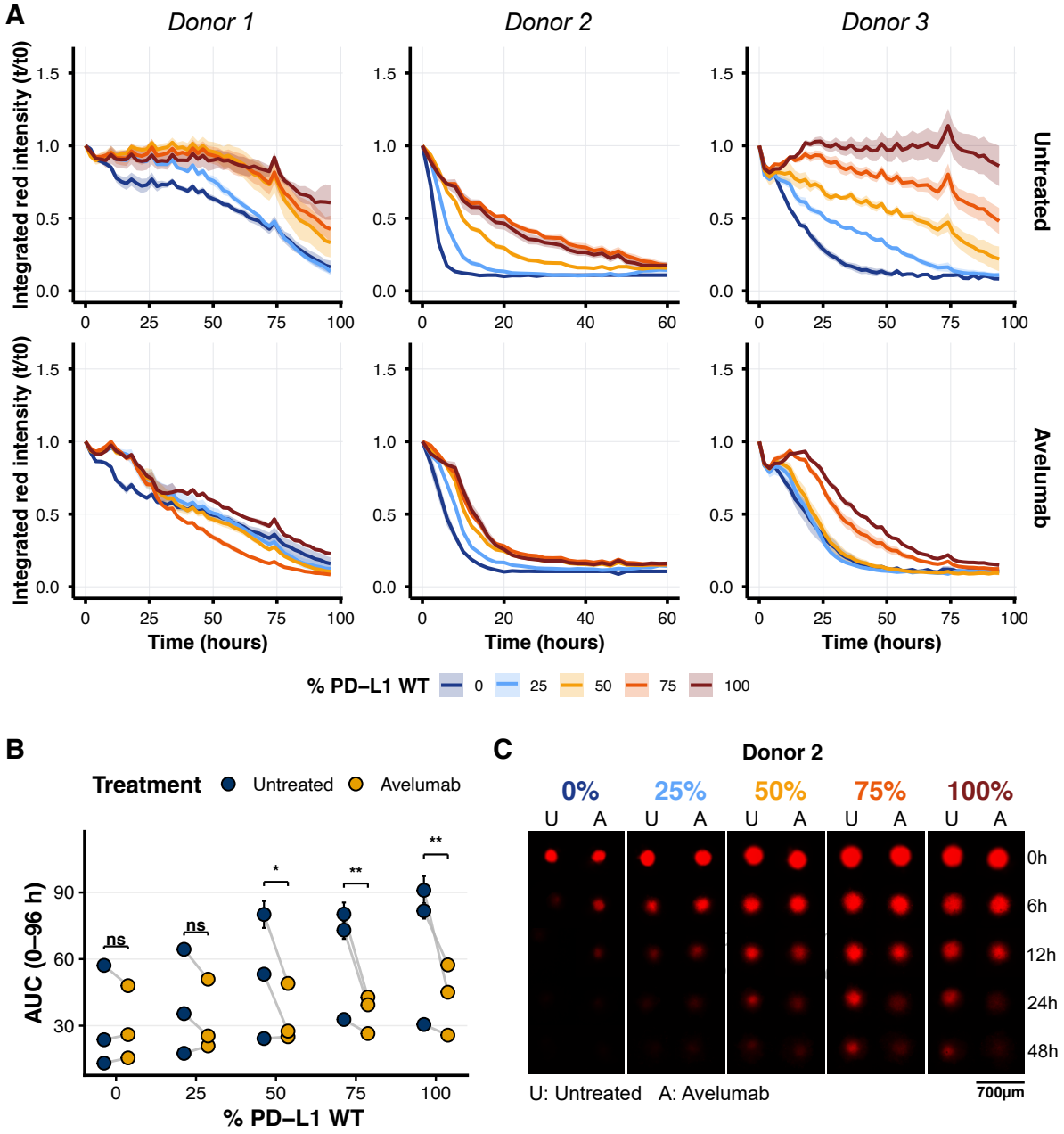

Figure 2: *PD-L1–dependent modulation of tumor spheroid killing by Avelumab.*
(A) Mixed RCC7 spheroids containing defined fractions of PD-L1^{+} (WT) cells (0–100 %) were co-cultured with allogeneic IL-15–activated PBMCs (E:T = 10:1). Red fluorescence (mCherry) was tracked over time as a proxy for residual tumor mass. Curves represent mean normalized fluorescence (t/t_0 ± SEM; n = 3 donors). (B) Quantification of cytotoxic activity expressed as the area under the curve ($AUC_{0–96}$ h) for each donor and condition. Statistical significance was assessed using a linear mixed-effects model (donor as random intercept), followed by pairwise post hoc contrasts between untreated and Avelumab-treated conditions at each PD-L1 fraction. (C) Representative fluorescence images (Donor 2) at indicated time points. PD-L1^{+} fraction and treatment are shown above panels (U, untreated; A, Avelumab). Scale bar = 700 µm.

3. *SPATIALLY RESOLVED ASSESSMENT OF PD-L1–DEPENDENT PROTECTION USING A FUSION SPHEROID MODEL*

To evaluate the spatial contribution of PD-L1 expression to immune protection, we established a two-compartment spheroid fusion model combining fluorescently distinct ccRCC populations. Each fusion consisted of a PD-L1 KO spheroid expressing mCherry (red) and a PD-L1 WT spheroid co-expressing mCherry and GFP (red+green). After 72 h of preformation, both spheroids were fused for 24 h to generate a stable chimeric structure with red-only (PD-L1$^-$) and red + green (PD-L1$^+$) compartments. Double-KO fusions (mCherry$^+$/GFP$^+$ + mCherry$^+$/GFP$^-$) served as negative controls. Fused spheroids were then co-cultured for 96 h with IL-15–activated PBMCs (E:T = 10:1).

Compartment-specific cytotoxicity was quantified from time-lapse images. Mean red fluorescence intensity (mCherry) within each region, normalized to t_0, served as a proxy for viable tumor mass. Differential persistence between compartments was summarized by the integrated ΔAUC (AUC_green – AUC_red), representing the cumulative survival advantage of the green region.

In untreated fusions, the PD-L1$^+$ (green) compartment displayed a clear survival advantage over the PD-L1$^-$ (red) compartment (Fig. 3A middle), resulting in slower red-signal loss (Fig. 3B upper) and a positive ΔAUC (dark blue; median = 10.6 [2.4]) compared with double-KO controls (light blue; median = 1.0 [2.4]; p = 0.002, Wilcoxon). No difference was observed between zones in PD-L1 KO/KO spheroids (Fig. 3A left; 4B upper, dotted). These data confirm that PD-L1 expression locally protects tumor cells from PBMC-mediated killing.

Upon Avelumab treatment, this protection was abolished: fluorescence in the green zone declined as rapidly as in the red zone (Fig. 3A right; 4B lower), and ΔAUC values in treated PD-L1 KO/WT spheroids (dark yellow; median = –2.9 [1.6]) decreased relative to untreated controls (p = 0.004), reaching levels similar to PD-L1 KO/KO fusions (median = –0.7 [0.8]). As expected, Avelumab had no effect in PD-L1 KO/KO spheroids (light yellow vs light blue, p = 0.25).

Overall, this experiment demonstrates that the spheroid system can resolve spatially restricted PD-L1–mediated immune protection and its neutralization by checkpoint blockade. These results validate the model as a sensitive, spatially resolved assay for quantifying immune–tumor interactions in 3D.

However, all experiments so far were performed under static conditions, limiting medium renewal, immune-cell circulation, and temporal control of treatments. To overcome these constraints and extend assay flexibility, we next adapted the model into a perfusable microfluidic platform enabling continuous medium flow and controlled immune co-culture.

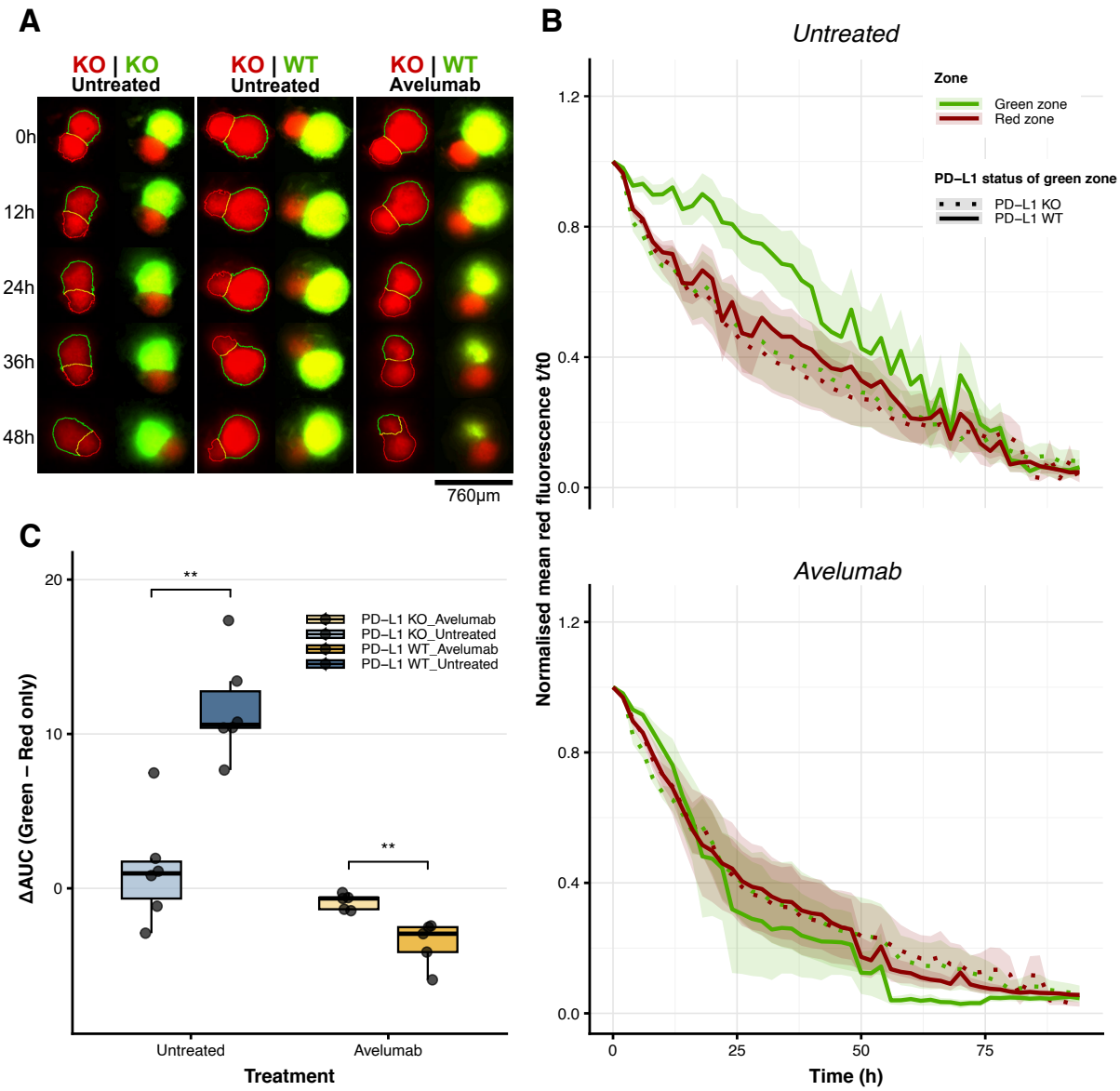

Figure 3: *PD-L1 expression protects tumour zones from immune destruction in fused ccRCC spheroids.*
*(A) Representative time-lapse images of fused RCC7 spheroids co-cultured with allogeneic IL-15–activated PBMCs (E:T = 10:1). Each fusion combined a PD-L1⁻ spheroid (KO, mCherry⁺) with either a PD-L1⁺ spheroid (WT, mCherry⁺/GFP⁺; columns 2–3) or a second PD-L1⁻ spheroid as a double-KO control (mCherry⁺/GFP⁺ + mCherry⁺/GFP⁻; column 1). For each condition, red-fluorescence images show segmentation masks for PD-L1⁻ (red) and PD-L1⁺ (red + green) zones (left), and merged channels illustrate segmentation accuracy (right). Scale bars = 760 µm. (B) Mean red-fluorescence intensity (normalized to t_0) in PD-L1⁺ (green) and PD-L1⁻ (red) compartments over time (three pooled PBMC donors). Solid lines represent PD-L1⁺/PD-L1⁻ fusions; dotted lines indicate double-KO controls. Shaded ribbons denote SEM. (C) Differential fluorescence between PD-L1⁺ and PD-L1⁻ compartments, expressed as ΔAUC (green – red). Each dot represents one well (two donors pooled); boxplots show median ± IQR. P values from two-sided Wilcoxon rank-sum tests * p<0.05, ** p < 0.01).*

INTEGRATION OF THE MODEL INTO A DYNAMIC MICROFLUIDIC PLATFORM

1. *DETERMINATION OF AN OPTIMAL NUMBER OF PATIENT-DERIVED SPHEROIDS.*

In our previously-described model, patient-derived immunocompetent spheroids were generated directly from freshly dissociated ccRCC tumors, without any 2D culture step, to preserve the cellular heterogeneity and transcriptional state of the parental tissue. This setup restored autologous immune–tumor interactions *ex vivo* while maintaining short culture times to minimize phenotypic drift, we showed in previous work that this model retains key immune components in relevant proportions, immune checkpoint expression and comparable TIDE score to the original tissue.

However, spheroid formation is inherently governed by a stochastic process, driven by physical and biological factors that determine which cells participate in aggregation and which immune cells infiltrate the structure. As a result, individual spheroids from the same patient can display variable immune and stromal compositions, reflecting intratumoral heterogeneity. To quantitatively assess how such variability impacts tumor representativity and chose an appropriate amount of spheroid to include in our chip design, we analyzed how the number of spheroids combined influences their transcriptomic similarity to the parental tumor. Using BRB-seq data from our previous study, we simulated *in silico* pools of increasing spheroid numbers (n = 1–10) and computed the Pearson correlation coefficients (PCC) between each pool and its matched tumor tissue. This analysis allowed us to define the minimal pool size required to capture the transcriptional complexity of the tumor while maintaining experimental feasibility (Fig. 4A–D), serving as a rational basis for subsequent microfluidic co-culture assays.

Transcriptomic similarity between pooled spheroids and the parental tumor tissue increased with the number of spheroids combined (Fig. 4A–C). The most pronounced improvement occurred when increasing from one to three spheroids, after which Pearson correlation coefficients (PCC) progressively reached a plateau. To quantify this convergence, we computed the marginal gain in transcriptomic representativity for each pool size, defined as the change in mean correlation between consecutive pool sizes ($\Delta meanPCC = PCC_n - PCC_{n-1}$). This metric reflects how much additional representativity is gained when adding one more spheroid to the pool. The incremental transcriptomic gain from adding one spheroid to the pool (ΔmeanPCC) rapidly decreased, plateauing at 4–6 spheroids for Patients 1 and 2, and around 8 spheroids for Patient 3 (Fig. 4D), suggesting a patient-specific saturation in transcriptomic convergence. The 0.005 ΔPCC threshold, used to define this plateau, was reached with 5 spheroids for Patients 1 and 2, and with 8 spheroids for Patient 3.

To benchmark these results, we compared the transcriptomic correlation of spheroid pools to that observed between three replicate tumor fragments from the same patient.

While pooling significantly improved spheroid representativity, the mean PCC values of even the largest pools remained below the tumor-tumor correlation for Patients 1 and 2 (0.791 and 0.974, respectively). In contrast, for Patient 3, pooling just 4–5 spheroids was sufficient to reach a similar level of correlation (tumor-tumor PCC = 0.801), indicating lower variability and higher intrinsic representativity among spheroids from this patient. This indicates that the spheroid model captures most of the transcriptional complexity of the parental tumor, though the degree of fidelity remains patient dependent.

Overall, the number of spheroids required to approach the transcriptomic plateau ranged from five to eight, providing an experimental reference for balancing representativity and practicality. These values are not absolute and may vary depending on tumor composition, cell viability, or the method of spheroid formation. Nevertheless, they define an order of magnitude that can guide experimental design in similar patient-derived immunocompetent models, approximately five to ten spheroids of 10,000 cells each, reconstituted with their autologous immune components. Based on these findings, we designed our microfluidic chip to host ten spheroids per chamber, corresponding to the upper end of this representativity range. This configuration should ensure optimal fidelity while maintaining a manageable format for dynamic co-culture and immune–tumor interaction studies under flow.

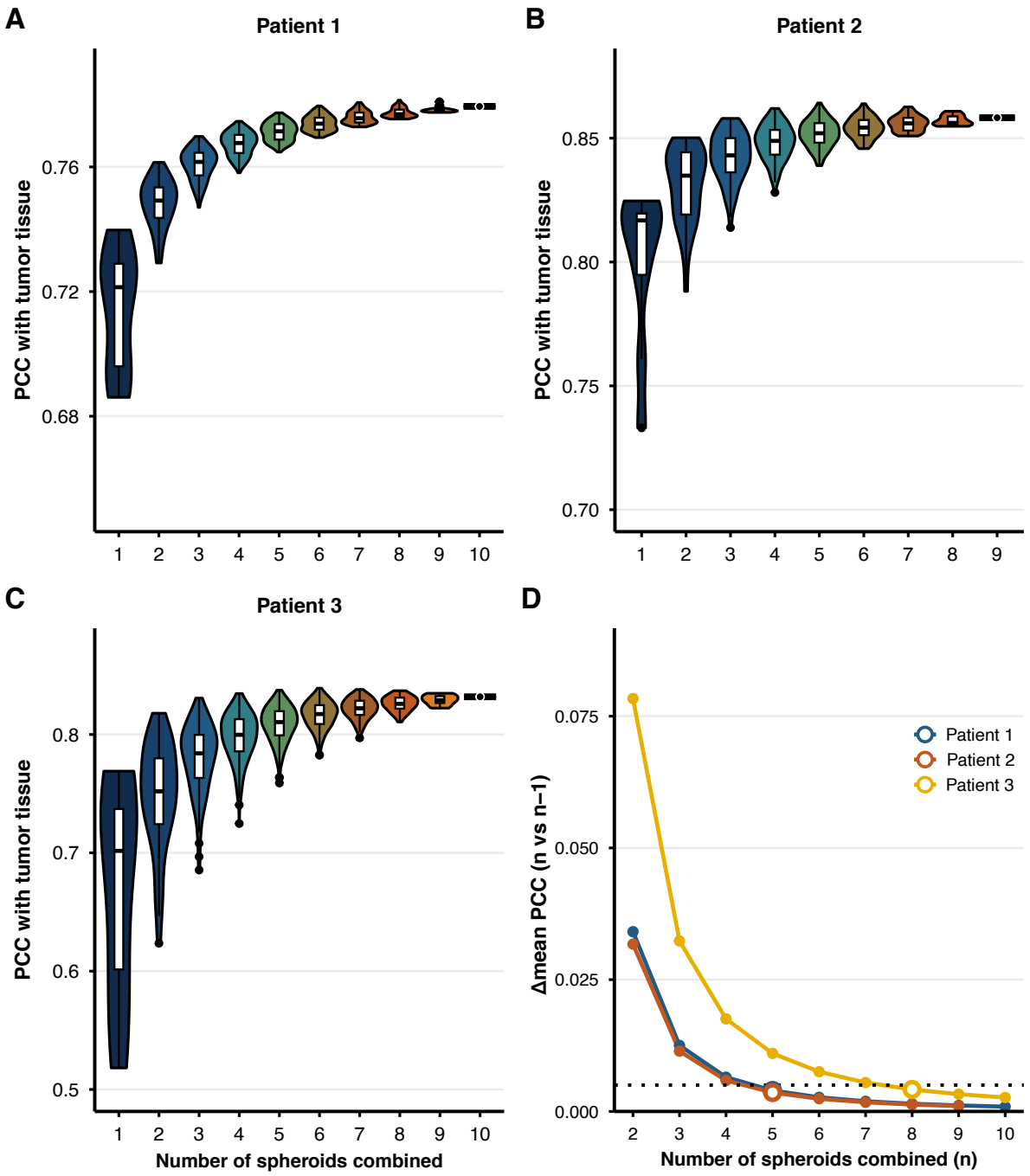

Figure 4 : *Transcriptomic representativity of pooled ccRCC spheroids. (A–C) Pearson correlation coefficients (PCC) between parental tumor tissue and simulated pools of 1–10 spheroids from three patients (P1–P3). Each violin shows the PCC distribution across all possible spheroid combinations for a given pool size. (D) Marginal gain in representativity ($\Delta meanPCC_n = PCC_n - PCC_{n-1}$) plotted as a function of pool size. The dotted line indicates the 0.005 ΔPCC threshold, beyond which additional spheroids provide negligible improvement. Data are derived from BRB-seq transcriptomic profiles of ten individual spheroids per patient (nine for Patient 2)*

2. *CHIP DESIGN AND SETUP*

To expand the versatility of our immunocompetent spheroid model, we developed a reusable microfluidic platform enabling continuous medium perfusion and controlled immune co-culture (Fig. 5). The chip design was adapted from the hydrodynamic bypass trapping

principle of Quintard et al. (21), which exploits local flow resistance to direct spheroids into available traps. Each serpentine circuit contained ten U-shaped bypass traps in series, allowing sequential capture and perfusion of up to ten spheroids per track (Fig. 5B). Five parallel tracks were integrated within a single cyclic olefin copolymer (COC) chip (85 × 54 mm; Fig. 5C), providing a total capacity of 50 spheroids across five independent conditions. Channel dimensions were optimized for spheroids of 400–600 µm, ensuring stable immobilization and homogeneous low-shear flow compatible with prolonged culture.

Perfusion was driven by a multichannel syringe pump operating in aspiration mode (Fig. 5A), keeping inlet reservoirs accessible for medium renewal, sequential drug addition, or immune-cell injection without interrupting flow. Inlet wells were fabricated from shortened 5 mL syringes (4 mL final volume) compatible with direct pipette loading. Pre-formed spheroids were injected into each inlet reservoir at 50 $\mu L \cdot min^{-1}$; chip geometry automatically guided and distributed them into individual traps within the target size range.

After loading, the chip and aspiration system were placed in a standard cell-culture incubator (37 °C, 5 % CO_2) for continuous perfusion at 1 $\mu L \cdot min^{-1}$. Trapped spheroids were visualized under a stereomicroscope, and correct positioning was verified before co-culture (Fig. 5D). The COC material and MicroAmp™ film sealing confer robustness and reusability: a single chip was used for more than thirty independent experiments without performance loss. The film closure also allows recovery of individual traps at the end of culture.

Fluorescence microscopy was used for illustration: panel D shows brightfield imaging of a trapped $mCherry^+$ RCC7 spheroid; panel E, red fluorescence; and panel F, perfused fluorescent immune cells (cyan) contacting the spheroid surface. Together, these features make the device a simple yet versatile platform for reproducible spheroid trapping, long-term culture, and facile on-chip immune manipulation.

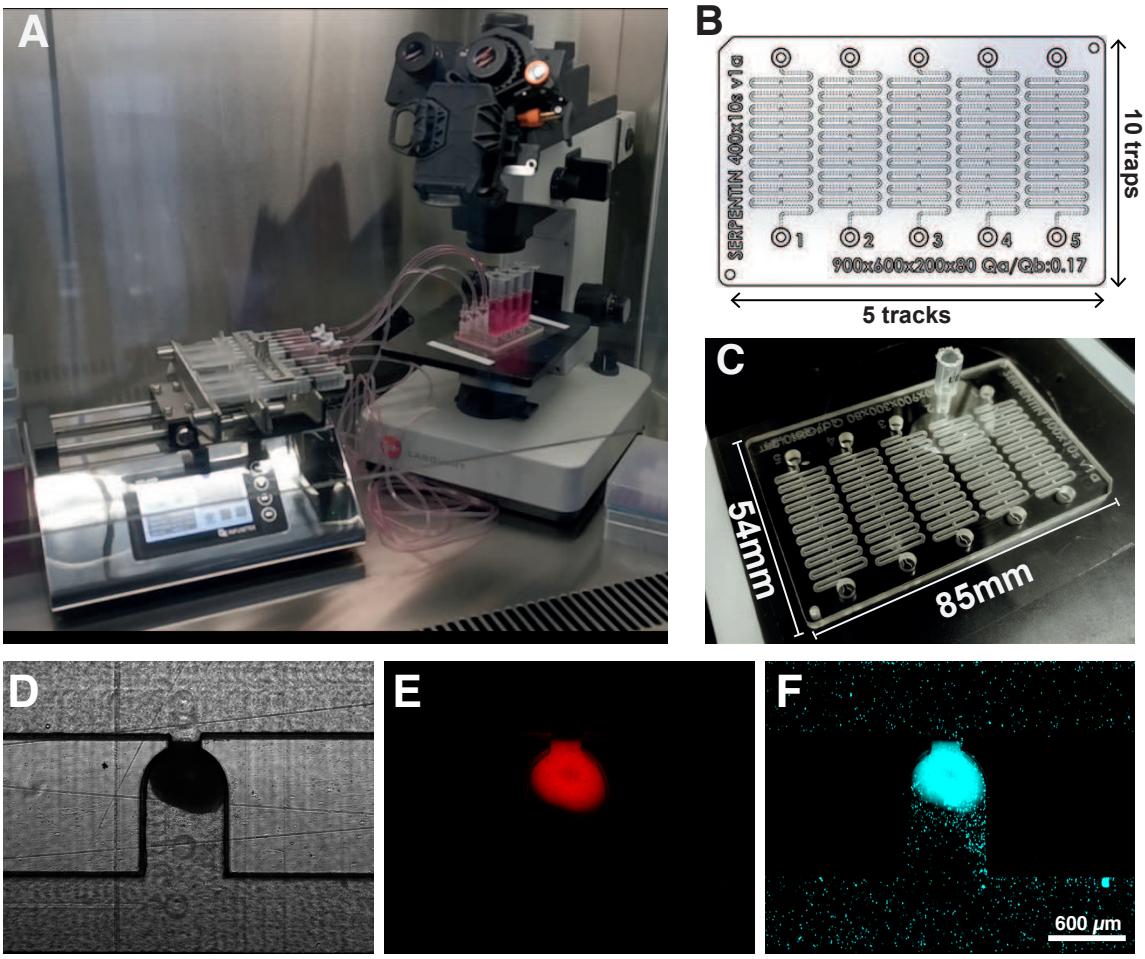

Figure 5: *Integration of tumor spheroids into a reusable microfluidic perfusion platform. (A) Experimental setup showing the microfluidic chip connected to a multichannel syringe pump operating in aspiration mode, enabling continuous medium perfusion and direct access to inlet reservoirs for medium renewal or cell addition. (B) Computer-assisted design of the chip layout based on hydrodynamic bypass trapping, with ten sequential traps per serpentine track. (C) Fabricated cyclic olefin copolymer (COC) chip (85 × 54 mm) containing five independent circuits (50 traps total). (D) Brightfield image of an RCC7 spheroid immobilized in a U-shaped hydrodynamic trap. (E) Fluorescence image of the trapped mCherry^{+} spheroid. (F) Perfusion of CellTrace-Far-Red–labeled PBMCs through the microchannel, showing circulating immune cells contacting the trapped spheroid under continuous flow. Scale bar = 600 µm.*

After confirming the stability of spheroid trapping and medium perfusion in the microfluidic platform, we next assessed whether circulating lymphocytes could effectively reach and infiltrate immobilized spheroids under dynamic flow. Unlike static co-cultures, perfused systems continuously expose cells to shear stress and constrained trajectories, potentially limiting effector–target interactions. Demonstrating preserved infiltration capacity under these conditions was therefore a prerequisite for subsequent functional assays.

2. *DYNAMIC INFILTRATION OF ACTIVATED LYMPHOCYTES INTO TUMOR SPHEROIDS UNDER FLOW CONDITIONS*

To assess whether circulating lymphocytes could reach and infiltrate spheroids under

dynamic flow, IL-15–activated PBMCs were pre-stained with CellTrace Violet (CTV) and perfused through the chip at a density of 10^6 cells per circuit for 72 h. Each track contained pre-trapped mCherry$^+$ RCC7 spheroids maintained under continuous perfusion. After co-culture, spheroids were retrieved by gentle back-flushing with PBS, fixed, and processed for confocal microscopy. CTV fluorescence enabled visualization of immune cells within tumor spheroids after 24 h of passive optical clearing, allowing volumetric imaging of the entire structure with minimal scattering.

This experiment was designed as a technical proof of concept to validate the workflow's compatibility with immune-cell perfusion, spheroid recovery, and 3D imaging, rather than to draw biological comparisons between treatment conditions. Three spheroids per condition (untreated and Avelumab-treated) were analyzed to illustrate the method's feasibility.

After 72 h of co-culture, spheroids remained compact and viable, as indicated by persistent mCherry signal in tumor cells (Fig. 6A). Circulating IL-15–activated lymphocytes labeled with CTV were readily detected throughout the spheroid volume (Fig. 6B), confirming effective infiltration under flow. Immune cells were segmented using Fiji's 3D Maxima Finder and Spot Segmentation tools, yielding consistent performance as illustrated by 3D reconstructions (Fig. 6D–E).

To quantify infiltration depth, we computed the Euclidean Volume Fraction (EVF), a normalized radial metric ranging from 0 (surface) to 1 (center). Concentric iso-depth layers ($\Delta EVF = 0.05$) were generated from the spheroid mask (Fig. 6C, yellow contours), and mean CTV$^+$ cell density was calculated per layer (Fig. 6F). Analyses were performed on three spheroids per condition to derive representative radial profiles.

In untreated spheroids (blue), immune-cell infiltration showed a mean density of 0.036 a.u. and a median depth of EVF = 0.4, indicating that half of the cumulative signal was within the outer half of the spheroid. Density peaked at 0.0457 a.u. (EVF = 0.5) and decreased toward both surface and core, corresponding to a 1.5-fold reduction between outer ($EVF \leq 0.2$) and inner ($EVF \geq 0.8$) regions.

Under Avelumab (yellow), the overall immune-cell density appeared lower (0.025 a.u., 0.68× vs untreated), and the distribution more homogeneous, with a reduced surface-to-core ratio (1.48 → 0.62) and decreased standard deviation (0.0072 → 0.0051 a.u.). The profiles intersected near $EVF \approx 0.85$, suggesting deeper but more uniform infiltration. These trends should not be overinterpreted given the single-donor origin and absence of biological replicates, and are reported here to illustrate the analytical workflow.

To complement these profiles, individual lymphocyte positions were mapped to compute full depth distributions (Fig. 6G). Each lymphocyte was assigned a normalized radial co-

ordinate (0 = surface, 1 = center). Across samples, 5,737 lymphocytes were detected in untreated and 3,269 under Avelumab (–43 %), likely reflecting inter-spheroid variability. Median normalized depths were 0.42 (IQR = 0.46) and 0.55 (IQR = 0.50), with mean lymphocyte volumes (372 ± 172 μm^3 untreated; 345 ± 214 μm^3 Avelumab) matching expected sizes, confirming segmentation accuracy.

Although based on a single donor and limited sample size, these results demonstrate that immune cells can infiltrate tumor spheroids under continuous perfusion and that chip-recovered samples are suitable for volumetric imaging and spatial analysis. This endpoint imaging approach thus serves primarily as a validation of technical feasibility, offering a reliable alternative to real-time on-chip microscopy for studying immune infiltration under dynamic flow.

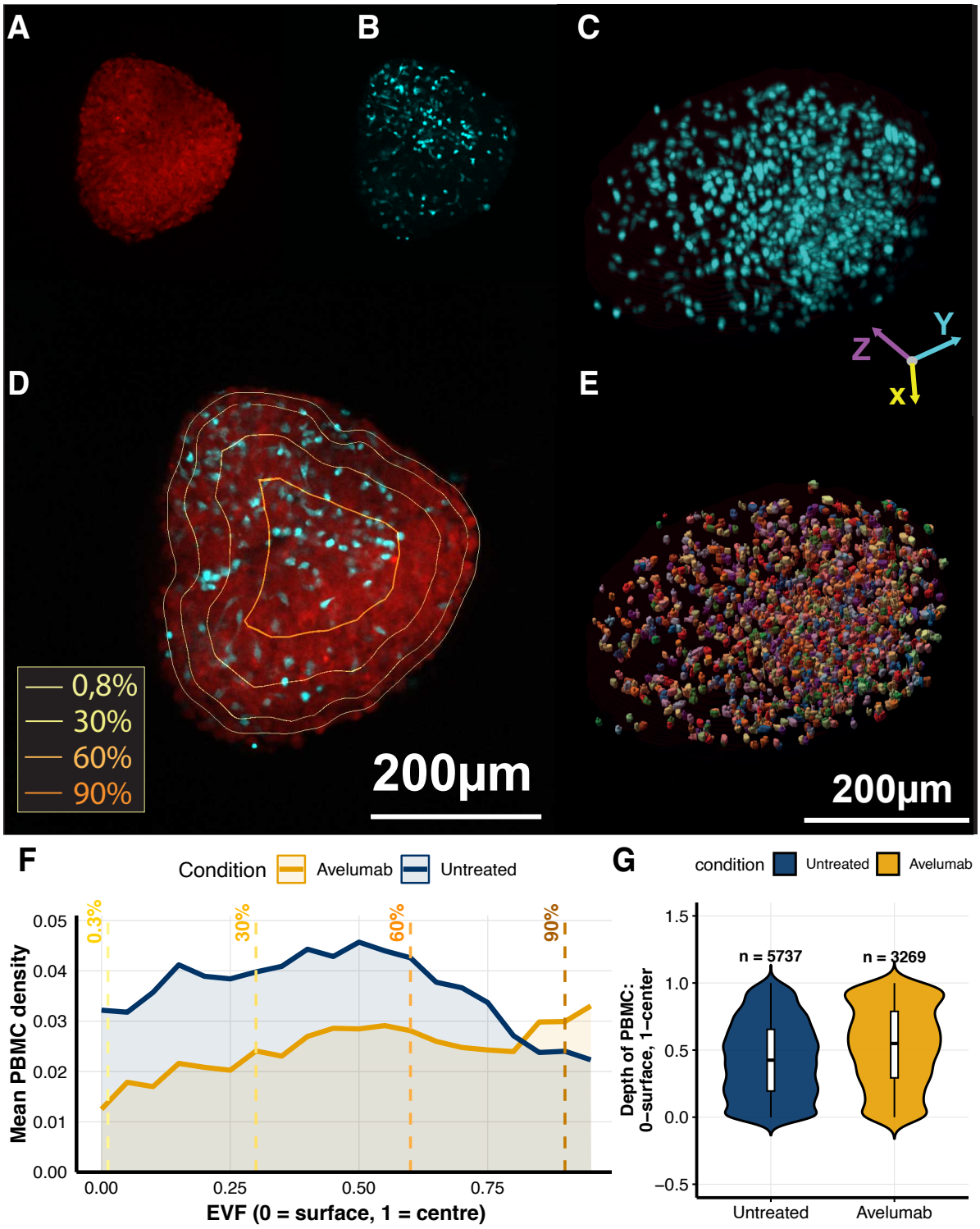

***Figure 6** : Spatial distribution of immune cells within tumor spheroids following on-chip co-culture with PBMCs under continuous flow.*
(A–E) Confocal imaging of an mCherry⁺ RCC7 spheroid after 72 h of co-culture under continuous perfusion with IL-15–activated, CellTrace Violet (CTV)–labeled PBMCs. (A) mCherry fluorescence (tumor cells). (B) CTV signal showing infiltrating PBMCs distributed throughout the spheroid volume. (C) Overlay of mCherry and CTV channels with Euclidean Volume Fraction (EVF) iso-depth contours (yellow), used to quantify immune-cell depth Scale bar = 200 µm (D) Three-dimensional reconstruction of CTV (cyan) and spheroid mask (red) using Napari. (E) 3D rendering of segmented CTV⁺, confirming accurate single-cell detection. Scale bar = 100 µm (F) Representative radial pro-

files of immune-cell density as a function of normalized spheroid depth (EVF; 0 = surface, 1 = center). In untreated spheroids (blue), PBMCs accumulated mainly in outer and intermediate layers, whereas under Avelumab (yellow), appeared deeper and more evenly distributed, based on representative spheroids from a single donor (technical proof of concept, not a biological comparison). (G) Distribution of individual lymphocyte positions normalized from 0 (surface) to 1 (center). Comparable cell sizes and diffuse distributions across the spheroid confirm segmentation accuracy and infiltration under flow. For these proof-of-concept experiments (single donor, n = 3 spheroids per condition), spheroids were optically cleared for 24 h after recovery from the microfluidic chip. Together, these results demonstrate that circulating immune cells can infiltrate 3D tumor spheroids under continuous perfusion and that the workflow enables volumetric imaging and spatial analysis after dynamic co-culture.

3. *PHENOTYPIC AND FUNCTIONAL CHARACTERIZATION OF IMMUNE INFILTRATES IN MICROFLUIDIC CO-CULTURES*

a) Flow cytometry on on-chip cocultures confirms interaction between circulating immune cells and cell line tumor spheroids

After confirming that activated lymphocytes could infiltrate tumor spheroids under continuous flow, we next characterized the immune populations recovered from the microfluidic system. IL-15–stimulated PBMCs from a healthy donor were perfused for three days through RCC7 spheroids under continuous flow (1 $\mu L \cdot min^{-1}$). Three fractions were analyzed by flow cytometry: (1) PBMC controls cultured under identical IL-15 and flow conditions but without spheroids; (2) circulating, non-infiltrated cells collected from the chip outlet; and (3) infiltrated cells dissociated from spheroids after perfusion. All samples were processed with identical enzymatic treatment to avoid bias between conditions.

We first analyzed immune composition (Fig. 7A) to determine how infiltration into tumor spheroids affected effector subset distribution. PBMCs and circulating cells were dominated by $CD4^+$ T cells (≈ 75–80 %), whereas infiltrated spheroids showed an enrichment in $CD8^+$ (≈ 35 %) and NK (≈ 8 %) subsets. This redistribution suggests selective retention of cytotoxic and innate effectors within the tumor compartment, while circulating cells remained phenotypically similar to IL-15–activated PBMCs.

Flow-cytometry phenotyping revealed a progressive activation gradient across compartments (Fig. 7B–D). $CD4^+$ T cells displayed strong upregulation of CD69, PD-1, Ki-67, and ILT2 within infiltrates, consistent with robust activation, proliferation, and induction of inhibitory pathways. $CD8^+$ T cells showed the most pronounced shift, with near-universal CD69 and PD-1 co-expression and high Ki-67 positivity, indicating local proliferation upon tumor contact. NK cells were highly activated across all compartments owing to IL-15 stimulation but exhibited additional PD-1 and ILT2 induction within infiltrates. Interestingly, circulating NKs showed slightly higher CD69 and Ki-67 expression than infiltrated NKs, possibly reflecting differential exposure to cytokines and physical constraints within the spheroid.

Overall, lymphocytes retained within tumor spheroids exhibited (1) selective enrichment

in $CD8^+$ and NK subsets, (2) strong activation and proliferative reprogramming, and (3) moderate checkpoint induction. In contrast, circulating cells remained largely similar to IL-15–stimulated PBMCs, suggesting that direct tumor contact and spatial confinement are key drivers of immune activation within the microfluidic model.

As expected from IL-15 stimulation, the overall phenotype was biased toward activated and proliferative NK cells. This cytokine-driven bias was deliberately maintained to sustain effector viability and PBMC–tumor interactions within the 3D co-culture, at the cost of a reduced representation of resting or naïve populations. Importantly, these results primarily reflect allogeneic, cytokine-driven dynamics and should not be extrapolated to autologous contexts. Together, they demonstrate the feasibility of recovering and characterizing distinct immune compartments from perfused tumor co-cultures, establishing a foundation for subsequent multi-donor and autologous experiments.

b) Cytokine profiling confirms measurable immune activation under PD-L1 blockade

To determine whether immune activation in the microfluidic co-culture translated into functional outputs, cytokine concentrations were measured in chip supernatants after 72 hours of perfused co-culture with or without Avelumab (Fig. 7E). Multiplex analysis was performed on three independent donors for interferon γ (IFNγ), tumor necrosis factor α (TNFα), granzyme B (GzmB), perforin (Prf), and granulysin (Gnly).

All five cytokines were consistently detectable in the chip supernatants, confirming the feasibility of direct cytokine monitoring from the perfused microenvironment without additional processing. Mean concentrations in untreated chips ranged between 30–300 pg/mL for TNFα, 400–3300 pg/mL for IFNγ, 7–49 ng/mL for GzmB, 0.35–2.2 ng/mL for Prf, and 1.6–15.6 ng/mL for Gnly. These values fell well within the dynamic range of bead-based immunoassays, demonstrating assay robustness in a low-volume microfluidic setting.

Upon Avelumab treatment, two of the three donors displayed a coordinated cytokine upregulation, whereas one donor showed an inverse trend. IFNγ increased from 391 to 776 pg/mL in Donor 1 and from 950 to 5551 pg/mL in Donor 3, while it decreased from 3321 to 835 pg/mL in Donor 2. TNFα rose modestly in all donors (1.3–3.7-fold, up to 303 pg/mL in Donor 3). Prf and Gnly followed similar donor-dependent patterns, increasing 1.4–3.8-fold in Donors 1 and 3 but declining in Donor 2. GzmB secretion reached 49 ng/mL in Donor 1 (saturation ceiling), doubled in Donor 3 (9.1 → 19 ng/mL), and decreased in Donor 2 (7.5 → 4.2 ng/mL).

Although none of these changes reached statistical significance due to the limited sample size (n = 3), within-donor trends were reproducible, confirming that effector cytokine modulation by Avelumab can be captured in this format. The heterogeneity observed

across donors likely reflects intrinsic differences in immune responsiveness and allogeneic reactivity under IL-15 stimulation.

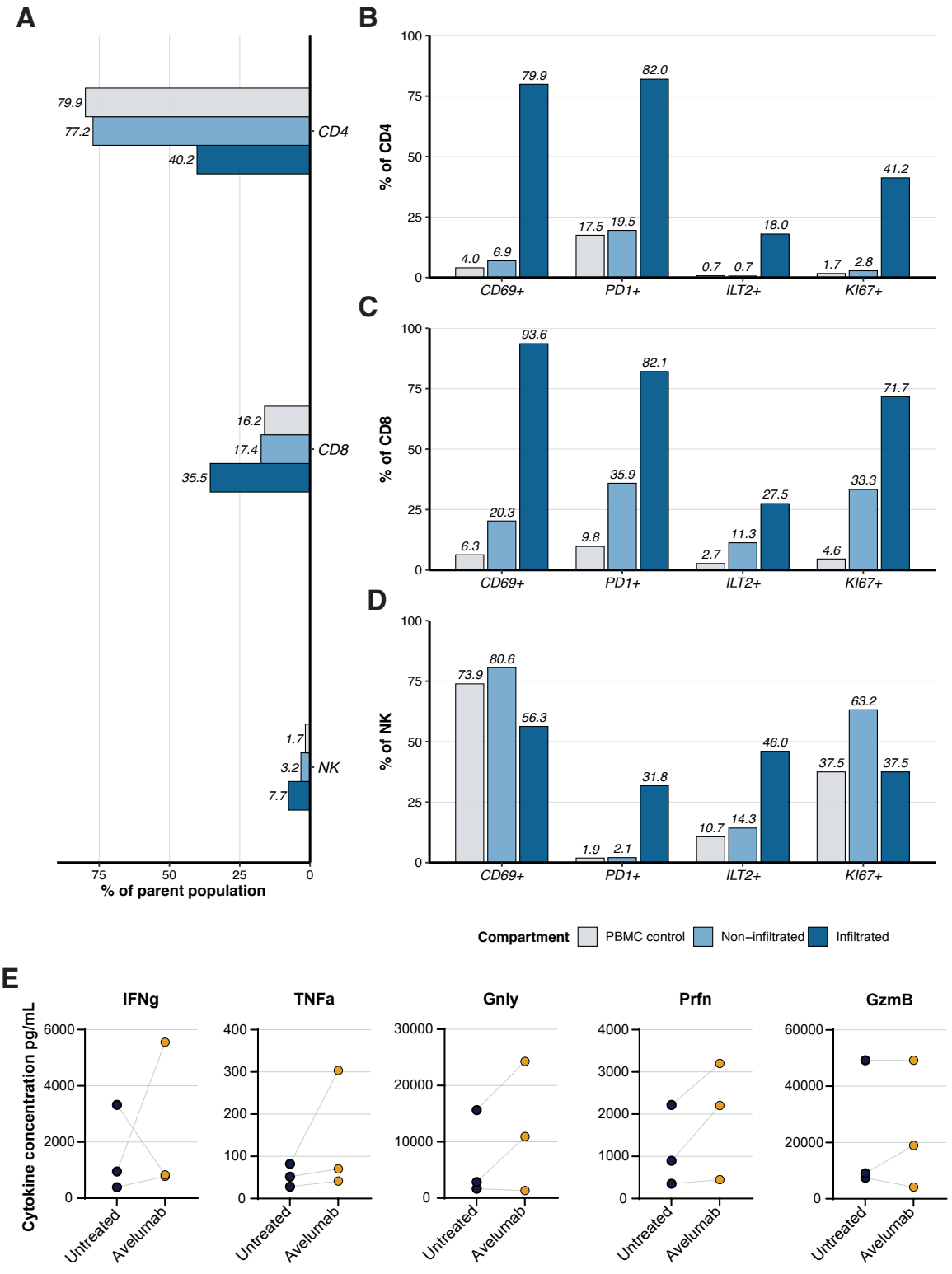

Figure 7: *Phenotypic and functional characterization of immune infiltrates in microfluidic co-cultures.*
(A) Flow cytometry analysis of global lymphocyte composition after 72 h of perfused co-culture in

the microfluidic chip. Fractions correspond to IL-15–activated PBMC controls (light gray), circulating non-infiltrated cells recovered from the chip outlet (mid-blue), and infiltrated cells dissociated from tumor spheroids (dark blue). Percentages represent the relative proportions of $CD4^+$, $CD8^+$, and NK cells within the lymphocyte population. (B–D) Expression of activation (CD69), checkpoint (PD-1, ILT2), and proliferation (Ki-67) markers in $CD4^+$ (B), $CD8^+$ (C), and NK (D) subsets. (E) Cytokine concentrations in chip supernatants after 72 h of co-culture under continuous flow, untreated (blue) or Avelumab-treated (yellow), measured by multiplex assay for IFNγ, TNFα, granulysin (Gnly), perforin (Prf), and granzyme B (GzmB). Each point represents one donor duplicate (n = 3). Statistical comparisons were not significant (paired Wilcoxon test, n = 3).

INTEGRATION OF A FULLY AUTOLOGOUS TUMOR–IMMUNE WORKFLOW

After validating the microfluidic co-culture platform under allogeneic conditions, we next evaluated whether it could be adapted to a fully autologous tumor–immune configuration. The preceding experiments primarily served as system calibration, covering chip design, operation, and readout validation, and confirmed that lymphocyte infiltration, activation, and functional cytokine responses can be monitored under continuous perfusion. These results provided the methodological basis to attempt an autologous adaptation.

In this proof-of-feasibility phase, tumor samples from patients with clear-cell renal carcinoma were processed as described in our previous work and formed spheroids in 48h (Fig. 8A). Following IL-15 stimulation, TILs were re-introduced into tumor spheroids by a 24h coculture. This complete model was then cultured for 72 h in microfluidic chips perfused with the corresponding autologous PBMCs, in the presence or absence of anti–PD-L1 (avelumab). Remarkably, the entire workflow, from tumor excision to the acquisition of functional readouts, is completed within six days, without any intermediate amplification or 2D culture step. This rapid turnaround is itself a key strength of this model, demonstrating that complex autologous co-cultures and endpoint analyses can be established within a clinically compatible timeframe, while preserving the native immune and stromal composition.

Despite these constraints, the full workflow succeeded for two out of three patient samples (patient characteristics in supplementary table 1), enabling cytokine profiling (Fig. 8C) in both, and high-dimensional spectral cytometry on immune cells contained in chip-recovered spheroids in one case (Fig. 8B, D). Although limited in scale, these results confirm the feasibility of performing complex autologous tumor–immune co-cultures in a microfluidic chip, demonstrate that viable immune populations can be resolved after perfusion, and establish a framework for individualized functional testing of immunotherapies under dynamic flow conditions.

1. *CYTOKINE PROFILING*

In both patients, cytokine secretion was readily detectable after 72 h of perfusion, confirming the feasibility of multiplex quantification in the fully autologous microfluidic setup (Fig. 8C). Quantifiable levels were obtained for TNFα (2.5–92 pg/mL), IFNγ (10.7–

15.6 pg/mL), Perforin (171–191 pg/mL), Granulysin (351–360 pg/mL), and Granzyme B (122–1,098 pg/mL), which represented the most abundant effector molecule. Overall cytokine output differed between patients (152 pg/mL vs 331 pg/mL on average), illustrating inter-patient heterogeneity in baseline immune activity.

Upon PD-L1 blockade, secretion profiles diverged sharply. In Patient 1, Avelumab induced a broad and coordinated rise in effector molecules, with total cytokine output increasing more than sixfold (761 → 4,592 pg/mL, +503%). This response was dominated by strong increases in Granzyme B (×28) and Perforin (×4), consistent with enhanced cytolytic activation. Granulysin and IFNγ rose modestly (+7% and +15%, respectively), while TNFα decreased (–60%). In Patient 2, baseline effector activity was already high (Granzyme B = 1,098 pg/mL), and Avelumab produced a distinct pattern characterized by reduced degranulation markers (Granzyme B –74%, Granulysin –22%) but a pronounced rise in IFNγ (×5, +413%) and a mild increase in TNFα (+86%). This shift suggests a transition from cytolytic toward inflammatory cytokine dominance.

Although exploratory (n = 2), these results demonstrate that the autologous microfluidic system supports direct quantification of soluble effectors within limited chip volumes and captures distinct, patient-specific functional responses to PD-L1 blockade.

2. SPECTRAL FLOW CYTOMETRY

In this proof-of-concept experiment performed on patient 1, lymphocytes were analyzed after 72 h of perfusion using a 37-color spectral cytometry panel (full list in Supplementary Table 1). Sufficient viable cells were recovered from dissociated spheroids to enable unsupervised clustering and UMAP projection (Fig. 8B), confirming that high-dimensional phenotyping can be directly applied to microfluidic chip outputs. In contrast, spheroids cultured without circulating PBMCs yielded too few live lymphocytes for reliable analysis, highlighting current limitations in dissociation efficiency and TIL recovery. Global mapping (Fig. 8B) identified the three major lymphocyte subsets: $CD4^+$ T, $CD8^+$ T, and NK cells, clearly separated by their high-dimensional profiles. Clusters were annotated by conventional gating (FSC/SSC → singlets → $LiveDead^-$ → $Dump^-$ → $CD3^+$ for CD4 and CD8 and $CD3^-$ → $CD56^+$/$CD16^+$ for NK cells). A small $CD4^+$ population clustered near $CD8^+$ cells despite lacking CD8 expression, corresponding to a cytotoxic CCR7-, $CD45RA^+$, $NKp80^+$, $GzmB^+$, $CXCR6^+$, $GPR56^+$, $ILT2^+$, $CD57^+$ population probably induced by IL-15, underrepresented in the spheroids compared to the PBMC alone control (7.64 vs 1.58% of CD4+ cells, data not shown).

Subset proportions differed slightly from those in IL-15–activated PBMCs cultured in parallel in standard conditions without a spheroid (Fig. 8D): $CD4^+$ T cells were enriched in chip-derived spheroids (≈ 64 % vs 52 %), whereas $CD8^+$ T cells (≈ 25 % vs 38 %) and NK cells (≈ 7 % vs 10 %) were reduced.

Together, these results show that high-dimensional spectral flow cytometry can be successfully performed on cells recovered from autologous microfluidic chips, providing sufficient resolution to resolve major effector subsets and capture patient-specific immune landscapes, while emphasizing remaining technical challenges, chiefly spheroid dissociation efficiency and IL-15-related biases, to be optimized for future studies.

We next focused on CD8 T cells by conducting unsupervised clustering.

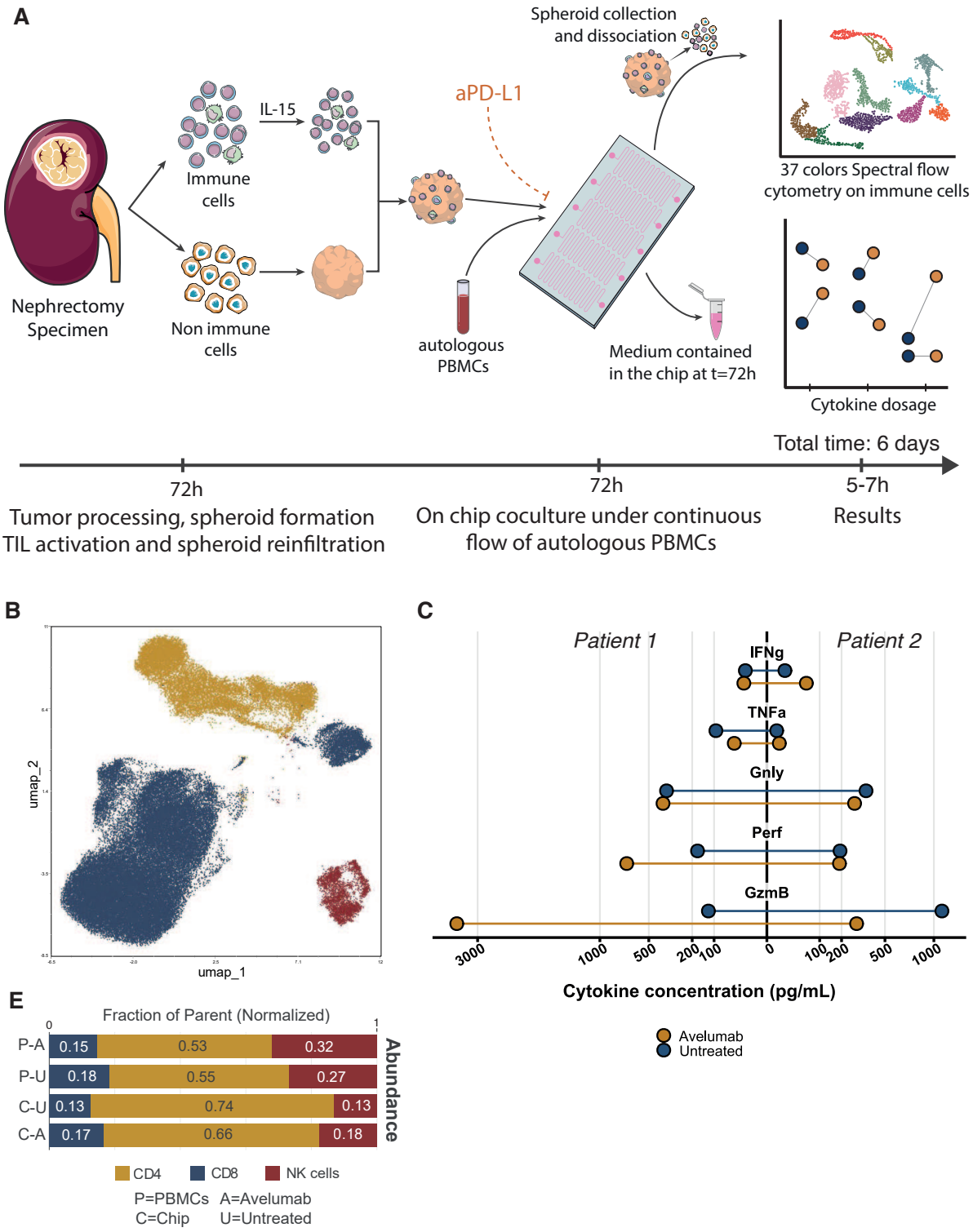

***Figure 8**: Overview of the autologous microfluidic tumor–immune model and global immune features under IL-15 stimulation.*
(A) Workflow of the autologous setup. Fresh tumor tissue from nephrectomy specimens was processed into spheroids and matched tumor-infiltrating lymphocytes (TILs). After IL-15 activation, TILs were re-introduced into tumor spheroids, which were subsequently cultured for 72 h in microfluidic chips perfused with autologous PBMCs ± anti-PD-L1 (Avelumab). Media and dissociated spheroids were collected for multiplex cytokine quantification and 37-color spectral cytometry, respectively.
(B) Global UMAP projection of pooled lymphocytes from the autologous chip, showing distinct

CD8⁺ (yellow), CD4⁺ (blue), and NK (red) clusters. (C) Patient-specific cytokine secretion profiles after 72 h of perfusion. Lollipop plots indicate the mean concentration (pg/mL) of each cytokine in untreated (blue) and Avelumab-treated (yellow) tracks, displayed on a square-root scale. (D) Relative abundance of CD4⁺, CD8⁺, and NK cells across experimental conditions.

1. *CD8 T CELLS LANDSCAPE IN OUR AUTOLOGOUS ON CHIP MODEL UNDER IL-15 ACTIVATION*

Unsupervised clustering of CD8⁺ T cells across all conditions resolved ten phenotypically distinct subsets that segregated clearly on the UMAP projection (Fig. 9A). Their marker expression patterns (Fig. 9D) enabled precise annotation of the ten clusters:

- Cluster 1 – "TEMRA cytotoxic (CD57⁺ ILT2⁺)": Canonical terminal effector population with high GzmB and NKp80 expression, characteristic of fully differentiated cytotoxic TEMRA cells often expanded under IL-15 stimulation.
- Cluster 2 – "Restrained TEMRA (TIM-3⁺ TIGIT⁺)": Checkpoint⁺ CXCR4^{high} CD45RA⁺ subset lacking CD57 and ILT2 but retaining cytotoxic potential, consistent with restrained TEMRA cells exhibiting partial functional limitation rather than full exhaustion.
- Cluster 3 – "Primed-naïve (CCR7⁺ CD45RA⁺)": Naïve-like cells maintaining a CCR7⁺ CD45RA⁺ backbone but expressing TIM-3 and CD25, indicative of IL-15–alerted, cytokine-primed lymphocytes that have not undergone antigenic activation.
- Cluster 4 – "Proliferative hypercytotoxic (CD25⁺ ILT2⁺ CD57⁺)": Highly activated Ki-67⁺ effectors expressing GzmB, NKp80, and NKG2C, probably reflecting acute IL-15-driven proliferation and effector differentiation.
- Cluster 5 – "Checkpoint-free TEMRA (CD69⁺)": CD45RA⁺ CD69⁺ TIM-3⁻ GzmB⁺ subset corresponding to cytotoxic TEMRA cells devoid of inhibitory receptor expression, representing checkpoint-independent terminal effectors.
- Cluster 6 – "Early-memory": CCR7⁺ CD45RA⁺/⁻ CD25^low TIM-3⁻ subset corresponding to low-activation early-memory or central-memory–like cells maintained by cytokine signaling.
- Cluster 7 – "Adaptive-memory (CXCR6⁺)": Transitional memory subset co-expressing CXCR6 and CXCR4 with low GzmB and high CD127, consistent with tissue-adapted or long-lived adaptive-memory cells bridging effector and memory compartments.
- Cluster 8 – "Exhausted-like (PD-1⁺ TIGIT⁺ CD39⁺)": Checkpoint-rich PD-1⁺ TIGIT⁺ TIM-3⁺ CD39⁺ CD69⁺ subset with reduced cytotoxic machinery.
- Cluster 9 – "Pre-exhausted EM (PD-1⁺ CD27⁺ CD28⁺)": Effector-memory subset re-

taining costimulatory receptors (CD27, CD28) but limited cytotoxicity, consistent with a transitional pre-exhausted phenotype.

- Cluster 10 – "Proliferative PD-1$^+$ EM (TIM-3$^+$ Ki-67$^+$)": Actively cycling effector-memory cells expressing PD-1, TIM-3, CD69, HLA-DR and GzmB, indicative of recently activated cells beginning to acquire inhibitory features.

Although all ten subsets corresponded to circulating CD8$^+$ phenotypes, their distribution and activation profiles diverged from those typically described in resting peripheral blood. In our dataset, naïve-like cells ("Primed-naïve (CCR7$^+$ CD45RA$^+$)", cluster 3, yellow) accounted for ≈ 25 % of CD8$^+$ cells, while early-memory–like cells ("Early-memory", cluster 6, blue) represented ≈ 29 %. Highly differentiated TEMRA and effector populations (clusters 1, 2 and 5) together made up ≈ 30 % of CD8$^+$ cells (16.5 %, 1.3 % and 11.6 %, respectively), and minor checkpoint-positive or exhausted-like subsets (clusters 8–9) accounted for ≈ 9 %. For reference, in resting peripheral blood, naïve CD8$^+$ T cells typically constitute 45–60 % of the population, and TEMRA or checkpoint-positive subsets are comparatively rare (<10 %). The observed distribution therefore reflects a cytokine-driven reshaping of the CD8$^+$ landscape under IL-15 activation, characterized by depletion of true naïve cells, maintenance of early-memory populations, and emergence of partially differentiated, checkpoint-expressing effectors.

Cluster composition varied moderately across the four experimental conditions (Fig. 9B). These shifts likely reflect differential recruitment, survival, or retention of pre-existing subsets within the microfluidic spheroids. We observed an apparent enrichment of naïve-like cells ("Primed-naïve (CCR7$^+$ CD45RA$^+$)", cluster 3, yellow) within spheroids (25.2 % → 55.8 %), unlike what is typically seen in tumor tissue. This increase is unlikely to result from naïve T-cell recruitment, but rather from the persistence of IL-15–maintained "primed-naïve" CCR7$^+$ CD45RA$^+$ TIM-3$^+$ CD25$^+$ cells. Within the TEMRA compartment, overall abundance decreased markedly in spheroids, accompanied by a phenotypic redistribution. Cytotoxic TEMRA subsets ("TEMRA cytotoxic (CD57$^+$ ILT2$^+$)", cluster 1, red, and "Checkpoint-free TEMRA (CD69$^+$)", cluster 5, pink-orange) contracted sharply (16.5 % → 7.1 % and 11.6 % → 2.6 %, respectively), while the "Restrained TEMRA (TIM-3$^+$ TIGIT$^+$)" subset (cluster 2, orange) became relatively enriched (1.3 % → 6.0 %). This enrichment likely reflects selective retention of restrained, CXCR4high checkpoint-expressing effectors with a tissue-adapted orientation. In parallel, all proliferative subsets ("Proliferative hypercytotoxic", cluster 4, and "Proliferative PD-1$^+$ EM", cluster 10) virtually disappeared (1.9 % and 2.4 % → < 0.6 %), suggesting that the 3D tumor-like microenvironment or the chip impose strong metabolic or inhibitory constraints limiting CD8$^+$ proliferation.

In Avelumab-treated spheroids, cytotoxic TEMRA clusters 1 and 5 were more abundant (10.8 % and 7.8 %, respectively) than in untreated counterparts (7.1 % and 2.6 %), con-

sistent with improved persistence or reactivation of pre-existing effector populations. Conversely, the "Restrained TEMRA (TIM-3$^+$ TIGIT$^+$)" subset (cluster 2) was reduced (4.0 % vs 6.0 %), and the "Primed-naïve" cluster 3 declined also declined (37.8 % vs 55.8 %), indicating that PD-L1 blockade preferentially favors cytotoxic rather than naïve-like populations. Checkpoint-positive or exhausted-like subsets ("Exhausted-like (PD-1$^+$ TIGIT$^+$ CD39$^+$)", cluster 8, and "Pre-exhausted EM (PD-1$^+$ CD27$^+$ CD28$^+$)", cluster 9) showed slight increases (2.7 % and 3.4 % vs 1.1 % and 1.3 % in untreated spheroids), possibly reflecting selective retention of checkpoint-expressing cells within the spheroid environment rather than true functional reactivation. In contrast, PBMC + Avelumab controls remained globally stable, supporting a tumor-dependent effect of PD-L1 blockade consistent with the PD-L1–positive CPS of the corresponding patient.

Functionally (Fig. 9C), GzmB and NKp80 median of intensities decreased across all clusters within spheroids (mean −65 % and −55 % vs PBMCs), indicating a global reduction in cytotoxic potential under 3D culture on chip vs control PBMCs. PD-L1 blockade restored these markers across most subsets, irrespective of PD-1 status, with mean gains of +90 % for GzmB and +65 % for NKp80. Only the least cytotoxic clusters (2, 3, 6, 9) showed minimal reactivation, confirming that functional recovery primarily concerned pre-existing effector populations.

In summary, this single-patient analysis confirms that high-dimensional spectral cytometry can be successfully applied to microfluidic chip–derived cells, resolving distinct CD8$^+$ phenotypes and capturing PD-L1-dependent modulation of cytotoxic markers. These results establish the technical feasibility of the approach and point to the need for optimized activation protocols and larger patient cohorts.

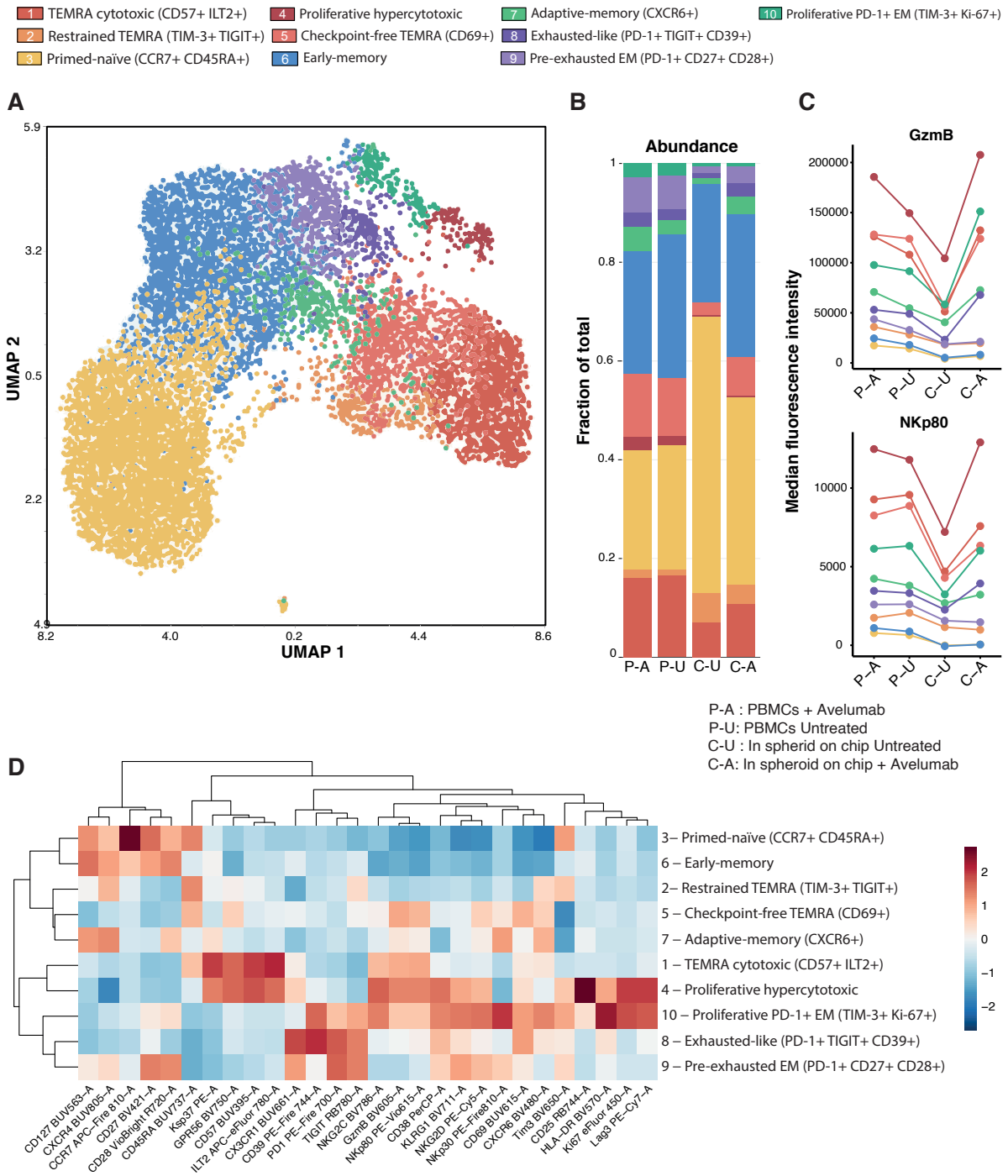

Figure 9: *High-dimensional spectral cytometry analysis of CD8⁺ T cells recovered from the autologous microfluidic co-culture.*
(A) UMAP projection of all CD8⁺ T cells pooled across conditions, colored by unsupervised FlowSOM clustering. Ten phenotypically distinct subsets were identified based on surface and intracellular marker expression and annotated as: (1) TEMRA cytotoxic (CD57⁺ ILT2⁺), (2) Restrained TEMRA (TIM-3⁺ TIGIT⁺), (3) Primed-naïve (CCR7⁺ CD45RA⁺), (4) Proliferative hypercytotoxic (CD25⁺ ILT2⁺ CD57⁺), (5) Checkpoint-free TEMRA (CD69⁺), (6) Early-memory (CCR7⁺ CD45RA⁺/⁻), (7) Adaptive-memory (CXCR6⁺), (8) Exhausted-like (PD-1⁺ TIGIT⁺ CD39⁺), (9) Pre-exhausted EM (PD-1⁺ CD27⁺ CD28⁺), and (10) Proliferative PD-1⁺ EM (TIM-3⁺ Ki-67⁺). (B) Relative abundance of each cluster across the four experimental conditions: PBMCs treated with Avelumab kept in stan-

dard culture without spheroid (P–A), untreated PBMCs (P–U), cells infiltrating spheroids without treatment (C–U), and cells infiltrating spheroids under Avelumab (C–A). (C) Median fluorescence intensity (MFI) of cytotoxic markers GzmB (top) and NKp80 (bottom) across the four conditions. Lines connect corresponding clusters between conditions. (D) Heatmap of scaled median marker expression for all clusters. Marker intensities were normalized (z-score) per marker across all clusters.

DISCUSSION

This study establishes a dynamic, autologous model of clear cell renal cell carcinoma (ccRCC) integrating patient-derived tumor spheroids and immune components within a reusable microfluidic platform. Building on our previous development of standardized and immune-reconstituted spheroid systems (22) (LIANGWEI YIN 2025), we were able to extend this approach by introducing a controlled perfused environment that supports continuous circulation of autologous immune cells and real-time analysis of immune–tumor interactions under immunotherapeutic conditions. To our knowledge, this is the first instance of an autologous tumor on chip including immune components for immunotherapy in a microfluidic chip in RCC.

Several of the results presented here were obtained as proof-of-feasibility of the workflow and should therefore not be interpreted as comparative between experimental conditions. The confocal imaging analyses, performed on only three spheroids per condition from a single donor under two conditions, were intended primarily to demonstrate the feasibility of immune-cell infiltration under continuous flow and to validate that the clearing and imaging methods enable visualization and accurate segmentation of infiltrating cells throughout the spheroid depth.

Similarly, spectral cytometry assays were conducted on a single biological replicate and mainly served as a technical validation of the staining panel and of its applicability to limited cell numbers recovered from the microfluidic chip. Cytokine assays, performed on three independent donors, revealed substantial inter-donor variability and were primarily designed to confirm detectable effector activity and assay sensitivity within the expected dynamic range.

Altogether, these exploratory datasets establish technical feasibility and identify measurable readouts, but larger-scale experiments involving additional donors, alternative activation conditions, and appropriate resting and activation controls will be required to validate the reproducibility and generalizability of these findings.

Methodologically, this platform consolidates prior optimizations in tissue processing and spheroid generation. Adjustments to dissociation procedures, media formulation, and optional use of growth factor–depleted Matrigel increased the success rate of spheroid formation to ~70%. The entire workflow, from surgical sampling to microfluidic experimentation, is completed within three days, minimizing culture-induced drift and preserv-

ing immune functionality. The ten spheroids used per condition exceed the empirically defined representativity threshold identified in the present work, ensuring robust transcriptomic fidelity without unnecessary redundancy.

Cytokine quantification in the circulating medium provided a convenient functional endpoint. Yet, the absence of continuous sampling precludes kinetic interpretation. Integrating a simple outlet loop for serial sampling will enable time-resolved cytokine profiling to distinguish transient from sustained immune activation and clarify whether low cytokine levels correspond to target clearance or limited immune engagement.

Beyond soluble readouts, the model supports high-content phenotyping. A 37-color spectral flow cytometry panel was developed to analyze cells recovered after chip culture, validating downstream compatibility with single-cell–level assays. Spheroid retrieval proved straightforward, but dissociation efficiency remains a limitation, particularly to enable TILs visualization given their fragility, most of the lymphocytes in the conditions without PBMCs contained few live cells. Optimization of enzymatic digestion and mechanical disruption should enhance recovery, enabling simultaneous analysis of infiltrated and non-infiltrated immune fractions, a key next step for quantifying recruitment and effector polarization.

Our primary objective was to determine whether patient-derived, immune-competent spheroids could retain functional behavior within a dynamic environment. Tumor-infiltrating lymphocytes (TILs) were first reintroduced into tumor spheroids after short-term IL-15 activation, ensuring viability and re-engagement with the autologous tumor compartment. These immune-reconstituted aggregates were then integrated into the microfluidic device, where autologous peripheral blood mononuclear cells (PBMCs), also IL-15–activated, were perfused through the circulation channel to form a third, dynamic immune compartment. This configuration demonstrated that immune cells in circulation could infiltrate and interact with tumor spheroids under flow, validating the technical feasibility of a three-compartment autologous ccRCC-on-chip system. The strong IL-15 activation used here served to maximize immune engagement and confirm proof of principle.

Our spectral cytometry revealed a cytokine-driven, rather than antigen-driven, $CD8^+$ T-cell landscape, characterized by reduced naïve frequencies and expansion of early-memory and TEMRA subsets. Compared with the allogeneic experiments, the difference between PBMC and spheroid-derived populations was smaller, and no surge in cytotoxic cells was observed within the spheroid mass under autologous conditions which is reassuring,

However, the limited divergence between control PBMCs and spheroid-infiltrating immune cells may raise concern that infiltration in the autologous setting is not fully specific, as only modest phenotypic differences were detected between circulating and infiltrated lymphocytes. Such similarity may at once indicate (i) reduced non-specific inflammatory

activation, consistent with a more physiological autologous context, and (ii) partial masking of tumor-driven modulation by the strong IL-15–induced activation used in this proof-of-concept. The persistence of "primed-naïve" cells within spheroids and the loss of proliferative subsets likely reflect both cytokine bias and local metabolic constraints within the 3D microenvironment. Although residual attachment of non-specific lymphocytes cannot be fully excluded, repeated perfusion and extensive washing make this explanation unlikely. Notably, IL-15 has been reported to promote bystander infiltration and TCR-independent effector functions in T cells (23,24), which may contribute to the low specificity observed here. Moving forward, the main improvement for this autologous system will be to identify more physiologically relevant strategies to sustain immune viability and function without inducing cytokine-driven drift away from tumor- or tissue-like conditions.

Altogether, these findings indicate that while the system remains biologically responsive to PD-L1 blockade, further optimization will be required to elicit truly tumor-specific immune effects and to improve the recovery of endogenous TILs. In future iterations, quantitative outlet sampling and labeling controls will be essential to determine how much of the observed variation arises from intrinsic biological modulation versus culture-dependent effects.

Preclinical modeling of ccRCC has historically relied on systems that capture partial aspects of tumor biology. Patient-derived xenografts preserve architecture and stromal composition but preclude the study of human immunity due to their dependence on immunodeficient hosts. Even humanized PDXs, while conceptually attractive, remain slow, costly, and unsuitable for parallelized precision testing, and raise ethical questions (18,20). Organoid models have revolutionized the field by enabling expansion of patient-derived tumor cells and recapitulation of epithelial heterogeneity; however, conventional 3D cultures are generally devoid of stromal or immune compartments, and extended culture times promote phenotypic drift.

The air–liquid interface (ALI) system developed by Neal et al. (25) addressed these shortcomings by maintaining stromal and immune components in short-term organoid cultures. Esser et al. (26) subsequently adapted this approach to ccRCC, generating 42 patient-derived ALI organoids that retained T cells, fibroblasts, and endothelial cells and showed responsiveness to cabozantinib and nivolumab. Such ALI PDOs, typically used within a week of derivation, are highly relevant for immunotherapy testing but remain limited by their static nature. The biological material underpinning these models could, however, be seamlessly adapted to a perfused microfluidic environment to capture dynamic immune processes, an approach implemented here.

Microfluidic systems provide unique control over perfusion, nutrient exchange, and cytokine gradients, allowing dynamic investigation of tumor–immune interactions under

physiologically relevant flow. In renal cancer, Miller et al. (27) established a cell line–based "RCC-on-a-chip" supporting CAR T-cell infiltration and antigen-specific cytotoxicity, while other platforms have primarily focused on vascularization and angiogenic signaling (28,29). However, none to date has combined autologous tumor and immune components from the same patient.

Our platform's simplicity, reusability, and compatibility with standard laboratory workflows directly address practical barriers often cited as limiting factors for the adoption of microfluidic systems (19). Comparable autologous immune-on-chip models have recently emerged in NSCLC (30) but to our knowledge, no such implementation has yet been reported for renal cell carcinoma.

Aside from our autologous chip, among the methods developed in this paper, the dual-color "red–green" spheroid assay, in which tumor cells are labeled with distinct fluorophores, provides a simple and elegant means to visualize infiltration and localized killing in real time. Given the profound spatial heterogeneity of ccRCC (31), including region-specific expression of immune checkpoints such as PD-L1 and HLA-G (32,33), this approach offers a promising foundation to study local immune escape and selective immune pressure. While developed with cell lines, this concept could be extended to patient-derived material through fluorescent tagging or genetic barcoding, creating "bi-zone" spheroids that model intra-tumoral diversity and subclonal coexistence. The clinical relevance of such an approach is highlighted by the work of Dijkstra et al.(34), who used multi-region organoid–T cell co-cultures to show that tumor subclones differ intrinsically in immune evasion capacity, differences not predictable from genomic data alone. Extending this principle to ccRCC using our dynamic, autologous microfluidic platform could provide a powerful experimental framework to dissect subclonal immune escape mechanisms and assess therapeutic strategies targeting spatially distinct tumor regions.

Beyond checkpoint inhibition, this platform is compatible with emerging immunotherapies, including bispecific engagers, CAR or TCR-engineered lymphocytes, and antibodies directed against non-canonical pathways. The integration of a controlled circulation compartment allows the study of immune recruitment, trafficking, and systemic cytokine modulation in a reproducible, patient-specific context.

CONCLUSION

In summary, this work establishes a fast, practical, and fully autologous microfluidic model of ccRCC that integrates tumor spheroids and immune cells within a reusable, experimentally accessible device. The workflow requires less than three days from tissue sampling to experimentation, preserving the viability and phenotypic integrity of tumor and immune compartments. By combining biological representativity with operational sim-

plicity, this system bridges static immunocompetent cultures and dynamic organ-on-chip technologies.

Ultimately, the aim of this approach is to enable rapid and individualized prediction of therapeutic responses for personalized immunotherapy guidance. Its modularity, and adaptability to multiple analytical readouts, including imaging, cytokine measurement, spectral flow cytometry, and transcriptomics, make it a versatile foundation for dynamic, patient-specific immuno-oncology studies.

MATERIAL AND METHODS:

HUMAN SAMPLES AND ETHICS

Human tumor specimens were obtained as residual surgical material from patients with clear cell renal cell carcinoma (ccRCC). All patients underwent partial or radical nephrectomy at the Department of Urology, Saint-Louis Hospital (Paris, France). Tissue collection and experimental use were conducted in accordance with institutional and national ethical regulations. All patients provided written informed consent authorizing the use of residual material for research purposes, in compliance with the Declaration of Helsinki and French bioethics law.

Fresh ccRCC tissue was selected by an experienced pathologist immediately after surgical resection. Specimens were first rinsed in sterile phosphate-buffered saline (PBS, Gibco) to remove residual blood and debris, then transferred into cold RPMI 1640 medium (Gibco) supplemented with gentamicin (50 µg/mL, Gibco) and amphotericin B (0.25 µg/mL, Sigma-Aldrich). Samples were maintained at 4 °C during transport and delivered to the research laboratory within 30 minutes after excision to ensure maximal cell viability and integrity prior to enzymatic dissociation.

Peripheral blood mononuclear cells (PBMCs) were obtained from the residual volume of cytapheresis cassettes provided by healthy donors through a formal agreement with the Établissement Français du Sang (EFS, agreement no.13/EFS/101). The material was collected following routine platelet or plasma donation and processed within 1 hour of collection. PBMCs were isolated at room temperature by standard density-gradient centrifugation using Histopaque-1077 (Sigma-Aldrich) according to the manufacturer's instructions. Cells were washed twice in PBS and resuspended in complete medium for immediate use or cryopreserved as described below.

All human biological materials (tumor specimens, PBMCs, and TILs) were collected, handled, and transferred in compliance with GDPR requirements, ensuring donor anonymity and confidentiality.

GENERAL CELL CULTURE CONDITIONS

All cell cultures were maintained under sterile conditions at 37 °C in a humidified incubator with 5% CO_2. Three types of media were used depending on the cell model.

(i) For renal carcinoma cell lines, DMEM (GlutaMAX, Gibco) was supplemented with 10% fetal calf serum (FCS, Sigma-Aldrich), gentamicin (50 µg/mL, Gibco), and amphotericin B (0.25 µg/mL, Sigma-Aldrich).

(ii) For immune-cell cultures and co-culture assays, RPMI 1640 (Gibco) supplemented with 2 mM L-glutamine, 10% FCS, and the same antibiotic/antifungal mixture was used. No penicillin–streptomycin was added to prevent interference with cytokine signaling.

(iii) The renal carcinoma complete medium (RCCM), composed of DMEM:F12 (3:1) supplemented with 10% FCS, 2 mM L-glutamine, 10 ng/mL EGF (PeproTech), and 0.4 µg/mL hydrocortisone (Sigma-Aldrich), was used specifically for the culture and formation of Patient-Derived Spheroids (PDS). Cells were passaged at 70–80% confluence using TrypLE Express (Gibco) and replaced after a maximum of 10 passages to preserve phenotypic stability. All cultures were regularly tested for mycoplasma contamination, and any culture testing positive was immediately discarded. Cryopreserved vials were thawed rapidly at 37 °C and expanded for at least one passage before experimental use.

CELL LINE AND PD-L1 GENETIC ENGINEERING

2. *CELL LINE ORIGIN AND MAINTENANCE*

The human clear cell renal carcinoma cell line RCC7 was kindly provided by Dr. Anne Caignard (INSERM U1160 Team 3, Paris, France). Cells were maintained under the standard culture conditions described above and routinely monitored for morphology and growth rate. Cells were expanded from cryopreserved stocks and maintained at low-passage before replacement to prevent phenotypic drift. Parental RCC7 cells were used to generate PD-L1 wild-type (WT) and PD-L1 knockout (KO) derivatives, as described below. All derivatives were maintained under identical culture conditions to ensure experimental comparability.

3. *CRISPR PD-L1 KNOCKOUT*

RCC7 cells were edited using a commercial CRISPR/Cas9 lentiviral system targeting CD274 (PD-L1, Cat. #78057, BPS Bioscience). The construct encodes SpCas9 driven by an EF-1α promoter and four sgRNAs under a U6 promoter, targeting exons 2–3 of CD274 (GenBank NM_021893). Representative guide sequence: 5′-GGTTCCCAAGGACCTATATG-3′ (exon 2, PAM = TGG). Cells were transduced at a multiplicity of infection (MOI = 4) without polybrene, and selected with puromycin (1 µg/mL) for 5 days to enrich transduced populations. PD-L1 loss of surface expression was assessed by flow cytometry.

c) Single-cell cloning by sorting (MA900)

Single-cell clones were isolated by fluorescence-activated cell sorting (FACS) on a Sony MA900 equipped with a 100 µm nozzle operated at 20 psi. The gating strategy was FSC-A/SSC-A → singlets (FSC-H vs FSC-W) → live cells (Zombie NIR$^+$ exclusion) → PD-L1 negative. One cell per well was sorted into 96-well flat-bottom plates containing 200 µL of pre-warmed complete DMEM medium supplemented with 20 % FBS and 1% gentamicin.

d) KO validation

For 10 clones, PD-L1 surface expression was quantified by flow cytometry using anti-PD-L1-BV421 (clone 29E.2A3, BioLegend, 5 µg/mL). Knockout (KO) clones were defined as overlapping the isotype distribution and showing <0.5% PD-L1-positive cells. In selected clones, KO was corroborated by Western blot for PD-L1 (anti-PD-L1, clone E1L3N, Cell Signaling Technology, 1:1000) using β-actin as loading control.

e) Fluorescent tagging (mCherry/GFP) and clonal selection

Validated PD-L1 clones and parental cells were transduced with mCherry Lentifect™ purified lentiviral particles at MOI=3 (CMV promoter, puromycin resistance; GeneCopoeia, Cat. No. LP441-025) to act as a marker for spheroid persistence in our assays. Single mCherry$^+$ were cloned by FACS as described above. Homogeneous expressers were confirmed by analytical flow cytometry, and the fluorescence intensity of eGFP and mCherry populations was cross-checked to ensure comparable expression levels across colors. Fluorescent signal stability was verified over ≥ 3 passages prior to experiments.

f) Safety & QC

All lentiviral procedures were conducted under BSL-2 conditions. Cultures were regularly tested for mycoplasma, and any positive culture was discarded.

SPHEROID GENERATION

Three-dimensional tumor spheroids were generated from RCC7 cells to establish the calibration model. Briefly, 10,000 cells per well (or 20,000 if the spheroid was aimed to be included in the microfluidic chip) were seeded in ultra–low-attachment 96-well plates (Greiner Bio-One) in complete DMEM medium, centrifuged briefly (1 minute 500 rcf, low acceleration and deceleration) to promote spheroid initiation, and incubated at 37 °C in a humidified atmosphere with 5% CO_2. Spheroid formation occurred spontaneously within 72 hours, yielding compact, single spheroids per well. The morphology and size of spheroids were monitored by brightfield microscopy to confirm uniformity before downstream assays.

Spheroids could be composed of two fluorescent RCC7 populations mixed at defined ratios to modulate PD-L1 expression, either cells could be singles labeled with mCherry or double-labeled with PD-L1 and mCherry as described above. The total cell number per

well was kept constant at 10,000 (except for on chip experiments where this number was pushed to 20,000 to better accommodate the size of the traps), with PD-L1 WT cells representing varying proportions according to the experimental design.

Three experimental series were performed:

Homogeneous spheroids composed entirely of PD-L1 WT (mCherry$^+$) or PD-L1 KO (mCherry$^+$) cells, to assess immune response and treatment sensitivity.

Gradient spheroids mixing both mCherry$^+$ populations at 100%, 75%, 25%, or 0% PD-L1 WT to evaluate the impact of PD-L1 abundance on immune resistance.

Detection-limit spheroids containing 0%, 1%, 5%, or 10% PD-L1 WT (mCherry$^+$) cells to determine the threshold sensitivity of the model.

In addition to homogeneous and mixed spheroids, zonal spheroids were generated to reproduce spatial heterogeneity in PD-L1 expression, as detailed in the following section.

FORMATION OF ZONAL (FUSED) SPHEROIDS

Zonal spheroids were generated by physical fusion of two pre-formed spheroids composed of distinct RCC7 derivatives. Independent spheroids were first produced as described above for 72 hours. After complete formation, one spheroid of each type (e.g., PD-L1 WT mCherry$^+$GFP$^+$ and PD-L1 KO mCherry$^+$) was transferred into the same well containing fresh complete medium. The two spheroids were maintained in close contact for 24 hours, during which spontaneous fusion occurred, yielding a single compact spheroid displaying two visually distinct zones corresponding to the respective cell populations. Control fused spheroids were generated in parallel by combining PD-L1 KO mCherry$^+$ and PD-L1 KO mCherry$^+$GFP$^+$ spheroids, to verify that fluorescence labeling alone did not affect fusion efficiency, morphology, or downstream image quantification.

All spheroid configurations were then subjected to immune co-culture assays and longitudinal fluorescence imaging, as described below.

IMMUNE CO-CULTURE ASSAY AND LIVE IMAGING

Formed spheroids were co-cultured with allogeneic PBMCs from healthy donors. PBMCs were pre-activated for 48 h with recombinant human IL-15 (30 ng/mL; PeproTech) in RPMI 1640 complete medium before co-culture. Immediately before immune cell addition, spheroids were either left untreated or pre-incubated for 30 min with anti–PD-L1 antibody (avelumab, 10 µg/mL) to evaluate the effect of PD-L1 blockade on subsequent immune-mediated cytotoxicity. Activated PBMCs were then added at an effector-to-target (E:T) ratio of 10:1, based on 10,000 tumor cells per spheroid.

Co-cultures were monitored in real time using an Incucyte® S2 Live-Cell Analysis System

(Sartorius) equipped with the Spheroid module. Imaging was performed under standard culture conditions (37 °C, 5 % CO_2) with a 4× objective, acquiring both red (mCherry) and green (GFP) fluorescence channels (250 ms exposure each). Brightfield and fluorescence images were captured every 2 h throughout the experiment. Identical imaging parameters were applied across all experimental series.

IMAGE ANALYSIS FROM INCUCYTE

Fluorescence quantification was adapted to each experimental design, using automated or custom pipelines depending on signal composition.

1. *AUTOMATED KINETIC ANALYSIS (100% PD-L1 WT VS PD-L1 KO)*

Homogeneous spheroids were analyzed directly in the Incucyte Analysis Suite (Sartorius) using the Spheroid module. Object detection was based on the mCherry channel, defining each spheroid as a single region of interest (ROI). For each time point, the software reported the integrated red fluorescence intensity (RFI) and object area. CSV exports were processed in R 4.5.1 to compute normalized kinetics of spheroid integrity (RFI_t / RFI_t0) and immune-mediated cytotoxicity. Statistical analyses (± anti–PD-L1, PD-L1 WT vs PD-L1 KO) used two-way ANOVA or non-parametric equivalents.

For experiments involving heterogeneous PD-L1 WT/KO ratios or spatially fused spheroids, calibrated 32-bit TIFF images (“red calibrated” and “green calibrated”) were exported from the Incucyte system and processed in Fiji 1.54p (35) through dedicated in-house macros. All macros can be found in supplementary materials.

4. *NON-ZONAL ANALYSIS.*

a) Hyperstack generation

A first in-house macro assembled the two-channel time-lapse datasets (red and green) extracted from the Incucyte into 3D + time hyperstacks (Macro 1). Briefly, the macro expects a parent directory containing two subfolders named red/ and green/, each including time-ordered image sequences named according to the pattern: <ExperimentName>_red_<Well>_…tif

<ExperimentName>_green_<Well>_…tif

For each well (e.g., A1, B2, C3), the macro:

1. Reads all .tif files from red/ and green/ whose names contain the well identifier.
2. Loads each time series as a stack (Image Sequence), renames them RED_<well> and GREEN_<well>.
3. Merges the two stacks into a 2-channel hyperstack (C1 = red, C2 = green).

4. Saves the resulting file as <ExperimentName>_<Well>_hyperstack.tif in the hyperstack/ folder.
5. Closes all images before proceeding to the next well.

After obtention of these hyperstack regrouping every channel at every timepoint for each well, images were processed to generated segmentation masks of the spheroid using another macro.

g) Binary mask generation from red and green hyperstacks

Binary masks of red and green fluorescence channels were generated using Macro 2.

1. The macro processes all two-channel image stacks located in the /hyperstack/ folder of the experiment directory and produces corresponding binary stacks in /mask/.
2. Each input file followed the naming pattern <Experiment>_<Well>_hyperstack.tif.
3. For every hyperstack (C = 2, typically red and green), both channels were converted to 8-bit and individually thresholded using the "Moments" automatic thresholding method (background = Default; ImageJ AutoThreshold implementation).
4. Thresholding was applied to the entire z-stack of each channel (calculate stack mode), generating a binary mask per channel (C1 = red mask, C2 = green mask).
5. Resulting masks were saved in the /mask/ directory under the same base filename, following the convention: /mask/<Experiment>_<Well>_mask_hyperstack.tif

A third Macro (Macro 3) was then developed to use these sets of masks to measure the required data:

1. The macro reads paired image stacks corresponding to each experimental well, consisting of:
2. /hyperstack/ → two-channel raw images (<exp>_<well>_hyperstack.tif), and /mask/ → binary masks (<exp>_<well>_mask_hyperstack.tif) delimiting the region of interest (ROI). (output from previous macro).
3. All image stacks were aligned in x-y dimensions, and analysis was performed slice by slice (z-axis).
4. For each z-slice, the binary mask (C1) was converted into a ROI, which was then applied to the corresponding red (C1) and green (C2) channels of the hyperstack.
5. The macro extracted, for both channels, the mean fluorescence intensity (Mean) and integrated density (IntDen = Mean × Area) within the ROI, together with the ROI area (in pixels and μm^2, using stored pixel dimensions).

6. The first valid slice was defined as t0 and used as a baseline for normalization.
7. For each subsequent slice, relative fluorescence ratios were computed as: Mean_rel_t0=Mean_t/Mean_t0 and IntDen_rel_t0=IntDen_t/IntDen_t0
8. If no ROI was detected in a slice, zeros were written for all values to preserve data continuity.
9. Results were appended to a global comma-separated file (measurements_RG.csv) created in the parent directory, containing the following columns:
    - Exp, Well, Slice as identifiers
    - Area_px, Area_μm^2 as the computed fluorescent spheroid area
    - Mean_red, Mean_green as the average intensity in red/green
    - IntDen_Red, IntDen_Green as the integrated Red/Green fluorescence intensity (=Mean*Area)
    - Mean_Red_relT0, Mean_Green_relT0, IntDen_Red_relT0, IntDen_Green_relT0 their counterpart values normalized to t0

The results stored in the csv file were then processed in R v4.5.1.

5. *ZONAL (FUSED) SPHEROID ANALYSIS.*

The same initial macro (Macro 1) created one hyperstack per well. To distinguish tumor zones according to fluorescence composition another macro was developed Fusion_bicolor_spheroids_masks_v0.1.

1. For each spheroid "hyperstack," the red (R) and green (G) channels were split, converted to 8-bit, and processed slice by slice.
2. First, the total tumor volume was delineated on the red channel using an automatic Moments threshold yielding a binary mask (*mask_Rmoments*).
3. In parallel, a normalized intensity ratio G / (R + G) was computed and blurred (σ = 1 px); pixels with ratio > 0.5 were binarized to define the mixed (red + green) interface zone (mask_RGplus).
4. Logical operations were then used to separate the two subvolumes:
    - RG^+ zone (mixed) = intersection of total tumor and green-dominant regions → RGplus = mask_Rmoments ∧ mask_RGplus
    - R-only zone (pure red) = total tumor minus the mixed zone → Ronly = mask_Rmoments − RGplus

5. These two masks were stacked over all z-slices to produce 3D "raw" mask hyperstacks (channels 1–3 = Ronly, RGplus, mask_Rmoments).
6. A global correction step was then applied to homogenize boundaries: the Moments mask was used as a clipping mask to restrict both Ronly and RGplus stacks to the tumor volume, yielding a "corrected" hyperstack (C1 = Ronly_corr, C2 = RGplus_corr, C3 = MaskGlobal). The macro automatically processed all wells within a chosen parent directory, saving outputs as:

   /mask_hyperstack_raw/ → _mask.tif

   /mask_hyperstack_corrected/ → _mask_corrected.tif

Another macro (Macro 4) was then used to measure red fluorescence in each region : Measure_fusion_spheroids_v0.1.

For each well, the macro:

1. Opens the two-channel hyperstack (C1 = red) and its three-channel corrected mask stack (C1 = Ronly, C2 = Green, C3 = Rtot).
2. Iterates through all z-slices (time points) of the red channel.
3. For each slice and each mask channel, extracts the ROI corresponding to the binary mask and measures:
   - Area (px and μm^2)
   - Mean red intensity
   - Integrated density (IntDen = Mean × Area)

1. Writes all results to a global CSV file (measurements_RG.csv), with the following columns:

   IntDen_R_in_Ronly, Area_Ronly, Mean_Ronly: red intensity in pure red zone

   IntDen_R_in_Green, Area_Green, Mean_Green: red intensity in red+green zone

   IntDen_R_in_Rtot, Area_Rtot, Mean_Rtot: total red signal across tumor

For this experiment specifically, we used mean intensity rather than integrated signal to avoid artifacts from frame-to-frame mask fluctuations due to spheroid reshaping. Because the mask was defined by local GFP/(GFP + RFP) ratios, small shifts could occur between compartments; using mean intensity limits false gains from spillover and favors specific-

ity over sensitivity, ensuring that fluorescence changes reflect genuine differential cytotoxicity.

COMPUTATIONAL ANALYSIS OF SPHEROID REPRESENTATIVITY

To estimate the minimal number of spheroids required to capture the transcriptomic heterogeneity of parental tumors, we re-analyzed previously generated BRB-seq datasets from our earlier study on clear cell renal cell carcinoma (ccRCC) spheroids. In that work, RNA was extracted from dissociated patient tumors and from spheroids re-infiltrated with autologous tumor-infiltrating lymphocytes (TILs), at multiple stages of spheroid formation. For each patient sample, triplicate BRB-seq libraries were generated from bulk tumor tissue and from ten individual spheroids derived from the same dissociation. Normalized count matrices (TPM) and corresponding Pearson correlation coefficients (PCC) between each spheroid and its parental tumor replicate were retrieved from the original dataset. All possible combinations of n spheroids ($1 \leq n \leq 10$) were simulated in silico by averaging their normalized gene expression profiles, followed by recalculation of the PCC between each simulated pool and the mean of the tumor triplicates. For each patient, the mean and standard deviation of PCC values were computed for every pool size n, across all possible combinations. The marginal gain in representativity was defined as the incremental increase in PCC between successive pool sizes: $\Delta meanPCC_n = PCC_n - PCC_n\text{-}1$. The empirical "representativity plateau" was defined as the smallest n for which $\Delta meanPCC < 0.005$.

MICROFLUIDIC DEVICE DESIGN AND FABRICATION

A microfluidic chip was designed to trap individual tumor spheroids using SolidWorks CAD software (Dassault Systèmes, France), based on the principle of hydrodynamic bypass trapping. This design exploits local flow resistance differences to direct the incoming spheroid into the shortest available path, as initially described by Tan and Takeuchi et al. (36). The overall microfluidic layout followed a serpentine main channel, along which ten bypass traps were integrated in series, allowing the sequential capture and perfusion of up to ten spheroids per circuit.

Each trap connected two consecutive bends of the serpentine path through a short, straight bypass channel offering a lower hydrodynamic resistance than the curved main path. When a trap was empty, the flow preferentially passed through it, carrying the spheroid into the trap. Once the trap became occupied, its local resistance increased, redirecting the flow back along the serpentine path and automatically preventing additional spheroids from entering the same site. This passive self-regulation ensured efficient single-spheroid trapping and stable positioning under continuous perfusion.

To accommodate spheroids of 400–600 µm in diameter, the serpentine main channel had

a square cross-section of 800 × 800 µm. Each U-shaped bypass trap connected two consecutive bends of the serpentine and featured an entrance width of 900 µm (1.125 × 800 µm) leading to a narrow final restriction 300 µm wide (0.375 × 800 µm) and 100 µm long (0.125 × 800 µm) before rejoining the main path. The channel height remained constant at 800 µm throughout the circuit.

This trap geometry was derived from the framework established by Quintard et al. ensuring robust trapping efficiency (21). The final design complied with ISO 22916:2022 standards for microfluidic device fabrication and interoperability. Each chip (credit-card size, 85 × 54 mm) comprised five independent serpentine circuits, each containing ten hydrodynamic traps arranged in series. Fluidic inlets and outlets were configured with standard Luer connectors, ensuring compatibility with syringe or peristaltic pumps for controlled perfusion.

Design files were processed using MasterCAM software (CNC Software, LLC, USA), and the chips were micromachined in cyclic olefin copolymer (COC 6013S; Topas Advanced Polymers, Oberhausen, Germany) on a DATRON M7HP milling platform (Datron AG, Germany) by Axxicon (Eindhoven, The Netherlands).

TUMOR PROCESSING

Within 30 minutes following nephrectomy, ccRCC tumor specimens were collected in ice-cold RPMI 1640 medium (Gibco). Fibrous and necrotic areas were carefully removed, and viable tissue fragments were finely minced into ~1 mm^3 pieces using sterile scalpels. To maximize viability, excessive mechanical dissociation was avoided. Tumor fragments were enzymatically digested in 6 mL of dissociation buffer consisting of Hank's Balanced Salt Solution (HBSS, Gibco), Liberase TM (0.28 Wünsch units/mL, Sigma-Aldrich), and recombinant DNase I (125 U/mL, Sigma-Aldrich). The digestion was performed at 37°C in a water bath for 30–40 minutes, with manual agitation every 10 minutes to enhance enzymatic efficiency.

Following digestion, the cell suspension was filtered through a 100 µm nylon mesh (Corning) into a 50 mL conical tube (Falcon). Enzymatic activity was stopped by adding 35 mL of ice-cold complete RPMI medium containing 10% fetal calf serum (FCS, Sigma-Aldrich), L-glutamine (300 µg/mL, Gibco), gentamicin (50 µg/mL, Gibco), and amphotericin B (2.5 µg/mL, Gibco). After centrifugation and red blood cell lysis (RBC Lysis Buffer, BioLegend), cells were washed, resuspended in complete RPMI, and counted. Cell viability was assessed by trypan blue exclusion.

Immune ($CD45^+$) and non-immune ($CD45^-$) fractions were separated using magnetic bead selection (Miltenyi Biotec, QuadroMACS Separator) according to the manufacturer's instructions. Both fractions were processed independently for downstream culture.

FORMATION OF PATIENT DERIVED IMMUNE INFILTRATED SPHEROIDS

1. *TUMOR SPHEROID FORMATION*

Following tumor processing (see above), non-immune ($CD45^-$) cells were seeded in ultra-low attachment 96-well round-bottom plates. Cell density was adjusted between 10,000 and 20,000 cells per well to accommodate the chip's trap size. A duplicate of these cell seedings was made and 5% growth factor–depleted Matrigel (Corning) was added to facilitate aggregation in challenging samples; however, Matrigel-free conditions were preferred and successfully used for all experiments presented in this study.

Plates were centrifuged briefly (500 × g, 1 min) to promote cell settling, then incubated for 48 hours at 37°C and 5% CO_2 to allow compact spheroid formation. Morphology and size uniformity were verified under phase-contrast microscopy before proceeding to co-culture experiments.

6. *TUMOR-INFILTRATING LYMPHOCYTE (TIL) ACTIVATION AND RE-INFILTRATION*

Autologous $CD45^+$ cells were plated in complete RPMI supplemented with recombinant human IL-15 (30 ng/mL, PeproTech) at a density of 1×10^5 cells per well in 96-well plates and incubated for 48 hours to promote survival and activation.

Following spheroid formation and TIL pre-activation, tumor spheroids were co-cultured with activated TILs at a 3:1 (TIL:tumor) ratio in U-bottom 96-well plates. After 24 hours of static co-culture, reinfiltrated spheroids were gently transferred to the microfluidic device for dynamic perfusion experiments.

SPHEROID LOADING AND ON-CHIP OPERATION

Before each experiment, microfluidic chips were cleaned by sequential rinsing with distilled water and 90% ethanol, then air-dried under sterile conditions. The channels were sealed using MicroAmp™ optical-grade PCR film (Applied Biosystems, USA). For inlet reservoirs, 5-mL plastic syringes (BD Plastipak) were shortened to a 4-mL volume using a heat-cut blade to create open wells compatible with pipette loading.

Perfusion and suction were controlled by a 6-channel syringe pump (Shenchen, China) operating in aspiration mode, using 10-mL syringes connected to the chip outlets via medical sterile perfusion tubes (Braun, Germany). Operations were performed under a stereomicroscope to allow real-time visualization of fluid interfaces and spheroid positioning.

Prior to biological loading, chips were filled ("primed") with pre-warmed and degassed culture medium (RPMI or RCCM, depending on experiment) to prevent bubble formation. Degassing was performed under vacuum for 5 min. The circuit was fully wetted at a flow rate of 50 µL/min until all channels were filled and free of air bubbles.

Pre-formed spheroids (12 per circuit) were collected in 200-µL pipette tips with the cone end cut off and gently injected directly into the inlet syringe barrel. The spheroids were transported by gravity and hydrodynamic flow toward the trapping region and captured sequentially in individual hydrodynamic traps. Trapping efficiency was confirmed visually under brightfield illumination

Once all traps were filled, perfusion continued until the inlet reservoir reached approximately 500 µL of residual volume. At this stage, pre-activated PBMCs (typically 10^6 per track, activated as described in Section 4.2) were added directly to the inlet reservoir in RPMI complete medium, bringing the total inlet volume to 1 mL. The perfusion flow was maintained at 50 µL/min until circulating immune cells were observed passing through the last trap, ensuring full chip perfusion and immune saturation.

Flow was then paused, and the chip and syringe-pump were transferred to a cell-culture incubator (37 °C, 5% CO_2). Immediately after transfer, a short flow pulse (50 µL/min, 10s) was applied to reposition spheroids within the traps, followed by steady-state perfusion at 1 µL/min in RPMI containing IL-15 (30 ng/mL, Peprotech, USA) for long-term co-culture.

CONFOCAL IMAGING: HARVESTING, OPTICAL CLEARING AND IMAGE ANALYSIS

1. *CELL LABELING WITH CELLTRACE VIOLET*

When mentioned, cells were pre-labeled with CellTrace™ Violet (CTV) following the manufacturer's instructions (Thermo Fisher Scientific, USA).

7. *SPHEROID HARVESTING*

For confocal imaging after chip co-culture, spheroids were harvested by backflushing. The outlet and its tubing were disconnected and replaced with a syringe connected to new tubing containing 5 mL of PBS, while the inlet was replaced by an empty 5 mL syringe with the plunger fully depressed. To optimize recovery, one operator gently pushed the PBS through the outlet-side syringe while holding the tubing in place, whereas a second operator simultaneously lifted the plunger of the inlet-side syringe to facilitate flow. Once the 5 mL of PBS had completely passed through the chip, the procedure was stopped, and the collecting syringe containing the backflushed spheroids was emptied into a 15 mL conical tube. Spheroids were then rinsed 3 times in 10mL PBS to avoid any contaminant non-infiltrated immune cell.

8. *SPHEROID OPTICAL CLEARING*

Optical clearing was adapted from the protocol by Gunasingh et al. (37) with minor modifications. Tumor spheroids generated by the agarose overlay method were fixed in 4% paraformaldehyde for 20 min at 37 °C, washed twice in PBS, and permeabilized with 0.5 % Triton X-100 (Sigma-Aldrich) in PBS for 2 h at room temperature under gentle rotation.

The spheroids were then incubated overnight in PBS-TT (PBS containing 0.1 % Tween-20 and 0.1 % Triton X-100, Sigma-Aldrich, Germany). A 2 % (w/v) low-melting agarose solution was prepared by dissolving 0.5 g agarose (ThermoFisher, USA) in 25 mL PBS, and the clearing solution was prepared by dissolving 9 g N,N,N′,N′-tetrakis(2-hydroxypropyl)ethylenediamine (Sigma-Aldrich, Germany), 22 g urea, 44 g sucrose, and 0.1 g Triton X-100 (all Sigma-Aldrich, Germany) in 24.9 g deionized water at 56 °C with gentle agitation until complete dissolution.

Spheroids were embedded in liquid agarose (≈ 50 µL per sample) and dispensed onto 24-well glass-bottom plates (3-5 spheroids per well, MatTek Corporation, USA). After gel solidification, 500 µL of clearing solution were added per well, ensuring full immersion of the gel. Samples were incubated at room temperature for at least 24 h and imaged directly in the clearing solution. Immunofluorescence and nuclear counterstaining steps from the original JOVE protocol were omitted, as only endogenous fluorescent reporters were analyzed.

9. *IMAGING AND IMAGE ANALYSIS*

Confocal imaging was performed on a Zeiss LSM 800 inverted microscope using an EC Plan-Neofluar 20×/0.5 M27 air objective (working distance = 2 mm). Z-stacks were acquired using the optimal number of optical sections automatically suggested by the Zeiss ZEN software, typically resulting in 30–40 planes per stack. Images were imported into Fiji 1.54p (ImageJ)(35) for preprocessing and segmentation. The lymphocyte channel (CTV) was first smoothed using a 2-pixel median filter, followed by a Gaussian filter (σ = 2 px). Cell candidates were detected using the 3D Maxima Finder plugin (3D suite)(38) with the noise level set to 1 and the background value manually adjusted according to visual inspection of the raw image. These detected peaks were then used as seeds for 3D segmentation. Segmentation was performed using the 3D Spot Segmentation plugin, initialized with the previously generated seeds. Parameters were as follows:

- Seed threshold = 1
- Local background = auto
- Threshold method = Local Mean
- Local Mean parameters: Radius 0 = 2, Radius 1 = 4, Radius 2 = 6, Weight = 0.5
- Watershed = enabled
- Minimum object volume = 50 voxels; maximum = full stack volume
- Seed radius = 2

All segmented objects were added to the 3D Manager with unique index labels. The tumor

spheroid was segmented independently from the red channel by automatic Otsu thresholding. Because the red fluorescence intensity decreased at the top and bottom optical planes, the resulting binary mask was visually inspected and manually corrected: slices preceding and following the visually defined spheroid boundaries were filled with black to avoid false surfaces. Subsequently, the Euclidean Distance Map (EVF) of the spheroid was computed using the 3D Distance Map tool from 3D Suite. Immune cell density was computed using the 3D EVF Layers tool with a step size of 0.05. Quantification of individual lymphocyte positions relative to the spheroid surface was obtained from 3D measurements, including centroid-to-surface distances. The data was exported and further analyzed in R v4.5.1.

3D visualization was performed using Napari (version 0.6.6) (39). The preprocessed CTV channel, the corrected spheroid mask, and the 3D index image obtained from the Spot Segmentation plugin were imported as separate layers. The spheroid mask was converted into a 3D surface representation using the marching_cubes algorithm (skimage.measure.marching_cubes) (40).

Segmented lymphocytes were rendered as colored 3D surfaces using a Paired colormap (Matplotlib, 12 colors) (41), assigned by modulo indexing to ensure visual distinction between adjacent cells while maintaining color-blind accessibility. The spheroid surface was displayed in semi-transparent red (opacity = 0.1). The CTV signal was manually adjusted for optimal visualization.

Napari scenes were displayed under the dark theme with voxel scaling corresponding to acquisition parameters. Camera angles were adjusted individually for each spheroid to optimize the visualization of infiltration patterns and segmentation quality, rather than fixed across samples. Screenshots were exported for figure assembly.

FLOW CYTOMETRY AFTER SPHEROID HARVESTING

1. *SAMPLE COLLECTION*

For spheroid immune composition analysis after on-chip cocultures, 3 types of samples were used: on chip PBMCs taken from the outlet (tubing+syringe), “non-infiltrated” on chip PBMCs contained in the outlet of tracks containing spheroids, and “infiltrated” samples: immune cells contained in the spheroid after 72h of coculture under continuous 1µL/min flow.

The first two types were obtained by centrifugation of the collected outlets. For the third type, spheroids were harvested by backflushing (as described above), thoroughly rinsed, and processed for flow cytometry, starting with enzymatic dissociation.

10. *SPHEROID DISSOCIATION*

Spheroids were transferred to 1.5-mL Eppendorf tubes and further washed once in PBS. PBS was then replaced with 50 µL of Accutase (Stemcell Technologies, Canada) to dissociate the spheroids according to the protocol given by Grässer et al. (42). Every 10 minutes, each sample was pipetted 10 times up and down to combine mechanical and enzymatic dissociation, as older spheroids get difficult to dissociate. Three rounds of 10 minutes were performed before spheroids were finally dissociated.

In our immune composition experiment, control conditions (PBMCs without spheroids) as well as the "non-infiltrated" condition were submitted to the same enzymatic digestion as the spheroids to avoid bias.

Tubes were then centrifuged and processed for flow cytometry.

11. *CONVENTIONAL FLOW CYTOMETRY*

Conventional flow cytometry was performed on PBMCs recovered from co-cultures. Cells were adjusted to 1×10^6 cells/mL in PBS and preincubated for 10 min with human polyclonal IgG (Sigma-Aldrich) to block Fc receptors. Viability was assessed using Zombie Aqua™ (BioLegend). Surface staining was performed for 30 min at 4 °C with the following antibodies: CD3 PerCP-Vio700 (Miltenyi), CD4 BV711 (BD Biosciences), CD8 AF700 (BioLegend), CD56 PE-Vio770 (Miltenyi), CD69 BV421 (BioLegend), and ILT2 APC (eBioscience). After washing, intracellular staining for Ki-67 PE (BD Biosciences) was performed using the FoxP3/Transcription Factor Staining Buffer Set (Thermo Fisher Scientific) according to the manufacturer's protocol.

Samples were acquired on an Attune NxT 3-laser flow cytometer (Thermo Fisher Scientific) and analyzed using FlowJo™ v10 (BD Life Sciences). Compensation was performed with UltraComp eBeads™ (Invitrogen), and gating was applied to live, singlet lymphocytes.

12. *CYTOKINE DOSAGE IN CHIP EFFLUENTS*

Cytokine levels in microfluidic chip effluents were quantified using a LEGENDplex™ Human CD8/NK Panel (BioLegend) according to the manufacturer's instructions and without dilution. The panel simultaneously measured IFN-γ, TNF-α, Granzyme B (GzmB), Granulysin (GNLY), and Perforin (PRF1) to assess cytotoxic and inflammatory immune activity within the circulating compartment.

Effluent samples were collected at the end of perfusion by removing the outlet tube and gently aspirating the forming 200 µL drop corresponding to the volume presently in the chip at the end of experiment. Samples were then centrifuged to remove cellular debris, and stored at −80°C until analysis. Following thawing, samples were incubated with antibody-coated capture beads for 2 hours at room temperature under gentle agitation. Af-

ter washing, detection antibodies and streptavidin-PE were added sequentially. Samples were acquired on a Attune NxT flow cytometer (Thermofisher), and cytokine concentrations were calculated using the Qognit Data Analysis Suite (BioLegend).

Cytokine concentrations are reported in pg/mL. All measurements were performed in technical duplicates, and background values from control medium were subtracted.

13. *SPECTRAL FLOW CYTOMETRY*

Before antibody staining, cells were incubated with human polyclonal IgG (Sigma-Aldrich) for 10 minutes to block Fc receptors and prevent nonspecific binding. Cells were then incubated for 30 minutes at room temperature in PBS containing the extracellular antibody mix. Following surface staining, cells were fixed and permeabilized using the FoxP3 Fixation/Permeabilization kit (ThermoFisher) for 30 minutes at room temperature, then incubated with the intracellular antibody mix in permeabilization buffer for an additional 30 minutes.

The complete list of antibodies and fluorochrome conjugates used in this 37-color panel is provided in Supplementary Table 1. Stained PBMCs were acquired on a five-laser Cytek Aurora spectral cytometer (Cytek Biosciences). The same acquisition settings were applied across all batches.

Data were deconvoluted on SpectroFlo and compensated and then imported to OMIQ application (Dotmatics).

Data were further compensated and scaled, and FSC SSC compatible single, LiveDead- $CD3^+$ lymphocytes from all conditions were concatenated and subsampled to equal event counts per condition. Unsupervised clustering and dimensionality reduction were performed using the FlowSOM (using the elbow method for cluster number choice) and UMAP workflows. Clusters were manually annotated based on median marker expression and grouped by shared expression patterns.

14. *STATISTICAL ANALYSIS*

For IncuCyte time-lapse experiments, the integrated mCherry fluorescence intensity was quantified at each time point (0–96 h) and normalized to baseline (t_0). The area under the fluorescence decay curve (AUC_{0-96} h) was computed by trapezoidal integration and used as a surrogate of spheroid persistence: high AUC values indicate limited PBMC-mediated killing, whereas low AUC values reflect enhanced cytotoxic activity.

The mean AUC per donor was used as the biological replicate, and technical variability was represented by the standard error of the mean (SEM) across replicate wells.

A linear mixed-effects model was fitted using the *lme4* and *lmerTest* packages:

AUC~Treatment×PD-L1 status+(1|Donor) with *Treatment* (Avelumab vs no treatment) and *PD-L1 status* (PD-L1WT vs PD-L1KO) as fixed effects and *Donor* as a random intercept. Degrees of freedom were computed with the Kenward–Roger method, and pairwise contrasts were estimated using emmeans.

Three planned comparisons were tested:

1. *Avelumab effect* within each PD-L1 status (PD-L1KO: $p = 0.005$; PD-L1WT: $p < 0.001$).
2. *Baseline protection* by PD-L1 (WT vs KO under no treatment: Δ = +64.9 ± 2.4, $p < 0.0001$).
3. *Cross-arm comparison* (WT + Avelumab vs KO no treatment: Δ = +32.2 ± 2.5, $p < 0.0001$).

Equivalence between these two latter conditions was formally assessed using a two one-sided test (TOST) with an a-priori equivalence margin of ±10 % of the KO/no-treatment mean (Δ = 3.26 AUC). The 90 % confidence interval of the contrast ([28.1, 36.4]) lay entirely outside this margin ($p_{\text{tost}} = 1$), indicating absence of equivalence. Model diagnostics (QQ-plots and residual-vs-fitted) supported normality and homoscedasticity.

For experiments using variable PD-L1$^+$ target proportions, the AUC was modeled as a function of both Treatment and PD-L1$^+$ fraction (continuous variable, 0–100%) with donor as a random effect (AUC ~ Treatment × PD-L1$^+$% + (1|Donor)). Interaction terms were evaluated using Type III ANOVA (Satterthwaite correction), and fitted slopes were extracted with emtrends (emmeans). This allowed assessment of dose-dependent modulation of cytotoxicity by PD-L1 expression and checkpoint blockade.

Cytokine concentrations were analyzed using descriptive statistics and non-parametric paired tests (Wilcoxon signed-rank test, two-tailed) given the small sample size (n = 3 biological replicates). Data are presented as mean ± SEM for inter-donor comparisons and as individual paired values for within-donor contrasts. Fold changes were computed from donor-matched mean concentrations. For exploratory visualization, cytokine profiles were scaled per donor and plotted using ggplot2 (tidyverse). No multiple-testing correction was applied due to the limited number of planned comparisons.

All analyses were performed in R v4.5.1 using the tidyverse, lme4, lmerTest, emmeans, and ggplot2 packages. Data are presented as either mean ± SEM (parametric) or median [IQR] (non-parametric). All tests were two-tailed, and p-values < 0.05 were considered statistically significant unless stated otherwise.

ACKNOWLEDGMENTS

We would like to thank the Saint-Louis Research Institute Core Facility, particularly Niclas Setterblad, Claire Maillard and Christelle Doliger, for their valuable advice and kind assistance with the cytometry experiments.

The chip drawing in Fig 8 is based on "microfluids_chip" by Marcel Tisch (CC0), modified to represent our 5-channel chip design.

Blood tube icon from "tube_blood" by Helicase 11, licensed under CC BY 4.0

REFERENCES

1. Ferlay J, Laversanne M, Ervik M, Lam F, Colombet M, Mery L, et al. International Agency for Research on Cancer (IARC). 2024 [cited 2025 Sept 2]. Global Cancer Observatory: Cancer Tomorrow (version 1.1). Available from: https://gco.iarc.who.int/tomorrow

2. Bex A, Albiges L, Bedke J, Capitano U, Dabestani S, Hora M, et al. EAU Guidelines on Renal Cell Carcinoma 2025 update. In: EAU Guidelines Edn presented at the EAU Annual Congress, Madrid 2025 [Internet]. Arnhem, The Netherlands: EAU Guidelines Office; 2025 [cited 2025 Aug 29]. Available from: https://uroweb.org/guidelines/compilations-of-all-guidelines/

3. Moch H, Cubilla AL, Humphrey PA, Reuter VE, Ulbright TM. The 2016 WHO Classification of Tumours of the Urinary System and Male Genital Organs—Part A: Renal, Penile, and Testicular Tumours. Eur Urol. 2016;70(1):93–105.

4. Motzer RJ, Escudier B, McDermott DF, George S, Hammers HJ, Srinivas S, et al. Nivolumab versus Everolimus in Advanced Renal Cell Carcinoma. N Engl J Med. 2015 Nov 5;373(19):1803–13.

5. Motzer RJ, Tannir NM, McDermott DF, Frontera OA, Melichar B, Choueiri TK, et al. Nivolumab plus Ipilimumab versus Sunitinib in Advanced Renal-Cell Carcinoma. N Engl J Med. 2018;378(14):1277–90.

6. Tannir NM, Albigès L, McDermott DF, Burotto M, Choueiri TK, Hammers HJ, et al. Nivolumab plus ipilimumab versus sunitinib for first-line treatment of advanced renal cell carcinoma: extended 8-year follow-up results of efficacy and safety from the phase III CheckMate 214 trial. Ann Oncol Off J Eur Soc Med Oncol. 2024 Nov;35(11):1026–38.

7. Choueiri TK, Powles T, Burotto M, Escudier B, Bourlon MT, Zurawski B, et al. Nivolumab plus Cabozantinib versus Sunitinib for Advanced Renal-Cell Carcinoma. N Engl J Med. 2021 Mar 3;384(9):829–41.

8. Choueiri TK, Eto M, Motzer R, De Giorgi U, Buchler T, Basappa NS, et al. Lenvatinib plus pembrolizumab versus sunitinib as first-line treatment of patients with advanced renal cell carcinoma (CLEAR): extended follow-up from the phase 3, ran-

domised, open-label study. Lancet Oncol. 2023 Mar;24(3):228–38.

9. Motzer R, Alekseev B, Rha SY, Porta C, Eto M, Powles T, et al. Lenvatinib plus Pembrolizumab or Everolimus for Advanced Renal Cell Carcinoma. N Engl J Med. 2021 Apr 7;384(14):1289–300.

10. Powles T, Burotto M, Escudier B, Apolo AB, Bourlon MT, Shah AY, et al. Nivolumab plus cabozantinib versus sunitinib for first-line treatment of advanced renal cell carcinoma: extended follow-up from the phase III randomised CheckMate 9ER trial. ESMO Open. 2024 May;9(5):102994.

11. Rini BI, Plimack ER, Stus V, Gafanov R, Hawkins R, Nosov D, et al. Pembrolizumab plus Axitinib versus Sunitinib for Advanced Renal-Cell Carcinoma. N Engl J Med. 2019 Mar 21;380(12):1116–27.

12. Rini BI, Plimack ER, Stus V, Gafanov R, Waddell T, Nosov D, et al. Pembrolizumab plus axitinib versus sunitinib for advanced clear cell renal cell carcinoma: 5-year survival and biomarker analyses of the phase 3 KEYNOTE-426 trial. Nat Med. 2025 Aug 1;1–10.

13. Choueiri TK, Tomczak P, Park SH, Venugopal B, Ferguson T, Chang YH, et al. Adjuvant Pembrolizumab after Nephrectomy in Renal-Cell Carcinoma. N Engl J Med. 2021 Aug 19;385(8):683–94.

14. Haas NB, Powles T, Tomczak P, Park SH, Venugopal B, Symeonides SN, et al. Five-year follow-up results from the phase 3 KEYNOTE-564 study of adjuvant pembrolizumab (pembro) for the treatment of clear cell renal cell carcinoma (ccRCC). J Clin Oncol. 2025 June;43(16_suppl):4514–4514.

15. Robert C. A decade of immune-checkpoint inhibitors in cancer therapy. Nat Commun. 2020 July 30;11(1):3801.

16. Braun DA, Street K, Burke KP, Cookmeyer DL, Denize T, Pedersen CB, et al. Progressive immune dysfunction with advancing disease stage in renal cell carcinoma. Cancer Cell. 2021 May 10;39(5):632-648.e8.

17. Vuong L, Kotecha RR, Voss MH, Hakimi AA. Tumor Microenvironment Dynamics in Clear Cell Renal Cell Carcinoma. Cancer Discov. 2019 Oct;9(10):1349–57.

18. Sobczuk P, Brodziak A, Khan MI, Chhabra S, Fiedorowicz M, Wełniak-Kamińska M, et al. Choosing The Right Animal Model for Renal Cancer Research. Transl Oncol. 2020 Mar 1;13(3):100745.

19. Gao J, Luo H, Wang S, Zhou C, Li Z, Kimhoy C, et al. Renal cell carcinoma organoids for precision medicine: bridging the gap between models and patients. J Transl Med. 2025 Oct 21;23(1):1152.

20. Zhang C, Sui Y, Liu S, Yang M. In vitro and in vivo experimental models for cancer immunotherapy study. Curr Res Biotechnol. 2024 Jan 1;7:100210.

21. Quintard C, Tubbs E, Jonsson G, Jiao J, Wang J, Werschler N, et al. A microfluidic

platform integrating functional vascularized organoids-on-chip. Nat Commun. 2024 Feb 16;15(1):1452.

22. Lugand L, Mestrallet G, Laboureur R, Dumont C, Bouhidel F, Djouadou M, et al. Methods for Establishing a Renal Cell Carcinoma Tumor Spheroid Model With Immune Infiltration for Immunotherapeutic Studies. Front Oncol [Internet]. 2022 [cited 2022 Nov 29];12. Available from: https://www.frontiersin.org/articles/10.3389/fonc.2022.898732

23. Lee H, Park SH, Shin EC. IL-15 in T-Cell Responses and Immunopathogenesis. Immune Netw. 2024 Feb 16;24(1):e11.

24. Tietze JK, Wilkins DEC, Sckisel GD, Bouchlaka MN, Alderson KL, Weiss JM, et al. Delineation of antigen-specific and antigen-nonspecific CD8+ memory T-cell responses after cytokine-based cancer immunotherapy. Blood. 2012 Mar 29;119(13):3073–83.

25. Neal JT, Li X, Zhu J, Giangarra V, Grzeskowiak CL, Ju J, et al. Organoid Modeling of the Tumor Immune Microenvironment. Cell. 2018 Dec 13;175(7):1972-1988.e16.

26. Esser LK, Branchi V, Leonardelli S, Pelusi N, Simon AG, Klümper N, et al. Cultivation of Clear Cell Renal Cell Carcinoma Patient-Derived Organoids in an Air-Liquid Interface System as a Tool for Studying Individualized Therapy. Front Oncol [Internet]. 2020 Sept 22 [cited 2025 Oct 28];10. Available from: https://www.frontiersin.org/journals/oncology/articles/10.3389/fonc.2020.01775/full

27. Miller CP, Tsuchida C, Zheng Y, Himmelfarb J, Akilesh S. A 3D Human Renal Cell Carcinoma-on-a-Chip for the Study of Tumor Angiogenesis. Neoplasia. 2018 June 1;20(6):610–20.

28. Miller CP, Tsuchida C, Zheng Y, Himmelfarb J, Akilesh S. A 3D Human Renal Cell Carcinoma-on-a-Chip for the Study of Tumor Angiogenesis. Neoplasia N Y N. 2018 May 7;20(6):610–20.

29. Virumbrales-Muñoz M, Chen J, Ayuso J, Lee M, Abel EJ, Beebe DJ. Organotypic primary blood vessel models of clear cell renal cell carcinoma for single-patient clinical trials. Lab Chip. 2020 Nov 24;20(23):4420–32.

30. Veith I, Nurmik M, Mencattini A, Damei I, Lansche C, Brosseau S, et al. Assessing personalized responses to anti-PD-1 treatment using patient-derived lung tumor-on-chip. Cell Rep Med [Internet]. 2024 May 21 [cited 2025 Oct 29];5(5). Available from: https://www.cell.com/cell-reports-medicine/abstract/S2666-3791(24)00241-6

31. Li Y, Lih TSM, Dhanasekaran SM, Mannan R, Chen L, Cieslik M, et al. Histopathologic and proteogenomic heterogeneity reveals features of clear cell renal cell carcinoma aggressiveness. Cancer Cell. 2023 Jan 9;41(1):139-163.e17.

32. Bukur J, Rebmann V, Grosse-Wilde H, Luboldt H, Ruebben H, Drexler I, et al. Functional Role of Human Leukocyte Antigen-G Up-Regulation in Renal Cell Carcinoma1. Cancer Res. 2003 July 21;63(14):4107–11.

33. Rouas-Freiss N, LeMaoult J, Verine J, Tronik-Le Roux D, Culine S, Hennequin C, et al. Intratumor heterogeneity of immune checkpoints in primary renal cell cancer: Focus on HLA-G/ILT2/ILT4. OncoImmunology. 2017 Sept 2;6(9):e1342023.

34. Dijkstra KK, Vendramin R, Karagianni D, Witsen M, Gálvez-Cancino F, Hill MS, et al. Subclonal immune evasion in non-small cell lung cancer. Cancer Cell. 2025 Oct 13;43(10):1833-1849.e10.

35. Schindelin J, Arganda-Carreras I, Frise E, Kaynig V, Longair M, Pietzsch T, et al. Fiji: an open-source platform for biological-image analysis. Nat Methods. 2012 July;9(7):676–82.

36. Tan WH, Takeuchi S. A trap-and-release integrated microfluidic system for dynamic microarray applications. Proc Natl Acad Sci U S A. 2007 Jan 23;104(4):1146–51.

37. Gunasingh G, Browning AP, Haass NK. Rapid Optical Clearing for Semi-High-Throughput Analysis of Tumor Spheroids. JoVE J Vis Exp. 2022 Aug 23;(186):e64103.

38. Ollion J, Cochennec J, Loll F, Escudé C, Boudier T. TANGO: a generic tool for high-throughput 3D image analysis for studying nuclear organization. Bioinformatics. 2013 July 15;29(14):1840–1.

39. Perkel JM. Python power-up: new image tool visualizes complex data. Nature. 2021 Dec 6;600(7888):347–8.

40. Walt S van der, Schönberger JL, Nunez-Iglesias J, Boulogne F, Warner JD, Yager N, et al. scikit-image: image processing in Python. PeerJ. 2014 June 19;2:e453.

41. Hunter JD. Matplotlib: A 2D Graphics Environment. Comput Sci Eng. 2007 May;9(3):90–5.

42. Grässer U, Bubel M, Sossong D, Oberringer M, Pohlemann T, Metzger W. Dissociation of mono- and co-culture spheroids into single cells for subsequent flow cytometric analysis. Ann Anat - Anat Anz. 2018 Mar 1;216:1–8.

SUPPLEMENTARY MATERIALS :

MACROS

MACRO 1

```
// ========================
// Hyperstacks Incucyte (R+G) par puit -> dossier parent/hyperstack/
// ========================

macro "Build Hyperstacks R+G per well" {
  // 1) Choix du dossier parent
  parentDir = getDirectory("Choisir le dossier parent (contenant 'red' et 'green')");
  sep = File.separator;
```

```
  redDir   = parentDir + “red”   + sep;
  greenDir = parentDir + «green» + sep;

  // Dossier de sortie
  outDir = parentDir + “hyperstack” + sep;
  if (!File.exists(outDir)) File.makeDirectory(outDir);

  if (!File.exists(redDir))   exit(«Dossier ‘red’ introuvable : « + redDir);
  if (!File.exists(greenDir)) exit(«Dossier ‘green’ introuvable : « + greenDir);

  // 2) Récupérer la liste des puits présents depuis ‘red’
  listRed = getFileList(redDir);
  if (listRed.length==0) exit(“Aucune image dans “ + redDir);

  // Déduire le nom d’expérience et les puits depuis les fichiers ‘red’
  wells = newArray();
  nW = 0;
  expName = “”;

  for (i=0; i<listRed.length; i++) {
    name = listRed[i];
    if (!endsWith(name, “.tif”) && !endsWith(name, “.tiff”)) continue;
    parts = split(name, “_”);
    if (parts.length < 5) continue; // non conforme

    if (expName==””) expName = parts[0]; // premier rencontré
    color = parts[1]; // “red”
    if (color!=”red”) continue;

    well = parts[2]; // ex: “C3”
    if (indexOf(wells, nW, well) < 0) {
      wells = Array.concat(wells, newArray(well));
      nW++;
    }
  }

  if (nW==0) exit(«Aucun puit détecté dans les fichiers ‘red’.»);

  print(«\\Clear»);
  print(«Expérience détectée : « + expName);
  print(«Puits détectés (« + nW + «): « + joinArray(wells, «, «));

  // 3) Boucle sur les puits
  for (w=0; w<nW; w++) {
    well = wells[w];
    print(“\\Update: Traitement puit “ + well + “ (“+(w+1)+”/”+nW+”)”);
    run(“Close All”);

    // 3a) Import RED
    redFilter = “(“ + well + “)”;
    run(“Image Sequence…”, “open=[“+redDir+”] sort filter=[“+redFilter+”]”);
    if (nImages<1) { print(“Avertissement: pas de RED pour “ + well + “.”); run(“Close All”); continue; }
    rename(“RED_”+well);

    // 3b) Import GREEN
    greenFilter = “(“ + well + “)”;
    run(“Image Sequence…”, “open=[“+greenDir+”] sort filter=[“+greenFilter+”]”);
    if (nImages<2) { print(“Avertissement: pas de GREEN pour “ + well + “.”); run(“Close All”); continue; }
    rename(“GREEN_”+well);

    // 3c) Merge -> Hyperstack (C=2, T=time)
    run(“Merge Channels…”, “c1=[RED_”+well+”] c2=[GREEN_”+well+”] create”);

    // 3d) Enregistrement dans /hyperstack
    outName = expName + “_” + well + “_hyperstack.tif”;
    outPath = outDir + outName;
    saveAs(“Tiff”, outPath);
    print(“Enregistré : “ + outPath);

    // 3e) Fermetures
    run(“Close All”);
  }

  print(“Terminé.”);
}

// ---- Helpers ----
```

```
function indexOf(arr, len, value) {
  for (ii=0; ii<len; ii++) if (arr[ii]==value) return ii;
  return -1;
}
function joinArray(arr, sep) {
  s = "";
  for (i = 0; i < arr.length; i++) { if (i > 0) s += sep; s += arr[i]; }
  return s;
}
```

MACRO 2

```
// =========================
// Bloc 2 minimal : masque Sphéroïde depuis le canal Rouge via Moments
// Entrée  : parent/hyperstack/{exp}_{WELL}_hyperstack.tif   (C=2, T=...)
// Sortie  : parent/mask/{exp}_{WELL}_mask_hyperstack.tif    (C=1, T=...)
// Aucune correction, seuillage = Moments (comme avant).
// =========================

macro "Mask (RED only) via Moments on hyperstack" {
  parentDir = getDirectory(«Choisir le dossier parent (contenant 'hyperstack')»);
  sep = File.separator;

  hyperDir = parentDir + "hyperstack" + sep;
  if (!File.exists(hyperDir)) exit("Dossier 'hyperstack' introuvable : " + hyperDir);

  outDir = parentDir + "mask" + sep;
  if (!File.exists(outDir)) File.makeDirectory(outDir);

  // 0 = batch silencieux ; 1 = debug/affiche fenêtres
  showWindows = 0;
  if (showWindows==0) setBatchMode(true); else setBatchMode(false);

  files = getFileList(hyperDir);
  if (files.length==0) exit("Aucun hyperstack dans " + hyperDir);

  for (i=0; i<files.length; i++) {
    run("Close All");
    name = files[i];
    if (!endsWith(name, ".tif") && !endsWith(name, ".tiff")) continue;
    if (!endsWith(name, "_hyperstack.tif") && !endsWith(name, "_hyperstack.tiff")) continue;

    // Ouvrir hyperstack (2 canaux attendus)
    open(hyperDir + name);
    run(«8-bit»);

    // Dupliquer le seul canal Rouge (canal 1)
    // -> crée une copie C=1, T=...
    run("Duplicate...", "title=RED_only duplicate channels=1");

    // Seuillage binaire = Moments (identique à ta méthode)
    selectWindow("RED_only");
    run("Make Binary", "method=Moments background=Default calculate stack");

    // Sauvegarde masque (C=1)
    outName = replace(name, "_hyperstack.tif", "_mask_hyperstack.tif");
    outName = replace(outName, "_hyperstack.tiff", "_mask_hyperstack.tif");
    saveAs("Tiff", outDir + outName);

    if (showWindows==1) { wait(200); }
    run("Close All");
    print("Masque enregistré : " + outDir + outName);
  }
```

```
  setBatchMode(false);
  print("Terminé.");

}
```

MACRO 3

```
// ====================================================
// MASK (Z-slices) -> mesures C1 (Red) & C2 (Green) par slice -> CSV global
// + Normalisation au t0 (slice 1 valide) pour Rouge & Vert (Mean, IntDen)
// Dossiers attendus dans le dossier parent choisi :
//   hyperstack/{exp}_{well}_hyperstack.tif(.tiff)
//   mask/{exp}_{well}_mask_hyperstack.tif(.tiff)
// Sortie (append) :
//   {parent}/measurements_RG.csv
// Colonnes :
//   Exp,Well,Slice,
//   Area_px,Area_um2,
//   Mean_Red,Mean_Green,IntDen_Red,IntDen_Green,
//   Mean_Red_relT0,Mean_Green_relT0,IntDen_Red_relT0,IntDen_Green_relT0
// ====================================================
macro "MASK Z -> C1/C2 per-slice -> CSV + relT0 (Red & Green)" {
  sep = File.separator;

  // 0) Dossier parent
  parentDir = getDirectory(«Choisir le dossier parent (avec 'hyperstack' et 'mask')»);
  if (parentDir==»») exit(«Aucun dossier choisi.»);
  hyperDir = parentDir + "hyperstack" + sep;
  maskDir  = parentDir + "mask" + sep;
  if (!File.exists(hyperDir)) exit(«Dossier 'hyperstack' introuvable : « + hyperDir);
  if (!File.exists(maskDir))  exit(«Dossier 'mask' introuvable : « + maskDir);

  // 1) CSV global (créé s'il n'existe pas)
  outCSV = parentDir + "measurements_RG.csv";
  header = "Exp,Well,Slice"
      + ",Area_px,Area_um2"
      + ",Mean_Red,Mean_Green,IntDen_Red,IntDen_Green"
      + ",Mean_Red_relT0,Mean_Green_relT0,IntDen_Red_relT0,IntDen_Green_relT0";
  if (!File.exists(outCSV)) File.saveString(header + "\n", outCSV);

  setBatchMode(true);
  files = getFileList(maskDir);
  nProcessed = 0;

  // 2) Parcours des masques (un puits = un fichier)
  for (i=0; i<files.length; i++) {
    run("Close All");
    name = files[i];

    // on ne prend que *_mask_hyperstack.tif/.tiff
    if (!(endsWith(name, "_mask_hyperstack.tif") || endsWith(name, "_mask_hyperstack.tiff"))) continue;

    // {exp}_{well}_mask_hyperstack.tif
    parts = split(name, "_");
    if (parts.length < 3) { print("Nom inattendu: "+name+" (skip)"); continue; }
    expName = parts[0];
    well    = parts[1];

    // brut correspondant
    rawPath = hyperDir + expName + "_" + well + "_hyperstack.tif";
    if (!File.exists(rawPath)) rawPath = hyperDir + expName + "_" + well + "_hyperstack.tiff";
    if (!File.exists(rawPath)) { print("Brut introuvable pour: "+expName+"_"+well+" (skip)"); continue; }

    // --- Ouvrir MASK (binaire). Si multi-canaux, garder C1.
    open(maskDir + name);
    maskTitle = getTitle();
```

```
getDimensions(Wm,Hm,Cm,Zm,Tm);
if (Cm>1) {
   run("Split Channels");
   selectWindow("C1-"+maskTitle);
   rename(maskTitle+"_C1");
   maskTitle = getTitle();
}
selectWindow(maskTitle);
getDimensions(Wm,Hm,Cm,Zm,Tm); // Zm = nb de slices mask

// --- Ouvrir HYPERSTACK puis split C1/C2
open(rawPath);
hsTitle = getTitle();
run("Split Channels");

// récupérer les IDs des fenêtres C1/C2 relatives à cet hyperstack
titles = getList("image.titles");
idRed = -1; idGreen = -1;
for (k=0; k<titles.length; k++) {
   if (startsWith(titles[k], "C1-"+hsTitle)) { selectWindow(titles[k]); idRed = getImageID(); }
   if (startsWith(titles[k], "C2-"+hsTitle)) { selectWindow(titles[k]); idGreen = getImageID(); }
}
if (idRed==-1 || idGreen==-1) { print("C1/C2 introuvables pour "+expName+"_"+well+" (skip)"); run("Close All");
continue; }

// Sanity XY + nb de slices commun
selectWindow(maskTitle); getDimensions(Wm,Hm,Cm,Zm,Tm);
selectImage(idRed);     getDimensions(Wr,Hr,Cr,Zr,Tr);
selectImage(idGreen);   getDimensions(Wg,Hg,Cg,Zg,Tg);
if (Wm!=Wr || Hm!=Hr || Wm!=Wg || Hm!=Hg) { print("Dims mismatch "+expName+"_"+well+" -> skip"); run("Close
All"); continue; }

nZ = Zm;
if (Zr < nZ) nZ = Zr;
if (Zg < nZ) nZ = Zg;
if (nZ < 1) { print("0 slice "+expName+"_"+well+" -> skip"); run("Close All"); continue; }

// --- Baselines t0 (premier slice avec ROI valide) ---
baseSet = 0;
baseMeanR = 0; baseMeanG = 0;
baseIntR  = 0; baseIntG  = 0;

// --- Mesures slice par slice (mask -> C1 -> C2)
roiManager("Reset");
for (s=1; s<=nZ; s++) {
   // MASK : Edit > Selection > Create Selection au slice s
   selectWindow(maskTitle);
   setSlice(s);
   run("Create Selection"); // mask binaire -> contour direct

   if (selectionType()==-1) {
      // Pas de ROI à ce slice : on écrit des zéros (et on ne change pas les baselines)
      line = expName+","+well+","+s
          + ",0,0"
          + ",0,0,0,0"
          + ",0,0,0,0\n";
      File.append(line, outCSV);
      continue;
   }

   // Propager la sélection via le ROI Manager
   roiManager("Reset");
   roiManager("Add"); // index 0

   // C1 (Red)
   selectImage(idRed);
   setSlice(s);
   roiManager("Select", 0);
   getRawStatistics(nPixR, meanR, minR, maxR, stdR);
   getPixelSize(unitR, pwR, phR, pdR);
   area_px  = nPixR;
```

```
        area_um2 = nPixR * pwR * phR;
        intDenR  = meanR * nPixR;

        // C2 (Green)
        selectImage(idGreen);
        setSlice(s);
        roiManager("Select", 0);
        getRawStatistics(nPixG, meanG, minG, maxG, stdG);
        intDenG = meanG * nPixG;

        // Baselines (prise au premier slice avec ROI valide)
        if (baseSet==0) {
           baseMeanR = meanR;
           baseMeanG = meanG;
           baseIntR  = intDenR;
           baseIntG  = intDenG;
           baseSet   = 1;
        }

        // Ratios rel. t0 (protégés)
        meanR_rel = safeDiv(meanR,  baseMeanR);
        meanG_rel = safeDiv(meanG,  baseMeanG);
        intR_rel  = safeDiv(intDenR, baseIntR);
        intG_rel  = safeDiv(intDenG, baseIntG);

        // Append une ligne / slice
        line = expName+","+well+","+s
            + ","+d2s(area_px,0)+","+d2s(area_um2,6)
            + ","+d2s(meanR,6)+","+d2s(meanG,6)+","+d2s(intDenR,6)+","+d2s(intDenG,6)
            + ","+d2s(meanR_rel,6)+","+d2s(meanG_rel,6)+","+d2s(intR_rel,6)+","+d2s(intG_rel,6)
            + "\n";
        File.append(line, outCSV);
      }

      nProcessed++;
      run("Close All");
      print("OK: "+expName+" "+well+" ("+nZ+" slices)");
   }

   setBatchMode(false);
   print(«Terminé. Puits traités : «+nProcessed+». CSV : "+outCSV);
}

// -------- Helper ----------
function safeDiv(num, den) {
   if (den==0) return 0;
   return num/den;
}
```

MACRO 4

```
// ============================================================================
// Generate Mask Hyperstacks (raw + corrected)
// C1 = red-only zone
// C2 = red+green zone
// C3 = red mask (Moments) used for clipping
// Sorties:
//   /mask_hyperstack_raw/      → _mask.tif
//   /mask_hyperstack_corrected/ → _mask_corrected.tif
// Fix: on renomme R/G par puit (R_src/G_src) et on les ferme avant puit suivant
// ============================================================================

macro "Generate Mask Hyperstacks (raw + corrected)" {
   setBatchMode(true);
   sep = File.separator;
```

```
master = getDirectory(«Choisir le dossier maître (avec 'hyperstack')»);
if (master == «») exit(«Aucun dossier choisi.»);

inDir  = master + "hyperstack" + sep;
outRaw = master + "mask_hyperstack_raw" + sep;
outCor = master + "mask_hyperstack_corrected" + sep;
File.makeDirectory(outRaw);
File.makeDirectory(outCor);

list = getFileList(inDir);

for (i = 0; i < list.length; i++) {
  if (!endsWith(list[i], ".tif") && !endsWith(list[i], ".tiff")) continue;
  base = replace(list[i], «_hyperstack», «»); // nom de base propre
  print(«\\n=== Traitement : « + base + « ===»);

  // --- Ouverture de l'hyperstack ---
  open(inDir + list[i]);

  // --- Split + renommage sûr des canaux source ---
  run("Split Channels");
  titles = getList("image.titles");
  selectWindow(titles[0]); run("8-bit"); rename("R_src");
  selectWindow(titles[1]); run("8-bit"); rename("G_src");

  // --- Dimensions ---
  selectWindow("R_src");
  w = getWidth(); h = getHeight(); nZ = nSlices();

  // --- Stacks de sortie (RAW) ---
  newImage("Ronly_stack",      "8-bit black", w, h, nZ);
  newImage("RGplus_stack",     "8-bit black", w, h, nZ);
  newImage("MaskMoments_stack", "8-bit black", w, h, nZ);

  for (z = 1; z <= nZ; z++) {
    // Duplique la slice courante de chaque source
    selectWindow("R_src"); setSlice(z); run("Duplicate...", "title=Rtemp");
    selectWindow("G_src"); setSlice(z); run("Duplicate...", "title=Gtemp");

    // Passer en 32-bit pour calculs (sélection explicite)
    selectWindow("Rtemp"); run("32-bit");
    selectWindow("Gtemp"); run("32-bit");

    // === Ratio G/(R+G) → masque RG+ (ou autre méthode) ===
    imageCalculator("Add create", "Rtemp","Gtemp");
    rename("Sum");
    imageCalculator("Divide create", "Gtemp","Sum");
    rename("Ratio");
    run("Gaussian Blur...", "sigma=1");
    setThreshold(0.5, 1.0);       // ajuste si besoin
    run("Convert to Mask");
    rename(«Mask_RGplus»);

    // === Masque rouge total (Moments) ===
    selectWindow("Rtemp");
    run("Make Binary", "method=Moments background=Dark");
    rename(«Mask_Rmoments»);

     // === Séparation zones ===
    imageCalculator("AND create", "Mask_RGplus", "Mask_Rmoments");
    rename("RGplus");
    imageCalculator("Subtract create", "Mask_Rmoments", "RGplus");
    rename("Ronly");
```

```
    // === Copie dans stacks RAW ===
    selectWindow("Ronly_stack"); setSlice(z);
    selectWindow("Ronly"); run("Copy");
    selectWindow("Ronly_stack"); run("Paste");

    selectWindow("RGplus_stack"); setSlice(z);
    selectWindow("RGplus"); run("Copy");
    selectWindow("RGplus_stack"); run("Paste");

    selectWindow("MaskMoments_stack"); setSlice(z);
    selectWindow("Mask_Rmoments"); run("Copy");
    selectWindow("MaskMoments_stack"); run("Paste");

    // Nettoyage temporaires de la slice
    close(«Rtemp»); close(«Gtemp»); close(«Sum»);
    close("Ratio"); close("Mask_RGplus");
    close("Mask_Rmoments"); close("RGplus"); close("Ronly");
}

// --- Fusion RAW + sauvegarde (flush sûr) ---
run("Merge Channels...", "c1=Ronly_stack c2=RGplus_stack c3=MaskMoments_stack create keep");
rename("MaskRaw_"+base);
selectWindow("MaskRaw_"+base);
wait(400);
saveAs("Tiff", outRaw + base + "_mask.tif");
wait(200);
close(«MaskRaw_»+base);
// ferme aussi les sources pour ne pas polluer le puit suivant
close("R_src");
close("G_src");
// ferme les 3 stacks constituants
close(«Ronly_stack»);
close(«RGplus_stack»);
close(«MaskMoments_stack»);
wait(100);

// --- Correction : on repart du RAW enregistré (en environnement propre) ---
close(«*»);                    // contexte propre pour éviter collisions
open(outRaw + base + "_mask.tif");
run("Split Channels");
ctitles = getList("image.titles");
ron  = ctitles[0];
rgp  = ctitles[1];
rmom = ctitles[2];

// Normalise type du masque global sans re-seuiller
selectWindow(rmom); rename("MaskGlobal");
if (bitDepth()!=8) run("8-bit");

// Si MaskGlobal est mono-slice, duplique sur nSlices de C1
selectWindow(ron); nR = nSlices();
selectWindow("MaskGlobal"); nMask = nSlices();
if (nMask == 1 && nR > 1) {
    selectWindow("MaskGlobal");
    run("Duplicate...", "duplicate slices=1-" + nR + " title=MaskGlobal_full");
    rename(«MaskGlobal»);
}

// Applique le masque global en mode stack
selectWindow(ron);
run("8-bit");
imageCalculator("AND create stack", ron, "MaskGlobal");
rename("Ronly_corr");
```

```
    selectWindow(rgp);
    run("8-bit");
    imageCalculator("AND create stack", rgp, "MaskGlobal");
    rename(«RGplus_corr»);

    // Fusion CORR + sauvegarde (flush sûr)
    run("Merge Channels...", "c1=Ronly_corr c2=RGplus_corr c3=MaskGlobal create keep");
    rename("MaskCorr_"+base);
    selectWindow("MaskCorr_"+base);
    wait(400);
    saveAs("Tiff", outCor + base + "_mask_corrected.tif");
    wait(200);
    close("MaskCorr_"+base);
    close("Ronly_corr");
    close("RGplus_corr");
    close("MaskGlobal");
    wait(100);

    // Fin puit : tout est fermé → on passe au suivant proprement
    close(«*»);
  }

  setBatchMode(false);
  print(«\\n=== Terminé (tous les puits) ===»);
}
```

MACRO 5

```
// ====================================================
// Mesure de la fluorescence rouge (C1) dans 3 zones (Ronly, Green, Rtot)
// Temps = axe Z (slices)
// Sortie : measurements_RG.csv
// Version stable + focus lock (BatchMode)
// ====================================================

macro "Measure Red Intensity per Slice (BatchMode)" {
  sep = File.separator;

  // --- Choix du dossier maître ---
  masterDir = getDirectory(«Choisir le dossier maître (avec 'hyperstack' et 'mask_hyperstack_corrected')»);
  if (masterDir == «») exit(«Aucun dossier choisi.»);

  hyperDir = masterDir + "hyperstack" + sep;
  maskDir  = masterDir + "mask_hyperstack_corrected" + sep;
  outputCSV = masterDir + "measurements_RG.csv";

  // --- En-tête CSV ---
  header = "Exp,Well,Slice," +
       "IntDen_R_in_Ronly,Area_Ronly,Mean_Ronly," +
       "IntDen_R_in_Green,Area_Green,Mean_Green," +
       "IntDen_R_in_Rtot,Area_Rtot,Mean_Rtot\n";
  File.saveString(header, outputCSV);

  // --- Mesures activées ---
  run("Set Measurements...", "area mean integrated redirect=None decimal=3");

  // --- Active le mode batch pour éviter tout clic/focus ---
  setBatchMode(true);

  list = getFileList(hyperDir);
  for (i = 0; i < list.length; i++) {
    if (!endsWith(list[i], "_hyperstack.tif")) continue;
```

```
expNameFull = substring(list[i], 0, lastIndexOf(list[i], "_"));
parts = split(expNameFull, "_");
if (parts.length < 2) continue;
expName = parts[0];
well = parts[1];

print("\\n=== Traitement : " + expName + " / " + well + " ===");

open(hyperDir + list[i]);
rename("hyper");
Stack.getDimensions(width, height, channels, slices, frames);
if (frames < slices) frames = slices;

maskName = expName + "_" + well + ".tif_mask_corrected.tif";
if (!File.exists(maskDir + maskName)) {
   print("⚠ Masque introuvable : " + maskName);
   close("hyper");
   continue;
}
open(maskDir + maskName);
rename("mask");

for (z = 1; z <= slices; z++) {
   selectWindow("hyper");
   Stack.setPosition(1, z, 1);

   Ronly_IntDen=0; Ronly_Area=0; Ronly_Mean=0;
   Green_IntDen=0; Green_Area=0; Green_Mean=0;
   Rtot_IntDen=0; Rtot_Area=0; Rtot_Mean=0;

   // ---- C1 Ronly ----
   selectWindow("mask"); Stack.setPosition(1, z, 1);
   run("Select None");
   run("Create Selection"); run("Make Inverse");
   if (selectionType != -1) {
      run("Copy");
      selectWindow("hyper"); Stack.setPosition(1, z, 1);
      run("Restore Selection"); run("Measure");
      n=nResults;
      if (n>0){
         Ronly_IntDen=getResult("IntDen",n-1);
         Ronly_Area=getResult("Area",n-1);
         Ronly_Mean=getResult("Mean",n-1);
      }
   }
   run("Clear Results");

   // ---- C2 Green ----
   selectWindow("mask"); Stack.setPosition(2, z, 1);
   run("Select None");
   run("Create Selection"); run("Make Inverse");
   if (selectionType != -1) {
      run("Copy");
      selectWindow("hyper"); Stack.setPosition(1, z, 1);
      run("Restore Selection"); run("Measure");
      n=nResults;
      if (n>0){
         Green_IntDen=getResult("IntDen",n-1);
         Green_Area=getResult("Area",n-1);
         Green_Mean=getResult("Mean",n-1);
      }
   }
   run("Clear Results");
```

```
        // ---- C3 Rtot ----
        selectWindow("mask"); Stack.setPosition(3, z, 1);
        run("Select None");
        run("Create Selection"); run("Make Inverse");
        if (selectionType != -1) {
           run("Copy");
           selectWindow("hyper"); Stack.setPosition(1, z, 1);
           run("Restore Selection"); run("Measure");
           n=nResults;
           if (n>0){
              Rtot_IntDen=getResult("IntDen",n-1);
              Rtot_Area=getResult("Area",n-1);
              Rtot_Mean=getResult("Mean",n-1);
           }
        }
        run("Clear Results");

        // --- Écriture CSV ---
        line = expName + "," + well + "," + z + "," +
             Ronly_IntDen + "," + Ronly_Area + "," + Ronly_Mean + "," +
             Green_IntDen + "," + Green_Area + "," + Green_Mean + "," +
             Rtot_IntDen + "," + Rtot_Area + "," + Rtot_Mean + "\n";
        File.append(line, outputCSV);
     }

     close("hyper");
     close(«mask»);
  }

  // --- On rend la main à l'interface ---
  setBatchMode(false);

  print(«\\n☑ Mesures terminées. Fichier enregistré dans : " + outputCSV);

}
```

Supplementary Table 1. Patients characteristics

	Sample number	***Age***	***Sex***	***pT Stage***	***ISUP Grade***	***PD-L1 CPS***
Patient 1	26	90	F	1	3	Positive
Patient 2	27	87	M	3	3	Positive

Supplementary Table 2. Full spectral cytometry panel used for immunophenotyping of blood- and tumor-infiltrating lymphocytes.

Laser (nm)	**Fluorochrome**	**Marker**	**Target Immune Population**
488	FITC	CD14, CD19, TCRVα7.2, TCRγ/δ	Monocytes, B cells, MAIT cells, γδ T cells (Dump)
	Alexa Fluor 532	CD8	CD8+ T cells
	Spark Blue 574	CD3	T cells, NKT cells
	RB613	FoxP3	Regulatory T cells
	PerCP	CD38	Activated T cells
	PerCP-Cy5.5	CD16	Cytotoxic NK cells
	RB744	CD25	Tregs or activated T cells
	RB780	TIGIT	Exhausted/regulatory T cells, exhausted NK cells
405	BV421	CD27	Naive or early memory T cells
	eFluor450	Ki-67	Proliferating cells
	BV480	CXCR6	NK cells
	BV570	HLA-DR	Activated T cells, B cells, monocytes
	BV605	Granzyme B	Cytotoxic T cells, NK cells
	BV650	TIM-3	Exhausted T cells
	BV711	KLRG1	Late-differentiated T cells, NK cells
	BV750	GPR56	Effector memory T cells, TEMRA
	BV786	NKG2C	NK cells, some CD8+ T cells
633	APC	KIRs	NK cells
	Alexa Fluor 660	CD56	NK cells
	VioBright R720	CD28	Naive/effector T cells
	APC-eFluor780	ILT2	Target of interest across immune subsets

	APC-Fire810	CCR7	Naive T cells
561	PE	Ksp37	Cytotoxic cells
	PE-Vio615	NKp80	NK cells, some T cells
	PE-Cy5	NKG2D	NK cells, some T cells
	PE-Fire700	PD-1	Exhausted T cells
	PE-Fire744	CD39	Exhausted or regulatory T cells
	PE-Cy7	LAG-3	Exhausted T cells
	PE-Fire810	NKp30	NK cells, some T cells
355	BUV395	CD57	Effector memory T cells, TEMRA
	Live/Dead Blue	Live/Dead	Cell viability
	BUV496	CD4	CD4+ T cells, monocytes
	BUV563	CD127	Naive/effector T cells
	BUV615	CD69	Activated T cells
	BUV661	CX3CR1	Effector memory T cells, TEMRA
	BUV737	CD45RA	Naive and TEMRA T cells
	BUV805	CXCR4	Naive, memory, and homing T cells

Summary and perspectives

Thus, this study demonstrated the successful integration of the autologous immune-infiltrated spheroid model into a perfused microfluidic system, providing a functional proof of concept for dynamic modeling of tumor–immune interactions and paving the way for further methodological developments.

The implementation of a Tumor-on-Chip system marked a pivotal step in this work, extending the autologous immune-infiltrated spheroid model into a dynamic model. Beyond the proof-of-concept data presented in the article, this phase of the project involved extensive technical optimization and the establishment of analytical pipelines that now form the foundation for future developments.

Our microfluidic chip has reached a reliable and reproducible level of performance. It readily captures spheroids derived from both established ccRCC cell lines and freshly dissociated and reinfiltrated patient tumors, maintaining their integrity and viability under continuous perfusion. The chip is reusable, compatible with standard incubator conditions, and adaptable to multiple readouts, including microscopy, cytokine quantification, and flow cytometry.

Alongside the hardware optimization, a dedicated imaging and analytical workflow was established to enable consistent quantification of tumor–immune interactions. Custom imaging analysis macros for ImageJ were developed to process dual-channel fluorescence images, allowing reliable monitoring of immune infiltration and spheroid integrity. These tools, specifically adapted to the format of IncuCyte outputs, could eventually be released as a standalone analysis package to facilitate accessibility to this type of model across laboratories. Furthermore, the implementation of rapid optical clearing protocols combined with confocal microscopy enabled 3D imaging of large spheroids, providing high-resolution visualization of immune cell distribution within the tumor mass. This imaging strategy opens new possibilities for endpoint analysis, including the assessment of effector cell entry in models that rely on circulating effectors such as CAR-T cells or bispecific antibodies.

Among the imaging developments initiated during this work, the “fusion” spheroid model represents a particularly interesting tool to investigate the impact of spatially segregated checkpoint expression within the same tumor mass. In this configuration, we attempted to challenge this concept by combining HLA-G and PD-L1 expression, either co-expressed or arranged in alternating zones, to reproduce the heterogeneous checkpoint patterns observed in renal tumors. Although stable HLA-G–expressing cell lines were successfully generated, these preliminary experiments did not demonstrate a protective effect or any major functional impact of HLA-G under the tested conditions, likely related to IL-15 activation. For now, the approach remains exploratory, but the model itself provides a solid basis for future investigations aimed at evaluating how spatially distinct checkpoint expression may shape immune infiltration or response

to therapy. This model could also be used by mixing the two fluorescent cell populations within the same spheroid and independently tracking their respective signals over time, to assess the relative behavior or survival of distinct cellular subsets within a complex tumor mass.

Functional readouts were also refined during this phase. Cytokine quantification in chip effluents confirmed that, even under continuous flow, secreted factors such as IFNγ or granzyme B remain within detectable concentrations after three days of culture. These findings encourage the future implementation of time-resolved sampling to better capture cytokine dynamics before and after therapeutic intervention. In parallel, spectral flow cytometry was established as a deep immune-profiling readout, confirming the feasibility of endpoint phenotypic characterization of infiltrating lymphocytes. However, this analysis remains technically demanding: dissociation of older spheroids often results in the loss or damage of infiltrating cells, particularly TILs.

Despite these advances, several aspects still warrant optimization. Controlled comparisons between chip effluents and spheroid lysates, fine-tuning of perfusion rates, and better calibration of circulating immune cell numbers are needed to improve data standardization. In parallel, implementing non-invasive live imaging compatible with perfusion would provide valuable kinetic insight into immune–tumor dynamics. Preliminary tests using the EVOS platform (automated microscope) demonstrated that the device can operate within controlled incubation environments with minimal adaptation and allows sequential imaging of our chip for at least 24 hours under continuous flow, confirming its robustness and experimental flexibility. Such integration could enable longitudinal multicolor monitoring of T cell infiltration and spheroid integrity using fluorescent reporters, thereby complementing cytokine profiling and endpoint cytometric analyses with continuous dynamic readouts and provide visual assessment of efficacy.

Throughout this work, IL-15 activation has been an essential component of the model, allowing the maintenance, survival, and infiltration of immune cells within spheroids under ex vivo culture conditions. In the absence of IL-15, most immune populations rapidly declined or failed to penetrate the spheroid core, highlighting the need for cytokine support to sustain viable and functionally competent effectors. However, the use of relatively high and continuous doses of IL-15, while ensuring reproducibility and robust immune activation, introduced a substantial biological bias. This hyperactivated state blurred the distinction between experimental conditions and controls, as both PBMCs and infiltrated spheroids exhibited comparable inflammatory phenotypes, thereby limiting the interpretability of short-term immunotherapy assays.

To overcome these limitations, several strategies could be explored. One option would be to shorten the IL-15 exposure window, limiting cytokine stimulation to the early activation phase prior to infiltration. Alternatively, maintaining very low IL-15 concentrations after activation might help preserve effector viability while minimizing excessive stimulation. Combinatorial cytokine regimens involving IL-7 or IL-2, either in pulsed or alternating formats, have also been proposed to sustain immune cells under more physiological conditions. Finally, a longer

term direction would be to promote immune activation indirectly through tumor-derived cues or chemokine gradients, potentially restoring more natural infiltration dynamics.

In its current form, this work would greatly benefit from an additional section dedicated to the histological representativity of the model, complementing the transcriptomic data presented through BRB-seq. Such a component would help contextualize the model by visually illustrating its cellular composition and architectural fidelity relative to the original tumor. Once immunostaining protocols are finalized, we plan to use our existing and coming slides to generate comparative images of patient tumor sections and their corresponding spheroids or alternatively produce a representative immunofluorescence panel of cleared spheroids. These images would provide a valuable visual counterpart to the molecular data, facilitating a more intuitive understanding of the model's relevance and complexity.

Collectively, the results and methodological advances presented in this chapter consolidate the foundations of a reproducible and physiologically relevant autologous tumor–immune model. Beyond the technical achievements, these studies now raise broader questions regarding the biological fidelity, predictive value, and translational potential of such ex vivo systems, aspects that will be further discussed in the general discussion.

General Discussion

I. Current state and limitations

In this work, we progressively developed a model, starting from the establishment of the methods required for spheroid formation from tumor samples, followed by the development of an autologous immune-infiltrated model and its transcriptomic characterization, up to its implementation in a microfluidic workflow and the associated readouts to study immune responses under dynamic conditions.

The overall objective of this thesis was to establish a robust, patient-derived in vitro system capable of capturing the complex interactions between tumor and immune cells in ccRCC. The project was guided by a set of criteria defined in **Box 1**. The first stage focused on the technical establishment of reproducible spheroid formation methods, ensuring structural consistency and experimental control. The second phase was dedicated to validating the cellular composition and transcriptional representativity of autologous immune-infiltrated patient-derived spheroids, confirming that the model faithfully retained the key components of the tumor microenvironment. Finally, these advances culminated in the transition to a dynamic, perfused microfluidic system integrating autologous circulating and tumor compartments under continuous flow.

The model developed throughout this thesis fulfills most of the criteria defined for a relevant preclinical system of ccRCC. It preserves tumor heterogeneity as well as key immune subsets, and stromal components, as confirmed by transcriptomic and cellular analyses. The maintenance of extracellular matrix and stromal integrity are ensured by the spheroid format, as well as the preservation of hypoxia and metabolic tumor characteristics. Multiple immune checkpoints were conserved, and immune scores matched that of the original tissue. The autologous nature of the model is ensured, while the microfluidic implementation introduced dynamic flow and circulating cells. The system was designed to be compatible with functional readouts, including cytokine secretion, flow or spectral cytometry, and live imaging, thereby enabling quantitative assessment of immune responses. In its current form, the workflow takes approximately one week, ensuring biological fidelity and potential compatibility with clinically relevant timeframes.

However, the model is still in an early phase and its usability for immunotherapeutic prediction is not yet established and significant limitations still have to be addressed.

First, although the overall cellular composition of our model appears close to that of the original tumor tissue, it still lacks some essential components. As shown in Chapter 2, the myeloid compartment, and particularly its macrophagic fraction, is severely reduced. The critical role of these cells in both antitumoral activity and immune tolerance, as well as in shaping immune ex-

clusion and accessibility to the tumor, has been discussed in the introduction (31,81). Interestingly, despite this apparent loss of macrophages, BRB-seq analysis suggested that myeloid-derived suppressor cells (MDSCs) might still be conserved within the model, although this result remains unexpected and requires further validation. Histological or flow cytometry confirmation of these populations will therefore be necessary to clarify their presence and contribution.

From a technical standpoint, myeloid depletion could occur during the 48-hour activation phase on plastic, as these cells are highly adherent and no detachment step was performed prior to spheroid formation. As demonstrated in the first article, myeloid populations can be successfully incorporated into spheroids through simple co-culture. It should therefore be technically feasible to separate them from TILs and reintegrate them either concurrently with the rest of the lymphocytes or at the initiation of spheroid formation (day 0). Such inclusion has been reported in other studies without impairing spheroid assembly (298–301) and would likely restore part of the innate compartment, thereby enriching the biological relevance of the model.

Another major limitation of the model concerns immune activation and infiltration. In our system, efficient lymphocyte migration into spheroids critically depends on pre-activation with IL-15. Without cytokine stimulation, immune cells fail to infiltrate the spheroid core and rapidly lose viability, preventing the establishment of a functional immune compartment. Attempts to include lymphocytes directly during spheroid formation were not successful: under such conditions, spheroid assembly was markedly delayed or did not occur at all, suggesting that simultaneous aggregation of tumor and immune cells interferes with proper spheroid organization.

IL-15 was selected to promote T- and NK-cell survival without relying on anti-CD3/CD28 stimulation, thereby avoiding strong TCR-driven recruitment and maintaining the autologous specificity of the model. Yet, IL-15 is also known to induce potent TCR-independent effector functions, which likely contribute to the transcriptional and phenotypic discrepancies observed in our system (302,303). Although this activation ensures immune persistence, reinfiltration, and measurable functional readouts, it also introduces a significant bias that may obscure subtle treatment-related responses and limit the interpretability of short-term immunotherapy assays.

Identifying more optimal strategies for TIL reinfiltration and survival without introducing such strong immunological bias will therefore be crucial. More conservative cytokine regimens could rely on lower doses or combinations of IL-2, IL-7, IL-15, and IL-21 (304), administered either continuously or in pulsed settings. Unfortunately, cytokine protocols specifically designed to support immune cell migration while minimizing activation or skewing of the original immune composition remain poorly documented, as most studies have focused on generating specific effector subsets or optimizing expansion for adoptive transfer applications (305–307).

Another approach would be to eliminate any activation step prior to TIL reinfiltration. Several alternative techniques have been described to directly incorporate immune cells during spheroid formation. Among them, magnetic-directed aggregation has shown promising results in fa-

cilitating the assembly of mixed tumor–immune spheroids (230,308). This method relies on the transient coating of cells with biologically inert magnetic nanoparticles, followed by seeding onto low-attachment multiwell plates. A magnetic field applied beneath each well draws tumor and immune cells together, promoting the formation of composite spheroids.

In our hands, however, reproducing consistent spheroid formation using this technique has proven challenging, both in terms of timing and structural integrity. Further optimization is currently underway to refine the parameters of this approach and evaluate its compatibility with freshly dissociated tumor and immune cells.

While most of these limitations appear technically addressable and the model shows promising biological relevance, this alone does not establish its predictive value.

In this regard, the transcriptomic analysis presented in Chapter 2 provided an interesting exploratory perspective. Using the TIDE framework, we observed that the predicted response profiles of patient-derived spheroids tended to align with those of their corresponding tumor tissues. Tumors predicted as non-responders by TIDE generated spheroids with similarly low immune-response scores, whereas, in the one patient confidently classified as a responder, all derived spheroids displayed high predicted sensitivity, although based on a limited sample size (n = 3). The TIDE algorithm was originally developed as a computational biomarker integrating two complementary mechanisms of resistance to immune checkpoint blockade: T cell dysfunction in infiltrated but non-responsive tumors, and T cell exclusion in poorly infiltrated tumors (309). It has been validated in several cancers, including melanoma and non-small-cell lung carcinoma, where it often outperforms classical markers such as PD-L1 expression or tumor mutational burden. In renal cell carcinoma, however, its predictive performance remains indicative and has never been formally proven. While some studies have reported associations between TIDE scores and survival or immune infiltration patterns (310), none has linked it directly to clinical response to immune inhibitors. In parallel, more advanced integrative approaches are emerging. Recent multimodal algorithms combining genomic, histopathological, and clinical data through artificial intelligence, have shown predictive accuracy for both immunotherapy and targeted therapy outcomes in ccRCC (311). Testing our ex vivo model against such comprehensive predictive frameworks could provide valuable complementary insights into its representativity and translational relevance.

Ultimately, demonstrating that our system can reliably anticipate therapeutic outcomes will require evaluation across multiple patients and repeated assays, to determine how to distinguish responders from non-responders based on the available readouts.

To put these findings into perspective, it is important to consider how our system compares with existing preclinical tumor models developed for immunotherapy research, and to what extent it addresses some of their current limitations.

II. Positioning of the model

When considering its place within the broader landscape of preclinical tumor models, our system aligns with and extends recent efforts to develop patient-derived, immunocompetent platforms for translational oncology.

Over the past decade, multiple preclinical systems have been developed to model renal cancer, each capturing distinct aspects of its biological and immunological complexity.

Patient-derived xenografts (PDXs) remain invaluable for preserving native tumor architecture and stromal composition, yet their dependence on immunodeficient hosts makes them unsuitable for studying human immune mechanisms. Even humanized versions, while conceptually attractive, remain technically demanding, costly, and incompatible with the timelines and scalability required for patient-specific testing (130,134).

In parallel, organoid-based models have considerably advanced the study of renal cancer by enabling expansion of patient-derived epithelial cells and partial retention of tumor heterogeneity. Conventional ECM-embedded organoids, however, lack stromal and immune elements and require extended culture times that can induce phenotypic drift. The emergence of the air–liquid interface (ALI) format represented a significant step forward, allowing maintenance of tumor fragments that retain immune and stromal compartments (239). In ccRCC, Esser et al. successfully applied this approach to generate organoids preserving T cells, fibroblasts, and endothelial cells, and demonstrated responsiveness to cabozantinib and nivolumab (312). More recently, Xue et al. confirmed that such ALI-derived organoids could recapitulate PD-1–induced immune activation ex vivo, reinforcing their potential as immunocompetent tumor models (295). Similarly, Voabil et al. established that the reactivation capacity of tumor-infiltrating lymphocytes in ex vivo tumor fragments correlated with clinical responses to anti–PD-1 therapy, highlighting the translational promise of short-term patient-derived systems (262).

Despite these advances, all these models share a common limitation: they operate under static conditions. This configuration restricts the study of dynamic processes, such as migration, infiltration, sequential treatment, that are central to understanding and studying immune checkpoint responses. From a technical perspective, however, the same biological material used for ALI cultures or tumor fragments could readily be integrated in chip models similar to ours.

Microfluidic tumor-on-chip systems provide this missing dynamic dimension, allowing precise control over perfusion, nutrient gradients, and shear stress, thereby recreating more physiologically relevant microenvironments. In renal cancer, Miller et al. developed a first-generation RCC-on-chip using cell line spheroids and CAR-T cells, successfully visualizing antigen-specific infiltration under flow (313). However, the model relied on immortalized cells and engineered effectors, and thus did not reproduce the complexity or autologous context of patient-derived tumors. More recent systems have extended this approach to other cancers. Veith et al.

proposed a lung tumor-on-chip integrating tumor cells, autologous $CD8^+$ T cells, and fibroblasts in a perfused collagen matrix, demonstrating anti–PD-1–induced cytotoxicity (293). Jenkins et al. introduced an autologous PDOTS system derived from patient tumors, enabling checkpoint blockade testing in spheroids retaining native tumor–immune architecture. Yet, perfusion in these two settings was primarily used for medium renewal, and immune cells were not perfused dynamically, limiting the modeling of circulation-dependent processes, which were not the goal of these studies.

Finally, Cui et al. developed a glioblastoma-on-chip with perfusable vascular channels and perfused immune cells, successfully modeling PD-1 blockade in a microphysiologically relevant context and Maulana et al. created a endothelial barrier on chip to assess T cells and CAR-T extravasation. However, these systems employed allogeneic immune cells and were not specific to renal cancer, leaving open the question of fully autologous modeling under flow (314,315).

Within this landscape, the model developed in this work positions itself at the convergence of these approaches. It integrates freshly dissociated patient tumors and their corresponding autologous immune cells into a dynamically perfused microenvironment, preserving the architectural, stromal, and immune diversity of the original tumor while introducing circulation.

III. Perspectives

A. Vascularization

Beyond immune–tumor interactions, one of the most critical feature for next-generation tumor models lies in the integration of vascular components. This limitation is particularly critical in ccRCC, a tumor type that is both highly vascularized and strongly dependent on angiogenic signaling pathways. The absence of perfusable vessels leads to non-physiological oxygen and nutrient gradients, distorts immune cell trafficking, and prevents realistic redistribution of soluble factors that regulate immune activation, angiogenesis, and tumor behavior, as well as the delivery and diffusion of therapeutic agents. These processes are key to understanding immune–tumor interactions and therapeutic responses.

Historically, vascularization could only be achieved in vivo, through xenografts or chick chorioallantoic membrane (CAM) assays. However, recent bioengineering advances have demonstrated that perfusable and functional vasculature can now be engineered in vitro, using preformed endothelial channels, vasculogenesis-driven networks, or hybrid microfluidic systems (316).

Several microfluidic studies have specifically addressed the vascular dimension of ccRCC. Miller et al. (317) first reported a vascularized RCC-on-chip combining primary tumor cells with endothelial networks to study angiogenic sprouting under flow, while Virumbrales-Muñoz

et al. (318) established organotypic microvessels capturing patient-specific angiogenesis. Other RCC microtumor models integrating human umbilical vein endothelial cells (HUVECs) revealed aberrant vascular structures and distinct sensitivities to anti-angiogenic agents such as sunitinib or cabozantinib (319). More recently, tri-culture systems combining RCC cells, endothelial cells, and patient-derived lymphocytes demonstrated that $CD4^+$ T cell subsets can promote resistance to VEGF-TKI therapy through secretion of pro-angiogenic cytokines, linking immune dysfunction to vascular remodeling (320).

These observations echo the abnormal peritumoral vasculature described in ccRCC, where disorganized and leaky vessels create heterogeneous perfusion, local hypoxia, and physical barriers to immune infiltration. Modeling such vascular irregularities could therefore provide critical insights into both immune exclusion and therapeutic resistance mechanisms.

Furthermore, colorectal and lung tumor-on-chip models have established the feasibility of immune perfusion through vascularized microenvironments. In both systems, endothelialized channels were connected to tumor compartments, allowing the flow of THP-1 monocytes or peripheral blood lymphocytes and their active transmigration into tumor tissue under controlled shear stress (321,322). These studies provided compelling proof that vascularized microfluidics can reproduce immune trafficking and barrier crossing under physiologically relevant flow.

Our microfluidic chip model was originally derived from a platform designed to enable vascularization of trapped organoids (323). In that system, organoids were first positioned within microfluidic traps, after which a hydrogel containing HUVECs was perfused through the chip. Following a controlled rinse step, the gel remained confined to the trap regions, allowing endothelial cells from the organoid to connect with the surrounding HUVEC network. This process led to the formation of a continuous and perfusable microvascular network bridging the organoid and the external channels.

Building on this principle, combining such vascular integration with the immune perfusion strategies demonstrated in colorectal and lung tumor-on-chip models could represent a promising future evolution for our platform. This approach might eventually allow the reconstruction of a functional endothelial barrier and the modeling of immune cell transmigration toward the tumor spheroid under dynamic flow conditions. In this context, our model, which already contains endogenous endothelial populations within patient-derived spheroids as demonstrated in Chapter 2, could provide a starting point for exploring vascular integration. However, whether these endothelial cells can be functionally activated and form stable vascular connections remains to be demonstrated.

B. Reproducibility

Despite their promise, 3D tumor models still face major challenges in reproducibility and standardization. Variability in spheroid size and morphology has been shown to significantly in-

fluence experimental outcomes, particularly in cytotoxicity assays, as both volume and shape directly affect diffusion dynamics and cell viability (229). Without harmonized procedures and reliable readouts adapted to large aggregates, such heterogeneity ultimately limits the translational reliability of these systems.

In the first part of this work, a workflow was established to assess key morphological parameters of spheroids and to select homogeneous populations prior to experimentation. However, this selection process was not systematically implemented in the subsequent stages of model development. Establishing a standardized workflow ensuring morphological consistency across experiments therefore remains an important step to improve reproducibility and comparability of results.

Beyond this variability, there is an inherent trade-off between speed and control of complexity. Multicellular tumor spheroids (MCTS), which self-assemble rapidly and in large numbers, offer high throughput but limited architectural fidelity. By contrast, patient-derived organoids (PDOs) or engineered systems reproduce native tissue organization and cellular heterogeneity with greater reproducibility, but at the expense of longer culture times and reduced scalability.

Emerging bioengineering strategies aim to reconcile this tension by combining reproducibility with complexity. One example is the use of self-assembling nucleic acid nanostructures (NACs) to decorate living cells and guide their assembly into reproducible "designer spheroids." This approach allows controlled organization of tumor, stromal, and immune compartments, thereby integrating physiological relevance with improved standardization (324). In parallel, 3D bioprinting provides another route toward reproducible complexity. Based on the precise deposition of bio-inks containing cells and extracellular matrix components, bioprinting enables the spatial arrangement of multiple compartments in a controlled manner. While issues of long-term stability remain, this technique is increasingly combined with organoid technology to generate more standardized yet physiologically relevant tumor platform (325).

C. Scalability

Beyond reproducibility, scalability and throughput represent another major bottleneck, particularly when aiming for translational applications. In the long term, integrating this workflow into a precision medicine framework will require further optimization to ensure its compatibility with clinical use.

Spheroid formation, in particular, still relies on several manual steps that are not easily scalable. Recently, automated organoid-printing platforms have been developed to generate hundreds of uniform organoids within a week. By encapsulating heterogeneous tumor cells into standardized Matrigel droplets, these systems preserved the mutational landscape of the parental tumor and enabled high-throughput drug testing. Strikingly, organoid-based predictions matched pa-

tient outcomes in most cases (17 out of 21 patients) (326).

The readout used in this work are readily reproducible in research laboratory but not necessarily in a clinical context.

The readouts implemented in this work are readily reproducible in a research setting but not yet adapted to clinical workflows. Recent advances in on-chip automation and real-time monitoring, although still largely outside immuno-oncology, may offer valuable perspectives. For instance, a nanoplasmonic optofluidic biosensor was recently designed to monitor single tumoroids in real time (327). This device uses nanoscale metallic resonators that change their optical properties when secreted proteins (VEGF-A in this example) accumulate nearby, allowing label-free detection of cytokine secretion while simultaneously tracking morphology and motility. Applied to colorectal tumoroids from both cell lines and patient samples, this approach captured dynamic VEGF-A secretion in response to hypoxia and therapy, demonstrating its potential for functional drug screening. Similar biosensing strategies could help make our microfluidic platform more easily interpretable in a clinical context.

Artificial intelligence (AI) is also beginning to complement these technological advances. Deep learning models trained on annotated imaging datasets can automatically detect, segment, and track organoids at high throughput, offering a more efficient alternative to the semi-automated macros developed in this work (328,329). Beyond image analysis, AI-based in silico simulations are being explored to model immune–tumor interactions, including T cell infiltration or checkpoint dynamics, thereby providing predictive insights that could guide experimental design (325).

Collectively, these developments illustrate the trajectory of the field toward increasingly standardized, automated, and scalable tumor models. Although integrating such strategies into immuno-oncology remains challenging due to the additional complexity of immune components, they pave the way for the next generation of patient-specific platforms. Their translation to ccRCC applications, however, remains at an early stage.

D. Adaptation to other cancers and samples

While the present work focused on clear cell renal cell carcinoma, many other cancers could benefit from similar autologous ex vivo models to investigate immune–tumor interactions and evaluate immunotherapies. However, there is no guarantee that the current workflow can be directly transferred to other tumor types, as several parameters are specific to renal cancer, particularly the culture medium formulation and the intrinsic ability of ccRCC cells to self-aggregate into spheroids. Indeed, tumor types differ considerably in their capacity to spontaneously form cohesive 3D structures.

Preliminary trials using bladder cancer samples illustrated these differences: spheroid formation

proved less efficient and reproducibility was lower compared with renal tumors. Nevertheless, since our microfluidic chip captures structures based on size rather than biological composition, it could readily accommodate alternative tissue formats such as small tumor fragments or patient-derived organotypic tumor spheroids (PDOTS). This technical flexibility opens the possibility of extending the platform to explant- or fragment-based cultures in future developments.

One advantage of the spheroid-based format in renal cancer is its ability to encompass the full tumor heterogeneity. In our workflow, each spheroid derives from the complete dissociation of a transversal tumor slice encompassing multiple histological regions, thereby averaging spatial heterogeneity, an important consideration given the well-documented intratumoral variability in ccRCC (330,331). In contrast, when shifting toward fragment- or explant-based formats, careful attention will be required regarding sampling location, as our current chip design accommodates only a limited number of traps (n = 10).

Technically, we have already explored this transition by successfully introducing finely minced and size-filtered tumor fragments into the chip using the same trapping system. Although functional validation remains to be performed, these preliminary results demonstrated the compatibility of the platform with different input materials.

To further enhance the clinical translatability of the system, adapting the workflow to biopsy-derived material represents a key next step. While nephrectomy specimens provide abundant tissue for model establishment in renal cancer, many solid tumors are primarily diagnosed and monitored through small biopsies. Developing a protocol enabling the generation of viable spheroids and functional assays from such limited samples would substantially broaden the applicability of this approach. Moreover, in renal cancer itself, immunotherapy is mainly indicated in the metastatic setting, where surgical resection is uncommon. Establishing a workflow compatible with needle biopsy material will therefore be critical. This will require optimization of both the dissociation and capture steps to accommodate the low number of viable cells typically recovered from biopsies. Once established, such a workflow could enable rapid ex vivo evaluation of immunotherapeutic responses directly from patient biopsies, moving this system closer to a functional predictive tool for precision immuno-oncology.

Altogether, this work lays the foundation for a reproducible and physiologically relevant autologous Tumor-on-Chip platform, bridging the gap between basic tumor immunology and translational applications. Further refinement and validation across larger patient cohorts will determine its true potential as a predictive tool for precision immuno-oncology.

Appendix

Appendix 1. Characteristics and mutated genes in the main RCC cell lines.

wt- wild-type gene, m- mutated, p- polymorphism, nd- no data on gene modifications, t- mRNA (transcript) detected, + protein expression, - no protein expression, C- changed protein structure/ size, ND- no data on protein, OP- original patient, SP and NSP- side population and non-side populations, * clear cell according to describing authors; before 1995, # inconsistent data.

Cell line	Source	Culture conditions	Molecular characteristics	Histological type	Other features
769-P	Primary 1970-75	RPMI, 2 mM Glutamine,1 mM sodium pyruvate, 10% FBS	VHL m -/+# HIF1 nd -/+# HIF2 nd t -/+# c-MET nd + VHL (codon 2, 180 - point mutations, Pro2Ser, Ile180Asn) and VHL promoter hypermethylation-no VHL mRNA, no HIF-1α [1]	OP- unknown; RCC Clear cell by vhl status	TICs No lung metastases, tumours by SP and NSP or no tumours in xenografts # High VEGF Genes mutated: 74 in CCLE (incl. CXCL12, MAPK kinases, Ncam, PDGFR, VEGFC, VHL), 317 in COSMIC (incl. ABC, MAPK kinases, PDGFR, VHL) Mutated BAP1
786-O	Primary 1970-75	RPMI, 2 mM Glutamine,1 mM sodium pyruvate, 10% FBS	VHL m t -/+# HIF1 m t - HIF2 nd + c-MET nd + non-functional VHL (codon104 -1 base deletion), no HIF-1α , high HIF-2α	OP- unknown; RCC Clear cell by vhl status CD10 positive	Agar colonies TICs Tumorigenic in nude mice; tumours by SP and lung metastases in xenografts Fuhrman 4 ccRCC in mice High VEGF Cell line transfected with Luciferase available Genes mutated: 90 in CCLE (incl. FGFR, IL-1, MAPK kinases, PTEN, TP53, VEGFC), 344 in COSMIC (incl. ABC, FLT1, PTEN, TP53, VHL) [2]
A-498	primary 1973 [3]	EMEM, 2 mM Glutamine, 1% Non-Essential Amino Acids,1 mM sodium pyruvate, 10% FBS	VHL m/wt# t - HIF1 nd t C HIF2 nd t + c-MET nd + codones 142-3 - 4 bases deletion), no HIF-1α mRNA, high HIF-2α, SETD2 mutation,	OP- kidney carcinoma Moderately differentiated clear cell* in xenografts Clear cell by vhl status Papillary in xenografts and by chromosome analysis	Tumorigenic in nude mice (sc and iv) Wt p53# TICs High VEGF Genes mutated: 86 in CCLE (incl. CXCL12, EGF, FGFR, MAPK kinases, Ncam, PIK3, TP53, VHL), 282 in COSMIC (incl. PIK3, VHL)
A-704	primary 1973	EMEM, 2 mM Glutamine, 1% Non-Essential Amino Acids, 1 mM sodium pyruvate, 10% FBS	VHL m - HIF1 nd + HIF2 nd + c-MET nd ND	OP- kidney carcinoma Clear cell by vhl status	Not tumorigenic in nude mice Genes mutated: 477 in COSMIC (incl. FGF, FGFR, MAPK kinases, TLR5, VHL), 105 in CCLE (incl. BAX, EGF, HGF, Ncam, PDGFR, PIK3, TLR3, TNFR, VEGF, VHL) Mutated PBRM1

ACHN	Metastatic (pleural effusion) 1979 [4]	1.EMEM, 2 mM Glutamine, 1% non-essential amino acids, 1 mM sodium pyruvate, 10% FBS 2. DMEM, 10% FBS, 2 mM Glutamine	VHL wt + HIF1 nd + HIF2 nd + c-MET p +	OP- unknown; RCC Clear cell by gene expression analysis Papillary# by copy number alteration and chromosome analysis [5]http://www.jurology.com/article/S0022-	Growth inhibition by IFN Agar colonies Sphere formation TICs Wt p53 Tumorigenic in nude mice Tumours by SP in xenografts Genes mutated: 168 in COSMIC (incl. ABCA genes, MAPK kinases, PBMR1#, TLR2), 62 in CCLE (incl. Ncam, MAPK kinases, PIK3, VEGFC). PBMR1 wildtype/m#
Caki-1	Metastatic (skin) 1975	1. McCoy's 5a, 10% FBS, 2 mM Glutamine 2. EMEM, 2 mM Glutamine, 1% non-essential amino acids	VHL wt + HIF1 m + HIF2 nd + c-MET m +	OP- adenocarcinoma Poorly differentiated clear cell*or clear cell in xenografts [6]	Sphere formation Wt p53 Tumorigenic, lung metastases Tumours with sarcomatoid changes by SP in xenografts High VEGF Cell line transfected with Luciferase available Genes mutated: 76 in CCLE (incl. HIF1A, MAPK kinases, MET, MMP9, Ncam, VEGFC), 336 in COSMIC (incl. ABC, FGFR, HLA, IL-10R, MAPK kinases, MET, NES, PIUK3, TRAF)
Caki-2	Primary 1975	1. McCoy's 5a, 10% FBS, 2 mM Glutamine 2. EMEM, 2 mM Glutamine, 1% non-essential amino acids	VHL wt/m# - HIF1 nd + HIF2 nd + c-MET nd + [7]	OP- adenocarcinoma Papillary# by MET expression and in xenografts Papillary in xenografts	Wt p53 TICs Tumorigenic in nude mice Tumours by SP Genes mutated: 80 in CCLE (incl. ABC, EGF, FGFR, MAPK kinases, Ncam, PDGFR, VEGF, VHL#) Mutated PBRM1

Source: (115), under CC BY 4.0

Bibliography

1. Ferlay J, Ervik M, Lam F, Laversanne M, Colombet M, Mery L, et al. Global Cancer Observatory: Cancer Today. 2024 [cited 2025 Sept 2]. Global Cancer Observatory: Cancer Today. Available from: https://gco.iarc.fr/

2. Ferlay J, Laversanne M, Ervik M, Lam F, Colombet M, Mery L, et al. International Agency for Research on Cancer (IARC). 2024 [cited 2025 Sept 2]. Global Cancer Observatory: Cancer Tomorrow (version 1.1). Available from: https://gco.iarc.who.int/tomorrow

3. Boveri T. Concerning the Origin of Malignant Tumours by Theodor Boveri. Translated and annotated by Henry Harris. J Cell Sci. 2008 Jan 1;121(Supplement_1):1–84.

4. Aaltonen LA, Abascal F, Abeshouse A, Aburatani H, Adams DJ, Agrawal N, et al. Pan-cancer analysis of whole genomes. Nature. 2020 Feb;578(7793):82–93.

5. Zhang S, Xiao X, Yi Y, Wang X, Zhu L, Shen Y, et al. Tumor initiation and early tumorigenesis: molecular mechanisms and interventional targets. Signal Transduct Target Ther. 2024 June 19;9(1):149.

6. Stratton MR, Campbell PJ, Futreal PA. The cancer genome. Nature. 2009 Apr;458(7239):719–24.

7. Hanahan D. Hallmarks of Cancer: New Dimensions. Cancer Discov. 2022 Jan 12;12(1):31–46.

8. Hanahan D, Weinberg RA. The Hallmarks of Cancer. Cell. 2000 Jan 7;100(1):57–70.

9. Hanahan D, Weinberg RA. Hallmarks of Cancer: The Next Generation. Cell. 2011 Mar 4;144(5):646–74.

10. Ehrlich P. Ueber den jetzigen Stand der Karzinomforschung. Nederlands Tijdschrift voor Geneeskunde. 1909;273–90.

11. Burnet FM. The Concept of Immunological Surveillance. 1970 Sept 24 [cited 2025 Sept 3]; Available from: https://karger.com/books/book/483/chapter/5575692/The-Concept-of-Immunological-Surveillance

12. Burnet M. Cancer—A Biological Approach. Br Med J. 1957 Apr 6;1(5022):779–86.

13. Foley EJ. Antigenic properties of methylcholanthrene-induced tumors in mice of the strain of origin. Cancer Res. 1953 Dec;13(12):835–7.

14. Gross L. Intradermal Immunization of C3H Mice against a Sarcoma That Originated in an Animal of the Same Line. Cancer Res. 1943 May 1;3(5):326–33.

15. Dunn GP, Bruce AT, Ikeda H, Old LJ, Schreiber RD. Cancer immunoediting: from immunosurveillance to tumor escape. Nat Immunol. 2002 Nov;3(11):991–8.

16. O'Donnell JS, Teng MWL, Smyth MJ. Cancer immunoediting and resistance to T cell-based immunotherapy. Nat Rev Clin Oncol. 2019 Mar;16(3):151–67.

17. Coulie PG, Van den Eynde BJ, van der Bruggen P, Boon T. Tumour antigens recognized by T lymphocytes: at the core of cancer immunotherapy. Nat Rev Cancer. 2014 Feb;14(2):135–46.

18. Peña-Romero AC, Orenes-Piñero E. Dual Effect of Immune Cells within Tumour Microenvironment: Pro- and Anti-Tumour Effects and Their Triggers. Cancers. 2022 Mar 25;14(7):1681.

19. Ahmed H, Mahmud AR, Siddiquee MohdFR, Shahriar A, Biswas P, Shimul MdEK, et al. Role of T cells in cancer immunotherapy: Opportunities and challenges. Cancer Pathog Ther. 2022 Dec 20;1(2):116–26.

20. Fridman WH, Meylan M, Pupier G, Calvez A, Hernandez I, Sautès-Fridman C. Tertiary lymphoid structures and B cells: An intratumoral immunity cycle. Immunity. 2023 Oct 10;56(10):2254–69.

21. Chen DS, Mellman I. Oncology Meets Immunology: The Cancer-Immunity Cycle. Immunity. 2013 July 25;39(1):1–10.

22. Mellman I, Chen DS, Powles T, Turley SJ. The cancer-immunity cycle: Indication, genotype, and immunotype. Immunity. 2023 Oct 10;56(10):2188–205.

23. Pardoll DM. The blockade of immune checkpoints in cancer immunotherapy. Nat Rev Cancer. 2012 Apr;12(4):252–64.

24. Cai L, Li Y, Tan J, Xu L, Li Y. Targeting LAG-3, TIM-3, and TIGIT for cancer immunotherapy. J Hematol OncolJ Hematol Oncol. 2023 Sept 5;16(1):101.

25. Wang S, Wang J, Xia Y, Zhang L, Jiang Y, Liu M, et al. Harnessing the potential of HLA-G in cancer therapy: advances, challenges, and prospects. J Transl Med. 2024 Feb 3;22(1):130.

26. Borst L, van der Burg SH, van Hall T. The NKG2A–HLA-E Axis as a Novel Checkpoint in the Tumor Microenvironment. Clin Cancer Res. 2020 Nov 2;26(21):5549–56.

27. Kong X, Zhang J, Chen S, Wang X, Xi Q, Shen H, et al. Immune checkpoint inhibitors: breakthroughs in cancer treatment. Cancer Biol Med. 2024 June 15;21(6):451–72.

28. de Visser KE, Joyce JA. The evolving tumor microenvironment: From cancer initiation to metastatic outgrowth. Cancer Cell. 2023 Mar 13;41(3):374–403.

29. Togashi Y, Shitara K, Nishikawa H. Regulatory T cells in cancer immunosuppression — implications for anticancer therapy. Nat Rev Clin Oncol. 2019 June;16(6):356–71.

30. Veglia F, Sanseviero E, Gabrilovich DI. Myeloid-derived suppressor cells in the era of increasing myeloid cell diversity. Nat Rev Immunol. 2021 Aug;21(8):485–98.

31. DeNardo DG, Ruffell B. Macrophages as regulators of tumour immunity and immuno-

therapy. Nat Rev Immunol. 2019 June;19(6):369–82.

32. Kalluri R. The biology and function of fibroblasts in cancer. Nat Rev Cancer. 2016 Sept;16(9):582–98.

33. Sahai E, Astsaturov I, Cukierman E, DeNardo DG, Egeblad M, Evans RM, et al. A framework for advancing our understanding of cancer-associated fibroblasts. Nat Rev Cancer. 2020 Mar;20(3):174–86.

34. De Palma M, Biziato D, Petrova TV. Microenvironmental regulation of tumour angiogenesis. Nat Rev Cancer. 2017 Aug;17(8):457–74.

35. van der Leun AM, Thommen DS, Schumacher TN. CD8+ T cell states in human cancer: insights from single-cell analysis. Nat Rev Cancer. 2020 Apr;20(4):218–32.

36. Baessler A, Vignali DAA. T Cell Exhaustion. Annu Rev Immunol. 2024 June 28;42(Volume 42, 2024):179–206.

37. Escobar G, Mangani D, Anderson AC. T cell factor 1 (Tcf1): a master regulator of the T cell response in disease. Sci Immunol. 2020 Nov 6;5(53):eabb9726.

38. Tufail M, Jiang CH, Li N. Immune evasion in cancer: mechanisms and cutting-edge therapeutic approaches. Signal Transduct Target Ther. 2025 July 31;10(1):227.

39. Min HY, Lee HY. Molecular targeted therapy for anticancer treatment. Exp Mol Med. 2022 Oct;54(10):1670–94.

40. Hoption Cann SA, van Netten JP, van Netten C. Dr William Coley and tumour regression: a place in history or in the future. Postgrad Med J. 2003 Dec;79(938):672–80.

41. Lipson EJ, Drake CG. Ipilimumab: an anti-CTLA-4 antibody for metastatic melanoma. Clin Cancer Res Off J Am Assoc Cancer Res. 2011 Nov 15;17(22):6958–62.

42. Leach DR, Krummel MF, Allison JP. Enhancement of antitumor immunity by CTLA-4 blockade. Science. 1996 Mar 22;271(5256):1734–6.

43. Ishida Y, Agata Y, Shibahara K, Honjo T. Induced expression of PD-1, a novel member of the immunoglobulin gene superfamily, upon programmed cell death. EMBO J. 1992 Nov;11(11):3887–95.

44. Robert C. A decade of immune-checkpoint inhibitors in cancer therapy. Nat Commun. 2020 July 30;11(1):3801.

45. Du X, Tang F, Liu M, Su J, Zhang Y, Wu W, et al. A reappraisal of CTLA-4 checkpoint blockade in cancer immunotherapy. Cell Res. 2018 Apr;28(4):416–32.

46. Ferlay J, Ervik M, Laversanne M, Colombet M, Mery L, Piñeros M, et al. Global Cancer Observatory: Cancer Today (version 1.1) [Internet]. Lyon, France: International Agency for Research on Cancer; 2024 [cited 2025 Aug 29]. Available from: https://gco.iarc.who.int/today

47. Bex A, Albiges L, Bedke J, Capitano U, Dabestani S, Hora M, et al. EAU Guidelines on Renal Cell Carcinoma 2025 update. In: EAU Guidelines Edn presented at the EAU Annual Congress, Madrid 2025 [Internet]. Arnhem, The Netherlands: EAU Guidelines Office; 2025 [cited 2025 Aug 29]. Available from: https://uroweb.org/guidelines/compilations-of-all-guidelines/

48. Haas NB, Nathanson KL. Hereditary Kidney Cancer Syndromes. Adv Chronic Kidney Dis. 2014 Jan 1;21(1):81–90.

49. Powles T, Albiges L, Bex A, Comperat E, Grünwald V, Kanesvaran R, et al. Renal cell carcinoma: ESMO Clinical Practice Guideline for diagnosis, treatment and follow-up☆. Ann Oncol. 2024 Aug 1;35(8):692–706.

50. Moch H, Amin MB, Berney DM, Compérat EM, Gill AJ, Hartmann A, et al. The 2022 World Health Organization Classification of Tumours of the Urinary System and Male Genital Organs—Part A: Renal, Penile, and Testicular Tumours. Eur Urol. 2022 Nov 1;82(5):458–68.

51. Lindgren D, Sjölund J, Axelson H. Tracing Renal Cell Carcinomas back to the Nephron. Trends Cancer. 2018 July 1;4(7):472–84.

52. Kelly CR, Landman J. The Netter Collection of Medical Illustrations: Urinary System. 2nd edn. Vol. 5. Philadelphia: Saunders; 2012.

53. Amin MB, Greene FL, Edge SB, Compton CC, Gershenwald JE, Brookland RK, et al. The Eighth Edition AJCC Cancer Staging Manual: Continuing to build a bridge from a population-based to a more "personalized" approach to cancer staging. CA Cancer J Clin. 2017;67(2):93–9.

54. Hsieh JJ, Purdue MP, Signoretti S, Swanton C, Albiges L, Schmidinger M, et al. Renal cell carcinoma. Nat Rev Dis Primer. 2017 Mar 9;3(1):17009.

55. Swami U, Nussenzveig RH, Haaland B, Agarwal N. Revisiting AJCC TNM staging for renal cell carcinoma: quest for improvement. Ann Transl Med. 2019 Mar;7(Suppl 1):S18.

56. Capitanio U, Bedke J, Albiges L, Volpe A, Giles RH, Hora M, et al. A Renewal of the TNM Staging System for Patients with Renal Cancer To Comply with Current Decision-making: Proposal from the European Association of Urology Guidelines Panel. Eur Urol. 2023 Jan 1;83(1):3–5.

57. Dagher J, Delahunt B, Rioux-Leclercq N, Egevad L, Srigley JR, Coughlin G, et al. Clear cell renal cell carcinoma: validation of World Health Organization/International Society of Urological Pathology grading. Histopathology. 2017;71(6):918–25.

58. Delahunt B, Cheville JC, Martignoni G, Humphrey PA, Magi-Galluzzi C, McKenney J, et al. The International Society of Urological Pathology (ISUP) grading system for renal cell carcinoma and other prognostic parameters. Am J Surg Pathol. 2013 Oct;37(10):1490–504.

59. Mikami S, Kuroda N, Nagashima Y. Pathology of Renal Cell Carcinoma. In: Renal Cell Carcinoma [Internet]. Springer, Tokyo; 2017 [cited 2025 Aug 31]. p. 105–37. Available from: https://link.springer.com/chapter/10.1007/978-4-431-55531-5_4

60. Surveillance Research Program, National Cancer Institute. SEER*Explorer: An interactive website for SEER cancer statistics [Internet]. [Internet]. 2025 [cited 2025 Aug 31]. Available from: https://seer.cancer.gov/statistics-network/explorer/

61. Creighton CJ, Morgan M, Gunaratne PH, Wheeler DA, Gibbs RA, Gordon Robertson A, et al. Comprehensive molecular characterization of clear cell renal cell carcinoma. Nature. 2013 July 1;499(7456):43–9.

62. Jonasch E, Walker CL, Rathmell WK. Clear cell renal cell carcinoma ontogeny and mechanisms of lethality. Nat Rev Nephrol. 2021 Apr;17(4):245–61.

63. Linehan WM, Schmidt LS, Crooks DR, Wei D, Srinivasan R, Lang M, et al. The Metabolic Basis of Kidney Cancer. Cancer Discov. 2019 Aug 1;9(8):1006–21.

64. Monjaras-Avila CU, Lorenzo-Leal AC, Luque-Badillo AC, D'Costa N, Chavez-Muñoz C, Bach H. The Tumor Immune Microenvironment in Clear Cell Renal Cell Carcinoma. Int J Mol Sci. 2023 Jan;24(9):7946.

65. Atkins D, Ferrone S, Schmahl GE, Störkel S, Seliger B. Down-Regulation of HLA Class I Antigen Processing Molecules: An Immune Escape Mechanism of Renal Cell Carcinoma? J Urol. 2004 Feb 1;171(2, Part 1):885–9.

66. Hugaboom MB, Wirth LV, Street K, Ruthen N, Jegede OA, Schindler NR, et al. Presence of Tertiary Lymphoid Structures and Exhausted Tissue-Resident T Cells Determines Clinical Response to PD-1 Blockade in Renal Cell Carcinoma. Cancer Discov. 2025 May 2;15(5):948–68.

67. Zhu Z, Jin Y, Zhou J, Chen F, Chen M, Gao Z, et al. PD1/PD-L1 blockade in clear cell renal cell carcinoma: mechanistic insights, clinical efficacy, and future perspectives. Mol Cancer. 2024 July 16;23(1):146.

68. Bukur J, Rebmann V, Grosse-Wilde H, Luboldt H, Ruebben H, Drexler I, et al. Functional Role of Human Leukocyte Antigen-G Up-Regulation in Renal Cell Carcinoma1. Cancer Res. 2003 July 21;63(14):4107–11.

69. Ibrahim EC, Aractingi S, Allory Y, Borrini F, Dupuy A, Duvillard P, et al. Analysis of HLA antigen expression in benign and malignant melanocytic lesions reveals that upregulation of HLA-G expression correlates with malignant transformation, high inflammatory infiltration and HLA-A1 genotype. Int J Cancer. 2004;108(2):243–50.

70. Seliger B, Jasinski-Bergner S, Quandt D, Stoehr C, Bukur J, Wach S, et al. HLA-E expression and its clinical relevance in human renal cell carcinoma. Oncotarget. 2016 Aug 31;7(41):67360–72.

71. André P, Denis C, Soulas C, Bourbon-Caillet C, Lopez J, Arnoux T, et al. Anti-NKG2A mAb Is a Checkpoint Inhibitor that Promotes Anti-tumor Immunity by Unleashing

Both T and NK Cells. Cell. 2018 Dec 13;175(7):1731-1743.e13.

72. Crispen PL, Sheinin Y, Roth TJ, Lohse CM, Kuntz SM, Frigola X, et al. Tumor Cell and Tumor Vasculature Expression of B7-H3 Predict Survival in Clear Cell Renal Cell Carcinoma. Clin Cancer Res Off J Am Assoc Cancer Res. 2008 Aug 15;14(16):5150–7.

73. Hong S, Yuan Q, Xia H, Zhu G, Feng Y, Wang Q, et al. Analysis of VISTA expression and function in renal cell carcinoma highlights VISTA as a potential target for immunotherapy. Protein Cell. 2019 Nov 1;10(11):840–5.

74. Krambeck AE, Thompson RH, Dong H, Lohse CM, Park ES, Kuntz SM, et al. B7-H4 expression in renal cell carcinoma and tumor vasculature: Associations with cancer progression and survival. Proc Natl Acad Sci U S A. 2006 July 5;103(27):10391–6.

75. Özalp FR, Yörükoğlu K, Yıldırım EÇ, Uzun M, Semiz HS. Prognostic value of B7-H3 expression in metastatic renal cell carcinoma and its impact on immunotherapy response. BMC Cancer. 2024 Nov 29;24(1):1471.

76. Takamatsu K, Tanaka N, Hakozaki K, Takahashi R, Teranishi Y, Murakami T, et al. Profiling the inhibitory receptors LAG-3, TIM-3, and TIGIT in renal cell carcinoma reveals malignancy. Nat Commun. 2021 Sept 20;12(1):5547.

77. Jiang W, Zeng H, Liu Z, Jin K, Hu B, Chang Y, et al. Immune inactivation by CD47 expression predicts clinical outcomes and therapeutic responses in clear cell renal cell carcinoma patients. Urol Oncol Semin Orig Investig. 2022 Apr 1;40(4):166.e15-166.e25.

78. Zimarino C, Moody W, Davidson SE, Munir H, Shields JD. Disruption of CD47-SIRPα signaling restores inflammatory function in tumor-associated myeloid-derived suppressor cells. iScience [Internet]. 2024 Apr 19 [cited 2025 Sept 1];27(4). Available from: https://www.cell.com/iscience/abstract/S2589-0042(24)00768-5

79. Denize T, Jegede OA, Matar S, El Ahmar N, West DJ, Walton E, et al. PD-1 Expression on Intratumoral Regulatory T Cells Is Associated with Lack of Benefit from Anti–PD-1 Therapy in Metastatic Clear-Cell Renal Cell Carcinoma Patients. Clin Cancer Res. 2024 Feb 16;30(4):803–13.

80. Li K, Shi H, Zhang B, Ou X, Ma Q, Chen Y, et al. Myeloid-derived suppressor cells as immunosuppressive regulators and therapeutic targets in cancer. Signal Transduct Target Ther. 2021 Oct 7;6(1):362.

81. Komohara Y, Hasita H, Ohnishi K, Fujiwara Y, Suzu S, Eto M, et al. Macrophage infiltration and its prognostic relevance in clear cell renal cell carcinoma. Cancer Sci. 2011;102(7):1424–31.

82. Wang B, Zhao Q, Zhang Y, Liu Z, Zheng Z, Liu S, et al. Targeting hypoxia in the tumor microenvironment: a potential strategy to improve cancer immunotherapy. J Exp Clin Cancer Res. 2021 Jan 9;40(1):24.

83. D'Costa NM, Cina D, Shrestha R, Bell RH, Lin YY, Asghari H, et al. Identification of gene

signature for treatment response to guide precision oncology in clear-cell renal cell carcinoma. Sci Rep. 2020 Feb 6;10(1):2026.

84. McDermott DF, Huseni MA, Atkins MB, Motzer RJ, Rini BI, Escudier B, et al. Clinical activity and molecular correlates of response to atezolizumab alone or in combination with bevacizumab versus sunitinib in renal cell carcinoma. Nat Med. 2018 June;24(6):749–57.

85. Gouttefangeas C, Stenzl A, Stevanović S, Rammensee HG. Immunotherapy of renal cell carcinoma. Cancer Immunol Immunother CII. 2006 May 5;56(1):117–28.

86. Motzer RJ, Hutson TE, Tomczak P, Michaelson MD, Bukowski RM, Rixe O, et al. Sunitinib versus interferon alfa in metastatic renal-cell carcinoma. N Engl J Med. 2007;356(2):115–24.

87. Motzer RJ, Escudier B, McDermott DF, George S, Hammers HJ, Srinivas S, et al. Nivolumab versus Everolimus in Advanced Renal Cell Carcinoma. N Engl J Med. 2015 Nov 5;373(19):1803–13.

88. Motzer RJ, Tannir NM, McDermott DF, Frontera OA, Melichar B, Choueiri TK, et al. Nivolumab plus Ipilimumab versus Sunitinib in Advanced Renal-Cell Carcinoma. N Engl J Med. 2018;378(14):1277–90.

89. Tannir NM, Albigès L, McDermott DF, Burotto M, Choueiri TK, Hammers HJ, et al. Nivolumab plus ipilimumab versus sunitinib for first-line treatment of advanced renal cell carcinoma: extended 8-year follow-up results of efficacy and safety from the phase III CheckMate 214 trial. Ann Oncol Off J Eur Soc Med Oncol. 2024 Nov;35(11):1026–38.

90. Choueiri TK, Powles T, Burotto M, Escudier B, Bourlon MT, Zurawski B, et al. Nivolumab plus Cabozantinib versus Sunitinib for Advanced Renal-Cell Carcinoma. N Engl J Med. 2021 Mar 3;384(9):829–41.

91. Choueiri TK, Eto M, Motzer R, De Giorgi U, Buchler T, Basappa NS, et al. Lenvatinib plus pembrolizumab versus sunitinib as first-line treatment of patients with advanced renal cell carcinoma (CLEAR): extended follow-up from the phase 3, randomised, open-label study. Lancet Oncol. 2023 Mar;24(3):228–38.

92. Motzer R, Alekseev B, Rha SY, Porta C, Eto M, Powles T, et al. Lenvatinib plus Pembrolizumab or Everolimus for Advanced Renal Cell Carcinoma. N Engl J Med. 2021 Apr 7;384(14):1289–300.

93. Powles T, Burotto M, Escudier B, Apolo AB, Bourlon MT, Shah AY, et al. Nivolumab plus cabozantinib versus sunitinib for first-line treatment of advanced renal cell carcinoma: extended follow-up from the phase III randomised CheckMate 9ER trial. ESMO Open. 2024 May;9(5):102994.

94. Rini BI, Plimack ER, Stus V, Gafanov R, Hawkins R, Nosov D, et al. Pembrolizumab plus Axitinib versus Sunitinib for Advanced Renal-Cell Carcinoma. N Engl J Med. 2019 Mar 21;380(12):1116–27.

95. Rini BI, Plimack ER, Stus V, Gafanov R, Waddell T, Nosov D, et al. Pembrolizumab plus axitinib versus sunitinib for advanced clear cell renal cell carcinoma: 5-year survival and biomarker analyses of the phase 3 KEYNOTE-426 trial. Nat Med. 2025 Aug 1;1–10.

96. Cella D, Grünwald V, Escudier B, Hammers HJ, George S, Nathan P, et al. Patient-reported outcomes of patients with advanced renal cell carcinoma treated with nivolumab plus ipilimumab versus sunitinib (CheckMate 214): a randomised, phase 3 trial. Lancet Oncol. 2019 Feb;20(2):297–310.

97. Cella D, Motzer RJ, Suarez C, Blum SI, Ejzykowicz F, Hamilton M, et al. Patient-reported outcomes with first-line nivolumab plus cabozantinib versus sunitinib in patients with advanced renal cell carcinoma treated in CheckMate 9ER: an open-label, randomised, phase 3 trial. Lancet Oncol. 2022 Feb;23(2):292–303.

98. Motzer R, Porta C, Alekseev B, Rha SY, Choueiri TK, Mendez-Vidal MJ, et al. Health-related quality-of-life outcomes in patients with advanced renal cell carcinoma treated with lenvatinib plus pembrolizumab or everolimus versus sunitinib (CLEAR): a randomised, phase 3 study. Lancet Oncol. 2022 June;23(6):768–80.

99. Adhikari A, Sapkota S, Gogia S, Kc O. Changes in the overall survival of patients with metastatic renal cell carcinoma in the era of immune-checkpoint inhibitors. Cancer Epidemiol. 2024 Oct 1;92:102639.

100. Hutson T, Figlin RA. The current and evolving therapeutic paradigm in the management of metastatic renal cell carcinoma. Kidney Cancer J. 2021;19(3):102–7.

101. Xu W, Atkins MB, McDermott DF. Checkpoint inhibitor immunotherapy in kidney cancer. Nat Rev Urol. 2020 Mar;17(3):137–50.

102. Choueiri TK, Tomczak P, Park SH, Venugopal B, Ferguson T, Chang YH, et al. Adjuvant Pembrolizumab after Nephrectomy in Renal-Cell Carcinoma. N Engl J Med. 2021 Aug 19;385(8):683–94.

103. Haas NB, Powles T, Tomczak P, Park SH, Venugopal B, Symeonides SN, et al. Five-year follow-up results from the phase 3 KEYNOTE-564 study of adjuvant pembrolizumab (pembro) for the treatment of clear cell renal cell carcinoma (ccRCC). J Clin Oncol. 2025 June;43(16_suppl):4514–4514.

104. Motzer RJ, Russo P, Grünwald V, Tomita Y, Zurawski B, Parikh O, et al. Adjuvant nivolumab plus ipilimumab versus placebo for localised renal cell carcinoma after nephrectomy (CheckMate 914): a double-blind, randomised, phase 3 trial. Lancet Lond Engl. 2023 Mar 11;401(10379):821–32.

105. Pal SK, Uzzo R, Karam JA, Master VA, Donskov F, Suarez C, et al. Adjuvant atezolizumab versus placebo for patients with renal cell carcinoma at increased risk of recurrence following resection (IMmotion010): a multicentre, randomised, double-blind, phase 3 trial. Lancet Lond Engl. 2022 Oct 1;400(10358):1103–16.

106. Allaf ME, Kim SE, Master V, McDermott DF, Harshman LC, Cole SM, et al. Periopera-

tive nivolumab versus observation in patients with renal cell carcinoma undergoing nephrectomy (PROSPER ECOG-ACRIN EA8143): an open-label, randomised, phase 3 study. Lancet Oncol. 2024 Aug 1;25(8):1038–52.

107. Albiges L, Motzer RJ, Trevino S, Kanesvaran R, Centkowski P, Reimers MA, et al. Cabozantinib (C) in combination with nivolumab (N) and ipilimumab (I) in previously untreated advanced renal cell carcinoma (aRCC): Final results of COSMIC-313. J Clin Oncol. 2025 Feb 10;43(5_suppl):438–438.

108. Suárez C, Choueiri TK, Albiges L, Voss MH, McGregor BA, Khan O, et al. Efficacy and safety of second-line cabozantinib ± atezolizumab for patients with advanced renal cell carcinoma after progression on immuno-oncology combinations: Subgroup analysis of CONTACT-03. J Clin Oncol. 2025 June;43(16_suppl):4523–4523.

109. Srour SA, Chahoud J, Drakaki A, Curti BD, Gibney GT, Pal SK, et al. ALLO-316 in advanced clear cell renal cell carcinoma (ccRCC): Updated results from the phase 1 TRAVERSE study. J Clin Oncol. 2025 June;43(16_suppl):4508–4508.

110. Braun DA, Bakouny Z, Hirsch L, Flippot R, Van Allen EM, Wu CJ, et al. Beyond conventional immune-checkpoint inhibition — novel immunotherapies for renal cell carcinoma. Nat Rev Clin Oncol. 2021 Apr;18(4):199–214.

111. Wang Y, Shelton SE, Kastrunes G, Barbie DA, Freeman GJ, Marasco WA. Preclinical models for development of immune–oncology therapies. Immuno-Oncol Insights. 2022;3(8):379–98.

112. Lucey BP, Nelson-Rees WA, Hutchins GM. Henrietta Lacks, HeLa Cells, and Cell Culture Contamination. Arch Pathol Lab Med. 2009 Sept 1;133(9):1463–7.

113. Monks A, Scudiero D, Skehan P, Shoemaker R, Paull K, Vistica D, et al. Feasibility of a high-flux anticancer drug screen using a diverse panel of cultured human tumor cell lines. J Natl Cancer Inst. 1991 June 5;83(11):757–66.

114. Stinson SF, Alley MC, Kopp WC, Fiebig HH, Mullendore LA, Pittman AF, et al. Morphological and immunocytochemical characteristics of human tumor cell lines for use in a disease-oriented anticancer drug screen. Anticancer Res. 1992;12(4):1035–53.

115. Brodaczewska KK, Szczylik C, Fiedorowicz M, Porta C, Czarnecka AM. Choosing the right cell line for renal cell cancer research. Mol Cancer. 2016 Dec 19;15(1):83.

116. Yap NY, Ong TA, Morais C, Pailoor J, Gobe GC, Rajandram R. Establishment of epithelial and fibroblast cell cultures and cell lines from primary renal cancer nephrectomies. Cell Biol Int. 2019;43(6):715–25.

117. Furge KA, Chen J, Koeman J, Swiatek P, Dykema K, Lucin K, et al. Detection of DNA Copy Number Changes and Oncogenic Signaling Abnormalities from Gene Expression Data Reveals MYC Activation in High-Grade Papillary Renal Cell Carcinoma. Cancer Res. 2007 Apr 4;67(7):3171–6.

118. Pulkkanen KJ, Parkkinen JJ, Kettunen MI, Kauppinen RA, Lappalainen M, Ala-Opas

MY, et al. Characterization of a new animal model for human renal cell carcinoma. Vivo Athens Greece. 2000;14(3):393–400.

119. Sinha R, Winer AG, Chevinsky M, Jakubowski C, Chen YB, Dong Y, et al. Analysis of renal cancer cell lines from two major resources enables genomics-guided cell line selection. Nat Commun. 2017 May 10;8(1):15165.

120. Strefford JC, Stasevich I, Lane TM, Lu YJ, Oliver T, Young BD. A combination of molecular cytogenetic analyses reveals complex genetic alterations in conventional renal cell carcinoma. Cancer Genet Cytogenet. 2005 May 1;159(1):1–9.

121. Glube N, Giessl A, Wolfrum U, Langguth P. Caki-1 cells represent an in vitro model system for studying the human proximal tubule epithelium. Nephron Exp Nephrol. 2007;107(2):e47-56.

122. Wang Y, Suarez ER, Kastrunes G, de Campos NSP, Abbas R, Pivetta RS, et al. Evolution of cell therapy for renal cell carcinoma. Mol Cancer. 2024 Jan 9;23(1):8.

123. Chang DK, Moniz RJ, Xu Z, Sun J, Signoretti S, Zhu Q, et al. Human anti-CAIX antibodies mediate immune cell inhibition of renal cell carcinoma in vitro and in a humanized mouse model in vivo. Mol Cancer. 2015 June 11;14:119.

124. Zhu Q, Cai MY, Weng DS, Zhao JJ, Pan QZ, Wang QJ, et al. PD-L1 expression patterns in tumour cells and their association with CD8+ tumour infiltrating lymphocytes in clear cell renal cell carcinoma. J Cancer. 2019 Jan 29;10(5):1154–61.

125. Chang W, Zhang B, Yang S, Zhang X, Zhang L, Zhang S, et al. Genome-wide CRISPR/Cas9 screening identifies PTGR2 as a potential therapeutic target for sunitinib resistance in clear cell renal cell carcinoma. Sci Rep. 2025 July 19;15(1):26263.

126. Feng X, Li Z, Liu Y, Chen D, Zhou Z. CRISPR/Cas9 technology for advancements in cancer immunotherapy: from uncovering regulatory mechanisms to therapeutic applications. Exp Hematol Oncol. 2024 Oct 19;13(1):102.

127. Quevedo R, Smirnov P, Tkachuk D, Ho C, El-Hachem N, Safikhani Z, et al. Assessment of Genetic Drift in Large Pharmacogenomic Studies. Cell Syst. 2020 Oct 21;11(4):393-401.e2.

128. Claus C, Ferrara C, Xu W, Sam J, Lang S, Uhlenbrock F, et al. Tumor-targeted 4-1BB agonists for combination with T cell bispecific antibodies as off-the-shelf therapy. Sci Transl Med. 2019 June 12;11(496):eaav5989.

129. Barbosa GR, de Souza AM, Silva PF, Fávero CS, de Oliveira JL, Carvalho HF, et al. Zebrafish as a Model for Translational Immuno-Oncology. J Pers Med. 2025 July;15(7):304.

130. Zhang C, Sui Y, Liu S, Yang M. In vitro and in vivo experimental models for cancer immunotherapy study. Curr Res Biotechnol. 2024 Jan 1;7:100210.

131. Yu JW, Bhattacharya S, Yanamandra N, Kilian D, Shi H, Yadavilli S, et al. Tumor-immune profiling of murine syngeneic tumor models as a framework to guide mechanistic studies and predict therapy response in distinct tumor microenvironments.

PLOS ONE. 2018 Nov 2;13(11):e0206223.

132. Hrushesky WJ, Murphy GP. Investigation of a new renal tumor model. J Surg Res. 1973 Nov;15(5):327–36.

133. Salup RR, Wiltrout RH. Adjuvant Immunotherapy of Established Murine Renal Cancer by Interleukin 2-stimulated Cytotoxic Lymphocytes. Cancer Res. 1986;46(7):3358–63.

134. Sobczuk P, Brodziak A, Khan MI, Chhabra S, Fiedorowicz M, Wełniak-Kamińska M, et al. Choosing The Right Animal Model for Renal Cancer Research. Transl Oncol. 2020 Mar 1;13(3):100745.

135. Zhang X, Shi X, Li J, Hu Z, Gao J, Wu S, et al. Combination immunotherapy with interleukin-2 surface-modified tumor cell vaccine and programmed death receptor-1 blockade against renal cell carcinoma. Cancer Sci. 2019;110(1):31–9.

136. Alicke B, Totpal K, Schartner JM, Berkley AM, Lehar SM, Capietto AH, et al. Immunization associated with primary tumor growth leads to rejection of commonly used syngeneic tumors upon tumor rechallenge. J Immunother Cancer. 2020 July 15;8(2):e000532.

137. Dong H, Strome SE, Salomao DR, Tamura H, Hirano F, Flies DB, et al. Tumor-associated B7-H1 promotes T-cell apoptosis: A potential mechanism of immune evasion. Nat Med. 2002 Aug;8(8):793–800.

138. Leach DR, Krummel MF, Allison JP. Enhancement of Antitumor Immunity by CTLA-4 Blockade. Science. 1996 Mar 22;271(5256):1734–6.

139. Sanmamed MF, Chester C, Melero I, Kohrt H. Defining the optimal murine models to investigate immune checkpoint blockers and their combination with other immunotherapies. Ann Oncol. 2016 July 1;27(7):1190–8.

140. Sharpless NE, DePinho RA. The mighty mouse: genetically engineered mouse models in cancer drug development. Nat Rev Drug Discov. 2006 Sept;5(9):741–54.

141. Schokrpur S, Hu J, Moughon DL, Liu P, Lin LC, Hermann K, et al. CRISPR-Mediated VHL Knockout Generates an Improved Model for Metastatic Renal Cell Carcinoma. Sci Rep. 2016 June 30;6:29032.

142. Stransky LA, Gao W, Schmidt LS, Bi K, Ricketts CJ, Ramesh V, et al. Toward a CRISPR-based mouse model of Vhl-deficient clear cell kidney cancer: Initial experience and lessons learned. Proc Natl Acad Sci. 2024 Oct 8;121(41):e2408549121.

143. van der Mijn JC, Laursen KB, Fu L, Khani F, Dow LE, Nowak DG, et al. Novel genetically engineered mouse models for clear cell renal cell carcinoma. Sci Rep. 2023 May 22;13(1):8246.

144. Kim HM, Kim KJ, Lee K, Yoon MJ, Choih J, Hong TJ, et al. GNUV201, a novel human/mouse cross-reactive and low pH-selective anti-PD-1 monoclonal antibody for cancer immunotherapy. BMC Immunol. 2024 May 11;25:29.

145. Mancardi D, Daëron M. Fc Receptors in Immune Responses. Ref Module Biomed Sci. 2014;B978-0-12-801238-3.00119-7.

146. Terje Andersen J, Bekele Daba M, Berntzen G, Michaelsen TE, Sandlie I. Cross-species Binding Analyses of Mouse and Human Neonatal Fc Receptor Show Dramatic Differences in Immunoglobulin G and Albumin Binding2. J Biol Chem. 2010 Feb 12;285(7):4826–36.

147. Zhong W, Myers JS, Wang F, Wang K, Lucas J, Rosfjord E, et al. Comparison of the molecular and cellular phenotypes of common mouse syngeneic models with human tumors. BMC Genomics. 2020 Jan 2;21(1):2.

148. Rygaard J, Poulsen CO. Heterotransplantation of a Human Malignant Tumour to "Nude" Mice. Acta Pathol Microbiol Scand. 1969;77(4):758–60.

149. Shultz LD, Schweitzer PA, Christianson SW, Gott B, Schweitzer IB, Tennent B, et al. Multiple defects in innate and adaptive immunologic function in NOD/LtSz-scid mice. J Immunol Baltim Md 1950. 1995 Jan 1;154(1):180–91.

150. Beroukhim R, Brunet JP, Di Napoli A, Mertz KD, Seeley A, Pires MM, et al. Patterns of Gene Expression and Copy-Number Alterations in von-Hippel Lindau Disease-Associated and Sporadic Clear Cell Carcinoma of the Kidney. Cancer Res. 2009 June 1;69(11):4674–81.

151. Day CP, Merlino G, Van Dyke T. Preclinical Mouse Cancer Models: A Maze of Opportunities and Challenges. Cell. 2015 Sept 24;163(1):39–53.

152. Tentler JJ, Tan AC, Weekes CD, Jimeno A, Leong S, Pitts TM, et al. Patient-derived tumour xenografts as models for oncology drug development. Nat Rev Clin Oncol. 2012 June;9(6):338–50.

153. Grisanzio C, Seeley A, Chang M, Collins M, Di Napoli A, Cheng SC, et al. Orthotopic xenografts of RCC retain histological, immunophenotypic and genetic features of tumours in patients. J Pathol. 2011 Oct;225(2):212–21.

154. Sivanand S, Peña-Llopis S, Zhao H, Kucejova B, Spence P, Pavia-Jimenez A, et al. A Validated Tumorgraft Model Reveals Activity of Dovitinib Against Renal Cell Carcinoma. Sci Transl Med. 2012 June 6;4(137):137ra75-137ra75.

155. Qiu Z, Zhang D, Garcia-Marques FJ, Bermudez A, Zhao H, Peehl DM, et al. Identification of Molecular Subtypes of Clear-Cell Renal Cell Carcinoma in Patient-Derived Xenografts Using Multi-Omics. Cancers. 2025 Apr 18;17(8):1361.

156. Sanz L, Cuesta AM, Salas C, Corbacho C, Bellas C, Alvarez-Vallina L. Differential transplantability of human endothelial cells in colorectal cancer and renal cell carcinoma primary xenografts. Lab Investig J Tech Methods Pathol. 2009 Jan;89(1):91–7.

157. Yuen JSP, Sim MY, Siml HG, Chong TW, Lau WKO, Cheng CWS, et al. Inhibition of angiogenic and non-angiogenic targets by sorafenib in renal cell carcinoma (RCC) in a RCC xenograft model. Br J Cancer. 2011 Mar;104(6):941–7.

158. Diaz-Montero CM, Mao FJ, Barnard J, Parker Y, Zamanian-Daryoush M, Pink JJ, et al. MEK inhibition abrogates sunitinib resistance in a renal cell carcinoma patient-derived xenograft model. Br J Cancer. 2016 Oct;115(8):920–8.

159. Sakamoto H, Yamasaki T, Sumiyoshi T, Takeda M, Shibasaki N, Utsunomiya N, et al. Functional and genomic characterization of patient-derived xenograft model to study the adaptation to mTORC1 inhibitor in clear cell renal cell carcinoma. Cancer Med. 2021;10(1):119–34.

160. Pompili L, Porru M, Caruso C, Biroccio A, Leonetti C. Patient-derived xenografts: a relevant preclinical model for drug development. J Exp Clin Cancer Res. 2016 Dec 5;35(1):189.

161. Pearson T, Greiner DL, Shultz LD. Creation of "Humanized" Mice to Study Human Immunity. Curr Protoc Immunol Ed John E Coligan Al. 2008 May;CHAPTER:Unit-15.21.

162. Bosma GC, Custer RP, Bosma MJ. A severe combined immunodeficiency mutation in the mouse. Nature. 1983 Feb;301(5900):527–30.

163. Shultz LD, Lyons BL, Burzenski LM, Gott B, Chen X, Chaleff S, et al. Human lymphoid and myeloid cell development in NOD/LtSz-scid IL2R gamma null mice engrafted with mobilized human hemopoietic stem cells. J Immunol Baltim Md 1950. 2005 May 15;174(10):6477–89.

164. King MA, Covassin L, Brehm MA, Racki W, Pearson T, Leif J, et al. Human peripheral blood leucocyte non-obese diabetic-severe combined immunodeficiency interleukin-2 receptor gamma chain gene mouse model of xenogeneic graft-versus-host-like disease and the role of host major histocompatibility complex. Clin Exp Immunol. 2009 July 1;157(1):104–18.

165. Mosier DE, Gulizia RJ, Baird SM, Wilson DB. Transfer of a functional human immune system to mice with severe combined immunodeficiency. Nature. 1988 Sept 15;335(6187):256–9.

166. Matsumura T, Kametani Y, Ando K, Hirano Y, Katano I, Ito R, et al. Functional CD5+ B cells develop predominantly in the spleen of NOD/SCID/γcnull (NOG) mice transplanted either with human umbilical cord blood, bone marrow, or mobilized peripheral blood CD34+ cells. Exp Hematol. 2003 Sept 1;31(9):789–97.

167. Traggiai E, Chicha L, Mazzucchelli L, Bronz L, Piffaretti JC, Lanzavecchia A, et al. Development of a Human Adaptive Immune System in Cord Blood Cell-Transplanted Mice. Science. 2004 Apr 2;304(5667):104–7.

168. Lan P, Tonomura N, Shimizu A, Wang S, Yang YG. Reconstitution of a functional human immune system in immunodeficient mice through combined human fetal thymus/liver and CD34+ cell transplantation. Blood. 2006 July 15;108(2):487–92.

169. Melkus MW, Estes JD, Padgett-Thomas A, Gatlin J, Denton PW, Othieno FA, et al. Humanized mice mount specific adaptive and innate immune responses to EBV and TSST-1. Nat Med. 2006 Nov;12(11):1316–22.

170. Park CK, Khalil M, Pham NA, Wong S, Ly D, Sacher A, et al. Humanized Mouse Models for Immuno-Oncology Research: A Review and Implications in Lung Cancer Research. JTO Clin Res Rep [Internet]. 2025 Mar 1 [cited 2025 Aug 14];6(3). Available from: https://www.jtocrr.org/article/S2666-3643%2824%2900151-6/fulltext?utm_source=chatgpt.com

171. Brehm MA, Kenney LL, Wiles MV, Low BE, Tisch RM, Burzenski L, et al. Lack of acute xenogeneic graft-versus-host disease, but retention of T-cell function following engraftment of human peripheral blood mononuclear cells in NSG mice deficient in MHC class I and II expression. FASEB J. 2019 Mar;33(3):3137–51.

172. Ka Y, Katano I, Nishinaka E, Welcker J, Mochizuki M, Kawai K, et al. Improved engraftment of human peripheral blood mononuclear cells in NOG MHC double knockout mice generated using CRISPR/Cas9. Immunol Lett. 2021 Jan;229:55–61.

173. Yaguchi T, Kobayashi A, Inozume T, Morii K, Nagumo H, Nishio H, et al. Human PBMC-transferred murine MHC class I/II-deficient NOG mice enable long-term evaluation of human immune responses. Cell Mol Immunol. 2018 Nov;15(11):953–62.

174. Ashizawa T, Iizuka A, Nonomura C, Kondou R, Maeda C, Miyata H, et al. Antitumor Effect of Programmed Death-1 (PD-1) Blockade in Humanized the NOG-MHC Double Knockout Mouse. Clin Cancer Res Off J Am Assoc Cancer Res. 2017 Jan 1;23(1):149–58.

175. Gitto SB, Kim H, Rafail S, Omran DK, Medvedev S, Kinose Y, et al. An autologous humanized patient-derived-xenograft platform to evaluate immunotherapy in ovarian cancer. Gynecol Oncol. 2020 Jan 1;156(1):222–32.

176. Odunsi A, McGray AJR, Miliotto A, Zhang Y, Wang J, Abiola A, et al. Fidelity of human ovarian cancer patient-derived xenografts in a partially humanized mouse model for preclinical testing of immunotherapies. J Immunother Cancer. 2020 Nov 11;8(2):e001237.

177. Sanmamed MF, Rodriguez I, Schalper KA, Oñate C, Azpilikueta A, Rodriguez-Ruiz ME, et al. Nivolumab and Urelumab Enhance Antitumor Activity of Human T Lymphocytes Engrafted in Rag2−/−IL2Rγnull Immunodeficient Mice. Cancer Res. 2015 Aug 31;75(17):3466–78.

178. Jespersen H, Lindberg MF, Donia M, Söderberg EMV, Andersen R, Keller U, et al. Clinical responses to adoptive T-cell transfer can be modeled in an autologous immune-humanized mouse model. Nat Commun. 2017 Sept 27;8:707.

179. Bacac M, Fauti T, Sam J, Colombetti S, Weinzierl T, Ouaret D, et al. A Novel Carcinoembryonic Antigen T-Cell Bispecific Antibody (CEA TCB) for the Treatment of Solid Tumors. Clin Cancer Res. 2016 June 30;22(13):3286–97.

180. Boustany LM, LaPorte SL, Wong L, White C, Vinod V, Shen J, et al. A Probody T Cell–Engaging Bispecific Antibody Targeting EGFR and CD3 Inhibits Colon Cancer Growth with Limited Toxicity. Cancer Res. 2022 Nov 15;82(22):4288–98.

181. Lee SH, Chu SY, Rashid R, Phung S, Leung IW, Muchhal US, et al. Abstract 3633: Anti-SSTR2 × anti-CD3 bispecific antibody induces potent killing of human tumor cells in vitro and in mice, and stimulates target-dependent T cell activation in monkeys: A potential immunotherapy for neuroendocrine tumors. Cancer Res. 2017 July 1;77(13_Supplement):3633.

182. Seckinger A, Delgado JA, Moser S, Moreno L, Neuber B, Grab A, et al. Target Expression, Generation, Preclinical Activity, and Pharmacokinetics of the BCMA-T Cell Bispecific Antibody EM801 for Multiple Myeloma Treatment. Cancer Cell. 2017 Mar 13;31(3):396–410.

183. Lee YG, Marks I, Srinivasarao M, Kanduluru AK, Mahalingam SM, Liu X, et al. Use of a Single CAR T Cell and Several Bispecific Adapters Facilitates Eradication of Multiple Antigenically Different Solid Tumors. Cancer Res. 2019 Jan 15;79(2):387–96.

184. Amarnath S, Mangus CW, Wang JCM, Wei F, He A, Kapoor V, et al. The PDL1-PD1 Axis Converts Human Th1 Cells Into Regulatory T Cells. Sci Transl Med. 2011 Nov 30;3(111):111ra120.

185. Mutis T, van Rijn RS, Simonetti ER, Aarts-Riemens T, Emmelot ME, van Bloois L, et al. Human Regulatory T Cells Control Xenogeneic Graft-versus-Host Disease Induced by Autologous T Cells in RAG2−/−γc−/− Immunodeficient Mice. Clin Cancer Res. 2006 Sept 25;12(18):5520–5.

186. Carroll RG, Carpenito C, Shan X, Danet-Desnoyers G, Liu R, Jiang S, et al. Distinct Effects of IL-18 on the Engraftment and Function of Human Effector CD8+ T Cells and Regulatory T Cells. PLOS ONE. 2008 Sept 26;3(9):e3289.

187. Liu Z, Gunasekaran K, Wang W, Razinkov V, Sekirov L, Leng E, et al. Asymmetrical Fc Engineering Greatly Enhances Antibody-dependent Cellular Cytotoxicity (ADCC) Effector Function and Stability of the Modified Antibodies*. J Biol Chem. 2014 Feb 7;289(6):3571–90.

188. Suarez ER, Chang DK, Sun J, Sui J, Freeman GJ, Signoretti S, et al. Chimeric antigen receptor T cells secreting anti-PD-L1 antibodies more effectively regress renal cell carcinoma in a humanized mouse model. Oncotarget. 2016 Apr 29;7(23):34341–55.

189. Au KM, Li S, Zhang T, Wang AZ. Biologically targeted dual adaptive and innate nano-Immunotherapy for clear cell renal cell carcinoma treatment. Mol Cancer. 2025 June 18;24(1):181.

190. Sonntag K, Eckert F, Welker C, Müller H, Müller F, Zips D, et al. Chronic graft-versus-host-disease in CD34+-humanized NSG mice is associated with human susceptibility HLA haplotypes for autoimmune disease. J Autoimmun. 2015 Aug 1;62:55–66.

191. Chen A, Neuwirth I, Herndler-Brandstetter D. Modeling the Tumor Microenvironment and Cancer Immunotherapy in Next-Generation Humanized Mice. Cancers. 2023 May 30;15(11):2989.

192. Do ASMS, Amano T, Edwards LA, Zhang L, De Peralta-Venturina M, Yu JS. CD133 mR-

NA-Loaded Dendritic Cell Vaccination Abrogates Glioma Stem Cell Propagation in Humanized Glioblastoma Mouse Model. Mol Ther - Oncolytics. 2020 Sept 25;18:295–303.

193. Wang M, Yao LC, Cheng M, Cai D, Martinek J, Pan CX, et al. Humanized mice in studying efficacy and mechanisms of PD-1-targeted cancer immunotherapy. FASEB J. 2018;32(3):1537–49.

194. Capasso A, Lang J, Pitts TM, Jordan KR, Lieu CH, Davis SL, et al. Characterization of immune responses to anti-PD-1 mono and combination immunotherapy in hematopoietic humanized mice implanted with tumor xenografts. J Immunother Cancer. 2019 Feb 8;7:37.

195. Liu WN, Fong SY, Tan WWS, Tan SY, Liu M, Cheng JY, et al. Establishment and Characterization of Humanized Mouse NPC-PDX Model for Testing Immunotherapy. Cancers. 2020 Apr 22;12(4):1025.

196. Marín-Jiménez JA, Capasso A, Lewis MS, Bagby SM, Hartman SJ, Shulman J, et al. Testing Cancer Immunotherapy in a Human Immune System Mouse Model: Correlating Treatment Responses to Human Chimerism, Therapeutic Variables and Immune Cell Phenotypes. Front Immunol. 2021 Mar 29;12:607282.

197. Zhao Y, Shuen TWH, Toh TB, Chan XY, Liu M, Tan SY, et al. Development of a new patient-derived xenograft humanised mouse model to study human-specific tumour microenvironment and immunotherapy. Gut. 2018 Oct;67(10):1845–54.

198. Herndler-Brandstetter D, Shan L, Yao Y, Stecher C, Plajer V, Lietzenmayer M, et al. Humanized mouse model supports development, function, and tissue residency of human natural killer cells. Proc Natl Acad Sci U S A. 2017 Nov 7;114(45):E9626–34.

199. Maser IP, Hoves S, Bayer C, Heidkamp G, Nimmerjahn F, Eckmann J, et al. The Tumor Milieu Promotes Functional Human Tumor-Resident Plasmacytoid Dendritic Cells in Humanized Mouse Models. Front Immunol. 2020 Sept 8;11:2082.

200. Rongvaux A, Willinger T, Martinek J, Strowig T, Gearty SV, Teichmann LL, et al. Development and function of human innate immune cells in a humanized mouse model. Nat Biotechnol. 2014 Apr;32(4):364–72.

201. Lang J, Leal AD, Marín-Jiménez JA, Hartman SJ, Shulman J, Navarro NM, et al. Cabozantinib sensitizes microsatellite stable colorectal cancer to immune checkpoint blockade by immune modulation in human immune system mouse models. Front Oncol. 2022 Nov 7;12:877635.

202. Wang Y, Cho JW, Kastrunes G, Buck A, Razimbaud C, Culhane AC, et al. Immune-restoring CAR-T cells display antitumor activity and reverse immunosuppressive TME in a humanized ccRCC mouse model. iScience [Internet]. 2024 Feb 16 [cited 2025 Aug 16];27(2). Available from: https://www.cell.com/iscience/abstract/S2589-0042(24)00100-7

203. Kang Y, Armstrong AJ, Hsu DS. An autologous humanized patient-derived xenograft

(PDX) model for evaluation of nivolumab immunotherapy in renal cell cancer: a case report. Stem Cell Investig. 2022 Nov 8;9:8.

204. Mold JE, Venkatasubrahmanyam S, Burt TD, Michaëlsson J, Rivera JM, Galkina SA, et al. Fetal and adult hematopoietic stem cells give rise to distinct T cell lineages in humans. Science. 2010 Dec 17;330(6011):1695–9.

205. Pang WW, Price EA, Sahoo D, Beerman I, Maloney WJ, Rossi DJ, et al. Human bone marrow hematopoietic stem cells are increased in frequency and myeloid-biased with age. Proc Natl Acad Sci. 2011 Dec 13;108(50):20012–7.

206. Fu J, Kim YJ. Autologously Humanized Mice for Immune-Oncologic Studies. Curr Protoc Pharmacol. 2020 June;89(1):e76.

207. Chuprin J, Buettner H, Seedhom MO, Greiner DL, Keck JG, Ishikawa F, et al. Humanized mouse models for immuno-oncology research. Nat Rev Clin Oncol. 2023 Mar;20(3):192–206.

208. Diwanji R, O'Brien NA, Choi JE, Nguyen B, Laszewski T, Grauel AL, et al. Targeting the IL1β Pathway for Cancer Immunotherapy Remodels the Tumor Microenvironment and Enhances Antitumor Immune Responses. Cancer Immunol Res. 2023 June 2;11(6):777–91.

209. Somasundaram R, Connelly T, Choi R, Choi H, Samarkina A, Li L, et al. Tumor-infiltrating mast cells are associated with resistance to anti-PD-1 therapy. Nat Commun. 2021 Jan 12;12:346.

210. Vatakis DN, Koya RC, Nixon CC, Wei L, Kim SG, Avancena P, et al. Antitumor activity from antigen-specific CD8 T cells generated in vivo from genetically engineered human hematopoietic stem cells. Proc Natl Acad Sci. 2011 Dec 20;108(51):E1408–16.

211. Kaur K, Topchyan P, Kozlowska AK, Ohanian N, Chiang J, Maung PO, et al. Super-charged NK cells inhibit growth and progression of stem-like/poorly differentiated oral tumors in vivo in humanized BLT mice; effect on tumor differentiation and response to chemotherapeutic drugs. OncoImmunology. 2018 May 4;7(5):e1426518.

212. Park HB, Kim KH, Kim JH, Kim SI, Oh YM, Kang M, et al. Improved safety of chimeric antigen receptor T cells indirectly targeting antigens via switchable adapters. Nat Commun. 2024 Nov 18;15(1):9917.

213. Weaver JL, Zadrozny LM, Gabrielson K, Semple KM, Shea KI, Howard KE. BLT-Immune Humanized Mice as a Model for Nivolumab-Induced Immune-Mediated Adverse Events: Comparison of the NOG and NOG-EXL Strains. Toxicol Sci. 2019 May 1;169(1):194–208.

214. Zhang C, Zaman LA, Poluektova LY, Gorantla S, Gendelman HE, Dash PK. Humanized Mice for Studies of HIV-1 Persistence and Elimination. Pathogens. 2023 July;12(7):879.

215. Greenblatt MB, Vbranac V, Tivey T, Tsang K, Tager AM, Aliprantis AO. Graft versus Host Disease in the Bone Marrow, Liver and Thymus Humanized Mouse Model. PLOS

ONE. 2012 Sept 5;7(9):e44664.

216. Brown ME, Zhou Y, McIntosh BE, Norman IG, Lou HE, Biermann M, et al. A Humanized Mouse Model Generated Using Surplus Neonatal Tissue. Stem Cell Rep. 2018 Apr 10;10(4):1175–83.

217. Morton JJ, Bird G, Refaeli Y, Jimeno A. Humanized mouse xenograft models: narrowing the tumor-microenvironment gap. Cancer Res. 2016 Nov 1;76(21):6153–8.

218. Mestas J, Hughes CCW. Of mice and not men: differences between mouse and human immunology. J Immunol Baltim Md 1950. 2004 Mar 1;172(5):2731–8.

219. Delitto D, Pham K, Vlada AC, Sarosi GA, Thomas RM, Behrns KE, et al. Patient-Derived Xenograft Models for Pancreatic Adenocarcinoma Demonstrate Retention of Tumor Morphology through Incorporation of Murine Stromal Elements. Am J Pathol. 2015 May;185(5):1297–303.

220. Lang H, Béraud C, Bethry A, Danilin S, Lindner V, Coquard C, et al. Establishment of a large panel of patient-derived preclinical models of human renal cell carcinoma. Oncotarget. 2016 July 18;7(37):59336–59.

221. Ny L, Rizzo LY, Belgrano V, Karlsson J, Jespersen H, Carstam L, et al. Supporting clinical decision making in advanced melanoma by preclinical testing in personalized immune-humanized xenograft mouse models. Ann Oncol. 2020 Feb 1;31(2):266–73.

222. Stripecke R, Münz C, Schuringa JJ, Bissig K, Soper B, Meeham T, et al. Innovations, challenges, and minimal information for standardization of humanized mice. EMBO Mol Med. 2020 July 7;12(7):e8662.

223. Mellor DJ. Welfare-aligned Sentience: Enhanced Capacities to Experience, Interact, Anticipate, Choose and Survive. Animals. 2019 July;9(7):440.

224. Russell W, Burch R. The Principles of Humane Experimental Technique. Med J Aust. 1959;1(13):500–500.

225. Directive 2010/63/EU of the European Parliament and of the Council of 22 September 2010 on the protection of animals used for scientific purposes Text with EEA relevance [Internet]. OJ L Sept 22, 2010. Available from: http://data.europa.eu/eli/dir/2010/63/oj/eng

226. European Commission. Summary Report on the statistics on the use of animals for scientific purposes in the Member States of the European Union and Norway in 2022 [Internet]. Brussels: European Commission; 2024 July [cited 2025 Aug 18]. Report No.: Brussels, 19.7.2024 SWD(2024) 185 final. Available from: https://circabc.europa.eu/ui/group/8ee3c69a-bccb-4f22-89ca-277e35de7c63/library/051e5787-7746-46cf-8a0d-310f84fd1900/details

227. Miralles A, Raymond M, Lecointre G. Empathy and compassion toward other species decrease with evolutionary divergence time. Sci Rep. 2019 Dec 20;9(1):19555.

228. Vezirian K, Bègue L, Bastian B. Mindless furry test-tubes: Categorizing animals as

lab-subjects leads to their mind denial. J Exp Soc Psychol. 2024 Sept 1;114:104629.

229. Zanoni M, Piccinini F, Arienti C, Zamagni A, Santi S, Polico R, et al. 3D tumor spheroid models for in vitro therapeutic screening: a systematic approach to enhance the biological relevance of data obtained. Sci Rep. 2016 Jan 11;6(1):19103.

230. Séraudie I, Pillet C, Cesana B, Bazelle P, Jeanneret F, Evrard B, et al. A new scaffold-free tumoroid model provides a robust preclinical tool to investigate invasion and drug response in Renal Cell Carcinoma. Cell Death Dis. 2023 Sept 22;14(9):622.

231. Rodrigues DB, Reis RL, Pirraco RP. Modelling the complex nature of the tumor microenvironment: 3D tumor spheroids as an evolving tool. J Biomed Sci. 2024 Jan 23;31(1):13.

232. Rausch M, Blanc L, De Souza Silva O, Dormond O, Griffioen AW, Nowak-Sliwinska P. Characterization of Renal Cell Carcinoma Heterotypic 3D Co-Cultures with Immune Cell Subsets. Cancers. 2021 Jan;13(11):2551.

233. El Harane S, Zidi B, El Harane N, Krause KH, Matthes T, Preynat-Seauve O. Cancer Spheroids and Organoids as Novel Tools for Research and Therapy: State of the Art and Challenges to Guide Precision Medicine. Cells. 2023 Jan;12(7):1001.

234. Jenkins RW, Aref AR, Lizotte PH, Ivanova E, Stinson S, Zhou CW, et al. Ex Vivo Profiling of PD-1 Blockade Using Organotypic Tumor Spheroids. Cancer Discov. 2018 Feb 1;8(2):196–215.

235. Aref AR, Campisi M, Ivanova E, Portell A, Larios D, Piel BP, et al. 3D microfluidic ex vivo culture of organotypic tumor spheroids to model immune checkpoint blockade. Lab Chip. 2018 Oct 9;18(20):3129–43.

236. Yang S, Hu H, Kung H, Zou R, Dai Y, Hu Y, et al. Organoids: The current status and biomedical applications. MedComm. 2023 May 17;4(3):e274.

237. Spagnol G, Sensi F, De Tommasi O, Marchetti M, Bonaldo G, Xhindoli L, et al. Patient Derived Organoids (PDOs), Extracellular Matrix (ECM), Tumor Microenvironment (TME) and Drug Screening: State of the Art and Clinical Implications of Ovarian Cancer Organoids in the Era of Precision Medicine. Cancers. 2023 Jan;15(7):2059.

238. Sato T, Vries RG, Snippert HJ, van de Wetering M, Barker N, Stange DE, et al. Single Lgr5 stem cells build crypt-villus structures in vitro without a mesenchymal niche. Nature. 2009 May;459(7244):262–5.

239. Neal JT, Li X, Zhu J, Giangarra V, Grzeskowiak CL, Ju J, et al. Organoid Modeling of the Tumor Immune Microenvironment. Cell. 2018 Dec 13;175(7):1972-1988.e16.

240. Booij TH, Cattaneo CM, Hirt CK. Tumor Organoids as a Research Tool: How to Exploit Them. Cells. 2022 Jan;11(21):3440.

241. Lo YH, Karlsson K, Kuo CJ. Applications of organoids for cancer biology and precision medicine. Nat Cancer. 2020 Aug;1(8):761–73.

242. Kenerson HL, Sullivan KM, Labadie KP, Pillarisetty VG, Yeung RS. Protocol for tissue slice cultures from human solid tumors to study therapeutic response. STAR Protoc. 2021 June 18;2(2):100574.

243. Rodríguez-Merced NJ, Callaway MK, Provenzano PP. Protocol to culture and image pancreatic ductal adenocarcinoma tumor slices to study T cell migration. STAR Protoc. 2023 Mar 17;4(1):102135.

244. Donnadieu E, Michel Y, Hansmann ML. Live Imaging of Resident T-Cell Migration in Human Lymphoid Tissue Slices Using Confocal Microscopy. In: Verma NK, editor. T-Cell Motility: Methods and Protocols [Internet]. New York, NY: Springer; 2019 [cited 2021 May 18]. p. 75–82. (Methods in Molecular Biology). Available from: https://doi.org/10.1007/978-1-4939-9036-8_10

245. Jiang X, Seo YD, Chang JH, Coveler A, Nigjeh EN, Pan S, et al. Long-lived pancreatic ductal adenocarcinoma slice cultures enable precise study of the immune microenvironment. OncoImmunology. 2017 July 3;6(7):e1333210.

246. Runge A, Mayr M, Schwaiger T, Sprung S, Chetta P, Gottfried T, et al. Patient-derived head and neck tumor slice cultures: a versatile tool to study oncolytic virus action. Sci Rep. 2022 Sept 12;12(1):15334.

247. Powley IR, Patel M, Miles G, Pringle H, Howells L, Thomas A, et al. Patient-derived explants (PDEs) as a powerful preclinical platform for anti-cancer drug and biomarker discovery. Br J Cancer. 2020 Mar 17;122(6):735–44.

248. Costa EC, Moreira AF, de Melo-Diogo D, Gaspar VM, Carvalho MP, Correia IJ. 3D tumor spheroids: an overview on the tools and techniques used for their analysis. Biotechnol Adv. 2016 Dec 1;34(8):1427–41.

249. Duval K, Grover H, Han LH, Mou Y, Pegoraro AF, Fredberg J, et al. Modeling Physiological Events in 2D vs. 3D Cell Culture. Physiology. 2017 July;32(4):266–77.

250. Papamichail L, Koch LS, Veerman D, Broersen K, van der Meer AD. Organoids-on-a-chip: microfluidic technology enables culture of organoids with enhanced tissue function and potential for disease modeling. Front Bioeng Biotechnol [Internet]. 2025 Mar 11 [cited 2025 Sept 7];13. Available from: https://www.frontiersin.org/journals/bioengineering-and-biotechnology/articles/10.3389/fbioe.2025.1515340/full

251. Moshksayan K, Kashaninejad N, Warkiani ME, Lock JG, Moghadas H, Firoozabadi B, et al. Spheroids-on-a-chip: Recent advances and design considerations in microfluidic platforms for spheroid formation and culture. Sens Actuators B Chem. 2018 June;263:151–76.

252. Ildiz ES, Gvozdenovic A, Kovacs WJ, Aceto N. Travelling under pressure - hypoxia and shear stress in the metastatic journey. Clin Exp Metastasis. 2023 Oct 1;40(5):375–94.

253. Bertani F, Di Francesco D, Corrado MD, Talmon M, Fresu LG, Boccafoschi F. Paracrine Shear-Stress-Dependent Signaling from Endothelial Cells Affects Downstream Endothelial Function and Inflammation. Int J Mol Sci. 2021 Jan;22(24):13300.

254. Barnes JM, Nauseef JT, Henry MD. Resistance to Fluid Shear Stress Is a Conserved Biophysical Property of Malignant Cells. PLOS ONE. 2012 Dec 3;7(12):e50973.

255. Alcaide P. Mechanisms Regulating T Cell–Endothelial Cell Interactions. Cold Spring Harb Perspect Med. 2022 July;12(7):a041170.

256. Iakovlev AP, Erofeev AS, Gorelkin PV. Novel Pumping Methods for Microfluidic Devices: A Comprehensive Review. Biosensors. 2022 Nov 1;12(11):956.

257. Boucherit N, Gorvel L, Olive D. 3D Tumor Models and Their Use for the Testing of Immunotherapies. Front Immunol [Internet]. 2020 Dec 10 [cited 2025 Aug 25];11. Available from: https://www.frontiersin.org/journals/immunology/articles/10.3389/fimmu.2020.603640/full

258. Appleton KM, Elrod AK, Lassahn KA, Shuford S, Holmes LM, DesRochers TM. PD-1/PD-L1 checkpoint inhibitors in combination with olaparib display antitumor activity in ovarian cancer patient-derived three-dimensional spheroid cultures. Cancer Immunol Immunother. 2021 Mar 1;70(3):843–56.

259. Dijkstra KK, Cattaneo CM, Weeber F, Chalabi M, Haar J van de, Fanchi LF, et al. Generation of Tumor-Reactive T Cells by Co-culture of Peripheral Blood Lymphocytes and Tumor Organoids. Cell. 2018 Sept 6;174(6):1586-1598.e12.

260. Liu C, Li K, Sui X, Zhao T, Zhang T, Chen Z, et al. Patient-Derived Tumor Organoids Combined with Function-Associated ScRNA-Seq for Dissecting the Local Immune Response of Lung Cancer. Adv Sci. 2024;11(31):2400185.

261. Deng J, Wang ES, Jenkins RW, Li S, Dries R, Yates K, et al. CDK4/6 Inhibition Augments Anti-Tumor Immunity by Enhancing T Cell Activation. Cancer Discov. 2018 Feb;8(2):216–33.

262. Voabil P, de Bruijn M, Roelofsen LM, Hendriks SH, Brokamp S, van den Braber M, et al. An ex vivo tumor fragment platform to dissect response to PD-1 blockade in cancer. Nat Med. 2021 July;27(7):1250–61.

263. Salmon H, Franciszkiewicz K, Damotte D, Dieu-Nosjean MC, Validire P, Trautmann A, et al. Matrix architecture defines the preferential localization and migration of T cells into the stroma of human lung tumors. J Clin Invest. 2012 Mar 1;122(3):899–910.

264. Seo YD, Jiang X, Sullivan KM, Jalikis FG, Smythe KS, Abbasi A, et al. Mobilization of CD8+ T Cells via CXCR4 Blockade Facilitates PD-1 Checkpoint Therapy in Human Pancreatic Cancer. Clin Cancer Res. 2019 July 1;25(13):3934–45.

265. Courau T, Bonnereau J, Chicoteau J, Bottois H, Remark R, Miranda LA, et al. Cocultures of human colorectal tumor spheroids with immune cells reveal the therapeutic potential of MICA/B and NKG2A targeting for cancer treatment. J Immunother Cancer. 2019 Dec 1;7(1):74.

266. Gopal S, Kwon SJ, Ku B, Lee DW, Kim J, Dordick JS. 3D tumor spheroid microarray for high-throughput, high-content natural killer cell-mediated cytotoxicity. Commun

Biol. 2021 July 21;4(1):893.

267. Nguyen M, De Ninno A, Mencattini A, Mermet-Meillon F, Fornabaio G, Evans SS, et al. Dissecting Effects of Anti-cancer Drugs and Cancer-Associated Fibroblasts by On-Chip Reconstitution of Immunocompetent Tumor Microenvironments. Cell Rep. 2018 Dec 26;25(13):3884-3893.e3.

268. Tong L, Tay AHM, Cui W, Liu Y, Su Y, Lyu J, et al. VHL restoration in clear cell renal cell carcinoma improves NK cell infiltration and function. Cancer Immunol Immunother. 2025 Sept 1;74(9):1–14.

269. Zou F, Tan J, Liu T, Liu B, Tang Y, Zhang H, et al. The CD39+ HBV surface protein-targeted CAR-T and personalized tumor-reactive CD8+ T cells exhibit potent anti-HCC activity. Mol Ther. 2021 May 5;29(5):1794–807.

270. Dekkers JF, Alieva M, Cleven A, Keramati F, Wezenaar AKL, van Vliet EJ, et al. Uncovering the mode of action of engineered T cells in patient cancer organoids. Nat Biotechnol. 2023 Jan;41(1):60–9.

271. Schnalzger TE, de Groot MH, Zhang C, Mosa MH, Michels BE, Röder J, et al. 3D model for CAR-mediated cytotoxicity using patient-derived colorectal cancer organoids. EMBO J. 2019 June 17;38(12):e100928.

272. Stüber T, Monjezi R, Wallstabe L, Kühnemundt J, Nietzer SL, Dandekar G, et al. Inhibition of TGF-β-receptor signaling augments the antitumor function of ROR1-specific CAR T-cells against triple-negative breast cancer. J Immunother Cancer. 2020 Apr 16;8(1):e000676.

273. Greiner D, Xue Q, Waddell TQ, Kurudza E, Chaudhary P, Belote RL, et al. Human CSPG4-targeting CAR-macrophages inhibit melanoma growth. Oncogene. 2025 June;44(22):1665–77.

274. Li Z, Xu H, Yu L, Wang J, Meng Q, Mei H, et al. Patient-derived renal cell carcinoma organoids for personalized cancer therapy. Clin Transl Med. 2022;12(7):e970.

275. Wang Y, Buck A, Piel B, Zerefa L, Murugan N, Coherd CD, et al. Affinity fine-tuning anti-CAIX CAR-T cells mitigate on-target off-tumor side effects. Mol Cancer. 2024 Mar 16;23(1):56.

276. Guiet R, Van Goethem E, Cougoule C, Balor S, Valette A, Al Saati T, et al. The Process of Macrophage Migration Promotes Matrix Metalloproteinase-Independent Invasion by Tumor Cells. J Immunol. 2011 Oct 1;187(7):3806–14.

277. Rebelo SP, Pinto C, Martins TR, Harrer N, Estrada MF, Loza-Alvarez P, et al. 3D-3-culture: A tool to unveil macrophage plasticity in the tumour microenvironment. Biomaterials. 2018 May 1;163:185–97.

278. Kuen J, Darowski D, Kluge T, Majety M. Pancreatic cancer cell/fibroblast co-culture induces M2 like macrophages that influence therapeutic response in a 3D model. PLoS ONE. 2017 July 27;12(7):e0182039.

279. Raghavan S, Mehta P, Xie Y, Lei YL, Mehta G. Ovarian cancer stem cells and macrophages reciprocally interact through the WNT pathway to promote pro-tumoral and malignant phenotypes in 3D engineered microenvironments. J Immunother Cancer. 2019 July 19;7(1):190.

280. Li YR, Yu Y, Kramer A, Hon R, Wilson M, Brown J, et al. An Ex Vivo 3D Tumor Microenvironment-Mimicry Culture to Study TAM Modulation of Cancer Immunotherapy. Cells. 2022 Jan;11(9):1583.

281. Peranzoni E, Lemoine J, Vimeux L, Feuillet V, Barrin S, Kantari-Mimoun C, et al. Macrophages impede CD8 T cells from reaching tumor cells and limit the efficacy of anti–PD-1 treatment. Proc Natl Acad Sci [Internet]. 2018 Apr 24 [cited 2025 Aug 25];115(17). Available from: https://pnas.org/doi/full/10.1073/pnas.1720948115

282. Perucca A, Llonín AG, Benach OM, Hallopeau C, Rivas EI, Linares J, et al. Micro Immune Response On-chip (MIRO) models the tumour-stroma interface for immunotherapy testing. Nat Commun. 2025 Feb 3;16(1):1279.

283. López JI, Errarte P, Erramuzpe A, Guarch R, Cortés JM, Angulo JC, et al. Fibroblast activation protein predicts prognosis in clear cell renal cell carcinoma. Hum Pathol. 2016 Aug 1;54:100–5.

284. Owaki T, Iida T, Miyai Y, Kato K, Hase T, Ishii M, et al. Synthetic retinoid-mediated preconditioning of cancer-associated fibroblasts and macrophages improves cancer response to immune checkpoint blockade. Br J Cancer. 2024 July;131(2):372–86.

285. Zhou Z, Van der Jeught K, Li Y, Sharma S, Yu T, Moulana I, et al. A T Cell-Engaging Tumor Organoid Platform for Pancreatic Cancer Immunotherapy. Adv Sci. 2023;10(23):2300548.

286. Herter S, Morra L, Schlenker R, Sulcova J, Fahrni L, Waldhauer I, et al. A novel three-dimensional heterotypic spheroid model for the assessment of the activity of cancer immunotherapy agents. Cancer Immunol Immunother. 2017;66(1):129–40.

287. Teijeira A, Migueliz I, Garasa S, Karanikas V, Luri C, Cirella A, et al. Three-dimensional colon cancer organoids model the response to CEA-CD3 T-cell engagers. Theranostics. 2022 Jan 1;12(3):1373–87.

288. Zhang Y, Qian L, Chen K, Gu S, Meng Z, Wang J, et al. Oncolytic adenovirus in treating malignant ascites: A phase II trial and longitudinal single-cell study. Mol Ther. 2024 June 5;32(6):2000–20.

289. Yin Q, Yu W, Grzeskowiak CL, Li J, Huang H, Guo J, et al. Nanoparticle-enabled innate immune stimulation activates endogenous tumor-infiltrating T cells with broad antigen specificities. Proc Natl Acad Sci U S A. 2021 May 25;118(21):e2016168118.

290. Feodoroff M, Hamdan F, Antignani G, Feola S, Fusciello M, Russo S, et al. Enhancing T-cell recruitment in renal cell carcinoma with cytokine-armed adenoviruses. Oncoimmunology. 2024;13(1):2407532.

291. Ding S, Hsu C, Wang Z, Natesh NR, Millen R, Negrete M, et al. Patient-derived micro-organospheres enable clinical precision oncology. Cell Stem Cell. 2022 June 2;29(6):905-917.e6.

292. Votanopoulos KI, Forsythe S, Sivakumar H, Mazzocchi A, Aleman J, Miller L, et al. Model of Patient-Specific Immune-Enhanced Organoids for Immunotherapy Screening: Feasibility Study. Ann Surg Oncol. 2020 June;27(6):1956–67.

293. Veith I, Nurmik M, Mencattini A, Damei I, Lansche C, Brosseau S, et al. Assessing personalized responses to anti-PD-1 treatment using patient-derived lung tumor-on-chip. Cell Rep Med. 2024 May;5(5):101549.

294. Al-Samadi A, Poor B, Tuomainen K, Liu V, Hyytiäinen A, Suleymanova I, et al. *In vitro* humanized 3D microfluidic chip for testing personalized immunotherapeutics for head and neck cancer patients. Exp Cell Res. 2019 Oct 15;383(2):111508.

295. Xue Y, Wang B, Tao Y, Xia J, Yuan K, Zheng J, et al. Patient-derived organoids potentiate precision medicine in advanced clear cell renal cell carcinoma. Precis Clin Med. 2022 Dec;5(4):pbac028.

296. LeSavage BL, Suhar RA, Broguiere N, Lutolf MP, Heilshorn SC. Next-generation cancer organoids. Nat Mater. 2022 Feb;21(2):143–59.

297. Adashi EY, O'Mahony DP, Cohen IG. The FDA Modernization Act 2.0: Drug Testing in Animals is Rendered Optional. Am J Med. 2023 Sept;136(9):853–4.

298. Singh K, Gautam PK. Macrophage infiltration in 3D cancer spheroids to recapitulate the TME and unveil interactions within cancer cells and macrophages to modulate chemotherapeutic drug efficacy. BMC Cancer. 2023 Dec 7;23(1):1201.

299. Francois A, Dirheimer L, Chateau A, Lassalle HP, Yakavets I, Bezdetnaya L. A Macrophages-Enriched Head and Neck Tumor Spheroid Model to Study Foslip® Behavior in Tumor Microenvironment. Int J Nanomedicine. 2023 Nov 9;18:6545–62.

300. Seo J, Ha G, Lee G, Nasiri R, Lee J. Modeling tumor-immune interactions using hybrid spheroids and microfluidic platforms for studying tumor-associated macrophage polarization in melanoma. Acta Biomater. 2024 Dec 1;190:233–46.

301. Tan Y, Suarez A, Garza M, Khan AA, Elisseeff J, Coon D. Human fibroblast-macrophage tissue spheroids demonstrate ratio-dependent fibrotic activity for in vitro fibrogenesis model development. Biomater Sci. 2020 Mar 31;8(7):1951–60.

302. Liu K, Catalfamo M, Li Y, Henkart PA, Weng N ping. IL-15 mimics T cell receptor crosslinking in the induction of cellular proliferation, gene expression, and cytotoxicity in CD8+ memory T cells. Proc Natl Acad Sci. 2002 Apr 30;99(9):6192–7.

303. Meresse B, Chen Z, Ciszewski C, Tretiakova M, Bhagat G, Krausz TN, et al. Coordinated induction by IL15 of a TCR-independent NKG2D signaling pathway converts CTL into lymphokine-activated killer cells in celiac disease. Immunity. 2004 Sept;21(3):357–66.

304. Marton C, Mercier-Letondal P, Galaine J, Godet Y. An unmet need: Harmonization of IL-7 and IL-15 combination for the *ex vivo* generation of minimally differentiated T cells. Cell Immunol. 2021 May 1;363:104314.

305. Hopkins B, Fisher J, Chang M, Tang X, Du Z, Kelly WJ, et al. An In-Vitro Study of the Expansion and Transcriptomics of CD4+ and CD8+ Naïve and Memory T Cells Stimulated by IL-2, IL-7 and IL-15. Cells. 2022 Jan;11(10):1701.

306. Baldan V, Griffiths R, Hawkins RE, Gilham DE. Efficient and reproducible generation of tumour-infiltrating lymphocytes for renal cell carcinoma. Br J Cancer. 2015 Apr;112(9):1510–8.

307. Petrozziello E, Sturmheit T, Mondino A. Exploiting Cytokines in Adoptive T-Cell Therapy of Cancer. Immunotherapy. 2015 June 1;7(5):573–84.

308. Lo HC, Choi H, Kolahi K, Rodriguez S, Gonzalez L, Chu F, et al. A 3D tumor spheroid model with robust T cell infiltration for evaluating immune cell engagers. iScience. 2025 Aug 15;28(8):112996.

309. Jiang P, Gu S, Pan D, Fu J, Sahu A, Hu X, et al. Signatures of T cell dysfunction and exclusion predict cancer immunotherapy response. Nat Med. 2018 Oct;24(10):1550–8.

310. Xin S, Su J, Li R, Cao Q, Wang H, Wei Z, et al. Identification of a risk model for prognostic and therapeutic prediction in renal cell carcinoma based on infiltrating M0 cells. Sci Rep. 2024 June 11;14(1):13390.

311. Stupichev D, Miheecheva N, Postovalova E, Lyu Y, Ramachandran A, Galkin I, et al. AI-driven multimodal algorithm predicts immunotherapy and targeted therapy outcomes in clear cell renal cell carcinoma. Cell Rep Med. 2025 Aug 19;6(8):102299.

312. Esser LK, Branchi V, Leonardelli S, Pelusi N, Simon AG, Klümper N, et al. Cultivation of Clear Cell Renal Cell Carcinoma Patient-Derived Organoids in an Air-Liquid Interface System as a Tool for Studying Individualized Therapy. Front Oncol [Internet]. 2020 Sept 22 [cited 2025 Oct 28];10. Available from: https://www.frontiersin.org/journals/oncology/articles/10.3389/fonc.2020.01775/full

313. Miller CP, Shin W, Ahn EH, Kim HJ, Kim DH. Engineering Microphysiological Immune System Responses on Chips. Trends Biotechnol. 2020 Aug 1;38(8):857–72.

314. Maulana TI, Teufel C, Cipriano M, Roosz J, Lazarevski L, Hil FE van den, et al. Breast cancer-on-chip for patient-specific efficacy and safety testing of CAR-T cells. Cell Stem Cell. 2024 July 5;31(7):989-1002.e9.

315. Cui X, Ma C, Vasudevaraja V, Serrano J, Tong J, Peng Y, et al. Dissecting the immunosuppressive tumor microenvironments in Glioblastoma-on-a-Chip for optimized PD-1 immunotherapy. Reis e Sousa C, Settleman J, editors. eLife. 2020 Sept 10;9:e52253.

316. Wang X, Sun Q, Pei J. Microfluidic-Based 3D Engineered Microvascular Networks and Their Applications in Vascularized Microtumor Models. Micromachines. 2018 Sept 27;9(10):493.

317. Miller CP, Tsuchida C, Zheng Y, Himmelfarb J, Akilesh S. A 3D Human Renal Cell Carcinoma-on-a-Chip for the Study of Tumor Angiogenesis. Neoplasia. 2018 June 1;20(6):610–20.

318. Virumbrales-Muñoz M, Chen J, Ayuso J, Lee M, Abel EJ, Beebe DJ. Organotypic primary blood vessel models of clear cell renal cell carcinoma for single-patient clinical trials. Lab Chip. 2020 Nov 24;20(23):4420–32.

319. Brassard-Jollive N, Atlas Y, Compère CL, Ardidie-Robouant C, Mailly P, Bouchtaoui ME, et al. 3D vascularized microtumors unveil aberrant ccRCC vasculature and differential sensitivity to targeted treatments [Internet]. bioRxiv; 2025 [cited 2025 Aug 26]. p. 2025.03.27.645644. Available from: https://www.biorxiv.org/content/10.1101/2025.03.27.645644v1

320. Park KY, Hefti HO, Liu P, Lugo-Cintrón KM, Kerr SC, Beebe DJ. Immune cell mediated cabozantinib resistance for patients with renal cell carcinoma. Integr Biol. 2021 Nov 1;13(11):259–68.

321. Kim D, Hwang KS, Seo EU, Seo S, Lee BC, Choi N, et al. Vascularized Lung Cancer Model for Evaluating the Promoted Transport of Anticancer Drugs and Immune Cells in an Engineered Tumor Microenvironment. Adv Healthc Mater. 2022;11(12):2102581.

322. Song J, Choi H, Koh SK, Park D, Yu J, Kang H, et al. High-Throughput 3D In Vitro Tumor Vasculature Model for Real-Time Monitoring of Immune Cell Infiltration and Cytotoxicity. Front Immunol [Internet]. 2021 Sept 24 [cited 2025 Aug 26];12. Available from: https://www.frontiersin.org/journals/immunology/articles/10.3389/fimmu.2021.733317/full

323. Quintard C, Tubbs E, Jonsson G, Jiao J, Wang J, Werschler N, et al. A microfluidic platform integrating functional vascularized organoids-on-chip. Nat Commun. 2024 Feb 16;15(1):1452.

324. Wei J, Sun Y, Wang H, Zhu T, Li L, Zhou Y, et al. Designer cellular spheroids with DNA origami for drug screening. Sci Adv. 2024;10(29):eado9880.

325. Wang Q, Yuan F, Zuo X, Li M. Breakthroughs and challenges of organoid models for assessing cancer immunotherapy: a cutting-edge tool for advancing personalised treatments. Cell Death Discov. 2025 May 7;11(1):222.

326. Jiang S, Zhao H, Zhang W, Wang J, Liu Y, Cao Y, et al. An Automated Organoid Platform with Inter-organoid Homogeneity and Inter-patient Heterogeneity. Cell Rep Med [Internet]. 2020 Dec 22 [cited 2025 Aug 26];1(9). Available from: https://www.cell.com/cell-reports-medicine/abstract/S2666-3791(20)30208-1

327. Liu YC, Ansaryan S, Tan J, Broguiere N, Lorenzo-Martín LF, Homicsko K, et al. Nanoplasmonic Single-Tumoroid Microarray for Real-Time Secretion Analysis. Adv Sci. 2024;11(34):2401539.

328. Bian X, Li G, Wang C, Liu W, Lin X, Chen Z, et al. A deep learning model for detection and tracking in high-throughput images of organoid. Comput Biol Med. 2021 July

1;134:104490.

329. Park T, Kim TK, Han YD, Kim KA, Kim H, Kim HS. Development of a deep learning based image processing tool for enhanced organoid analysis. Sci Rep. 2023 Nov 13;13(1):19841.

330. Gerlinger M, Rowan AJ, Horswell S, Larkin J, Endesfelder D, Gronroos E, et al. Intratumor Heterogeneity and Branched Evolution Revealed by Multiregion Sequencing. N Engl J Med. 2012 Mar 8;366(10):883–92.

331. Turajlic S, Xu H, Litchfield K, Rowan A, Horswell S, Chambers T, et al. Deterministic Evolutionary Trajectories Influence Primary Tumor Growth: TRACERx Renal. Cell. 2018 Apr 19;173(3):595-610.e11.

Résumé substantiel en français

Le cancer constitue l'un des enjeux majeurs de santé mondiale, avec 20 millions de nouveaux cas et 9,7 millions de décès en 2022, des chiffres appelés à croître du fait du vieillissement démographique et de l'exposition accrue aux facteurs environnementaux. Ce fardeau épidémiologique s'inscrit dans un cadre biologique complexe où le cancer est aujourd'hui compris comme une maladie génétique et évolutive, façonnée par l'accumulation progressive d'altérations somatiques affectant oncogènes, suppresseurs tumoraux, mécanismes de réparation, voies métaboliques et programmes épigénétiques. Cette vision s'est construite au fil des avancées historiques, depuis les intuitions cellulaires de Virchow et les hypothèses chromosomiques de Boveri, jusqu'aux projets contemporains de caractérisation moléculaire à grande échelle tels que TCGA, ICGC et PCAWG, qui ont révélé l'ampleur des mutations structurales, des remaniements épigénétiques et de l'hétérogénéité intra-tumorale.

Face à cette diversité, les Hallmarks of Cancer de Hanahan et Weinberg offrent un cadre conceptuel unificateur décrivant les propriétés fonctionnelles acquises par les cellules tumorales au cours de leur évolution : autosuffisance proliférative, échappement aux signaux antiprolifératifs, résistance à la mort programmée, immortalité réplicative, angiogenèse, invasion et métastases. À ces traits s'ajoutent des capacités émergentes telles que la plasticité phénotypique, la reprogrammation métabolique, les remodelages épigénétiques ou encore l'impact des microbiotes, ainsi que des caractéristiques habilitantes comme l'instabilité génomique ou l'inflammation chronique. L'intégration du microenvironnement tumoral (TME) comme dimension essentielle du modèle souligne que la progression tumorale ne dépend pas uniquement des altérations intrinsèques des cellules cancéreuses, mais également des interactions dynamiques qu'elles entretiennent avec l'ensemble des éléments non tumoraux qui les entourent : fibroblastes, cellules endothéliales, matrice extracellulaire, cellules immunitaires infiltrantes, facteurs solubles et gradients métaboliques, constituent un écosystème complexe qui façonne la croissance, la plasticité et les capacités d'échappement immunitaire des tumeurs.

L'interface entre tumeur et immunité est précisément structurée par le modèle de l'immunoédition, qui décrit trois phases successives : élimination, équilibre et échappement. Dans la phase d'élimination, l'immunité innée (NK, macrophages M1, cellules dendritiques) et l'immunité adaptative (lymphocytes T cytotoxiques $CD8^+$, lymphocytes $CD4^+$ Th1, lymphocytes B organisés en structures lymphoïdes tertiaires) coopèrent pour reconnaître et détruire les cellules transformées grâce à la présentation d'antigènes tumoraux, incluant néoantigènes mutés, antigènes aberrants ou protéines surexprimées. Lorsque l'élimination est incomplète, la phase d'équilibre maintient des clones tumoraux résiduels dans un état de dormance sous pression immunitaire, tout en sélectionnant des variantes moins immunogènes. Cette co-évolution, véritable filtre darwinien, façonne des tumeurs dites « chaudes » ou « froides » selon leur degré d'infiltration immune.

La phase d'échappement survient lorsque les cellules tumorales acquièrent des mécanismes leur permettant d'éviter la détection ou de paralyser la réponse immunitaire. Ceux-ci incluent la perte d'antigènes, la diminution du CMH-I ou de β2-microglobuline, l'expression accrue de checkpoints inhibiteurs (PD-L1, CTLA-4, TIM-3, LAG-3, TIGIT, HLA-G, HLA-E), ou encore des modifications métaboliques et cytokiniques qui favorisent la tolérance. Parallèlement, le TME devient profondément immunosuppresseur : accumulation de T régulateurs, expansion de cellules myéloïdes suppressives, polarisation de macrophages en M2-like tolérogènes, remodelage matriciel par les fibroblastes associés au cancer (CAFs), angiogenèse désorganisée, hypoxie, acidose et déplétion en nutriments essentiels tels que l'arginine ou le tryptophane. Ces contraintes multifactorielles entravent l'accès, la survie et l'activité cytotoxique des lymphocytes T, renforçant l'état d'épuisement T caractérisé par une stimulation chronique, une diminution des fonctions effectrices et une surexpression de multiples récepteurs inhibiteurs.

Cette compréhension mécanistique des interactions immuno-tumorales a conduit au développement des immunothérapies modernes, principalement les inhibiteurs de points de contrôle immunitaire (ICIs) ciblant les axes CTLA-4–CD80/86 et PD-1–PD-L1. Ces traitements, aujourd'hui standards dans plusieurs cancers, exploitent la réactivation de cellules T pré-existantes, restaurent la fonction effectrice dans le TME et peuvent entraîner des réponses durables chez certains patients. Toutefois, l'hétérogénéité des réponses observées en clinique souligne l'absence de modèles précliniques capables de reproduire de manière fidèle et rapide l'organisation immuno-tumorale des cancers solides et, en particulier, de tumeurs fortement immunomodulées comme le carcinome rénal à cellules claires.

Le carcinome rénal à cellules claires (ccRCC), forme la plus fréquente de cancer du rein, se caractérise par une hétérogénéité clinique, génétique et microenvironnementale particulièrement marquée. Son incidence, en hausse dans les pays industrialisés, reflète l'impact combiné de facteurs environnementaux tels que l'obésité, le tabagisme, l'hypertension ou l'insuffisance rénale chronique, ainsi que de syndromes héréditaires spécifiques, incluant la maladie de von Hippel–Lindau (VHL), BHD, HLRCC ou les altérations germinales de TSC et SDH. Ces formes héréditaires ont permis d'identifier les circuits moléculaires majeurs impliqués dans cette tumeur, notamment la voie VHL/HIF, dont la dérégulation entraîne une stabilisation de HIF-1α et HIF-2α, une activation excessive de l'angiogenèse et une reprogrammation métabolique profonde.

Le pronostic du ccRCC dépend étroitement du stade TNM, du grade ISUP et des scores cliniques tels que MSKCC ou IMDC, aujourd'hui essentiels dans la stratification des formes métastatiques. Sur le plan génomique, les mutations récurrentes de PBRM1, SETD2 et BAP1 affectent la structure de la chromatine, la réparation de l'ADN, la différenciation cellulaire et l'immunogénicité tumorale. Parallèlement, la tumeur adopte un profil métabolique singulier, incluant une accumulation lipidique, des altérations mitochondriales et une dépendance accrue à certains substrats énergétiques, éléments déterminants pour comprendre sa physiopathologie et ses mécanismes de résistance thérapeutique.

Le microenvironnement tumoral du ccRCC est défini par une infiltration immune dense mais paradoxale. Malgré la présence importante de lymphocytes T, les réponses aux immunothérapies demeurent hétérogènes et difficilement prévisibles. Les TILs présentent fréquemment un état d'épuisement marqué (PD-1, LAG-3, TIM-3), les macrophages adoptent majoritairement un phénotype M2 immunosuppresseur, tandis que fibroblastes et cellules endothéliales contribuent au remodelage matriciel, à l'organisation des gradients métaboliques et à la modulation de l'accessibilité des cellules effectrices. L'intense angiogenèse induite par l'axe HIF-2α/VEGF renforce encore ce microenvironnement permissif à la progression tumorale mais défavorable à l'immunité cytotoxique.

Sur le plan thérapeutique, la chirurgie demeure le traitement de référence pour les formes localisées, tandis que les thérapies ciblant VEGF ou mTOR ont longtemps constitué l'arsenal principal dans la maladie métastatique. L'introduction des immunothérapies, notamment les combinaisons aPD-1/PD-L1-aCTLA-4 et aPD-1/PD-L1-TKI (nivolumab–ipilimumab, pembrolizumab–axitinib, nivolumab–cabozantinib, pembrolizumab–lenvatinib), a profondément modifié les standards de prise en charge, avec des gains démontrés en survie globale et en survie sans progression. Malgré ces progrès, aucun biomarqueur fiable ne permet aujourd'hui d'anticiper la réponse individuelle aux ICIs : l'expression de PD-L1 est variable, la charge mutationnelle faible, et les signatures transcriptomiques, bien que prometteuses, restent difficilement transposables en pratique clinique.

L'ensemble de ces caractéristiques positionne le ccRCC comme une tumeur immunogène, façonnée par la convergence de dérégulations génétiques, de plasticité métabolique, d'angiogenèse active et d'immunomodulation complexe. Cette configuration, combinée à l'absence de biomarqueurs prédictifs robustes et à une hétérogénéité intra-tumorale marquée, souligne la nécessité de disposer de modèles précliniques ex vivo capables de conserver l'architecture cellulaire, la diversité immunitaire et les spécificités microenvironnementales du ccRCC, tout en permettant l'évaluation fonctionnelle des réponses immunitaires et des immunothérapies.

Les cultures bidimensionnelles traditionnelles constituent l'outil historique de la recherche en cancérologie. Elles permettent un contrôle précis des paramètres expérimentaux, une grande reproductibilité et une compatibilité avec des approches à haut débit. Cependant, ces modèles perdent rapidement l'hétérogénéité cellulaire d'origine, induisent une adaptation artificielle au plastique et ne conservent ni l'architecture tridimensionnelle, ni les gradients métaboliques, ni la composition stromale caractéristiques des tumeurs in vivo Leur pertinence pour l'immuno-oncologie demeure toutefois limitée : les cultures 2D ne conservent ni l'architecture tridimensionnelle, ni la diversité stromale ou immunitaire des tumeurs in vivo, et ne permettent donc pas de modéliser l'infiltration, l'exclusion ou les interactions immunosuppressives caractéristiques du microenvironnement tumoral. Elles restent utiles pour des études mécanistiques ciblées ou des approches à haut débit, mais ne peuvent reproduire la complexité cellulaire et fonctionnelle nécessaire à l'étude fine des réponses immunitaires antitumorales.

Les modèles in vivo constituent un cadre expérimental plus intégratif, permettant de préserver une partie de la complexité anatomique et physiologique des tumeurs dans la dynamique d'un organisme entier. Leur diversité reflète des stratégies expérimentales complémentaires, mais aucune d'entre elles ne permet de reproduire simultanément l'ensemble des dimensions immunologiques, stromales et génétiques propres aux tumeurs humaines.

Les modèles syngéniques murins représentent la forme la plus simple de cancérogenèse immunocompétente : des lignées ou tumeurs murines sont implantées dans des souris génétiquement compatibles. Ce format permet l'étude de réponses immunitaires complètes, mais repose sur des tumeurs strictement murines, souvent très éloignées des cancers humains sur les plans génétique, transcriptomique et immunobiologique. Leur microenvironnement diffère profondément de celui des tumeurs solides humaines et limite leur transposabilité, en particulier pour des tumeurs fortement immunomodulées comme le ccRCC.

Les modèles génétiquement modifiés (GEMMs) permettent d'induire in vivo des événements oncogéniques spécifiques et de suivre la formation de tumeurs spontanées dans un organisme immunocompétent. Ils reproduisent certains aspects du contexte tissulaire et des interactions précoces tumeur–immunité, mais souffrent généralement d'une latence importante, d'une disponibilité restreinte et d'une forte variabilité d'un modèle à l'autre. Leur mise en œuvre demeure coûteuse et techniquement lourde, ce qui limite leur utilisation à grande échelle.

Les xénogreffes dérivées de lignées (CDX) sont faciles à établir et largement utilisées dans les criblages précliniques. Elles permettent d'obtenir des masses tumorales reproductibles, mais doivent être implantées dans des souris immunodéficientes, ce qui supprime tout compartiment immunitaire fonctionnel. Leur intérêt pour l'immuno-oncologie reste donc limité, malgré leur utilité pour des études pharmacologiques élémentaires.

Les xénogreffes dérivées de patients (PDX) conservent mieux l'hétérogénéité génétique et l'architecture du tissu d'origine, et reproduisent certaines réponses thérapeutiques observées en clinique. Toutefois, comme les CDX, elles nécessitent un hôte immunodéficient, impliquant une perte quasi complète du compartiment immunitaire humain. De plus, les cellules immunitaires résiduelles du patient, lorsqu'elles sont transférées avec le fragment tumoral, ne persistent que transitoirement et ne permettent pas de reconstituer un infiltrat intratumoral fonctionnel.

Afin de pallier cette limitation, des modèles humanisés ont été développés en reconstituant une immunité humaine dans des souris dépourvues d'immunité adaptative. Cette reconstitution repose sur l'injection de cellules $CD34^+$, de PBMC, ou sur la greffe de fragments thymiques, chacune de ces approches générant un degré variable de restauration immunitaire. Malgré un intérêt conceptuel majeur, ces systèmes présentent plusieurs contraintes :

– la reconstitution est souvent incomplète, avec un déséquilibre marqué des sous-populations immunitaires (expansion des T, faible reconstitution myéloïde) ;

– le système immunitaire est instable dans le temps, sujet à des dérégulations ou au développe-

ment de réactions xénogéniques ;

– les modèles sont coûteux, nécessitent de longues périodes de prise de greffe, et dépendent de sources cellulaires difficiles à standardiser ;

– l'interaction entre cellules immunitaires humaines et stroma murin reste non physiologique, ce qui limite la fidélité des réponses immunitaires, notamment pour les thérapies ciblant les checkpoints.

En conséquence, si les modèles humanisés demeurent une voie importante pour l'étude de certaines dimensions de l'immunité anticancéreuse, leur lenteur, leur variabilité et leurs contraintes techniques les rendent difficiles à mobiliser dans un cadre de médecine translationnelle ou pour des applications patient-spécifiques.

Aux contraintes organisationnelles et biologiques inhérentes aux modèles animaux s'ajoutent des considérations éthiques et sociétales majeures. La reconnaissance de la sentience des animaux de laboratoire, ainsi que l'évolution des attentes sociétales, ont conduit à un encadrement réglementaire strict visant à limiter le recours à l'expérimentation animale. Ce contexte a motivé l'adoption du principe des 3R (Reduction, Refinement, Replacement), désormais au cœur des politiques européennes de recherche biomédicale.

Malgré ces évolutions, l'emploi d'animaux demeure massif : plusieurs millions de sujets sont encore utilisés chaque année en recherche biomédicale, avec une proportion particulièrement élevée en cancérologie. Les données récentes montrent que, contrairement à d'autres domaines où l'usage tend à diminuer, l'oncologie reste l'un des secteurs où la réduction est la plus difficile à atteindre, et où la consommation animale a plutôt stagné que réellement reculé. Cette tendance reflète en partie la dépendance persistante aux modèles in vivo pour l'étude des interactions tumeur–microenvironnement, de la pharmacodynamie et des réponses immunitaires.

Ces contraintes éthiques, combinées aux limites méthodologiques, temporelles et immunologiques décrites précédemment, réduisent la pertinence des modèles animaux pour l'évaluation de l'efficacité des immunothérapies. Elles renforcent la nécessité de développer des alternatives complémentaires ex vivo, plus rapides et mieux alignées avec les objectifs de réduction de l'expérimentation animale. Entre les modèles 2D et les modèles animaux, un ensemble de systèmes tridimensionnels in vitro a émergé pour tenter de combiner réalisme biologique et accessibilité expérimentale.

Les sphéroïdes tumoraux sont des micro-agrégats tridimensionnels obtenus par l'auto-organisation de cellules tumorales en structures compactes. Ils se distinguent des cultures 2D par la capacité à reconstruire une architecture multicellulaire plus physiologique, caractérisée par des gradients d'oxygène, de nutriments, de signaux paracrines et une organisation tissulaire partiellement comparable à celle observée in vivo. Ces structures peuvent être générées à partir de lignées établies ou directement à partir de cellules tumorales primaires, par agrégation spontanée ou sous contrainte physique (liquid overlay, goutte pendante, agitation douce). Leur rapidité de

formation, leur coût réduit et leur facilité de standardisation expliquent leur utilisation très large dans les modèles précliniques.

Ainsi, si les sphéroïdes dérivés de patients représentent un compromis intéressant combinant rapidité, accessibilité et conservation partielle de la complexité tumorale, ils nécessitent souvent des stratégies additionnelles (co-culture, ré-infiltration autologue, matrices enrichies) pour approcher plus fidèlement un microenvironnement immunocompétent.

Les organoïdes sont des structures tridimensionnelles auto-organisées dérivées de cellules souches ou de cellules épithéliales, capables de reproduire certains aspects architecturaux, fonctionnels et transcriptomiques d'un tissu d'origine. Cultivés le plus souvent dans une matrice extracellulaire (type Matrigel) et exposés à des milieux de différenciation spécifiques, ils génèrent des microstructures présentant des domaines luminalisés, une polarité épithéliale et une organisation cellulaire plus proche de la physiologie que les cultures bidimensionnelles. Leur principal intérêt réside dans leur capacité à conserver des programmes de différenciation et des altérations génétiques propres au tissu dont ils dérivent, ce qui en fait un outil puissant pour l'étude de la biologie tumorale.

Les organoïdes dérivés de patients (PDOs) appliquent ce principe aux tumeurs solides en permettant de préserver une partie des programmes transcriptionnels, de l'hétérogénéité cellulaire et des altérations génétiques du tissu tumoral originel. Plusieurs déclinaisons existent. Les PDO « classiques », obtenus par mise en culture dans du Matrigel, conservent robustement l'épithélium tumoral mais perdent rapidement les cellules immunitaires, stromales et endothéliales.

Les explants tumoraux, ainsi que les tranches tumorales, sont des fragments de tumeur conservant l'architecture histologique native, les interactions épithéliales, stromales et immunitaires, ainsi que les gradients locaux d'oxygène et de nutriments. Leur culture à court terme permet d'étudier des interactions cellulaires dans un environnement fidèle au tissu d'origine, mais leur durée de vie limitée et l'absence de dynamique restreignent les possibilités d'analyse fonctionnelle prolongée.

Dans la continuité de ces approches, les patient-derived organotypic tumor spheroids (PDOTs) représentent une variante intermédiaire entre l'explant et le sphéroïde. Contrairement aux sphéroïdes dérivés de cellules dissociées, les PDOTs sont obtenus par fragmentation contrôlée de tissu tumoral frais, sans dissociation enzymatique complète. Chaque micro-fragment conserve ainsi un « noyau organotypique » comprenant les cellules tumorales, un contingent stromal, une matrice extracellulaire native, des cellules endothéliales résiduelles et, surtout, une fraction de l'infiltrat immunitaire intratumoral initial. En d'autres termes, le PDOT fonctionne comme une micro-section tridimensionnelle de la tumeur, plus maniable et standardisable qu'un explant, mais nettement plus représentative de l'architecture initiale qu'un sphéroïde reconstruit.

Enfin, les systèmes microfluidiques et plateformes « organ-on-chip » constituent une extension technologique majeure des modèles tridimensionnels classiques. Plus qu'une catégorie

de modèles supplémentaires, ces dispositifs ajoutent une couche fonctionnelle intégrative permettant d'exposer des structures 3D : sphéroïdes, PDOTS, PDOs ou fragments tumoraux, à un environnement dynamique recréant des paramètres physiologiques essentiels : gradients de pression et de nutriments, perfusion contrôlée, forces de cisaillement, ou encore circulation cellulaire. Cette dimension sous flux ouvre l'accès à des readouts impossibles en culture statique, tels que l'observation en temps réel de l'infiltration de lymphocytes, l'analyse de migrations directionnelles, la quantification dynamique de cytokines dans l'effluent, ou la modélisation de micro-interactions vascularisées.

Malgré leur potentiel, ces plateformes demeurent techniquement exigeantes, nécessitant un matériel spécialisé, une fabrication micro-ingénierique et des compétences avancées pour assurer stabilité et reproductibilité. Elles restent par ailleurs rarement immunocompétentes : l'intégration de cellules immunitaires dans des conditions physiologiques de circulation est encore peu fréquente, et leur application spécifique au carcinome rénal à cellules claires demeure limitée. Toutefois, lorsqu'elles sont couplées à des modèles 3D dérivés de patients, elles permettent de franchir une étape supplémentaire en capturant des phénomènes dynamiques, infiltration, activation, cytotoxicité sous flux, essentiels pour l'étude des immunothérapies.

Bien que le paysage des modèles précliniques soit aujourd'hui extrêmement riche, cultures 2D, lignées, sphéroïdes, organoïdes, explants, modèles animaux ou systèmes microfluidiques, chacun de ces outils répond d'abord à un objectif particulier. Certains privilégient la simplicité et le contrôle expérimental, d'autres la conservation de l'architecture tissulaire, d'autres encore la dynamique vasculaire ou la possibilité d'explorer des interactions immunitaires complexes. Aucun modèle n'a vocation à être universel : leur pertinence dépend étroitement de l'application envisagée, qu'il s'agisse de biologie fondamentale, de pharmacologie, de modélisation immunitaire ou d'évaluation thérapeutique.

Dans ce contexte, notre démarche s'est inscrite dans un besoin spécifique : disposer d'un modèle ex vivo rapide, autologue et immunocompétent, adapté à l'étude fonctionnelle des interactions tumeur–immunité dans le carcinome rénal à cellules claires et à l'évaluation de réponses aux immunothérapies. Pour guider cette construction, nous nous sommes appuyés sur un ensemble de critères considérés comme essentiels pour un modèle pertinent du ccRCC : préservation de l'hétérogénéité tumorale et des populations immunitaires majeures, maintien des composantes stromales et matricielles, conservation de multiples checkpoints immunitaires, reproduction de gradients métaboliques et d'hypoxie, compatibilité avec des readouts fonctionnels multiparamétriques, délai d'obtention court et respect du contexte autologue.

L'objectif a donc été de développer un modèle ex vivo qui réponde de manière pragmatique à ces exigences, en combinant :

— une dérivation directe à partir de tumeurs fraîches,

— une ré-infiltration par les TILs autologues,

— un format tridimensionnel,

— et une intégration dans un environnement microfluidique dynamique permettant l'étude de phénomènes dépendants du flux.

Cette approche ne vise pas à se substituer aux modèles préexistants, mais à proposer un outil complémentaire, spécifiquement conçu pour explorer les interactions immunitaires et les mécanismes de réponse ou de résistance aux ICIs dans un cadre autologue et fonctionnel.

Le premier volet des résultats présente le développement complet d'un modèle tridimensionnel de sphéroïdes dérivés de carcinome rénal à cellules claires (ccRCC), conçu pour permettre l'étude fine des interactions entre cellules tumorales et effecteurs immunitaires. L'établissement de ce modèle repose d'abord sur l'optimisation de la dissociation tumorale. Un protocole enzymatique doux est défini afin de maximiser la viabilité cellulaire et de limiter les artefacts transcriptionnels induits par les contraintes mécaniques. L'obtention de suspensions primaires de haute qualité s'accompagne de l'élaboration d'un milieu de culture simplifié spécifiquement adapté aux cellules de ccRCC.

La formation des sphéroïdes est ensuite évaluée à l'aide de plusieurs méthodes. La technique de « liquid overlay », utilisant des plaques à faible adhérence, s'avère la plus efficace pour obtenir des structures compactes, homogènes et reproductibles, tant à partir de lignées établies que de cellules primaires. La qualité morphologique des sphéroïdes est contrôlée via une analyse quantitative fondée sur quatre paramètres : aire, circularité, roundness et solidity, calculés automatiquement grâce à une macro dédiée. Cette étape permet de sélectionner, en amont des expérimentations fonctionnelles, des sphéroïdes répondant à des critères objectifs d'homogénéité et d'exclure les agrégats irréguliers ou incomplets. Cette standardisation constitue un point clé, garantissant la reproductibilité expérimentale et réduisant la variabilité inhérente aux cultures tridimensionnelles.

Une fois ce socle méthodologique établi, le modèle est utilisé pour étudier des interactions immunitaires. Des PBMC activés, principalement par IL-15, montrent une capacité d'infiltration profonde dans les sphéroïdes tumoraux. L'imagerie en temps réel permet d'observer directement la migration et la pénétration des cellules immunitaires, tandis que l'analyse cytométrique après dissociation confirme la présence de populations $CD45^+$ au sein des structures. L'infiltration par des macrophages dérivés de monocytes est également démontrée, illustrant la capacité du modèle à accueillir différents types effecteurs et à reproduire des interactions immunitaires diversifiées.

La fonctionnalité du modèle est évaluée par des essais de cytotoxicité en imagerie temps réel utilisant l'iodure de propidium. Les PBMC activés induisent une augmentation progressive de la mort cellulaire tumorale, traduisant leur activité cytotoxique. Cette réponse est amplifiée par l'ajout d'un anticorps anti-PD-1, fournissant une preuve de concept de la capacité du système à détecter les effets modulés par une immunothérapie montrant qu'un modèle tridimensionnel

simplifié peut révéler des différences fonctionnelles liées à des stratégies thérapeutiques ciblant les checkpoints immunitaires.

Dans son ensemble, ce premier volet établit une plateforme tridimensionnelle robuste, modulable et compatible avec des analyses dynamiques de l'infiltration immunitaire et de la cytotoxicité. Il met également en évidence plusieurs limites, principalement liées au fait que ce modèle repose encore sur une étape préalable de culture en flasque. Cette phase de mise en culture induit une sélection cellulaire, un éloignement du contexte patient-dérivé et la perte complète du compartiment immunitaire natif. L'infiltration observée dépend exclusivement de l'ajout de PBMC activés ex vivo, dans un environnement immunologique reconstitué et non autologue. Ces contraintes soulignent la nécessité de passer à des approches dérivées directement de tumeurs fraîches sans culture préalable, capables de préserver davantage de complexité cellulaire et de permettre l'étude d'interactions immunitaires dans un contexte plus physiologique.

Dans un second volet expérimental, l'objectif est d'évaluer dans quelle mesure un modèle tridimensionnel dérivé directement de tumeurs humaines, sans phase préalable de culture en flasque, contrairement au volet précédent, peut préserver la complexité cellulaire et les propriétés immunologiques caractéristiques du ccRCC. Pour cela, un workflow séquentiel a été mis en place, comprenant des prélèvements de matériel ARN à quatre étapes clés : le tissu tumoral natif, la tumeur fraîchement dissociée, les sphéroïdes formés en 48 heures à partir des cellules dissociées, puis les sphéroïdes ré-infiltrés pendant 24 heures par leurs TILs autologues (pour trois patients).

À chacune de ces étapes, des échantillons ont été collectés pour un séquençage BRB-seq, permettant de comparer de manière systématique l'évolution transcriptionnelle et la composition cellulaire au cours de la formation du modèle.

Les premières analyses montrent que la dissociation enzymatique génère un signal transcriptionnel marqué par des signatures de stress, d'inflammation aiguë et de modifications métaboliques, ainsi qu'un enrichissement relatif en cellules immunitaires confirmant que cette étape introduit un biais important dans l'état cellulaire initial. Toutefois, la formation rapide de sphéroïdes permet une restauration partielle des programmes observés dans le tissu parental, notamment des signatures d'hypoxie, de remodelage matriciel et d'activités métaboliques typiques du ccRCC.

En termes de composition cellulaire, l'analyse de révèle que les sphéroïdes dérivés de tumeurs humaines conservent les principaux compartiments du microenvironnement tumoral : cellules épithéliales malignes, fibroblastes, cellules endothéliales et populations immunitaires. Cette conservation n'est pas parfaite, mais elle demeure robuste malgré les variations inter-patients, ce qui témoigne d'une bonne stabilité structurelle du modèle. L'étape de ré-infiltration autologue permet de restaurer un compartiment immunitaire intratumoral cohérent, enrichi en lymphocytes T effecteurs exprimant des signatures d'activation et de cytotoxicité. En revanche, les populations myéloïdes, en particulier les macrophages, cruciaux dans le ccRCC, apparaissent

significativement sous-représentées à ce stade. Cette observation, répétée dans plusieurs échantillons, suggère que le protocole favorise la survie et la réactivation des TILs mais n'assure pas la préservation des macrophages, probablement en raison de conditions de culture et de stimulation peu compatibles avec leur maintien.

L'analyse s'attache également à évaluer la fidélité biologique du modèle par rapport aux tumeurs d'origine. Les transcriptomes montrent une conservation de signatures de différenciation épithéliale, de programmes de signalisation HIF-dépendants, de voies associées au remodelage matriciel, ainsi que l'expression de points de contrôle immunitaire tels que PD-1, PD-L1, LAG3 ou TIGIT. De plus, les scores prédictifs de réponse aux ICIs dérivés de signatures publiées présentent une bonne concordance entre les fragments tumoraux initiaux et les sphéroïdes ré-infiltrés, ce qui soutient la pertinence fonctionnelle du modèle. Fait notable, l'hétérogénéité inter-patient, caractéristique du ccRCC, est préservée dans les transcriptomes sphéroïdes, renforçant la vocation du modèle pour des approches ex vivo individualisées.

Une lecture intégrative des capacités et limites du modèle met en avant, d'un côté, la rapidité du workflow (moins de 72 heures entre la dissociation et les premières mesures) et la conservation des compartiments clés, qui rendent le système compatible avec des tests fonctionnels rapides, et de l'autre, l'appauvrissement du compartiment myéloïde, la dépendance à une activation intense des TILs et la perte d'une partie de l'architecture stromale initiale, qui constituent des limites majeures pour modéliser fidèlement le TME du ccRCC. Ces observations orientent déjà des pistes d'optimisation : protocoles de co-culture dédiés aux macrophages, ajustement plus physiologique des cytokines de stimulation, intégration de matrices extracellulaires enrichies.

Dans son ensemble, l'ensemble de ce volet montre qu'un modèle tridimensionnel dérivé de tumeur fraîche et ré-infiltré par des TILs autologues peut reconstituer de manière rapide et fiable une part substantielle de la complexité immuno-biologique du ccRCC. Ce résultat constitue une avancée structurante dans la mise en place d'un modèle ex vivo pertinent pour explorer la sensibilité ou la résistance aux immunothérapies, et préfigure son intégration dans des systèmes plus sophistiqués, en particulier la plateforme microfluidique décrite dans la suite.

Un troisième volet des résultats décrit l'intégration du modèle patient-dérivé de ccRCC au sein d'une plateforme microfluidique de type tumor-on-chip permettant de reconstituer un environnement dynamique et de modéliser, sous flux, les interactions entre tumeur et système immunitaire. L'objectif est de dépasser les limites des cultures statiques et de créer un système capable d'accueillir un compartiment tumoral tridimensionnel, un compartiment infiltrant et un compartiment circulant, tout en permettant l'observation en temps réel des interactions cellulaires et l'évaluation fonctionnelle d'immunothérapies.

La puce microfluidique développée présente une architecture reposant sur une série de pièges hydrodynamiques capables de capturer les sphéroïde ré-infiltrés décrits précédemment et de permettre la circulation continue de cellules du sang périphérique (PBMCs) autologues.

Dans un premier temps, la plateforme est validée à l'aide de sphéroïdes dérivés de lignées tumorales, en combinant une étape préalable d'imagerie confocale sur sphéroïdes transparisés afin de vérifier la capacité des cellules immunitaires à s'infiltrer dans les structures tridimensionnelles. Des PBMCs activés sont co-cultivées avec les sphéroïdes, puis ces derniers sont clarifiés et imagés en profondeur, ce qui permet de visualiser directement la migration et la pénétration cellulaire au sein du volume tumoral. Cette étape constitue une validation essentielle démontrant que le modèle sphéroïdal est compatible avec l'analyse en imagerie 3D haute résolution et que l'infiltration immune peut être quantifiée de manière robuste.

La plateforme est ensuite appliquée au modèle patient-dérivé complet : des sphéroïdes générés directement à partir de tumeurs fraîchement dissociées, ré-infiltrés par leurs TILs autologues, sont perfusés pendant 72 heures avec des PBMC du même patient, reconstituant ex vivo un système comprenant un compartiment tumoral tridimensionnel, un compartiment infiltrant et un compartiment circulant. Les PBMC circulants infiltrent efficacement les sphéroïdes, et le milieu collecté met en évidence des variations du profil cytokine, notamment sous blocage PD-L1. À l'issue de la perfusion, les cellules récupérées dans les sphéroïdes dissociés sont analysées par cytométrie spectrale 37 couleurs, démontrant la faisabilité d'un phénotypage en haute dimension directement à partir de la puce.

Cette analyse permet d'identifier les principaux sous-ensembles lymphocytaires autologues ($CD4^+$, $CD8^+$, NK) ainsi qu'une diversité de phénotypes $CD8^+$, allant de populations naïves et mémoire à des effecteurs cytotoxiques, TEMRA et sous-ensembles pré-épuisés ou checkpoint-positifs. La distribution observée diffère de celle de PBMC activés en conditions statiques, traduisant des mécanismes de rétention, de survie ou de recrutement propres au microenvironnement 3D sous flux. Globalement, les marqueurs cytotoxiques sont diminués dans les sphéroïdes, mais restaurés après blocage PD-L1, indiquant une modulation fonctionnelle mesurable au niveau de plusieurs sous-populations T.

Dans son ensemble, ce volet démontre qu'un modèle autologue sous flux permet non seulement une infiltration immunitaire mesurable et une modulation cytokine dépendante d'un anti-PD-L1, mais également un phénotypage immunitaire en haute dimension. Il valide la faisabilité d'intégrer la cytométrie spectrale comme readout fonctionnel et positionne la plateforme comme un outil pertinent pour étudier les réponses immunitaires patient-spécifiques dans un environnement dynamique.

Ce dispositif met en évidence la capacité d'un modèle patient-dérivé à générer rapidement des réponses immunitaires mesurables dans un environnement dynamique, et à distinguer des conditions traitées ou non par immunothérapie. L'intégration microfluidique apporte ainsi une dimension supplémentaire au modèle testé dans les volets précédents, en permettant d'analyser des comportements cellulaires dépendants du flux, d'accéder à des lectures fonctionnelles multiparamétriques et de reconstituer des interactions immunitaires complexes dans un cadre autologue.

Plusieurs limites doivent être prises en compte dans l'interprétation de ce modèle, qui reste présenté ici comme une preuve de faisabilité. Les analyses d'imagerie et de cytométrie ont été réalisées sur un nombre restreint d'échantillons, parfois à partir d'un seul donneur, ce qui ne permet pas encore de conclusions comparatives robustes entre conditions. La récupération cellulaire après dissociation des sphéroïdes demeure perfectible et limite l'analyse détaillée des TILs infiltrants, en particulier en l'absence de PBMC circulants. L'utilisation d'une activation IL-15 forte, choisie pour garantir la viabilité et l'engagement des compartiments immunitaires dans ce contexte exploratoire, induit un remodelage cytokine-dépendant des lymphocytes et peut masquer une partie des modulations induites spécifiquement par la tumeur. Par ailleurs, l'absence d'échantillonnage cinétique restreint l'interprétation fonctionnelle des profils cytokiniques à un point final unique.

Ces éléments soulignent la nécessité de futures optimisations, notamment en termes de conditions d'activation plus physiologiques, d'amélioration de la dissociation sphéroïdale, d'intégration d'un suivi temporel des sécrétions et de l'extension des validations à un nombre plus large de patients, afin de consolider la robustesse, la sensibilité et la portée translationnelle du système.

Dans son ensemble, ce troisième volet montre qu'un modèle tumor-on-chip autologue appliqué au ccRCC est capable de capturer des phénomènes dynamiques d'infiltration et de réponse immunitaire, tout en offrant un cadre rapide et potentiellement prédictif pour l'évaluation fonctionnelle d'inhibiteurs de checkpoints. Il représente ainsi une avancée importante pour le développement de modèles ex vivo personnalisés en immuno-oncologie.

Ainsi la plateforme expérimentale élaborée repose sur un modèle ex vivo de carcinome rénal à cellules claires (ccRCC) construit par étapes successives : formation de sphéroïdes à partir de tumeurs fraîchement dissociées, réinfiltration par des TIL autologues, caractérisation transcriptomique et intégration finale dans une puce microfluidique perfusée. L'ensemble vise à approcher un système in vitro robuste, dérivé du patient, capable de capturer les interactions complexes entre compartiments tumoral, stromal et immunitaire. Le modèle ainsi obtenu préserve une part importante de l'hétérogénéité tumorale, conserve des sous-populations immunitaires clés et des éléments stromaux, ainsi que des caractéristiques de microenvironnement telles que l'hypoxie, la matrice extracellulaire et des signatures métaboliques typiques du ccRCC. Plusieurs checkpoints immunitaires sont maintenus, les scores immunologiques restent globalement concordants avec ceux du tissu initial, et l'organisation autologue des compartiments est respectée. L'implémentation microfluidique introduit un flux continu et un compartiment circulant, tandis que les readouts fonctionnels : sécrétion de cytokines, cytométrie en flux ou spectrale, imagerie en temps réel, permettent de quantifier des réponses immunitaires dynamiques. Le workflow complet, de la chirurgie aux premières mesures fonctionnelles, s'étale sur environ une semaine, ce qui rend envisageable une utilisation dans des délais compatibles avec le contexte clinique.

Malgré ces atouts, plusieurs limites majeures subsistent. Sur le plan cellulaire, le modèle

conserve bien les compartiments épithéliaux, stromaux et une partie du compartiment lymphocytaire, mais le compartiment myéloïde, et en particulier la fraction macrophagique, apparaît sévèrement appauvri. Or ces cellules jouent un rôle central dans la balance entre activité antitumorale et tolérance, dans la structuration de l'exclusion ou de l'accessibilité immunitaire et dans le remodelage de la matrice. De façon intrigante, les analyses BRB-seq suggèrent néanmoins la persistance possible de signatures de cellules suppressives d'origine myéloïde (MDSC), observation inattendue qui demande à être confirmée par des approches histologiques ou cytométriques ciblées. Sur le plan technique, cette déplétion myéloïde peut s'expliquer par la phase de 48 heures d'activation sur plastique, durant laquelle les cellules fortement adhérentes restent fixées et ne sont pas récupérées avant la formation des sphéroïdes. Des données antérieures montrent pourtant que des populations myéloïdes peuvent être efficacement intégrées à des sphéroïdes par simple co-culture, ce qui ouvre la voie à une stratégie consistant à séparer ces cellules des TILs, puis à les réintroduire au moment de la formation sphéroïde (jour 0) ou en parallèle de la réinfiltration lymphocytaire, comme cela a été démontré dans d'autres modèles sans compromettre l'assemblage sphéroïdal.

Une seconde limite concerne les modalités d'activation et de survie des lymphocytes. Dans ce système, l'infiltration efficace des sphéroïdes par les TILs dépend fortement d'une préactivation par l'IL-15 : en l'absence de stimulation cytokine, les cellules immunitaires n'infiltre pas les sphéroïdes, perdent rapidement leur viabilité et ne permettent pas l'établissement d'un compartiment immunitaire fonctionnel. Les essais visant à inclure directement les lymphocytes pendant la formation des sphéroïdes se sont soldés par une organisation défectueuse ou très retardée des structures, suggérant une interférence entre co-agrégation précoce et architecture sphéroïdale stable. L'IL-15 a été choisie pour favoriser la survie et la fonction T et NK sans engager directement le TCR, afin de conserver autant que possible le contexte autologue. Toutefois, cette cytokine est connue pour induire des fonctions effectrices puissantes indépendantes du TCR, ce qui contribue probablement aux divergences transcriptionnelles et phénotypiques observées et introduit un biais d'hyperactivation. Celui-ci garantit la persistance, la réinfiltration et des readouts fonctionnels mesurables, mais risque d'écraser des différences fines entre conditions expérimentales et de limiter la sensibilité des tests à des effets d'immunothérapie modestes ou subtils.

L'identification de stratégies d'activation plus « physiologiques » de TILs, compatibles avec la migration et la survie sans induire de biais trop marqué, constitue donc un enjeu méthodologique important. Des schémas plus conservateurs pourraient reposer sur des combinaisons de faibles doses d'IL-2, IL-7, IL-15 ou IL-21, administrées de manière continue ou pulsée, dans le but de soutenir la viabilité et la motilité sans reprogrammer complètement le compartiment immunitaire. La littérature existante décrit toutefois essentiellement des protocoles visant à générer des effecteurs spécifiques ou à maximiser l'amplification ex vivo en vue de transfert adoptif, plutôt qu'à préserver la composition et l'état fonctionnel d'un infiltrat intratumoral. Une autre

piste consisterait à supprimer toute étape d'activation préalable et à favoriser l'intégration des TILs au moment de la formation sphéroïde. Des techniques d'agrégation dirigée par champ magnétique, reposant sur l'utilisation transitoire de nanoparticules magnétiques inertes, ont été proposées pour forcer l'assemblage rapide de sphéroïdes mixtes tumeur–immunité. Dans la pratique, la reproductibilité de cette approche s'est révélée difficile, tant en termes de cinétique de formation que d'intégrité structurelle, ce qui nécessite des optimisations supplémentaires avant d'envisager une intégration routinière dans le workflow.

La question de la valeur prédictive du modèle, au-delà de sa seule fidélité biologique, reste ouverte. L'analyse transcriptomique exploratoire menée dans le second volet à l'aide de l'algorithme TIDE suggère une certaine cohérence entre les profils prédits de réponse aux inhibiteurs de checkpoints dans les tissus tumoraux et ceux observés dans les sphéroïdes dérivés. Les tumeurs classées comme non répondeuses présentaient des sphéroïdes avec des scores TIDE concordants, tandis que, pour un patient catégorisé comme répondeur, les sphéroïdes affichaient également une sensibilité prédite élevée, malgré un effectif encore très limité (n = 3). TIDE a été conçu comme un biomarqueur computationnel intégrant deux dimensions clés de résistance à l'immunothérapie : la dysfonction des lymphocytes T dans les tumeurs infiltrées mais non répondeuses, et l'exclusion des T dans les tumeurs faiblement infiltrées. Il a été validé dans plusieurs cancers, où il surpasse parfois des marqueurs classiques tels que l'expression de PD-L1 ou la charge mutationnelle tumorale. Dans le ccRCC, cependant, ses performances restent indicatives : certaines études l'ont corrélé à la survie ou à des patterns d'infiltration, mais aucune ne l'a formellement relié à la réponse clinique effective. Parallèlement, des approches multimodales récentes combinant données génomiques, histologiques et cliniques via l'intelligence artificielle ont montré une capacité à prédire les réponses aux immunothérapies et aux thérapies ciblées dans le ccRCC. Confronter le modèle ex vivo à ces outils prédictifs avancés, sur des séries plus larges, permettrait d'évaluer plus finement sa représentativité fonctionnelle et son potentiel translationnel.

La mise en perspective avec les modèles précliniques existants en oncologie rénale situe ce système au croisement de plusieurs approches. Les xénogreffes dérivées de patients conservent la structure et une partie de la complexité stromale, mais leur nécessité de recourir à des hôtes immunodéficients les rend inadaptées à l'étude directe de l'immunité humaine, même dans leurs versions « humanisées », lourdes, coûteuses et lentes. Les organoïdes dérivés de patients permettent l'expansion de compartiments épithéliaux tumoraux en conservant une fraction de l'hétérogénéité génétique, mais perdent rapidement les cellules immunitaires et stromales et exigent des temps de culture prolongés exposant au drift phénotypique. Les formats air–liquid interface et les fragments tumoraux ex vivo ont constitué une avancée importante en permettant le maintien concomitant de TILs, fibroblastes et endothélium, et des travaux dans le ccRCC ont montré qu'ils peuvent refléter des réponses à des inhibiteurs de PD-1 ou de VEGFR. Ces systèmes restent toutefois essentiellement statiques, ne modélisent ni la circulation, ni les pro-

cessus d'infiltration sous flux, ni les cinétiques de réponse, alors que les mêmes matériaux biologiques pourraient, en principe, être transférés dans des dispositifs microfluidiques.

Les plateformes tumor-on-chip comblent précisément ce manque en ajoutant une dimension dynamique. Les premiers modèles RCC-on-chip utilisant des sphéroïdes de lignée et des CAR-T ont démontré la faisabilité d'observer une infiltration antigène-spécifique sous flux, mais au prix d'un contexte non autologue et d'une immunité artificiellement reconstituée. D'autres systèmes développés dans des cancers pulmonaires ou cérébraux ont intégré des cellules tumorales, des lymphocytes autologues et des fibroblastes dans des matrices perfusées, révélant la possibilité de modéliser la réponse à des anti-PD-1 dans des conditions microphysiologiquement pertinentes. Dans la plupart de ces approches, cependant, le flux sert avant tout au renouvellement du milieu, les cellules immunitaires n'étant pas systématiquement perfusées comme un véritable compartiment circulant, et l'autologité complète n'est pas toujours assurée. Le modèle microfluidique décrit ici se distingue en combinant des tumeurs dissociées fraîches donnant des sphéroïdes autologues réinfiltrés par leurs TILs et une perfusion continue de PBMCs du même patient, réunissant dans un même dispositif les compartiments tumoral infiltré et sanguin dans un contexte dynamique.

Les perspectives d'évolution identifiées prolongent plusieurs lignes fortes. L'intégration d'une vascularisation fonctionnelle apparaît comme une étape intéressante, particulièrement dans le ccRCC, tumeur hautement angiogénique dont la vascularisation désorganisée contribue à l'hypoxie, à l'hétérogénéité de perfusion et aux barrières physiques à l'infiltration immunitaire. L'absence de vaisseaux perfusables dans les modèles actuels conduit à des gradients d'oxygène et de nutriments non physiologiques et à une distribution imparfaite des facteurs solubles et des agents thérapeutiques. Des microenvironnements vasculaires sur puce ont déjà été développés dans le ccRCC, montrant la possibilité de recréer des réseaux endothéliaux aberrants et d'explorer leurs réponses à des anti-angiogéniques ou à des signaux dérivés des lymphocytes T $CD4^+$. Par ailleurs, la puce utilisée dérive d'une plateforme initialement conçue pour vasculariser des organoïdes capturés par des trappes microfluidiques, via l'injection contrôlée d'hydrogels contenant des cellules endothéliales (HUVEC) et l'établissement de réseaux connectant l'organoïde aux canaux de perfusion. Le fait que les sphéroïdes patient-dérivés conservent des cellules endothéliales offre un point de départ théorique pour tenter de reconstruire une interface vasculaire fonctionnelle autour des structures tumorales et d'y greffer des modules de perfusion immunitaire, à l'image des modèles colorectaux et pulmonaires où des monocytes ou lymphocytes perfusés traversent une barrière endothéliale avant d'atteindre le compartiment tumoral.

D'autres défis concernent la reproductibilité et l'échelle. La variabilité de taille et de morphologie des sphéroïdes influence directement la diffusion, la viabilité et les résultats de cytotoxicité, ce qui impose des procédures de sélection et des critères morphométriques stricts pour garantir l'homogénéité des lots expérimentaux. Un pipeline a été mis en place pour mesurer aire, circularité et roundness et sélectionner des populations homogènes, mais il n'a pas encore été

systématisé à toutes les étapes de développement du modèle. De manière plus générale, il existe une tension entre vitesse et complexité : les sphéroïdes multicellulaires auto-assemblés offrent un haut débit mais une fidélité architecturale limitée, tandis que les organoïdes structurés et les systèmes bio-ingénierés plus riches en compartiments sont plus longs à établir et moins adaptés au criblage. Des approches émergentes visent à concilier ces exigences, par exemple en utilisant des nanostructures d'acides nucléiques auto-assemblées pour « programmer » l'adhérence et l'organisation relative de différents types cellulaires au sein de sphéroïdes dessinés, ou en mobilisant l'impression 3D et la bio-impression pour positionner spatialement des compartiments tumoraux, stromaux et immunitaires dans des architectures reproductibles.

Enfin, les questions de scalabilité et de transposition clinique impliquent l'automatisation de la génération des structures 3D et l'adaptation des readouts. Des plateformes d'impression d'organoïdes permettent déjà de produire en quelques jours des centaines de mini-tumeurs standardisées encapsulées dans des gouttelettes de Matrigel, avec des corrélations encourageantes entre les réponses ex vivo et les évolutions cliniques. À l'échelle des microfluidiques, des capteurs optofluidiques nanoplasmoniques ont été utilisés pour suivre en temps réel la sécrétion de facteurs tels que VEGF-A par des tumoroïdes, sans marquage, tout en surveillant morphologie et motilité. De telles stratégies pourraient rendre les réponses immunitaires mesurées sur puce plus facilement interprétables dans un cadre clinique. Parallèlement, l'intelligence artificielle commence à soutenir ces développements : des modèles d'apprentissage profond automatisent la détection, la segmentation et le suivi d'organoïdes à haut débit, tandis que des simulations in silico explorent les dynamiques d'infiltration T ou les flux de checkpoints au sein de microenvironnements modélisés, fournissant des hypothèses pour guider les expériences ex vivo.

L'adaptabilité du système à d'autres types tumoraux et à des échantillons plus limités représente enfin un enjeu de généralisation. Si la formulation du milieu et la capacité intrinsèque des cellules de ccRCC à s'auto-agréger facilitent la mise en œuvre dans ce contexte précis, d'autres tumeurs, comme les carcinomes vésicaux testés de manière préliminaire, forment des sphéroïdes plus difficilement et de manière moins reproductible. La géométrie de la puce permet toutefois de capturer non seulement des sphéroïdes, mais aussi des fragments tissulaires ou des PDOTS, ce qui ouvre la possibilité d'étendre la plateforme à ces formats. Dans le ccRCC lui-même, le recours principal à la néphrectomie fournit un matériau abondant, mais la plupart des indications d'immunothérapie concernent les formes métastatiques, où les décisions reposent sur des biopsies. Adapter le workflow à des prélèvements de très faible volume, en optimisant dissociation, capture et agrégation, est donc une étape clé vers une réelle intégration en médecine de précision.

Pris dans son ensemble, ce dispositif autologue tumor-on-chip, fondé sur des sphéroïdes dérivés de tumeurs fraîches, réinfiltrés par leurs TILs et exposés à un flux de PBMCs, constitue une base méthodologique solide pour relier la complexité immunobiologique du ccRCC à des réponses fonctionnelles mesurables ex vivo. L'avenir de cette approche dépendra de son raffi-

nement technique, de l'enrichissement des compartiments myéloïdes et vasculaires, de sa standardisation et de sa validation sur des cohortes élargies, afin de déterminer dans quelle mesure elle pourra devenir un véritable outil prédictif en immuno-oncologie de précision.

List of Figures

Figure 1. Historical milestones in the development of the somatic mutation theory of cancer. 3
Figure 2. Updated framework of the hallmarks of cancer as proposed by Hanahan (2022). 6
Figure 3. Cancer immunoediting. 8
Figure 4. Processing and sources of tumor antigens. 9
Figure 5. The cancer-immunity cycle and its intratumoral subcycle. 11
Figure 6. Distinct roles of CTLA-4 and PD-1 in regulating T cell responses. 14
Figure 7. Co-stimulatory and inhibitory interactions regulating T cell responses. 15
Figure 8. Mechanisms of immune suppression mediated by regulatory T cells (Tregs). 17
Figure 9. Distinguishing MDSCs from classical neutrophils and monocytes. 18
Figure 10. Direct and indirect mechanisms of immunosuppression mediated by TAMs. 19
Figure 11. Summary of cancer-associated fibroblast functions and the mechanisms by which they are achieved. 20
Figure 12. Functional and molecular differences between effector and exhausted $CD8^+$ T cells. 22
Figure 13. Differentiation trajectory of exhausted $CD8^+$ T cells during chronic antigen exposure. 23
Figure 14. Mechanisms of immune evasion in cancer. 24
Figure 15. Proposed effects of anti-PD-1 therapy on $CD8^+$ T cell states. 27
Figure 16. Major RCC subtypes and their cellular origins. 34
Figure 17. Macroscopic features of clear cell renal cell carcinoma (RCC). 35
Figure 18. Schematic representation of renal cell carcinoma staging according to the TNM classification (UICC/AJCC, 8th edition). 38
Figure 19. WHO/ISUP grade of ccRCC. 40
Figure 21. International Metastatic RCC Database Consortium (IMDC) risk stratification model for metastatic renal cell carcinoma. 43
Figure 22. Chromosome 3 Deletions in CcRCC and the VHL/HIF Signaling Cascade. 45
Figure 23. Current ESMO-recommended treatment algorithm for localized and locoregional RCC. 49
Figure 24. Current ESMO-recommended treatment algorithm for advanced and metastatic clear-cell renal cell carcinoma (ccRCC), stratified by IMDC risk group. 51
Figure 25. Evolution of systemic therapies for metastatic renal cell carcinoma (mRCC). 53
Figure 26. Timeline of pivotal clinical trials of ICIs in metastatic renal cell carcinoma (mRCC). 54
Box 1. Requirements for a Relevant Preclinical Model of ccRCC 59
Figure 27. Histological sections of clear cell RCC (top) and sarcomatoid-transformed ccRCC (bottom) compared with the corresponding cell line cultures. 61
Figure 28. Summary of mouse models. 66
Figure 29. Methods of immune engraftment for humanized mouse models. 71
Figure 30. Proposed animal model selection for ccRCC biological research. 76
Figure 31. Strategies for spheroid generation and example of obtained patient-derived tumoroids (spheroids equivalent). 85
Figure 32. Generation and immunofluorescence characterization of patient-derived organotypic tumor spheroids (PDOTS). 87
Figure 33. Organoid methodologies and preservation of tumor microenvironment components in ccRCC patient-derived organoids cultured under air–liquid interface conditions. 90
Figure 34. Workflow and example of application of tumor slice model. 92
Figure 35. Main features of 3D tumor models compared with 2D cultures. 94
Box 2. How are microfluidic chips made? 99
Figure 36. Biological complexity that 3D cancer models can potentially recapitulate. 109
Figure 37: Estimation of non-immune cells and immune cells signatures in tumor tissues, dissociated tumors, PDTOs, and infiltrated-PDTOs. 149

List of Tables

Table 1. TNM classification of renal cell carcinoma (AJCC 8th edition) 37
Table 2. World Health Organization (WHO)/International Society of Urological Pathology (ISUP) and Fuhrman grading systems. 40
Table 3. Selected emerging immunotherapies for RCC. 57
Table 4. Comparative advantages and limits of animal models for ccRCC immunotherapeutic studies. 75
Table 5. Axes of classification for ex vivo models. 82
Appendix 1. Characteristics and mutated genes in the main RCC cell lines. 231

Université Paris Cité

LISTE DES ÉLÉMENTS SOUS DROITS

Liste de **tous les éléments retirés** de la version complète de la thèse
faute d'en détenir les droits

Document à intégrer dans la version partielle de la thèse

Illustrations, figures, images…

Figure 17. Macroscopic features of clear cell renal cell carcinoma (RCC). A. Schematic illustration of gross pathologic findings in RCC, highlighting pseudocapsule, necrosis, hemorrhage, cystic changes, and venous extension. Adapted from (52)	17A	35

Table of all Contents

Acknowledgements / Remerciements v

List of Abbreviations xvii

Introduction 1

Chapter 1: Cancer Immunology 1

I. Cancer as a Genetic and Evolving Disease 1

II. The Hallmarks of Cancer 3

III. Cancer Immunology: Elimination, Equilibrium, and Escape 7

A. Elimination *8*

1. Neoantigens and tumor immunogenicity 8
2. Effectors of immunosurveillance 10

B. Equilibrium: selection and coevolution *12*

C. Escape: tolerance and progression *12*

1. Loss of antigenicity 12
2. Immune checkpoints 13
   - *a. Canonical checkpoints* *13*
   - *b. Additional inhibitory checkpoints* *14*
3. The immunosuppressive tumor microenvironment 16
   - *a. Regulatory T cells (Tregs)* *16*
   - *b. Myeloid-derived suppressor cells (MDSCs)* *17*
   - *c. Tumor-associated macrophages (TAMs)* *18*
   - *d. Cancer-associated fibroblasts (CAFs) and the extracellular matrix* *20*
   - *e. Endothelium and angiogenesis* *20*
   - *f. Metabolic constraints* *21*
   - *g. Conclusion* *21*
4. T cell exhaustion 21

IV. Cancer Immunotherapy 25

A. General principles *25*

1. Immune Checkpoint Inhibitors (ICIs): Canonical Targets 26
2. Immune checkpoint blockade: non canonical 28
3. Combination strategies 28
4. Other classes of cancer immunotherapy 29
   - *a. Cytokine therapies* *29*
   - *b. Adoptive cell therapies (ACT)* *29*
   - *c. Cancer vaccines* *29*
   - *d. Oncolytic viruses* *30*
5. Conclusion on immunotherapy 30

Chapter 2: Renal Cell Carcinoma **31**

I. Epidemiology, Risk Factors, and Hereditary Syndromes 31

II. Diagnosis and Prognosis 32

A. Histological subtypes of RCC 32

B. Macroscopic pathology, staging, and grading 35

C. Prognosis 41

III. Molecular and Biological Characteristics of Clear Cell RCC 43

IV. Immune Landscape and Tumor Microenvironment of Clear Cell RCC 46

A. Immune infiltration and immunogenicity 46

B. Canonical immune checkpoints 46

C. Non-classical and emerging checkpoints 47

D. Regulatory populations and myeloid suppression 47

E. Angiogenesis and hypoxia 47

F. Transcriptomic TME subtypes 48

G. Summary 48

V. Current Management of RCC 48

A. Localized disease 48

B. Metastatic disease — first-line systemic therapies 49

C. Metastatic Disease — Subsequent-Line Treatments 49

VI. Place of immunotherapy in RCC 52

A. Historical background 52

B. The immune checkpoint inhibitor revolution 52

C. Immunotherapy in the adjuvant and neoadjuvant setting 54

D. Future directions in RCC immunotherapy 55

E. Current positioning and unmet needs 57

Chapter 3: Preclinical Models for Immuno-Oncology **60**

I. Classical 2D Culture Cell Line Model 60

A. Cancer cell lines in oncology and in RCC research 60

B. Molecular and phenotypic characterization of RCC cell lines 62

1. RCC subtypes 62
2. Genetic alterations captured in RCC lines 62
3. Phenotypic features and tumorigenic potential 63

C. RCC cell lines in immuno-oncology: applications, strengths and limitations 63

1. Applications in immuno-oncology 63
2. Strengths of RCC cell lines in immuno-oncology research 64

3. Limitations and partial alternatives 64
4. Positioning and conclusion 64

II. In Vivo Models 66

A. Syngeneic murine models 67

B. Genetically Engineered Mouse Models (GEMMs) 68

C. Cell line-Derived Xenografts 69

D. Patient-Derived Xenografts (PDX) 69

E. Humanized PDX models 70

1. Principles 70
2. Applications in immuno-oncology 71

F. Conclusion on animal models 74

III. Complex in Vitro Models for Immuno-Oncology 80

A. Introduction and comparative framework 80

B. Complex in vitro model types 83

1. Spheroids 83
2. Patient-derived organotypic tumor spheroids (PDOTs) 86
3. Organoids 88
4. Tumor slices 91

C. Key features and advantages of 3D tumor models 93

1. Gradients 94
2. Enhanced cell–cell and cell–matrix interactions 95
3. Immune–tumor interactions 95
4. Heterogeneity and translational relevance 95

D. Microfluidic systems 96

1. Microfluidic systems advantages for immuno-oncology 96
2. Types of microfluidic devices 97
3. Flow control in microfluidic culture 98
4. Possible readouts 100
   a. Live imaging 100
   b. Effluent analysis 100
   c. End-point assays 100
   d. Integration with omics and high-throughput platforms 100

E. In vitro complex models applications in immuno-oncology 101

1. T cell cytotoxicity and canonical checkpoint blockade 101
2. NK cell activity in 3D tumor models 102
3. CAR-engineered immune cells in 3D systems 103
4. Myeloid cells in 3D tumor models for immuno-oncology 104
5. Fibroblasts and stromal immunoregulation in 3D models 105
6. Next-generation immunotherapies in 3D models 105
7. 3D personalized platforms for immunotherapy response prediction 106

F. General conclusion on preclinical models in immuno-oncology 108

G. Project Rationale and Methodological Framework 110

Results **111**

Chapter 1: Methods for Establishing a Renal Cell Carcinoma Tumor Spheroid Model with Immune Infiltration for Immunotherapeutic Studies **112**

Summary and perspectives 127

Chapter 2: Transcriptomic evaluation of immune-infiltrated patient-derived tumor spheroids as preclinical models in renal cell carcinoma **128**

Summary and perspective 149

Chapter 3: A Tumor-on-Chip Platform for Modeling Immunotherapy Response in Clear Cell Renal Cell Carcinoma **151**

Summary and perspectives 218

General Discussion **221**

I. Current state and limitations 221

II. Positioning of the model 224

III. Perspectives 225

A. Vascularization 225

B. Reproducibility 226

C. Scalability 227

D. Adaptation to other cancers and samples 228

Appendix **230**

Bibliography **233**

Résumé substantiel en français **260**

List of Figures **277**

List of Tables **278**

Liste des éléments sous droits **279**